BULGARIAN CHEMICAL COMMUNICATIONS

2013 Volume 45 / Number 4

Journal of the Chemical Institutes
of the Bulgarian Academy of Sciences
and of the Union of Chemists in Bulgaria

Preface

Dear reader,

This special issue of the "Bulgarian Chemical Communication" contains selected full texts from reports presented during the 4th National Crystallographic Symposium (**NCS'12**), which took place on 01-03 November, 2012 in the "Assen Zlatarov" hall of the University of Chemical Technology Metallurgy (UCTM), Sofia. For a third consecutive year, the participants in this event gratefully obtained opportunity to publish in this journal. The acceptance of the papers was based on the Journal's normal reviewing procedure.

NCS'12 was conducted under the auspices of the Bulgarian Crystallographic Society (**BCS**) with the invaluable effort of organizing committee members from the Institute of Mineralogy and Crystallography (BAS), University of Chemical Technology and Metallurgy, Sofia, Institute of General and Inorganic Chemistry (BAS), Institute of Geology (BAS), Institute of Catalysis (BAS), and Institute of Physical Chemistry (BAS).

The organizers of **NCS'12** invited leading researchers from abroad to inspire the interdisciplinary audience and attract young researchers to this interdisciplinary field of science.

Main purpose of such meetings is to gather the crystallographic community in Bulgaria to meet and share knowledge in modern crystallographic approaches on study of new materials achieved by scientists from national research institutes and universities in the fields of structural crystallography, crystal chemistry, crystal physics, mineralogy and materials science.

The National Crystallographic Symposium (NCS) is the annual meeting of the growing Bulgarian crystallographic community and is the principal activity of the recently established Bulgarian Crystallographic Society (**BCS**). These symposia became the leading scientific events, not only for the Bulgarian crystallographers, but also for participants from different European countries. A testimony for the growing interest to the National Crystallographic Symposium is the fact that this special issue collected 37 papers – a number exceeding by about 60% the ones in previous **NCS** issues.

The papers in the present issue outline the latest developments in the research of the Bulgarian crystallographers. They cover a wide interdisciplinary range – main essence is the synthesis, structure and properties studies on a great variety of materials – "glaserite" type compounds, ion-exchanged natural zeolites and microporous titanosilicates, sedimentary apatite, Ni-Al layered double hydroxides, ZnO powders, borate materials, $ZnFe_2O_4$, $LiNbO_3$ and $LiTaO_3$, TeO_2/TiO_2 powders, Fe-doped TiO_2 nanoparticles, magnesium chlorates, amorphous Ge–Te–In system, molybdenum modified aluminum bronze, bacteria and DNA samples, proteins, urea and thiourea adducts, orthodontic archwires, polycaprolactam, hybrid materials, organic dyes.

Special attention is paid to the 100 years Anniversary of X-ray diffraction discovery.

We very much hope that this issue, representing the accepted full texts, reveals the high quality work of the Bulgarian crystallographers, is good basis for provoking business interest in investment in production of high technological materials and is an in-time product at the dawn of 2014 – The International Year of Crystallography. The decision was proclaimed by the United Nations General Assembly in July 2012. The official Opening Ceremony of the International Year of Crystallography (IYCr2014) will take place at UNESCO Headquarters in Paris on 20 and 21 January 2014.

We are looking forward to successful organization of the Fifth National Crystallographic Symposium to be held in Sofia in 2014.

Special acknowledgements are due to the sponsors of the 4th National Crystallographic Symposium – ASTEL, PANalytical, Bruker, RETSCH, and **Labexpert Ltd.** for their help and making the symposium a success and this special issue possible.

Prof. Ognyan Petrov
Guest editor of the special issue of the Journal
Bulgarian Chemical Communications,
and President of the Bulgarian Crystallographic Society

Bulgarian Chemical Communications, Volume 45, Number 4 (pp. 411–417) 2013

100 years of X-ray diffraction: from Röntgen's discovery to top-of-the-art synchrotron source applications

V. Krastev[1], G. K. Exner[2]*

[1] *Sofia University "St. Kliment Ohridski", 5 James Bourcher Blvd., 1164 Sofia, Bulgaria*
[2] *Department of Experimental Physics, Faculty of Physics and Engineering Technologies, PU "Paisii Hilendarski", 24 Tzar Asen Str., 4000 Plovdiv, Bulgaria*

Received February, 2013; Revised May, 2013

The paper invites the reader to recall the 100 years long history of X-rays diffraction discovery, advancement and achievements with great impact on our daily life. Let us pay a tribute to the founders of X-ray diffraction and emphasize the importance of their work for our modern understanding of matter. Special honor has to be given to Max von Laue, who discovered in 1912 that X-rays are electromagnetic in nature, with wavelength short enough, to cause diffraction when passing through a periodic crystal medium. Shortly afterwards, the importance of his work was recognized and he received Nobel Prize two years later. Other distinguished researchers are Sir William Henry Bragg and William Lawrence Bragg, who were awarded a Nobel Prize in 1915 "for their services in the analysis of crystal structure by means of X-rays". Bulgarian history of X-ray diffraction analysis started around 1939, when Ivan Stranski and Rostislaw Kaishev performed the first experiments. One of the very first publications by Bulgarian authors on this topic belongs to Strashimir Dimitrov in collaboration with Kaishev.

At present, the X-ray diffraction is irreplaceable, unique method for structural investigation of inorganic and organic materials, biomolecules, including human DNA, nanocomposites and many others, especially after the development of more than 40 X-ray synchrotron sources worldwide.

Key words: X-ray diffraction history, Bulgarian X-rays science history.

INTRODUCTION

Since the discovery of X-rays not only the scientific community, but the entire society have recognized their importance for our daily life. X-rays are employed in structural investigation of inorganic and organic materials, for chemical elemental analysis and biological imaging.

Hundred years of X-ray diffraction analysis, is a good occasion to recall the people, whom we have to thank for our achievements today. The article invites the reader to recall the significant moments in the 100 years long history of advancement and achievements since the scientific discovery of X-rays diffraction.

Prehistory

Before dealing with the essentials of X-ray diffraction applications, let us recall the story of the X-ray discovery, marked with at least 5 related Nobel Prizes in a period of only 10 years.

The very first Nobel Prize, in the remote 1901, was awarded to Wilhelm Conrad Röntgen "in recognition of the extraordinary services he has rendered by the discovery of the remarkable rays, subsequently named after him" [1]. At the time of his discovery, Röntgen was appointed Professor at the University of Würzburg. His scientific interests since then were far from that field, but since the investigations on cathode rays were very new and modern, he decided to perform some experiments similar to those of Herz and Lenard. In the autumn of 1895 he assembled equipment, consisting of Ruhmkorff's coil and evacuated Lenard's tube covered with paperboard. What he observed amazed him [2]! In the dark room, a barium-platinum-cyanide screen, located 2 meters away from the equip-

* To whom all correspondence should be sent:
E-mail: ginka@yahoo.com

ment, was fluorescencing. Röntgen was famous for his diligence, so he closed the door of his lab and spent six weeks repeating and trying different experiments to convince himself that the observation came really from the experiment and is not a fiction. He even did not speak to his assistant or his wife, who started to worry about him.

The amount of work he performed in this period is indeed impressing! The first results were published as a short communication in the local scientific journal [3], where as a footnote to the main text Röntgen wrote *"for shortcut I would like to use the expression „rays" and more precisely, to make the difference with all other rays, I will use the name X-rays"*. The communication was sent as a Christmas present to almost 90 scientists all over the world and it actually became the Christmas present to the humanity as well.

The first communication was followed by a second one, issued a month later. There was only one more communication written by Röntgen on this topic, published a year later in Berlin [4]. So, the new X-rays were born and described in only 30 pages!

The main part of the experimental work of Röntgen aimed on proving the properties of the "agent", if it was really rays, if they differed from light and cathode rays and in which way. It has to be mentioned here, that he also tried to observe diffraction but did not succeed. His achievement had a profound effect. Researchers worldwide could experiment with X-rays as Röntgen refused to patent his findings, convinced that his inventions and discoveries belong to the entire world.

The next, very important person in our story is Charles Glover Barkla, who devoted his life to the investigations on X-rays. His extraordinary work, honored with Nobel Prize in 1917, is described on the Nobel Prize site as follows [1]: *"His discovery of homogeneous radiations characteristic of the elements showed that these elements had their characteristic line spectra in X-ray and he was the first to show that secondary emission is of two kinds, one consisting of X-rays scattered unchanged, and the other a fluorescent radiation peculiar to the particular substance. He discovered the polarization of X-rays, an experimental result of considerable importance for it meant that X-radiation could be regarded as similar to ordinary light. Barkla made valuable contributions to present knowledge on the absorption and photographic action of X-rays and his later work demonstrated the relation between the characteristic X-radiation and the corpuscular radiation accompanying it. He has also shown both the applicability and the limitation of the quantum theory in relation to Röntgen radiation ...Barkla's discovery of the characteristic X-radiation has proved to be a phenomenon of extraordinary importance as regards physical research, a fact which has been made increasingly manifest by the subsequent researches of other investigators..."*

Once upon a time in Munich

Now the time line goes to Munich, where Röntgen had moved to in the beginning of the 20th century. The scientific community there had good traditions. One of them was that every day professors and students were discussing modern scientific topics at the Café Hofgarten. Under discussion were crystallography, X-rays and their polarization, different new theories, ideas mostly inspired by the interests of the appointed at that time professors at the University of Munich and on the first place by professor Röntgen, of course.

On the second place – Professor Groth, who was the Director of the Institute of Crystallography. He used to invite famous crystallographers from all over the world, which gave the possibility to the students and professors for real and spontaneous transfer of knowledge and generation of new ideas. Although at that time some facts were already known, for instance the existence of 32 symmetry classes and 230 Space Groups, and the theory of "molécular intégrantes", according to which crystals were supposed to be a periodic arrangement of identical particles, crystallography was still rather a mathematical exercise. This was also the time when the theory of the atoms and their inner structure did not exist yet. Knowing this, Groth's great contribution can be highly appreciated. In 1876, he wrote "Physical crystallography", which became a leading book in Crystallography for decades [5]. The most famous book, written by him is "Chemical crystallography" (1906, in 5 volumes), where he classified crystal forms according to their chemical structure. This way he established for the first time the connection between physical shape and chemical nature of the crystals.

Another very important person in our story is professor Sommerfeld. At the time when Röngen invited him for the position of a Director of the Theoretical institute at the University of Munich, Sommerfeld's scientific interests had been connected with the theory of diffraction in the optical range. Curiously, Sommerfeld stated that his condition to accept the position was to have a laboratory with appropriate equipment for proving his theories. Professor Sommerfeld was easy going, charming and open person who soon became the center of all scientific meetings at the Café Hofgarten. About his extraordinary scientific capacity one could judge from the success of his students such as P. Debye, P. Ewald, W. Pauli, W. Heisenberg. All these students

participated in the café and some of the students of Röntgen like P. Knipping, J. Brentano, R. Glocker, and Joffe can be added to this list.

All mentioned students are renowned scientists of course but we will pay special attention only to Paul Ewald (1888–1985). In one of his books Ewald wrote [6]: "*Towards the end of summer semester of 1910 the present author, Paul Ewald, had belonged to the group of students centered about Sommerfeld for about two years, and he felt that he could venture to ask his teacher to accept him as a doctorant.*"

Ewald chose a thesis problem with the working title "To find the optical properties of an anisotropic arrangement of isotropic resonators", the basic idea of which he explained as [6]: *"...If the same type resonators were placed in a lattice array, with perfect regularity but different distances along the three coordinate axes – would the dispersive and refractive properties of this medium be those of a crystal?"*

Almost ready, Ewald met some difficulties explaining his calculations. According to Munich university traditions, he asked the newly appointed assistant Max von Laue for help. Laue was actually the favorite student of Max Plank in Berlin, but he insisted to move to Munich and in 1909 he was appointed in the Theoretical institute under the supervision of Sommerfeld. Laue invited Ewald for a supper at home. They met (in late January 1912) and took a walk in the English Garden (near the University), where Ewald started explaining his problems. Ewald wrote [6] about this walk: *"Meanwhile they were entering the park, when Laue asked: "what is the distance between the resonators?". To this Ewald answered that it was very small compared to the wave-length of visible light, perhaps 1/500 or 1/1000 of the wave-length, but that an exact value could not be given because of the unknown nature of the "molecules integrantes" or "particles" of the structure theory; that, however, the exact distance was immaterial for his problem because it was sufficient to know that it was only a minute fraction of the wave-length."*

Let us now draw our attention to Laue and his point of view. In his Nobel Prize lecture he explained how much all professors at Munich University influenced him [1]: *"It turned to be a matter of great good fortune that Sommerfeld passed to me the article "Wellenoptik" at that time to work upon for the Encyclopedia of Mathematical Science. For it was during that object that I was obliged to seek a mathematical presentation of the lattice theory… On my arrival in Munich in 1909 my attention was drawn constantly – first owing to the influence of Röntgen's work at this University and subsequently by Sommerfeld's active interest in X-rays and γ-rays, which he had also testified in several works-back to the question of their actual nature … it was Groth who expressed his defense of it (the space-lattices model), both orally and in writing, and I, also thus learned from him."* and then concluded [1]: *"Such was the state of affair as, one evening in February 1912, P.P. Ewald came to visit me… he was faced at that time with certain difficulties and came to me with a request for advice."*

Through the memories of Ewald [5] and Laue [1] one can reconstruct the remarkable conversation on that day. Laue said that during the conversation with Ewald in his mind was: *"...lattice spectra have to be ensued. The fact that the lattice constant in crystals is of an order of 10^{-8} cm was sufficiently known from the analogy with other interatomic distances in solid and liquid substances, and in addition, this could easily be argued from the density, molecular weight and the mass of the hydrogen atom which, just at that time, had been particularly well determined. The order of X-ray wavelengths was estimated by Wien and Sommerfeld at 10^{-9} cm, so …"*

Ewald explained about the time after the supper: "*When this time came, he found Laue listening in a slightly distracted way. He again insisted on knowing the distance between the resonators and when he received the same answer as before, he asked: "what would happen if you assume very much shorter waves to travel in a crystal?"...*"

Ewald was on a hurry finishing his thesis, so he only copied the calculations to Laue. After finishing his PhD, Ewald got a job and forgot about this issue. However, the interest of Laue and respectively of the other scientists at Munich University continued. Meanwhile, Ewald continued working on X-rays and became later the father of the dynamic theory of the X-ray diffraction.

In 1912 during the Easter holydays, completely in accordance with the good university traditions, a group of professors, assistants and students were skiing in the Alps. During the vacation, Laue shared his idea with Sommerfeld, Wien and other scientists, but encountered a strong disbelief in a significant outcome of any diffraction experiment based on the regularity of the internal structure of crystals. On the other hand, Walter Friedrich, who was newly appointed as an experimental assistant in Sommerfeld's group, immediately expressed his willingness to carry out a relevant test. Also Paul Knipping, who had just finished his thesis in Röntgen's institute, volunteered for assisting in the experiment. Finally, the opinion prevailed that experiment was safer than theory and that since the diffraction experiment required no sophisticated set-up, it should at least be tried.

Friedrich and Knipping performed series of experiments with $CuSO_4$ and they had success when

experimented on transmission. Visiting the scientific café, Laue was informed about that progress and was so excited that he even remembered the house, where he solved the equations. He wrote [1]: "*Only shortly before this, when writing an article for Enzyklopaedie der matematischen Wissenschaften, I had given the old theory of diffraction by an optical grating, which went back to Schwerd (1835), a new formulation in order that by applying the equation of the theory twice over, the theory of diffraction by a cross-grating could be obtained. I had only to write out this equation three times, corresponding to the three periodicities of the space lattice, so as to obtain the interpretation of the discovery. In particular the observed rings of rays could thus be related to the cones of rays demanded separately by each of the three conditions of constructive interference.*"

The last events happened in 1912. The results were then presented (8.06.1912) by Sommerfeld at the Bavarian Academy of Sciences. Meanwhile Laue delivered a lecture in Berlin, presenting the results to his former colleagues and the scientific society in Berlin. On his way back to Munich, Laue went to visit Professor Wien and introduced the recent achievements to the group there and a professor from Göttingen. The presentations were followed by publication of the significant results. The first publication was written by Friedrich, Knipping and Laue [7], followed by another one written by Laue [8]. These publications gave the birth of X-ray diffraction science. Shortly, the importance of Laue's work was recognized and he received the Nobel Prize in 1914 "*for his discovery of the diffraction of X-rays by crystals*" [1].

Practical application

The theory of Laue for the diffraction of X-rays by crystal lattice and its mathematical formulation was a ground breaking discovery a ground breaking discovery. However, as Professor Granqvist explained [1]: "*...calculating the crystal structures, from von Laue's formulae, was an exceedingly complicated one, in as much as not only the space lattices, but also the wavelengths and the intensity-distribution over the various wavelengths in the spectra of the X-rays, were unknown quantities.*"

This is the reason why Ewald defined [5] the beginning of the real X-ray diffraction analysis as follows: "*Crystal Structure Analysis began in November 1912 with the first papers of W. L. Bragg, then still student in Cambridge, in which, by analysis of the Laue diagrams of zink blende, he determined the correct lattice upon which the structure of this crystal is built. Soon afterwards he obtained the first complete structure determinations, namely of NaCl, KCl, KBr, KI, a series of alkali halides having similar structures. By this determination a scale for measuring of atomic distances in crystals and, simultaneously, of X-ray wave-lengths obtained.*"

The real progress was possible due to the subsequent discovery of W. L. Bragg, who found out that the phenomenon could be treated mathematically as a reflection by successive parallel planes that may be placed so as to pass through the lattice points, and that in this way the ratio between the wavelengths and the distances of the said planes from each other can be calculated by a simple formula from the angle of reflection [1]. The other very important event was that W.H. Bragg and W. L. Bragg constructed the first X-ray spectrometer, based on reflection principle, which admitted a definite, even though initially unknown, wavelength being made use of. Exactly this spectrometer allowed the Bragg's to gain the first, extremely important insights into the structure of crystals. The rays falling on the crystal were produced by X-ray tubes, platinum being at first used for the anticathode while consequently anticathodes were produced from palladium and rhodium. In order to take practical advantage of those different X-rays W. L. Bragg developed a method for calculating their intensity in the case of a complex space lattice.

If one has to summarize the contribution of the Bragg's to science, one has to mention that these two investigators determined the crystal structures of various materials, the wavelengths of the X-rays and the distances between the successive planes, placed with such exactitude, that the error, if any, is probably at most some few units per cent. Thanks to the methods that the Bragg, father and son, have devised for investigating crystal structures, an entirely new world has been opened and has already in part been explored with marvelous exactitude.

In recognition of the great practical importance of their method, the Nobel Prize in Physics in 1915 was awarded jointly to Sir William Henry Bragg and William Lawrence Bragg "*for their services in the analysis of crystal structure by means of X-rays*".

Bulgarian contribution to X-ray diffraction science

In the book of Ewald, devoted to the 50 year anniversary of X-ray diffraction [5], the author makes a comprehensive review of historical developments in the field, pretending to cover all achievements over the world. Somehow the Balkan region is scarcely mentioned. He describes only an experiment on a mineral, employing the Debye method, performed in Yugoslavia in 1947. In the same text, Ewald admits that for countries like Romania and Bulgaria there is nothing to be said because of their isolation.

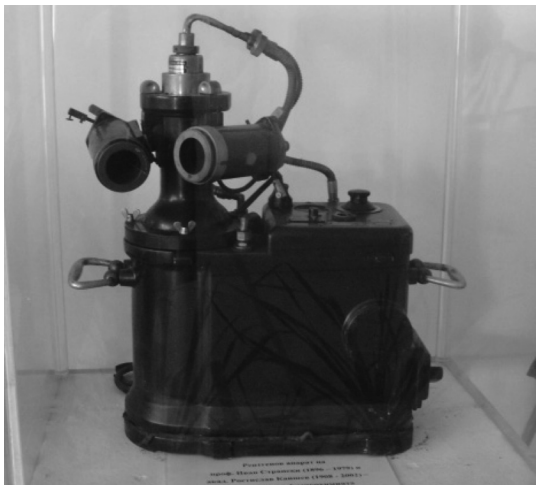

Fig. 1. First X-ray diffractometer, used for research purposes in Bulgaria

The very first experiments, performed in in Bulgaria, date back from the time before World War II. Bulgarian X-ray diffraction analysis is closely connected with one very prominent and distinguished scientist – Iwan Nicolá Stranski, who brought from abroad the first X-ray apparatus, made by the "Siemens" company (Fig. 1). At that time, Stranski was appointed professor at the Institute of Physical Chemistry, belonging to the Bulgarian Academy of Sciences.

Actually Iwan Nicolá Stranski [9] (Fig. 2) left a profound imprint on the world science record with his famous theory of crystal growth (theory of Kossel-Stranski) and he is the father of the Bulgarian school of physical chemistry. He studied chemistry and graduated in Sofia in 1922, but he got his doctorate in 1925 in Germany (at Physikalisch-chemische Institut of the University, Berlin). His doctoral research was devoted to X-ray spectroscopic analysis. He started his career as lecturer in Physical Chemistry at the Department of Physical Chemistry Sofia University in 1926, becoming the first teacher in physical chemistry in Bulgaria. In 1937 he was the first elected Professor there. In 1941 Stranski moved to Germany. During the years 1941–44 he was visiting professor at the University and the TH Breslau (now Wroclaw, Poland). In 1944 he became a scientific fellow of the Kaiser-Wilhelm-Institut für physikalische Chemie und Elektrochemie (Kaiser Wilhelm Institute for Physical Chemistry and Electrochemistry) in Dahlem, Berlin, becoming its associate director in 1953. The TU Berlin made him the successor to Max Volmer as professor of Physical Chemistry in 1946. He taught at the Free University of Berlin as an honorary professor until 1963. Two research institutes in Germany have been named after him: the Iwan N. Stranski Institute of the TU Berlin and the I. N. Stranski Institute for Metallurgy in Oberhausen.

Rostislaw Kaishev [10] (Fig. 2) was appointed as assistant to Stanski in 1933. Both are the cofounders of the contemporary theory of crystal nucleation and growth. They both were connected with Germany (Kaischew obtained his PhD in 1932 under the supervision of the famous F. Simon) and their fruitful cooperation continues also by working on the first X-ray diffraction experiments. In 1958 Kaischew became the founder of the Institute of Physical Chemistry, within the Bulgarian Academy

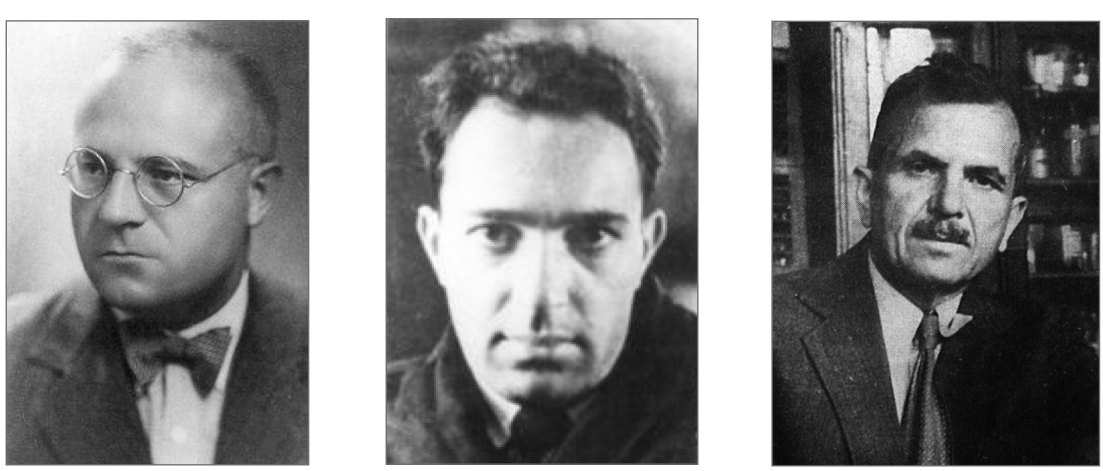

Iwan Stranski **Rostislaw Kaischew** **Strashimir Dimitrov**

Fig. 2. Bulgarian pioneers in X-ray diffraction analysis

of Sciences, named after him today, and held the position of director there until his retirement in 1989.

The first publication with Bulgarian contribution, devoted to X-ray diffraction experiments dated from 1939, on clay material, provided by Strashimir Dimitrov, and were performed by Kaischew. Dimitrov (Fig. 2) graduated in 1914 from Sofia University. He made a specialty of mineralogy and petrology in Heidelberg, Germany in 1927. His career is closely connected with Sofia University, where he became a professor in 1941. He was the Dean of the Department of mineralogy and petrography. In 1947 Dimitrov became one of the founders and director of the Geological Institute of BAS, named today after him. His great contribution to the Bulgarian science was recognized by naming a mineral after him (*Strashimirite* $Cu_8(AsO_4)_4(OH)_4{\cdot}5(H_2O)$).

Advancement and achievements

If one can use the Nobel Prizes as a measure of the recognition and significance of any scientific field, here is the place to state, that since 1901, more than 24 Nobel Prize holders belong to the family of researches, connected with X-ray diffraction [1]. Even the Nobel Prize in chemistry for 2012 is evidence of the great impact of the Laue's discovery on our daily life. Most of the recent progress is due to the development of synchrotron sources, starting in 1970. Nowadays there are more than 40 such sourced all over the world. Thanks to the extended possibilities, X-rays diffraction analysis is applied in biology, earth and environmental science, soft matter, polymers, complex and nanostructured materials sciences, in investigations of semiconductors, surfaces, and interfaces, in chemical dynamics, for ultrafast/time-resolved studies, etc. [11, 12].

REFERENES

1. http://www.nobelprize.org/nobel_prizes/physics/laureates/.
2. O. Glasser, Wilhelm Conrad Röntgen and the Early History of the Roentgen Rays, Norman Publishing, 1993.
3. W. C. Röntgen, Aus den Sitzungsberichte der Würzburger Physik.-medic. Gesellschaft, Verlag und Druck der Stahel'schen K. Hof- und Universitäts-Buch- und Kunsthandlung, 1895.
4. W. C. Röntgen, Sitzungsberichte der Königlich Preußischen Akademie der Wissenschaften zu Berlin. Jahrgang 1897. Erster Halbband. Berlin: Georg Reimer, 576 (1897).
5. http://www.deutsche-biographie.de/sfz24096.html.
6. 50 years of X-ray diffraction, P. P. Ewald (ed.): Copyright © 1962, 1999 International Union of Crystallography (http://www.iucr.org/publ/50years ofxraydiffraction).
7. W. Friedrich, P. Knipping, M. von Laue, Sitzungsberichte der Königlich Bayerischen Akademie der Wissenschaften Mathematisch-physikalische Klasse, 302 (1912), reprinted in: Annalen der Physik, **41**, 971 (1913).
8. M. von Laue, Sitzungsberichte der Königlich Bayerischen Akademie der Wissenschaften Mathematisch-physikalische Klasse, 363 (1912).
9. http://opus.kobv.de/tuberlin/volltexte/2008/2012/html/festschrift/stranski_e.htm.
10. http://en.wikipedia.org/wiki/Rostislaw_Kaischew.
11. http://www.als.lbl.gov/als/science/.
12. W. Paszkowicz, Ninety years of powder diffraction /Synchrotron Radiation in Natural Science, **5** (1–2), 115 (2006).

100 ГОДИНИ РЕНТГЕНОВА ДИФРАКЦИЯ: ОТ ОТКРИТИЕТО НА РЬОНТГЕН ДО МОДЕРНИТЕ ПРИЛОЖЕНИЯ НА СИНХРОТРОННИТЕ ИЗТОЧНИЦИ

В. Кръстев, Г. Екснер*

[1] Софийски университет „Св. Климент Охридски", бул. „Джеймс Баучер" № 5, 1164 София, България
[2] Катедра „Експериментална физика", Факултет по физика и инженерни технологии, ПУ „Паисий Хилендарски", ул. „Цар Асен" № 24, 4000 Пловдив, България

Постъпила февруари, 2013 г.; приета май, 2013 г.

(Резюме)

Статията приканва читателя да проследи 100-годишната история от откриването на рентгеновите лъчи, напредъка и достиженията при тяхното използване и ефекта върху нашето ежедневие. Отдаваме почит на откривателите на рентгеновата дифракция и подчертаваме важността на техните усилия за съвременното ни познание при изследване на материята. Специално уважение трябва да отдадем на Макс фон Лауе, който през 1912 година установи, че рентгеновите лъчи са електромагнитни по природа с достатъчно къси дължини на вълните за да предизвикат дифракция, когато преминават през една периодична кристална среда. Скоро след това важността на неговата работа беше оценена високо и след две години той бе удостоен с Нобелова награда. В същата сфера работят и други авторитетни учени като Сър Уилиам Хенри Брег и Уилиам Лоуренсе Грег, които получават Нобелова награда през 1915 „за техния принос за анализ на кристални структури с рентгенови лъчи". В България стартирането на рентгено-дифракционния анализ води началото си от 1939 г., когато Иван Странски и Ростислав Каишев правят първите експерименти. Една от най-първите публикации от български автори по тази тема принадлежи на Страшимир Димитров в колаборация с Каишев. В днешно време рентгеновата дифракция е незаменим, уникален метод за структурни изследвания на неорганични и органични материали, биоматериали, включващи човешкото ДНК, нанокомпозити, особено стимулирани след разработването и пускане в действие на повече от 40 рентгенови синхротронни източника по света.

Bulgarian Chemical Communications, Volume 45, Number 4 (pp. 418–426) 2013

Crystal chemistry of "glaserite" type compounds

R. Nikolova, V. Kostov-Kytin

Institute of Mineralogy and Crystallography, Bulgarian Academy of Sciences, "Acad. G. Bonchev" Str., bl. 107,1113, Sofia, Bulgaria

Received February, 2013; Revised May, 2013

Crystal chemical data for more than 100 compounds with "glaserite" type structure are summarized and evaluated. A revised general formula for "glaserite" type compounds (GTC) is deduced – $X_{(\square;1)}Y_{(\square;2)}[M(TO_4)_2]$. It gives information for two important structural characteristics of GTC. The first one is that main structural unit is the $^2_\infty[M(TO_4)_2]$ layer where all the atomic positions are fully occupied. The second one is that the occupancy of X and Y positions depends on the layer charge and these positions can either be both unoccupied, one can be entirely occupied whereas the other is totally unoccupied, or both can be entirely occupied. Precise criteria for "glaserite" type topology (GTT) are proposed distinguishing GTT from other topologies built by similar or identical layers. The range of structural stability of the "glaserite" type compounds is outlined in terms of the established up to now cation composition and site occupancy. The topological flexibility is evaluated through geometrical criteria based on the lattice parameters or certain dimensional and angular correlations. The established compositional diversity, topological versatility and wide range of formation conditions are good prerequisite for preparation of new materials adopting the "glaserite" topology and estimation of certain physical phenomena such as temperature induced phase transitions.

Key words: glaserite, "glaserite" type topology, "glaserite" type compounds.

INTRODUCTION

The structure of the mineral glaserite was originally determined by Gossner (1928) [1] and confirmed later by Bellanca (1943) [2] and Pontonnier et al. (1972) [3]. The structure of its synthetic analogue was solved by Okada and Ossaka in 1980 [4]. Later on, it has been established that there are many substances which are isostructural with glaserite. In the course of gathering information for new compounds with such topology different approaches have been applied to describe this structural type. Moore (1981) [5] reported that in glaserite, the cations and anions form two types of columns in a hexagonal arrangement: type I containing only, Na^+ and K^+ cations and type II, containing both cations and anions (K^+ and SO_4^{2-}). Since the ions in each column are tightly bound along its length, the structure has been considered as a hexagonal packing of rods. Such an approach was applied by Takagy *et al.* (1983) [6] for the structure of $CaK_3H(PO_4)_2$ and used also by other authors, e.g. Lazoryak (1996) [7]. Later on, the results from investigations of various physical phenomena (phase transitions without topological changes, luminescence properties, etc.) occurring in certain "glaserite" type compounds (GTC) suggested that their structures can be considered as alternating layers composed by corner-sharing octahedra and tetrahedra with or without additional charge compensating cations [8–17]. An interesting approach for presentation of the "glaserite" type compound $Ba_3MgSi_2O_8$ was reported by Park *et al*. [18]. The authors have derived its structure from the perovskite one by considering variations on the stacking of layers of the type AX_3 and AX_2.

Upon accumulation of crystal chemical data many authors have tried to classify the GTC and clarify their structural features. Based on approximately 10 compounds known at that time Moor (1973) and Eysel (1973) independently from each other found out that "The glaserite structure and its deformed derivatives can be predicted for $(A,C)_yBX_4$ solid solution" [19, 20]. Later on, Lazoryak (1996) defined criteria for stability of the "glaserite" type topology and postulated that "Glaserite structural type $X^{[6+6]}Y_2^{[4+6]}M^{[6]}(EO_4)_2$ is stable for compounds where $0.59 < \Delta r < 0.89$

* To whom all correspondence should be sent:
E-mail: rosica.pn@clmc.bas.bg

(Δr = rX(Y) – rM; Shanon ionic radii)" [7]. The superscripts denote the coordination number expressed in terms of the bond lengths between the central cation and the ligand oxygen atoms.

Recently, it has been established that a synthetic sodium zirconosilicate material – $Na_{3-x}H_{1+x}Zr(SiO)_4.yH_2O$ ($0<x<3$, $0<y<1$) exhibits a "glaserite" type topology [21, 22]. Two features of this compound attract attention. The first one is the presence of water molecules in a structural topology known as an anhydrous one. The second feature is related with the possibility for protonation of this compound. Sodium ions could be leached out upon treatment with hydrochloric acid without destroying the structural topology. Such behavior is indicative of a "microporous" or a "layered" structure rather than of a dense-packed one. To better understand the crystal-chemical relation of this zirconosilicate to other materials adopting "glaserite" topology a search of such compounds in the available structural databases has been undertaken [23, 24]. Detailed analysis of the crystal-chemical characteristics of the collected compounds has revealed the amazing chemical diversity and structural versatility of the "glaserite" materials.

This work summarizes data from the crystal-chemical characterization of over 100 compounds with "glaserite" type topology. All of them are oxides. In fact, only one compound with "glaserite" type structure and fluorine instead of oxygen was found [3]. Precise criteria for GTT definition are introduced. The general formula previously reported for these materials [7] is reconsidered and new features and limitations are added to it. The topological flexibility is evaluated through introduced here geometrical criteria. Based on the gathered crystal-chemical information the range of structural stability of the "glaserite" type compounds is outlined in terms of the established up to now cation composition and site occupancy. This work is not an attempt to classify the "glaserite" type compounds but rather to comprise, to describe, and to evaluate the chemical diversity and structural versatility of the "glaserite" type topology.

RESULTS AND DISCUSSION

Crystal-chemical characterization of the "glaserite" type topology

In this paper the layer model for description of GTT is adopted as presented in Figure 1.

The TO_4 tetrahedron can be defined as a primary building unit of the "glaserite" structure type. Three of the oxygen atoms of a TO_4 tetrahedron are shared with the adjacent MO_6 octahedra, whereas one oxygen atom is non-bridging. Each of the M atoms is linked to six different TO_4 groups. Repetition of such connectivity results in the formation of a secondary building unit – a $^2_\infty[M(TO_4)_2]$ layer of corner-sharing MO_6 octahedra and TO_4 tetrahedra (see Fig. 1a). The resulting construction upon "glaserite" type stacking of the layers allows the appearance of two additional cationic positions (Fig. 1b and Fig. 2). For the highest symmetry case they can be defined as follows: a twelve coordinated position located between the layers and surrounded by six oxygen atoms from one of the layers and six more oxygens from the other layer ($X^{[6+6]}$) (Fig. 2a) and a ten coordinated position which is layer embedded and surrounded by nine oxygen atoms from the same layer and one oxygen from the adjacent layer ($Y^{[9+1]}$) (Fig. 2b). Such presentation of the X

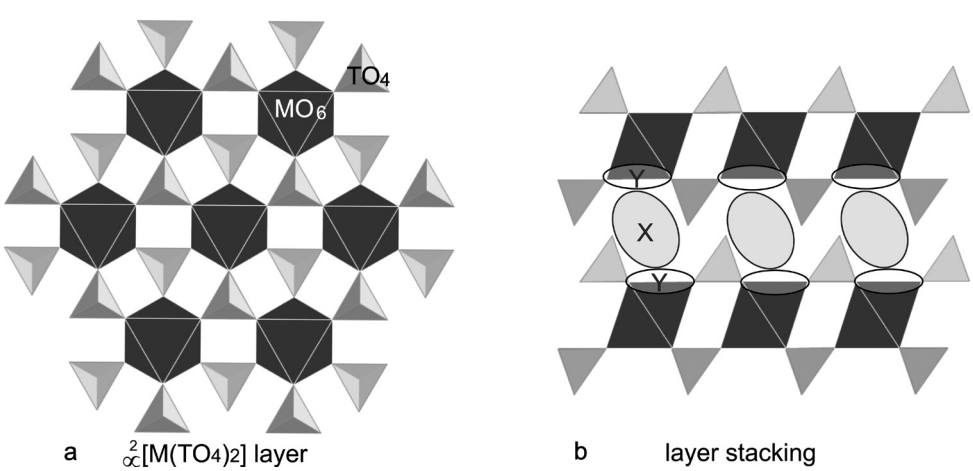

Fig. 1. Schematic presentation of the "glaserite" type topology: a) $^2_\infty[M(TO_4)_2]$ layer– top view; b) layers stacking – side view and possible interlayer cations positions (X, Y)

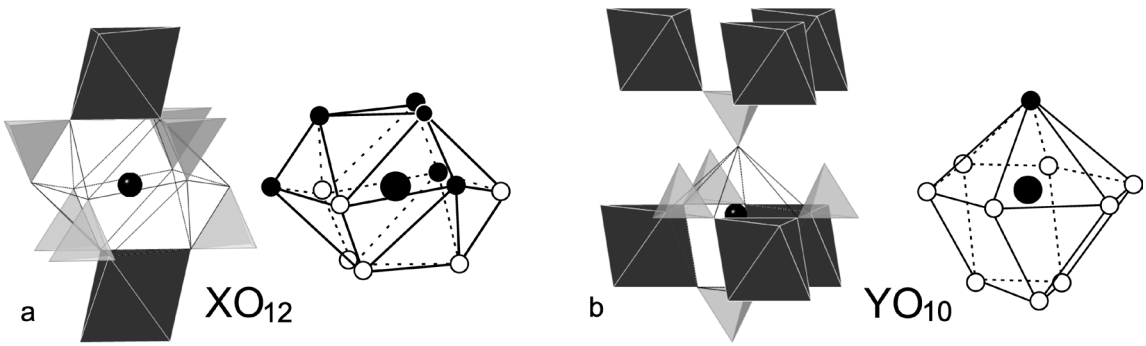

Fig. 2. Interlayer cations environment in the highest symmetry GTT case expressed in terms of the oxygen ligands from the "upper" (filled circles) and the "lower" (empty circles) layer

and Y atoms coordination does not match the one proposed by Lazoryak in his general formula – $X^{[6+6]}Y_2^{[4+6]}M^{[6]}(EO_4)_2$ [7]. It is because this author applies the columnar model for description of the glaserite construction. It is worth noting that the multiplicity of the Y position in GTT is always twice that one of X (X:Y=1:2).

The $^2_\infty[M(TO_4)_2]$ layer is common for a large number of compounds e.g. $Zr(HPO_4)_2.2H_2O$ (αZrP) [25], palmierite [26], $A_{2(3)}MT_2O_7$ [27] and references therein (Fig. 3).

In this work three essential structural characteristics are introduced to strictly define the "glaserite" type topology and distinguish it from other topologies with $^2_\infty[M(TO_4)_2]$ layers. The first one is that GTT does not contain additional atomic positions except the described M, T, X, and Y ones. For example, the structure of $Zr(HPO_4)_2.2H_2O$ (αZrP) provides opportunity for appearance of different interlayer positions due to its well-known capability for intercalation interrelated with the presence of OH^- group at the free apexes of the TO_4 tetrahedra (Fig. 3a). Another essential structural feature of GTT is that the free tetrahedral apexes point outside the layer towards the interlayer space. Up to now, the authors applying the layer model in the description of GTT point out only that the unshared corners of the tertahedra are oriented alternatively up and down in direction perpendicular to the layer [4, 7–9, 16, 19]. In the "palmierite" type structures this rule is observed however the free apexes point inside the layer (Fig. 3b) and the consequences of this is a different configuration of the charge compensating cations (see the stacking sequence of palmierite in [19]). The third one is that the layer stacking in GTT is realized without bridging oxygen atoms as shown in Fig. 1b. In contrast, in the $A_{2(3)}MT_2O_7$ compounds (Fig. 3c) the $^2_\infty[M(TO_4)_2]$ layers are linked by a bridging oxygen atoms leading to less pronounced characteristics of layeredness as compared with the GTT.

Quite obviously the $^2_\infty[M(TO_4)_2]$ layer charge depends on the type and valence of the M and T positioned cations. On its side, the layer charge is predetermining the occupancy, type, and valence of the

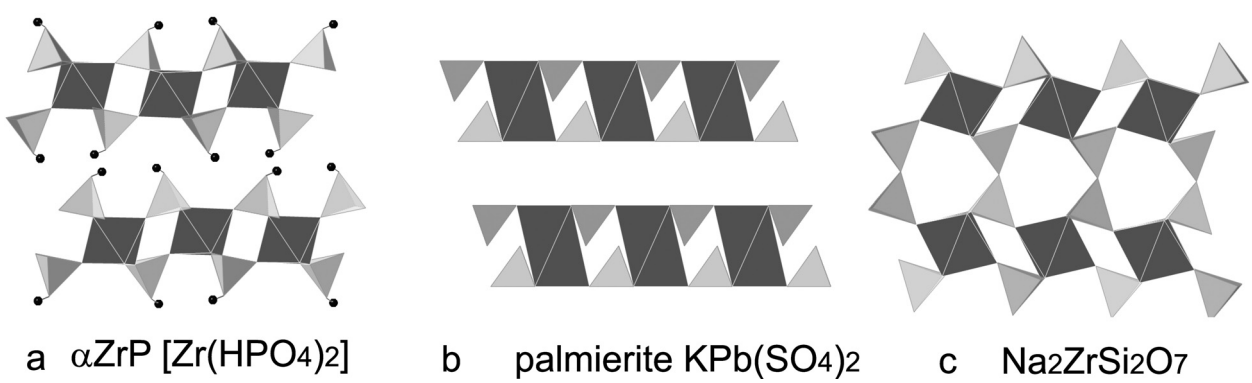

Fig. 3. Non-GTT compounds containing $^2_\infty[M(TO_4)_2]$ layers. Filled circles in Fig. 3a denote hydrogen atoms. $Na_2ZrSi_2O_7$ is a representative of the group of compounds with general formula $A_{2(3)}MT_2O_7$

X and Y positioned cations. Thus, when the layer is electroneutral both charge compensation cation positions will be unoccupied. In all other cases either X, or Y, or both X and Y positions will be occupied by appropriate in charge cations. Lazoryak's general formula, however, does not provide information about the cationic positions occupancy and their actual coordination in case of structural deviations from the highest symmetry.

Thus, a reconsideration of the general formula of GTC has been undertaken in terms of the postulated above essential structural features for GTT. A check-up in the available structural data bases has been performed and some of the results are summarized below.

- among the compounds adopting GTT there are 5 minerals and more than 100 synthetic compounds;
- altogether 47 elements from the periodic table can occupy the established four cationic positions (X, Y, M, and T) in the studied group;
- the T position (always fully occupied) includes the following elements: transition metals (V, Cr, Mo, W, Re, Fe, Ru) and non-metals (Si, P, S, Se). Altogether – 11;
- the M position (always fully occupied) is taken by: alkali metals (Na), alkali earth metals (Mg, Ca), transition metals (Sc, Y, Ti, Zr, Hf, V, Cr, Mo, Mn, Fe, Co, Ni, Cu, Zn, Cd) including lanthanides (Gd, Tb, Dy, Ho, Er, Tm, Yb, Lu), and poor metals (Al, In, Tl, Ge, Sn, Sb). Altogether – 32;
- if occupied the X and Y positions are taken by alkali metals (Na, K, Rb, Cs), alkali earth metals (Ca, Sr, Ba), transition metals (Ag), and poor metals (Tl, Pb). All of them – 10;
- the $^{2}_{\infty}[M(TO_4)_2]$ layer charge can take up the following values: 0, –1, –2, –3, –4, –6;

Based on the performed crystal chemical review a precise general formula (GF) for "glaserite" type compounds can be deduced and presented as follows: $X_{(\square;1)}Y_{(\square;2)}[M(TO_4)_2]$ (X+Y = 0; 1; 2; 3; M = 1; T = 2). Additional limitations and variety ranges for the general formula are presented in Table 1.

The amazing compositional diversity, the possibility for some chemical elements to occupy more than one cationic position (sometimes even in a single compound), the availability of mixed cationic positions, and the opportunity for X and Y to be both either free (unoccupied) or entirely occupied bring to a great variety of records for the general formula. Table 2 presents derivatives of the as introduced GTC general formula in accordance with the specificity (see third column) and occupancy of the cationic positions X, Y, M, and T ("conditions"). Each one is illustrated with the long and short formula of a particular "glaserite" compound in order to clarify the way the empirical chemical formulas for certain GTC can be derived. The last column shows the number of compounds found in the available structural data bases.

The distribution of GTC in groups according to the specificity of the cationic positions reveal that the conditions indicated in lines 2 and 4 of Table 2 are most favorable for the formation of such materials. According to the X and Y positions occupancy three groups of GTC can be differentiated. There are only 8 compounds with electroneutral layers and free X and Y positions. In 45 compounds only the X position is occupied (always completely) and 55 other phases contain both X and Y cations (full occupancy). Up to now only one compound – $K_2Zr(PO_4)_2$ (line 7 in Table 2) is established in which the Y position is occupied whereas the X one is free. This is indicative that the X position is more occupationally preferred than the Y one.

The proposed crystal-chemical formula does not contain information about the coordination numbers of the charge compensating cations since these values are not constant (Table 1, last column). These are strongly influenced by the structural deviations from the highest symmetry case for GTT occurring upon variations of the cationic positions specificity (Table 2). In some GTC H atoms are added to the chemical formula to overwhelm the spatial limitations affecting the charge compensating cations.

Table 1. Limitations and variety ranges of the GTC general formula $X_{(\square;1)}Y_{(\square;2)}[M(TO_4)_2]$ (X+Y = 0; 1; 2; 3;)

Cation position	number of elements occupying the position	valence of elements occupying the position	CN (BVS)*
X	0; 1; 2	1+, 2+	6, 7, 8, 9, 10, 12
Y	0; 1; 2	1+, 2+	4, 5, 7, 8, 9, 10, 12
M	1; 2	1+, 2+, 3+, 4+	6
T	1; 2	4+, 5+, 6+, 7+	4

* The coordination number CN is determined on the basis of the bond valence sums (BVS) after testing each CIF file with the ***soft BV 0.96*** software [28]

Table 2. Derivatives of the general formula $X_{(□;1)}Y_{(□;2)}[M(TO_4)_2]$ in accordance with the specificity and occupancy of the cationic positions (X, Y, M, and T)

No	General formula	Conditions	Examples		Ref.	Number of GTC
			Long formula	Short formula		
1	$XY_2[M(TO_4)_2]$	X≠Y≠M≠T	$BaNa_2[Mg(PO_4)_2]$	$BaNa_2Mg(PO_4)_2$	[12]	12
2	$XY_2[M(TO_4)_2]$	X=Y≠M≠T	$AgAg_2[Fe(VO_4)_2]$	$Ag_3Fe(VO_4)_2$	[29]	31
3	$XY_2[M(TO_4)_2]$	X≠Y; X=M; Y≠M≠T	$NaK_2[Na(SO_4)_2]$ = $K_2Na_2(SO_4)_2$	$KNaSO_4$	[2]	1
4	$XY_□[M(TO_4)_2]$	X≠M≠T; Y=0	$Rb□[Fe(MoO_4)_2]$	$RbFe(MoO_4)_2$	[30]	41
5	$(X1,X2)Y_□[M(TO_4)_2]$	X1≠X2≠M≠T; Y=0	$(Ba_{0.3}Sr_{0.7})[Zr(PO_4)_2]$	$Ba_{0.3}Sr_{0.7}Zr(PO_4)_2$	[31]	1
6	$X(Y1,Y2)_2[M(TO_4)_2]$	X=Y1≠Y2;Y2=M≠T	$Ba(Ba_{0.5},Na_{0.5})_2[Na(PO_4)_2]$ = $Ba_2Na_2(PO_4)_2$	$BaNaPO_4$	[32]	4
7	$X_□Y_2[M(TO_4)_2]$	Y≠M≠T; X=0	$□K_2[Zr(PO_4)_2]$	$K_2Zr(PO_4)_2$	[33]	1
8	$X_□Y_□[M(TO_4)_2]$	M≠T; X=0, Y=0	$□□[Ni(ReO_4)_2]$	$Ni(ReO_4)_2$	[34]	7
9	$X_□Y_□[M(T1,T2O_4)_2]$	M≠T1; T1≠T2; X=0, Y=0	$□□[Zr(Mo,WO_4)_2]$	$Zr(Mo,WO_4)_2$	[35]	1
10	$XY_□[(M1,M2)(TO_4)_2]$	X≠M1≠M2≠T; Y=0	$K□[(Mg_{0.5}Zr_{0.5})(MoO_4)_2]$	$K(Mg_{0.5}Zr_{0.5})(MoO_4)_2$	[36]	1
11	$XY_2[M(TO_4)_2]$	X=Y=M≠T	$TlTl_2[Tl(WO_4)_2]$= $Tl_4(WO_4)_2$	Tl_2WO_4	[37]	2
12	$XY_2H[M(TO_4)_2]$	X=Y≠M≠T	$NaNa_2H[Mg(PO_4)_2]$	$Na_3HMg(PO_4)_2$	[38]	5
13	$XY_□H[M(TO_4)_2]$	X≠M≠T; Y=0	$K□H[Zr(PO_4)_2]$	$KHZr(PO_4)_2$	[39]	2

For example, in $Na_3HZr(GeO_4)_2$, $K_3HCa(PO_4)_2$ and $Na_3HMg(PO_4)_2$ this occurs on the account of a randomly attached to the framework hydrogen [40–42]. The $Na_{3-x}H_{1+x}Zr(SiO)_4.yH_2O$ material also accommodates charge compensating H^+ as well as water molecules in its structure [21, 22]. Interestingly, the water is trapped between the charge compensating Na atoms and not positioned in the interlayer space, the way this occurs in the αZrP. Since the $Na_{3-x}H_{1+x}Zr(SiO)_4.yH_2O$ material does not exhibit rehydration or intercalation properties we are prone to classify this zirconosilicate as a GTC.

No doubt, the cations radiuses play a key role for the structural versatility and range of stability of GTC. As reported in the Introduction section in 1996 Lazoryak defined criteria for stability of "glaserite" type topology and postulated that "Glaserite structural type is stable for compounds where $0.59 < \Delta r < 0.89$ Å (Δr = r X(Y) – rM; Shanon ionic radii). When this difference decreases, metastable or β-K_2SO_4–like structures are formed" [7]. Later on, Morozov *et al.* expanded the lower limit of the range to $0.375 \leq \Delta r \leq 0.89$ Å, reporting the structure of $Na_3Fe(PO_4)_2$ [43]. As a result of the performed here review of GTC this range is further expanded and can be written as $0 < \Delta r < 1.345$ Å. The lower value is obtained for the structure of Tl_2WO_4 [37] and the upper one – for $CsAl(MoO_4)_2$ [44].

The "glaserite" layer stability and structural flexibility

Inspection of the collected structures brought forward certain facts and observations and suggest that the main structural motif of the investigated materials is the $^2_\infty[M(TO_4)_2]$ layer. One example concerns compounds which undergo phase transitions upon thermal treatment without destroying their topology. It was noticed that this process affects noticeably only the environment of the charge compensating interlayer cations. The adjacent layers may mutually off-shift when a phase transition occurs but the layer structure itself remains almost intact and only slight deviation can be detected for the bond distances and angles of the atoms constituting them. The XO_n and YO_n polyhedra in the higher temperature phases (HTP) have higher symmetry and are larger in volume than the corresponding coordination polyhedral in the lower temperature phases (LTP). The latter ones exhibit noticeable non-equivalence in the bond lengths. In general, the thermal expansion of the XO_n and YO_n polyhedra is most pronounced in the direction perpendicular to the layers. An expected effect of the bond distances elongation occurring in the HTP is the lowering of the bond valence sums calculated for the charge compensating cations there as compared to those ones obtained in the LTP. $K_3Na(SeO_4)_2$,

$K_3Na(RuO_4)_2$, $BaZr(PO_4)_2$ are "glaserite" type materials which undergo phase transformation upon thermal treatment and the comparison of their high and low modifications characteristics is a pretty fair illustration of the above said [10, 45, 46]. The structural transformations that occur with the latter compound are such that the charge compensating Ba even changes its coordination number from 10 (LTP) to 12 (HTP) thus making its bonds with the layer weaker.

As mentioned above in some "glaserite" type compounds the layers are electroneutral and their structures do not contain charge compensating cations, i.e. X and Y are vacant: $Ni(ReO_4)_2$, $Co(ReO_4)_2$, $Zn(ReO_4)_2$, $Mn(ReO_4)_2$, $Zr(Mo,WO_4)_2$, $Zr(MoO_4)_2$, $Hf(MoO_4)_2$, [34, 35, 47, 48]. The lack of any bonds between the layers provide for their comparatively high mobility and various opportunities for mutual orientation. Thus, a remarkable number of different polymorphs of $Zr(MoO_4)_2$ with GTT have been reported in the literature ([47, 48] and references therein).

In general, GTC with compositionally identical layers and various in size charge compensating interlayer cations are interesting because they illustrate the "layer-splitting" role of the latter. The intralayer cations are, in fact, framework cations and hence, it is possible to calculate the framework density (FD) of such compounds the way this is made for microporous materials (FD = number of framework cations per 1000 Å^3). Best candidates for this procedure are GTT orthophosphates, orthovanadates and orthotungstates of rare earth elements (REE) and differing in size alkali elements (rK < rRb < rCs) with general formula $X_{(\square;1)}Y_{(\square;2)}[M(TO_4)_2]$ (X,Y = K, Rb, Cs; M = Gd, Tb, Dy, Ho, Er, Tm, Yb, Lu; T = P, V, W). These materials have been investigated in details by many authors and although not all theoretically possible structures have been experimentally observed or refined, there is sufficient amount GTC with refined lattice parameters and chemical formulas to perform such calculations [13–17]. As expected the FD values drop with the increase of the alkali cation radius. For example, in $K_2RbGd(VO)_4$ [16] this value is 12.8 whereas in $Rb_3Gd(VO)_4$ [14] FD = 12.5. Another examples are $KAl(MoO)_4$ [49] (FD = 15.94) *vs.* $CsAl(MoO)_4$ [44] (FD = 13.99); $NaCr(CrO)_4$ (FD = 18.98) – $KCr(CrO)_4$ (FD = 16.88) – $CsCr(CrO)_4$ [50] (FD = 16.11), *etc*. In practice, the "layer-splitting" role of the interlayer cation was noticed for $M_3Ln(PO_4)_2$ compounds (M = K, Rb, Cs) in terms of the correlation between their hygroscopicity and the alkali cation radius. Most hygroscopic are the Rb and Cs phosphates [13].

As a whole, the "glaserite" topology is quite flexible and able to endure deformations preserving however its main structural motif. This is manifested through a variety of symmetry related Space Groups in which the members of GTC crystalize, e.g. P–3m – C2/m – P2/m – P–1 or C2/c – P2/c *etc*.

The flexibility of GTT can be expressed by comparing unit cell parameters which actually describe the translational symmetry of each particular crystal structure. For many GTC two crystallographic unit-cell parameters lie within the plane of the layer and hence, the a and b parameters are assumed to describe the intralayer translational symmetry, whereas the c parameter describes the stacking sequence repetition. For structures with a and b inclined to the plane of layer appropriate coordinate-system transformations are performed as to meet the above assumption. Therefore, the a and b parameters are related with the layer dimensionality and the value of their ratio is indicative for the degree of intralayer deformation (Fig. 4a).

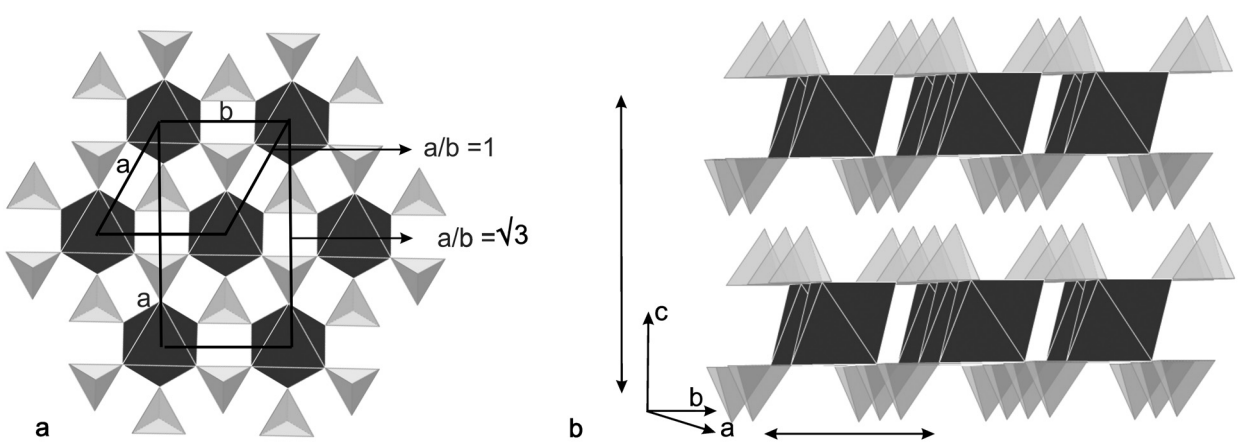

Fig. 4. GTT flexibility expressed in terms of lattice parameters ratios: a) two cell choices within the layer; b) schematic presentation of the magnitude of deformation within the layers and along their stacking

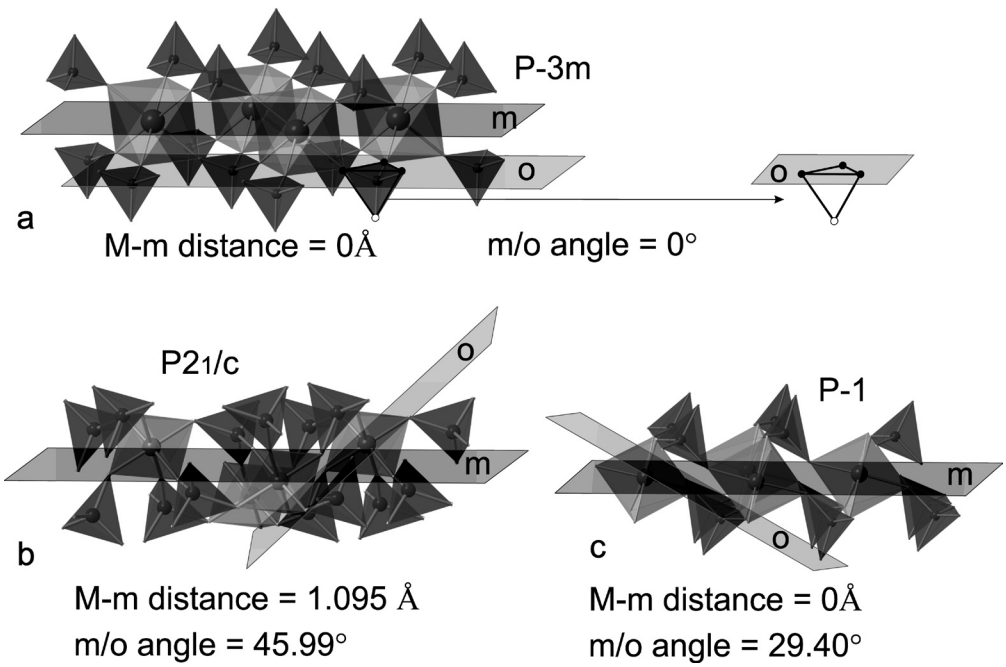

Fig. 5. Torsion of $^{2}_{\infty}[M(TO_4)_2]$ layer in terms of the relationship between atoms and planes. a) glaserite $K_3Na(SO_4)_2$; b) $CsSb(VO_4)_2$; c) $Na_3HZr(SiO_4)_2 \times 0.2H_2O$

On the other hand, the c value refers to the flexibility of the layer stacking. The highest possible symmetry of GTT is P–3*m*. In this "ideal" case of hexagonal setting $a_h = b_h$ or in the case of orthogonal choice the cell used is characterized with the ratio $a_o:b_o = \sqrt{3}$ (Fig. 4a). For the studied compounds the $a_0:b_0$ ratio deviates from the "ideal" value of $\sqrt{3}$ within the range 0.001 to 0.247 for $BaNa(PO_4)$ [51] and $KM(SeO_4)_2$ [52], respectively. On the other hand, the value of the *c* parameter varies between 5.285(1) Å in $\delta Zr(MoO_4)_2$ [47] to 25.409(4) Å in $KSb(PO_4)_2$ [53]. From these figures it can be concluded that similarly to other layered structures the deformation in GTT is anisotropic being more pronounced in direction of the layer stacking rather than within the layer (Fig. 4b).

Another set of parameters characterizing the topological flexibility is presented in Fig. 3 on the example of three particular GTC. By considering the $^{2}_{\infty}[M(TO_4)_2]$ layer two planes can be clearly defined: the mean plane defined by the M atoms – denoted here with (**m)** and the plane defined by the three bridged oxygen atoms from a given TO_4 tetrahedron is denoted here with (**o)**. In the "ideal" case all M atoms lie in a single plane and both **m** and **o** planes are parallel to each other (Fig. 5a). However, deviations from these values are possible as the maximum measured distance of M atom from the mean *m* plane is 1.09 Å and the largest established angle between **o** and **m** planes is 45.99° for $CsSb(VO_4)_2$ [54] (Fig. 3b).

Obviously, the chemical diversity and structural versatility of GTC are closely related and depend also on the formation conditions which impress with the broadness of their range. Thus, three of the minerals are products of volcanic fumarolic activity e.g. glaserite (aphthitalite) – $K_3Na(SO_4)_2$ [1–3], yavapaiite – $KFe(SO_4)_2$ [55], eldfellite – $NaFe(SO_4)_2$ [56]. Merwinite – $Ca_3Mg(SiO_4)_2$ is of scarn origin (high temperature, low pressure contact metamorphic zones with marbles) [57]. Brianite – $Na_2CaMg(PO_4)_2$ is an exotic find established only in meteorite rocks [58]. The synthetic compounds can be prepared through a great variety of methods (from solution, hydrothermally, solid state reactions, electrosynthesis, *etc*.) and within temperature ranges from room temperature to 1800 °C.

The established compositional variety and wide range of formation conditions are good prerequisite for preparation of new materials adopting the "glaserite" topology.

CONCLUSIONS

Crystal chemical data for more than 100 compounds with "glaserite" type structure have been summarized, analyzed, and evaluated. A revised

general formula for "glaserite" type compounds has been deduced – $X_{(\square;1)}Y_{(\square;2)}[M(TO_4)_2]$ (X+Y = 0; 1; 2; 3;). It gives information for two important structural characteristics of GTC. The first one is that main structural unit is the $^2_\infty[M(TO_4)_2]$ layer in which all the atomic positions are fully occupied. The second one is that the occupancy of X and Y positions depends on the layer charge and these positions can either be both free, separately or both of them entirely occupied. Additional limitations and variety ranges of the general formula are presented with respect to the cationic characteristics most important of which is the great variety of coordination numbers for the X and Y positions.

Precise criteria for the "glaserite" type topology are proposed distinguishing it from other topologies constructed by similar or identical layers. One of them is that the free apexes of the layer constructing tetrahedral should point outside the layer towards the interlayer space and another one is that the layers stacking should be realized without bridging oxygen atoms.

The range of structural stability of the "glaserite" type compounds is outlined in terms of the established up to now cations composition and site occupancy. The topological flexibility is evaluated through purposely introduced here geometrical parameters based on the lattice parameters or certain dimensional and angular interrelations.

The established compositional diversity, topological versatility and wide range of formation conditions are good prerequisite for preparation of new materials adopting the "glaserite" topology and estimation of certain physical phenomena such as temperature induced phase transitions.

***Acknowledgments**: Financial support by the Bulgarian National Fund of Scientific Research (contract DRNF 02/1) is gratefully acknowledged.*

REFERENCES

1. B. Gossner, *Neues Jahrb, Mineral*., B.-Band **57A**, 89 (1928).
2. A. Bellanca *Period. di mineral*., **14**, 67 (1943).
3. L. Pontonnier, M. Caillet and S. Aleonard, *Mat. Res. Bull.*, **7**, 799 (1972).
4. K. Okada and J. Ossaka, *Acta Cryst. B*, **36**, 919 (1980).
5. P. B. Moore, *Bulletin de la societe Francaise de Mineralogie et de Cristsllographie*, **104**, 536 (1981).
6. S. Takagi, M. Mathew, W. E. Brown, *Acta Cryst. C*, **39**, 166 (1983).
7. B. I. Lazoryak, *Russ. Chem. Rev.*, **65(4)**, 287 (1996).
8. M. Auray, M. Quarton, P. Tarte, *Acta Cryst. C*, **42**, 257 (1986).
9. L. Rghioui, L. El Ammari, L. Benarafa, J. P. Wignacourt, *Acta Cryst. C*, **58**, i90 (2002).
10. J. Fabry, T. Breczewski, V. Petricek, *Acta Cryst. B*, **49**, 826 (1993).
11. J. Fabry, V. Petricek, P. Vanek, I. Cisarova, *Acta Cryst. B*, **53**, 596 (1997).
12. Y. Yonesaki, C. Matsuda, *Journal of Solid State Chemistry*, **184**, 3247 (2011).
13. P. P. Mel'nikov, L. N. Komissarova *Koord. Khim.*, **12(10)**, 1299 (1986).
14. P. P. Mel'nikov, G. Y. Pushkina, V. A. Efremov, V. B. Kalinin, L. N. Komissarova, *Russ. J. Inorg. Chem. (Engl. Transl.)*, **26**, 142 (1981).
15. V. A. Efremov, P. P. Mel'nikov, L. N. Komissarova, *Revue de Chimie Minerale*, **22**, 666 (1985).
16. V. A. Efremov, P. P. Mel'nikov, H. D. K. Eredero, V. K. Trunov, *Izvestiya Akademii Nauk SSSR, Neorganicheskie Materialy*, **27**, 88 (1991).
17. V. A. Efremov, P. P. Mel'nikov, L.N. Komissarova, *Koord. Khim.*, **7(3)**, 467 (1981).
18. C. Park, S. Hong, D. A. Keszler *Journal of Solid State Chemistry*, **182,** 496 (2009).
19. P. B. Moore, *Am. Mineral.*, **58**, 32 (1973).
20. W. Eysel, *Am. Mineral.*, **58**, 736 (1973).
21. V. Kostov-Kytin, R. Nikolova, D. Nihtianova, *Materials Research Bulletin*, **47,** 2324 (2012).
22. V. Kostov-Kytin**,** R. Nikolova, T. Kerestedjian, P. Bezdicka, *Materials Research Bulletin*, **48**, 2029 (2013).
23. International Centre for Diffraction Data ICDD DD view+ 4.10.0.4 using PDF-4+2010 RDB 4.1002.
24. Inorganic Crystal Structure Database (ICSD), Karlsruhe: Gmelin institute fur anorganische Chemie, (2005).
25. J. M. Toup, A. Clearfield, *Inorg. Chem*., **16***,* 3311 (1977).
26. R. G. Tissot, M. A. Rodriguez, D. L. Sipola, J. A. Voigt, *Powder Diffraction*, **16(2)**, 92 (2001).
27. R. P. Nikolova, K. Fujiwara, N. Nakayama, V. Kostov-Kytin, *Solid State Sciences*, **11**, 382 (2009).
28. http://www.kristall.uni-mki.gwdg.de/softbv/
29. G. A. Becht, J. T, Vaughey, S. Hwu, *Chemistry of Materials*, **22(3)**, 1149 (2010).
30. T. Inami, *Journal of Solid State Chemistry*, **180**, 2075 (2007).
31. K. Fukuda, T. Iwata, A. Moriyama, S. Hashimoto, *Journal of Solid State Chemistry*, **179**, 3870 (2006).
32. C. Calvo, R. Faggiani, *Canadian Journal of Chemistry*, **53**, 1849 (1975).
33. M. Doerffel, J. Liebertz, *Zeitschrift fuer Kristallographie*, **193**, 155 (1990).
34. A. Butz, G. Miehe, H. Paulus, P. Strauss, H. Fuess, *Journal of Solid State Chemistry*, **138**, 232 (1998).
35. X. Deng, J. Tao, X. Yang, H. Ma, J. W. Richardson, Jr. X. Zhao, *Chemistry of Materials*, **20(5)**, 1733 (2008).
36. R. F. Klevtsova, Zh. G. Bazarova, L. A. Glinskaya, V. I. Alekseev, S. I. Arkhincheeva, B. G. Bazarov, P. V. Klevtsov, *Zhurnal Strukturnoi Khimii*, **36(5)**, 891 (1995).
37. K. Okada, J. Osaka, *Acta Cryst. B*, **35**, 2189 (1979).
38. Natl. Bur. Stand. (U.S.) Monogr. 25 21, 117 (1985).

39. A. Clearfield, L. B. McCusker, P. R. Rudolf, *Inorganic Chemistry*, **23**, 4679 (1984).
40. N. A. Nosyrev, E. N. Treushnikov, V. V. Ilyukhin, N. V. Belov, *Dokl. Akad. Nauk*, **218(4)**, 830 (1974).
41. J. C. Grenier, A. Durif, C. Martin, *Bulletin de la Societe Francaise de Mineralogie et de Cristallographie*, **92**, 30 (1969).
42. A. Kawahara, J. Yamakawa, T. Yamada, D. Kobashi, *Acta Cryst. C*, **51**, 2220 (1995).
43. V. A. Morozov, B. I. Lazoryak, A. P. Malakho, K. V. Pokholok, S. N. Polyakov, T. P. Terekhina, *Journal of Solid State Chemistry*, **160**, 377 (2001).
44. P. E. Tomaszewski, A. Pietraszko, M. Maczka, J. Hanuza, *Acta Cryst. E*, 58, i119 (2002).
45. K. Mogare, W. Klein, Eva-Maria Peters, M. Jansen, *Solid State Sciences*, **8,** 500 (2006).
46. D. Bregiroux, K. Popa, R. Jardin, P. E. Raison, G. Wallez, M. Quarton, M. Brunelli, C. Ferrero, R. Caciuffo, *Journal of Solid State Chemistry*, **182**(5), 1115 (2009).
47. A. M. K. Andersen, S. Carlson, *Acta Cryst. B*, **57**, 20 (2001).
48. S. Allen, R. J. Ward, M. R. Hampson, R. K. B. Gover, J S. O. Evans, *Acta Cryst. B*, **60**, 32 (2004).
49. R. F. Klevtsova, P. V. Klevtsov, *Kristallografiya*, **15**, 953 (1970).
50. R. Vidya, P. Ravindran, P. Vajeeston, H. Fjellvag, A. Kjekshus, *Physical Review, Serie 3. B – Condensed Matter*, **72***,* 014411 (2005).
51. A. W. Kolsi, M. Quarton, W. Freundlich, *Journal of Solid State Chemistry*, **36**, 107 (1981).
52. G. Giester, *Mineralogy and Petrology*, **53**, 165 (1995).
53. Y. Piffard, S. Oyetola, S. Courant, A. Lachgar, *Journal of Solid State Chemistry*, **60**, 209 (1985).
54. D. R. Nandini, K. Vidyasagar, *J. Chem. Soc., Dalton Trans*, **18,** 3013 (1998).
55. E. J. Graeber, A. Rosenzweig, *Am. Mineral.*, **56**, 1917 (1971).
56. T. Balić-Žunić A. Garavelli, P. Acquafredda, E. Leonardsen, S. P. Jakobsson, *Mineralogical Magazine*, **73(1)**, 51 (2009).
57. P. B. Moore, T. Araki, *Am. Mineral.*, **57**, 1355 (1972).
58. J. Alkemper, H. Fuess, *Zeitschrift fuer Kristallographie*, **213**, 282 (1998).

КРИСТАЛОХИМИЯ НА СЪЕДИНЕНИЯ С "GLASERITE" ТИП СТРУКТУРА

Р. Николова*, В. Костов-Китин

Институт по минералогия и кристалография, Българската академия на науките, ул. „Г. Бончев", бл. 107, 1113, София, България

Постъпила февруари, 2013 г.; приета май, 2013 г.

(Резюме)

Обобщени и са кристалохимични данни за повече от 100 съединения с "glaserite" тип структура. Предложена е ревизирана кристалохимичната обща формула на "glaserite" тип съединения (GTC) – $X_{(\square;1)}Y_{(\square;2)}[M(TO_4)_2]$, която дава информация за две важни структурни характеристики на GTC. Първата е, че основната структурна единица в този тип съединения е слой – $^{2}_{\infty}[M(TO_4)_2]$, в който всички атомни позиции са напълно заети. Втората е, че заетостта на X и Y позиции зависи от заряда на слоя и тези позиции могат или да бъдат изцяло заети и двете заедно или по отделно, като и да бъдат незаети, ако заряда на слоя е нулев. Предложени са точни критерии за "glaserite" тип топология (GTT), които позволяват разграничаване на GTT от други такива, изградени от сходни или еднакви слоеве. Границите на структурна стабилност на "glaserite" тип съединения е описан от гледна точка на установените до сега катионен състав и заетост на междуслойните катионни позиции. Възможностите за деформация на GTT при запазване на основните и характеристики е оценена чрез геометрични критерии, основани на решетъчни параметри и определени разстояния и ъглови. Установеното голямо разнообразие в структурните параметри, химичния състав и условията на образуване на "glaserite" тип съединения са добра предпоставка за получаване на нови материали с подобна топология, предлагаща възможности за нереконструктивни фазови преходи. Ключови думи: глазерит, "glaserite" тип топология, "glaserite" тип съединения.

Bulgarian Chemical Communications, Volume 45, Number 4 (pp. 427–433) 2013

XRD and TEM characterization of the morphology of ZnO powders prepared by different methods

M. Markova-Velichkova[1], S. Veleva[2], V. Tumbalev[1], L. Stoyanov[2], D. Nihtianova[1,3], M. Mladenov[2], R. Raicheff[2], D. Kovacheva[1]*

[1] *Institute of General and Inorganic Chemistry, BAS - Acad. G. Bontchev str. Bd. 11*
[2] *Institute of Electrochemistry and Energy Systems, BAS - Acad. G. Bontchev str. Bd. 10*
[3] *Institute of Mineralogy and Crystallography, BAS - Acad. G. Bontchev str. Bd. 107*

Received February, 2013; Revised May, 2013

Three different synthesis techniques were applied in order to prepare ZnO powder samples with different crystallite size. The first method is thermal decomposition of $Zn(NO_3)_2.6H_2O$. The second synthesis method is a sucrose-assisted solution combustion method. The third technique used is ultrasound assisted precipitation. A short-time thermal treatment is used to obtain ZnO materials with the required mean crystallite size. Materials were studied by means of powder XRD and TEM. The detailed morphology of the materials was first studied by XRD utilizing the special features of Fullprof program. This study revealed that different synthesis methods lead to products with different morphology. Materials obtained by the first method have an average crystallite size of 130–150 nm with irregular but isometric shape of the crystallites, while those obtained by the second method are almost spherical particles with size of about 30–40 nm. Regardless of the similar average crystallite size of the material obtained by the third method, its morphology is spindle-like, derived from different broadening of the XRD lines. The results from XRD analyses were confirmed by TEM observations. The influence of crystal morphology on the performance of ZnO as a main active material in zinc electrodes is discussed.

Key words: ZnO, synthesis, morphology, zinc electrodes.

INTRODUCTION

In recent years, many studies have been focused both on the synthesis and the morphological-structural characterization of new functional materials. Zinc oxide (ZnO) is a challenging inorganic material with various applications in many industrial branches, namely: in ceramic and rubber production; in electronics – for field emitters, gas sensors, ultraviolet lasers, solar cells, piezoelectric and optoelectronic devices; in chemical industry for photocatalysts; in energy production – for hydrogen-storage and alkaline batteries; and in environmental protection as biosensors, etc. [1–8]. Zinc oxide micro- and nanoparticles have attracted great interest due to their unique and remarkable chemical, electrical, mechanical, optical, and piezoelectric properties. It was established that the properties and possible applications of the ZnO are strongly influenced by structure and morphology of the obtained products which depend on the method of synthesis and synthesis conditions [9–11]. Therefore, it is important to synthesize ZnO with different size and morphologies to explore its performance for certain applications. Experience in the use of ZnO in alkaline secondary batteries shows that many of the battery problems are related to the physical and electrochemical properties of ZnO. As an example, the initial morphology of the active ZnO anode material was found to influence strongly the electrochemical performance of the battery altogether. For example, the use of ZnO with prismatic shape improves the cycling life of the battery [12]. Many synthesis techniques are known for the ZnO preparation. Recently, several soft chemistry (chimie douce) methods have been developed, allowing modification of the morphology and the particle size, by affecting diameters and aspect ratios of ZnO particles. The aim of the present work is to obtain ZnO nanomaterial and to investigate the relation between

* To whom all correspondence should be sent:
E-mail: didka@svr.igic.bas.bg

its morphological characteristics and electrochemical properties. In the present work we also explore the ability of X-ray diffraction to obtain information about the crystallite morphology. This is possible by crystal structure refinement using the Rietveld method, where crystallite size and morphology are modeled with spherical harmonics.

EXPERIMENTAL

Three different techniques were applied in order to prepare ZnO powder samples with different crystallite size and morphology. The first method is thermal decomposition of $Zn(NO_3)_2.6H_2O$. Aqueous solution of initial nitrate was placed in glass beaker and heated till evaporation. The obtained powders were heat-treated in air at 400 or 500 °C for 1 hour.

The second synthesis method is sucrose-assisted solution combustion method. For this purpose a $Zn(NO_3)_2.6H_2O$ solution was mixed with sucrose-in-water solution in 1:1 ratio oxidizing to reduce the power ratio of the corresponding nitrates and organic fuel [13, 14]. The solutions were placed on a heating plate until evaporation of the water. After that, a foamy mass was formed, which produces an amorphous powder oxide material. The calculated average crystallite size of the as prepared sample is 5 nm. Consequently, materials were thermally treated in air at 350, 400 and 500 °C for 1h. Finally, the materials were grinded for homogeneity.

The third technique used is ultrasound-assisted precipitation. The sonication of the precipitate was performed by a 20 KHz, 750W ultrasonic processor SONIX, USA. The total sonication time was from 5 to 30 minutes. The obtained product was repeatedly washed with distilled water, filtered and finally dried at 80 °C.

Powder XRD patterns were recorded at room temperature on a Bruker D8 Advance diffractometer with Cu K_α radiation and LynxEye detector. TEM investigations were performed by transmission electron microscope JEOL 2100 at 200 kV accelerating voltage.

Electrochemical charge-discharge characteristics were collected using specialized laboratory cycling equipment allowing galvanostatic mode charge and discharge, as well as mixed mode constant current/ constant voltage. Nickel electrode was commercial cathode produced in Bulgaria. Zinc electrode is prepared by introducing the zinc paste on the matrix (modified metallic or conductive ceramic composite). The pasted electrode is dried at 90 °C for 2 hours and then is pressed under 30 MPa for 2 min. Electrodes in the cell package are separated by a microporous polymer separator and immersed in alkaline (7M solution of KOH) electrolyte.

RESULTS AND DISCUSSION

This study revealed that different synthesis methods lead to products with different size and morphology. The diffraction patterns of ZnO materials obtained by the three methods are presented on Fig. 1. According to the X-ray diffraction patterns the products obtained through the first method are single phase ZnO. The average crystallite size of this material heated to 400 °C is about 100 nm. The increase of the temperature up to 500 °C leads to an increase in the crystallite size to about 150–200 nm.

The powders of ZnO prepared by the second method have crystallite size of about 6 nm. Additional heating to 400 and to 500 °C leads to an increase of crystallite size up to 10–12 and 25–30 nm, respectively. After one hour heat treatment at 600 °C, the sizes of crystallites were 45–50 nm. Thus this method allows easy preparation of ZnO material with predefined crystallite size.

The calculated mean crystallite size of the ZnO powders prepared by the third method is 24 nm. After thermal treatment at 600 °C for 1 h the mean crystallite size increases to about 50 nm. Powder diffraction pattern indicates the morphological peculiarities of this material. The diffraction peaks with indices (00l) are significantly narrower than those with other indices, which mean larger size in this direction indicating rod-like or needle-like morphology of the crystallites.

The calculated crystallite sizes within the main directions and the calculated mean crystallite sizes are summarized in Table 1. The crystallite sizes within the main directions were estimated by single line fitting of the corresponding peaks with the

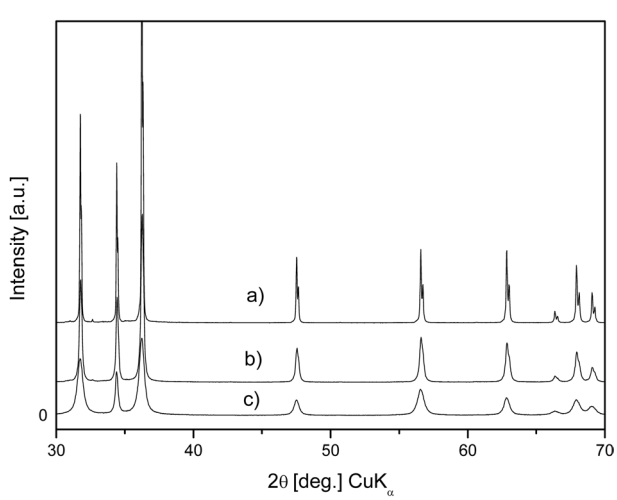

Fig. 1. XRD powder patterns of the materials obtained by the a) – decomposition; b) combustion; c) sonochemical methods

Table1. Calculated crystallite size within main directions of ZnO obtained by different methods

Line	100 (nm)	002 (nm)	101 (nm)	110 (nm)	Mean (nm)	$D_{(002)}/D_{(100)}$
ZnO – sonochemical as prepared	22	36	22	22	24	1.63
ZnO – sonochemical, heated	50	62	49	44	48	1.24
ZnO – combustion	52	49	46	50	47	0.94
ZnO – combustion (doped)	55	42	50	49	46	0.76
ZnO – decomposition	145	192	116	153	144	1.32

program Topas 4.2 [15] using the fundamental parameters peak shape description including appropriate corrections for instrumental broadening and diffractometer geometry.

Microstructural effects of materials may significantly hinder the successful crystal structure determination via Rietveld refinement method. The standard peak profile functions as well as the Caglioti equation fit patterns of materials with isometric crystallites well, but when the morphology is somehow different from the spherical symmetry some peaks of the diffraction pattern could not be

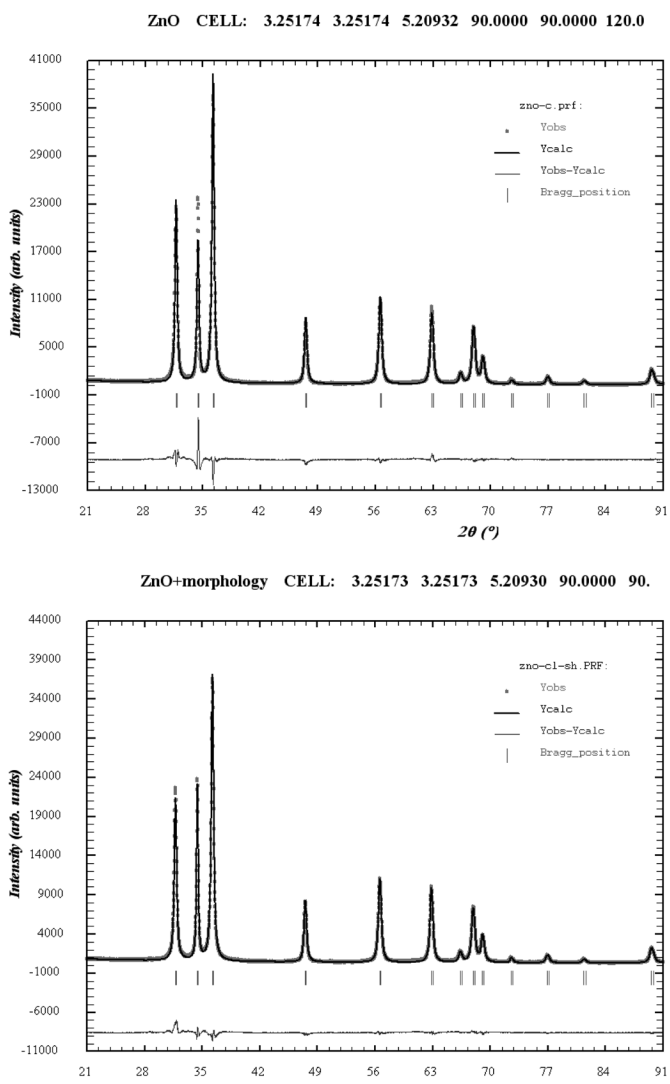

Fig. 2. Rietveld plot for ZnO obtained by the sonochemical method with the use of a) isotropic model for size broadening and b) using spherical harmonics

fit so good. As a result the refined structural parameters and their standard deviation may have values different from the expected ones for a well balanced structure. Such refinement may lead to unacceptable interatomic distances and highly distorted coordination polyhedra. Figure 2 illustrates the influence of microstructural effects by showing two Rietveld plots resulting from refinement of the crystal structure of ZnO using a) an isotropic model for size effects, and b) an appropriate crystallite morphology modelling.

The morphology of the materials synthesized by the three methods was first studied by XRD applying the special features of Fullprof [16] program. The microstructural effects in the program are introduced into the line broadening. For this purpose, instrumental and sample profiles are described by a convolution of Lorentzian and Gaussian functions, thus ensuring the simultaneous treatment of size and strain contribution to the line broadening. Spherical harmonics (SPH) are used for modeling the shape of the particles. Spherical harmonics are the angular parts of some solutions to Laplace's equation and they are widely used in different field of physics as a tool for gravitational, electric and magnetic fields description. In quantum chemistry they represent the atomic orbital electron configurations. Recently, spherical harmonics are used in the computer graphics in lightening effects and recognition of 3D shapes. The explicit formula for the SPH treatment of size broadening in Fullprof is the following [17]:

$$\beta_h = \frac{\lambda}{D_h \cos\theta} = \frac{\lambda}{\cos\theta} \sum_{lmp} a_{lmp} y_{lmp}(\Theta_h, \Phi_h)$$

Fig. 3. TEM photograph of ZnO prepared by the decomposition method

Where β_h is the size contribution to the integral breadth of reflection h, and $y_{lmp}(\Theta, \Phi)$ are the real spherical harmonics with normalization. For the proper use of this particular treatment of line broadening the instrumental resolution function should be preliminary determined by collecting the powder diffraction pattern of a standard sample with high crystallite size. After refinement of the coefficients the program calculates the apparent size (in angstroms) along each reciprocal lattice vectors.

It should be mentioned that the effect of the crystallite size on the broadening of diffraction lines is negligible for large crystallites (above 200 nm). As a result the attempt for modeling the size for the sample prepared from nitrate decomposition was not successful. Therefore, Transmission Electron Microscopy was used to confirm the findings of X-Ray diffraction. TEM photograph of the sample prepared by the decomposition method is presented on Fig. 3.

Figure 4a shows the XY, XZ and YZ projection of the "mean" crystallite as derived from XRD line broadening for ZnO prepared via the combustion method. TEM photograph of the ZnO prepared by this method is presented on Figure 4b. It can be seen that the particles are isometric, and that the shape derived from XRD analysis fits well with the shape observed in TEM.

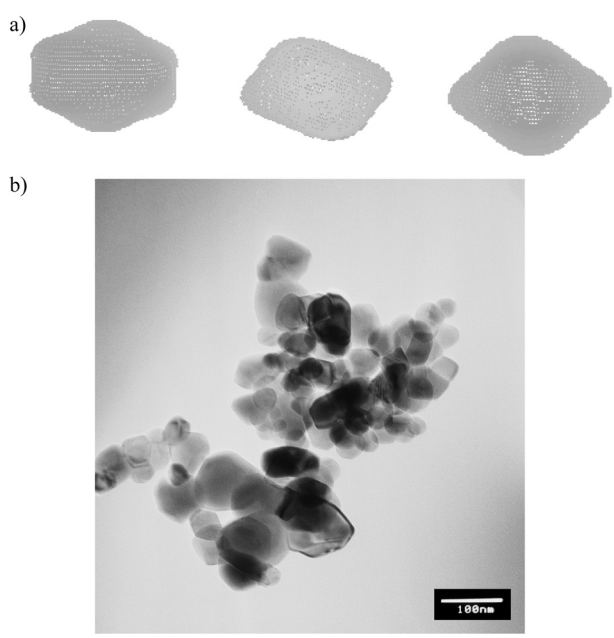

Fig. 4. a) XY, XZ and YZ projection of the "mean" crystallite, derived from the XRD line broadening for ZnO prepared via the combustion method; b) TEM photograph of ZnO prepared via combustion method

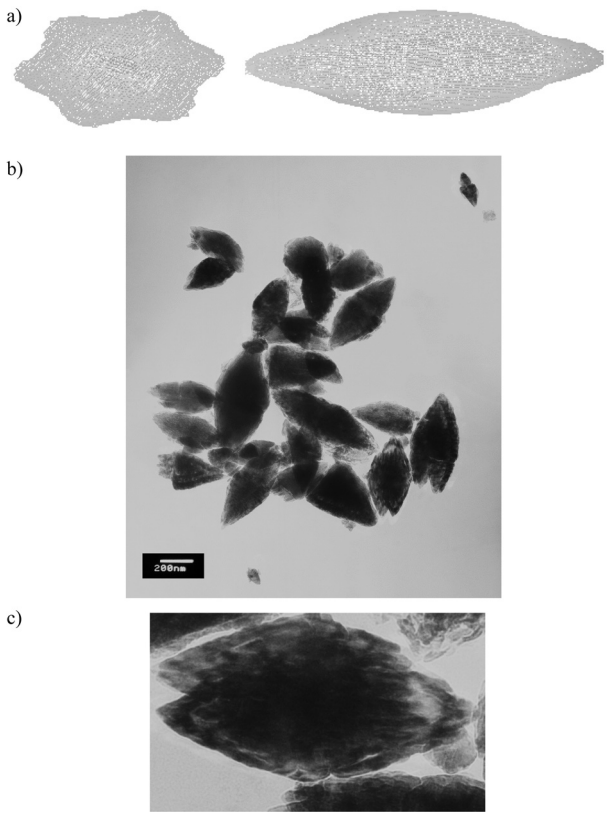

Fig. 5. a) The XY and XZ projection of the particles,derived from XRD line broadening for ZnO prepared via sonochemical method; b) TEM photograph of ZnO prepared by the sonochemical method; c) detail of the TEM photograph of ZnO prepared by the sonochemical method

A different morphology was observed for samples prepared via the sonochemical method. As it can be seen on Figure 5, both analytical methods give similar results representing spindle-like particles with different sizes within different crystallographic directions. The details in TEM photographs revealed also that spindle-like crystallites aggregate together within particles with same shape. Each big particle (with a size of about 200 nm) in fact consists of several smaller crystallites.

The electrochemical cycling behavior of pasted zinc electrodes with ZnO prepared by different methods is presented in Figure 6. The charge/discharge capacity of electrode with ZnO prepared via combustion method shows good stability during cycling as well as good capacity retention at different charge/discharge current rates. The initial capacity value for this material is about 200 mAh/g and decreases gradually to 180mAh/g within 50 charge-discharge cycles at C/5 rate, where C is the theoretical capacity of ZnO (978 mAh/g). The increase of the discharge rate to C/1.5 at charge rate C/2.5 lead to decrease of the capacity to about 75 mAh/g within the next 90 cycles. When the initial charge/discharge rate is restored, the capacity increases to its initial values. Cycling efficiency of this electrode is about 90–95%. Analogous behavior but higher values for the charge and discharge capacities (about 240 mAh/g) were observed for the capacity during cycling of electrodes with ZnO prepared via the sonochemical method. The dependence of charge and discharge capacity of the corresponding cell on cycle number demonstrates good electrochemical characteristics and cycling behaviour but relatively lower cycling efficiency (80–85%), compared to the zinc electrode with ZnO synthesized by combustion method. Nevertheless, the initial capacity of the ZnO prepared by decomposition method is relatively low (about 100 mAh/g) while the capacity fade during cycling is also very low.

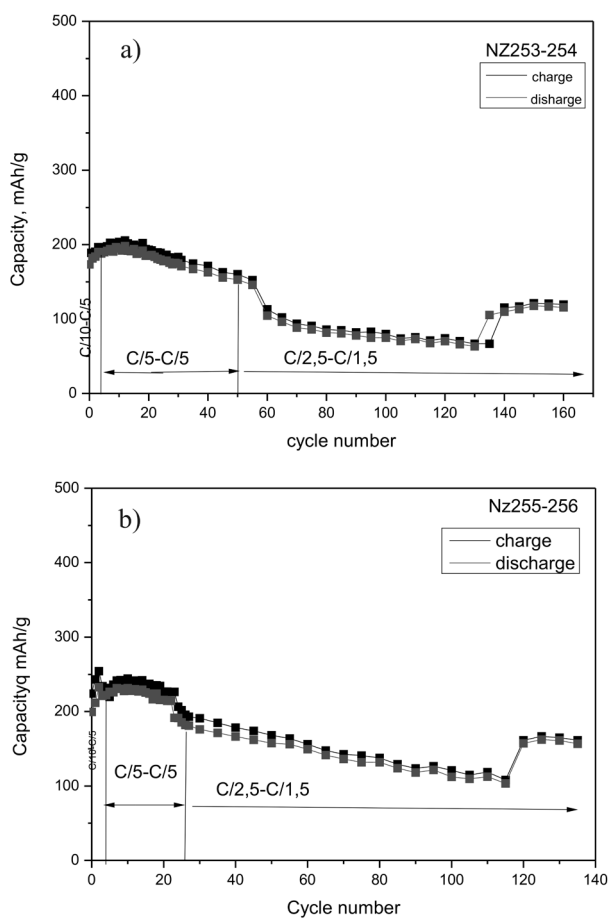

Fig. 6. a) Capacity during charge/discharge of electrode made with ZnO prepared via the combustion method; b) Capacity during charge/discharge of electrode made with ZnO prepared via sonochemical method

CONCLUSIONS

Compared to the conventional ZnO, nanosized ZnO anode material in Ni-Zn batteries shows better electrochemical characteristics – higher capacity and long cycling life. The reasons for such behavior could be attributed to higher specific surface area of the electrode prepared from nanoparticles thus ensuring better contact with the electrolyte. The morphology of the particles also influences the electrochemical behavior. ZnO with spindle-like particles showed higher capacity but lower electrochemical efficiency compared to ZnO with isometric particles.

REFERENCES

1. P. Yang, H. Yan, S. Mao, R. Russo, J. Johnson, R. Saykally, N. Morris, J. Pham, R. He and H.-J. Choi, *Adv. Funct. Mater.*, **12**, 323 (2002).
2. S. Chen, J. Zhang, X. Feng, X. Wang, L. Luo, Y. Shi, Q. Xue, C. Wang, J. Zhu, *Appl. Surf. Sci.*, **241**, 384 (2005).
3. J. Aranovich, D. Golmayo, A. Fahrenbruch, R. Bube, *J. Appl. Phys.*, **51**, 4260 (1980).
4. M. Wang, J. Wang, W. Chen, Y. Cui, L. Wang, *Mater. Chem. Phys.*, **97**, 219 (2006).
5. Y.W. Zhu, H.Z. Zhang, X.C. Sun, S.Q. Feng, J. Xu, Q. Zhao, B. Xiang, R.M. Wang, *Appl. Phys. Lett.*, **83**, 144 (2003).
6. K. Keis, C. Bauer, G. Boschloo, A. Hagfeldt, K. Westermark, H. Rensmo, H. Siegbahn, *J. Photochem. Photobiol. A Chem.* **148**, 57 (2002).
7. L. Luo, Y. Zhang, S.S. Mao, L. Lin, *Sens. Actuators A Phys.* , **127**, 201 (2006).
8. Y. Zhang, F. Zhu, J. Zhang, L. Xia, *Nanoscale Res. Lett.*, **3**, 201 (2008).
9. R. Wahab, Y.-S. Kim and H.-S. Shin, *Materials Transaction*, **50**, 2092 (2009).
10. S. Music, D. Dragcevic, S. Popovic, *J. of Alloys and Compounds*, **429**, 242 (2007).
11. Y. F. Yuan, J. P. Tu, H. M. Wu, Y. Z. Yang, D. Q. Shi, X. B. Zhao, *Electrochimica Acta*, **51**, 3632 (2006).
12. M. Ma, J. P. Tu, Y. F. Yuan, X. L. Wang, K. F. Li, F. Mao, Z. Y. Zeng, *Journal of Power Sources*, **179**, 395 (2008).
13. S. R. Jain, K. C. Adiga and V. R. Pai Verneker, *Combust. Flame*, **40**, 71 (1981).
14. M. M. A. Sekar and K. C. Patil, *J. Mater. Chem.*, **2**, 739 (1992).
15. TOPAS V4: General profile and structure analysis 14. software for powder diffraction data, User's Manual, Bruker AXS, Karlsruhe, Germany Bruker AXS (2008).
16. J. Rodríguez-Carvajal, FULLPROF: A Program for Rietveld Refinement and Pattern Matching Analysis, *Abstracts of the Satellite Meeting on Powder Diffraction of the XV thCongress of the International Union of Crystallography*, Toulouse, 127 (1990).
17. J. Rodríguez-Carvajal, Study of Micro-Structural Effects by Powder Diffraction Using the Program FullProf, *IV Congreso de la Sociedad Mexicana de Cristalografía*, Morelia, Michoacan, México, Libro de Resúmenes, 66 (2003).

РЕНТГЕНОГРАФСКО И ТЕМ ХАРАКТЕРИЗИРАНЕ НА МОРФОЛОГИЯТА НА ПРАХООБРАЗЕН ZnO, ПОЛУЧЕН ПО РАЗЛИЧНИ МЕТОДИ

М. Маркова-Величкова[1], С. Велева[2], В. Тумбалев[1], Л. Стоянов[2], Д. Нихтянова[1,3], М. Младенов[2], Р. Райчев[2], Д. Ковачева[1]*

[1] Институт по Обща и неорганична химия, БАН – ул. Акад. Г. Бончев, бл 11
[2] Институт по Електрохимия и енергийни системи, БАН – ул. Акад. Г. Бончев, бл 10
[3] Институт по Минералогия и кристалография, БАН – ул. Акад. Г. Бончев, бл 107

Постъпила февруари, 2013 г.; приета май, 2013 г.

(Резюме)

Поликристални образци от ZnO с различни размери на кристалитите бяха получени по три различни метода на синтез. Първият метод е чрез термично разлагане на Zn $(NO_3)_2 \cdot 6H_2O$. Вторият синтез е по метода на изгаряне от разтвор. Третата използвана техника е чрез ултразвуково третиране на утайка. Сравнително кратки времена на термична обработка са необходими за получаване на ZnO материали с желан среден размер на кристалитите. Материалите са изследвани с рентгенова дифракция и трансмисионна електронна микроскопия. Морфологията на материалите първоначално е изследвана с рентгенографски методи чрез прилагане на специалните възможности на програмата Fullprof. Изследването показа, че различните методи за синтез водят до получаване на продукти с различна морфология. Материалите, получени по първия метод имат среден размер на кристалитите 130–150 nm с неправилна но изометрична форма на кристалите, тези, получени по втория метод имат почти сферични частици с размер от около 30–40 nm. Въпреки същия среден размер на кристалитите на материала, получен по третия метод морфология на частиците е вретеновидна, съгласно резултатите от анализа на уширението на дифракционните линии. Резултатите от рентгенографските анализи бяха потвърдени от снимките получени от ТЕМ. Обсъдено е влиянието на морфологията на ZnO върху работата му като активен материал в цинкови електроди.

Bulgarian Chemical Communications, Volume 45, Number 4 (pp. 434–439) 2013

Preparation, structure and catalytic properties of $ZnFe_2O_4$

K. V. Koleva[1]*, N. I. Velinov[1], T. S. Tsoncheva[2],
I. G. Mitov[1], B. N. Kunev[1]

[1] *Institute of Catalysis, BAS, Sofia, 1113, Bulgaria*
[2] *Institute of Organic Chemistry with Centre of Phytochemistry, BAS, Sofia, 1113, Bulgaria*

Received February, 2013; Revised May, 2013

Zinc ferrite ($ZnFe_2O_4$) nanopowders were prepared by co-precipitation method from the corresponding nitrate precursors and thermal treating of the obtained precursor at different temperatures. X-ray diffraction and ^{57}Fe Mössbauer spectroscopy were used for the characterization of the obtained materials. The results of X-ray analysis confirm formation of nanocrystalline zinc ferrite phase with cubic structure and crystallite size 6–46 nm depending on the annealing temperature. The obtained ferrites were tested as catalysts in methanol decomposition to CO and hydrogen. The analyses of the samples after the catalytic test reveal a significant phase transformation of the ferrite phase by the influence of the reaction medium.

Key words: zinc ferrite, Mössbauer spectroscopy, methanol decomposition.

INTRODUCTION

The magnetic, dielectric and electrical behavior of the ferrite materials provides their large scale of applications, as semiconductors [1], pigments [2], magnetic resonance imaging [3], computer memory chips. Their catalytic properties have been tested in number of industrial process, such as oxidative dehydrogenation of hydrocarbons, decomposition of alcohols [4] and hydrogen peroxide, treatment of automobile-exhausted gases, phenol hydroxylation (oxidation), photocatalytic ozonation of dyes [5] and alkylation of hydrocarbons [6].

Recent studies concerned methanol as a potential source of hydrogen for fuel cells because of its relatively low temperature of decomposition to hydrogen, high energy density, safety handle, low cost and possibility of production from renewable sources as biomass [7–11].

The aim of present work is to study preparation of zinc ferrite nanopowders by co-precipitation method following by thermal treatment and to study the catalytic activity in methanol decomposition to CO and hydrogen. The changes in the phase composition of materials after the catalytic test were also in the focus of investigation. Mössbauer technique was used due to its high sensitivity to investigate the phase composition, magnetic behavior and iron ions emplacement of unit cell [12].

In our previous work the synthesis of $CuFe_2O_4$ [13, 14], $CoFe_2O_4$ [15, 16], $NiFe_2O_4$ [17] and mixed Ni-$ZnFe_2O_4$ ferrite materials [18] was reported. Methods of Spark Plasma Sintering, sol-gel, thermal and mechanochemical treatments [19, 20] have been applied successfully. The relationship between parameter of synthesis, phase composition, particle size, microstrain and catalytic behavior of ferrite materials has been discussed. Application of Cu, Ni, and Co based ferrites is well known, especially when these elements are substituted with Zn ions, which prefer the tetrahedral position in spinel lattice and has strong effect on the properties. It is well known that Zn content exerts important role on structure and properties of ferrites [21, 22]. In this work we demonstrate synthesis, structure and catalytic properties of pure zinc ferrite.

EXPERIMENTAL

Synthesis

Four samples of zinc-iron oxide powders were prepared by co-precipitation method. Water solution containing Zn- and Fe-ions was prepared of stoichiometric amount of nitrate salts [$Zn(NO_3)_2.6H_2O$;

* To whom all correspondence should be sent:
E-mail: kremena_vassileva@abv.bg

$Fe(NO_3)_3.9H_2O$]. As a precipitation agent was used 1M Na_2CO_3 and pH was kept of 9. The obtained precipitates were washed with distilled water and dried at room temperature to form precursor powders. The heat treatment of precursors was conducted in air at 573 K, 673 K, 773 K, 973 K for four hours to obtain ferrite samples.

Characterisation

The powder XRD patterns were recorded by a TUR M62 diffractometer with Co Kα radiation. The observed patterns were cross-matched with those in the JCPDS database [23]. The average crystallites size (D), the degree of microstrain (e) and the lattice parameters (a) of the studied ferrites were determined from the experimental XRD profiles by using the PowderCell-2.4 software [24]. The instrumental broadening of diffraction peaks is equal to 0.020° Bragg angle. It was determined by Al standard and was excluded at calculation of crystallites size and the degree of microstrain. The Mössbauer spectra were obtained at room temperature (RT) with a Wissel (Wissenschaftliche Elektronik GmbH, Germany) electromechanical spectrometer working in a constant acceleration mode. $^{57}Co/Rh$ (activity ≅50 Ci) source and α-Fe standard were used. The experimentally obtained spectra were fitted using CONFIT2000 software [25]. The parameters of hyperfine interaction such as isomer shift (IS), quadrupole splitting (QS), effective internal magnetic field (Heff), line widths (FWHM), and relative weight (G) of the partial components in the spectra were determined.

Catalytic test

Methanol decomposition experiments were carried out in a flow reactor using argon as a carrier gas, at methanol partial pressure of 1.57 kPa and WHSV of 1.5 h^{-1}. On-line gas chromatographic analysis were performed on HP 5980 on PLOT Q column, with simultaneous using of detector of thermo conductivity and flame ionization detector and an absolute calibration method.

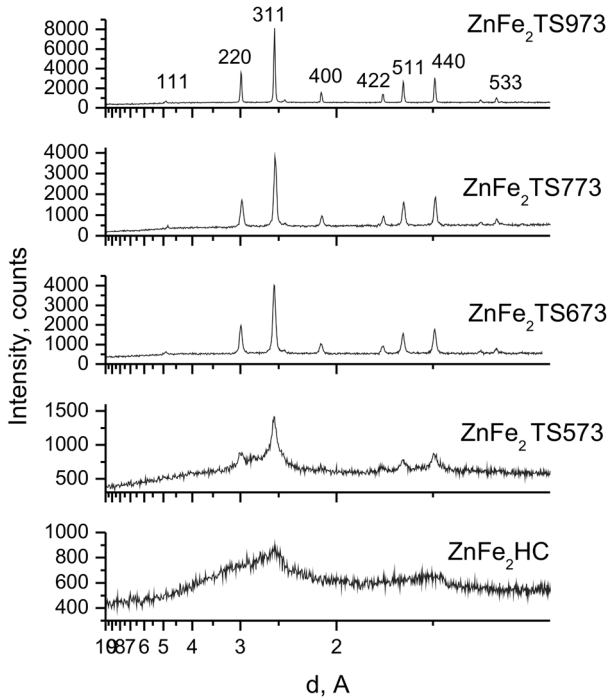

Fig. 1. X-ray diffraction patterns of synthesized samples

RESULTS AND DISCUSSION

XRD patterns of the precursor powder and thermally synthesized samples are presented in Fig. 1. Beginning of crystallization process was observed at temperature as low as 573K. The diffractograms of samples treated at higher temperatures show well defined reflexes corresponding to cubic spinel phase of zinc ferrite with lattice parameter a= 8.43–8.44 Å. Microstrain degree and average crystallite size of zinc ferrite powders was calculated using Williamson–Hall equation and presented in Table 1.

Table 1. Average crystallite size (D), degree of microstrain (e) and lattice parameters (a) determined from experimental XRD profiles

Sample	Phase	D, nm	$e.10^3$, a.u	a, A
$ZnFe_2TS573$	Fd3m(227) – cubic	5.89	7.894	8.43
$ZnFe_2TS673$	Fd3m(227) – cubic	19.09	1.228	8.43
$ZnFe_2TS773$	Fd3m(227) – cubic	19.08	1.323	8.44
$ZnFe_2TS973$	Fd3m(227) – cubic	45.84	1.187	8.43

Increasing of crystallite size from 6 to 46 nm and narrowing the width of the peaks with increasing of temperature in the range of 573–973 K can be explain with effect of sintering.

The room temperature Mössbauer spectroscopy is presented in Fig. 2. The Mössbauer spectra are consisted of well-defined doublet, typical of paramagnetic state of materials. The fitting parameters of Mössbauer spectra are presented in Table 2. Parameters of all spectra correspond to octahedral coordinated Fe^{3+} ions. Increasing of the value of superfine quadrupole splitting after treatment at 573 K could be assigned to additional deformation of octahedral Fe^{3+}, as a result of precursor decomposition. Further increasing of treatment temperature leads to decrease of QS to reach values typical for well crystallized zinc ferrite.

Temperature dependencies of conversion and CO selectivity in methanol decomposition of synthesized materials are presented in Figure 3. All ferrites started to decompose the methanol above 500 K and the conversion was about 90–95% at 600 K. Carbon monoxide was formed with 50–70% selectivity and methane and CO_2 were also registered as by products. A well defined tendency for the catalytic activity decrease with the increase of the temperature of ferrite synthesis was observed.

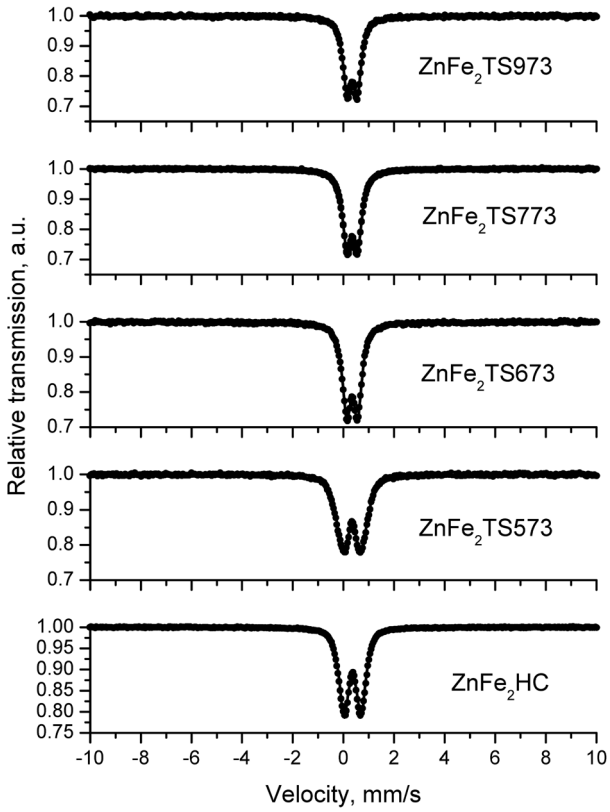

Fig. 2. Mössbauer spectra of synthesized samples

Table 2. Parameters of Mössbauer spectra of the investigated samples

Sample	Components	IS mm/s	QS mm/s	$H_{eff,}$ T	FWHM mm/s	G,%
$ZnFe_2HC$	Db	0.36	0.67	–	0.44	100
$ZnFe_2TS573$	Db	0.35	0.72	–	0.56	100
$ZnFe_2TS673$	Db	0.35	0.44	–	0.40	100
$ZnFe_2TS773$	Db	0.35	0.42	–	0.41	100
$ZnFe_2TS973$	Db	0.35	0.40	–	0.38	100

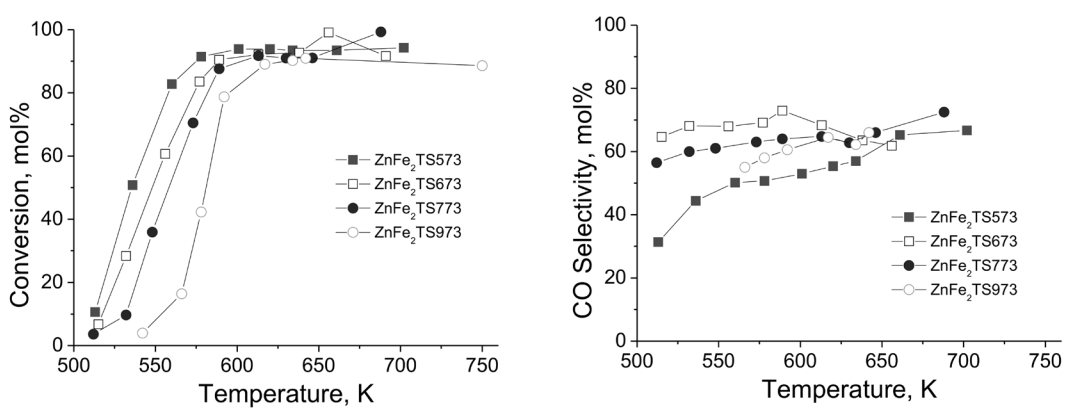

a) b)

Fig. 3. Methanol conversion (A) and CO selectivity (B) vs. temperature of investigated ferrite materials

The phase transformation of used materials after catalytic test has been obtained by Mössbauer measurement (Fig. 4). The Mössbauer spectra of used sample $ZnFe_2O_4$ TS-973 was well fitted with two sextets of Zn-substituted magnetite, one sextets of non-stoichiometric carbide (Fe_xC_x), α-Fe and doublet of wuestite (FeO). Spectra of the other materials consist of sextets with parameters corresponding to $Zn_xFe_{3-x}O_4$ and Fe_5C_2 phases and zinc ferrite with relative part of 4–13% was also registered (Table 3). The Zn-substituted magnetite could be presented with the formula $(Zn_x^{2+}Fe_{1-x}^{3+})_{tetra}[Fe_{1+x}^{3+}Fe_{1+x}^{2+}]_{octa}O_4$, as the spinel structure is preserved in the range $0 \leq x \leq 1$. Mössbauer spectrum of magnetite (Fe_3O_4) i.e. x = 0 consist of two Zeeman sextets. One of them is due to tetrahedral Fe^{3+} ions and other is due to octahedral Fe^{3+} and Fe^{2+} ions rendered indistinguishable by electron hopping at a frequency faster than that of the Larmor precession of the iron nucleus in the hyperfine field [26]. Therefore, the ratio of relative weight of two sextet components of unsubstituted magnetite should be 1:2 for Fe_{tetra}:Fe_{octa}, assuming of equal Mössbauer–Lamb factors for the different iron sites. The ratio of fitted relative weight of Sx1

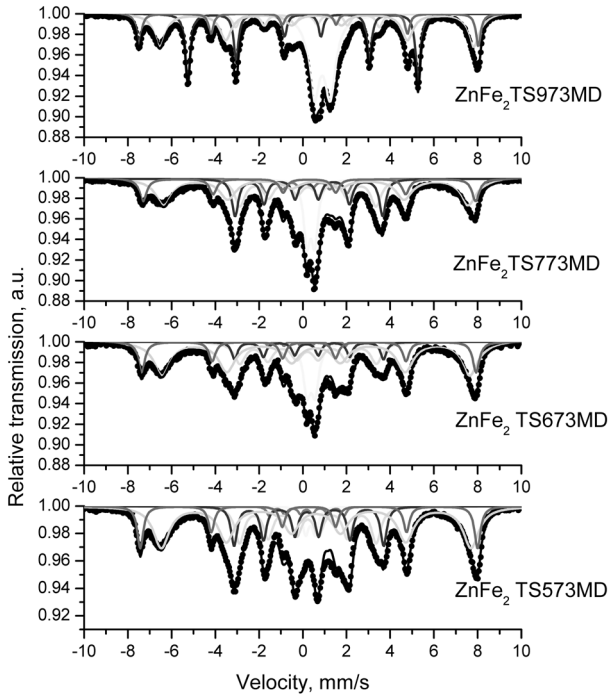

Fig. 4. Mössbauer spectra of samples after catalytic test

Table 3. Parameters of Mössbauer spectra of the investigated samples after catalytic test

Sample	Components		IS, mm/s	QS, mm/s	Heff, T	FWHM, mm/s	G, %
$ZnFe_2TS573$-MD	$Zn_xFe_{3-x}O_4$ (x = 0.30)	Sx1	0.28	0.00	47.9	0.33	14
		Sx2	0.60	0.01	44.0	0.87	40
	Fe_5C_2	Sx3	0.23	0.09	21.3	0.34	16
		Sx4	0.23	0.00	19.4	0.52	22
		Sx5	0.17	0.01	10.6	0.28	3
	$ZnFe_2O_4$	Db	0.35	0.44	–	–	4
$ZnFe_2TS673$-MD	$Zn_xFe_{3-x}O_4$ (x= 0.36)	Sx1	0.28	–0.01	47.5	0.36	14
		Sx2	0.60	0.00	43.7	0.89	44
	Fe_5C_2	Sx3	0.22	0.11	21.2	0.32	8
		Sx4	0.22	0.04	19.4	0.60	20
		Sx5	0.17	0.02	10.1	0.15	1
	$ZnFe_2O_4$	Db	0.37	0.37	–	–	12
$ZnFe_2TS773$-MD	$Zn_xFe_{3-x}O_4$ (x = 0.20)	Sx1	0.30	0.00	47.2	0.39	12
		Sx2	0.59	0.00	43.2	0.88	30
	Fe_5C_2	Sx3	0.30	0.10	21.0	0.36	18
		Sx4	0.23	0.00	19.3	0.57	20
		Sx5	0.17	0.02	11.5	0.38	7
	$ZnFe_2O_4$	Db	0.36	0.35	–	–	13
$ZnFe_2TS973$-MD	$Zn_xFe_{3-x}O_4$ (x = 0.21)	Sx1	0.28	–0.02	48.2	0.26	11
		Sx2	0.63	0.00	44.6	0.63	28
	α-Fe	Sx3	0.00	0.01	32.7	0.27	23
	Fe_xC_x	Sx4	0.17	0.07	20.4	0.36	8
	FeO	Db	0.88	0.73	–	0.60	30

and Sx2 of samples after catalytic reaction (Table 3) is higher than 1:2. This is due to presence of Zn-ions substitution of Fe^{3+} in tetrahedral position of magnetite lattice. The degree of Zn substitution x can be easily calculated by formula: x = 1 – 2A/B, where A and B are relative weight of Sx1 and Sx2, respectively.

CONCLUSION

Nanocrystalline zinc ferrites with cubic structure and particle size 6–45 nm were successfully synthesized by co-precipitation method. All investigated ferrite materials revealed good catalytic activity and selectivity to CO in methanol decomposition and it can be denoted that the final composition of the catalytic materials was formed in the reaction medium.

Acknowledgement: *Sponsorship by the Bulgarian National Science Fund at the Ministry of Education, Youth and Science under Project FFNNIPO_12_ 00182/2012 is gratefully acknowledged.*

REFERENCES

1. A. S. Kindyak, *Materials Letters*, **39**, 12 (1999).
2. A. C. F. M. Costa, A. M. D. Leite, H.S. Ferreira, R. H. G. A. Kiminami, S. Cava, L. Gama, *J. Europ. Ceram. Soc.*, **28**, 2033 (2008).
3. H. Wu, G. Liu, X. Wang, J. Zhang, Y. Chen, J. Shi, H. Yang, H. Hu, S.Yang , *Acta Biomaterialia*, **7**, 3496 (2011).
4. N. I. Maksimova, O. P. Krivoruchko, *Chemical Engineering Science*, **54**, 4351 (1999).
5. N. M. Mahmoodi, *Desalination*, **279**, 332 (2011).
6. P. Siwach, S. Singh, R. K. Gupta, *Catalysis Communications*, 1**0**, 1577 (2009).
7. J. Christopher Brown, Erdogan Gulari, *Catalysis Communications*, **5**, 431 (2004*)*.
8. C.-C. Chang, C.-T. Chang, S.-J. Chiang, B.-J. Liaw, Y.-Z. Chen, *Intern. J. Hydrogen Energy*, **35**, 7675 (2010).
9. R. A. Dagle, A. Platon, D. R. Palo, A. K. Datye, J. M. Vohs, Y. Wang, *Applied Catalysis A: General*, **342**, 63 (2008).
10. T. Tsoncheva, J. Roggenbuck, M. Tiemann, L. Ivanova, D. Paneva, I. Mitov, C. Minchev, *Microporous and Mesoporous materials*, **110**, 339 (2008).
11. T. Tsoncheva, J. Rosenholm, C. V. Teixeira, M. Dimitrov, M. Linden, C. Minchev, *Microporous and Mesoporous Materials*, **89**, 209 (2006).
12. S. Kamali-M., T. Ericsson, R. Wäppling, *Thin Solid Films*, **515**, 721 (2006).
13. T. Tsoncheva, E. Manova, N. Velinov, D. Paneva, M. Popova, B. Kunev, K. Tenchev. I. Mitov, *Catalysis Communications*, **12**, 105 (2010).
14. E. Manova, .Tsoncheva, D. Paneva, M. Popova, N. Velinov, B. Kunev, K. Tenchev, I. Mitov, *Journal of Solid State Chemistry*, **184**, 1153 (2011).
15. E. Manova, T. Tsoncheva, C. Estournes, D. Paneva, K. Tenchev, I. Mitov, L. Petrov, *Applied Catalysis A: General*, **300**, 170 (2006).
16. E. Manova, T. Tsoncheva, D. Paneva, , I. Mitov, K. Tenchev, L. Petrov, *Applied Catalysis A: General*, **277**, 119 (2004).
17. E. Manova, T. Tsoncheva, D. Paneva, J. L. Rehspringer, K. Tenchev, I. Mitov, L. Petrov, *Applied Catalysis A: General*, **317**, 34 (2007).
18. N. Velinov, E. Manova, T. Tsoncheva, C. Estournes, D. Paneva, K. Tenchev, V. Petkova, K. Koleva, B. Kunev, I. Mitov, *Solid State Sciences*, **14**, 1092 (2012).
19. X. Wang, O. Tanaike, M. Kodama, H. Hatori, *Journal of Power Sources*, **168**, 282 (2007).
20. G. A. El-Shobaky, A .M. Turky, N. Y. Mostafa, S. K. Mohamed, *Journal of Alloys and Compounds*, **493**, 415 (2010).
21. M. Ajmal, A. Maqsood, *Materials Science and Engineering B*, **139**, 164 (2007).
22. K. B. Modi, P. V. Tanna, S. S. Laghate, H. H. Joshi, *Journal Of Materials Science Letters* **19**, 1111 (2000).
23. International Centre for Diffraction Data, Alphabetical Indexes, Pannsylvania 19073–3273, sets 1–44 (1998).
24. W. Kraus, G. Nolze, PowderCell for Windows, Federal Institute for Materials Research and Testing, Berlin, (2000).
25. T. Žák, Y. Jirásková, CONFIT: Mössbauer spectra fitting program, *Surface and Interface Analysis*, **38**, 710 (2006).
26. D. C. Dobson, J. W. Linnet, M. M. Rahman, *J. Phys. Chem. Solids*, **31**, 2727 (1970).

СИНТЕЗ, СТРУКТУРА И КАТАЛИТИЧНИ СВОЙСТВА НА $ZnFe_2O_4$

К. В. Колева[1]*, Н. И. Велинов[1], Т. С. Цончева[2],
И. Г. Митов[1], Б. Н. Кунев[1]

[1] *Институт по Катализ, БАН, София, 1113, България*
[2] *Институт по Органична химия с център по Фитохимия, София, 1113, България*

Постъпила февруари, 2013 г.; приета май, 2013 г.

(Резюме)

Наноразмерен цинков ферит ($ZnFe_2O_4$) беше синтезиран по метод на съутаяване от съответните метални соли с последващо термично третиране на получените предходници при различни температури. Всички образци бяха охарактеризирани с Рентгенов дифракционен анализ и Мьосбауерова спектроскопия. Резултатите получени от Рентгенофазовия анализ показват формиране на добре изкристализирала феритна фаза с кубична структура и размери на кристалитите в граници 6–46 nm, в зависимост от прилаганата температура на синтез. Получените след термична обработка феритни материали бяха изследвани в реакция на разлагане на метанол до CO и водород. Проведените анализи на образците след каталитичния тест показват значителна фазова трансформация на феритната фаза под влияние на реакционната среда.

Bulgarian Chemical Communications, Volume 45, Number 4 (pp. 440–445) 2013

Crystallographic conditions of the heterologically expressed recombinant metal-binding protein Ts-PCHTP

H. I. Sbirkova[1]*, G. A. Radoslavov[2], P. I. Hristov[2], B. L. Shivachev[1]

[1] *Institute of Mineralogy and Crystallography, Bulgarian Academy of Sciences, Acad. G. Bonchev Str., Bl. 107, 1113 Sofia,Bulgaria*
[2] *Institute of Biodiversity and Ecosystem Research , Bulgarian Academy of Sciences, Acad. G. Bonchev Str., Bl. 25, 1113 Sofia,Bulgaria*

Received February, 2013; Revised May, 2013

We have optimized the expression of Polycysteine and histidine-tailed protein (Ts-PCHTP). The protein contains a natural His-tag for metal binding, used in the protein purification process. The "tag" amino acid sequence binds very strongly to conventional Ni affinity chromatography columns and permits the protein elution with EDTA. The protein purification should be monitored by Native-PAGE as the high content of cysteine in the Ts-PCHTP protein sequence produces false positives, when SDS-PAGE technique is used. According to the DLS data a dimmer form of Ts-PCHTP is observed. Sparse matrix crystallization screens were used for the determination of the most favorable conditions for growth of crystals suitable for X-ray single crystal.

Key words: recombinant protein; His Tag affinity chromatography; Metal binding protein; Dynamic Light Scattering; Protein crystallization.

INTRODUCTION

The ultimate goal of structural biology is to understand the structural basis of proteins in cellular processes. In structural biology, the most critical issue is the availability of high-quality samples. Thus "structural biology grade" proteins must be produced in a suitable quantity and quality allowing crystallization (screening for crystallization conditions) and structure determination. The purification procedure must be reproducible and yield homogeneous protein in milligram quantities. Therefore the choice of protein purification and quality control procedures play a key role in obtaining protein samples in sufficient amounts and with high purity.

Poly**C**ysteine and **H**istidine-**T**ailed protein (Ts-PCHTP) is a metalloprotein expressed in muscle larvae of nematode *Trichinella spiralis*. Metalloprotein is a term used for proteins (e.g. ferritin) which binds, transports or stores, metal ions or enzymes (metalloenzymes), in which the metal atom is involved in important catalytic processes. Ts-PCHTP is the first described member of a new nematode-specific protein family PCHTP – Poly-cysteine proteins, which are unique to Order Trichocephalida [1]. Ts-PCHTP binds different bivalent metal ions such as Fe, Ni and Zn. Its most probable function is transport or storage of the metal ions in the parasite. Heavy metal ions exhibit positive and negative effects on biological processes. On one hand they act as a cofactor for a number of enzymes, which catalyze numerous metabolic reactions. On the other hand, they can destroy the native structure of proteins or nucleic acids, which requires their detoxification. Proteins, which bind bivalent metal cations, contain specific amino acids (aa) sequences forming metal binding sites. These sequences contain numerous aa such as cysteine, histidine, methionine, serine, threonine, tyrosine, asparagine, glutamine, aspartate and glutamate [2, 3].

The *Ts-pchtp* gene length is 1896 *bp* [1]. It contains six exons and five introns. The nucleotide sequence of the mRNA comprises 1576 *bp*. The transcript has a single open reading frame consisting of 1272 *bp*. The primary structure of Ts-PCHTP includes 424 aa with a molecular weight of 47744 Da. Protein sequence shows a high content of the following amino acids: 36 cysteine (8.5%), histidine 26 (6.4%), 10 tyrosine and 8 tryptophan. The protein consists of a signal peptide for extracellular localization in

* To whom all correspondence should be sent:
E-mail: sbirkova@mail.bg

the N-term, two homologous polycysteine domains (pcd) – pcd-1 and pcd-2, poly-histidine domain (histidine tag) at the C-term. Another characteristic of the cysteine rich and metal binding proteins is predominantly β-structure [4, 5]. Ts-PCHTP is mainly characterized by β-structural conformation. It is typical for many metalloproteins that they can also bind specifically or nonspecifically hydrophobic ligands, such as fatty acids or hem [4, 6].

Poly-histidine regions are often associated with the binding of transition metal ions such as Ni^{2+}, Zn^{2+} Cu^{2+}, Co^{2+}, Mn^{2+}, Fe^{2+}, Fe^{3+}. These metal binding sites can be constructed either from consecutive histidine residues or repeats of histidine in combination with one to three aa between them [7–9]. The poly-histidine motifs common observed in the middle part of protein chain rather than C- and N-term (Histidine rich glycoproteins etc.).

The poly-histidine motif is one of the most frequently used in the purification of recombinant proteins (*his-tag* protein) [9]. Typically the construct (*his-tag*) is composed by six or more histidine residues, which are located in C-or N-term of a recombinant protein. The method is one of the most common and is based on the affinity of the histidine to bivalent metal ions. Purification was performed by metal affinity chromatography – Ni^{2+} or Co^{2+} chromatography.

In this study we present successful conditions for production of the recombinant Ts-PCHTP (r*Ts*-PCHTP) in *Escherichia coli* strains. Recombinant protein with natural His-tag at the C-end was obtained by metal affinity chromatography similarity to the common recombinant His-tag purification techniques. Purified r*Ts*-PCHTP was used for a crystallographic assay and Dynamic Light Scattering (DLS) analyses.

EXPERIMENTAL METHODS

cDNA synthesis and PCR amplification

The cDNA synthesis and amplification were performed as described by Radoslavov *et al.* [1]. Briefly, total RNA from *Trichinella spiralis* (T1 ISS03) muscle larvae was extracted after homogenization with Trizol reagent according to the manufacturer's instructions (Invitrogen).

Reverse cDNA transcription was performed with 4 μg of RNA, gene specific primer AS3 and M-MuLV Reverse Transcriptase (Fermentas). The nucleotide sequence from the second exon to the stop codon ORF of the Ts-TCHTP (GeneBank™ accession JF899252 and GQ497342) was amplified with the following primers: S22 5'-ggaattccatatga acaaaatttcgtcggccga-3' and AS3 5'-cgcggatccttatca atgatgatgatgatgatgatg-3', containing *Bam*HI and *Nde*I restriction sites for direct cloning into pJC20 expression vector [10]. PCR product and vector were ligated with T4-DNA Ligase (Fermentas) by standard protocol [11] and transformed into *Escherichia coli* DH5α cells. The positive colonies were checked by colony PCR and DNA sequencing (Macrogene).

Production and purification of recombinant protein

The *E. coli* BL21(DE3), C43(DE3) and Rosettagami(DE3) cells were used for the expression of the recombinant protein. The induction was performed with of 1 mM IPTG (final concentration), for 4 hours at 37 °C. Cells were lysed through sonication on ice. The soluble fraction contains Ts-PCHTP. In consequence Ni-affinity chromatography, HisTrap Kit (GE Healtcare BioSciences), was employed for rTs-PCHTP purification.

The protein concentration was determined initially by the method of Bradford [12] and spectrophotometrically using a molar extinction coefficient of 1.332 M^{-1} at 280 nm as calculated on the basis of the aromatic amino acid of 10 Tyrosine (Tyr) and 8 Tryptophan (Trp) residues with ProtParam tool [13] (www.expasy.org). Protein fractions were dialyzed with PD-10 desalting column, Sephadex G25 (Amersham Bioscience) against 0.02M Tris buffer, pH 7.2. The protein was concentrated up to 4 mg/ml with Centricon columns, 10kDa (Millipore).

The molecular size and purity of the protein was determined by 12% SDS-PAGE and 12% Native-PAGE [11]. Proteins were visualized by Colloidal Coomassie G-250 Blue Safe staining (National Diagnostics) (Fig. 1).

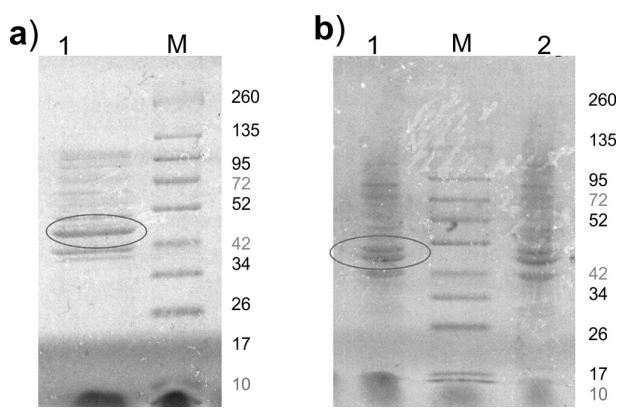

Fig. 1. a) 12% Native-PAGE gel of purified rTs-PCHTP lysate (elution with 0.05M EDTA) in to C43DE3 cells and b) 12% SDS-PAGE gel of purified rTs-PCHTP lysate (elution with 0.05M EDTA) in to C43DE3 cells. Proteins were visualized by Colloidal Coomassie Blue staining

Dynamic Light Scattering (DLS)

DLS measurements on the protein solutions were obtained using a 90Plus (Brookhaven Instruments), equipped with a 657 nm, 35mW laser. Time dependent fluctuations in the scattered intensity were measured using an avalanche photo detector (APD) and digital correlator. Protein solutions were analyzed in triplicate at 25.0 °C and scattering angle of 90°. The buffer solutions were filtered through 0.44 μm and 0.022 μm filters and were also analyzed by DLS. Standard NIST traceable polystyrene 22 nm ± 1.8 nm, 92 ± 2 nm latex standards and a blank, 0.02 μm filtered ultrapure water (Nanopure, Thermo Scientific), were also run as standards. Data was collected as co-added runs of 2 min collected for a total of 10 min. The autocorrelation functions were deconvoluted to obtain size distributions using both the non-negatively constrained least squares fit (multiple pass NNLS) algorithm. The size distributions obtained from the NNLS algorithm were presented since the distributions are bimodal. The intensity of scattered light is proportional to the particle size to the sixth power, which results in a higher scattered intensity for larger particles. The intensity weight distributions, measured by DLS, were converted to number weighted distributions using analysis software provided by Brookhaven (BIC).

Crystallographic conditions

Crystallization attempts were performed using the vapor-diffusion method, in which 1 μL of Ts-PCHTP (3.6 mg ml^{-1} in 0.02 M Tris 7.3 pH) solution was added to 1 μL of reservoir solution in a hanging drop suspended over 0.6 ml of reservoir solution. The reservoir (crystallization) conditions were those of the commercial Hampton Research Crystal screen HT, PEG/Ion and PEG/Ion 2.

RESULTS AND DISCUSSION

DNA sequencing of the pJC20 construct showed that the inserted fragment length is 1221 *bp*. Detailed analysis of the sequencing results showed that was the amplification and cloning, that the insert has an additional ATG initial codon at 5'end of the sequence. Thus the construct will translate 408 aa from the Native Ts-PCHTP (424 aa), with predicted molecule weight of 46 kDa. The 408 aa sequence includes the two full poly-cysteine domains and the poly His-Tag end, while the starting signaling peptide sequence is omitted. DNA sequencing showed also that the construct reading frame starts and ends correctly, so thus will allow subsequent expression.

The three *E. coli* bacterial strains were transformed with the expression vector: BL21(DE3), C43(DE3) and Rosetta-gami(DE3). The recombinant protein is isolated from soluble protein fraction under normal aerobic conditions, even that the cysteine constitutes 8.5% of all aa in Ts-PCHTP. 12% SDS-PAGE of bacterial lysates showed that only the C43(DE3) cells produced sufficient quantity of the recombinant protein (Fig. 2). The C43(DE3) cells are designed for expression of difficult or even toxic proteins. This suggests that Ts-PCHTP may be toxic due to its metal binding properties. Ts-PCHTP contains 26 histidine residues or 6.1% of the amino acid content in the protein. Fourteen histidine residues are localized in the C-terminus of the protein, which gives the name of the domain – poly-histidine tag. Seven consecutive histidine residues form a motif at the C-end of the protein. This histidine repeat at the C-term allows rTs-PCHTP to be purified with Ni-affinity chromatography (His Trap kit / GE Healtcare BioSciences). Sonication of C43(DE3) was performed in 10 mM imidazole pH 7.9, followed by centrifugation. The supernatant was used for loading on a HisTrap column. Attempting to elude the protein with high concentration of Imidazole (up to 1M) in some of the cases failed. The protein was successfully eluted with 0.05 M EDTA, pH 8.0. The concentration of the eluted protein was measured by Bradford [12] and spectrophotometrically at 280 nm. The molecular weight and purity of the protein was determined by 12% SDS-PAGE and 12% Native-PAGE. The protein is visualized on the gel at the expected molecular weight of 46 kDa (Fig. 1). The Native-PAGE showed better separation and single bands, in contrast to the SDS-PAGE, where multi bands

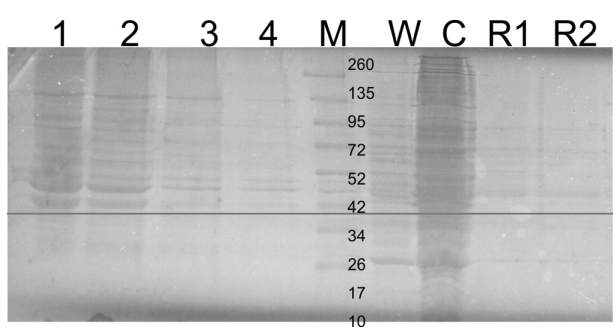

Fig. 2. 12% Native-PAGE of rTs-PCHTP lysate (elution with 0.05M EDTA): bands 1–4 correspond to C43DE3, M – protein marker, W – Wash cytosol after IPTG, C – Cytosol after IPTG, R1-R2 – rTs-PCHTP in Rosetta cells. Proteins were visualized by Colloidal Coomassie Blue staining

were visualized. This is an indication that the protein is more stable into non reductive conditions.

r*Ts*-PCHTP was used for DLS analysis to evaluate protein purity. The estimation of the molecular weight of rTs-PCHTP was carried out according to the Mark-Houwink-Sakurada equation $D = KM^a$ [15, 16] where D is the diffusion coefficient (assessed by DLS, $D = kT/(6\pi\eta R_h)$, M is the molecular weight and *K* and *a* are two empirically determined parameters that are solvent, temperature and protein specific. The molecular weight for the first size (peak of 39.4 nm) of the bimodal distribution corresponds to 110 kDa (Fig. 3b and 3c). This values is more than two time bigger than the theoretical one of 46 kDa. Thus the first peak in the size distribution can be related to a dimmer Ts-PCHTP. Although proteins generally fold into compact globular domains that are tightly packed (no voids or water molecules are accommodated in the interior of the protein) the surface of the protein is rather "bumpy" and is covered by an outer shell of water/solvent molecules. The DLS results for R_h will be affected by that shell and will overestimate the protein molecular weight. The second peak (82.6 nm, R_h of 41.3 nm) can be attributed to additional aggregation of Ts-PCHTP (octamer or dodecamer). As one can see from the multimodal distribution "number vs. diameter" the contribution of Ts-PCHTP dimmer is close to 100%, while the higher 8- or 12-mer is almost indiscernible (Fig. 3c).

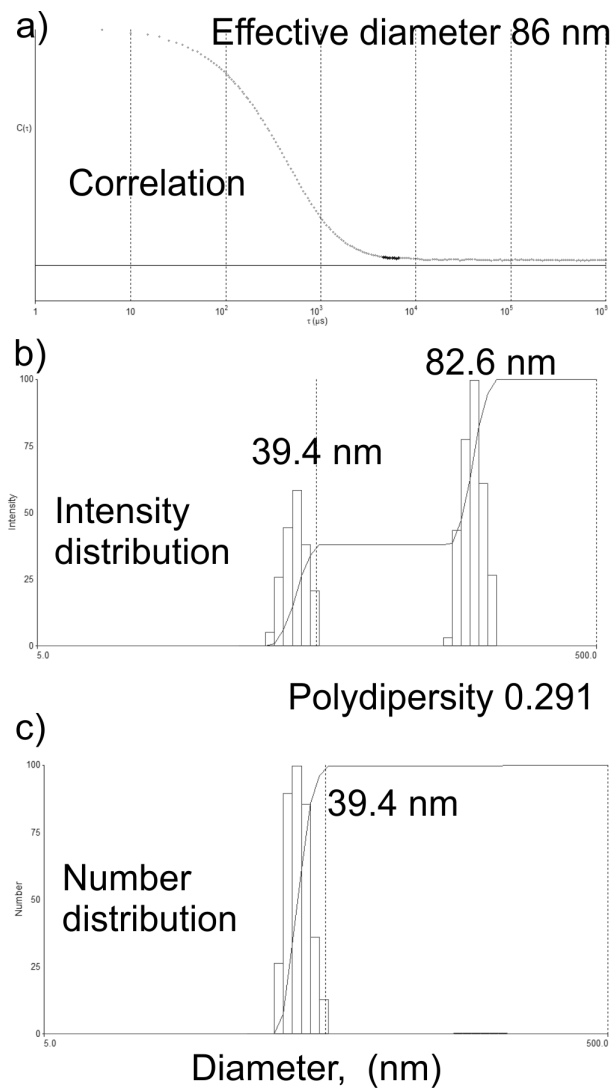

Fig. 3. Representative DLS for rTs-PCHTP 3.6 mg ml^{-1} in Tris pH 7.3 a) correlation function b) intensity particle size distribution and c) number particle size distribution

Preliminary crystallization results

The initial sparse matrix screening for Ts-PCHTP crystallization showed that the crystallization conditions listed in Table 1 are suitable for the growth of crystals for X-ray data collection (Fig. 4).

CONCLUSIONS

The present investigation provides insights into the heterologous expression, purification and crystallization of rTs-PCHTP. The protein was expressed and purified from soluble protein fraction at native condition. The purification of the rTs-PCHTP with Ni affinity chromatography is based of its nature poly his tag (7 histidine residues). Ts-PCHTP

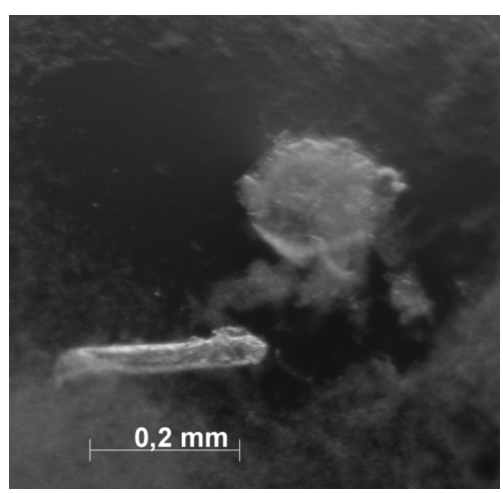

Fig. 4. Observed crystal of rTs-PCHTP, No 41 of Hampton Crystal screen 2

Table 1. Formulation of the crystallization conditions for Ts-PCHTP crystal growth

Hampton Screen	No	salt	buffer	precipitant
Crystal screen 1	46	0.2 M Ca acetate hydrate	0.1 M Na cacodylate trihydrate, pH 6.5	18% w/v PEG 800
Crystal screen 2	33	2M Ammonium formate	0.1M HEPES pH 7.5	
Crystal screen 2	41	0.01M Ni(II) chloride hexahydrate	1M Tris pH 8.5	1M Lithium sulfate monohydrate 0.
PEGI	2	0.2 M Potassium fluoride		20% w/v PEG 3350
PEGI	41	0.2 Potassium phosphate monobasic		20% w/v PEG 3350

describes for the first time a natural protein with this amino acid motif. DLS analysis showed that protein forms thoroughly dimmer formations which are not visualized at native gel conditions. There are identified several different suitable crystallization conditions for Ts-PCHTP. The data can be used for X-ray analysis.

Acknowledgments: *The authors thank the financial support of the Bulgarian National Science Fund through grant DRNF 02/1.*

REFERENCES

1. G. Radoslavov, R. Jordanova, D. Teofanova, K. Georgieva, P. Hristov, M. Salomone-Stagni, E. Liebau, I. Bankov, PLoS One, **5** (10), e13343 (2010).
2. D. Gregory, A. Martin, J. Cheetham, A. Rees, *Protein Engineering, Design and Selection*, **6**, 29 (1993).
3. M. Yamashita, L. Wesson, G. Eisenman, D. Eisenberg, *Proc. Natl. Acad. Sci*., USA, **87** (15), 5648 (1990).
4. D. Matthews, *Curr. Opin. Biotechnol*., **6** (4), 419 (1995).
5. N. Shu, T. Zhou, S. Hovmöller, *Bioinformatics*, **24** (6), 775 (2008).
6. L. Yi, Metalloprotein Design & Engineering. Encyclopedia of Inorganic Chemistry, Second Edition, ed. R. Bruce King, **5**, 3159 (2005).
7. A. Jones, M. Hulett, Immunol. *Cell Biol*., **83** (2), 106 (2005).
8. R. Garrett, C. Grisham, Biochemistry of Metal Ions. (Book Reviews: The Inorganic Chemistry of Biological Processes). *Science*, **4104**, 181, 1995, p. 1037.
9. P. Hengen, *Trends Biochem. Sci*., **20** (7), 285 (2005).
10. J. Clos, S. Brandau, *Protein Expr. Purif*., **5** (2), 133 (1994).
11. J. Sambrook, E. Fritsch, T. Maniatis, Molecular Cloning, A Laboratory Manual, 2nd edn. Cold Spring Harbor Laboratory Press, New York, USA, 1989.
12. M. Bradford, *Anal. Biochem.,* **72**, 248 (1976).
13. E. Gasteiger, C. Hoogland, A. Gattiker, S. Duvaud, M. Wilkins, Protein Identification and Analysis Tools on the ExPASy Server, in: John M. Walker (ed), The Proteomics Protocols Handbook, Humana Press, USA, 2005, p. 571.
14. P. Hiemenz, T. Lodge, Polymer Chemistry, Second ed. Boca Raton: CRC P, 336, (2007).
15. G. Borgstahl, *Methods Mol. Biol*., **363**, 109 (2007).
16. A. Ferre-D'Amare, S. Burley, *Structure*, **2**, 357 (1994).

КРИСТАЛИЗАЦИОННИ УСЛОВИЯ НА ХЕТЕРОЛОЖНО ЕКСПРЕСИРАН РЕКОМБИНАНТЕН МЕТАЛОСВЪРЗВАЩ БЕЛТЪК TS-PCHTP

Х. И. Сбиркова[1]*, Г. А. Радославов[2], П. И. Христов[2], Б. Л. Шивачев[1]

[1] Институт по Минералогия и Кристалография, Българска Академия на Науките, ул. „Акад. Г. Бончев“, бл. 107, 1113 София, България
[2] Институт по Биоразнообразие и Екосистемни Изследвания, Българска Академия на Науките, ул. „Акад. Г. Бончев“, бл. 25, 1113 София, България

Постъпила февруари, 2013 г.; приета май, 2013 г.

(Резюме)

В настоящата работа е оптимизирана експресията на протеин с полицистеинови домейни (Ts-PCHTP). Протеинът съдържа естествен фрагмент (His-Tag) за метална координация, използван в процеса на пречистване, чрез Ni афинитетна хроматография. Чистотата на белтъка се следи чрез нативна-полиакриламидна електрофореза, тъй като високото съдържание на цистеини в Ts-PCHTP протеиновата последователност води до подвеждащи резултати, когато се използвана техника с $CH_3(CH_2)_{11}OSO_3Na$ – полиакриламидна електрофореза. Според данните, получени чрез динамично светлоразсейване, се наблюдава димерната форма на Ts-PCHTP. За определяне на условията за кристализация на белтъка е използвана матрица от произволни условия за израстване на монокристали, подходящи за рентгеноструктурен анализ.

Bulgarian Chemical Communications, Volume 45, Number 4 (pp. 446–454) 2013

Crystal structure and properties of urea and thiourea adducts of tetraalkyl ammonium hydrogen sulphate

K. Kossev, H. Sbirkova, N. Petrova, B. Shivachev, R. Nikolova*

[1] *Institute of Mineralogy and Crystallography "Acad. Iv. Kostov", Bulgarian Academy of Sciences, acad. G. Bonchev str., building 107, 1113 Sofia, Bulgaria*

Received February, 2013; Revised May, 2013

Two inclusion complexes of tetraethylammonium hydrogen sulfate ($Et_4N.HSO_4$) with thiourea (TU) and urea (U) were prepared and characterized by X-ray diffraction (XRD) and differential thermal analysis (DTA). The crystal structures of the commercial salt $Et_4N.HSO_4$ (**1**) and both of the complexes $Et_4N.HSO_4.TU.H_2O$ (**2**) and $2Et_4N.2HSO_4.H_2SO_4.3U$ (**3**) were solved. Compounds **1** and **2** crystalize in the monoclinic $P2_1/n$ space group and compound **3** in the triclinic $P\bar{1}$ one. The cations and anions in **1** display a layered-like arrangement of alternating well-ordered tetraethylammonium cations and hydrogen-bonded hydrogen sulfate anions. In **2** and **3** the anionic layer is more complex and in addition to the hydrogen sulfate it includes thiourea and water or urea molecules, respectively. The thermal behavior of both adducts is more complicated than the one of $Et_4N.HSO_4$ and the melting temperature of the studied compounds decreases in the following order: **1** > **3** > **2**.

Key words: urea, thiourea; inclusion complex; hydrogen bonding; thermal decomposition.

INTRODUCTION

Tetraethylammonium salts are used as a source of tetraethylammonium ions (Et_4N) in pharmacological and physiological studies, but also in organic chemical synthesis and as structure-directing agents for synthesis of microporous materials [1, 2]. Besides, the urea and thiourea efficiency in formation of anionic host lattices is well defined due to the high dipole moment, planar geometry and good donor-acceptor properties of both molecules. A great number of urea and thiourea crystal complexes of different tetraethylammonium salts were synthesized aiming to study their crystal structures, phase transitions and temperature stability [3–10]. Varieties of host lattices were obtained depending on the combination of the employed anion and the number of urea/thiourea molecules. For instance, the inclusion complexes of $(Et_4N)C_4O_4$ with thiourea exhibit layered, one dimensional channel and two dimensional channel structures depending on the number of the incorporated thiourea molecules [11]. Many complex anions were employed including halides [12, 13], carbonate [14], perchlorate [15], borate [16], fumarate [17], etc. However, to date no structural information about the commercially distributed $Et_4N.HSO_4$ was reported [Cambridge Structural Database (CSD), 2011 release]. Moreover, bis(tetraethylammonium) hydrogen-sulfate dihydrogen-phosphate is the only reported compound containing both the Et_4N^+ and HSO_4^- ions. [18].

The present communication concerns the preparation of two new inclusion complexes of urea and thiourea with tetraethyl ammonium hydrogen-sulfate from aqueous or water/methanol solutions. The crystal structures of the studied compounds are discussed in relation to the differences in their thermal behavior.

MATERIALS AND METHODS

Synthesis

Tetraethylammonium hydrogen-sulfate, $Et_4N.HSO_4$ (**1**) is a commercial product and crystals suitable for single crystal X-ray diffraction measurements were obtained by slowly evaporation from water solution.

The other two compounds tetraethylammonium hydrogen sulfate thiourea hydrate, $Et_4N.HSO_4.TU.H_2O$ (**2**) and tetraethylammonium hydrogen-sulfate sulfonic acide ureate, $2Et_4N.2HSO_4.H_2SO_4.3U$

* To whom all correspondence should be sent:
E-mail: rosica.pn@clmc.bas.bg

(**3**) were obtained by slow evaporation from water solution of the components at room temperature:

$Et_4N.HSO_4.TU.H_2O$ (**2**): 0. 227 g (1.10^{-3} mol) $Et_4N.HSO_4$ and 0.078 g (1.10^{-3} mol) TU are dissolved in 20 ml of distillated water. The solution is slowly evaporated at room temperature leading to the formation of prismatic colorless crystals.

$2Et_4N.2HSO_4.H_2SO_4.3U$ (**3**): 0. 227 g (1.10^{-3} mol) $Et_4N.HSO_4$ and 0.060 g (1.10^{-3} mol) U are dissolved in 20 ml of distillated water. The solution is slowly evaporated at room temperature leading to the formation of prismatic colorless crystals.

Methods

XRD single crystal analyses: Crystals of the studied compounds were mounted on glass capillaries and diffraction data were collected at room temperature by ω-scan technique, on an Agilent Diffraction SuperNova Dual four-circle diffractometer equipped with Atlas CCD detector using mirror-monochromatized MoKα radiation from micro-focus source (λ = 0.7107 Å). The determination of cell parameters, data integration, and scaling and absorption correction were carried out using the CrysAlis Pro program package [19]. The structures were solved by direct methods (SHELXS-97) [20] and refined by full-matrix least-square procedures on F^2 (SHELXL-97) [20]. The non-hydrogen atoms were refined anisotropically and urea and thiourea hydrogen atoms were placed at idealized positions and refined using the riding model. The positions of hydrogen atoms of water molecule were calculated by DHA software [21]. A summary of the structural and refinement data is provided in Table 1. The data for publication were prepared using the program package WinGX [22]. Crystallographic data were deposited with the Cambridge Crystallographic Data Centre, CCDC No. 935080 (**1**) 93508 (**2**), 935082 (**3**). A copy of this information may be obtained free of charge from: The Director, CCDC, 12 Union Road, Cambridge, CB2 1EZ, UK. Fax: +44 1223 336 033, e-mail:deposit@ccdc.cam.ac.uk., or www.ccdc.cam.ac.uk.

Table 1. Crystal data and structure refinement results for the studied compounds

CCDC deposit number	1	2	3
Empirical formula	C8 H21 N O4 S	C9 H27 N3 O5 S2	C19 H56 N8 O15 S3
Moiety formula	C8 H20 N, O4 H S	C8 H20 N, H O4 S, C H4 N2 S, H2 O	3(O4 H S), 3(C H4 N2 O), 2(C8 H20 N)
Formula weight	227.32	321.46	732.9
Temperatute (K)	290(2)	290(2)	290(2)
Crystal system	Monoclinic	Monoclinic	Triclinic
Space group	P 2_1/n	P 2_1/n	P –1
a	9.7994(5)	9.4527(6)	7.4002(4)
b	13.812(3)	10.1222(6)	15.2365(8)
c	9.5968(17)	17.9932(11)	16.6134(8)
α	90	90	73.130(5)
β	89.368(15)	100.160(6)	88.137(4)
γ	90	90	84.630(4)
Volume (Å^3), *Z*	1190.2(4), 4	1694.63(18), 4	1784.71(16), 2
Calculated density (Mg m^{-3})	1.269	1.260	1.364
F(000)	496	696	788
Crystal color, shape, size (mm)	Colorless, prismatic 0.3 × 0.28 × 0.26	Colorless, prismatic 0.32 × 0.30 × 0.28	Colorless, prismatic 0.32 × 0.3 × 0.28
θ Range for data collection (deg)	2.95−29.58	3.52–29.12	2.99–29.45
Limiting indices *h*, *k*, *l*	$-12 \le h \le 11$, $-18 \le k \le 13$, $-11 \le l \le 13$	$-11 \le h \le 9$, $-13 \le k \le 10$, $-24 \le l \le 17$	$-10 \le h \le 9$, $-16 \le k \le 20$, $-22 \le l \le 22$
Reflections collected	6931	6277	14262
Independent reflections	2839	3513	7982
R_{int}	0.0446	0.0256	0.0438
Goodness-of-fit on F^2	1.058	1.047	1.019
Final *R* indices ($I > 2\sigma(I)$)	$R_1 = 0.0937$, $wR_2 = 0.2653$	$R_1 = 0.0681$, wR2 =0.1990	$R_1 = 0.0694$, $wR_2 = 0.1809$
R indices (all data)	$R_1 = 0.1308$, $wR_2 = 0.3061$	$R_1 = 0.1106$, $wR_2 = 0.2318$	$R_1 = 0.0958$, $wR_2 = 0.2082$
Largest diff. Peak/ hole (e Å^{-3})	0.873/ −0.574	0.652/ −0.277	0.957/ −0.498

Thermal analyses: Differential thermal analysis (DTA) and thermogravimetric measurements (TG) were carried out simultaneously in a thermal analyzer Stanton Redcroft 780 at the following conditions: heating rate of 10 °C/min, dry argon as a carrier gas, Al_2O_3 used as a referring material and sample weight of 8–10 mg.

RESULTS AND DISCUSSION

The asymmetric units of the studied compounds are shown in Figures 1, 2 and 3. Table 2 gives information about the bond distances and angles for HSO_4 group, urea and thiourea molecules in compounds **1**, **2** and **3**. The three dimensional packing of the discussed compounds and their hydrogen bonding systems are presented in Figure 4 and Table. 3.

Crystal structure of $Et_4N.HSO_4$ (**1**)

Figure 1 presents the asymmetric unit of compound **1**. It crystallizes in a monoclinic $P2_1/n$ space group and has pseudo orthorhombic lattice with a beta angle of 89.4°. The bond lengths and bond angles characterizing the Et_4N cation and hydrogen-sulfate anion agree with those reported previously [1–18] (Table 2.). There are four anions and four cations in the unit cell. The smaller hydrogen sulfate ion donates and accepts a hydrogen bond to form dimers. The dimers are arranged in layers parallel to $(10\bar{1})$ and are spaced at a distance of 6.53 Å (Fig. 4a, Tabl. 3). The larger Et_4N ions have a regular "Nordic cross" like shape with S_4 symmetry (Fig. 1). They are sandwiched between the anionic layers. Thus the 3D arrangement of $Et_4N.HSO_4$ is very similar to that in $2Et_4N.HSO_4.H_2PO_4$ [18] but the hydrogen-bonding network within the anionic layers is less extensive.

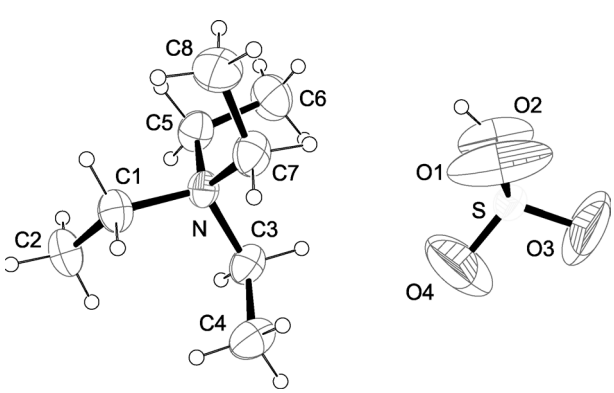

Fig. 1. ORTEP [23] view of complex ions in compound **1** with the atomic numbering scheme; ellipsoids are drawn at 50% probability; hydrogen atoms are shown as small spheres with arbitrary radii

Crystal structure of $Et_4N.HSO_4.TU.H_2O$ (**2**)

The TU adduct crystallizes as a neutral molecular adduct with one water molecule (Fig. 2). The crystal structure is monoclinic, space group $P2_1/n$ and there are four structural units per unit cell. The 3D arrangement is the same as in compound **1** and the larger Et_4N^+ ions are sandwiched between the layers built by hydrogen-sulfate anions and the rest of the molecules. As it is expected the TU and H_2O molecules are incorporated within the HSO_4^- layers

Table 2. Selected geometric parameters for the studied compounds. Bond lengths (Å)

Compound 1			
S – O(1)	1.409(5)	N – C(5)	1.505(5)
S – O(2)	1.515(4)	N – C(7)	1.512(5)
S – O(3)	1.310(5)	C(1) – C(2)	1.481(6)
S – O(4)	1.340(6)	C(3) – C(4)	1.497(7)
N – C(1)	1.515(5)	C(5) – C(6)	1.508(7)
N – C(3)	1.523(5)	C(7) – C(8)	1.504(8)
Compound 2			
S – O(1)	1.492(3)	C(11) – C(12)	1.529(8)
S – O(2)	1.435(3)	C(13) – C(14)	1.580(9)
S – O(3)	1.484(3)	C(15) – C(16)	1.574(9)
S – O(4)	1.433(3)	C(17) – C(18)	1.525(9)
N – C(11)	1.530(6)	S(1) – C(1)	1.696(4)
N – C(13)	1.474(7)	C(1) – N(11)	1.318(4)
N – C(15)	1.511(6)	C(1) – N(12)	1.326(4)
N – C(17)	1.554(7)		
Compound 3			
S(1) – O(11)	1.507(2)	C(11) – C(12)	1.514(5)
S(1) – O(12)	1.456(2)	C(13) – C(14)	1.509(7)
S(1) – O(13)	1.459(2)	C(15) – C(16)	1.505(5)
S(1) – O(14)	1.452(2)	C(17) – C(18)	1.499(6)
S(2) – O(21)	1.484(2)	C(21) – C(22)	1.516(6)
S(2) – O(22)	1.449(2)	C(23) – C(24)	1.507(6)
S(2) – O(23)	1.485(2)	C(25) – C(26)	1.499(6)
S(2) – O(24)	1.449(2)	C(27) – C(28)	1.499(6)
S(3) – O(31)	1.423(3)		
S(3) – O(32)	1.426(4)	O(1) – C(1)	1.289(4)
S(3) – O(33)	1.500(3)	O(2) – C(2)	1.302(4)
S(3) – O(34)	1.396(3)	O(3) – C(3)	1.302(4)
N(1) – C(11)	1.514(4)	C(1) – N(11)	1.325(4)
N(1) – C(13)	1.522(4)	C(1) – N(12)	1.314(4)
N(1) – C(15)	1.515(4)	C(2) – N(21)	1.295(4)
N(1) – C(17)	1.513(4)	C(2) – N(22)	1.304(4)
N(2) – C(21)	1.509(4)	C(3) – N(31)	1.305(4)
N(2) – C(23)	1.520(4)	C(3) – N(32)	1.310(4)
N(2) – C(25)	1.518(4)		
N(2) – C(27)	1.517(4)		

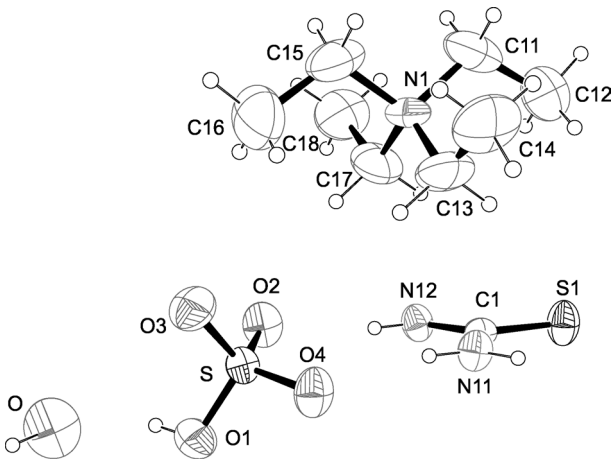

Fig. 2. ORTEP [23] view of complex ions and molecules in compound **2** with the atomic numbering scheme; ellipsoids are drawn at 50% probability; hydrogen atoms are shown as small spheres with arbitrary radii

and are involved in the hydrogen bonding network, which in this case is distributed over the whole layer (Fig. 4b, Table. 2). Thus, although the layer has similar thickness as in compound **1** the stacking is realized at a longer distance (7.64 Å in **2** versus 6.53 Å in **1**). This is accompanied with less compact shape of Et_4N ion exhibiting D2d symmetry in this structure (Fig. 2). The N….N distance between the closest Et_4N cations is 7.43Å, while the corresponding distance in compound **1** is 6.64 Å.

Crystal structure of $2Et_4N.2HSO_4.H_2SO_4.3Urea$ (**3**)

The asymmetric unit is presented in Figure 3. The organization of the crystal structure in this compound is very similar to that in **1** and **2**, but it crystallizes in triclinic P–1 space group. The sulfate groups and urea molecules are hydrogen bonded and built negatively charged layers, between which Et_4N^+ cations are situated. The hydrogen bonding network is presented in Fig. 4c. Hydrogen-sulfate groups and urea molecules are hydrogen-bonded to form anionic layers spaced at 8.30 Å from each other. The Et_4N cations are placed between the layers and the N…N distance between the closest ones is 7.40 Å. This is in agreement with the shape of Et_4N having D2d symmetry as in compound **2**. The structure determination shows a deficiency of Et_4N^+ ions and in order to balance the electro-neutrality of the compound it is assumed that it crystalizes with one molecule of sulfuric acid. However, this could not be confirmed by the X-ray diffraction data, because it was not possible to localize the positions of H atoms from the electron density map. On the other hand, the S-O distances for the symmetrically nonequivalent sulfate groups can give information about the presence of OH group because the corresponding S-O bond distance should be longer than the other three ones. This is actually the case for $(S2)O_4$ sulfate group only (Table 2). In contrast, the four S-O bonds in the $(S1)O_4$ and $(S3)O_4$ groups have similar lengths of about 1.46 Å. One possible explanation is that there is a migration of protons along the strong O-H…O hydrogen bonds formed between sulfate and urea oxygen atoms (Table 3). Besides, C-O distances in all of the urea molecules are longer than the standard C=O double bond (~1.2 Å) and have values of about 1.3 Å.

Table 2. Selected geometric parameters for the studied compounds. Bond lengths (Å)

Compound 1			
S – O(1)	1.409(5)	N – C(5)	1.505(5)
S – O(2)	1.515(4)	N – C(7)	1.512(5)
S – O(3)	1.310(5)	C(1) – C(2)	1.481(6)
S – O(4)	1.340(6)	C(3) – C(4)	1.497(7)
N – C(1)	1.515(5)	C(5) – C(6)	1.508(7)
N – C(3))	1.523(5)	C(7) – C(8)	1.504(8)
Compound 2			
S – O(1)	1.492(3)	C(11) – C(12)	1.529(8)
S – O(2)	1.435(3)	C(13) – C(14)	1.580(9)
S – O(3)	1.484(3)	C(15) – C(16)	1.574(9)
S – O(4)	1.433(3)	C(17) – C(18)	1.525(9)
N – C(11)	1.530(6)	S(1) – C(1)	1.696(4)
N – C(13)	1.474(7)	C(1) – N(11)	1.318(4)
N – C(15)	1.511(6)	C(1) – N(12)	1.326(4)
N – C(17)	1.554(7)		
Compound 3			
S(1) – O(11)	1.507(2)	C(11) – C(12)	1.514(5)
S(1) – O(12)	1.456(2)	C(13) – C(14)	1.509(7)
S(1) – O(13)	1.459(2)	C(15) – C(16)	1.505(5)
S(1) – O(14)	1.452(2)	C(17) – C(18)	1.499(6)
S(2) – O(21)	1.484(2)	C(21) – C(22)	1.516(6)
S(2) – O(22)	1.449(2)	C(23) – C(24)	1.507(6)
S(2) – O(23)	1.485(2)	C(25) – C(26)	1.499(6)
S(2) – O(24)	1.449(2)	C(27) – C(28)	1.499(6)
S(3) – O(31)	1.423(3)		
S(3) – O(32)	1.426(4)	O(1) – C(1)	1.289(4)
S(3) – O(33)	1.500(3)	O(2) – C(2)	1.302(4)
S(3) – O(34)	1.396(3)	O(3) – C(3)	1.302(4)
N(1) – C(11)	1.514(4)	C(1) – N(11)	1.325(4)
N(1) – C(13)	1.522(4)	C(1) – N(12)	1.314(4)
N(1) – C(15)	1.515(4)	C(2) – N(21)	1.295(4)
N(1) – C(17)	1.513(4)	C(2) – N(22)	1.304(4)
N(2) – C(21)	1.509(4)	C(3) – N(31)	1.305(4)
N(2) – C(23)	1.520(4)	C(3) – N(32)	1.310(4)
N(2) – C(25)	1.518(4)		
N(2) – C(27)	1.517(4)		

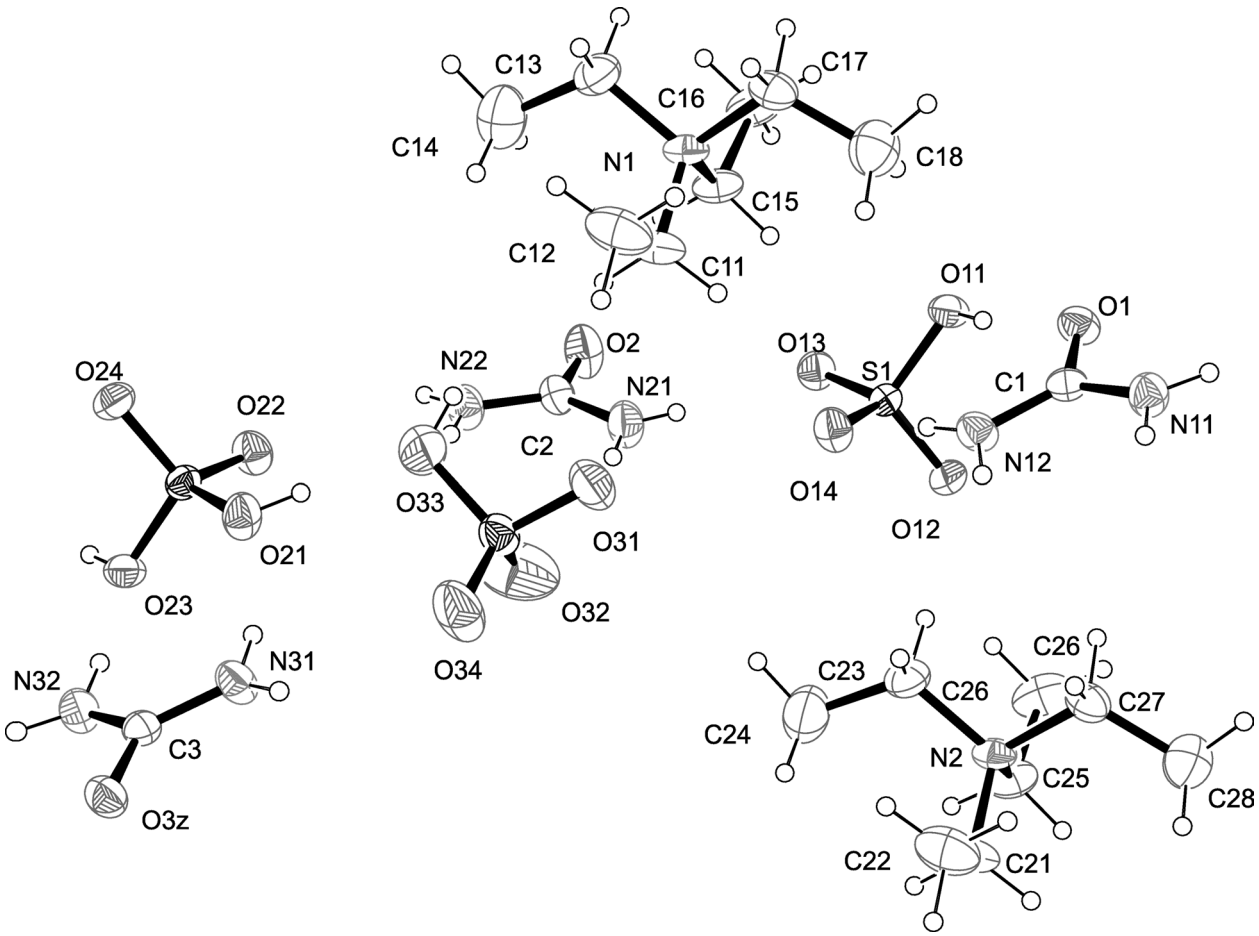

Fig. 3. ORTEP [23] view of complex ions and molecules in compound **3** with the atomic numbering scheme; ellipsoids are drawn at 50% probability; hydrogen atoms are shown as small spheres with arbitrary radii

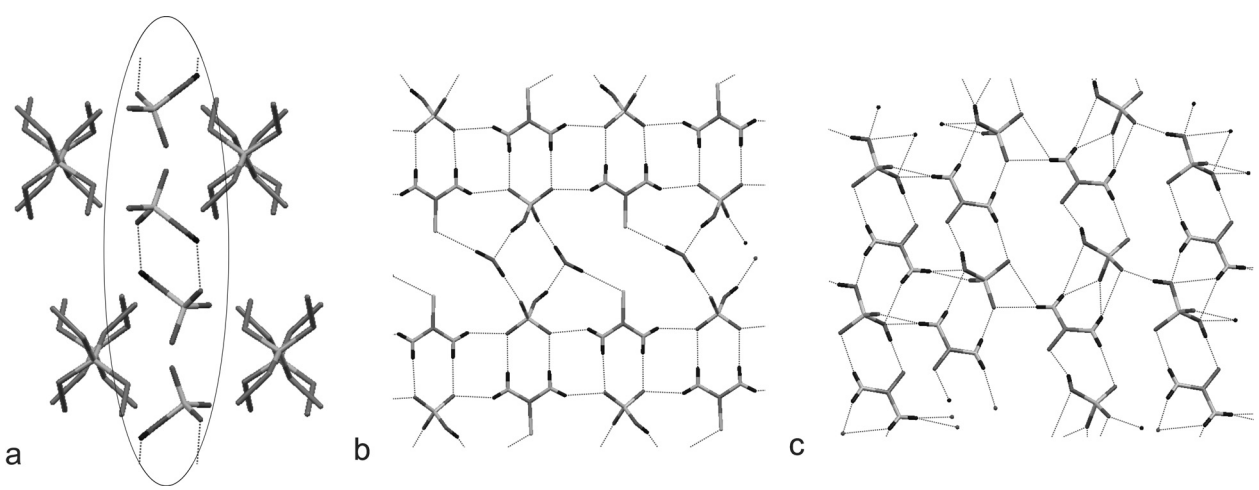

Fig. 4. Three dimensional packing and hydrogen bonding systems: a) stacking of cationic and anionic layers with hydrogen bonds between HSO_4 groups compound **1**; b) hydrogen-bonding system within the complex layer in compound **2**; c) hydrogen-bonding system within the complex layer in compound **3**

Table 3. Hydrogen-bond geometry (Å, °) for:

Compound 1				
D—H…A	*D—H*	H…A	D…A	D—H…A
O2-H2…O1^{i}	0.820	1.876	2.479	129.48
i: –x+1, –y +1, –z+1				
Compound 2				
D—H…A	*D—H*	H…A	D…A	D—H…A
O-H1…S1^{i}	0.960	2.490	3.450	179.60
O-H2…O3^{ii}	0.961	1.725	2.686	179.81
O1-H1A…O	0.820	1.864	2.644	158.32
N11-H11C…O4	0.860	2.127	2.977	169.51
N11-H11D…O2^{iii}	0.860	2.171	2.932	147.25
N12-H12D…O2	0.860	2.113	2.966	171.77
N12-H12E…O4^{iv}	0.860	2.145	2.916	149.12
i: –x+3/2, y–1/2, –z+1/2; ii: –x, –y+1, –z+1; iii: –x+3/2, y+1/2, –z+1/2; iv: –x+3/2, y–1/2, –z+1/2				
Compound 3				
D—H…A	*D—H*	H…A	D…A	D—H…A
O11-H11…O1	0.820	1.681	2.483	164.99
O21-H21…O33	0.820	1.706	2.512	167.15
O23-H23…O3^{i}	0.820	1.734	2.537	165.91
O31-H31…O2^{ii}	0.820	1.725	2.494	155.42
N11-H11C…O24^{iii}	0.852	2.079	2.920	168.75
N11-H11D…O11^{ii}	0.815	2.354	3.154	167.12
N12-H12D…O13^{ii}	0.805	2.047	2.851	176.37
N12-H12E…O14	0.813	2.036	2.830	165.22
N22-H22D…O32	0.812	2.133	2.920	163.27
N22-H22E…O34^{i}	0.794	2.505	3.143	138.46
N22-H22E…O33	0.794	2.558	3.294	154.93
N21-H21C…O13	0.745	2.130	2.875	176.81
N21-H21C…O14	0.745	2.657	3.124	122.75
N21-H21D…O32	0.743	2.238	2.926	154.45
N31-H31A…O21	0.874	2.051	2.896	162.17
N31-H31B…O22^{ii}	0.796	2.083	2.862	165.67
N32-H32A…O23	0.848	2.348	3.162	161.09
N32-H32A…O21	0.848	2.648	3.354	141.57
N32-H32B…O12^{iv}	0.816	2.049	2.856	170.33
i: x+1, y, z; ii: x–1, y, z; iii: x–1, y+1, z; iv: x, y–1, z;				

Thermal behavior

The thermal behavior of compounds **1**, **2** and **3** is investigated between room temperature and 400 °C using DTA-TG-DTG analysis (Fig. 5).

Compound **1**: DTA measurement shows a slow endothermic effect at 160 °C without loss of mass on the TG curve. Such kind of effect, assigned to phase transition, has been reported to be at 189 °C for tetramethylammonium sulfate [25] and in the interval 154–170 °C for tetraethylammonium tetrachloro-, bromotrichloro- and tribromochloroferrates(III) [26]. In the last work additional endo-effects corresponding to the melting point of the compounds are observed between 265–283 °C. However, in DTA curve of compound **1** similar effect cannot be clearly defined, because the melting and the main decomposition of the compound seem to occur simultaneously. These processes manifest a sequence of exo- and endo-effects maximizing at 297 and 330 °C, respectively, and are related to about 70% mass loss, which corresponds to a partial degradation. The described thermal behavior is rather similar to that in [26], where the thermal decomposition of tetraethylammonium salts had occurred in two main steps: first one, maximazing at 380–390 °C and corresponding to 60–79% mass loss and the second one – much slower, coming to an end at 700 °C and relating to the remaining sample mass loss.

The thermal behavior of compounds **2** and **3** (Fig. 5) becomes more complicated as compared with that of **1** and shows a complete degradation up to 400 °C. The first endothermic effect in the DTA curve (due to the melting of compounds without

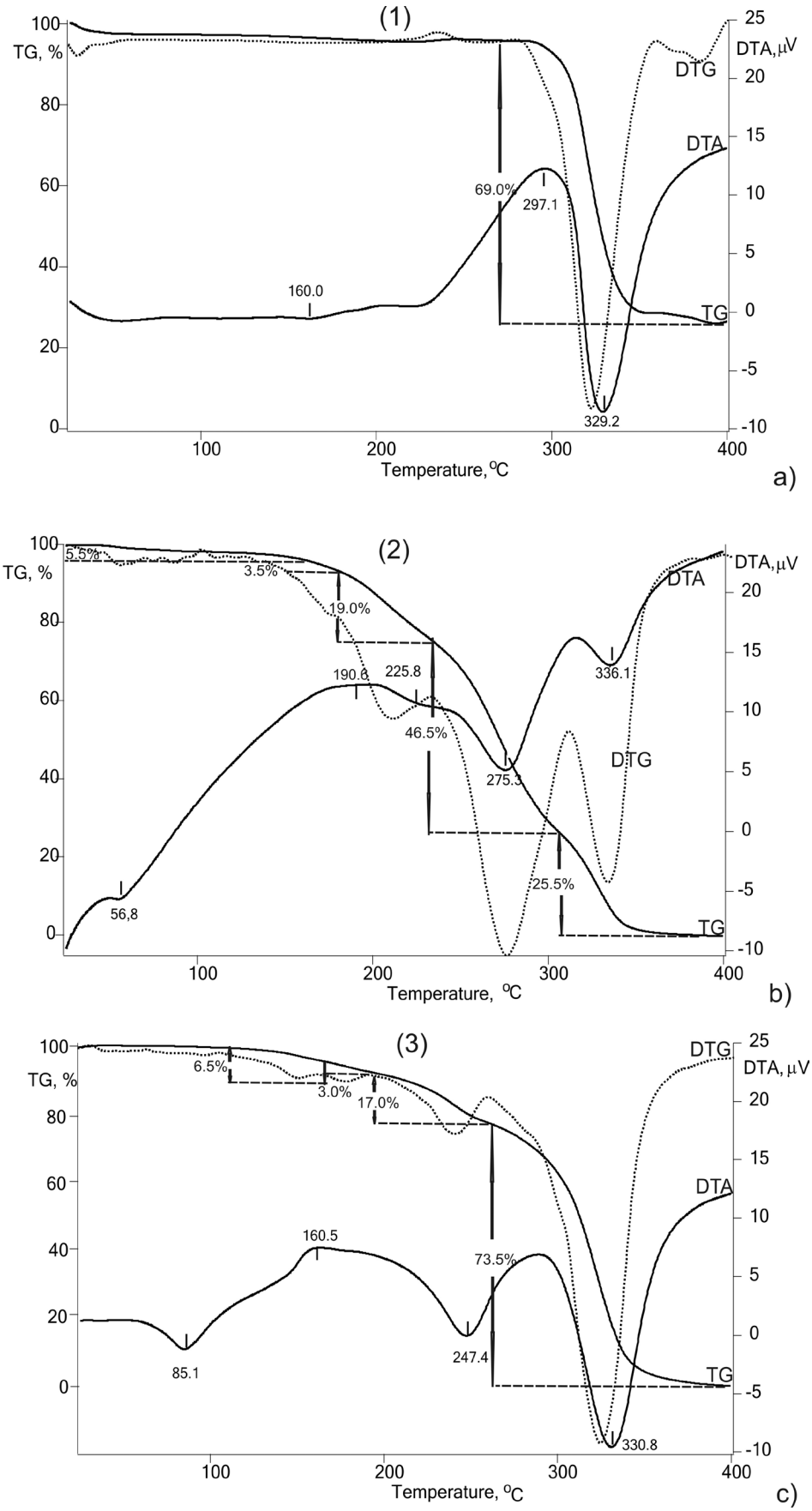

Fig. 5. DTA-TG-DTG curves: a) compound **1**; b) compound **2** and c) compound **3**

mass loss on the TG curves) of compounds **2** and **3** appears at 57 °C and 85 °C respectively, while the melting point of pure thiourea and urea has been observed respectively at 158 °C [27] and 132 °C [28]. Most probably, the presence of crystallization water in compound **2** decreases the melting temperature of that compound. At the same time the water in this sample continuously releases up to 150 °C with mass loss of about 5%, which corresponds to 1 molecule of H_2O (Fig. 5b). The melting temperature of the studied compounds decreases in the order: **1** > **3** > **2**.

As it is evident from the DTA-TG-DTG curves at least four events occur during the decomposition of both adducts being more clearly separated in compound **2** (Figures 5b and 5c). The process starts after the compound's melting with exothermal event on DTA curves following by series of endothermal events. These events manifest at lower tempereatures for the urea adduct (compound **3)** comparing with the thiourea one (compound **2)**.

The thermal degradation of tetraethylammonium salts has been investigated ever since the beginning of 20th century [29]. Two main ways of degradation have been defined both related to generation of a tertiary amine: beta degradation known also as "Hofmann degradation" and a nucleophilic substitution [30]. However, the decomposition processes of the studied compounds are more complicated due to the complex degradation of the HSO_4 group and the presence of Urea or Thiourea molecules.

CONCLUSIONS

Urea and Thiourea adducts of $Et_4N.HSO_4$ were synthesized and the crystal structures of the initial alkyl-ammonium salt and both adducts $Et_4N.HSO_4.TU.H_2O$ and $2Et_4N.2HSO_4.H_2SO_4.3U$ were solved. The structural analyses show that all three compounds have similar structures, where the large Et_4N cations are sandwiched between layers of hydrogen bonded anions or anions and molecules. The cation shape depends on the free space between the layers. In the initial alkyl-ammonium salt Et_4N has "Nordic cross" shape with 4s symmetry, while in both adducts it becomes less compact and has D2d symmetry.

The most complicated hydrogen bonding system with strong O–H…O bonds is observed in the Urea containing adduct. This supposes higher stability of that configuration compared to the thiourea compound, which is confirmed by the thermal analyses data. The structural features affect the melting point of the studied compounds and the observed melting temperature decreases in the following order: $Et_4N.HSO_4$ > $2Et_4N.2HSO_4.H_2SO_4.3U$ > $Et_4N.HSO_4.TU.H_2O$.

Acknowledgments: *This work was supported by Bulgarian National Fund of Scientific Research contract DRNF 02/1*

REFERENCES

1. M. Amany, A. Ibrahim, *Polyhedron*, **18(21)**, 2711 (1999).
2. J. Klinowski, P. J. Barrie in: *Studies in surface science and catalyses*, 1989, p. 19.
3. S. Mei; Z. Jinnan, L. Qi, *Acta Chim. Sinica*, **60(6)**, 1017 (2002).
4. Q. Li, F. Xue, T. C. W. Mak, *Inorg. Chem*., **38**, 4142 (1999).
5. T. C. W. Mak, R. K. McMullan, *Journal of inclusion phenomena*, **6(5)**, 473 (1988).
6. F. Xue, T. C. W. Mak, *Acta Cryst.*, **B56**, 142 (2000).
7. Q. Li, T. C. W. Mak, *J. Incl. Phenom. Mol. Recog. Chem.*, **20**, 73 (1995).
8. Q. Li, T. C. W. Mak, *Acta Cryst*., **B52**, 989 (1996).
9. Q. Li, T. C. W. Mak *J. Incl. Phenom. Mol. Recog. Chem.*, **28**, 151 (1997).
10. Y. V. Nelyubina, K. A. Lyssenko, D. G. Golovanov, M. Yu. Antipin, *Cryst. Eng. Comm*., **9**, 991 (2007).
11. C-K. Lam, T. C. W. Mak, *Tetrahedron*, **56**, 6657 (2000).
12. M. Ralle, J. C. Bryan, A. Habenschuss, B. Wunderlich, *Acta Cryst*., **C53**, 488 (1997).
13. M. A. Kandhaswamy, V. Srinivasan, *Bull. Mater. Sci*., **25(1)**, 41 (2002).
14. C-K. Lam, T. C. W. Mak. *Chem. Comm.*, 2660 (2003).
15. J. Kivikoski, J. A. K. Howard, P. Kelly, D. Parker, *Acta Cryst*., **C51**, 535 (1995).
16. Y. Yuan, Z. Jinnan, L. Surong, S. Xiaohong, L. Qi, *Front. Chem. China*, **2(3)**, 296 (2007).
17. Q. Li, T. C. W. Mak, *Acta Cryst*., **B53**, 252 (1997).
18. J. Fabry, R. Krupkova, I. Cisarova, K. Jurek, *Acta Cryst*., **C59**, o120 (2003).
19. Agilent. CrysAlisPro (version 1.171.35.15). Agilent Technologies Ltd, Yarnton England, (2010).
20. G. M. Sheldrick, *Acta Cryst*., **A64**, 112 (2008).
21. B. Shivachev, *Bull. Chem. Comm*., **45**(4), 461 (2013).
22. L. J. Farrugia, *J. Appl. Cryst*., **32**, 837 (1999).
23. L. J. Farrugia, *J. Appl. Cryst*., **30**, 565 (1997).
24. I. J. Bruno, J. C. Cole, P. R. Edgington, M. Kessler, C. F. Macrae, P. McCabe, J. Pearson, R. Taylor, *Acta Cryst*., **B58**, 389 (2002).
25. M. Malchus, M. Jansen, *Acta Crystal*., **B54**, 494 (1998).
26. N4. D. Wyrzykowski, A. Pattek-Janczyk, T. Maniecki, K. Zaremba, Z. Warnke, *Journal of Thermal Analysis and Calorimetry*, **91**, 279 (2008).
27. J. P. Chen, K. Isa, *J. Mass Spectrom. Soc. Jpn*., **46**, 299 (1998).
28. V. P. Timchenko, A. L. Novozhilov, O. A. Slepysheva, *Russian Journal of General Chemistry*, **74**, 1046 (2004).
29. V. Braun, *Ann*, **382(1)**, 1 (1911).
30. A. R. Katritzky, S. M. Roberts, in: *Comprehensive organic functional group transformations*, Otto Meth-Cohn, 1995, p. 627.

КРИСТАЛНА СТРУКТУРА И СВОЙСТВА НА УРЕА И ТИОУРЕА АДУКТИ НА ТЕТРАЕТИЛ АМОНИЕВ ХИДРОГЕН-СУЛФАТ

К. Косев, Х. Сбиркова, Н. Петрова, Б. Шивачев, Р. Николова*

Институт по минералогия и кристалография „Академик Иван Костов“,
Българска академия на науките, ул. академик Г. Бончев, бл. 107,
1113 София, България

Постъпила февруари, 2013 г.; приета май, 2013 г.

(Резюме)

Синтезирани са две съединения на тетраетил-амониев-хидроген сулфат ($Et_4N.HSO_4$) с тиоуреа (TU) и уреа (U). Първоначалния продукт тетраетил-амониев-хидроген сулфат ($Et_4N.HSO_4$) и двете нови съединения са характеризирани чрез рентгеноструктурен (XRD) и термичен (DTA-TG) анализи. Определени са кристалните структури на търговския продукт $Et_4N.HSO_4$ (**1**) и двете нови съединения $Et_4N.HSO_4.TU.H_2O$ (**2**) и $2Et_4N.2HSO_4.H_2SO_4.3U$ (**3**). Съединенията **1** и **2** кристализират в моноклинна пространствена $P2_1/n$, а съединения **3** в триклинна пространствена група $P\bar{1}$. Катионите и анионите в съединение **1** оформят слоисто-подобна структура в която се редуват слоеве от тетраетил-амониви катиони и свързани с водородни връзки хидроген-сулфатни аниони. Кристалните структури на новосинтезираните материали са подобни на тази на съединение **1**, но анионните слоеве има по-комлексен строеж, поради наличието на тиоуреа и вода или уреа молекули за съединения **2** и **3** съответно. Термичното поведение на двата адукта е по-сложно в сравнение с това на първоначалния продукт $Et_4N.HSO_4$, като температурата на топене на изследваните съединения намалява в посочената последователност: **1** > **3** > **2**.

Bulgarian Chemical Communications, Volume 45, Number 4 (pp. 455–460) 2013

Corrosive changes and chemical composition of the orthodontic archwires' surface during treatment

V. G. Petrov[1], S. D. Terzieva[2]*, Tz. I. Lazarova[3], V. Mikli[4], L. A. Andreeva[1], A. K. Stoyanova-Ivanova[2]

[1] *Faculty of Dental Medicine, Medical University Sofia, 1 St. St. Georgi Sofiiski Blvd., 1431 Sofia, Bulgaria*
[2] *Georgi Nadjakov Institute of Solid State Physics, Bulgarian Academy of Sciences, 72 Tzarigradsko Chaussee Blvd., 1784 Sofia, Bulgaria*
[3] *Institute of General and Inorganic Chemistry, Bulgarian Academy of Sciences, "Acad. Georgi Bonchev" str. bld.11, 1113 Sofia, Bulgaria*
[4] *Centre for Materials Research, Tallinn University of Technology, Ehitajate 5, Tallinn 19086, Estonia*

Received February, 2013; Revised May, 2013

The orthodontic archwires are an integral part of the fixed appliance used for treatment of orthodontic malocclusions. The chemical composition of the surface of three of the most frequently used archwires in orthodontic treatment worldwide and in Bulgaria is investigated, which consist of the following types of metal alloys: chromium-nickel stainless-steel, nickel-titanium, and titanium-molybdenum. The results of XRD, SEM and EDS show that the main element composition of the orthodontic archwires has not been changed for the examined residence time in the patient's mouth, which is an average of 6 and 10 weeks and the complex oral bacterial flora does not influence them.

Key words: orthodontic wires, XRD, SEM, EDX, surface chemical composition.

INTRODUCTION

The orthodontic wires are an integral part of the fixed appliance which is used to treat orthodontic malocclusions. The most frequently used archwires are made of the following alloys: chromium-nickel stainless steel, nickel-titanium, titanium-molybdenum and copper-nickel-titanium. Each of these alloys has its specific characteristics and the corresponding wires made by them possess the typical mechanical properties which enables choice in different treatment phases.

The orthodontic wires, made by stainless steel, classified by AISI (American Iron and Steel Institute) as type 304, are with chemical composition as follows: approximately 71% iron, 18–20% chromium, 8–11% nickel and quantities of carbon, manganese and silicon, respectively not exceeding 0.08%, 2% and 1% [1, 2]. Their mechanical properties are determined by the chemical composition and the microstructure and they are the most frequently used in their austenitic form. They are hard, elastic and have the smoothest surface, which leads to reducing of the friction between the wire and the brackets [3].

Nickel-titanium wires presented by Andreasen and Hilleman [4] in 1970 contain nearly equal amounts of nickel and titanium, respectively, 54–55% and 43-44%, and minimum amount of cobalt – 1.6–3%. They have very low modulus of elasticity and high elastic potential compared to the stainless steel and thus they are able to let out weak and continuous forces, which is desirable during the orthodontic treatment. These first wires are in martensite state and it is believed that they have curved monoclinic, three-clinic or hexagonal crystal structure [5]. They are known as non-super-elastic. The modern orthodontic nickel-titanium wires exist in the austenitic state with cubic crystal structure. They are called super-elastic and are able to undergo stress-induced transformation from austenite to martensite. When subjected to load or activated till elastic deformation they restore their shape approximately 8% of the initial [6].

* To whom all correspondence should be sent:
E-mail: mirolina@abv.bg

Later titanium-molybdenum wires are introduced (β-Ti, or TMA) [7], which are characterized by a high springy effect, low hardness, can be bent and directly soldered. The Element composition of these wires contains: 79% Ti, 11% Mo, 6% Zr and 4% Sn, and the adding of zirconium and zinc contributes to the strength and hardness of the arch. Their major disadvantage is the high friction coefficient.

A new generation of wires is the copper-nickel-titanium arches, which are known as orthodontic wires with shape memory, also called heat-activated. That's because they can be deformed in the martensite state but when increasing their temperature in the oral cavity a phase transformation is induced towards austenite and the form of the arch is returned to the original one [8].

The presented three types of orthodontic wires are used at certain treatment's stages with fixed equipment. They stay in the mouth a certain period, during which they are exposed to the aggressive environment of the oral cavity. The latter is characterized by the presence of complex oral microflora, which together with its bioproducts forms and accumulates plaque around the material [9]. Also the impact of food that the patient used, the type of tooth pastes and the temperature changes occurring in the oral cavity should not be overlooked. All this leads to changes in the surface characteristics of the retrieved orthodontic archwires.

It is established that the surface of the orthodontic wires is covered by the formed intraoral protein coat which covers up their topographic surface to a degree depending on the individual patient's oral circumstances and on the intraoral exposure period. The film's organic components founded on alloy's surface are amide, alcohol and carbonate while the predominant elements are sodium, potassium, chloride, calcium and phosphorus [10].

In the present study are considered three types (chromium-nickel stainless steel, nickel-titanium, titanium-molybdenum) orthodontic archwires and the changes in the chemical composition of the surface are observed when these wires are used for treatment.

MATERIAL AND METHODOLOGY

The research is on the orthodontic archwires of patients treated in 2012 by researchers – orthodontists. In relation to the study's objectives we provided the tested three main types of orthodontic wires in 3 pieces each, Table 1. The type A wires are with circular cross section 0.016 inches, and the remaining B, and C have a rectangular cross section – 0.016×0.022 inches. These are some of the most commonly used wires as a size and type that are offered by the distributors to the orthodontists in Bulgaria. The treatment of patients with orthodontic malocclusions is carried out with them as at certain treatment's stage the appropriate type and size wires are placed. Two wires are used of each type, which are compared with the corresponding starting wires, called control ones. The selected wires are used for the treatment and stayed in the patient's mouth, respectively 6 and 10 weeks. This period covers the average time of residence of the orthodontic wires at the mouth of the patient in order to perform a certain stage of orthodontic treatment. All wires, after removal from the patient's mouth, they are cleaned with disinfectant and placed in a resealable plastic bag each along with a note in which the following data is recorded: patient's name, his age, wires' type, the size, date of placement, date of removal, the total time of stay in the mouth.

Table 1. Characteristics of investigated orthodontic wires

Type of orthodontic wires	Cross section [inches]	Time of residence in the mouth
A – stainless steel, AISI 304*	0.016	A6 – 6 weeks A10 – 10 weeks
B – nickel-titanium alloys	0.016 × 0.022	B2 – 2 weeks B6 – 6 weeks B10 – 10 weeks
C – beta-titanium alloys	0.016 × 0.022	C6 – 6 weeks C10 – 10 weeks

The studied wires were analyzed by X-ray dispersive analysis (EDS), X-ray powder diffraction and scanning electron microscopy (SEM). Powder X-ray diffraction patterns were collected within the range from 5.3 to 80° 2θ with a constant step 0.02° 2θ on Bruker D8 Advance diffractometer with CuKα radiation and LynxEye position sensitive detector. Phase identification was performed by the program DiffracPlus EVA using ICDDPDF-2 (2009) database. The microstructure of the wires surface was studied by means of Zeiss EVO MA-15 scanning electron microscope (SEM) with LaB_6 cathode on the polished cross-section samples. The chemical composition was determined by the X-ray microanalysis using the energy dispersive spectroscopy (EDS) method and Oxford Instruments INCA Energy system. The qualitative and quantitative analyzes were carried out at an accelerating voltage 20 kV, an optimal condition for these samples.

RESULTS AND DISCUSSION

XRD patterns of the orthodontic archwires from the type A are amorphous, these of type B and C

are presented in Figure 1a) and 1b) respectively. On Fig. 1a) it can be seen the peaks of a crystalline phase marked with asterisk. The peaks correspond to the NiTi alloy with composition $Ni_{1.02}Ti_{0.98}$ (ICDDPDF#65-5746) with cubic type structure S.G. Pm-3m and unit cell parameter 3.01Å. For the peaks of the alloy presented in Fig. 1b) the best correspondence was found with a hexagonal phase (Ti_2Sn) with unit cell parameters a = 4. 65 Å and c = 5.7 Å. It is worth nothing that an amorphous hump is seen of the diffraction patterns of arches after prolonged usage for patient treatment. This amorphous part comes not only from corrosion processes on the wires surface but mostly from organic residues. The formed biofilms and calcification layers are well adsorbed to the wire surface and may play protective role towards the alloy surface. It should be mentioned that the presence of such films as well as their thickness and composition do not correlate well with the time of the wires application. The quality of the film is also patient dependant. These differences are mainly related to the nourishing traditions, composition of the saliva and the hygienic habits.

The information about the change in the surface morphology of the orthodontic wires is obtained by scanning electron microscopy (SEM), Fig 2. The observed change in the surface of the archwires is studied in details through energy dispersion study (EDS). The method used allows quantitative identification of the chemical composition by elements and focuses on the corrosion changes of the alloy rather than commenting on the complex oral flora. In Table 2 are presented the average values of the main components contained in the wires' alloy (Fe, Cr, Ni, Si and Mn) as well as the identified inclusions (P, S, Cl, K, Ca). For comparison are used the data of the studied as-received wires. The results indicate that the presence of the inclusions are as a result of the oral bacterial flora and of the oral hygiene

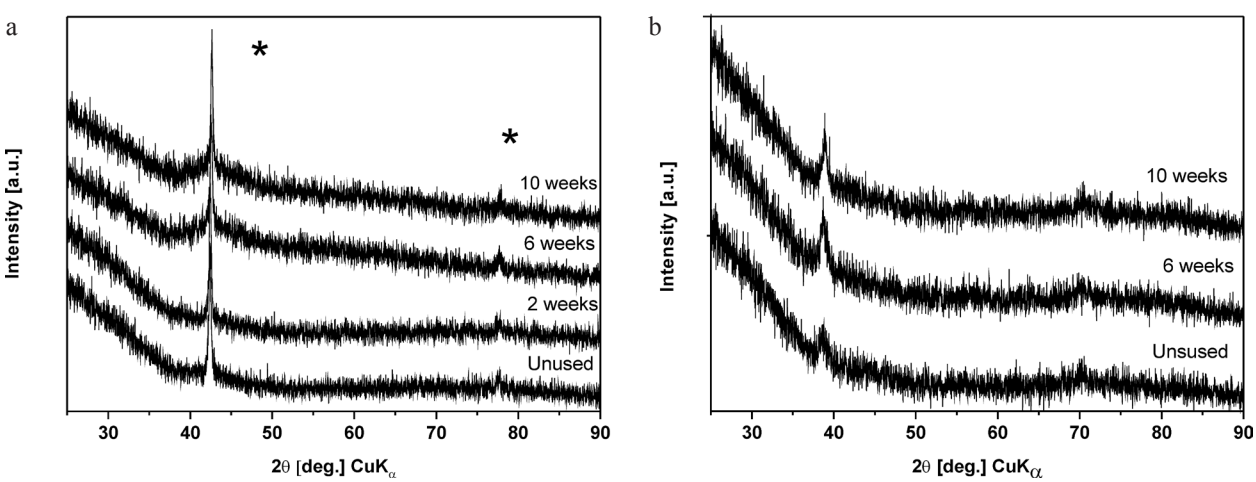

Fig. 1. a) XRD patterns of the orthodontic archwires type B at different stages of treatment; b) XRD patterns of the orthodontic archwires type C at different stages of treatment

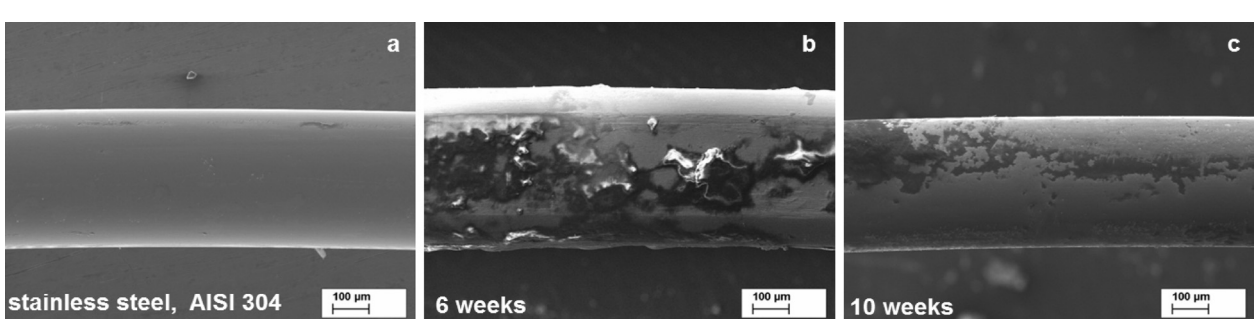

Fig. 2. Scanning electron microscopy images of A-austenitic stainless steel wires with cross section 0.016 inches: a) – as-received (A); b) – 6 weeks retrieved wire (A6) and c) – 10 weeks retrieved wire (A10)

Table 2. Elements content in new wire type A-stainless steel and used ones after 6 and 10 weeks

Elements, weight %	Si	Cr	Mn	Fe	Ni	P, S, Cl, K, Ca
Initial components content (new wire)	0.67	19.48	1.4	70.19	8.26	–
Mean components content after 6 weeks treatment	0.86	19.51	1.51	69.63	8.39	1.75
Mean components content after 10 weeks treatment	0.85	19.44	1.49	69.70	8.38	2.89

of the patient, while the main element composition of the orthodontic archwires from the stainless steel does not change for the examined period of treatment (6 and 10 weeks).

The second type of studied orthodontic wires is composed of nickel and titanium in almost equal amounts. Figure 3 shows the structure (3a) and the spectrum of the performed integral analysis of the element content by EDS (3b) of the as-received wires. The analysis confirms the two-component composition of nickel (54.67 wt.%) and titanium (45.38 wt.%).

After the usage of the wires correspondingly 6 and 10 weeks, which is shown in Figure 4, again changes of the surface are observed, which are associated with the presence of oral plaque. The presented scanning microscopical pictures are of selected areas of the wires' surface, where a point element analysis is made. The average values of the element composition are shown in Table 3. The quantity of nickel and titanium is not changed during the time of use. On the wires' surface that has stayed in for 10 weeks are observed surface irregularities, Figure 4c, which we assume, are as

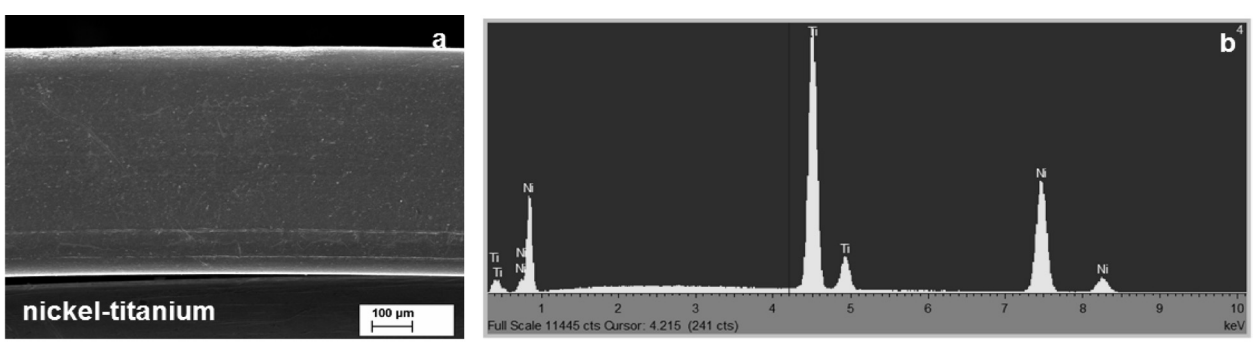

Fig. 3. Scanning electron microscopy images of as-received nickel-titanium wire and EDS spectrum of wire

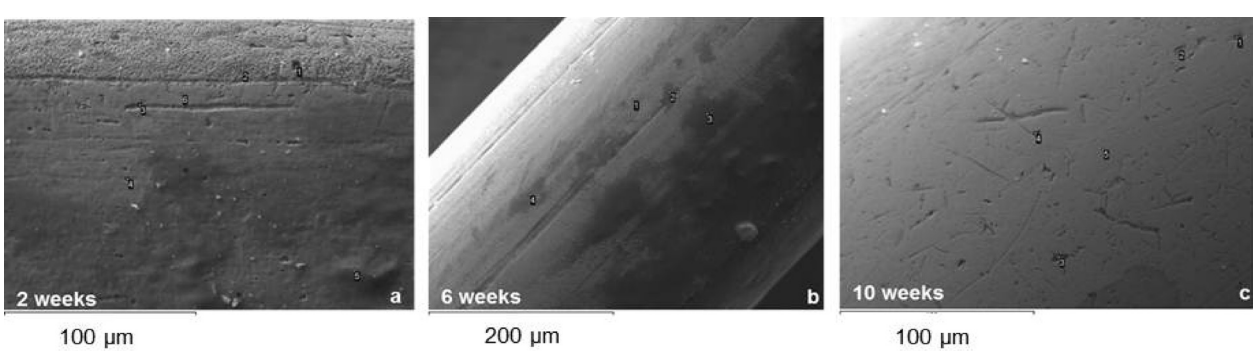

Fig. 4. Scanning electron microscopy images of retrieved nickel-titanium wires: a) – 2 weeks retrieved wire (B2); b) – 6 weeks retrieved wire (B6) and c) – 10 weeks retrieved wire (B10)

Table 3. Elements content in new wire type B – nickel-titanium alloys and used ones after 2, 6 and 10 weeks

Elements, weight %	Ni	Ti	Al, P, S, Cl, K, Ca
Initial components content (new wire)	54.67	45.38	–
Mean components content after 2 weeks treatment	54.85	45.16	2.06
Mean components content after 6 weeks treatment	54.33	45.48	1.48
Mean components content after 10 weeks treatment	54.74	45.30	0.22

a result of mechanical action. According to some authors [11] such surface alterations may be caused by loads during chewing. It is difficult to trace and investigate the corrosion according to the treatment's time stage and the wires' residence in the mouth due to the individuality of each patient (type of food, hygiene, age, gender, etc.). As an example we will point out the carried out analysis of nickel - titanium archwires used only for 2 weeks (B2), in which there is a large percentage of accumulated plaque on the surface in comparison with those used for 6 and 10 weeks, Fig. 4a, Table 3. From the analysis it appears that the coating deposits cannot be regarded as foci of corrosive change in wires. In-depth research on the mechanical resistance is about to be made.

Figure 5 shows the structures of titanium-molybdenum orthodontic archwires, respectively, 5a – as-received, 5b – after 6 weeks, and 5c, after 10 weeks of use. The determined chemical composition by EDS analysis is presented in Table 4. The trend to maintain the main components of the alloy (Ti, Mo, Zr, and Sn) is also observed in this type of orthodontic wires. The element study of the wires surface's changes indicate the presence of Na, Ca, Cl, which is associated with biofilm formation and

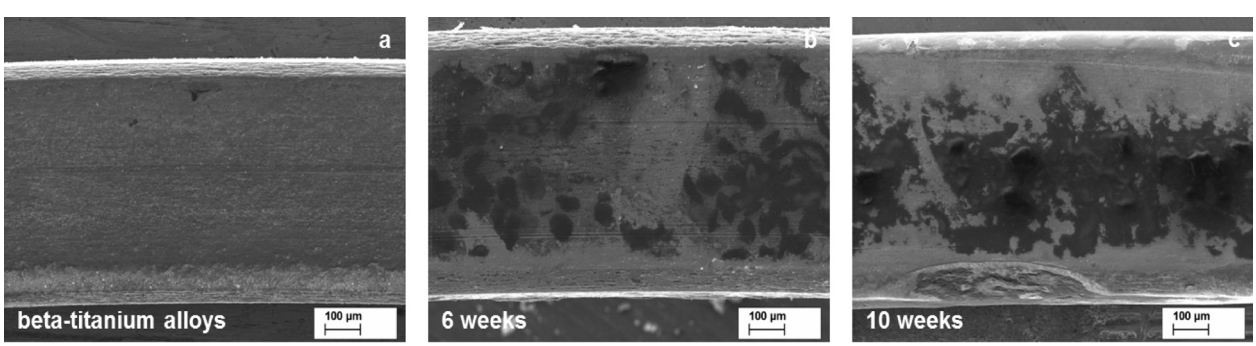

Fig. 5. Scanning electron microscopy images of retrieved beta-titanium wires with cross section 0.016×0.022 inches: a) – as-received (C); b) – 6 weeks retrieved wire (C6) and c) – 10 weeks retrieved wire (C10)

Table 4. Elements content in new wire type C beta – titanium alloys and used ones after 6 and 10 weeks

Elements, weight %	Ti	Zr	Mo	Sn	Na, Cl, Ca
Initial components content	76.90	6.36	11.87	4.86	–
Mean components content after 6 weeks treatment	76.80	7.11	11.45	4.65	0.52
Mean components content after 10 weeks treatment	77.09	6.54	12.4	3.95	4.27

does not contribute to a change of the initial wires' chemical composition.

CONCLUSION

The studied orthodontic archwires made of stainless steel, nickel-titanium and titanium-molybdenum is essential in orthodontic treatment. The analyses made and the achieved results show chemical resistance of all three wires. The orthodontic archwires are under continuous influence of the saliva, which is different from patient to patient and depends on the age, the hygiene of meal, the individual oral hygiene, which determines the plaque quality in the oral cavity, the presence of different diseases. From the carried out tests it is established that the complex oral flora, regardless of the changes it is subjected to according to the above described factors, it does not alter the major components of the alloys, which make them biocompatibility to the patient.

REFERENCES

1. R. S. de Biasi, A. C. O Ruela, C. N. Elias, O. Chevitarese, *J. Mater. Res*., **3**, 97 (2000).
2. W. A. Brantley, Orthodontic materials: scientific and clinical aspects, Stuttgart, New York, Thieme, 2001.
3. T. Eliades, et al., *Europ. J. Orthod*., **22**, 317 (2000).
4. G. F. Andreasen, T. B. Hilleman, *J. Am Dent. Assoc*., **82**, 1373 (1971).
5. R. P. Kusy, *Angle Orthod*., **67**, 197 (1997).
6. S. A. Thompson, *Int Endod J*., **33**, 297 (2000).
7. A. J. Goldberg, C.J. Burstone, *J. Dent. Res*., **58**, 593 (1979).
8. D. K. Pun, D. W. Berzins, *Dent. Mater.*, **24**, 221 (2008).
9. G. Eliades, T. Eliades, M. Vavuranakis, General aspects of biomaterials' surface alterations following exposure to biological fluids, D. C. Watts (ed.), Chicago, Quintessence, 2003.
10. T. Eliades, C. Bourauel, *Am J Orthod Dentofacial Orthop*., **127**, 403 (2005).
11. O. Prymak, A. Klocke, B. Kahl-Nieke, M. Epple, *Mater Sci Eng A*., **378**, 110 (2004).

КОРОЗИОННИ ПРОМЕНИ В ХИМИЧНИЯ СЪСТАВ НА ПОВЪРХНОСТТА НА ОРТОДОНТСКИ ДЪГИ ПРИ ИЗПОЛЗВАНЕТО ИМ ЗА ЛЕЧЕНИЕ

В. Г. Петров[1], С. Д. Терзиева[2]*, Ц. И. Лазарова[3], В. Микли[4], Л. А. Андреева[1], А. К. Стоянова-Иванова[2]

[1] Факултет по дентална медицина, Медицински Университет – София, Бул. „Св.Св. Георги Софийски“ 1, 1431 София, България, vpetrov@dentist.bg
[2] Институт по физика на твърдото тяло „Акад. Георги Наджаков“, Българска Академия на Науките, Бул. „Цариградско шосе“ 72, 1784 София, България, mirolina@abv.bg; aksi_bg@abv.bg
[3] Институт по органична и неорганична химия, Българска Академия на Науките, ул. „Акад. Георги Бончев“, бл. 11, 1113 София, България
[4] Център за изследване на материали към Технически Университет – Талин, Ehitajate 5, 19086 Талин, Естония

Постъпила февруари, 2013 г.; приета май, 2013 г.

(Резюме)

Ортодонтските дъги са неразделен елемент от фиксираната техника, използвана за лечение на ортодонтските деформации. Изследван е химичния състав на повърхността на три от най-използваните дъги за лечение в България, състоящи се от следните видове метални сплави: хром-никелова неръждаема стомана, никел-титан, титан-молибден и мед-никел-титан. Всяка една от тези сплави има своите специфични характеристики и направените от тях съответни дъги притежават характерни химични и механични свойства, давайки възможност за избор при употребата им в различните етапи от лечението. Резултатите от направените рентгенови и морфологични повърхностни изследвания показват, че основният химичен състав на ортодонските дъги не се променя в периода на лечение, който е между 2, 6 и 10 седмици. Наличието на химични примеси и отлагания се свързва с индивидуалната бактериална микрофлора в устната кухина на всеки пациентит.

Bulgarian Chemical Communications, Volume 45, Number 4 (pp. 461–465) 2013

DHA, a program for calculating hydrogen atom coordinates of solvent atom involved in hydrogen bonding interactions

B. Shivachev

Institute of Mineralogy and Crystallography, Bulgarian Academy of Sciences,
"Acad. Georgi Bonchev" str. building 107, Sofia 1113, Bulgaria

Received February, 2013; Revised May, 2013

Generally it is difficult to locate hydrogen atoms accurately using X-ray data because of their low scattering power and lack of core electrons. For many purposes the hydrogen positions can be calculated according to well-established geometrical criteria. Nevertheless, in some cases the positioning of the hydrogen atoms is tricky. Usually the problem arises when solvent molecules (e.g. water, OH groups or ammonia) are present in the crystal structure. Fortunately, hydrogen bonding interaction are characterized by an appropriate geometry and distance between the donor (**D**) and acceptor (**A**) atoms and requires the participation/presence of a hydrogen atom (D – H ••• A). Thus, if the coordinates of the donor and acceptor atoms are known one can calculate the coordinates of the "elusive" hydrogen atom. The program DHA uses an extremely simple mathematical apparatus to produce the coordinates of the hydrogen atom (**H**) participating in a D – H ••• A type of interaction.

Key words:

INTRODUCTION

Nowadays, single crystal X-ray data collection and structure solution has become a very accessible, popular and routine experimental technique. Interestingly, the most popular software, ShelX [1] used for structure solution and refinement has remained almost untouched since 1993, although 1997 and 2013 versions are available (Shelx, 2013). Various graphical user interfaces (GUI) were designed and implemented over the years to circumvent the "tedious" text typing, editing and manipulation of the input (*.ins) and output (*.res) files of Shelx programs [2, 3]. Certainly, several other free and commercial [4–6] software packages are available to the end-user but as the standard is set by ShelX most of the features are similar to those implemented in ShelX. One of the very few elusive options in those programs is the positioning of H atoms when suitable geometrical criteria fail and electron density from difference Fourier is not available. Usually the problem arises for solvent (water, OH, NH_3 etc.) atoms/molecules that are present in the crystal structure. However, if suitable hydrogen bonding geometry and distance (directionality) between such atoms (D ••• A) is detected the hydrogen atom should also be present. The DHA program targets the calculation of hydrogen atoms' coordinates when hydrogen bonding interaction criteria are encountered but the usual positioning of the hydrogen atom is either impossible or inaccurate.

METHODS

The mathematical apparatus required for the calculation of the H atoms coordinates is extremely simple. The distance D_{12} between two atoms A1 (with coordinates *x1, y1, z1*) and A2 (coordinates *x2, y2, z2*) can be calculated as:

$$D_{12} = \sqrt{(x1 - x2)^2 + (y1 - y2)^2 + (z1 - z2)^2} \quad (1)$$

The coordinates of the atom A_{mid} lying exactly in the middle between A1 and A2 are easily obtained:

$$x_{mid} = \frac{x1 + x2}{2}, y_{mid} = \frac{y1 + y2}{2}, z_{mid} = \frac{z1 + z2}{2} \quad (2)$$

The distance between A1 and A_{mid} (or A_{mid} and A2) can be obtained according to *eq.* 1. Using the

* To whom all correspondence should be sent:
E-mail: blshivachev@gmail.com

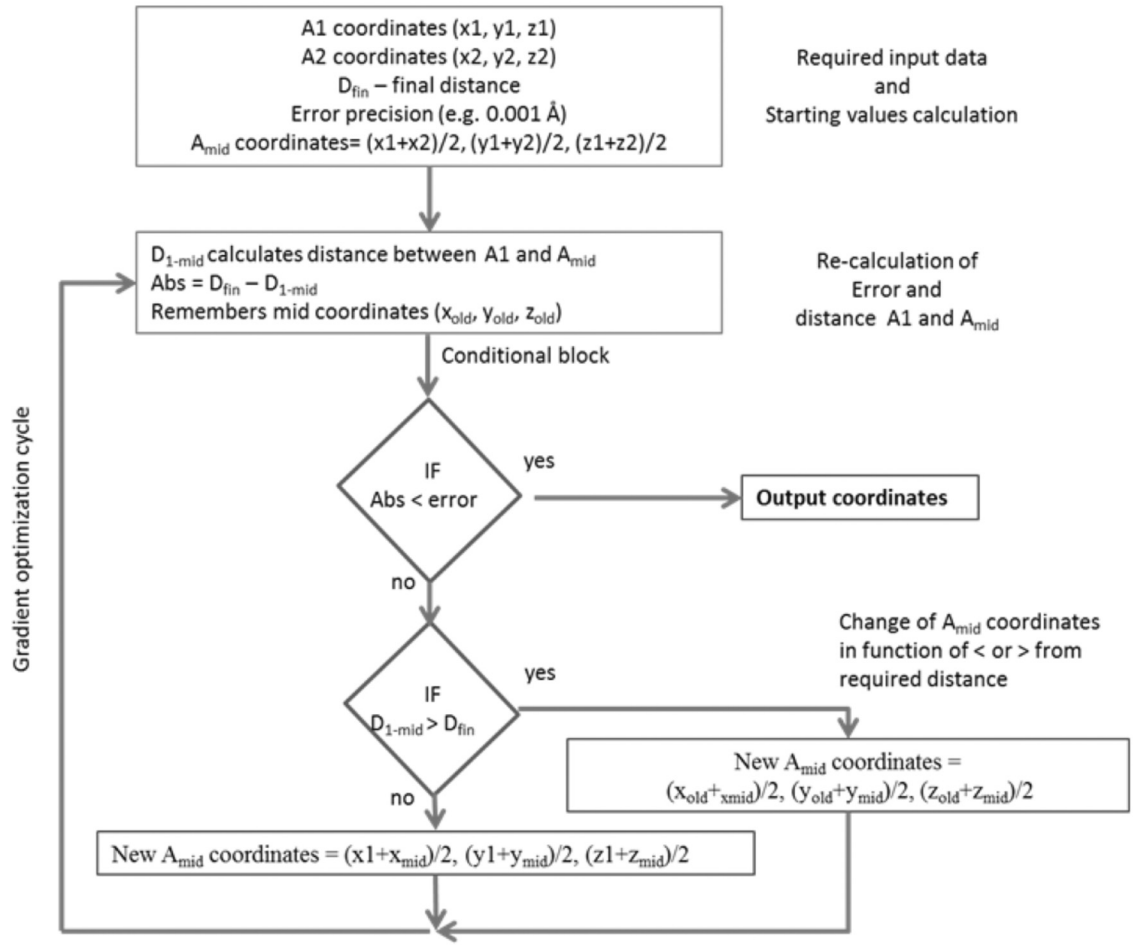

Fig. 1. Scheme of the algorithm of DHA program

coordinate descendent method [7] one can obtain the coordinates (within a predetermined error) of an atom located at the required distance from A1 (A1 -- A_{end}). The logical algorithm of the program is shown on Figure 1.

Hardware environment. The program is intended to run on personal computers and has minimal requirements for disk space and memory.

Software environment. The program is written in Visual Basic (VB) and utilizes the Dot.NET technology allowing it to be run on different operating systems.

For simplicity all of the calculations are carried out in Cartesian coordinate system. The conversion of fractional to Cartesian coordinates and backwards is performed as follows:

$$\begin{bmatrix} x \\ y \\ z \end{bmatrix} = \begin{bmatrix} a & b\cos(\gamma) & c\cos(\beta) \\ 0 & b\sin(\gamma) & c\dfrac{\cos(\alpha)-\cos(\beta)\cos(\gamma)}{\sin(\gamma)} \\ 0 & 0 & \dfrac{cv}{\sin(\gamma)} \end{bmatrix} \begin{bmatrix} a \\ b \\ c \end{bmatrix} \tag{3}$$

$$\begin{bmatrix} a \\ b \\ c \end{bmatrix} = \begin{bmatrix} \dfrac{1}{a} & -\dfrac{\cos(\gamma)}{\mathrm{a}\sin(\gamma)} & \dfrac{\cos(\alpha)\cos(\gamma)-\cos(\beta)}{\mathrm{a}\,v\sin(\gamma)} \\ 0 & \dfrac{1}{b\sin(\gamma)} & \dfrac{\cos(\beta)\cos(\gamma)-\cos(\alpha)}{bv\sin(\gamma)} \\ 0 & 0 & \dfrac{\sin(\gamma)}{cv} \end{bmatrix} \begin{bmatrix} x \\ y \\ z \end{bmatrix} \tag{4}$$

$$v = \sqrt{1 - cos^2(\alpha) - cos^2(\beta) - cos^2(\gamma) + 2cos(\alpha)\cos(\beta)\cos(\gamma)} \quad (5)$$

The assumption is that both coordinate system share the same origin, the *a*-axis is collinear with the *x*-axis, and the *b*-axis lies in the *xy*-plane.

INPUT DATA

The program requires the following data in order to return the Hydrogen coordinates (Fig. 2):

1. Unit cell parameters *a, b, c, α, β, γ* in Å,
2. Fractional coordinates of the donor (*x1, y1, z1*),
3. Fractional coordinates of the acceptor atom (*x2, y2, z2*),
4. Optionally a DH, donor-hydrogen distance (0.96 Å is pre-imputed).

OUTPUT DATA

The program outputs the Cartesian and fractional coordinates of an atom located at DH (Å) from the donor atom.

DISCUSSION

The choice of a suitable (default) O-H distance is very difficult. Internuclear O–H distances for isolated molecules in the gas phase are about 0.96 Å (*e.g.* 1.10 Å for C-H). However, the appropriate distance to use for X-ray diffraction must be appreciably shorter to allow displacement of the center of gravity of the electron distribution towards the oxygen atom, and also for oscillating effects. Fortunately SHELXL-97 provides a selection of options (AFIX and HFIX) for positioning and refining hydrogen atoms from geometrical criteria (ShelX manual [1]). For routine refinement, and when suitable geometrical criteria are available (e.g. tertiary CH (HFIX 13), secondary CH_2 (HFIX 23), ethylenic CH_2 (HFIX 93), acetylenic CH (HFIX 163), BH in polyhedral boranes (HFIX 153) and aromatic CH or amide NH (HFIX 43) etc.), the choices of hydrogen atoms generation are multiple (trough combination of AFIX and HFIX instructions). The hydrogen coordinates are re-idealized before each cycle, and "ride" on the atoms to which they are attached (i.e. the coordinate shifts are the same for both the heavy atom and riding H atom). Hydroxyl and methyl groups are more difficult to position accurately but if good data are available (e.g. low-temperature data) the method of choice is HFIX 137 for CH_3 and HFIX 147 for OH groups (torsion angles are allowed to refine while keeping the X–H distance and Y–X–H angle fixed).

OMIT instruction combined with L.S. 0, FMAP 2 (e.g. $F_o - F_c$) and PLAN-100 (list the coordinates and geometry of the highest 100 non-zero electron

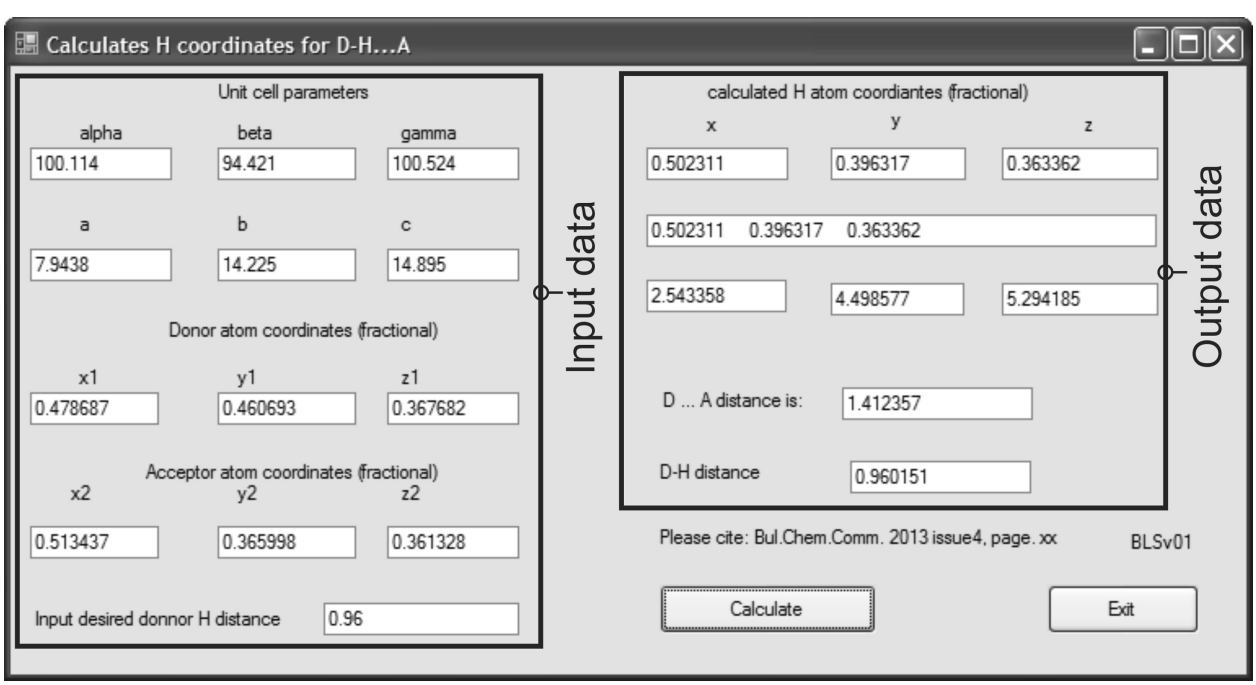

Fig. 2. Input/output window of DHA program

densities) enables an "omit map" to be calculated, which is a convenient way of checking whether there are actually electron density peaks close to the calculated atom positions (the H atom should not be already present). In this omit map, if a non-zero electron density (peak) appears in the Fourier output, then there is an actual peak in the difference electron density synthesis that can be assigned to a hydrogen position (AFIX 03).

In the case of isolated solvent molecules (water, OH, NH_3, etc.) no suitable geometric criteria are applicable and thus the location of the H atom(s) depends only on the data quality. Unfortunately, solvent molecules are usually far more mobile than the other atoms of the structure and thus their isotropic *U*'s are bigger. Therefore, the difference Fourier map may not allow the location of the solvent H atoms. Usually the solvent molecules that are present in the structures participate in hydrogen bonding interactions that stabilize the three-dimensional crystal packing. Thus if suitable hydrogen bonding geometry and distance (directionality) involving solvent (donor and/or acceptor) is detected, the hydrogen atom should also be present. Assuming that the D–H distance is known one can calculate the H atom coordinates from the ones of **D** and **A** (D ••• A).

The program has been used for the determination of solvent H atom coordinates for the structures cited in refs. 8 and 9.

CONCLUSION

The DHA program calculates hydrogen atoms coordinates when the usual positioning of the hydrogen atom is either impossible or inaccurate but hydrogen bonding interaction criteria are encountered.

Availability: The program is available free of charge and can be downloaded from the www.imc.bas.bg/dha site or supplied upon request.

Acknowledgments: *The financial support of Bulgarian Science Fund grant DRNF 02/1 is gratefully acknowledged.*

REFERENCES

1. G. M. Sheldrick, *Acta Cryst. A*, **64**, 112 (2008).
2. L. J. Farrugia, *J. Appl. Cryst.*, **32**, 837 (1999).
3. O. V. Dolomanov, L. J. Bourhis, R. J. Gildea, J. A. K. Howard, H. Puschmann, *J. Appl. Cryst.*, **42**, 339 (2009).
4. M. C. Burla, R. Caliandro, M. Camalli, B. Carrozzini, G. L. Cascarano, C. Giacovazzo, M. Mallamo, A. Mazzone, G. Polidori and R. Spagna, *J. Appl. Cryst.*, **45**, 357 (2012).
5. P. T. Beurskens, G. Beurskens, R. de Gelder, S. Garcia-Granda, R. O. Gould, J. M. M. Smits, The DIRDIF2008 program system, Crystallography Laboratory, University of Nijmegen, The Netherlands, 2008.
6. L. Palatinus and G. Chapuis, *J. Appl. Cryst*., **40**, 786 (2007).
7. P. Tseng. *J. Optim. Theory Appl.*, **109**, 475 (2001).
8. L. Dimowa, K. Kossev, H. I. Sbirkova, R. P. Nikolova, B. L. Shivachev, *Bul. Chem. Comm*., **45**(4), 505 (2013).
9. K. Kossev, L. Tsvetanova, L. Dimowa, R. Nikolova, B. L. Shivachev, *Bul. Chem. Comm*., **45**(4), 543 (2013).

DHA, ПРОГРАМА ЗА ИЗЧИСЛЯВАНЕ НА КООРДИНАТИТЕ НА ВОДОРОДЕН АТОМ КЪМ АТОМ РАЗТВОРИТЕЛ, УЧАСТВАЩ В ВОДОРОДНА ВРЪЗКА

Б. Шивачев

Институт по минералогия и кристалография – Акад. „Иван Костов“,
Българска Академия на Науките, ул. „Акад. Георги Бончев“,
блок 107, София 1113, България

Постъпила февруари, 2013 г.; приета май, 2013 г.

(Резюме)

При рентгеноструктурния анализ е сравнително трудно да се позиционират водородни атоми на база експериментални данни поради малкия брой електрони (в действителност един) а оттам и ниското им разсейване на рентгеновите лъчи. В много случаи водородните координати (позиции) могат да се изчислят въз основа на утвърдени геометрични критерии. Все пак, в някои случаи на позициониране на водородните атоми е трудно. Обикновено такъв проблем възниква, когато молекули на разтворителя (например вода, OH групи, амоняк и др.) са част от кристалната структура. За щастие, водородните атоми участват във водородни връзки (взаимодействия), които се характеризират с подходяща геометрия и разстоянието между донора (**D**) и акцептора (**A**) и изискват наличие на водороден атом (**D**–**H** • • • **A**). По този начин, ако координатите на атомите на донора и акцептора са известни, може да се изчислят координатите на „липсващият“ водороден атом. Програмата **DHA** използва изключително прост математически апарат за изчисляване на координатите на водороден атом (**H**), участващ във взаимодействия от типа **D**–**H** • • • **A**.

Bulgarian Chemical Communications, Volume 45, Number 4 (pp. 466–473) 2013

Natural and Zn exchanged clinoptilolite: *in situ* high temperature XRD study of structural behavior and cation positions

L. T. Dimowa[1]*, S. L. Petrov[2], B. L. Shivachev[1]

[1] *Institute of Mineralogy and Crystallography, Bulgarian Academy of Sciences,"Acad. Georgi Bonchev" str. building 107, Sofia 1113, Bulgaria*
[2] *Department of Chemistry, University of Toronto, 80 St. George Str., Toronto, ON, M5S 3H6 Canada*

Received February, 2013; Revised May, 2013

The thermal stability of the clinoptilolite's structure is reported to vary in a relatively wide range 600–800 °C depending on the sizes of the cations, their sites and occupancies. The aim of this study is to reveal and compare the thermal stability of a natural monomineral clinoptilolite (**CP**) that contains the most common cations: Na, Ca, K and Mg and its Zn-exchanged analogue (**CZN**) having high Zn content of 2.23 at%.

Two different modes of heating were applied: (1) conventional with time-dependent heating/cooling cycles in an electric oven and (2) *in situ* with the sample mounted on a high temperature attachment and continuously heated. In mode (1) the samples were heated up to 600 °C and maintained at this temperature for 3 and 6 hours. With retention time of 3 hours the CP structure collapses, while the CZN one remains stable and does not show visible structural changes. The prolonged retention time of (6 hours at 600 °C) results in the collapse of both structures.

In mode (2), the samples CP and CZN were heated from room temperature to 800 °C with steps of 100 °C and retention time of 20 min. on every step. It was found that the structure of CZN is stable up to 700 °C, while that one of CP collapses around at 600 °C.

Initially we assumed that the high Zn-content in CZN structure is the one that caused its higher short time thermal stability. However, the structural refinement conducted on X-ray powder diffraction patterns of heated samples (2) reveals a continuous displacement of the cations along *a*- and *c*-axis.

Key words: clinoptilolite, ion exchange, thermal stability, *in situ* HT X-ray diffraction.

INTRODUCTION

The zeolite minerals are known for having specific structural features based on the individual topology of their framework and the differences in the amount and type of cations located in the "cavities" of their structures. All these characteristics play a significant role in their thermal stability [1–3]. Thermal behavior is an important part of the overall knowledge of natural zeolites, and each study of these processes could provide a better recognition of their distinctive properties that can be used in various industrial applications. More specifically, the thermal stability may help understanding certain kinetic aspects related to: ion exchange, selective catalysis, molecular sieve properties etc.

The heulandite's group of zeolites is the most abundant on Earth and contains minerals with HEU topology [4]. Clinoptilolite is a member of HEU group with Si/Al ratio greater than four [5]. A widely used empirical method for distinguishing clinoptilolite from heulandite is the different thermal stability [6, 7]. Heulandite undergoes a structural collapse at 350 °C, while clinoptilolite remains stable above this temperature (undergoes structural collapse in the range 550~750 °C).

The clinoptilolite structure has cations and water molecules located inside its framework. The number of cations, their types, site occupancies and charge distribution over the framework are considered as being factors for its higher thermal stability. It is well known that the presence of K^+ and Cs^+ increases the thermal stability of clinoptilolite [8–12]. Although dehydration and some of the structural changes of heulandite group of minerals upon heating are studied [10, 11, 13, 14,] not all of the associated with heating internal processes are clarified.

* To whom all correspondence should be sent:
E-mail: louiza.dimova@gmail.com

In the current paper we study the thermal behavior of natural, poly-cationic clinoptilolite that was purified from additional phases (CP) and its Zn^{2+} exchanged analogue (CZN).

The thermal stability of both structures was monitored by diffraction patterns taken at various stages of heating. A detailed analysis of the diffraction patterns including Pawley whole pattern decomposition and Rietvled refinement were applied to access changes in lattice parameters, cation positions and site occupancies. In addition, a thermally stable K-exchanged clinoptilolite form was prepared (CK) and heated the same way as the other two in order to control the reliability of the applied heating procedures [1, 8].

Two different heating procedures were applied in this study:

1. Conventional (stationary) heating, in which the sample is placed in an electric furnace, heated and held at a certain temperature for a fixed period of time and then cooled down. This mode was used for evaluation of time-dependent short (3 hours) and long (6 hours) stability of the samples at the critical for CZN clinoptilolite temperature of 600 °C.

2. *In situ* heating process, in which the material is placed in a special "homemade" high temperature (HT) sample holder and mounted on the goniometer. This approach allows an instant monitoring of sample's compositional and structural changes during the entire process of continuous heating between the steps. This way, each diffraction pattern taken at a certain temperature will represent the actual status of the material at this moment of heating process.

EXPERIMENTAL

Materials

The studied material is a purified clinoptilolite tuff from Beli Plast deposit, Eastern Rhodopes, Bulgaria.

Ion exchange

The clinoptilolite sample was subject to preliminary removal of concomitant minerals such as: quartz, plagioclase, feldspar, mica and was labeled as CP. This material was used for Zn^{2+} and K^{+} exchange as described below.

Zn-exchange: 1 g of CP, 10 ml 1M $ZnCl_2$ solution and 50 ml distilled water were placed in a Teflon autoclave. The procedure of zinc exchange was performed at 100 °C for a period of 30 days. The autoclave was shook up every day while the solution of 1M $ZnCl_2$ was renewed every second day. The exchanged material (30^{th} day) was triple washed with distilled water, filtered and dried at room temperature. Zinc-exchanged clinoptilolite was labeled as CZN.

K-exchange: 1 g of CP, 10 ml 1M KCl and 50 ml distilled water were placed in a Teflon autoclave. The exchange was carried out at 60 °C for 5 days. The autoclave was shook up every day while the solution of 1M KC1 was renewed every 40 hours. The exchanged material was washed and dried. This potassium-exchanged clinoptilolite was labeled as CK.

Chemical analysis

The chemical composition of the samples was determined by ISP-OES, Varian Vista MPX CCD simultaneous analyses. The structural formulas of the CP, CZN and CK samples were calculated based on 72 framework oxygen atoms. Water molecules were determined using TG data (mass losses).

Differential Thermal analysis (DTA)/ Thermogravimetric (TG) analyses

The thermal effects and mass losses were monitored by DTA/TG analyses in the 30–750 °C temperature range and were obtained from samples CP and CZN (weight 12 ± 0.2 mg) under a constant heating rate of 10 °C min^{-1} and an air flow of 50 ml/min on a Stanton Redcroft thermoanalyzer.

Thermal treatment and heating procedures

Conventional heating: one set of samples CP, CZN and CK were placed in an electric oven, heated and retained at 600 °C for 3 hours. Another set of samples was heated and retained at 600 °C for a prolonged period of e.g. 6 hours.

In situ heating – the analyzed samples were placed and mounted on a homemade HT device adapted for powder X-ray diffractometer Dron 3M. They were heated from room temperature (RT) up to 800 °C. The heating scheme was: steps of 100 °C with a constant heating rate of 10 °C/min and 20 minutes retention time.

X-ray diffraction

The X-ray powder diffraction data collection for conventionally heated samples was carried out on a Bruker D2Phaser diffractometer, CuKα radiation, with scan step of 0.02°/s on a range of 5–35° 2θ.

X-ray diffractometer Dron 3M, CoKα radiation, with scan step of 0.02°/s on a range of 5–35° 2θ was used for data acquisition of *in situ* heated samples. A detailed description of high temperature equipment is represented [15].

Table 1. Agreement factors and unit cell parameters for samples CP and CZN at different temperatures

Sample	CP RT	CP 300 °C	CP 500 °C	CZN RT	CZN 300 °C	CZN 500 °C
R_{exp}	9.64	9.74	9.79	9.44	9.28	9.44
R_{wp}	12.7	11.8	11.85	11.37	11.22	12.05
R_p	9.68	9.22	8.96	8.69	8.73	9.46
GOF	1.32	1.21	1.19	1.23	1.21	1.28
DW	1.67	2.06	1.86	1.88	2.01	1.76
α (Å)	17.661(2)	17.635(3)	17.634(8)	17.649(2)	17.637(4)	17.613(4)
b (Å)	17.931(2)	17.612(3)	17.651(5)	17.960(3)	17.741(3)	17.593(4)
c (Å)	7.401(2)	7.394(4)	7.384(5)	7.401(3)	7.389(4)	7.382(5)
β(°)	116.33(4)	116.67(4)	116.71(6)	116.24(5)	116.29(5)	116.62(6)
V (Å^3)	2100(3)	2052.6(9)	2035.4(8)	2104(3)	2073(8)	2045(2)

Rietveld refinement

The structural properties at RT and high temperatures were investigated by Rietveld [16] analysis on the XRD powder patterns of the *in situ* heated samples using Bruker AXS Topas v. 4.0 [17] suite of programs. A pseudo-Voight profile function was applied. Profile parameters (2θ zero correction, background, cell parameters) were refined first and then the positional parameters (locations and site occupancies) of the cations at three different temperatures: RT (20 °C), 300 °C and 500 °C. Unit cell parameters for all samples (RT to 800 °C) were calculated by Pawley fitting procedure (Table 1).

RESULTS AND DISCUSSION

The chemical compositions of the samples CP, CZN and CK are shown in Table 2. The obtained formulas indicate that the exchanged samples CZN and CK contain predominantly zinc and potassium cations respectively.

The thermal behavior and mass losses illustrated by DTA/TG data are typical for clinoptilolite and both samples CP and CZN display similar curves (Fig. 1). The thermal curves for both samples are characterized by a broad single endothermic effect between ~100–300 ºC for CP and ~80–250 ºC for CZN. These losses are associated with continuous loss of mass mainly due to dehydration (removal of water molecules located in the channels).

The results of thermogravimetric analysis (RT-750 °C) of CP, CZN and CK show typical values for the mass losses of 14.5, 14.2 and 11.37 wt.%, respectively (Table 2).

XRD powder diffraction patterns obtained from RT, conventional heating (600 °C → 3 hrs) and conventional heating (600 °C → 6 hrs) for CK, CP and CZN samples are shown on Fig. 2 (a–c), respectively. As expected the diffractograms (RT, 600 °C → 3 hrs and 600 °C → 3 hrs) of the CK sample remains unchanged while those of CP and CZN samples exhibit a different behavior and are affected by the conducted thermal treatment. The most important result obtained from the conventional time-dependent mode of heating was the higher thermal stability of Zn-exchanged material after a short-term heating cycle (600 °C → 3 hrs) as shown on Figure 2b. One can see that the diffraction pattern of heated for 3 hours CZN is almost identical with its diffraction pattern at RT (Figure 2a). All

Table 2. Chemical composition of the analyzed samples: CP, CZN and CK (results from ICP-OES)

Oxides Wt %	SiO_2	Al_2O_3	Fe_2O_3	CaO	Na_2O	K_2O	MgO	ZnO	LOI*
CP	66.10	12.08	0.28	3.45	1.16	1.92	0.72	>0.01	14.20
CZN	64.75	11.74	0.31	0.80	0.21	0.70	0.29	6.59	14.56
CK	66.25	11.95	0.28	0.45	0.16	9.15	0.22	>0.01	11.37

Calculated chemical formulas:
CP: $(Na_{1.01}Ca_{1.66}K_{1.10}Mg_{0.48})\ Al_{6.39}Si_{29.52}O_{72}$ 21.20 H_2O;
CZN: $(Na_{0.19}Ca_{0.39}K_{0.41}Mg_{0.20}Zn_{2.23})Al_{6.31}Si_{29.61}O_{72}$ 22.20 H_2O;
CK: $(Na_{0.19}Ca_{0.39}K_{0.41}Mg_{0.20}Zn_{2.23})Al_{6.31}Si_{29.61}O_{72}$ 22.20 H_2O;
* LOI – Loss on ignition.

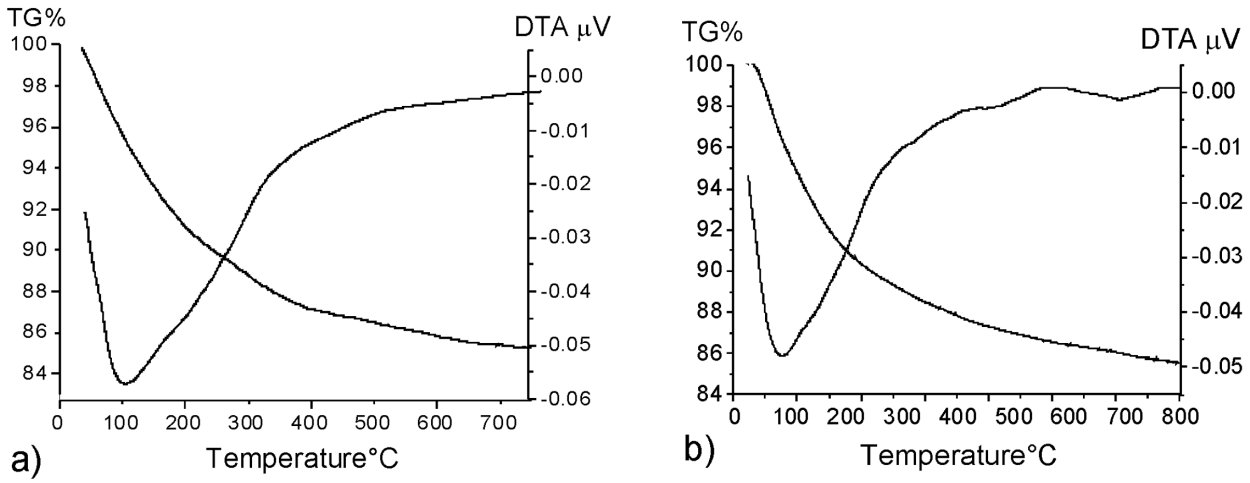

Fig. 1. The results obtained by DTA TG analysis for sample CP (a) and CZN (b)

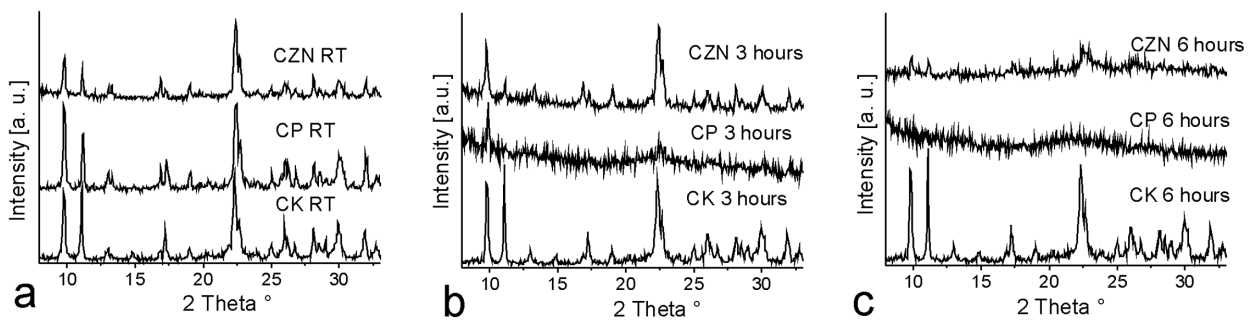

Fig. 2. XRD powder patterns of CP, CZN and CK obtained at RT (a), 300 °C (b) and 600 °C (c)

peak intensities and their positions on the pattern indicate that the structure of CZN retains its integrity and long-range ordering. This is a clear indication for unchanged crystal structure in contrast with the behavior of CP structure, which collapsed after identical short-term heating cycle. As shown on Figure 2c the long range order of samples CP and CZN subject to long-term heating cycle (600 °C → 6 hrs) disappears (amorphization).

The results from *in situ* HT x-ray experiments exploring a continuous heating mode do not show any significant structural changes up to 600 °C (Fig. 3). For the next step (700 °C) the structure of CP has collapsed, whereas that one of CZN remains stable. This shows again the enhanced thermal stability of Zn-exchanged material over the purified natural clinoptilolite. I*n situ* HT results show that CZN structure has collapsed at 800 °C.

As expected, there are some variations of the unit cell as a function of temperature. It was found that unit cell parameters *a*, *c* and *β* remain almost unchanged, whereas the heating affects mainly *b* (and thus way the volume, *V*) (Fig. 4). The reduction of *b* and *V* is slightly more noticeable below 300 °C due to ongoing dehydration process, while for next heating steps the contraction mechanism remains unclear. This mechanism could be related to the motion (kinetics and diffusion) of cations inside the channels.

We attempted to understand this short-term stability of the Zn^{2+}-exchanged sample by using *in situ* heating XRD powder data followed by Rietveld structural analysis on the diffraction patterns at different temperatures for both samples.

The crystal structure of our clinoptilolite (CP) was found to be very close to that one reported by Koyama et al. [9]. It has the same 4 cation sites for Na, Ca, K and Mg located at almost the same positions in the channels. The calculated XRD powder diffraction pattern is very close to that one obtained

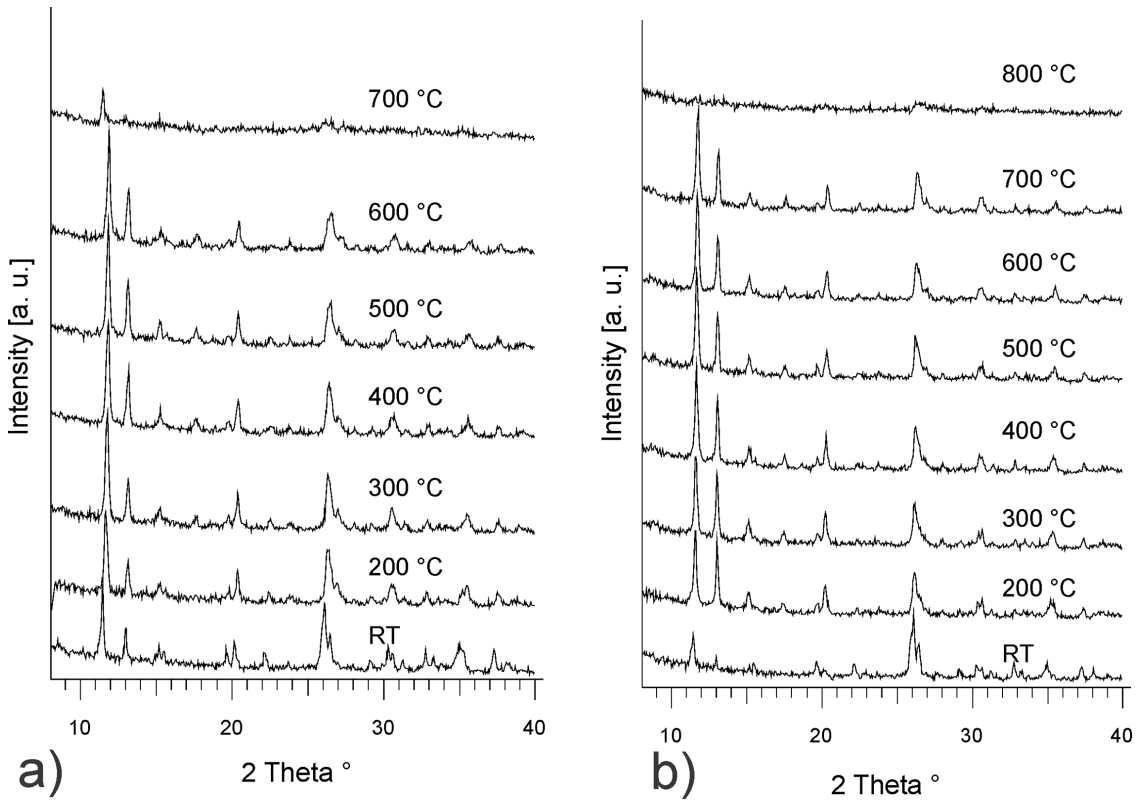

Fig. 3. XRD powder patterns of in situ heated samples CP (a) and CZN (b)

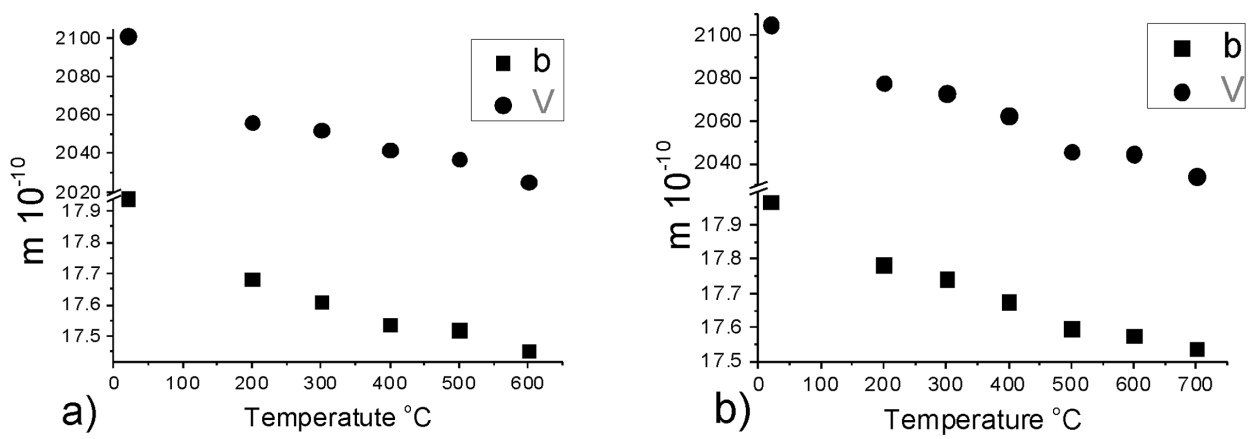

Fig. 4. The parameters that vary significantly: unit cell parameters b and V for samples CP (a) and CZN (b) during in situ heating process

for our clinoptilolite. Thus, the structure of Koyama and Takeuchi was used as a starting structural model in this study.

The results from the performed Rietvled refinement reveal that at high temperatures the cations move inside the channels. Some of their positions remain unchanged, while others experience shifts. This is shown on Table 2 and illustrated on Figure 5.

In the refined structure of CP at 300 and 500 °C, both Na^+ and Ca^{2+} positions have moved along *a*- and *c*-axes and as a result they have slightly been shifted away from the center of the channel, while K-position

remains steady. The most significant change here occurs with Mg^{2+} cation located at the center of the channel. At 300 °C its initial site splits creating new position labeled Mg'. At 500 °C it moves further to another position labeled Mg". This high-temperature transitions of Mg position to Mg' and Mg" changes the symmetry of its initial site from (*2c*) to (*4i*) and finally to (*8j*) (Table 3, Fig. 5).

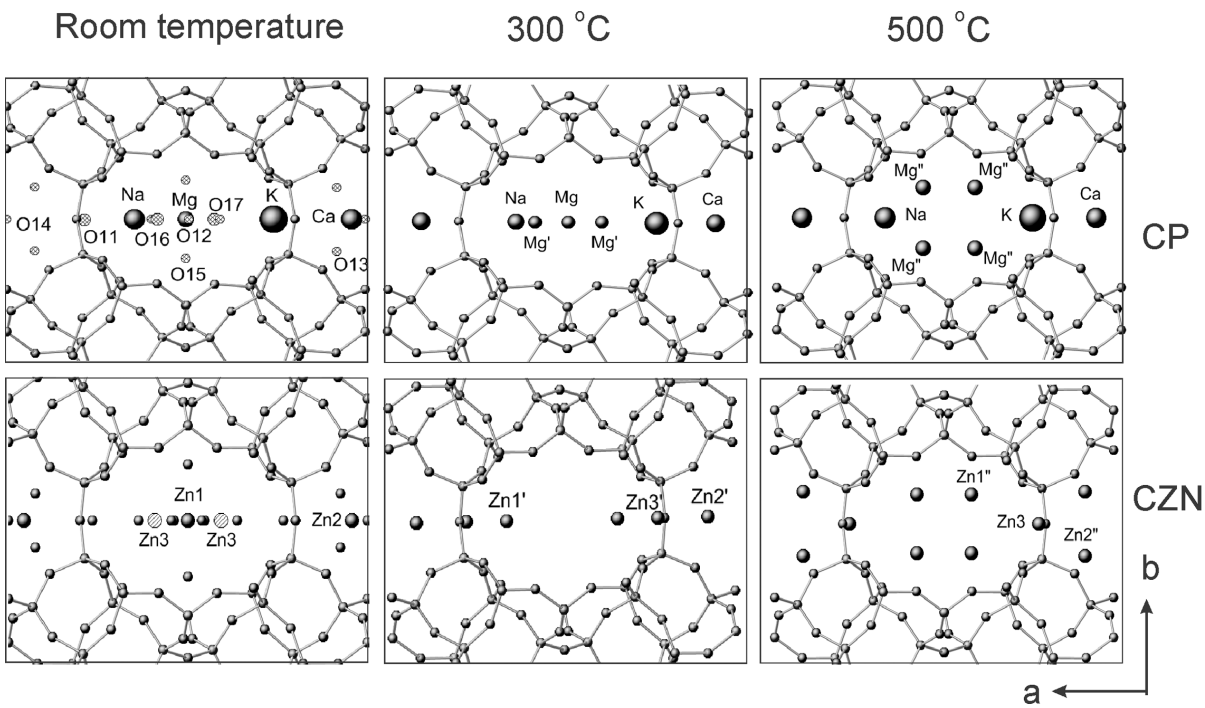

Fig. 5. The structures of CP and CZN samples refined in RT, 300 and 500 °C and cation positions obtained by using Rietveld method. The cation labeling is discussed in the text

Table 3. Cation positions, atomic coordinates (x, y, z) of the samples CP and CZN, their occupancies and Wyckoff positions (Wp) at RT, 300 and 500 °C. The cation labeling is discussed in the text

CP	Position	T °C	*x*	*y*	*z*	SOF	Wp
	Na	20	0.143(7)	0	0.664(8)	0.26(3)	*4i*
	Na	300	0.145(8)	0	0.664(8)	0.26(3)	*4i*
	Na	500	0.185(9)	0	0.858(9)	0.26(3)	*4i*
	Ca	20	0.038(8)	0.5	0.206(8)	0.44(2)	*4i*
	Ca	300	0.038(8)	0.5	0.131(9)	0.44(2)	*4i*
	Ca	500	0.950(8)	0.5	0.138(8)	0.44(2)	*4i*
	K	20	0.255(9)	0.5	0.088(9)	0.28(3)	*4i*
	K	300	0.255(9)	0.5	0.088(9)	0.28(3)	*4i*
	K	500	0.257(9)	0.50	0.080(9)	0.28(3)	*4i*
	Mg	20	0	0	0.5	0.24 (3)	*2c*
	Mg	300	0	0	0.5	0.09 (3)	*2c*
	Mg'	300	0.092(8)	0	0.051(8)	0.08(3)	*4i*
	Mg"	500	0.075(9)	0.077(8)	0.760(9)	0.07 (3)	*8j*
CZN	Zn1	20	0	0	0.5	0.52(3)	*2c*
	Zn1'	300	0.162(9)	0	0.076(9)	0.23(4)	*4i*
	Zn1"	500	0.080(8)	0.072(9)	0.838(8)	0.07(3)	*8j*
	Zn2	20	0.043(6)	0.5	0.27(9)	0.17(2)	*4i*
	Zn2'	300	0.075(8)	0.5	0.538(9)	0.20(3)	*4i*
	Zn2"	500	0.085(7)	0.42	0.109(9)	0.11(3)	*8j*
	Zn3	20	0.092(6)	0	0.464(9)	0.13(2)	*4i*
	Zn3'	300	0.721(9)	0	0.127(9)	0.13(2)	*4i*
	Zn3'	500	0.72(8)	0	0.127(9)	0.19(3)	*4i*

Similar changes occur in the structure of CZN sample where the high Zn-content is distributed in three Zn^{2+} positions. At RT Zn1 and Zn2 occupy the formerly occupied by Mg^{2+} and Ca^{2+} positions, respectively. The Zn3 position (with low occupancy) is very close to Zn1 and because of this both positions cannot be occupied simultaneously [18].

At 300 °C all three zinc positions: Zn1, Zn2 and Zn3 move along a-axis away from the center of the channels and along c-axis. The initial Zn1 position disappears and transforms to a new position labeled Zn1'. This changes its initial site symmetry from (*2c*) to (*4i*). The shifted position Zn2 and Zn3 are labeled as Zn2' and Zn3' and keep the same symmetry (*4i*).

At 500 °C both Zn1' and Zn2' continue their motion along b-axes. Thus Zn1' moves to a new position labeled Zn1" changing again its site symmetry to (*8i*). The Zn2' moves to a new position Zn2" changing its site symmetry from (*4i*) to (*8j*). The Zn3' position does not change.

We assume that the movements of Zn1 and Zn2 during the heating and the transformation of their initial positions symmetry from (*2c*) to (*4i*) and finally to (*8j*) could be the key factor that increases the HT stability of CZN structure. In the case of CP, Mg-position is the most mobile one, however its very low occupancy is insufficient, to hold the integrity of the structure above 600 °C. In contrast, the Zn-sites in CZN structure are highly occupied and their HT migration (movement) and re-arrangement most likely have an effect on charge balance between the framework and the cations that leads to the observed higher stability of the CZN structure. The smaller size of Zn^{2+} compared with the larger ones of Na^{+}, K^{+} and Ca^{2+} is in favor for its mobility. On the other hand, the Zn^{2+}-positions cannot be fully occupied even at high temperatures due to the limitations imposed by the existing framework's charge. Thus, the initial low symmetry cation positions at RT may uptake only three divalent cations per unit cell and because of this the observed thermal stability of CZN exists only for a limited time and eventually the structure would collapse as it has been observed.

CONCLUSION

The applied two different modes of heating on purified clinoptilolite and its Zn-analogue ultimately revealed the enhanced thermal stability of Zn-exchanged material. The steadiness of the reference sample CK structure confirmed the correctness of the applied heating procedure. The unit cell of CP and CZN shrinks during heating mainly due to continuous decrease of *b* parameter. The performed Rietveld structural analysis discloses the increased mobility of the cations in the channels. This leads to transformation of their initial crystallographic sites symmetry to new ones. This process is more significant in the Zn-exchanged form and it is assumed that it could be a stabilization factor for its higher thermal stability. Actually, the small Zn cation cannot 'hold' the structure the way this is made by as the bigger potassium one and this high temperature stability is temporary.

Acknowledgments: *The authors thank the financial support of the Bulgarian National Science Fund through grant DRNF 02/1.*

REFERENCES

1. D. L. Bish, *Clays and Clay Minerals*, **32**, 6, 444 (1984).
2. K. P. Kitsopoulos, *Clays and Clay Minerals*, **49**, 3, 236, (2001).
3. L. Filizova, G. N. Kirov, V. M. Balko, *Geochem. Miner. and Petr*., **2**, 32 (1975).
4. G. Gottardi, E. Galli, Natural Zeolites, Springer-Verlag, Berlin Heidelberg, Germany, 1985.
5. R. Tschernich, Zeolites of the World, Geoscience Press, Inc., Phoenix, 1992.
6. F. Mumpton, *Am. Mineral*., **45**, 351 (1960).
7. A. Alietti, *Am. Mineral*., **57**, 1448 (1972).
8. D. E. W. Vaughan, in: Natural Zeolites: Occurrence, Properties, Use, L. B. Sand, F. A. Mumpton, (eds), Pergamon, Oxford, 1978, p. 353.
9. K. Koyama, Y. Takeuchi, *Zeitschrift fur Kristallographie*, **145**, 216 (1977).
10. Th. Ambruster, M. E. Gunter, *Amer. Miner.*, **76**, 1872 (1991).
11. D. L. Bish, in: Occurrence, properties and utilization of natural zeolites, D. Kallo (ed.), Academiai Kiado, Budapest, 1988, p. 565.
12. T. Armbruster. *Amer. Miner.*, **78**, 260 (1993).
13. A. Alberti, G. Vezzalini, *Tschermaks mineralogische und petrographische Mitteilungen*, **31**, 259 (1983).
14. E. Galli, G. Gottardi, H. Mayer, A. Preisinger, E. Passaglia, *Acta Crustallografica,* **39B**, 189 (1983).
15. L. Dimova, B. Shivachev, S. Petrov, *Bull. Chem. Comm*., **45**(4), 479 (2013).
16. H. Rietveld, *Journal of Applied Crystallography*, **2**, 65 (1969).
17. Topas V4.2: General Profile and Structure Analysis Software for Powder Diffraction. Bruker AXS, Karlsruhe, Germany.
18. L. Dimova, PhD Thesis, IMC, Sofia, 2011.

ПРИРОДЕН И ZN ОБМЕНЕН КЛИНОПТИЛОЛИТ: *IN SITU* ВИСОКОТЕМПЕРАТУРНО ПРАХОВО РЕНТГЕНОСТРУКТУРНО ИЗСЛЕДВАНЕ НА ПОВЕДЕНИЕТО НА СТРУКТУРАТА И КАТИОННИТЕ ПОЗИЦИИ

Л. Т. Димова[1]*, С. Л. Петров[2], Б. Л. Шивачев[1]

[1] Институт по Минералогия и кристалография, БАН, ул. „Акад. Георги Бончев“, бл. 107, София 1113, България
[2] Университет в Торонто, Химически факултет, ул. „Сейнт Джордж“ 80, Торонто ON, M5S 3H6 Канада

Постъпила февруари, 2013 г.; приета май, 2013 г.

(Резюме)

Структурата на клиноптилолита е стабилна при високи температура (600 до 800 °C) в зависимост от типа на катионите в каналите, от техните позиции и от заетостта им. В настоящето изследване е сравнено термичното поведение на природен мономинерален клиноптилолит (CP) и на обменен с цинкови катиони (CZN). В природната CP форма се съдържат Na, Ca, K и Mg катиони, а в CZN 2,23 ат.% цинк. За целта на изследването се използват два метода за нагряване на пробите: (1) конвенционален в пещ и (2) *in situ*, при който пробата е монтирана на високо температурна приставка и постепенно се нагрява. При (1) се достига температура 600 °C, като продължителността е 3 и 6 часа. При образците загрявани 3 часа структурата на проба CP се разрушава, докато тази на CZN остава стабилна. При (2) загряването на образците CP и CZN започва от стайна температура и достига до 800 °C със стъпка 100 °C и задържане от 20 min за всяка стъпка (~ 3 часа). Структурата на проба CZN остава стабилна до 700 °C, докато тази на CP се разрушава при температура около 600 °C. Направено е структурно уточнение по метода на Rietveld на *in situ* нагряваните проби, за да се установи причината за кратката термична стабилност на цинково обменения клиноптилолит.

Bulgarian Chemical Communications, Volume 45, Number 4 (pp. 474–478) 2013

Surface phase detection of proton-exchanged layers in $LiNbO_3$ and $LiTaO_3$ by IR reflection spectroscopy

M. Kuneva

Institute of Solid State Physics – Bulgarian Academy of Sciences,
72 Tzarigradsko Chaussee Blvd, Sofia 1784, Bulgaria

Received February, 2013; Revised May, 2013

The proton exchange (PE) technology has focused scientists' attention for the last 30 years because of the easy and fast obtaining of waveguides with strong waveguiding effect in electro-optical crystals like $LiNbO_3$ (LN) and $LiTaO_3$ (LT). The $Li_{1-x}H_xNbO_3$/$Li_{1-x}H_xTaO_3$ layer, formed by Li-H ion exchange, shows complex phase behavior depending on the hydrogen concentration (value of x). Up to seven phases exist in PE-LN an up to five – in PE-LT. Each phase forms its own sublayer in the protonated region, the one with the highest value of x being on the top. That is why the recognition of the top sublayer phase in many cases could be used for some conclusions about the phases building the rest of the whole layer or for the optical and electro-optical quality of the optical waveguiding layer. It has been established that IR reflection spectra of proton-exchanged layers contain new bands within the range 850–1050 cm^{-1} and each phase has its own reflection spectrum. This way, IR reflection spectra in low-frequency range could determine the top-layer phase status. The samples investigated were obtained at different technological conditions and the analysis performed contributes to the accumulation of knowledge about the technological control of the phase composition of proton-exchanged waveguide layers in LN and LT.

Key words: $LiNbO_3$, $LiTaO_3$, optical waveguides, proton exchange, phase composition.

INTRODUCTION

Lithium niobate and lithium tantalate are among the most attractive ferroelectric crystals for integrated optics. Being an alternative of the most popular technology for obtaining optical waveguides in $LiNbO_3$ – Ti-indiffusion, proton exchange (PE) [1, 2] has undergone a strong development in the last two decades. PE represents a chemical reaction (diffusion and Li-H ion exchange) which takes place in the surface layer of a crystal immersed in an appropriate melt.

Going by the scheme:

$$LiMO_3 + xH^+ \Rightarrow Li_{1-x}H_xMO_3 + xLi^+ \ (M=Nb,Ta)$$

PE modifies the surface layer (several μm in depth) by Li–H ion exchange causing a large extraordinary index change Δn_e ($\Delta n_e \cong 0.12$ for $LiNbO_3$ and $\cong 0.02$ for $LiTaO_3$ at 0.633 μm). The PE layers show complex phase behaviour depending on the hydrogen concentration (value of x) and causing significant decrease in electro-optical coefficients and increase in optical losses and instabilities.

The phase model developed by Korkishko et al. [3, 4], on which contemporary ideas on phase formation in monocrystalline layers of $Li_{1-x}H_xMO_3$ are based, suggests that each phase originates as an individual sublayer of several hundred nm or less. In every single one of them Δn_e is a linear function of concentration. The lattice parameters vary among phases. Within each phase, the change of the extraordinary refractive index Δn_e is proportional to x; within a phase transition, the value of Δn_e and/or of the deformations perpendicular to the surface change by leap. Up to 7 phases could be formed in $LiNbO_3$ (α, κ_1, κ_2, $ß_1$, $ß_2$, $ß_3$, $ß_4$), and up to 5 – in $LiTaO_3$ (α, κ, ß, γ, δ).

The complicated phase composition of the proton-exchanged layers, determined by the degree of H^+–Li^+ substitution, has oriented the main efforts since the beginning of the technology to the ways for controlling the phase composition and to methods for waveguide phase characterization.

* To whom all correspondence should be sent:
E-mail: m_kuneva@yahoo.com

Table 1. Technological and waveguide parameters of the proton-exchanged waveguides: (T – temperature, t – duration of the PE process, T_a and t_a – temperature and duration of the annealing, M – number of waveguide modes at $\lambda = 633$ nm, Δn_e – extraordinary refractive index change, d – waveguide depth)

Material	Sample	Proton source	T [°C]	t [h]	Ta [h]	t_a [h]	M	d [μm]	Δn_e	Possible phase composition	Surface phase
$LiTaO_3$	TZ-2	$LiHSO_4$ (vapors)	250	20	–	–	1	1.23	0.0162	α, κ, δ	δ
$LiTaO_3$	TZ-3	$LiHSO_4$ (vapors)	220	48	–	–	1	1.44	0.0101	α, κ, δ	δ
$LiTaO_3$	TZ-4	$LiHSO_4$ (vapors)	200	72	–	–	1	2.09	0.0058	α, κ, δ	δ
$LiTaO_3$	T-1	Benzoic acid	240	8	265 295	1 1.5	2	2.18	0.0213	ß(γ)	γ
$LiTaO_3$	T-2	Benzoic acid	240	31	400	2	5	9.45	0.0155	A	α
$LiTaO_3$	Z-1	Benzoic acid	240	8	295 350	1 1	4	4.25	0.0189	α, κ	α, κ
$LiNbO_3$	LZ-1	$LiHSO_4$ (vapors)	250	3.5	–	–	6	2.66	0.1491	$ß_1$, $ß_3$, $ß_4$	$ß_4$
$LiNbO_3$	NM-1	NH_4HSO_4 (melt)	230	3.3	–	–	9	2.47	0.1508	$ß_1$, $ß_3$, $ß_4$	$ß_4$
$LiNbO_3$	NM-5	$LiHSO_4$ (melt)	175	1.5	–	–	1	0.62	0.1222	$ß_1$, $ß_2$, $ß_3$	$ß_1$

EXPERIMENTAL

Proton-exchanged optical waveguides in Z-cut $LiNbO_3$ and Z-cut $LiTaO_3$ were obtained by different technology conditions described in Table 1.

The phase analysis based on mode and IR absorption spectra was performed and reported earlier [5–8], the results being presented also in Table 1. In addition, infrared reflection spectra were registered in order to confirm the phase composition as well as to give some indications about the distribution of the different phases within the proton-exchanged layers.

IR reflection spectra were recorded at angle of incidence $\theta = 70°$ (measured from the normal to the surface) as shown in Fig. 1. The spectrometer accessories for specular reflectance were fixed- angle ones (for 20° and 70°). Since the penetration depth depends on the angle of incidence, at smaller angles (closer to the normal incidence) deeper penetration takes place and the measured spectra are affected by the presence of the various phases forming the waveguide. It was established [9] that at 70° the spectrum of the surface layer is separated from those of deeper situated layers in multiphase guides. This way only the surface phase could contribute to the reflection spectra of multiphase waveguides and the IR reflection spectroscopy allows the surface phase to be recognized.

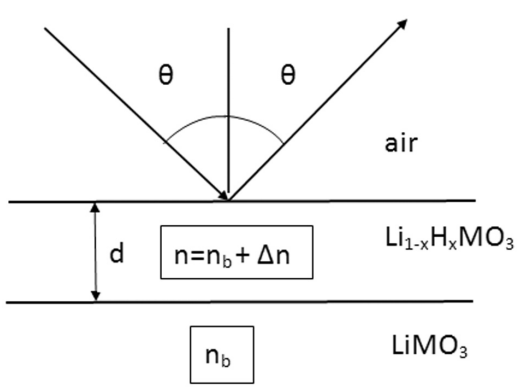

Fig. 1. Schematic sketch of IR reflection measurements

RESULTS AND DISCUSSION

$LiNbO_3$

The IR reflection spectra for LN samples are presented in Fig. 2.

The reflection IR spectra of protonated LN crystals have new bands compared to the spectra of virgin crystal (LZ-ref) or α-phase PE-$LiNbO_3$ [9]. These bands appear at frequences in the range of 890–1010 cm^{-1}, each phase having its own spectrum. It has been found that the new bands which can be attributed to new phases are 975 cm^{-1} for $ß_1$ phase, 980 cm^{-1} for $ß_2$ and $ß_3$ phases, 970 cm^{-1} for $ß_4$ phase [9, 10]. The new band at 890–985 cm^{-1} appears after PE in addition to the lattice spectrum of LN.

The low-frequency edges of the band correspond to the TO phonons of the NbO_6 vibration mode. Less distorted NbO_6 octahedra without any non-bridging oxygen ions are present in the α, $κ_1$ and $κ_2$ phases, as well as in pure LN. The appearance of weak extra bands in the region of IR reflection spectra from 800 to 900 cm^{-1} for all $ß_i$ phases suggests the presence of more distorted NbO_6 octahedra with non-bridging oxygen ions. Each $ß_i$ phase is marked by a very specific lattice vibration spectrum with unique charac-

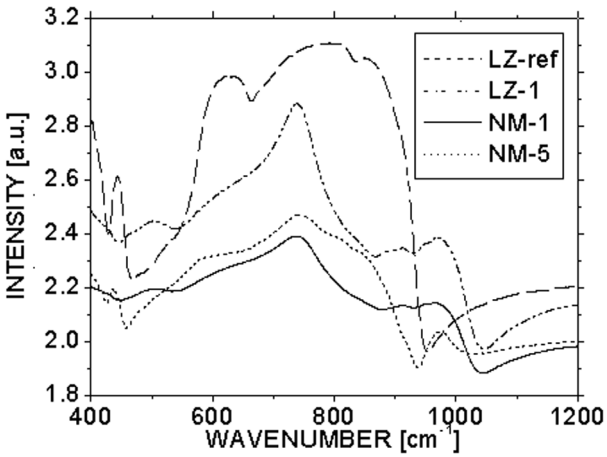

Fig. 2. IR reflection spectra measured at θ = 70° for the $LiNbO_3$ proton exchanged layers

teristic bands. A significant difference between the crystalline structures of different $ß_i$ phases exists, which is introduced by the added chemical bonds with characteristic frequencies of vibration. This feature can be used for accurate identification of $ß_i$ phases in any $H_xLi_{1-x}NbO_3$ waveguide.

Since the analysis based on mode and IR absorption spectroscopy suggests a particular phase composition, where the most strongly protonated phase is at the surface of the waveguide, particular changes in the reflection spectrum can be attributed to the respective phase. This way the analysis was made which allows a particular frequency band to be attributed to the presence of the definite phase on the surface.

The new bands which can be attributed to new phases are: 955 cm^{-1} and 970 cm^{-1} for κ_2-phase, 965 cm^{-1} for κ_1-phase and 965 cm^{-1} for α-phase.

Thus, looking at the spectra in Fig. 2 we could conclude that $ß_1$ phase is present on the top of sample NM-5 while $ß_4$ phase forms the top of the waveguiding layers of samples NM-1 and LZ-1, which are really strongly protonated. Also, it is seen that the spectrum of NM-5 is closest to the shape of the virgin sample (LZ-ref), which suggests that the contribution of the α-phase is larger than in the case of the other two samples. It could be seen that LZ-1 and NM-1 have almost the same spectra, confirming their equal phase composition determined by other methods, as it can be seen in Table 1.

In the case of analysis of the phase composition of the most weakly protonated waveguide, the reflection spectra give particularly important information since they show that the waveguide is a single-phase one. As it is known from the phase model, the single-phase layers form the layer in such way that the value of x increases towards the surface (i. e. the most strongly protonated layer is at the surface). In our case the uppermost layer is of the $ß_1$ phase and therefore, according to the phase analysis based on mode and IR spectroscopy, the possible $ß_2$ and $ß_3$ phases are not present in the protonated layer. (Another possibility is that the layer is slightly "buried" but the technological conditions do not suggest such a result).

$LiTaO_3$

The IR reflection spectra for LT samples are presented in Fig. 3 and Fig. 4.

The main changes in the reflection spectra introduced by proton exchange in Z-cut $LiTaO_3$ occur in the range of 850–1050 cm^{-1}. They were compared to the spectra of X-cut PE-$LiTaO_3$ given in [10] and some correlations with lattice deformations and reflection minimums were made in order to assign the spectral changes to a definite phase. According to [10], the changes observed at 899, 952 and 985 cm^{-1} in IR-reflection spectra of all samples could be assigned to the ß- and γ-phases, and the change at about 1000 cm^{-1} to the δ-phase, respectively. Since in the case of the waveguides (Fig. 3) obtained by proton exchange in vapors (PEV) the second perturbation is much stronger, we should conclude that the surface phase of all investigated waveguides is δ as their spectra are almost identical.

The phase composition of the annealed samples suggests the presence of α- and κ-phases, so the new bands in their reflection spectra (Fig. 4) could be assigned to these two phases: 960 cm^{-1} for the κ-phase, 974 cm^{-1} for the α-phase, 891 for both α- and κ-phases. For the ß- and γ-phases the

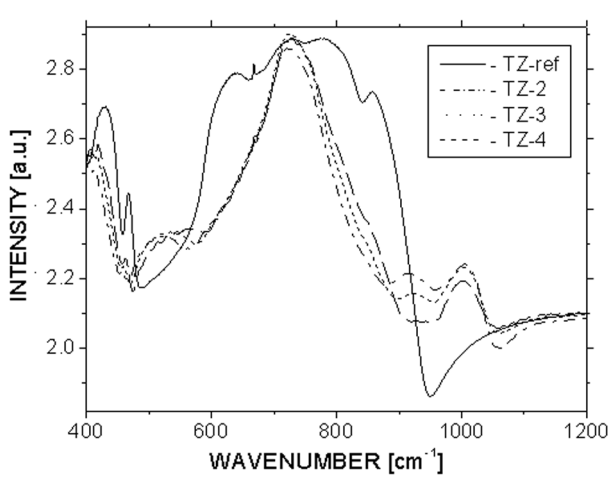

Fig. 3. Infrared reflection spectra measured at θ = 70° for the $LiTaO_3$-waveguides obtained in $LiHSO_4$ vapors

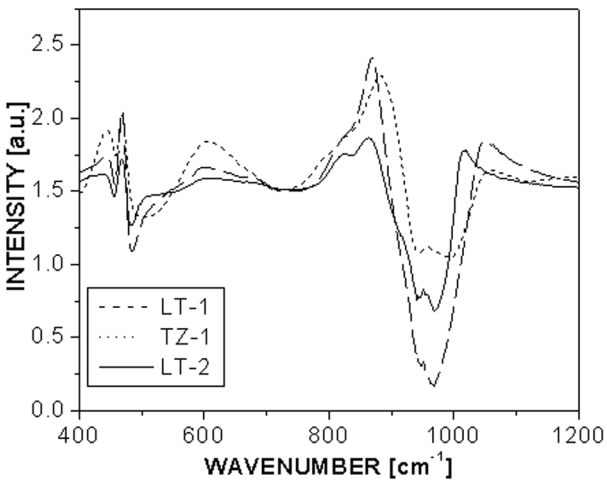

Fig. 4. Infrared reflection spectra measured at θ = 70° for the post-exchange annealed $LiTaO_3$-samples

band has three components at 890–915, 960 and 992 cm^{-1}, which are shifted to lower frequencies compared to the bands for the γ- and δ-phase of PEV waveguides.

The results of the IR-spectra analysis for the investigated LN and LT samples are shown in the rightmost two columns of Table 1. The information given by these spectra allows the determination to be made, which phase forms the uppermost layer of the waveguide. Thus, the information given by the analysis of the IR-reflection spectra allows us to be much more specific when determining which phases build the investigated waveguide layers.

CONCLUSIONS

• The phase composition of the entire PE-layers was determined by combined mode and IR absorption spectroscopy.

• IR reflection spectra of proton-exchanged layers contain new bands within the range 890–1010 cm^{-1} and each phase has its own reflection spectrum. This way, IR reflection spectra in the low-frequency range could determine the top-layer phase status.

• The low-frequency edges of the band correspond to the TO phonons of the NbO_6/TaO_6 vibration mode. The appearance of weak extra bands in the region of IR reflection spectra from 800 to 900 cm^{-1} suggests the presence of more distorted NbO_6/TaO_6 octahedra with non-bridging oxygen ions. There is a significant difference between the crystalline structures of different phases, which is introduced by the added chemical bonds with characteristic frequencies of vibration.

• The phase-characteristic bands for $LiNbO_3$ are at:

965 cm^{-1} for both α- and κ_1-phase;
955 cm^{-1} for κ_2-phase;
975 cm^{-1} for $ß_1$-phase;
980 cm^{-1} for $ß_2$- and $ß_3$-phases;
970 cm^{-1} for $ß_4$-phase.

• The new bands assigned to the definite phase in the case of $LiTaO_3$ are:

960 cm^{-1} for the κ-phase;
974 cm^{-1} for the α-phase;
890 cm^{-1} for both α- and κ-phases;
890–915, 960 and 992 cm^{-1} for ß- and γ-phases, the components of the first being shifted to lower frequencies compared to the bands of the second;
1000 cm^{-1} for the δ-phase.

• The presented results could contribute to the obtaining of waveguides with control of their phase composition and therefore of their optical and electro-optical properties.

REFERENCES

1. J. L. Jackel, C.E. Rice, J. J. Veselka, *Appl. Phys. Lett.*, **41,** 607 (1982).
2. W. B. Spillman, N.A. Sanford, R. A. Soref, *Opt. Lett.*, **8**, 497 (1983).
3. Yu. N. Korkishko, V. A. Fedorov, *IEEE J. Select. Top. Quant. El.*, **2**, 187 (1996).
4. K. El. Hadi, P. Baldi, S. Nouh, M. P. De Micheli, A. Leycuras, V. A. Fedorov, Yu. N. Korkishko, *Opt. Lett.*, **20**, 1698 (1995).
5. M. K. Kuneva, K. Christova, S. Tonchev, *J. Phys.: Conference Series* 398 012047 (2012).
6. M. K. Kuneva, S. H. Tonchev, D. Nesheva, P. Atanasov, *Solid State Sciences*, **12,** 1870 (2010).
7. M. K. Kuneva, S. H. Tonchev, P.S. Dimitrova, *J. Mater. Sci.: Mater. Electron*., **14**, 859 (2003).
8. M. K. Kuneva, S. H. Tonchev, M. Sendova-Vasileva, D. Dimova-Malinovska, P.A. Atanasov, *Sens. Actuators*, **A 99**, 154 (2002)
9. S. M. Kostritskii, Yu. N. Korkishko V. A. Fedorov, in: Properties of Lithium Niobate, K. K. Wong (ed.), INSPEC, London, 2002, p.161.
10. S. M. Kostritskii, Yu. N. Korkishko, V.A. Fedorov, D. B. Maring, R. F. Tavlykaev, R. V. Ramaswamy, *J. Appl. Phys*., **91,** 930 (2002).

ОПРЕДЕЛЯНЕ НА ПОВЪРХНИННАТА ФАЗА НА ПРОТОННО-ОБМЕНЕНИ СЛОЕВЕ В $LiNbO_3$ И $LiTaO_3$ ЧРЕЗ ОТРАЖАТЕЛНА ИЧ СПЕКТРОСКОПИЯ

М. Кънева

Институт по физика на твърдото тяло „Акад. Г. Наджаков“,
бул. Цариградско шосе 72, 1784 София

Постъпила февруари, 2013 г.; приета май, 2013 г.

(Резюме)

Протонният обмен (PE) е технология, която привлича вниманието на учените през последните 30 години поради лесното и бързо получаване на оптични вълноводи със силен вълноводен ефект в електрооптичните кристали $LiNbO_3$ (LN) и $LiTaO_3$ (LT). Слоят $Li_{1-x}H_xNbO_3$/$Li_{1-x}H_xTaO_3$, получен чрез Li–H йонен обмен, има сложен фазов състав, зависещ от концентрацията на водорода (стойността на x). До седем фази могат да съществуват в PE-LN и до пет – в PE-LT. Всяка фаза образува свой собствен подслой в протонираната област, като този с най-висока стойност на x се намира на повърхността. По тези причини от определянето на фазата на повърхинния слой в много случаи може да се направят изводи и за фазите, изграждащи целия слой или за оптичните и електрооптичните качества на вълноводния слой. Установено е, че ИЧ отражателни спектри на протонно-обменените слоеве съдържат нови ивици в областта 850–1050 cm^{-1} и всяка фаза има свой специфичен отражателен спектър. По този начин по ИЧ отражателни спектри в нискочестотната област може да се определи повърхнинната фаза. Тъй като изследваните проби са получени при различни технологични условия, проведеният анализ допринася за натрупване на знания по технологичен контрол на фазовия състав на протонно-обменени слоеве в LN и LT.

Bulgarian Chemical Communications, Volume 45, Number 4 (pp. 479–484) 2013

Design and application of a cost effective high temperature holder for *in-situ* powder X-ray diffraction experiments

L. Dimowa[1]*, B. Shivachev[1], S. Petrov[2]

[1] *Institute of Mineralogy and Crystallography, Bulgarian Academy of Sciences, "Acad. Georgi Bonchev" str. building 107, Sofia 1113, Bulgaria*
[2] *Department of Chemistry, University of Toronto, 80 St. George Street, Toronto, ON, M5S 3H6 (Canada)*

Received February, 2013; Revised May, 2013

We are presenting a simple and inexpensive, in-home made high-temperature (HT) device, suitable for high-temperature *in situ* investigations of phase transitions, crystallite growth and other thermal features of solid-state materials by X-ray diffraction (XRD). The attachment can be easily mounted on conventional laboratory X-ray diffractometer. The HT-device consists of sample holder and heating element combined together. The unit is made from fused quartz, which temperature resistance is above 1000 °C. The sample holder (the front part of the body) can be shaped to match the conventional front packing powder holder for the equipment that is used. The heating element consists of a khantal tape that is mounted on the backside of the body. Different ways of mounting the heating tape can be used to optimize the desired uniform heat distribution within the volume of the packed powder. The length of the heating tape can be adjusted, for tuning its total resistance and accordingly – its heating power. Both the sample holder and the heating element are made "small" to ensure a good thermal exchange and to save energy required for heating. Due to its small size, limited contact with the diffractometer and the good thermal stability of quartz in air, the HT-device does not require water-cooling and can be used for multiple routine *in situ* measurements up to 950 °C. Its functionality was studied on standard reference material (KNO_3) and on natural minerals: a mixture of clinoptilolite/opal-cristobalite and Zn-exchanged clinoptilolite. The advantages and limitations of the proposed design are discussed.

Key words: high-temperature XRD holder, XRD, *in situ* heating.

INTRODUCTION

X-ray powder diffraction (XRPD) is one of the most recognized analytical tools for compositional and structural analysis of solid-state materials including various natural and synthetic technological products. The ongoing investigations on many of these materials required more complex and detailed information for their features, including thermal behavior. The HT-X-ray diffraction analysis, especially when carried out *in situ*, is capable to display instantly physical, chemical and structural changes that occur at certain temperature, but remain "hidden" at ambient conditions [1]. A variety of attachments (chambers, furnaces, cameras etc.) are commercially available for conducting such *in situ* experiments [2, 3].

* To whom all correspondence should be sent:
E-mail: louiza.dimova@gmail.com

DESIGN AND DISCUSSION

The holder is made of fused quartz as a replica of the original plastic/metallic sample holders used for our conventional Bragg-Brentano diffractometer, Dron 3.0 M (Fig. 1). The heating element is mounted on the opposite side of the sample holder. Some advantages of fused quartz include:

- Its thermal expansion is negligible (coefficient of 5.5×10^{-7}/°C (20–320 °C),
- It is stable up to ~1100 °C (softening point is 1600 °C, annealing point is 1120 °C and strain point is 1025 °C),
- Multiple heating-cooling cycles can be carried out with temperature range up to 950 °C,
- It is inert (non-reactive) against very broad range of materials,
- When irradiated by X-rays fused quartz does not provide scattering or diffraction,
- Fused quartz is an insulator and cannot damage goniometer's base during the heating.

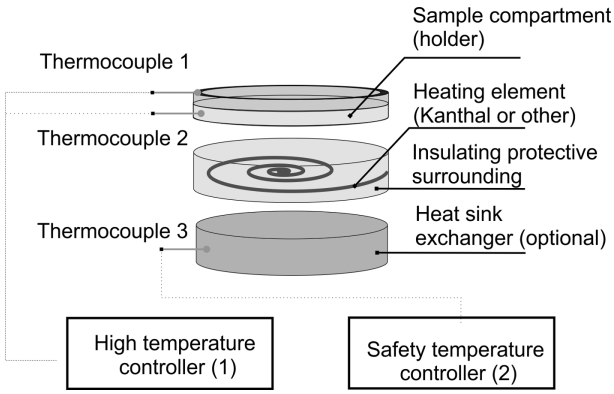

Fig. 1. Schematics of the high temperature holder

The body of the holder is made of cylindrical shaped piece of fused quartz with ø 25 mm, length 10 mm and consists of two parts:

1. Sample compartment (1 mm deep circle cavity with polished flat edges for precise alignment);

2. Heating element: in our case a kanthal tape, 1.5 mm width, 0.12 mm thickness;

The kanthal heating tape was inserted in thin-drilled channels on the backside of the sample compartment. Two modes of mounting the heating tape are possible: (1) – wire coiling and (2) – spiral coiling (Fig. 2). Wire coiling mounting of the heating tape has the advantage of allowing adjustments of its loops and distance between loops, which changes the total resistance of the tape and thus, its heating power. For fixed resistance parameters of the heating element, spiral coiling is the preferable option.

Two thin and flexible thermocouples (K-type) (~0.2 mm) are placed in different positions: (i) – inside the sample and near the diffracting surface and (ii) – closer to the heating element. Both of them are located on the border of the holder. They are used for control and adjustment of the temperature on the diffraction surface of the sample. The use of two thermal elements helps for monitoring the thermal gradient and heat distribution in the volume of the sample holder.

The temperature is controlled by adjusting the current/voltage provided to the heating element as a function of the output of the two thermocouples. Optionally, a third thermocouple may be placed inside the capping of the heating element.

The holder is mounted directly on the diffractometer. A self-adjustment ("in plane") of the diffracting surface is ensured by three contact points (stoppers) mounted on the goniometer. As it was stated above, due to insignificant thermal transfer of fused quartz, the heat exchange with the contact stoppers and other goniometer's parts is limited.

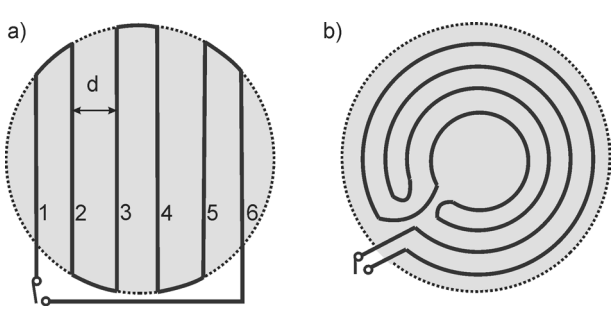

Fig. 2. Heating element placement: a) wire-coiling and b) spiral-coiling. The distance d between the channels could be adjusted by adding or subtracting turns, in order to obtain optimal total resistance and heating power

SIMULATION OF THE XRD HOLDER

In order to understand the heat transfer in the entire holder, it was modeled and numerically simulated by finite element method (FEM) analysis using RadTherm 8. For the solid phases (fused quartz) heat conduction, surface-to-surface (in the sample holder) and surface to ambient radiation (outside) was applied. For the gas phase, the heat transmission and free convection were taken into consideration. Due to the presence of a heating element without clear symmetry, the holder was simulated in a three dimensional model (x-, y- and z-axes). For simplicity, a constant value for the heat conductivity of 3.8 W m^{-1} K^{-1} was assumed for the sample in all simulations. The simulation of the temperature distribution in the cell in ambient atmosphere and a heating power of P = 85 W is shown in Fig. 3. The temperature of the cooling air has been set to 20 °C. Ideally, the sample temperature should be homogeneous over the entire sample volume. As the sample is heated from the inside and cooled from the surface, we expect a temperature gradient within the sample, especially for samples with very low heat conductivity. The highest temperature gradient is in the middle of the sample along the z-direction (Fig. 3). Due to the axial symmetry (along z) the contribution to the total sample volume is higher at the border than in the middle. Thus, the diffraction contribution from the sample volume near the "border" is going to be higher than that one from the center. This justifies the location of the thermocouples near the border.

THERMAL BEHAVIOR AND CALIBRATION OF THE HOLDER

Experimentally the overall cooling effect of the air was determined by measuring the heating power, necessary to reach a certain temperature of the sam-

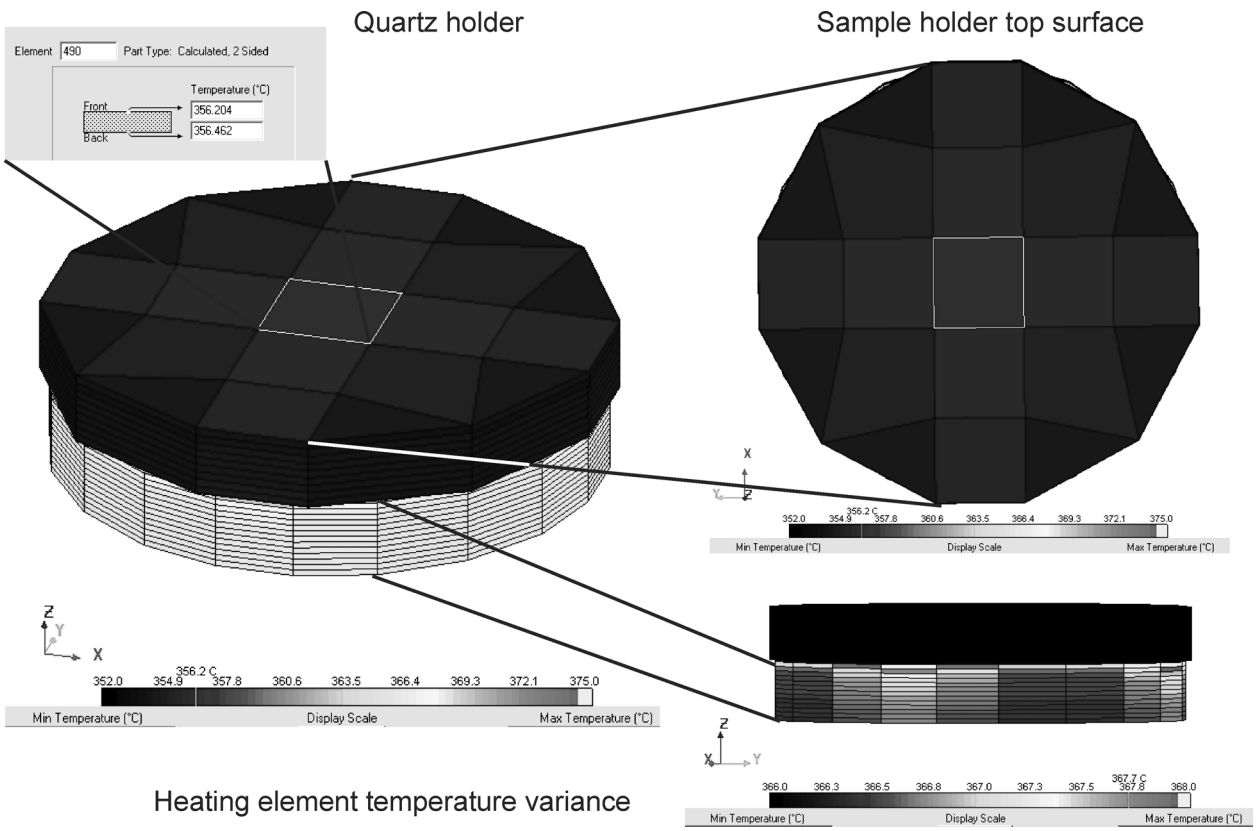

Fig. 3. Results from "finite element method" (FEM) simulation of the heat distribution in the sample holder in ambient atmosphere, heating power P = 85 W and temperature of the cooling air set at 20 °C

ple holder. Figure 4 shows the applied "input power" as a function of the temperatures, measured by the two thermocouples: T1 and T2. The measurements were carried out after reaching and maintaining for 10 min the temperatures 50–100, 200, 300, 400, 500, 600 and 700 °C. The heating power as a function of sample holder temperature was found almost linear. The experimental temperature variation, T1 vs. T2, that corresponds to the thermal gradient within the volume of the sample was found smallest in the range of 250–400 °C and more pronounced at lower and higher temperatures. The simulated heating power values required for the holder to reach the requested temperature and the experimentally measured ones correlate well up to ~300 °C; beyond that temperature the real power input becomes significantly higher than the calculated one. This is probably due to the different heat capacity of the sample and the thermocouple as already observed by Kerestedjian & Sergeeva [4].

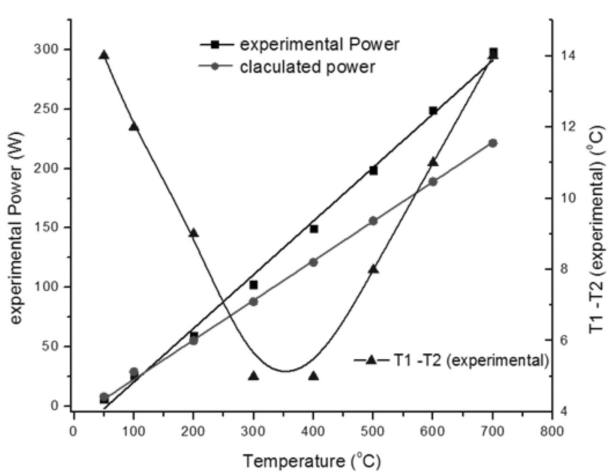

Fig. 4. Input power as a function of measured temperatures in the sample holder from the two thermocouples: T1 and T2

EXAMPLES OF APPLICATIONS OF HT-SAMPLE HOLDER

The holder was designed and mounted on a DRON 3M diffractometer (CoKα, 1.789 Å) equipped with position scintillation detector. The

system was interfaced with a personal computer. Data collection was carried out using a routine step scan mode with 0.02 or 0.04°.s^{-1}. Figure 5 shows the HT-sample holder as mounted on the goniometer and heated at 800 °C.

The holder has been tested against standard reference materials and used in our Lab for routine measurements on different materials [5, 6].

Here we are presenting the results from three HT *in situ* experiments carried out on different materials and at different temperature ranges.

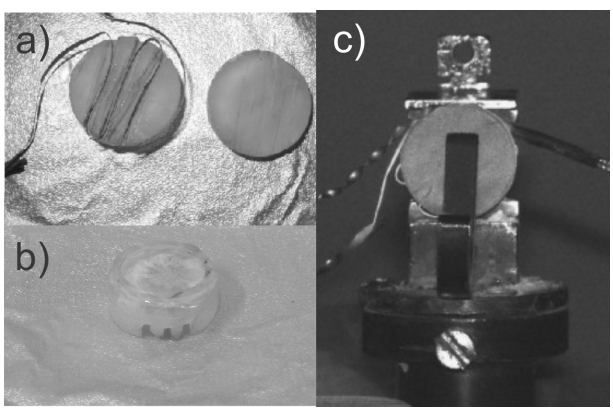

Fig. 5. View of: a) the heating element and its cover; b) the o-ring shaped sample compartment and c) the HT-holder mounted on a DRON 3M diffractometer and heated at 800 °C.

HT in situ experiment on reference material KNO_3

KNO_3 is known for having various polymorphous under certain thermodynamic conditions. Three of the polymorphs are stable at ambient pressure (7–10). At room temperature (RT) KNO_3 is orthorhombic, *Pnma*, with aragonite-type of structure (11). At temperatures above 129 °C it converts to calcite-type of structure $R\bar{3}m$, (8).

We used this material as a reference for testing the accuracy of our HT-sample holder. The observed structural transition of KNO_3 occurred at the same temperature as pointed out in the literature. This is illustrated on Figure 6, which displays the results from our *in situ* experiment carried out in routine step scan mode and elevating the temperature according to thermo couples showings with power control.

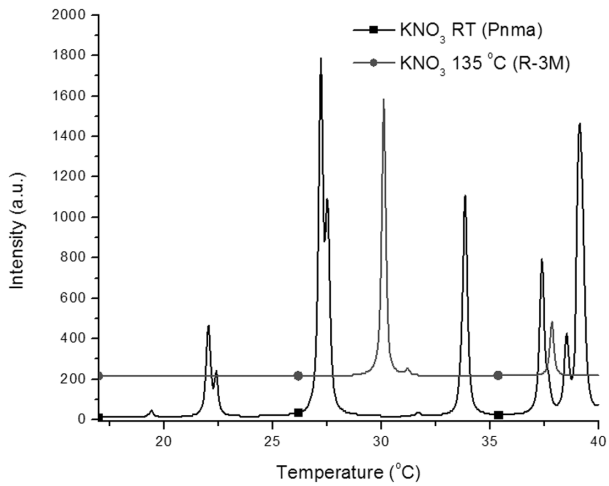

Fig. 6. In situ X-ray diffraction of reference material KNO_3: It shows a phase transition from orthorhombic (at room temperature) to rhomboherdal structure at 135 (±1) °C.

HT in situ experiment on natural mixture of clinoptilolite and opal-cristobalite

The natural zeolite mineral clinoptilolite from Beli Plast deposit, Bulgaria is commonly mixed with fine inter-grown sub-crystals of opal-cristobalite, having a visible peak on the diffraction pattern (d = 4.04 Å). It is well known that clinoptilolite undergoes lattice changes during heating, while opal-cristobalite has a stable structure that doesn't show lattice changes up to 1000 °C. A HT *in situ* experiment was done on this mixture in order to test and verify the overall alignment and possible positional displacements of the sample holder when heated. The heating was carried out up to 350 °C and the results are shown on Figure 7 – left plot. The position of the opal-cristobalite peak at 2θ = 25° is marked with black arrow. It does not move during the heating. In contrast, the strongest peak of clinoptilolite next to it (marked with red arrow) moves due to its well established lattice changes when heated.

HT in situ experiment Zn-exchanged clinoptilolite

Our previous investigation on the thermal stability of natural clinoptilolite with various cations incorporated in its framework shows their different thermal stability. Here we demonstrate the collapse of the structure at temperature above 700 °C (Figure 7 – right plot). The experiment was carried

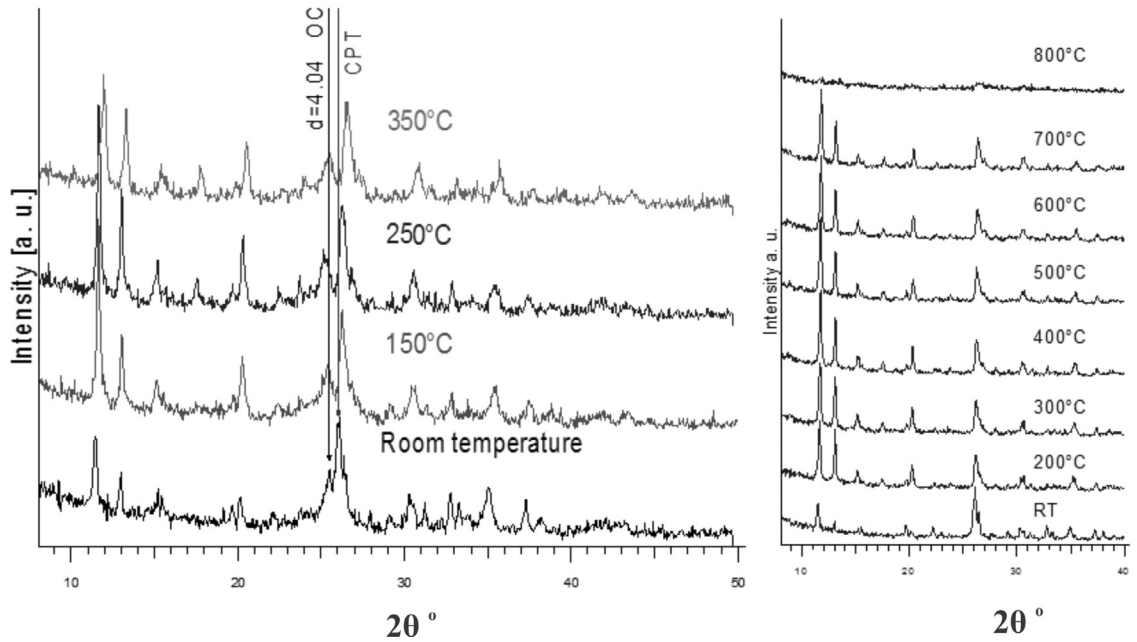

Fig. 7. Monitoring of CPT/Opal unit cells changes on heating (left plot) and thermal stability of Zn-exchanged natural clinoptilolite in the temperature range from RT to 700 °C (right plot)

out with our HT-sample holder and illustrates well its capabilities to be used for high-temperatures (up to 900–950 °C).

CONCLUSIONS

The design and construction of our "in home" HT-device, including sample holder and heating element are presented and explained in details. The design and setup were simulated and optimized by FEM analysis. The temperature can be properly controlled by two separate thermocouples and adjusted by power supply on the heating element. Due to the good thermal stability and negligible thermal expansion coefficient of fused quartz, the device can be used for multiple cycles of *in situ* heating/cooling in the temperature range from RT up to 900 °C. The accuracy of the alignment and its reliability has been tested and demonstrated here on three examples of HT *in situ* measurements on: reference material (KNO_3), natural mixture of clinoptilolite and opal-cristobalite and Zn-exchanged clinoptilolite.

The device is non-expensive, easy to be made and can be adapted and used on most of the conventional Bragg-Brenatano diffractometers.

Acknowledgments: *The authors thank the financial support of the Bulgarian National Science Fund through grant DRNF 02/1.*

REFERENCES

1. D. D. L. Chung, P. W. De Haven, H. Arnold, D. Ghosh, X-Ray Diffraction at Elevated Temperatures, A Method for in situ Process Analysis, VCH Publishers, 1993.
2. M. Dapiaggi, G. Artioli, L. Petras, *The Rigaku Journal*, **19**, 1 (2002).
3. http://www. anton-paar.com
4. T. Kerestedjian, I Sergeeva, *Bulgarian Chemical Communications*, **44**, 77 (2012).
5. A. R. Drews, *Advances in X-ray Analysis*, **44**, 44 (2001).
6. L. T. Dimowa, S. L. Petrov, B. L. Shivachev, *Bulgarian Chemical Communications,* **44**, 55 (2012).
7. P. E. Tomaszewski, Structural Phase Transitions in Crystals, I. Database, in: Phase Transitions **38**(3), 127 (1992).
8. J. K. Nimmo, B. W. Lucas, *Acta Cryst. B*, **32**, 1968 (1976).
9. E. Rapoport, G. C. Kennedy, *J. Phys. Chem. Solids*, **26**, 1995 (1965).
10. J. F. Scott, M. S. Zhang, R. B. Godfrey, C. Araujo, L. Mcmillan, *Phys. Rev. B*, **35**, 4044 (1987).
11. S. Sawada, S. Nomura, S. Fujii, *J. Phys. Soc. Jpn*, **13**, 1549 (1958).

ДИЗАЙН И ПРИЛОЖЕНИЕ НА ЛЕСНА ЗА НАПРАВА ВИСОКОТЕМПЕРАТУРНА ПРИСТАВКА ПОДХОДЯЩА ЗА *IN-SITU* ПРАХОВИ РЕНТГЕНО ДИФРАКЦИОНИ ИЗСЛЕДВАНИЯ

Л. Т. Димова[1]*, С. Л. Петров[2], Б. Л. Шивачев[1]

[1] *Институт по Минералогия и кристалография, БАН, ул. „Акад. Георги Бончев“, бл. 107, София 1113, България*
[2] *Университет в Торонто, Химически факултет, ул. „Сейнт Джордж“ 80, Торонто ON, M5S 3H6 Канада*

Постъпила февруари, 2013 г.; приета май, 2013 г.

(Резюме)

Представена е схема на високо температурна приставка (ВТП) подходяща за монтиране на прахов рентгенов дифрактометър и провеждане на *in situ* изследвания на свързани с фазови преходи, кристален растеж и други температурно зависими характеристики на твърдотелни материали. Приставката е сравнително лесна за направа и може да бъде монтирана на стандартен лабораторен рентгенов дифрактометър. ВТП се състои от два основни елемента: поставка за образеца и нагряващ елемент. Поставката е изработена от кварц с температура на топене над 1000 °C. Предната (фронталната част) на поставката трябва да е оформена така че да съответства на стандартния отражателен модел на съответния дифрактометър. Нагряващите елементи са от Кантал (ленти) които са прикрепени към задната част на поставката. За оптимизиране на равномерното разпределяне на температурата в обема на поставения прахов материал могат да се използват различни начини за монтиране на нагряващите елементи. Дължината на нагряващия елемент (съответно неговото съпротивление) може също да варира, което позволява по-точно нагласяне на мощността на нагряване. Размерите на приставката са минимизирани с оглед осигуряване на минимален температурен обмен с околната среда и консервиране на енергията. Поради малкия размер, ограничения контакт с дифрактометъра, добрата термична стабилност на кварца на въздух (до 950 °C при атмосферни условия) ВТП не изисква водно охлаждане и може да се използва многократно при рутинни *in situ* измервания. Функционалността на приставката е изпробвана върху стандартен еталонен материал (KNO_3) както и при *in situ* нагряване на природен клиноптилолит примесен с опал-кристобалит и клиноптилолит обменен с цинк. Представено е кратко разглеждане на предимствата и ограниченията на предложения дизайн и модел на ВТП.

Bulgarian Chemical Communications, Volume 45, Number 4 (pp. 485–490) 2013

Synthesis and characterization of TeO_2/TiO_2 powders obtained through Te (VI) acid

R. S. Iordanova[1], A. D. Bachvarova-Nedelcheva[1]*,
R. D. Gegova[1], Y. B. Dimitriev[2]

[1] *Institute of General and Inorganic Chemistry, BAS, "Acad. G. Bonchev" str., bl. 11, Sofia, 1113, Bulgaria*
[2] *University of Chemical Technology and Metallurgy, "Kl. Ohridski" blvd., 1756 Sofia, Bulgaria*

Received February, 2013; Revised May, 2013

The present study is focused on the possibility for obtaining TeO_2 containing powders in the TeO_2–TiO_2 system applying a low temperature wet chemistry method. Telluric (VI) acid (H_6TeO_6) and titanium butoxide were used as a new combination of precursors. Two compositions with high TeO_2 content (80, 90 mol%) were selected. Yellow coloured powders were obtained and they were characterized by XRD, IR and UV-Vis analysis. The crystallization tendency of the powders in the temperature range 300–600 °C was studied as well. The crystallization process started at heat treatment above 300 °C. Composite powders containing α-TeO_2 (paratellurite) and $TiTe_3O_8$ were obtained as final products.

Key words: telluric (VI) acid, TeO_2, $TiTe_3O_8$.

INTRODUCTION

Tellurium oxide – based materials have attracted considerable research interest in recent years due to their high refractive index, good non-linear optical properties and electrical semiconductivity appealing for various applications [1–4]. Up to now different methods for synthesis of Te-based materials were applied such as: melt quenching technique, chemical or physical vapour deposition, pulverization, molecular beam epitaxy or laser ablation [5]. It is known that most tellurium-based oxide materials can be synthesized at temperatures below 900 °C. Recently, much attention has been paid on applying the low temperature sol-gel method, which is an attractive alternative to the high temperature melt quenching route. The main disadvantage of this method is using of tellurium alkoxides, which possess high sensitivity to the moisture in air. Up to now, there are a few papers, which reported on sol-gel processing of TeO_2 powders and films using H_6TeO_6 as a precursor for obtaining Te (VI) alkoxide [4, 6]. Beaudry et al. [7] reported on synthesis of high purity TeO_2 powders applying a wet chemistry method, starting from elementary Te and HNO_3 as precursors. Several authors successfully prepared tellurium dioxide nanoparticles using different methods [8, 9].

On the other hand the binary TeO_2–TiO_2 system is very interesting one due to the existence of thermodynamically stable compound $TiTe_3O_8$, which possesses microwave-dielectric properties [10–12]. Up to now it has been synthesized mainly via solid-state reaction method in the temperature range 650–700 °C [12, 13]. However, it is difficult to obtain pure $TiTe_3O_8$ by solid state reaction of TiO_2 and TeO_2 because the volatilization of TeO_2 occurs rapidly at high temperatures [11].

The aim of this study was to verify the possibility for obtaining TeO_2 – based powders and $TiTe_3O_8$ compound in the TeO_2–TiO_2 system using telluric (VI) acid (H_6TeO_6) and titanium butoxide as a new combination of precursors. This investigation is an attempt to prepare such powders more readily and less expensively aiming to overcome the problems when using of tellurium alkoxides.

EXPERIMENTAL

Samples preparation

Two samples with high TeO_2 content and nominal compositions $90TeO_2.10TiO_2$ (sample 1, mol%)

* To whom all correspondence should be sent:
E-mail: albenadb@svr.igic.bas.bg

and $80TeO_2.20TiO_2$ (sample 2, mol%) were selected. It is well known that there are problems concerning the high hydrolysis rate of the tellurium alkoxides [4, 14]. In order to overcome this problem we used Te(VI) acid (Aldrich) in combination with Ti butoxide (Fluka AG) and ethylene glycol ($C_2H_6O_2$) (99% Aldrich). The scheme for synthesis is presented in Figure 1. Solutions (A and B) were prepared via dissolving of the precursors in ethylene glycol by means of vigorous magnetic stirring. Thus, white precipitates were obtained and subsequently they were subjected to evaporation at ~60 °C and heating on a hot plate at ~100–150 °C. A stepwise heating of the samples from 400 to 600 °C for 2 hours exposure time in air was performed, until obtaining powders (samples 1 and 2). The calcination temperature was selected on the basis of our previous investigations [15]. As we found earlier, there is no presence of organic constituents above 400 °C. The pH during the experiments was measured to be about 7.

Samples characterization

Powder X-ray diffraction (XRD) patterns of the samples were registered at room temperature with a Bruker D8 Advance diffractometer using Cu-Kα radiation. The main short range orders of the powders were determined by IR spectroscopy (Nicolet 320 FTIR spectrometer). The infrared spectra were registered in the range 1600–400 cm^{-1} using the KBr pellet technique on a Nicolet-320 FTIR spectrometer with 64 scans and a resolution of ±1 cm^{-1}. The optical absorption of the obtained powders was measured by UV-Vis analysis (Spectrophotometer Evolution 300).

RESULTS AND DISCUSSION

The XRD patterns of the yellow coloured TeO_2/TiO_2 powders (samples 1 and 2) are shown in Figure 2. As is seen, the metallic tellurium (ICDD, PDF 78-2312) is found predominantly in the samples up to 400 °C. It is possible this phase to be completely removed by oxidation at temperatures above 450 °C [16]. At this temperature separation of paratellurite (α-TeO_2, ICDD, PDF 42-1365) is also registered. With increasing the temperature (up to 500 °C) the paratellurite became a dominant phase and formation of the crystalline $TiTe_3O_8$ (ICDD, PDF 50-0250) phase occurred. With further increasing of the heating temperature (600 °C), all above pointed out crystalline phases were found to be present. In the XRD pattern of sample 1 (90 mol% TeO_2), α-TeO_2 remains as a main phase, while in the other sample 2 (80 mol% TeO_2), $TiTe_3O_8$ is the predominant one (Fig. 2). Probably, this phase ($TiTe_3O_8$) has wide primary crystallization field. Thus, our XRD data

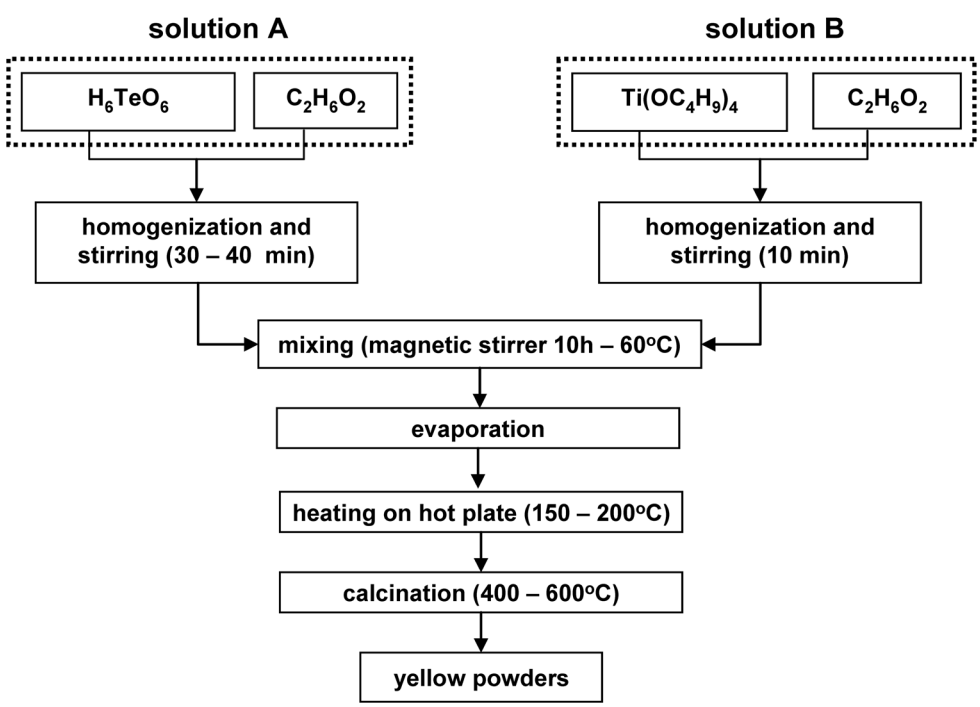

Fig. 1. Scheme for the low temperature synthesis of TeO_2/TiO_2 powders

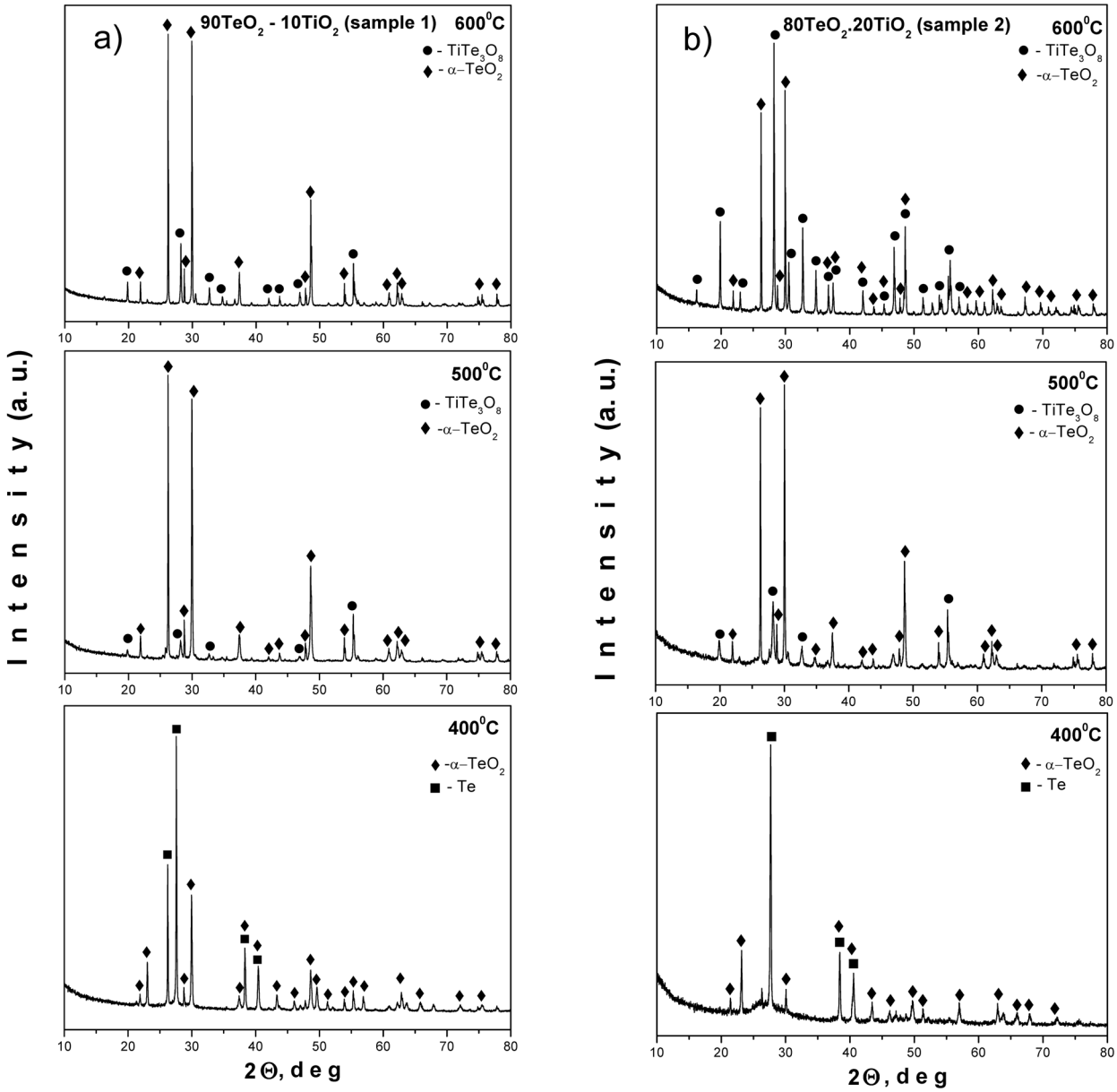

Fig. 2. XRD patterns of samples: a) $90TeO_2.10TiO_2$ (sample 1) and b) $80TeO_2.20TiO_2$ (sample 2)

are in good accordance with those obtained by other authors [2, 3, 17], who established formation of these phases using other precursors but at similar heating temperatures. By the way, for comparison XRD patterns of elementary tellurium, TeO_2 and H_6TeO_6 (JCPDS 70-1524) are shown as well (Fig. 3).

The phase transformations during the heat treatment were monitored also by IR spectroscopy. All IR spectra of the calcinated at different temperatures samples 1 and 2 are shown in Fig. 4a, b. At low temperatures (200 °C) characteristic bands in the range 1500–800 cm^{-1} were observed. Generally, they may be attributed to the C-OH stretching vibrations of $C_2H_6O_2$ and Ti butoxide [18]. The residual organic groups disappeared above 200 °C. At 400 °C the IR spectra of both samples are characterized by wide absorption bands in the range 770–460 cm^{-1}, which could be assigned to the vibrations of Me–O (Me = Ti, Te) complexes [19–21]. The IR spectra at 500 °C of both samples are very similar and vibrations at 770, 670-650, 630, 480-460 cm^{-1} were observed. The increase in the temperature (up to 600 °C) led to some changes in the IR spectra. The IR spectrum of sample 1 is typical for the crystalline TeO_2 [19].

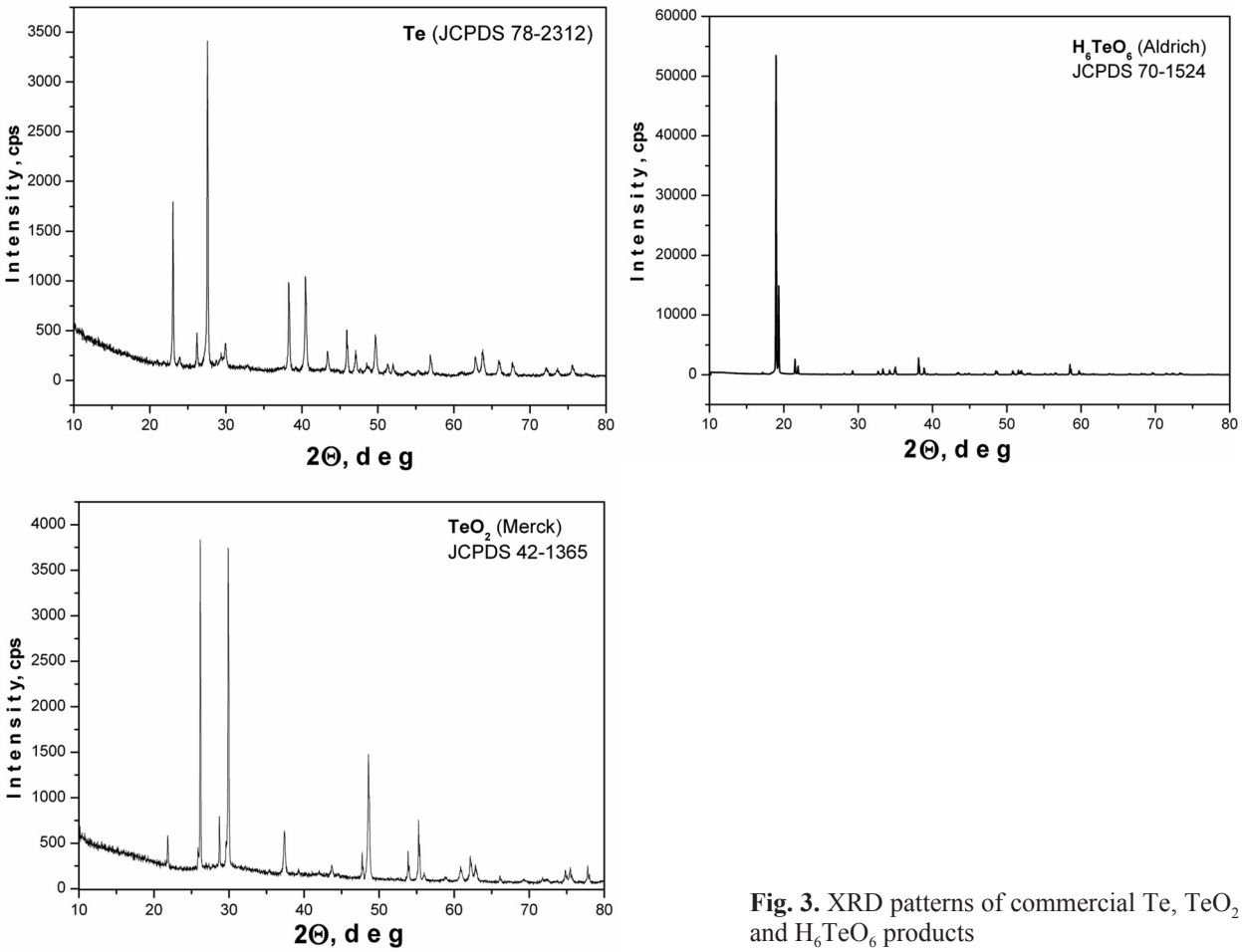

Fig. 3. XRD patterns of commercial Te, TeO_2 and H_6TeO_6 products

Intensive bands at 770 cm^{-1} (ν^s) and 670 cm^{-1} (ν^{as}) with a shoulder at 630 cm^{-1} (ν^s) were registered, which may be related to the stretching vibrations of TeO_4 groups (Fig. 4a). The IR spectrum of the other sample 2 is more close to that of the crystalline $TiTe_3O_8$ phase (Fig. 4b) [19]. The data obtained by IR spectroscopy are in good accordance with the XRD data.

The optical absorption spectra of the investigated samples are presented in Figure 5. As is seen from

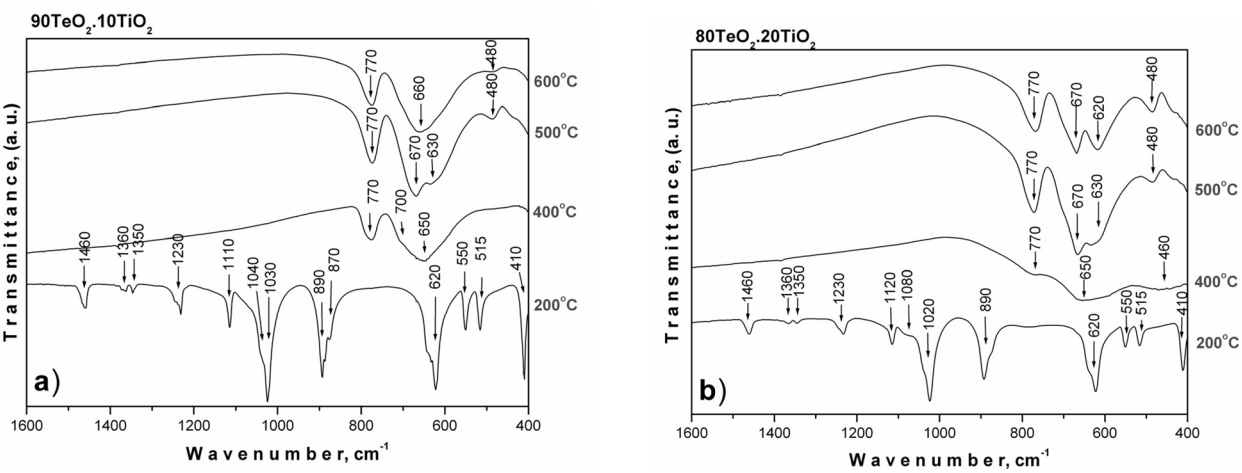

Fig. 4. IR spectra of samples 1 (a) and 2 (b)

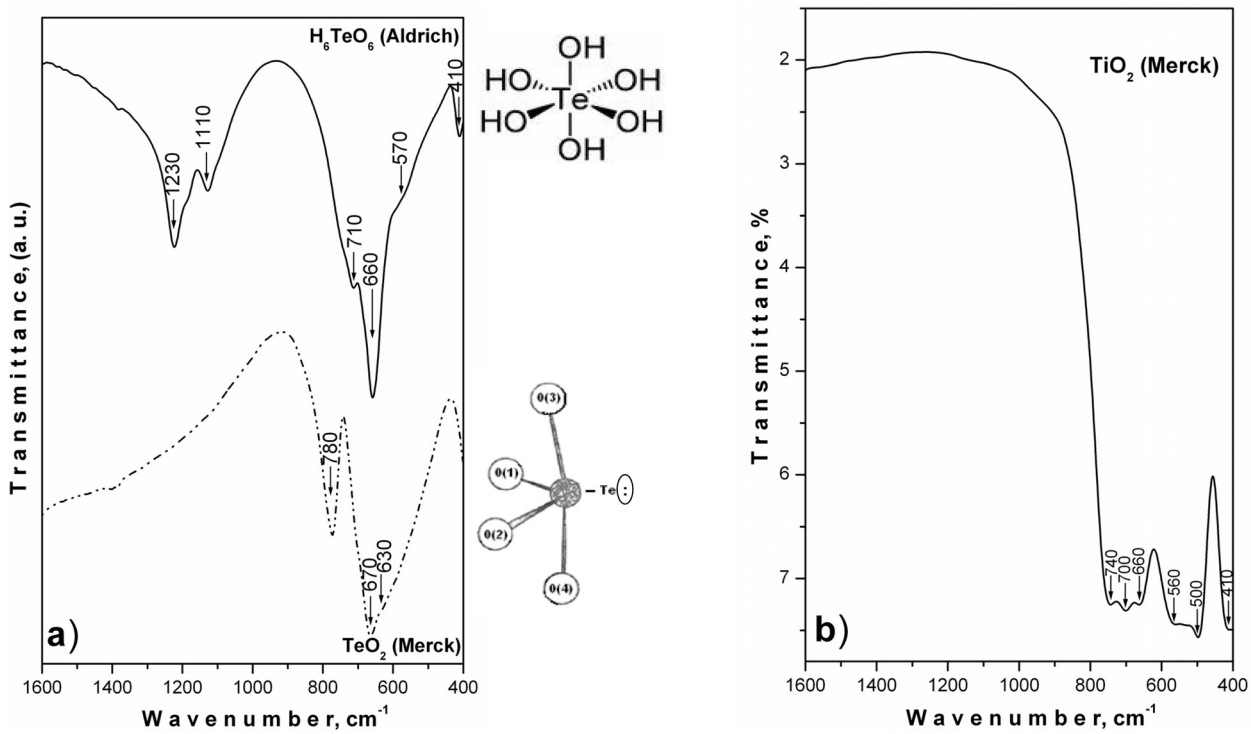

Fig. 5. IR spectra of: a) TeO_2 and H_6TeO_6; b) TiO_2

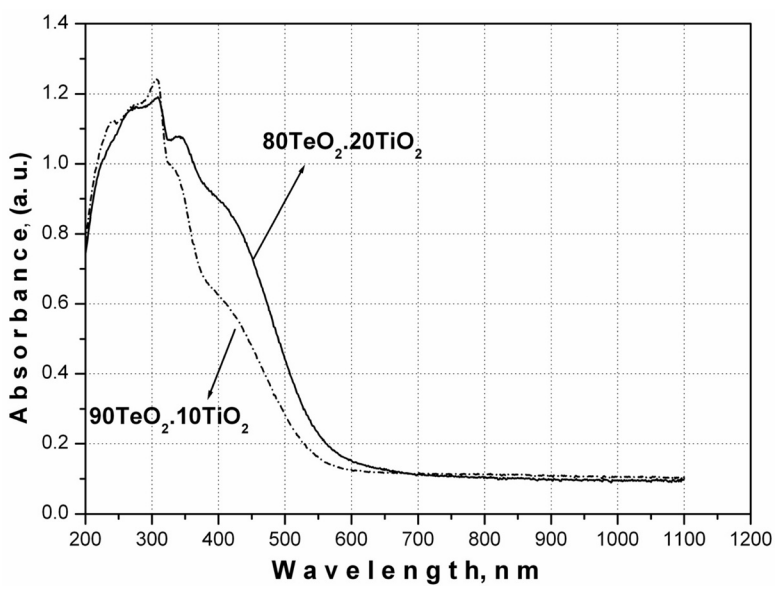

Fig. 6. UV-Vis absorption spectra of the investigated powder samples heated at 600 °C

the figure the sample containing lower TeO_2 content (80 mol%) exhibited more intensive absorbance in the UV spectra than those containing 90 mol% TeO_2. The absorption spectra were used to determine the optical band gap (E_{opt}) of both samples. For sample 1 E_{opt} is 3.45 eV, while for sample 2 it is 3.43 eV. According to Weng and Hodgson [3] similar powder compositions (containing 80, 90 mol% TeO_2) exhibited optical band gap value about 3.3 eV. Our values are higher than these obtained for the TeO_2/TiO_2 thin films (~3.29 eV) [14] but lower than the value of melted bulk tellurite glass (~3.79 eV).

CONCLUSIONS

Yellow coloured powders were obtained using a low temperature wet chemistry method. The crystallization tendency of the powders in the range 300–600 °C was studied. The crystallization process started at heat treatment above 300 °C and mixtures containing α-TeO_2 and $TiTe_3O_8$ were obtained depending on composition and heating temperature. The observed crystalline phases are in different quantity depending on the TeO_2/TiO_2 ratio. According to the IR results, the organic constituents existed below 400 °C and characteristic bands for α-TeO_2 and $TiTe_3O_8$ were observed at 600 °C. The obtained powders would be promising candidates for optical applications.

REFERENCES

1. A. Pierre, F. Duboudin et al., *J. Non-Cryst. Sol*., **147&148**, 569 (1994).
2. L. Weng and S. Hodgson, *J. Mater. Sci*., **36**, 4955 (2001).
3. S. Hodgson and L. Weng, *J. Mater. Sci*., **37**, 3059 (2002).
4. L. Weng, S. Hodgson, X. Bao, et al., *Mater. Sci. Engineer*., **B107**, 89 (2004).
5. A. Lecomte, F. Bamiere, S. Coste, P. Thomas, et al., *J. Eur. Cer. Soc*., **27**, 1151(2007).
6. H. Ikeda, S. Fujino et al., *J. Amer. Cer. Soc*., **92** (11), 2619 (2009).
7. J. Beaudry, S. Grenier, S. Amrate et al., *Metr. Chem. Phys*., **133**, 804 (2012).
8. B. Qin, Y. Bai, Y. Zhou, et al., *Mater. Lett*., **63**, 1949 (2009).
9. S. Cho, Y. Hong et al., *Chem. Phys. Lett*., **429**, 214 (2006).
10. G. Meunier, *J. Galy, Acta Cryst*., **B27**, 602 (1971).
11. O. Yamaguchi, D. Tomihisa et al., *J. Chem. Soc. Dalton Trans*., (1988) 2083.
12. M. Udovic, M. Valant et al*., J. Europ. Cer. Soc*., **21**, 1735 (2001).
13. M. Udovic, M. Valent, B. Jancar et al., *J. Amer. Ceram. Soc*., **89** (11), 3462 (2006).
14. L. Weng, S. Hodgson, *Optical Mater*., **19**, 313 (2002).
15. A. Shalaby, Y. Dimitriev, R. Iordanova, A. Bachvarova-Nedelcheva, Tz. Iliev, *J. Univ. Chem. Techn. Metall.*, **46** (2), 137 (2011).
16. S. Hodgson and L. Weng, *J. Mater. Sci: Mater. Electron*., **17**, 723 (2006).
17. T. Hayakawa, H. Koyama, et al., *J. Univ. Chem. Techn. Metall*., **47** (4) 381(2012).
18. H. Wei, J. Lin, W. Huang, et al., *Mater. Sci. Engineer*., **164B**, 51 (2009).
19. Y. Dimitriev, V. Dimitrov, M. Arnaudov, *J. Mater. Sci*., **18**, 1353 (1983).
20. A. Murashkevich, A. Lavitkaya, T. Barannikova et al., *J. Appl. Spectr*., **75** (5), 730 (2008).
21. E. Yurchenko, G. Kustovar, S. Bacanov, Vibratioanal spectroscopy of inorganic compounds, Moscow, Nauka, 1981 (in Russian).

СИНТЕЗ И ХАРАКТЕРИЗИРАНЕ НА TeO_2/TiO_2 ПРАХОВЕ, ПОЛУЧЕНИ ОТ Te (VI) КИСЕЛИНА

Р. С. Йорданова[1], А. Д. Бъчварова-Неделчева[1]*, Р. Д. Гегова[1], Я. Б. Димитриев[2]

[1] Институт по Обща и Неорганична Химия, БАН, ул. „Акад. Г. Бончев“, бл. 11, София, 1113, България
[2] Химикотехнологичен и Металургичен Университет, бул. “Кл. Охридски”, 1756 София, България

Постъпила февруари, 2013 г.; приета май, 2013 г.

(Резюме)

Настоящото изследване е фокусирано върху възможността за получаване на TeO_2 прахове в системата TiO_2–TeO_2 прилагайки един ниско температурен метод. Телурова (VI) киселина и титанов бутоксид са използвани като една нова комбинация от прекурсори. Като обекти на изследване бяха подбрани два състава с високо съдържание на TeO_2 (80, 90 mol%). Получени са жълти прахове, които са характеризирани с РФА, ИЧ и УВ-Вис спектроскопия. Изследвана е кристализационната тенденция на праховете в интервала 300–600 °C. Установено бе, че кристализационния процес започва при нагряване над 300 °C. Композитни прахове съдържащи α-TeO_2 (парателурит) и $TiTe_3O_8$ са получени като крайни продукти.

Bulgarian Chemical Communications, Volume 45, Number 4 (pp. 491–496) 2013

Synthesis, structural and optical characterization of TeO_2–GeO_2–Nd_2O_3 glasses

I. Piroeva[1], L. Dimowa[2]*, S. Atanasova-Vladimirova[1], N. Petrova[2], B. L. Shivachev[2]

[1] *Academician Rostislav Kaishev Institute of Physical Chemistry, Bulgarian Academy of Sciences, Acad. Georgi Bonchev str., building 11, Sofia 1113, Bulgaria*
[2] *Academician Ivan Kostov Institute of Mineralogy and Crystallography, Bulgarian Academy of Sciences, Acad. Georgi Bonchev str., building 107, 1113 Sofia, Bulgaria*

Received February, 2013; Revised May, 2013

Synthesis and optical properties of novel TeO_2–GeO_2–Nd_2O_3 glasses suitable for multiband calibration or multicolor filters in the 350–1000 nm wavelength region are reported. Differential thermal analysis (DTA), X-ray diffraction (XRD), Infrared FT-IR, UV/VIS spectroscopy, scanning and transmission electron microscopy (SEM, TEM) were complementarily applied to study the structural, thermal and optical properties of this ternary system. The UV-VIS spectrum shows outstanding absorption at specific wavelength suggesting that the glasses can be employed as multi-color-type filter.

Key words: tellurite glasses, multiband filter, XRD, FTIR.

INTRODUCTION

Tellurium oxide (TeO_2)-based glasses are of scientific and technical interest due to their optical properties: excellent transmission in the visible and near IR (up to 4.5 μm), low phonon energy, large third-order nonlinear susceptibility [1, 2]. In addition to their suitable optical properties tellurite glasses show other favorable properties, such as good mechanical strength and chemical durability, low processing temperature and large rare-earth solubility [3]. The combination of these properties makes tellurite glasses good candidates for the development of optical, nonlinear optical devices (e.g. optical amplifiers) [4]. Multi-band filters are relatively new to the commercial market and are significantly more expensive than traditional colored, dichroic, sequential or polarized filter/glasses [5]. Traditional optics for multiband applications covering regions of the SWIR, MWIR and LWIR include Zinc Sulfide (ZnS), Zinc Selenide (ZnSe) and Germanium (Ge) [6]. These materials have low strength, exhibit very low resistance to water, rain and dust erosion and ZnS and ZnSe are very soft and easily scratched or damaged. Ge, on the other hand, does not transmit in SWIR and becomes opaque in MWIR and LWIR at temperatures above 100 °C. Current multiband imaging systems with wide field of view use separate cameras and optics for each band region [6]. Achromats can be designed using materials having different dispersion profiles to minimize the focal shift between light from different wavebands when imaged through the lens system [7]. These achromats are currently available only in a narrow wavelength range due to the limited availability of suitable commercial materials.

The aim of this study was to obtain new tellurite glasses possessing suitable mechanical and optical properties for optical application [8]. As a result we report the synthesis, structural and optical properties of TeO_2–GeO_2–Nd_2O_3 glasses that exhibit suitable properties for multiband filter application.

MATERIALS AND METHODS

Synthesis

The tellurite glasses presented in our work were prepared by the melt-quenching technique in platinum crucible in an electrically-heated furnace under ambient atmosphere. High purity chemicals TeO_2

* To whom all correspondence should be sent:
E-mail: louiza.dimova@gmail.com

(99%), GeO_2 (99%), Nd_2O_3 (99%) were used for the batch melting. The raw material batches with composition $(1–x)TeO_2–xGeO_2–xNd_2O_3$ mol% (x = 5, 10 and 20) were carefully mixed (grounded) and then the batches were melted at 955 °C for 1 h. The glass melts were cast onto a preheated stainless steel mold at 120 °C and annealed at 150 °C (below the glass transition temperature) for 12 h in a separate electric oven to remove thermal strains. Then cooling down to room temperature was performed by switching off the oven. After the annealing the samples were sliced and polished into sizes of 3×3×1 mm^3 for the spectroscopic (UV-Vis) measurements.

Differential thermal analysis (DTA)

The DTA curves in the 20–750 °C temperature range were obtained from grounded samples (sample weight 14 ± 0.2 mg) of the as-quenched pieces under a constant heating rate of 10 °C/min in an air flow of 40 ml/min on a Stanton Redcroft thermoanalyzer. The glass transition (*Tg*) and crystallization (*Tc*) temperatures derived from these studies were employed in fixing the annealing-treatment temperatures for the various glass compositions.

X-ray diffraction (XRD)

X-ray powder diffraction analyses (Bruker, D2 Phaser diffractometer, Cu Kα, 0.02°.s^{-1}) were performed on the crushed powders of the annealed and heat-treated samples to verify the amorphous state of the sample and obtain information for the crystalline phases.

Infrared FT-IR

Infrared transmission properties of samples (KBr pellets) were measured with a Bruker Tensor 37 Fourier transform infrared (FTIR) spectrometer at a resolution of 4 cm^{-1} and accumulating 64 scans.

UV/VIS spectroscopy

The absorption spectra were measured on a Cary100, Varian spectrophotometer over the spectral range of 190–900 nm.

Scanning and transmission electron microscopy (SEM, TEM)

SEM analyses were performed on a JSM 6390 electron microscope (Japan) in conjunction with energy dispersive X-ray spectroscopy (EDS, Oxford INCA Energy 350) equipped with ultrahigh resolution scanning system (ASID-3D) in regimes of secondary electron image (SEI) and back scattered electrons (BEC) image. Before attempting SEM characterization, the sample must be clean and completely dry. Surface oils or dirt must be removed with solvents such as methanol or acetone. The sample is mounted on a double coated conductive carbon tape that holds the sample firmly to the stage surface and can be used as a ground strap from the sample surface to sample holder. The samples were Carbon coated (time of coating ~20 sec). Carbon at that thickness will have little or no effect on elemental analysis. The accelerating voltage was 20 kV, I ~65 mA. The pressure was of the order of 10^{-4} Pa.

TEM work was performed on a JEOL JEM 100B (100 kV). The accelerating voltage was 100 kV and the pressure was of the order of 10^{-6} Pa. The preparation of TEM specimens involves mechanical grinding, then dispersion in ethanol and finally depositing a drop of the dispersion on a Cu grid. The grid is dried on a filter paper and is ready for TEM observation.

RESULTS AND DISCUSSION

The XRD patterns of the annealed glasses samples corresponding to the TGN compositions x = 5, 10, and 20 mol% are shown on Fig. 1. The XRD patterns show the amorphous nature of the samples, with some broadening around 2θ = 28° are observed. In order to check for the presence/appearance of metastable phases TEM investigations were also performed to further complement XRD structural characterization. Low magnification TEM images of show the general morphology while the

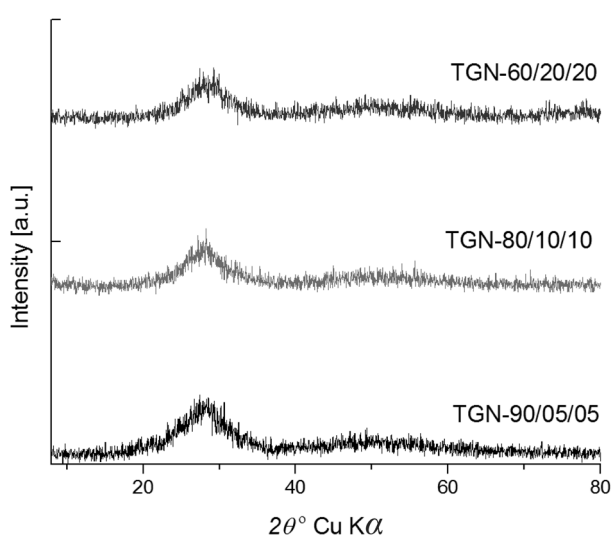

Fig. 1. XRD patterns of TGN-5, TGN-10 and TGN-20 samples after 12 h annealing at 150 °C

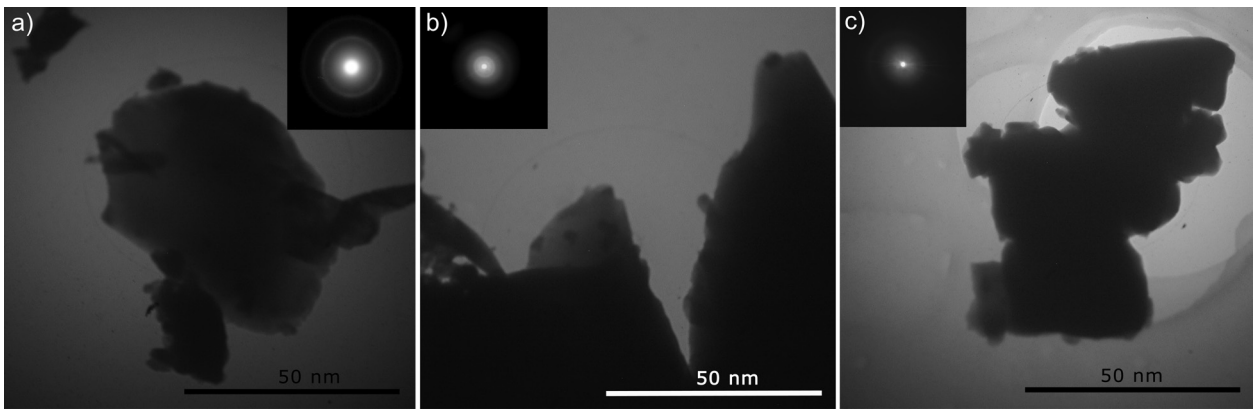

Fig. 2. Selected TEM images and SAED pattern demonstrating the amorphous nature of the samples; a) TGN-5, b) TGN-10 and c) TGN-20

SAED micro diffraction (Fig. 2) shows that samples are amorphous and are not subject to crystallization resulting from the interaction (heating) with the electron beam [9, 10]. The observed halo around the bright spot in the center indicates that the electrons are diffracted randomly by a material of amorphous structure. Indeed DTA data (Fig. 3) shows a good thermal stability of the glasses as the transition temperature (*Tg*) for all sample is around 320 °C and the first crystallization occurs around 420 °C (for TGN-5). The XRD patterns of the annealed TGN-5 at 300 and 610 °C (Fig. 4) confirm the suggested good thermal stability of the glasses [11]. The annealed at 300 °C (~12h) TGN-5 remains amorphous while the result of the annealing at 610 °C is the formation of the halite type (NaCl) cubic (SG 225) $Nd_{0.25}Te_{0.75}O_{1.875}$ crystal phase [12].

The compositions of the tellurite glasses and their surface morphology were assessed by SEM/EDS. As one can see the untreated surfaces of the samples exhibit very few visible defects (Fig. 5) and thus are very well suited for optical application (after cutting and polishing). Their chemical compositions were also close to the ones of the starting batches the major difference being for Nd_2O_3 in TGN-20.

The amorphous natures of the synthesized glasses can also be assessed from FTIR analysis [13]. The peaks of the FTIR spectra are very few and large

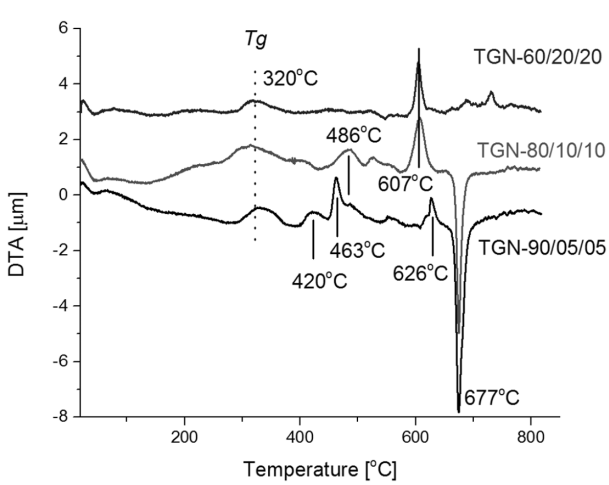

Fig. 3. Differential thermal analysis data of TGN-5, TGN-10 and TGN-20 glass samples

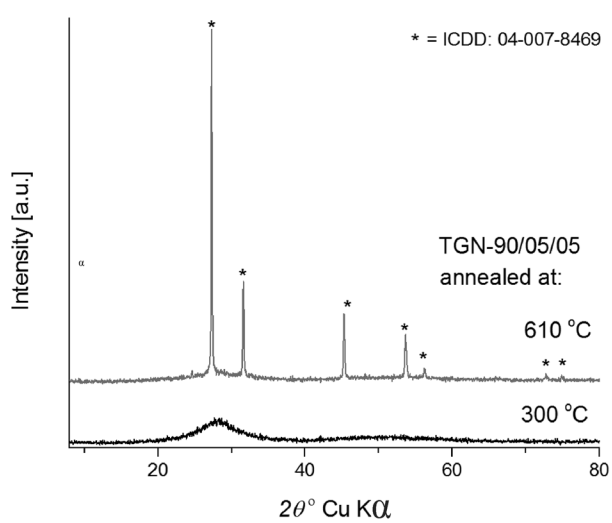

Fig. 4. XRD pattern of TGN-5 after annealing at 300 and 610 °C for 12 hours; JCPDS 04-007-8469 [12]

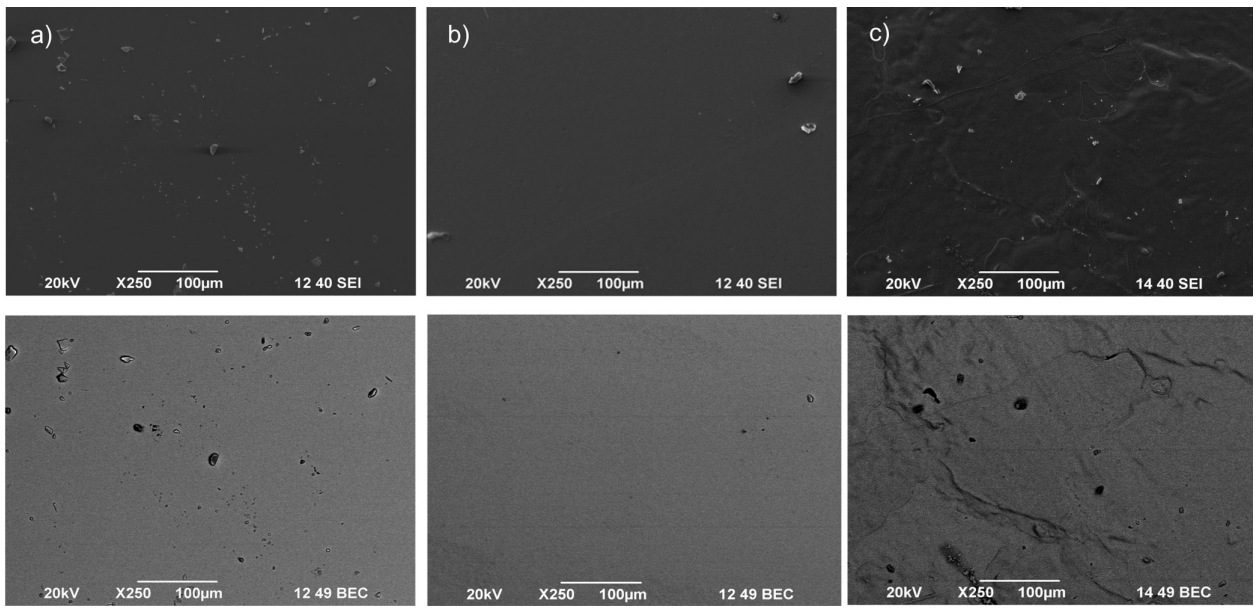

Fig. 5. SEM images of (a) TGN-5, (b) TGN-10 and c) TGN-20 surfaces. The top row shows images obtained by secondary electron imaging (SEI) while the bottom row are by Backscattered Electron contrast (BEC) imaging

Table 1. Starting chemical composition for TGN – x (x = 5, 10 and 20) mol% samples and subsequent EDS data for obtained samples TGN – x

Starting batch composition (mol%)	EDS data for obtained samples (mol%)	Resulting formula
90/05/05	88.92 / 6.52 / 4.54	88.92 TeO_2–6.52GeO_2–4.54Nd_2O_3
80/10/10	81.54 / 9.77 / 8.67	81.54 TeO_2–9.77GeO_2–8.67 Nd_2O_3
60/20/20	63.51 / 19.61 / 16.88	63.51 TeO_2–19.61GeO_2–16.88 Nd_2O_3

(broad) and thus they reveal only the presence of short order of Te, Ge and Nd oxides (a broad band around 670 cm^{-1} with a shoulder around 770 cm^{-1} Fig. 6a). This range is usually associated with stretching vibrations of the Te–O bond: [TeO_4] trigonal bipyramids and [TeO_3] trigonal pyramids units [14]. The performed deconvolution of these bands yield the same results for sample TGN-5 and 10 (90/05/05 and 80/10/10): four peaks with very close values for the peaks maxima. The deconvolution of the FTIR broad band of TGN-20 sample produced seven peaks. Four of those (2, 4, 5 and 6) having approximately the same maxima as the ones in TGN-5 and 10 samples (Fig. 6 b-d). The new peaks are not very intensive and appear on both sides of the broad band at 670–770 cm^{-1}: 471 cm^{-1}, 613 cm^{-1} and at 900 cm^{-1}. In our case, the absorption band at ~769, 781, 720 cm^{-1} correlates with [TeO_3] and the one at ~658, 672, 655 cm^{-1} with [TeO4] units [14, 15]. The band located around ~580 cm^{-1} (584, 587 and 578) can be associated with Te–O–M (M = Nd or Ge) while the band at 828, 845 and 829 cm^{-1} in the different composition may linked to M–O–M (M = Nd or Ge). The increased amounts of and Nd_2O_3 and GeO_2 lead to additional separation of the M–O–M linkages as Te–O–Ge ones are characterized by the 471 cm^{-1} band while the 613 cm^{-1} and 900 cm^{-1} ones can be attributed to Te–O–Nd and Nd–O–Nd. Those additional bands are could be obtained only in the deconvolution of the TGN-20 spectrum and attempts to introduce them in TGN-5 and TGN-10 processing failed.

The UV-Vis absorbance spectra of the TGN-x samples are shown on Fig. 7. The observed minima of the absorbance are located approximately at 885, 845, 780, 710 (700–725 range), 653 (667–647

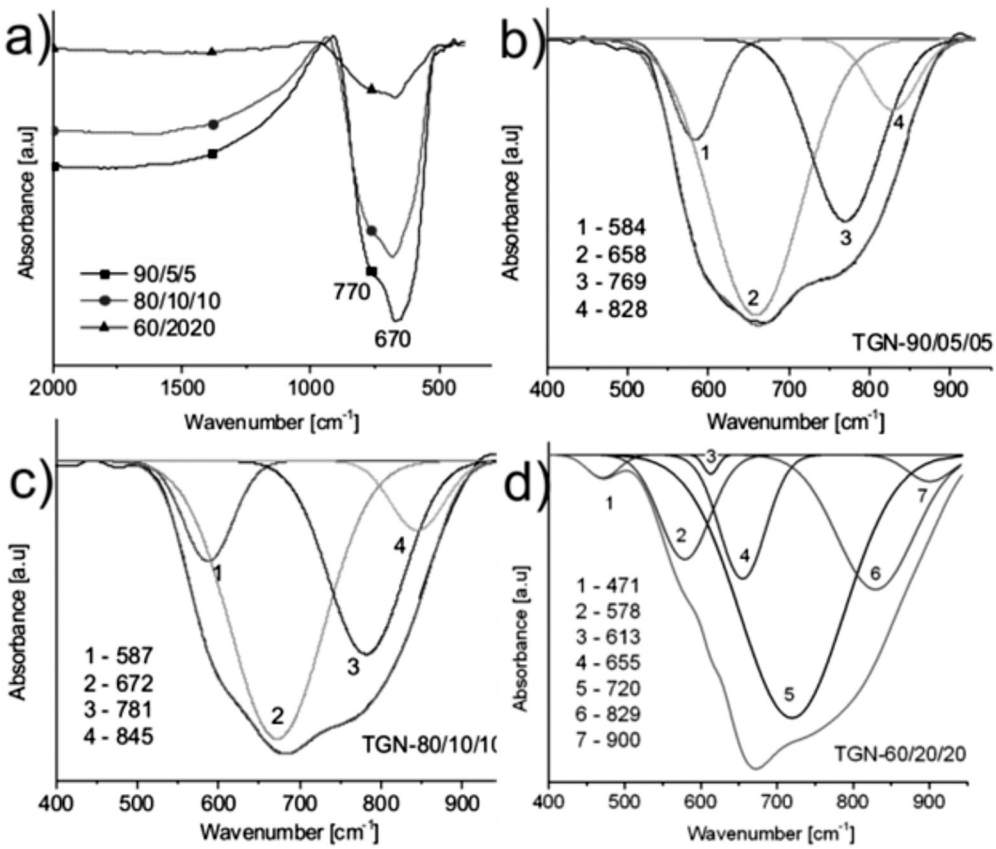

Fig. 6. FTIR spectra of TeO_2–GeO_2–Nd_2O_3 glass: a) Overview of the FTIR of the three TGN – x (x = 5, 10 and 20) samples and deconvolution of the band around 760 cm^{-1} for each sample b) TGN – 5, c) TGN – 10 and d) TGN – 20

range), 547, 491 and 447 nm [16]. The maxima of the absorption correspond to Nd^{3+} transitions from ground state of $^4I_{9/2}$ to the excited state of $^4F_{3/2}$ (876 nm), $^4F_{5/2}$ (804 nm), $^4F_{7/2}$ (747 nm), $^4F_{9/2}$ (682 nm), $^2H_{11/2}$ (628 nm), $^4G_{5/2}$ (583 nm), $^4G_{7/2}$ (525 nm), $^4G_{9/2}$ (511 nm), $^4G_{11/2}$ (465 nm) and $^2P_{1/2}$ (431 nm) respectively. The most interesting feature of the obtained glasses is probably their UV-Vis optical characteristics showing that they can be used as multiband filters.

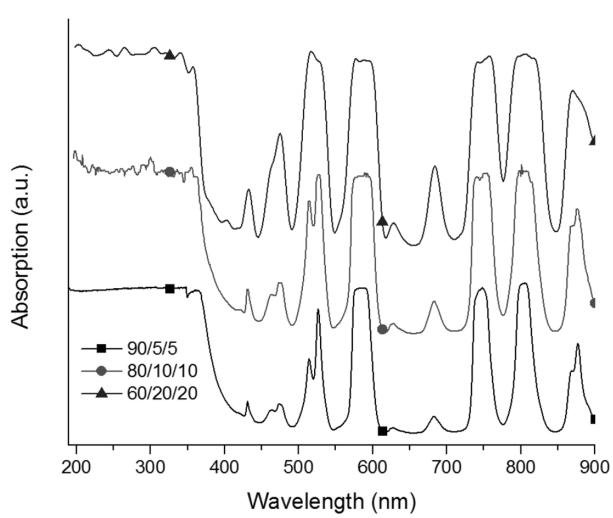

Fig. 7. UV-Visible transmittance spectra of polished 1 mm thick TeO_2–GeO_2–Nd_2O_3 glasses

CONCLUSIONS

In summary we have were prepared TeO_2–GeO_2–Nd_2O_3 glasses by conventional melt-quenching technique. The glasses show good thermal stability, with respect to other tellurite glasses, which makes them suitable for usage up to ~250 °C. The optical absorbance/transmission properties of the glasses are comparable to those of the multiband filters and make them ready for this type of application.

Acknowledgments: *The authors would like to thank the Bulgarian National Science Fund (bulfund.com) support through grant DRNF 02/1.*

REFERENCES

1. R. El-Mallawany, Tellurite Glasses Handbook: Physical Properties and Data, 2-nd ed. CRC Press, Proc. conf., Bordeaux, France, 2011.
2. A. Bachvarova-Nedelcheva, R. Iordanova, K. L. Kostov, St. Yordanov, V. Ganev, *Optical Mater*., **34**, 1781 (2012).
3. G. Yankov, L. Dimowa, N. Petrova, M. Tarassov, K. Dimitrov, T. Petrov, B. L. Shivachev, *Optical Mater*., **35**, 248 (2012).
4. H. Hu, Y. Bai, M. Huang, B. Qin, J. Liu, W. Zheng, *Optical Mater*., **34**, 274 (2011).
5. H. T. Bookey, J. Lousteau, A. Jha, N. Gayraud, R. R. Thomson, N. D. Psaila, H. Li, W. N. MacPherson, J. S. Barton, A. K. Kar., *Optics Express*, **15**, 17554 (2007).
6. I. Jlassi, H. Elhouichet, M. Ferid, C. Barthou, *J. Lumi.*, **130**, 2394 (2010).
7. S. Bayya, J. Sanghera, W. Kim, G. Villalobos, I. Aggarwal, *Optical Components and Materials*, IX, 825703 (2012); doi:10.1117/12.910149.
8. Y. Dimitriev, A. Bachvarova-Nedelcheva, R. Iordanova, S. Yordanov, *Phys. Chem. Glasses*, B, **48**, 138 (2007).
9. B. Fultz, J. Howe, Transmission Electron Microscopy and Diffractometry of Materials, 3-rd edition, Springer, 2007.
10. P. Binev, W. Dahmen, R. DeVore, P. Lamby, D.l Savu, R. Sharpley, *Nanostructure Science and Technology*, 73 (2012).
11. Z. Luo, A. Lu, G. Qu, Y. Lei, *Journal of Non-Crystalline Solids*, **362**, 1, 207 (2013).
12. M. Tromel, W. Hutzler, E. Munch, *J. Less-Common Met*., **110**, 421 (1985).
13. Y. Dimitriev, V. Dimitrov, M. Arnaudov, *Journal of Materials Science*, **18**, 5 1353 (1983).
14. E. I. Kamitsos, A. Patsis, M. Karakassides, G. Chryssikos, *Journal of Non-Crystalline Solids*, **126**, 1–2, 52 (1990).
15. Q. Li, L. Tian, K. Chi, H. Yang, M. Sun, W .Fu, *Applied Surface Science*, **270**, 707 (2013).
16. G. Singh, P. Kaur, S. Kaur, D. Arora, P. Singh, D. Sing, *Materials Physics and Mechanics*, **14**, 31 (2012).

СИНТЕЗ, СТРУКТУРНА И ОПТИЧНА ХАРАКТЕРИСТИКА НА TeO_2-GeO_2-Nd_2O_3 СТЪКЛА

И. Пироева[2], Л. Димова[1], С. Атанасова-Владимирова[2], Н. Петрова[1], Б. Шивачев[1]

[1] Институт по минералогия и кристалография, БАН, ул. „Акад. Георги Бончев“, бл. 107, София 1113, България

[2] Институт по физикохимия „Акад. Ростислав Каишев“, БАН, ул. „Акад. Георги Бончев“, бл. 11, София 1113, България

Постъпила февруари, 2013 г.; приета май, 2013 г.

(Резюме)

В настоящата работа са представени синтезът, структурните, термичните и оптичните особености на нови стъкла от системата TeO_2–GeO_2–Nd_2O_3. Получените стъкла могат да намерят приложение като цветни филтри при калибриране, изискващо наличие на няколко дължини на вълните в диапазона 350–1000 nm и т.н. При охарактеризирането на стъклата са използвани диференциално термичен анализ (ДТА), прахова рентгенова дифракция (ПРД), инфрачервена спектроскопия (ИР), ултравиолетова и видима абсорбция (УВ-Вис) и електронна микроскопия (сканираща и трансмисионна). УВ-Вис спектърът на поглъщане на изследваните образци показа специфично поглъщане на определени дължини на вълната.

Bulgarian Chemical Communications, Volume 45, Number 4 (pp. 497–504) 2013

Photocatalytic and antibacterial activity of Fe-doped TiO_2 nanoparticles prepared by nonhydrolytic sol-gel method

A. M. Stoyanova[1]*, H. Y. Hitkova[1], N. K. Ivanova[1], A. D. Bachvarova-Nedelcheva[2], R. S. Iordanova[2], M. P. Sredkova[1]

[1] *Medical University-Pleven, 5800 Pleven, Bulgaria*
[2] *Institute of General and Inorganic Chemistry, Bulgarian Academy of Sciences, 1113 Sofia, Bulgaria*

Received February, 2013; Revised May, 2013

In the present work we report synthesis of pure and iron doped TiO_2 by nonhydrolytic sol-gel method using titanium tetrachloride, benzyl alcohol and iron(III) nitrate.

The structure of the resulting particles was characterized by XRD, IR and UV-Vis spectroscopy. The average particles size of Fe-doped TiO_2 was 12–15 nm.

The photocatalytic activity of the as-prepared TiO_2 powders was tested by photodegradation of the organic dye Reactive Black 5 under UV and visible irradiation in an aqueous suspension.

Antibacterial action of pure and Fe-modified titanium dioxide samples was tested using *Escherichia coli* ATCC 25922. The bacterial growth was examined in the presence of a synthesized preparations – in dark and with UV light. The photodisinfection activity was assessed by plotting of survival curves and calculation of removal efficiency. In order to estimate the post-irradiation effect, the behavior of the bacterial suspension in presence of each photocatalyst after 24 h dark period was tested.

The optimal iron content was found to be 0.5 mol% for the photocatalytic decomposition of Reactive Black 5 dye under ultra violet (UV) and visible (Vis) irradiation, and also for antibacterial activity in the presence of UV light. At higher iron contents (1–2 mol%) the photocatalytic performance under both UV and Vis irradiation was worse relative to the undoped TiO_2.

Key words: Fe-doped titanium dioxide, sol-gel, photocatalytic, antibacterial activity.

INTRODUCTION

Titanium dioxide is a wide-band-gap semiconductor and a well-known photocatalytic material. Nanosized titanium dioxide is used in a variety of applications, such as fine ceramics, cosmetics, gas sensors, inorganic membranes, electronic devices and solar cells [1, 2]. Other photochemical and photophysical applications include photolysis of water and light-induced superhydrophylicity [2]. Because of its favorable physico-chemical properties it is now under intensive investigations for practical application to environmental and antimicrobial purification [2–4]. Many organic compounds can be decomposed in aqueous solution in the presence of TiO_2 powders or coatings illuminated with near UV or sunlight [5–7].

Most investigations on semiconductor catalysis focus on anatase type TiO_2, because of its high photocatalytic activity under UV irradiation ($\lambda \geq 388$ nm) [8–10]. Photocatalytic reactions occur on the surface of TiO_2 particles. When TiO_2 is irradiated by UV rays, pairs of positively charged holes are created in the valency band and electrons in the conductivity band. The holes react with water molecules or with the hydroxyl ions and as a result hydroxyl radicals are formed, which are strong oxidants of the organic molecules [2]. Hydroxyl radicals and other photogenerated reactive oxygen species can cause oxidative attack of the bacterial cell membrane and some internal cellular components that finally leads to cell death [11, 12].

However, there are still problems needed to be solved concerning its application in photocatalysis. Its shortcomings include a large band gap energy (3.2 eV) which causes most of the solar spectrum unutilized. In a number of cases, the photocatalytic reactions on TiO_2 nanoparticles can usually be in-

* To whom all correspondence should be sent:
E-mail: astoy@abv.bg

duced only by ultraviolet light, which limits the application of TiO_2 as a photocatalyst with visible light [2, 13]. In addition, the holes may recombine rapidly with conduction band electrons, thus decreasing the photocatalytic oxidation efficiency. Therefore, prolongation of the holes lifetime is favourable for the photocatalytic efficiency. In order to accomplish solar-driven photocatalysis and at the same time retard possible electron-hole recombination, doping of TiO_2 with various transition metals is one of the most successful strategies. Multivalent metal ions act as electron scavengers at the surface of the titanium dioxide, thus preventing electron-hole recombination and improving the oxidation performance [14, 15].

Among various metal ions, doping with iron(III) has been widely investigated because of its unique electronic structure and its size that closely match those of titanium(IV). The favorable electronic states of iron ions in titania contribute to formation of efficient trapping sites for electrons and holes [16, 17]. Enhanced photocatalytic activity was reported for iron-doped TiO_2 under UV and also for visible light irradiation in several publications [16–20]. On the contrary, some authors observed no or even negative effect of iron on the photocatalytic performance [21–24].

The effect of metal ion doping strongly depends on many factors such as synthetic procedure, doping method and the dopant concentration [14, 16]. Iron-doped titania samples have been prepared by various methods, including hydrothermal, controlled hydrolysis, co-precipitation, impregnation, solvothermal, etc. [20]. Among the most popular synthetic methods is sol-gel technology induced by traces of water. However, in most cases the reaction rates in aqueous sol-gel chemistry are very fast, especially with transition metal precursors, making it uneasy to control the processes. A simple way to circumvent this problem is applying of so called nonaqueous or nonhydrolytic procedures – syntheses performed in organic solvents under exclusion of water [25, 26]. The slower reaction rate of nonhydrolytic processes allow for better control over particle size and crystallinity [27].

In view of increasing the photocatalytic activity of TiO_2, we prepared pure and iron doped TiO_2 by nonhydrolytic sol-gel method and further evaluated their photocatalytic and antibacterial activity.

EXPERIMENTAL

Materials

Titanium(IV) chloride (purity ≥99.0%) was purchased from Fluka, benzyl alcohol (≥99.5%) from Merck, iron(III) nitrate, Reactive Black 5 dye ($C_{26}H_{21}N_5Na_4O_{19}S_6$, dye content, 55%), absolute ethanol and diethyl ether were supplied by Sigma-Aldrich. All the chemicals were used without further purification.

Preparation and characterization of titania catalysts

The synthesis of pure and Fe-doped titanium oxide nanoparticles was carried out following the nonhydrolytic procedure described by Niederberger et al. [27]. For the synthesis of undoped TiO_2 titanium tetrachloride was slowly added to a beaker containing benzyl alcohol under vigorous stirring and the resulting sols were heated at 150 °C for 1 h, at continued stirring [28]. For the preparation of Fe-modified TiO_2, initially, proper amount of iron(III) nitrate was dissolved in ethanol and fed to benzyl alcohol according to Figure 1. The reaction mixtures were left for aging at room temperature for 10–14 days. The resulting white thick suspensions were centrifuged at 4500 rpm for 15 min and the supernatant was discarded by decantation. The precipitates were then washed two times with absolute ethanol and three times with diethyl ether. After every washing

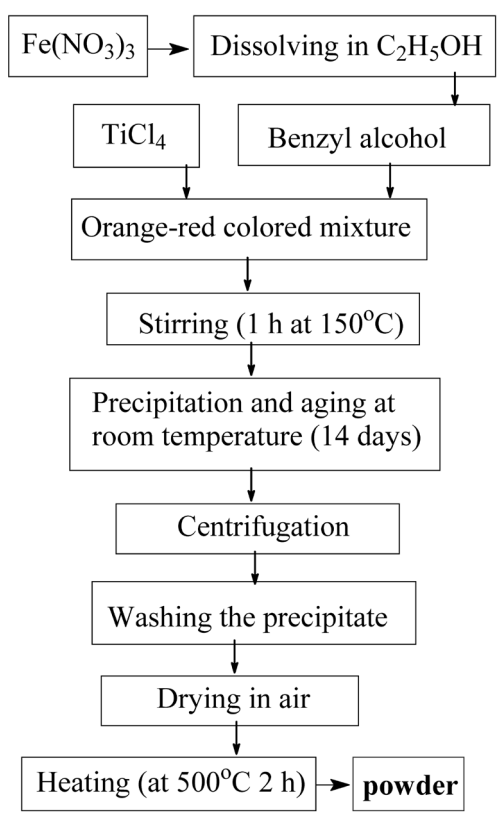

Fig. 1. Scheme of nonhydrolytic synthesis of Fe-doped TiO_2

step, the solvent was separated by centrifugation. The collected material was dried in air overnight and then ground into a fine powder. The obtained powders were calcinated at 500 °C for 2 hours. The as–prepared samples are denoted as TiO_2 for pure and xFe/TiO_2 for doped titania, where x represents the Fe/Ti mol ratio. In this way three modified TiO_2 samples were obtained: 0.5Fe/TiO_2, 1Fe/TiO_2, and 2Fe/TiO_2.

The structure and morphology of the resulting particles were characterized by X-ray diffraction (XRD, Bruker D8 Advance X-ray apparatus), infrared (IR, using the KBr pellets method (Nicolet-320, FTIR spectrometer with a resolution of ±1 cm^{-1}, by collecting 64 scans in the range 4000–400 cm^{-1}) and UV-Vis spectroscopy (Spectrophotometer Evolution 300).

Photocatalytic activity experiments

The photocatalytic activities of the synthesized powders were evaluated by degradation of a model aqueous solution of the azo dye Reactive Black 5 (RB5) under UV-Vis illumination. The molecular structure of this commercially used dye is given in Figure 2.

The initial concentration of RB5 aqueous solution was 20 mg/l. Titanium sample (100 mg) was added to 150 ml dye solution to form suspension. After sonicated for 10 min, the suspension was magnetically stirred in dark for 30 min to ensure the establishment of an adsorption-desorption equilibrium. The UV-irradiation source was a black light blue lamp (Sylvania BLB 50 Hz 8W T5) with the major fraction of irradiation occurring at 365 nm. The lamp was fixed 10 cm above the solution surface. The intensity of UV-light reaching the surface of the suspension was measured with a numeric Luxmeter (LM 37, Dostmann electronic). The mean value of the radiation power impinging on the reacting suspension was estimated to be 150 Lx.

The visible light source was a 500W halogen lamp (Sylvania) fixed at 40 cm above the treated solution. The mean value of the radiation power reaching on the suspension was estimated to be 14000 Lx.

All photocatalytic tests were performed at constant stirring rate (450 rpm) and room temperature of 25 °C. At regular time intervals of illumination, aliquot samples of the mixture (3 mL) were collected and centrifuged in order to remove the solid particles. The absorbances of clear aliquots were measured by a Jenway 6505 UV-Vis spectrophotometer at 597 nm, the maximum absorption wavelength of RB5.

Antibacterial activity experiments

Bacterial strain and preparation of bacterial suspension

Escherichia coli ATCC 25922 was used as a model microorganism. To prepare bacterial suspension, one colony from a fresh culture of the tested strain was introduced into Tryptic Soy Broth (Difco) and then grown under aerobic conditions at 37 °C. After 15 hours incubation, the broth culture was centrifuged at 1000xg for 10 min. The bacterial cells were washed two times and finally resuspended with a sterile phosphate buffered saline (PBS) – pH 7.2. The obtained suspension was standardized using densitometer (Densimat, bioMerieux) to 0.5 Mc Farland and then diluted 1:1000 to the required cell density of approximately 10^5 colony forming units per milliliter (CFU/ml). The exact initial cell count was determined by spread plate method.

Experimental procedure

The antibacterial activity of pure and Fe-modified titanium dioxide substrates were tested as a part of the experimental setup, previously described [28]. The disinfection process was carried out at a volume of 100 ml bacterial suspension with an initial cell density of 10^5 CFU/ml and a catalyst concentration of 1 mg/ml. Each sample was poured in a sterile glass flask of 200 ml. Three flasks were used in the photodisinfection experiment: first flask served as a control of bacteria growth – no catalytic powder or radiation was applied and it was kept in dark; to the second and third flask, 100 mg of synthesized powder was added. The second flask was kept in dark, while the third flask was irradiated with UV light. All samples were conducted in continuous stirring with magnetic stirrers to ensure maximum mixing

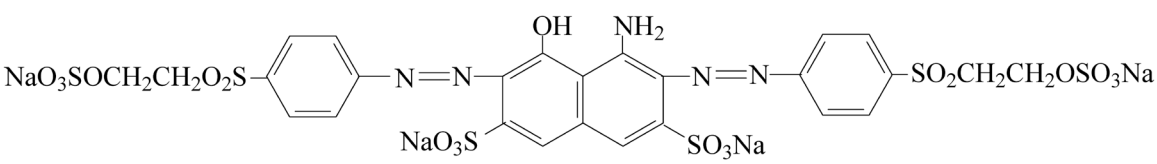

Fig. 2. Molecular structure of Reactive Black 5

of the powder particles. The experiment continued up to 1 hour at room temperature (25 °C).

At regular intervals of time (5 or 10 min) during the experimental period, and after 24 hours in dark, the definite amounts of samples were withdrawn and serial dilutions were prepared. 100 μl of the undiluted samples, and 10^{-1} and 10^{-2} dilutions were plated on Mueller-Hinton agar, BD Microbiology Systems (Cockeysville, Md). To reduce the detection limit, each undiluted and diluted sample was streaked on 3 agar plates. The number of viable cells in all samples was determined by spread plate method.

Antibacterial effect was evaluated by the decrease in the colony forming units on agar plates and presented as survival curves. The survival curves were constructed by plotting mean survival rate versus time. The removal efficiency, *E*, was calculated as:

$$E = \frac{C_i - C_f}{C_i} \times 100$$

where *Ci* and *Cf* are the initial and final CFU/ml, respectively.

RESULTS AND DISCUSSION

Characterization of titania samples

XRD measurements were performed to identify the crystalline phases synthesized by the nonhydrolytic sol–gel process at 500 °C calcination temperature. The XRD patterns of the as obtained powders, undoped and iron doped TiO_2 (0.5, 1 and 2 mol% Fe), are shown in Figure 3 a and b, respectively. As is seen in both figures, the three strongest interplanar distances of anatase (TiO_2) appear at 3.51; 1.89 and 1.66 Å (JCPDS 78-2486). The anatase structure is preferred over other polymorphs for photocatalytic applications because of its higher electron mobility, low dielectric constant and lower density. All commonly known polymorphs of titania consist of TiO_6 octahedra, which share edges and corners in different manners. The TiO_6 octahedron of anatase is slightly distorted [29]. It has to be noticed that iron was not found in the XRD patterns of the investigated samples due to its very low concentrations. The average crystallite size of as prepared undoped TiO_2 and iron doped TiO_2 (0.5, 1 and 2 mol% Fe) calculated from the broadening of the diffraction line using Sherrer's equation is about 20 and 12–15 nm, respectively. As is seen from the obtained values, the crystallite size of undoped TiO_2 is larger than those of Fe-doped TiO_2. Obviously, the Fe-doping leads to decrease of the crystallite sizes. Our results are in good accordance to the results obtained by Yang et al. [30]. However, there are previous studies which reported controversial results concerning the Fe^{3+} doping effect on the crystallite sizes. For example, Wang et al. [31] claimed that Fe^{3+} increase the crystallite sizes. Figure 4 presents the infrared spectra of investigated powder samples in the range 1200–400 cm^{-1}. As a more sensitive method, the IR spectroscopy was used to verify the main short range orders of the obtained submicron powders. As is seen from the figure, vibrations of the inorganic building units were recognized only. In the spectrum of all samples (Figure 4) bands in the range 470–420 cm^{-1} are observed. It is well known and it was also proved in our previous studies, that bands in the absorption range 700–400 cm^{-1} could be related to the vibrations of TiO_6 units [32, 33]. Despite

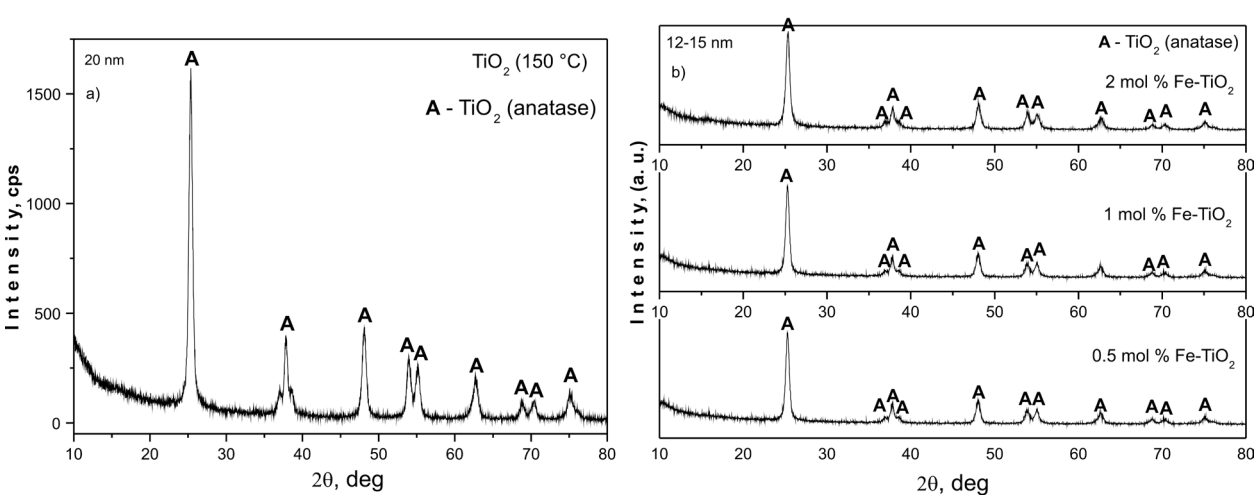

Fig. 3. XRD patterns of undoped (a) and doped with Fe (b) TiO_2

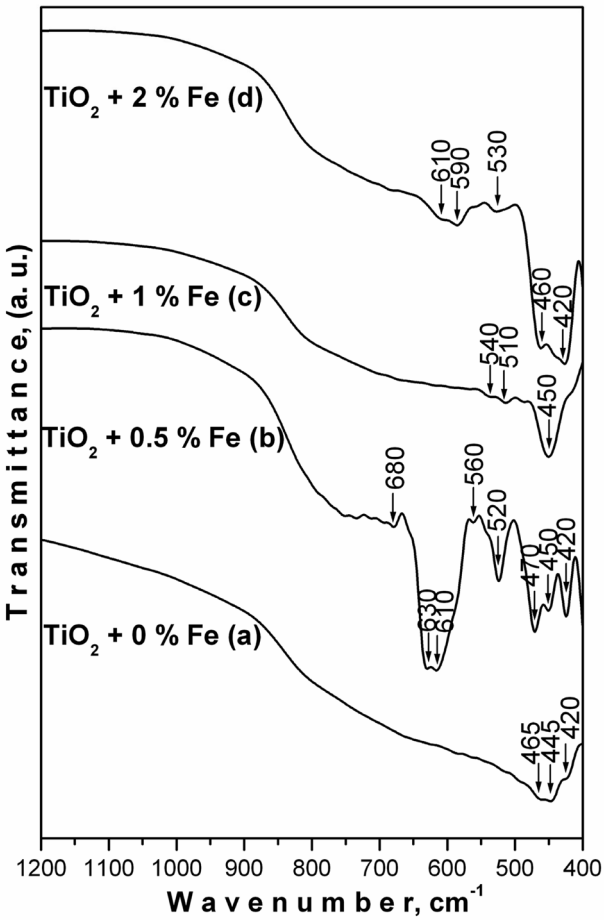

Fig. 4. IR of the investigated samples

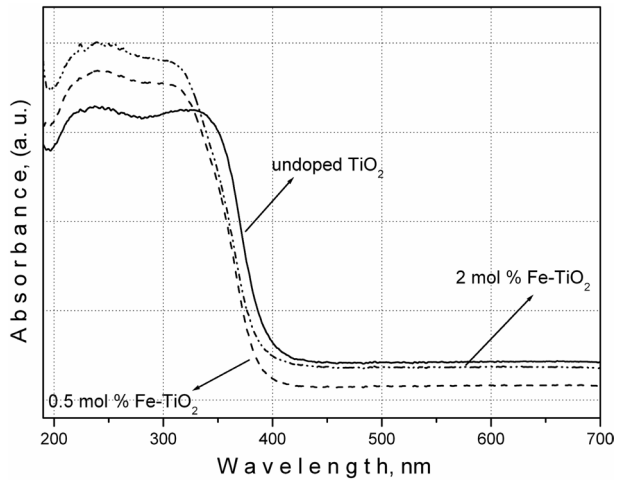

Fig. 5. UV-Vis spectra of undoped and doped with 0.5 and 2 mol% Fe–TiO_2

the fact that iron was not detected in the XRD patterns, its presence was registered by IR spectroscopy (bands in the range 680–470 cm^{-1}). The doping of even small amount of iron (0.5 mol%) led to changes in the IR spectra. The absorption intensity of the new bands changes with the iron content. The observed bands in the range 590–510 cm^{-1} could be assigned to the vibrations of FeO_6 structural units, while those above 600 cm^{-1} may be related to the vibrations of FeO_4 polyhedra [34].

The ultraviolet-visible (UV-Vis) absorption spectra of different TiO_2 powders are illustrated in Figure 5. As is seen from the figure, the increase in Fe^{3+} content increased the absorbance in the UV spectra. The UV-Vis spectra were used to determine the optical band gap (E_{opt}) of investigated samples. For undoped TiO_2 E_{opt} was 2.92 eV, while for the other two samples (0.5 and 2 mol%) it was about 2.95 eV. It is known that the band gap value of Degussa P25 is 3.03 eV [35], while for pure anatase is 3.2 eV [36]. Obviously, the band gap energy values of the synthesized undoped and Fe^{3+} doped TiO_2 samples are lower than those pointed out in the literature [35, 36]. According to Wu et al. [36] the narrowing of the band gap can improve the photocatalytic activity under visible light. This could explain our results for the photocatalytic activity of investigated samples. However, more experiments are needed in order to elucidate this fact.

Photocatalytic activity

The water soluble dye RB5 was selected as a model pollutant because it has been extensively used for dyeing cotton fabrics. Reactive Black 5 dye has two reactive vinylsulfonil groups and two azo groups (Figure 2). The dye is not degradable by direct photolysis and by TiO_2 in dark. Decoloration by TiO_2 adsorption under dark conditions did not exceeded 10% for all treatments (data not shown), determining that decoloration was conducted primarily by the photocatalytic process.

The changes in RB5 dye concentration C/C_o (C_o initial concentration and C reaction concentration of the dye) by the synthesized samples with the time of UV and visible radiation are shown in Figures 6 and 7. As can be seen, the iron content is an essential factor to define the photocatalytic activities of the samples. The preparations containing 0.5% Fe showed higher photocatalytic activities than pure TiO_2 either under UV or visible light irradiation. On the other hand, doping with higher concentrations of Fe^{3+} ions led to marked decrease in photocatalytic activity.

It is believed that Fe^{3+} ions can act as shallow traps in the titania lattice although their role during photooxidation processes remains controversial [37]. Introducing of small amounth of dopant ion

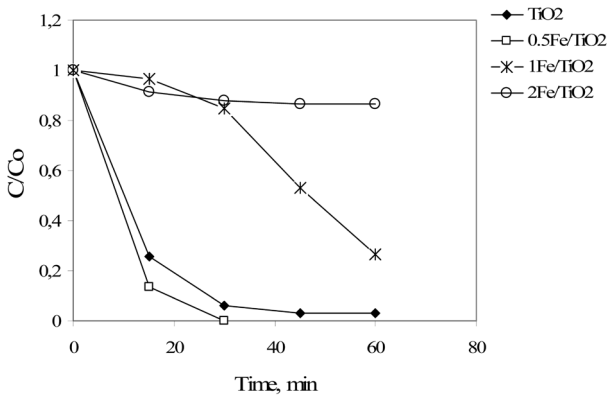

Fig. 6. Photocatalytic activity of TiO_2 samples under UV irradiation

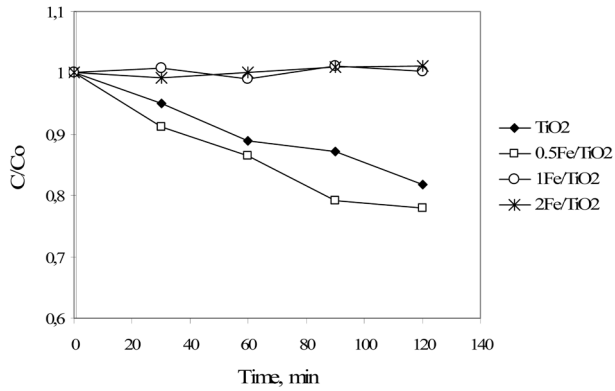

Fig. 7. Photocatalytic activity of TiO_2 samples under visible light irradiation

can retard possible electron-hole recombination thus leading to enhanced photoactivity. However, on increasing the dopant content the probability of charge carrier recombination is increased, explained by surplus Fe^{3+} ions which can cover the active sites on the surface of TiO_2 particles and as a result the photocatalytic activity decreases [38]. Sources of this controversy could also be due to differences in the preparation methods and doping procedure which can lead to different structural and electronic characteristics of the samples [39, 40]. For a particular synthesis method, optimum dopant concentration directly affect the photocatalytic activity [17, 37]. Such photocatalytic behavior of Fe-doped TiO_2 was observed by us and other researchers. In our study, maximum photoactivity toward RB5 dye was exhibited for the 0.5% Fe sample. The activity of this sample was higher than that of pure TiO_2 (Figures 6 and 7) under both – UV and visible light irradiation.

Antibacterial activity

The results from all experiments show that the inactivation of bacteria strongly depends on the presence of UVA light and concentration of the dopant. In the absence of radiation and after 60 min treatment, the number of cells slightly decreased, as follows: from an initial cell count 2.16×10^5 CFU/ml to 1.67×10^5 CFU/ml in contact with pure TiO_2, and from 2.24×10^5 CFU/ml to 7.40×10^4 CFU/ml with 0.5% Fe-doped TiO_2. Despite the fact that during dark conditions 0.5% Fe sample had showed better activity and reduced 66.8% of bacterial cells in the first 60 min, in the next 60 min the number of viable cells reached 1.65×10^5 CFU/ml. After 24 hours subsequent dark period, the bacterial growth was the same as at the beginning of the experiment in both studied powders – pure and 0.5% Fe-doped TiO_2. It can be concluded, that disinfection with TiO_2 nanosized materials under dark conditions does not proceed. This corresponds to the principle of photocatalytic disinfection activity [11] and is in agreement with other reports [12]. Antibacterial action of the synthesized preparations in the presence of UVA light is illustrated as survival curves in Figure 8. As can be seen, pure TiO_2 exhibited significant photoinduced activity against *E. coli* ATCC 25922: For the initial cell concentration 2.16×10^5 CFU/ml, the removal efficiency in the first 5 and 10 minutes was 49.3% and 98.4%, respectively, and 100% reduction was achieved in 15 min.

Fe-modified titanium dioxide substrates have shown different activities against the tested strain at illumination conditions. It is obvious, that in the presence of UVA light 0.5% Fe-doped TiO_2 ex-

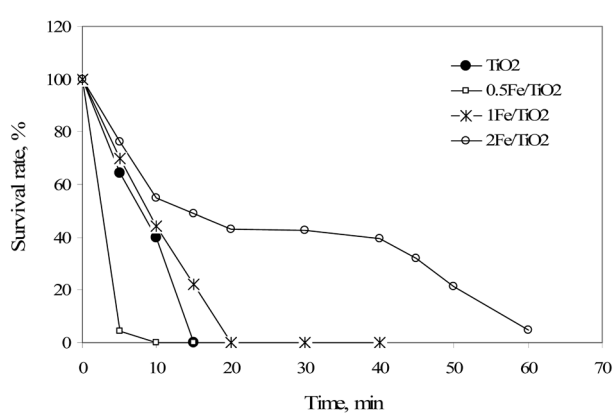

Fig. 8. Survival curves of *Escherichia coli* ATCC 25922 in presence of different substances and UVA radiation

hibited strongest antibacterial action – removal efficiency in the first 5 min was 95.7% and complete killing of bacteria was observed in 10 min. Concerning other preparations with higher iron content, the sample $1Fe/TiO_2$ showed better antibacterial activity than those of $2Fe/TiO_2$ (Figure 8). After 20 min UVA light treatment by 1% Fe-doped TiO_2, almost all cells were destroyed (99.9%), whereas by using 2% Fe-doped TiO_2 for the same period only half of them were destructed (56.7%) and subsequent 95.3% reduction was achieved after 60 min.

In most studies, TiO_2 photo-inactivation of bacteria has been examined as levels of inactivation without taking into account the levels of repair that may follow [12]. That is why we estimated the post-irradiation effect of all synthesized preparations after 24 h dark period. The subcultures from UVA illuminated TiO_2, $0.5Fe/TiO_2$ and $1Fe/TiO_2$ samples did not show any bacterial growth after overnight in the dark. This suggests that photoactivated treatment by these agents induced strong and lethal bacterial damages. In contrast to them, 2% Fe-doped TiO_2 did not show bactericidal effect – *E.coli* re-growth of more than 10^5 CFU/ml was observed after 24 h dark period. Finally, we may assume that some nanosized materials, such as pure TiO_2, 0.5% and 1% Fe-doped TiO_2 in the presence of UVA light possess bactericidal activity, whereas 2% Fe-doped TiO_2 only inhibits bacterial cells and probably has bacteriostatic effect. Antibacterial activity of Fe-modified titanium dioxide preparations initiated by visible light will be object of further investigations.

CONCLUSIONS

• Iron-doped titanium dioxide was prepared by a nonhydrolytic sol-gel method using titanium tetrachloride, benzyl alcohol and iron(III) nitrate.

• The optimal iron content for the photocatalytic decomposition of Reactive Black 5 dye under UV-Vis irradiation was found to be 0.5 mol%.

• At higher iron contents (1–2 mol%) the photocatalytic performance under both UV and visible irradiation was worse relative to the undoped TiO_2.

• In the presence of UV light, both 0.5% and 1% Fe-doped TiO_2 had strong bactericidal activity against *E. coli,* similar to that of the pure TiO_2. In comparison to them, 2% Fe-doped TiO_2 exhibited only weak bacteriostatic effect.

• The best antibacterial properties under UV illumination were presented by 0.5 mol% Fe-doped TiO_2, that correlates with highest photocatalytic action of this sample under UVA and Vis irradiation.

Acknowledgements: *Authors are grateful to the financial support of Medical University-Pleven, Contract No10/2013.*

REFERENCES

1. G. K. Mor, M. A. Carvalho, O. K. Varghese, M. V. Pishko, C. A. Grimes, *J. Mater. Res.*, **19**(2), 628 (2004).
2. O. Carp, C. L. Huisman, A. Reller, *Progr. Solid State Chem.*, **32,** 33 (2004).
3. C. McCullagh, J. M. C. Robertson, D. W. Bahnemann, P. K. .J. Robertson, *Res. Chem. Intermed.*, **33**(3–5), 359 (2007).
4. A. Sobczynski, A. Dobosz, *Pol. J. Environ. Studies*, **10**(4), 195 (2001).
5. D. M. Blake, J. Webb, C. Turch, K. Magrini, *Sol. Energy Mater.*, **24,** 584 (1991).
6. T. Tanizaki, Y. Murakami, Y. Hanada, S. Ishikawa, M. Suzuki, R. Shinohara, *J. Health Sci.*, **53**(5), 514 (2007).
7. H. Yang, K. Zhang, R. Shi, X. Li, X. Dong, and Y. Yu, *J. Alloys Compd.*, **413**(1–2), 302 (2006).
8. A. Fujishima, T. N. Rao, D. A. Tryk, *J. Photochem. Photobiol.* C, **1,** 1 (2000).
9. A. R. Khataee, G. Ali Mansoori, Nanostructured Titanium Dioxide Materials: Properties, Preparation and Applications, World Scientific Publishing Co, 2011.
10. S. M. Gupta, M. Tripathi, *Chin. Sci. Bull.*, **56**, 1639 (2011).
11. D. Blake, P. C. Maness, Z. Huang, E. Wolfrum, J. Huang, W. Jacoby, *Sep. Purif. Methods*, **28**(1), 1 (1999).
12. A. G. Rincón, C. Pulgarin, *Appl. Catal. B*, **4**, 99 (2004).
13. D. L. Liao, C. A. Badour, B. Q. Liao, *J. Photochem. Photobiol. A: Chem*., **194**, 11 (2008).
14. P. Yang, C. Lu, N. Hua, Y. Du, *Mater. Lett.*, **57**(4), 794 (2002).
15. D. Klauson, S. Preis, *Int. J. Photoenergy*, **7**(4), 175 (2005).
16. W. K. Choi, A. Termin, M. R. Hoffmann, *J. Phys. Chem.*, **98**(51), 13669 (1994).
17. A. Kumbhar, G. Chumanov, *J. Nanoparticle Res.*, **7**, 489 (2005).
18. Z. Ambrus, N. Balázs, T. Alapi, G. Wittmann, P. Sipos, A. Dombi, K. Mogyorósi, *Appl. Catal. B: Environ.*, **81,** 27 (2008).
19. W.-C. Hung, S.-H. Fu, J.-J. Tseng, H. Chu, T.-H. Ko, *Chemosphere*, **66**, 2142 (2007).
20. S. Liu, X. Liu, Y. Chen, R. Jiang, *J. Alloys Compd.*, **506**, 877 (2010).
21. E. Piera, M. I. Tejedor-Tejedor, M. E. Zorn, M. A. Anderson, *Appl. Catal. B*, **46**(4), 671 (2003).
22. Z. Li, W. Shen, W. He, X. Zu, *J. Hazard. Mater.*, **155,** 590 (2008).
23. N. D. Abazović, L. Mirenghi, I. A. Janković, N. Bibić, D. V. Šojić, B. F. Abramović, M. I. Čomor, *Nanoscale Res. Lett*., **4**, 518 (2009).

24. A. Di Paola, E. Garcia-Lopez, G. Marci, C. Martin, L. Palmisano, V. Rives, A. M. Venecia, *Appl. Catal. B: Environ.*, **48**, 223 (2004).
25. M. Niederberger, N. Pina, Metal Oxide Nanoparticles in Organic Solvents, Springer, 2009.
26. D. P. Debecker, P. H. Mutin, *Chem. Soc. Rev.*, **41**(9), 3624 (2012).
27. M. Niederberger, M. H. Bartl, G. D. Stucky, J. Am. Chem. Soc., **124**, 13642 (2002).
28. A. Stoyanova, M. Sredkova, A. Bachvarova-Nedelcheva, R. Iordanova, Y. Dimitriev, H. Hitkova, Tz. Iliev, *Optoelectron. Advan. Mater.-Rapid Commun.*, **4**(12), 2059 (2010).
29. S. M. Gupta, M. Tripathi. A review of TiO_2 nanoparticles, *Chinese Sci. Bull.*, **56**, 1639 (2011).
30. X. Yang, C. Cao, L. Erickson, K. Hohn, R. Maghirang, K. Klabunde, *Appl. Catal. B: Environ.*, **91,** 657 (2009).
31. Q. Wang, S. Xu, F., Shen, *Appl. Surf. Sci.*, **257**, 7671 (2011).
32. A. N. Murashkevich, A. S. Lavitskaya, T. I. Barannikova, I. M. Zharskii, *J. Appl. Spectr.*, **75**(5), 730 (2008).
33. A. M. Stoyanova, H. Y. Hitkova, A. D. Bachvarova-Nedelcheva, R. S. Iordanova, N. K. Ivanova, M. P. Sredkova, *J. Univ. Chem. Techn. Metall.*, in press.
34. K. Marinaga, Y. Suginohara, Y. Yanagase, *J. Jpn. Inst. Met.*, **40,** 775 (1976).
35. S. Boonyod, W. Sutthisripok, L. Sikong, *Adv. Mater. Res.*, **214**, 197 (2011).
36. H.-C. Wu, S.-H. Li, S.-W. Lin, *Int. J. Photoenergy*, Volume 2012, Article ID 823498.
37. X. Li, P.-L. Yue, C. Kutal, *New J. Chem.*, **27**(8), 1264 (2003).
38. J. Wang, R. Li, L. Zhang, Y. Xie, Z. Jiang, R. Xu, Z. Xing, X. Zhang, *Russ. J. Inorg. Chem.*, **55**(5), 692 (2010).
39. C. Adan, A. Bahamonde, M. Fernandez-Garcia, A. Martinez-Arias, *Appl. Catal. B: Environ.,* **72,** 11 (2007).
40. M. Litter, J. Navio, *J. Photochem. Photobiol. A: Chem.*, **98**(3), 171 (1996).

ФОТОКАТАЛИТИЧНА И АНТИБАКТЕРИАЛНА АКТИВНОСТ НА ДОТИРАНИ С ЖЕЛЯЗО TiO_2 НАНОЧАСТИЦИ, ПОЛУЧЕНИ ПО НЕХИДРОЛИТИЧЕН ЗОЛ-ГЕЛ МЕТОД

А. М. Стоянова[1]*, Х. Й. Хиткова[1], Н. К. Иванова[1], А. Д. Бъчварова-Неделчева[2], Р. С. Йорданова[2], М. П. Средкова[1]

[1] Медицински Университет-Плевен, 5800 Плевен, България
[2] Институт по Обща и Неорганична Химия, Българска Академия на Науките, 1113 София, България

Постъпила февруари, 2013 г.; приета май, 2013 г.

(Резюме)

В настоящата работа е представен синтез на дотиран с желязо TiO_2 синтезиран по нехидролитичен зол-гел метод от титанов тетрахлорид, бензилов алкохол и железен(III) нитрат.

Получените образци са охарактеризирани с помощта на РФА, ИЧ и УВ-Вис спектроскопия. Относителният размер на получените Fe-дотирани TiO_2 частици е 12–15 nm.

Фотокаталитичната активност на синтезираните прахове от TiO_2 е изследвана чрез фотодеградацията на органичното багрило Reactive Black 5 при осветяване с УВ и видима светлина.

Антибактериалната активност на чист и Fe-модифициран TiO_2 е изследвана спрямо щам *Escherichia coli* ATCC 25922. Бактериалният растеж беше изпитван в присъствие на съответния синтезиран препарат на тъмно и в присъствие на УВ светлина. Фотодезинфекционната активност е оценена чрез конструиране на „криви на преживяемост“ и определяне на ефективността на отстраняване на бактериалните клетки. За оценка на постирадиационния ефект бактериалната суспензия е тествана отново след 24 ч престой на тъмно. Установено е, че с най-добра фотокаталитична и антибактериална активност е препаратът, съдържащ 0,5 mol% желязо. При по-високо съдържание на желязо (1–2 mol%) фотокаталитичните тестове показаха по-лоши резултати спрямо чистия TiO_2 както в УВ, така и във видимата област.

Bulgarian Chemical Communications, Volume 45, Number 4 (pp. 505–509) 2013

Synthesis and crystal structure of oxonium 2,4,8,10-tetrahydroxy-1,3,5,7,9,11-hexaoxa-2,4,6,8,10-pentaboraspiro[5.5]undecan-6-uide hydrate

L. Dimowa, K. Kossev, H. I. Sbirkova, R. P. Nikolova, B. L. Shivachev*

Institute of Mineralogy and Crystallography "Academician Ivan Kostov", Bulgarian Academy of Sciences, 1113 Sofia, Acad. Georgi Bonchev Str., Building 107, Bulgaria

Received February, 2013; Revised May, 2013

Oxonium 2,4,8,10-tetrahydroxy-1,3,5,7,9,11-hexaoxa-2,4,6,8,10-pentaboraspiro[5.5]undecan-6-uide hydrate, was synthesized and its structure was investigated by single crystal X-ray diffraction and ^{11}B NMR analyses. The title compound, $B_5H_9O_{12}$, crystallizes in the orthorhombic crystal system, space group *Aba2* with cell parameters a = 11.3286(5) Å, b = 11.0118(4) Å, c = 9.2314(4) Å, Z = 4 and V = 1151.60(8) Å^3. The crystal structure is stabilized through hydrogen-bonding interactions, involving all possible donors and acceptors.

Key words: boroxine, single crystal, ^{11}B NMR.

INTRODUCTION

Borate materials are very attractive due to their use in various applications, ranging from agriculture, nuclear containment shields, in the production of glasses and ceramics, in chemistry synthesis, wood treatment, optical materials, treatments for cancer etc. Amongst the multitude of borate compounds (crystals, ceramics, glasses) employed in the optical field one should pay special attention to borate crystal phases that exhibit non-linear optical activity (barium borates, β-BBO, cesium borate, cesium lithium borate etc.). Aforementioned crystal phases are nowadays used routinely in laser setups for second- and third- harmonic generation (SHG and THG), phase-matching etc. A large number of inorganic (potassium, cesium), organic (alkylammonium, heterocyclic) or coordination (tris(ethylenediamine-N,N')-cobalt(II)) [1, 2] salts of the unknown in free state pentaboric acid $H^+[B_5O_6(OH)_4]^-$ have been described. They have been obtained mainly within attempts to optimize the optical, thermal and structural properties of known borate phases. Attempts to introduce organic molecular fragments to enhance the polarization or charge transfer while maintaining the boron surrounding have been also made. Amongst the factors contributing to the large diversity of borate crystal phases are the performed variations of the molar ratio of the reactants, the temperature, the solvent media and the presence of impurities (hampering or initiating the crystallization). Continuing our investigation on boronic acids crystallization and co-crystallization [3–5] here we present the crystal structure of oxonium 2,4,8,10-tetrahydroxy-1,3,5,7,9,11-hexaoxa-2,4,6,8,10-pentaboraspiro[5.5]undecan-6-uide hydrate (**I**), $B_5H_9O_{12}$.

EXPERIMENTAL

Synthesis and characterization

The title compound (**1**) was obtained according to the reaction scheme 1.

Boric acid (165 mg, 2.67 mmol) and triethylbenzylammonium chloride (TEBA.Cl) (600 mg, 2.64 mmol), were dissolved in 50 ml distilled water. Colorless (transparent) crystals of **1**, suitable for single crystal X-ray diffraction analyses have been obtained after slow evaporation of water at room temperature.

* To whom all correspondence should be sent:
E-mail: blshivachev@gmail.com

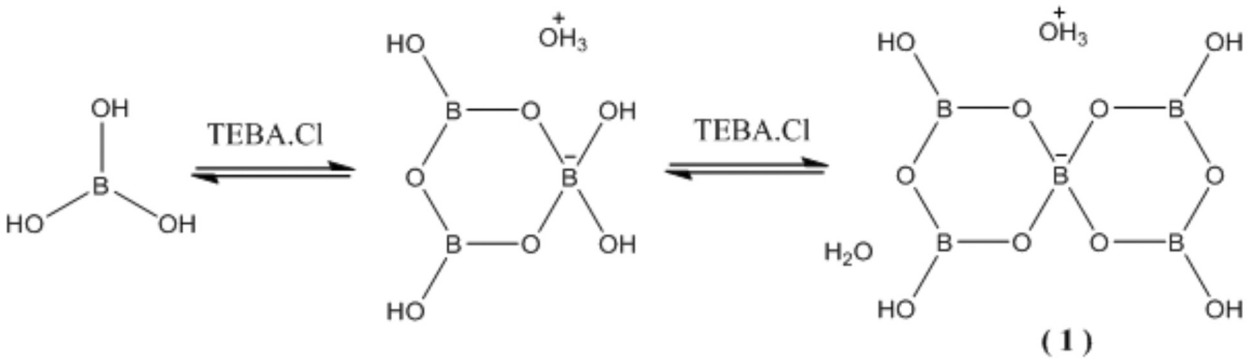

Scheme 1. Reaction scheme and chemical diagram of the title compound (1)

X-ray – single crystal analyses

A crystal of the title compound having approximate dimension 0.22×0.20×0.16 mm^3 was placed on a glass fiber and mounted on an Agilent, SuperNovaDual four-circle diffractometer equipped with Atlas CCD detector and using mirror-monochromatized MoKα (λ = 0.7107 Å) radiation from micro-focus source. Diffraction data were collected at room temperature by the ω-scan technique. The determination of cell parameters, data integration, scaling and absorption correction were carried out using the CrysAlisPro program package [6]. The structure was solved by direct methods using

Table 1. Crystal data and most important structure refinement indicators for **1**

$B_5H_9O_{12}$ (PBA)	D_x = 1.581 Mg m^{-3}
M_r = 255.11	Melting point: 314 K
Orthorhombic, *Aba*2	Mo *K*α radiation, λ = 0.7107 Å
a = 11.3286 (5) Å	Cell parameters from 3322 reflections
b = 11.0118 (4) Å	θ = 2.9–32.7°
c = 9.2314 (4) Å	μ = 0.16 mm^{-1}
V = 1151.60 (8) Å^3	*T* = 290 K
Z = 4	Prism, colorless
F(000) = 564	0.22 × 0.20 × 0.16 mm
Supernova Dual, Atlas CCD diffractometer	1704 independent reflections
Radiation source: Mova (Mo) X-ray Source	1671 reflections with $I > 2\sigma(I)$
mirror	R_{int} = 0.025
Detector resolution: 10.3974 pixels mm^{-1}	θ_{max} = 32.7°, θ_{min} = 2.9°
ω scans	*h* = −14→16
Absorption correction: multi-scan *CrysAlis PRO*, Oxford Diffraction Ltd., Version 1.171.34.40	*k* = −15→15
T_{min} = 0.837, T_{max} = 1.000	*l* = −13→12
4244 measured reflections	Primary atom site location: structure-invariant direct methods
Refinement on F^2	Hydrogen site location: from difference Fourier map and inferred from neighboring sites
Least-squares matrix: full	H-atom parameters constrained
$R[F^2 > 2\sigma(F^2)]$ = 0.050	$w = 1/[\sigma^2(F_o^2) + (0.1086P)^2 + 0.2796P]$ where $P = (F_o^2 + 2F_c^2)/3$
$wR(F^2)$ = 0.150	$(\Delta/\sigma)_{max} < 0.001$
S = 1.10	Secondary atom site location: difference Fourier map
1702 reflections	$\Delta\rho_{max}$ = 0.32 e Å^{-3}
85 parameters	$\Delta\rho_{min}$ = −0.30 e Å^{-3}
1 restraint	Extinction correction: none

ShelxS [7] and refined by full-matrix least-square procedures on F^2 with ShelxL-97 [7]. The boroxin and oxonium (Ow2) hydrogen atoms were located from difference Fourier map and refined as riding on their parent atoms, with $U_{iso}(H) = 1.2U_{eq}(O)$. Ow1 hydrogen atoms were placed on calculated position fulfilling hydrogen bonding criteria with acceptor atoms and refined as riding on their parent atoms, with $U_{iso}(H) = 1.2U_{eq}(O)$.

NMR

The ^{11}B NMR data were obtained on a Bruker AMX 500MHz at 300K. The data were referenced to a H_3BO_3 solution D_2O (35 ppm). ^{11}B NMR (THF-D_8, 160.4 MHz): δ = –4.8 (O_4B^-), 16.9 (BO_3).

RESULTS AND DISCUSSION

The chemical diagram of the studied compound (**1**) is illustrated in Scheme 1 and experimental conditions are summarized in Table 1. Selected bond distances and bond angles are listed in Table 2. Hydrogen bonding geometry is presented in Table 3. A diagram of the molecular structure with 50% probability and the atom numbering scheme is shown in Fig. 1. The data for publication were prepared with

Table 2. Selected geometrical parameters for **1** (Å, °)

Bond distance			
B1 — O2	1.372 (2)	B2 — O1^{i}	1.4659 (19)
B3 — O5	1.353 (2)	B2 — O3	1.475 (2)
B1 — O3	1.3557 (19)	B2 — O3^{i}	1.475 (2)
B1 — O4	1.353 (2)	B3 — O1	1.351 (2)
B2 — O1	1.4660 (19)	B3 — O2	1.379 (2)
Bond angle			
O3 —B1 — O2	121.74 (13)	O3^{i}— B2 — O3	108.1 (2)
O4 —B1 — O2	118.38 (14)	O1 — B3 — O2	121.77 (14)
O4 —B1 — O3	119.88 (14)	O1 — B3 — O5	124.23 (14)
O1^{i}—B2 — O1	108.7 (2)	O5 — B3 — O2	113.98 (15)
O1 —B2 — O3	111.39 (6)	B3 — O1 — B2	123.16 (11)
O1^{i}—B2 — O3	108.62 (8)	B1 — O2 — B3	119.01 (13)
O1^{i}—B2 — O3^{i}	111.39 (6)	B1 — O3 — B2	122.91 (11)
O1 —B2 — O3^{i}	108.62 (8)		
Torsion angle			
O1^{i}— B2 — O1 — B3	120.73 (19)	O3^{i}— B2 — O1 — B3	−117.91 (17)
O1^{i}— B2 — O3 — B1	−120.07 (14)	O3— B2 — O1 — B3	1.1 (3)
O1 — B2 — O3 — B1	−0.4 (2)	O3^{i}— B2 — O3 — B1	118.91 (16)
O1 — B3 — O2 — B1	0.3 (3)	O4 — B1 — O2 — B3	179.93 (19)
O2 — B1 — O3 — B2	−0.3 (3)	O4 — B1 — O3 — B2	−179.86 (17)
O2 — B3 — O1 — B2	−1.1 (3)	O5 —B3 — O1 — B2	−179.6 (2)
O3 — B1 — O2 — B3	0.4 (3)	O5 —B3 — O2 — B1	178.95 (19)

Symmetry code: (i) *−x+1, −y+1, z*

Table 3. Hydrogen bond for **I** (Å, °)

D—H···A	D—H	d(H···A)	d(D···A)	<(DHA)
OW2—HW2B···O1	0.954	1.912	2.857(5)	170.2
O4—H4···OW2^{i}	0.949	1.741	2.687(4)	174.5
O5—H5···O4^{ii}	0.820	1.907	2.664(4)	152.9
OW1—HW1A···O5^{iii}	1.152	1.844	2.962(5)	161.9
OW1—HW1B···O2^{iv}	1.068	1.888	2.935(5)	166.1
OW1—HW1B···O5^{iv}	1.068	2.332	2.962(5)	116.2
OW2—HW2A···O3^{v}	0.783	2.116	2.881(4)	164.9
OW2—HW2C···OW1^{vi}	0.748	2.342	2.992(5)	146.0

Symmetry codes : (i) *x+1/2, -y+1, z+1/2*; (ii) *x, y-1/2, z-1/2*; (iii) *x-1/2, -y+1, z+1/2*; (iv) *-x+3/2, y, z+1/2*; (v) *x, y-1/2, z-1/2*; (vi) *x, y, z-1*.

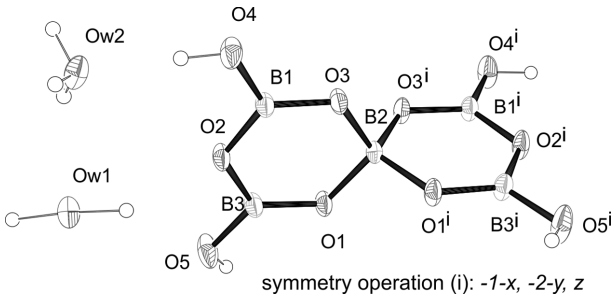

Fig. 1. View of molecule with an atom-numbering scheme. Displacement ellipsoids for the non-H atoms are drawn at the 50% probability level. The H atoms are presented with spheres with arbitrary radii

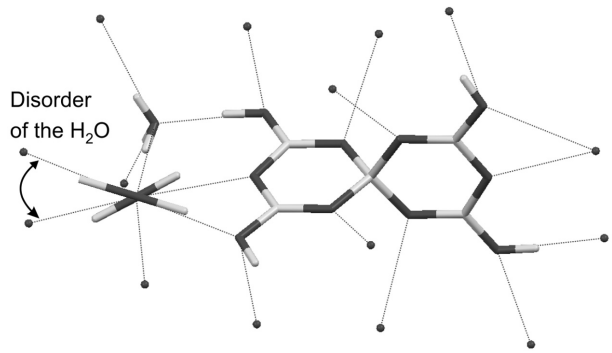

Fig. 2. The PBA, water, and oxonium ion hydrogen bonding interactions (see Table 3) are shown as dotted lines

WinGX [8], *ORTEP* [9], and Mercury [10] program packages. The location of the disordered H atoms of the solvent water (Ow1) has been performed using DHA program. [11]

The title compound crystallizes in the noncentrosymmetric space group *Aba2* (No 41) and thus possesses the prerequisites for potential (non-linear) optical application. Unfortunately we could not grow sufficiently large crystals for performing such investigations. The structural parameters (bond lengths and angles) of the title compound are comparable with those reported earlier [12, 13]. The boroxin ring systems (B1/O1/B2/O2B3/O3) is essentially planar with r.m.s. deviation of 0.0038(4) Å. The two hydroxy groups (O4 and O5) are also situated in the plane of the boroxin ring (OH groups are strong π-donor). In the three-dimensional arrangement of the molecules of **1** all possible donors and acceptors are involved in hydrogen bonding interactions (Fig. 2, 3 and Table 3). A closer inspection of the short distances and contacts present in crystal structure of **1** could not locate π… π or other weak interactions. The ^{11}B NMR shifts are consistent with O_4B^- and O_3B arrangement [14] ^{11}B NMR (THF-D_8, 160.4 MHz): δ = –4.8 (O_4B^-), 16.9 (BO_3).

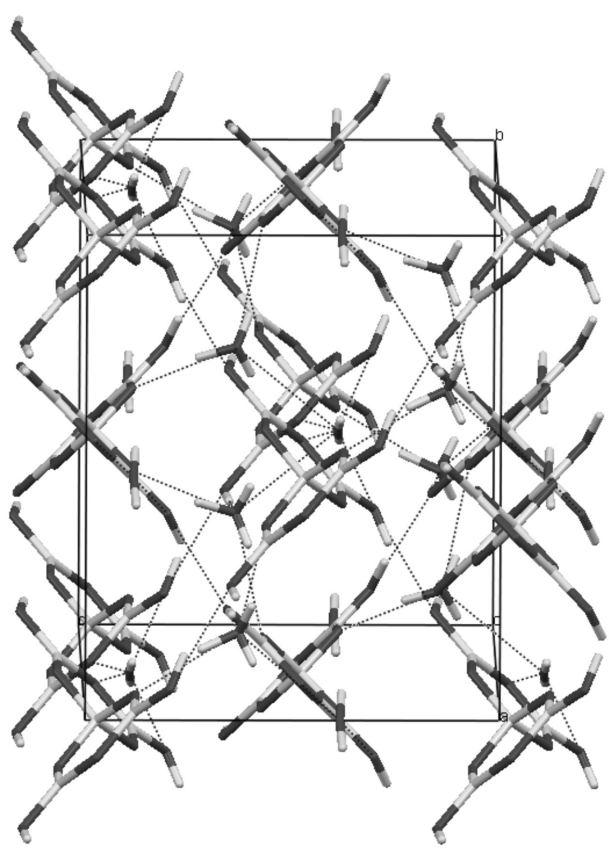

Fig. 3. Three-dimensional packing of the molecules in the crystal structure; hydrogen bonds are shown as dotted lines

The observed formation of the title compound (pentaboric acid) in the presence of triethylbenzylammonium chloride can be explained with the assumption that the alkylammonium salt enhances the solubility of orthoboric acid and prevents crystallization of orthoboric acid. In addition, the bulky and less polar cation locally decreases the medium polarity and favors the equilibrium shift to pentaboric acid.

SUPPLEMENTARY MATERIALS

ICSD 425613 contains the supplementary crystallographic data for this paper. Further details of the crystal structure investigation(s) may be obtained from Fachinformationszentrum Karlsruhe, 76344 Eggenstein-Leopoldshafen, Germany (fax: (+49)7247-808-666; e-mail: crysdata(at)fiz-karlsruhe.de, http://www.fiz-karlsruhe.de/request_for_

deposited_data.html) on quoting the appropriate ICSD number.

Acknowledgments: *The authors thank the financial support of the Bulgarian National Science Fund through contract DRNF 02/1.*

REFERENCES

1. M. A. Becketta, P. N. Horton, M. B. Hursthouse, J. L. Timmis, K. Sukumar Varma, *Collect. Czech. Chem. Commun*., **75**, 971 (2010).
2. Y. Yang, J. B. Sun, M. Cui, R. B. Liu, Y. Wang, C. G. Meng, *J. Sol State Chem.*, **184**, 1666 (2011).
3. V. Dyulgerov, R. P. Nikolova, L. T. Dimova and B. L. Shivachev, *Acta Cryst*. E, **68**, o2320 (2012).
4. M. D. Apostolova, R. P. Nikolova and B. L. Shivachev, *Acta Cryst.* E, **66**, o1273(2010).
5. B. Shivachev, R. Petrova, E. Naydenova, *Acta Cryst.* E, **62**, o3887 (2006).
6. Agilent. CrysAlisPro (version 1.171.35.15). Agilent Technologies Ltd, Yarnton England, 2010.
7. G. M. Sheldrick, *Acta Cryst. A*, **64**, 112 (2008).
8. L. J. Farrugia, *J. Appl. Cryst.*, **32**, 837 (1999).
9. L. J. Farrugia, *J. Appl. Cryst.*, **30**, 565 (1997).
10. I. J. Bruno, J.C. Cole, P. R. Edgington, M. Kessler, C. F. Macrae, P. McCabe, J. Pearson, R. Taylor, *Acta Cryst. B*, **58**, 389 (2002).
11. B. Shivachev, *Bull. Chem. Comm*., **45**(4), 461 (2013).
12. R. A. Baber, J. P. H. Charmant, N. C. Norman, A. G. Orpen, J. Rossi, *Acta Cryst*. E, **60**, o1086 (2004).
13. Hong-Xia Zhang, Jie Zhang, Shou-Tian Zheng, Guo-Yu Yang, *Cryst. Growth Des*., **5**, 157 (2005).
14. B. Wrackmeyer, NMR Spectroscopy of Boron Compounds Containing Two-, Three- and Four-Coordinate Boron, *Annu. Rep. NMR Spectrosc*., **20**, 61 (1988).

СИНТЕЗ И КРИСТАЛНА СТРУКТУРА НА ОКСОНИЕВ 2,4,8,10-ТЕТРАХИДРОКСИ-1,3,5,7,9,11-ХЕКСАОКСА-2,4,6,8,10-ПЕНТА-БИСПИРО[5.5]УНДЕКАН-6-ОИД ХИДРАТ

Л. Димова, К. Косев, Х. И. Сбиркова, Р. П. Николова, Б. Л. Шивачев

Институт по минералогия и кристалография „Акад. Иван Костов“,
Българска академия на науките, ул. „Акад. Георги Бончев“,
блок 107, София 1113, България

Постъпила февруари, 2013 г.; приета май, 2013 г.

(Резюме)

Синтезираният оксониев 2,4,8,10-тетрахидрокси-1,3,5,7,9,11-хексаокса-2,4,6,8,10-пентабиспиро[5.5]ундекан-6-оид хидрат бе охарактеризиран посредством монокристална рентгенова дифракция и ^{11}H ЯМР анализи. Така наименуваното вещество, $B_5H_9O_{12}$, кристализира в орторомбична кристална система и *Aba2* пространствена група, с параметри на елементарната клетка a = 11.3286(5) Å, b = 11.0118(4) Å, c = 9.2314(4) Å, Z = 4 and V = 1151.60(8) Å^3. Тримерната кристална структура е стабилизирана от мрежа от водородни връзки, като всички потенциални донори и акцептори участват в стабилизиращи взаимодействия.

Bulgarian Chemical Communications, Volume 45, Number 4 (pp. 510–515) 2013

A simple and rapid scanning electron microscope preparative technique for observation of biological samples: application on bacteria and DNA samples

I. Piroeva[1], S. Atanassova-Vladimirova[1], L. Dimowa[2], H. Sbirkova[2], G. Radoslavov[3], P. Hristov[3], B. L. Shivachev[2]*

[1] *Academician Rostislav Kaishev Institute of Physical Chemistry, Acad. Georgi Bonchev str., building 11, Sofia 1113, Bulgaria*
[2] *Institute of Mineralogy and Crystallography, Bulgarian Academy of Sciences, Acad. G. Bonchev Str., Bl. 107, 1113 Sofia, Bulgaria*
[3] *Institute of Biodiversity and Ecosystem Research , Bulgarian Academy of Sciences, Acad. G. Bonchev Str., Bl. 25, 1113 Sofia, Bulgaria*

Received February, 2013; Revised May, 2013

This protocol details a rapid preparative procedure enabling the visualization of biological samples like DNA and bacteria by scanning electron microscopy (SEM). This involves the fixation of the samples, followed by subsequent dehydration and the processing for electron microscopy observation. The fixation step is performed by allowing the samples to embed into an agar matrix. The dehydration of the samples ensures that they will not disrupt when processing for SEM observation or in the SEM vacuum camera. The whole process may be achieved for 6–24 hours and has been optimized for the visualization of bacteria, DNA. Samples once processed for SEM can be stored mild vacuum for weeks, allowing sufficient time for image acquisition.

Key words: scanning electron microscopy, SEM, *Esherichia Coli, Thermobispora bispora*.

INTRODUCTION

Biological samples e.g. bacteria, DNA, proteins, contain significant amounts of water and exhibit low conductivity. In their natural state, these samples cannot be observed directly by conventional scanning electron microscope (SEM) because the surface and subsurface water quickly evaporates under the high vacuum conditions necessary for electron microscopy observation [1, 2]. As a result usually the sample distorts collapses or destructs. In addition, water vapor from the specimen chamber decreases the vacuum and contaminates the detectors and column. The low conductivity of the biological samples also results in electrical charging that interferes with the electron beam and the secondary electron (SE) emission from the sample. Therefore, biological samples must be fixed, dehydrated, critical-point dried and coated before they can be observed in a conventional high-vacuum SEM [3]. Currently used protocols enabling electron microscopy observation are focused for obtaining high-quality data and involve successive series of procedures. While high quality data is achieved the protocols often include hazardous materials (OsO_4 or glutaraldehyde), are long-lasted and in some cases may extend for more than 7–8 days [4]. Our aim has been to adapt a protocol that will reduce significantly the processing time of such samples without significant loss of data collection quality. The protocol described hereafter provides a fast alternative for biological samples preparation [5, 6]. It can be used for rapid assessment of samples shapes, structural morphology etc.

MATERIALS AND METHODS

Although that there are many conditions to be met for "ideal" sample preparation for electron microscopy (EM) observation the most important and necessary condition is to maintain the integrity of the biological sample during sample preparation and subsequent work in the electron microscope [7]. Thus for biological samples the first difficulty lies in

* To whom all correspondence should be sent:
E-mail: blshivachev@gmail.com

the stable fixation of the samples onto a suitable surface as not to violate their integrity. The second difficulty is related to the high water content present in such samples. Unfortunately EM requires relatively high vacuum (10^{-6} to 10^{-7} torr) and if the samples are subject to such harsh conditions the water dehydration process of the samples is accompanied by the distortion, collapse or destruction. Fortunately, this drawback of EM can be circumvent by dehydration of the biological samples [8]. The last but not always the least difficulty is related to the low contrast provided by the samples build up predominantly by amino acids or nucleic acids e.g. C, N and O atoms [9]. Fortunately negative and positive staining may be used for enhancing the contrast – having in mind that DNA backbone is negatively charged [10].

Specific safety measures

- Because of the toxicity of the reagents and because possible biological contamination cannot be entirely excluded it is highly recommended to wear gloves during this procedure.
- NB! Staining with osmium should be done wearing gloves and under a fume hood.
- All waste materials generated during this procedure, such as the sheets of Whatman filter paper should be appropriately disposed (e.g. autoclavable waste container).

Materials

- Distilled water, sterile (dH_2O);
- Agar, biology grade;
- Optional: contrast enhancement (OsO_4, $UO_2(CH_3COO)_2$, WO_3).

Small laboratory material

- Small (60 mm diameter) or large (120 mm diameter) polyethylene petri dishes;
- Sterile centrifuge tubes (1.5 or 2 ml);
- sterile filter (<0.44 μm);
- Microbiology laboratory slides (18×18) – suitable for EM holder;
- Beaker glass, 50 ml,
- Filter paper (Whatman, 54 hardened);
- Forceps to manipulate laboratory slides;
- Permanent, waterproof marker (Staedler Lumocolor);
- Ball point to indicate references on filter paper.

Equipment

- Scanning electron microscope (Jeol, JSM 6390);
- Ultraviolet lamp;
- Laboratory oven;
- Centrifuge (~5000 rpm);
- Pipettes.

Sample processing preparation

Growth of bacteria and genomic DNA isolation

Two bacterial strains were employed: *Escherichia coli* (*E. coli*) *DH5α* strain and *Thermobispora bispora* (DSMZ 43038) [11]. *DH5α* is nowadays the most frequently used *E. coli* strain for routine cloning applications. It grows easily at 37 °C and its exponential growth can be controlled by spectrophotometric technique. *Thermobispora bispora* is a thermophilic strain that grows at 55 °C and in addition slowly than *E. coli*.

For the DNA investigation we isolated genomic *E. coli* DNA by standard procedure (PureLink, Invitrogen). The successful isolation was monitored electrophoretically (1% agarose gel, stained with 5 μl ethidium bromide, 10 mg ml^{-1}).

Harvesting of the samples

DNA elution was performed with 20 μl PCR water in order to avoid the presence of additional parasite salts from buffers.

The *E. coli* and *Thermobispora bispora* samples were collected by centrifugation at 3500 rpm for 5 min from the growth cultures (from 2 ml or more). The supernatant was discarded and the procedure was repeated two times with the addition of distilled water. The two additional steps are required in order to dissolves the salts and remains from the growth media. Finally 5–20 μl of dH_2O are added and the pellet is carefully homogenized thus ready for fixation for EM observation

Preparation for fixation and embedding of biological samples

1. 0.8% wt Agar-water solution: 400 mg agar were dissolved in 50 ml of distilled water by heating in a microwave oven without allowing the solution to boil.

2. Clean cover slips 18×18 mm^2 are sterilized by UV irradiation 10 for minutes. After what the slides are dipped in the agar solution (the 0.8% wt Agar solution is kept at ~ 50–60 °C in order to remain liquid) and left horizontally allowing a thin agar film to materialize. NB!!! Agar polymerization starts with temperature drop however it takes more than 30 min to obtain a sufficient degree of cross linking of the matrix.

3. The biological sample (bacteria, DNA) is carefully placed (pipetted) on the agar film and spread if

necessary. The fixation/embedding of the samples is achieved with agar cross-linking after approximately 30–45 min.

4. The agar is dehydrated in an oven at 37 °C for 12 hours (if necessary a low vacuum 0.8 atm may be additionally employed).

5. Dehydration of the samples: we choose to utilize a classical dehydration processing of the fixed samples by successive immersion in ethanol solutions starting from low to high concentration: 10, 25, 50, 75, 96 and absolute 99.99%). The samples were maintained in each ethanol solution for at least 30 minutes. Finally a drying at 37 °C for about 1 hour is performed.

6. The prepared samples are coated with a thin gold film (<10 nm).

Contrast enhancement by negative or positive staining can be optionally performed (OsO_4, $UO_2(CH_3COO)_2$, WO_3 etc.) of the samples before the first ethanol dehydration steps or immediately after the dehydration process depending on the samples.

RESULTS

SEM analyses were performed on a JSM 6390 electron microscope (JEOL, Japan) in conjunction with energy dispersive X-ray spectroscopy (EDS, Oxford INCA Energy 350) equipped with ultrahigh resolution scanning system (ASID-3D) in regimes of secondary electron image (SEI). The sample (cover slip) is mounted on a double coated conductive carbon tape that holds the sample firmly to the stage surface and can be used as a ground strap from the sample surface to sample holder. The samples were gold coated (time of coating ~30 s). This thickness of gold layer resulted in decent image quality without causing any electric charging. With thinner gold films (decrease of coating time below 30 s) electric charging was observed [12, 13]. When the coating time was longer (more than 40 s), the gold layer was thicker but no improvement of image quality was observed. The accelerating voltage was adjusted to 15 kV, I ~ 65 mA. Lower voltages (e.g. 10 kV) resulted in loss of contrast while higher voltages lead to rapid degradation of the imaging [14–16]. The pressure was of the order of 10^{-4} Pa [17].

The production of cover slips and embedding of the samples into the "agar" layer was achieved without difficulty. One should adjust carefully the required amounts of sample (not as on Fig. 1 were we intentionally overestimates the amounts for better visualization) as to have a "horizontal" (flat) surface allowing facile focusing of EM observation.

Figure 2 shows the observation of *E. coli* cells. As one can see the centrifugation and subsequent spreading of the water-cell solution over the cover slip allows better separation of individual cells. If a single colony of the same cells is directly embedded onto the cover slip the surface roughness can be observed. Interestingly, the average size of the cells is different (single colony shows that the cells are smaller). This is probably due to the centrifugation as the process collects more easily bigger ones. Thus an adjustment of centrifugation speed will be necessary in function of the size and consistency of the sample.

The results from the *Thermobispora bispora* observation are shown on Fig. 3. As one can see the quality of the visualization is reasonable. The concentration of the sample (Fig. 3a) leads to a some-

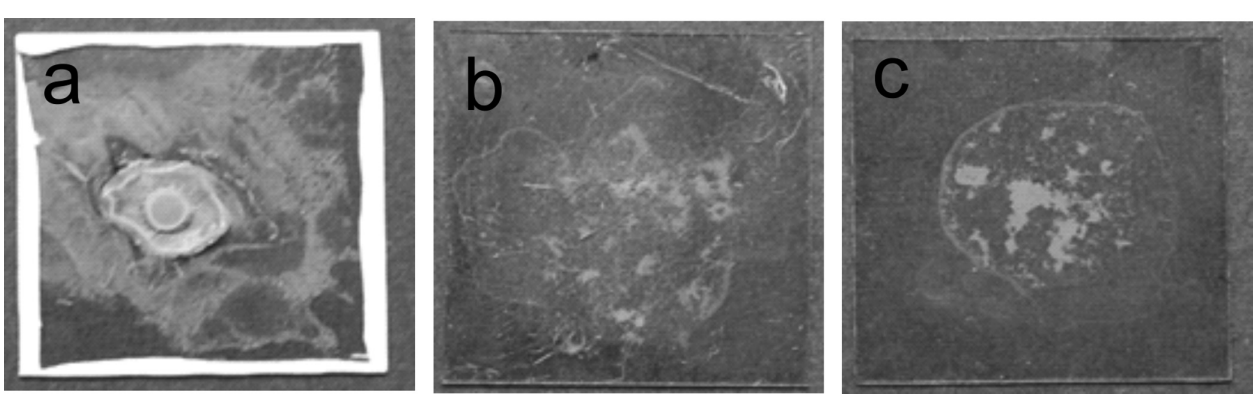

Fig. 1. Covers slips 18 mm^2 with embedded samples that were subject to dehydration and covering with gold layer a) Single *E. coli* colony from agar plate b) *E. coli* collected by centrifugation and spread over and c) *Thermobispora bispora* collected by centrifugation from media contaminated with TiO_2 (nano)particles. The amounts of samples here were intentionally overestimated

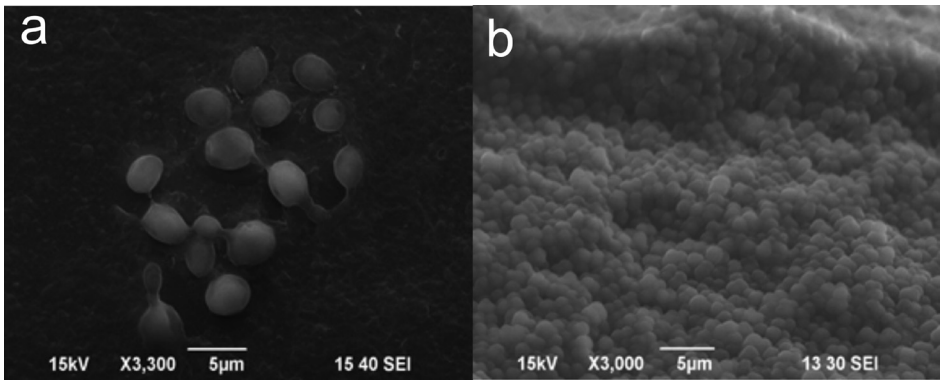

Fig. 2. SEM images of *E. coli* a) spreading after centrifugation b) single colony taken directly from plate (solid media)

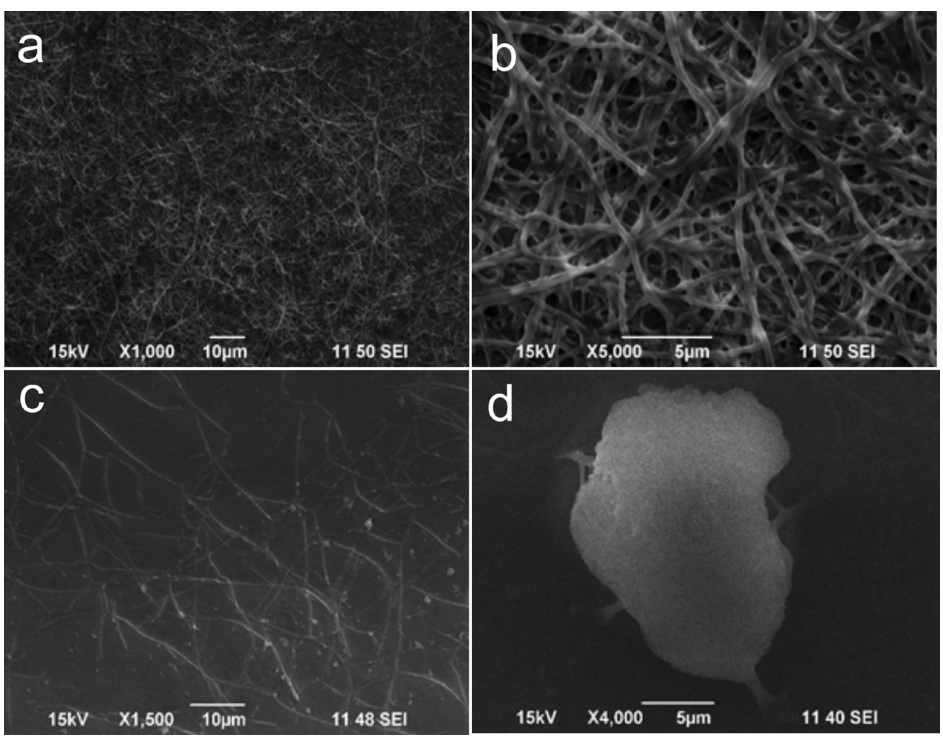

Fig. 3. SEM images of *Thermobispora bispora* with different concentration a) and b) centrifugation of 3×1.5 ml and c) and d) centrifugation of 1.5 ml

what higher contrast of the images – probably due to the fact that the "denser" surface allows a more uniform coverage of the gold layer and thus better conductance. The lower concentration of the sample, as for *E. coli*, gives better individual resolution and is able to discern bigger aggregates.

In order to estimate the use of the protocol in relatively unfriendly conditions *Thermobispora bispora* was grown in the presence of TiO_2 nanoparticles (Fig. 4). The TiO_2 particle cannot dissolve in the used water and thus bigger aggregates of them will be present after the centrifugation. Figure 4a shows that the TiO_2 particles are positioned "on top" of the bacteria. Of course this observation can be an artifact due to the employed centrifugation or to the pipetting or spreading of the samples. Nevertheless the bacterial network is clearly visible (Fig. 4b).

Finally the protocol has been used for DNA observation (Fig. 5). The DNA backbone features a negative charge and thus cations (Na, K, Zn, Cu etc.)

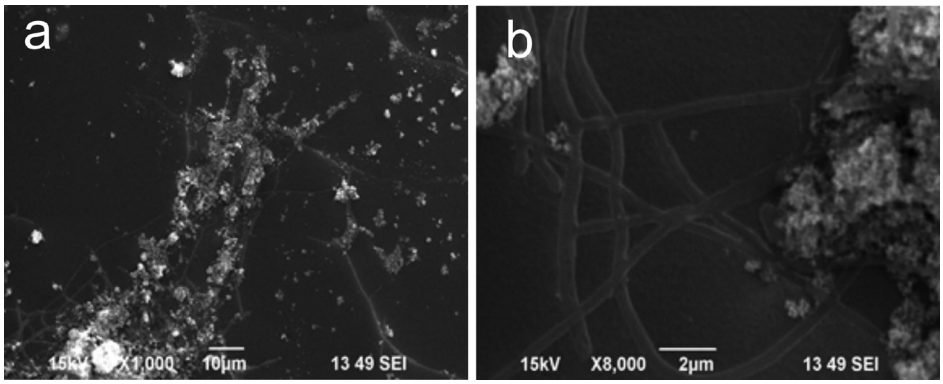

Fig. 4. SEM images of *Thermobispora bispora* grown with TiO_2 contamination

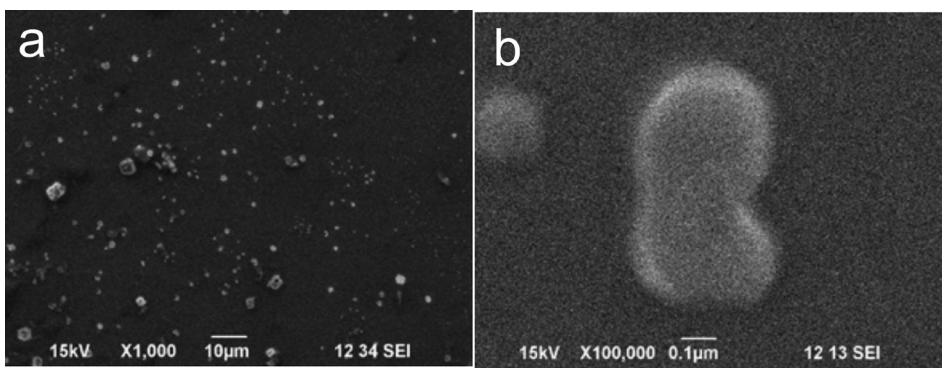

Fig. 5. SEM images of a) NaCl, $MgCl_2$ salts and b) genomic DNA

are needed to balance its charge. Thus the elimination of salts is more difficult than in the case of uncharged samples. Although the elution of DNA yields sufficient quantities for molecular biology work its concentration is typically ng/mL to µg/mL and thus very limited. More over DNA tends to compact tightly and thus its primary aggregate size is smaller – usually below 1 µm. Thus the routine SEM observations of DNA are more difficult than bacterial ones. As one can see from Fig. 5 the presence of salt is easily observable while the imaging of the DNA and its contrast are not as good as for the bigger biological samples.

CONCLUSIONS

We have adapted a rapid preparative procedure for preparing biological samples for SEM visualization. The processing is relatively rapid and may be performed for one day. The SEM visualization and data quality allows sufficient detail for samples that are bigger than 1 µm while for smaller size a contrast enhancement is suited. Compared to classical procedures the developed one is cost and time effective with minimal loss of data quality (mainly contrast lost).

Acknowledgments: *The authors are grateful for the financial support of Project BG051 PO 001-3.3.06-0038 funded by OP Human Resources Development 2007–2013 of EU Structural Funds and of the Bulgarian National Science Fund through grant DRNF 02/1.*

REFERENCES

1. T. Ogura, *Biochem. Biophys. Res. Comm*., **391** (1), 198 (2010).
2. F. Iwata, Y. Mizuguchi, H. Ko, T. Ushiki, *J.* El. Microscopy, **60** (6), 359 (2011).
3. Ye J., X. Zhang, C. Young, X. Zhao, Q. Hao, L. Cheng, O. Jensen. *J. Proteome Res*., **9** (7), 3561 (2010).
4. A. Dwiranti, L. Lin, E. Mochizuki, S. Kuwabata, A. Takaoka, S. Uchiyama, K. Fukui, *Microscopy Res. Tech.*, **75** (8), 1113 (2012).

5. J. Castillo, M. Dimaki, W. E. Svendsen. *Integr. Biology*, 1, 30 (2009).
6. T. Miyazaki, T. Nomoto, Y. Shimada, T. Tanaka, K. *Watanabe patent* No. US 8243266 B2 (2012).
7. S. Susan, W. Tai, M. Tang, *Journal of Scanning Microscopies*, 23, 267 (2001).
8. H. Vlčková, D. Solichová, M. Bláha, P. Solich, L. Nováková, *J. Pharm. Biomed. Anal.*, **55(**2), 301 (2011).
9. D. J. Billingsley, J. Kirkham, W. Bonass, N. Thomson, *Phys. Chem. Chem. Phys*., 12, 14727 (2010).
10. M. Kircher, J. Kelso, *Bio Essays*, **32(**6), 524 (2010).
11. K. Liolios, J. Sikorski, M. Jando, A. Lapidus, A. Copeland, Tijana Glavina Del Rio, M. Nolan, S. Lucas, H. Tice, Jan-Fang Cheng, Cliff Han, T. Woyke, L. Goodwin, S. Pitluck, N. Ivanova, K. Mavromatis, N. Mikhailova, O. Chertkov, Ch. Kuske, Amy Chen, Krishna Palaniappan, M. Land, L. Hauser, Yun-Juan Chang, C. D. Jeffries, J. C. Detter, T. Brettin, M. Rohde, M. Göker, J. Bristow, J. A. Eisen, V. Markowitz, P. Hugenholtz, H.-P. Klenk, N. C. Kyrpides, *Stand. Genomic Sci.*, **6** (2), 265 (2010).
12. M. Ohring, *Mater. Sci. Thin Films*, **42**, 794 (2002).
13. D. C. Bell, N. Erdman (eds), Low Voltage Electron Microscopy: Principles and Applications, 2012, p. 238.
14. L. Reimer, Image Formation in Low-voltage Scanning Electron Microscopy, 1993.
15. J. Bozzola, L. Russell, Electron Microscopy: Principles and Techniques for Biologists, 1998.
16. Scanning Electron Microscopy for the Life Sciences, H. Schatten (ed), 2012.
17. P. Mestres, N. Pütz, S. de las Heras, E. Poblete, A. Morguet, M. Laue, *Annals of Anatomy – Anatomischer Anzeiger*, **193** (3), 197 (2011).

БЪРЗА И ОПРОСТЕНА ПРЕПАРАТИВНА ПРОЦЕДУРА НА БИОЛОГИЧНИ ПРОБИ, ПОЗВОЛЯВАЩА ПОСЛЕДВАЩА ВИЗУАЛИЗАЦИЯ ЧРЕЗ СКАНИРАЩА ЕЛЕКТРОННА МИКРОСКОПИЯ

И. Пироева[1], С. Атанасова-Владимирова[1], Л. Т. Димова[2], Х. И. Сбиркова[2], Г. Радославов[3], П. Христов[3], Б. Л. Шивачев[2]

[1] Институт по физикохимия, Българска академия на науките, ул. „Акад. Георги Бончев“, бл. 11, 1113 София, България
[2] Институт по минералогия и кристалография „Акад. Иван Костов“, Българска академия на науките, ул. „Акад. Георги Бончев“, бл. 107, 1113 София, България
[3] Институт по биоразнообразие и екосистемни изследвания, Българска академия на науките, ул. „Акад. Георги Бончев“, бл. 25, 1113 София, България

Постъпила февруари, 2013 г.; приета май, 2013 г.

(Резюме)

Настоящият протокол описва бърза препаративна методика за биологични проби, като ДНК и бактерии, позволяваща последваща визуализация чрез сканираща електронна микроскопия (СЕМ). Това включва закрепването на пробите върху агарозна подложка, последвано от дехидратация на биологичните образци и нанасяне на тънко проводимо покритие за наблюдение чрез електронна микроскопия. Обезводняване на пробите гарантира, че те няма да деструктират във вакуумната камера на СЕМ. Нанасянето на тънък слой допълнително фиксира пробите и подобрява контраста. Процесът на пробоподготовка се извършва от 6 до 24 часа и е оптимизиран за визуализация на бактерии и ДНК. Пробите могат да се съхраняват във вакуум в продължение на седмица, което дава достатъчно време за получаване на СЕМ изображения. Протоколът не включва токсични, канцерогенни или други вредни химикали и реактиви.

Bulgarian Chemical Communications, Volume 45, Number 4 (pp. 516–521) 2013

Silica-based hybrid materials as biocompatible coatings for xenobiotics sensors

L. Yotova*, S. Yaneva

Department of Biotechnology, University of Chemical Technology and Metallurgy, 8 Str. K. Ohridski Blvd., 1756 Sofia, Bulgaria

Received February, 2013; Revised May, 2013

In the recent years many types of biosensors have been developed and used in a wide variety of analytical settings with applications in biomedicine, health care, drug design, environmental monitoring, and detection of biological, chemical and toxic agents.

Tailored surface properties such as tunable reactivity, biocompatibility or wettability could be obtained by different approaches of surface modification, so that the design of biofunctional surface is of great interest in bioanalysis research.

A good combination of support material and immobilization methods is of fundamental importance to achieve the desired performances from the sensing system.

The aim of this research is immobilization of tyrosinase onto silica hybrid membranes based on ethyltrimethoxy silane (ETMS) and methylthrietoxy silane MTES and cellulose derivatives. Tyrosinase was covalently immobilized by acrylamide/acrylonitrile copolymer included on hybrid membranes. pH and temperature optimum were determined for immobilized tyrosinase preparations as well as for the free enzyme.

Key words: hybrid membranes, enzymes, optical biosensors.

INTRODUCTION

Organic/inorganic hybrid materials prepared by the sol–gel approach have rapidly become a fascinating new field of research in materials science.

Organic molecules other than the solvent can be added to the sol and become physically entrapped in the cavities of the formed network upon gelation where the molecules have to endure the pH of the environment [1]. Most sol–gel bioencapsulates reported to date have used inorganic materials or carbon composite derived from either ethyltrimethoxy silane (ETMS) or methylthrietoxy silane (MTES) [2, 3]. The use of some organic molecules in the gel formation process that may influence the dimensions of the forming pores represents another way to increase the immobilized enzyme activity. Within such meso-or macroporous silica gels, substrate molecules diffusion is easier, explaining the increase of the enzymatic activity [4].

Porosity is a feature that allows analyte molecules to diffuse into the matrix and react with the enzymes or another biomolecules. As it was mentioned, many different molecules can be incorporated into the sol–gel matrix. Surface characteristics as well as uniformity in monoliths/thin films are one of the desirable criteria for sensing applications [5–6].

During the drying phase, some of the larger pores are emptied while smaller pores remained wet by the solvent, creating large internal pressure gradients. This stress causes cracks in large monoliths and is responsible for fractures in dry monolithic sensors upon immersion in water. Further addition of polymers as poly dimethil siloxane, polyamides, polyacrilates and polyethylene glycol (PEG) provide regulation of inorganic condensation-polymerization process and is also under investigation for improving sol-gel material. Polyethers were also used in sol-gel processing mixtures to control pore size distribution [7].

Phenols due to their toxicity, persistence and common occurrence in the biosphere are one of the most important groups of ecotoxins. These compounds are in a common use such as ingredients (components) and precursors of other chemicals including organic polymers, solvents, dyes (aminophenols), explosives (nitrophenols), surfactants (alkylphenols) or drugs [8].

* To whom all correspondence should be sent:
E-mail: lkyotova@yahoo.com

Photometric analyses by standard methods are commonly used for determination of phenols, and these analyses usually require sample pretreatment by filtration and distillation. Recently, tyrosinase based biosensors have been shown to be useful for this purpose. Easy fabrication, fast analysis, and low-cost are the main advantages of the biosensor method [9, 10].

The optical sensing techniques, in comparison with electrical methods, have some advantages, such as selectivity. They are also sensitive, inexpensive, non-destructive, and have wide capabilities. The idea behind these sensors is based on changes of optical parameters of sensing molecules entrapped usually in thin films. Optical fibers used in optical sensors to transmit the light in and out of the detection area assure such advantages as flexibility, directionality, low signal losses, low costs, etc. Since then, this technology is widely applied among others for immobilization of active molecules onto the tip of an optical fiber to fabricate a point sensor [11]. The most popular chemical immobilization utilized for the preparation of enzyme-based optical fiber sensors is the covalent coupling of enzymes to polymeric support [12].

This technique offers the most stable immobilized enzyme preparation by which the immobilization process is not easily reversed by pH, ionic strength, temperature, or solvent variations [13]. The main advantages of the biosensors over other kinds of sensors are their specificity of response and in some cases, their ability to work in very dirty environments [14].

Tyrosinase (EC 1.14.18.1, monophenol monooxygenase) is an enzyme which catalyzes the incorporation of molecular oxygen into phenolic compounds. Tyrosinase active site contains a coupled binuclear copper complex (type 3 copper). Recently, the mechanism of catalytic function of tyrosinase has been proposed and actively investigated. [15–17].

One of the key issues to develop biosensing platforms concerns the processes involved in enzyme immobilization on surfaces. The understanding of their fundamentals is crucial to obtain stable and catalytically active protein layers for developing successful biosensing devices [18, 19].

EXPERIMENTS AND EQUIPMENT

Reagents

Tyrosinase isolated from mushrooms, (E.C.1.14. 18.1) was supplied by Sigma-Aldrich; L-DOPA (L-3,4-dihydroxyphenylalanine) by Fluka; ethyltrimethoxy silane (ETMS) and methylthrietoxy silane (MTES) by Merck; cellulose acetate propionate with high and low molecule weight (CAP/H (~25 000 m.w.) (CAP/L (~15 000 m.w., respectively) by Sigma-Aldrich, copolymer from acrylamide and acrylonitrile (AA) were provided by the Biotechnology Department of UCTM, Sofia, Bulgaria [20], dimethyl formamide (DMF) by Merck.

Synthesis of hybrid membranes by the sol-gel method and visualization of the sufraces

Groups of hybrid materials were synthesised by the sol-gel method with the participation of silica precursors ETMS and MTES. Cellulose acetate propionate with high molecule weight CAP/H and CAP/L were used as an organic component of the system. A third component was included in the system as a carrier of active groups for covalent immobilization, namely copolymer of acrylamide/ acrylonitrile (AA). The precursors were hydrolysed in methyl alcohol for ETMS and ethyl alcohol for and MTES. Dimethylformamide was used as a solvent of the organic component. Hybrid membranes contained 5 ml ETMS (MTES), 3 g cellulose acetate propionate with high (low) molecular weight and 100 mg copolymer from poly-acrylamide and poly-acrylonitrile. The quantities and components for the synthesis and the conditions are described in a previous paper [21].

For visualization of membranes surfaces a microscope “Carlzeiss”, Jena, Jenatech Inspection, monochromatic light source “Infinity 22” with CCD camera – “Lumenera”, Canada was used.

Oxidation method for tyrosinase and covalent immobilization

Oxidation of the carbohydrate residues of tyrosinase was done with periodic acid according to Zaborsky and Ogletree’s method (0.04 mM in 0.05 mM acetate buffer, pH 5.0, in the dark) [28]. The oxidized enzyme was dialysed in a dialysis membrane from Serva, Germany by submerging in a 50 mM phosphate buffer with pH = 6.0 for 24 h. The immobilization of tyrosinase was carried out in the following sequence: 1.0 g of the hybrid membranes was added to 20 mL of the oxidized dialysed solution of tyrosinase. Immobilization was done under continuous stirring for 24 h at 4 °C.

Spectrophotometrically measurement of enzymatic activity and determination content of protein

Diphenolase activity was determined spectrophotometrically with 10 mM substrate L-DOPA as a substrate, at 25 °C, using spectrophotometer with

optical fibers (AvaSpec, Avantes, USA). The diphenolase activity does not show any lag period. The dopachrome assay was performed. The increase in absorption at 475 nm, due to the formation of dopachrome (ε 475 = 3 600 $M^{-1}cm^{-1}$), was monitored as a function of time. The activity is expressed as mole of L-DOPA oxidized per minute.

The total content of protein in the immobilized enzyme was determined by the Lowry [23] modified method using bovine serum albumin as a standard.

pH and temperature optimum

For determination of the pH optimum for tyrosinase, the residual activities of free and immobilized enzymes were determined in the sodium phosphate buffer with pH range from 5.0 to 8.0. To determine the temperature optimum for tyrosinase, the residual activities of free and immobilized enzyme were determined in the range from 20 °C to 50 °C.

RESULTS AND DISCUSSION

Groups of hybrid membranes were synthesised using different silica precursors. All membranes are mechanically resistant plastic and transparent, which is a necessary condition for the experiment. In such hybrid materials is possible to expect very interesting characteristics that are not found in organic polymer or inorganic material independently. For example, they can have features such as plastics flexibility and have excellent mechanical strength and thermal stability in the same time [24]. On the surface of the membranes different size aggregates (from 20 to 100 μm) are observed. For visualization of the surface series of images were made by microscope at different magnification. On Figure 1 images of the membranes surfaces are presented.

A comparison of the catalytic properties of immobilized enzymes on hybrid membranes containing ETMS and MTES CAP/L or CAP/H was made. In the table below catalytic properties of free tyrosinase and tyrosinase immobilized onto matrices are presented (Table 1).

The covalent binding of the enzyme to copolymer of acrylamide/acrylonitrile is effected between the amide groups of the copolymer and the oxidized carbohydrate residues of the enzyme. This method was applied in previous research as well. The advantage of the method is that immobilization does not change the conformation of the enzyme molecule and binding always takes place outside the active centres [20].

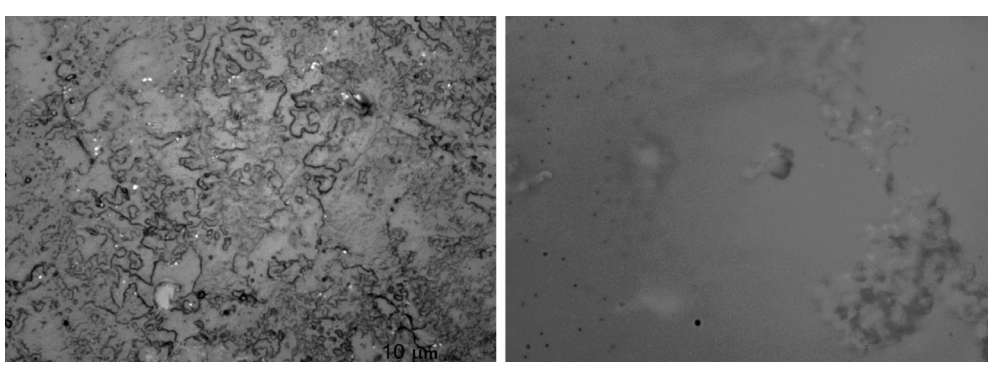

Fig. 1. Optical microscopy image of the surface on ETMS – left and MTES – right side at magnification ×50, light field

Table 1. Catalytic properties of free and immobilized tyrosinase

Membrane	Amount of bound protein [mg/g]	Specific activity [U/mg]	Relative activity [%]	pH optimum	Temperature optimum [°C]
Free tyrosinase	–	421	–	6.0	30
ETMS/CAP/H/AA	1.82	322	76.48	6.5	35
MTES/CAP/H/AA	2.34	312	74.10	5.5	35
ETMS/ CAP/L/AA	1.91	317	75.29	7.5	35
MTES/CAP/ L/AA	2.06	306	72.68	7.0	30

The results for specific activity of immobilized membranes are identical with results described in our previous work with substrate L-tyrosine [25]. For L-DOPA substrate tyrosinase immobilized onto hybrid membranes shows higher parameters of relative activity. Researchers have demonstrated that the silica sol-gel materials can retain the catalytic activities of enzymes to a large extent. The inorganic silica sol-gel material is biocompatible, has high thermal stability, chemical inertness and negligible swelling in non-aqueous solutions [26].

One of the most important parameters to be considered in enzyme immobilization is storage stability. The stabilities of the free and immobilized tyrosinase were determined after stored in phosphate buffer solution (50 mM, pH 6.5) at 4 °C for a predetermined period. Under the same storage conditions, the activities of the immobilized tyrosinase preparations decreased slower than that of the free tyrosinase. The free enzyme lost all of its activity within 4 weeks. The immobilized tyrosinase preserved its initial activity during several months storage period [27], which corresponds with the data reported by other authors [28]. On the figure below stored stability of immobilized tyrosinase activity are presented (Fig. 2).

The enzyme activities were seriously affected by the buffer solution pH value [29], so the effect of the pH value of buffer solution was investigated in the range from 5.0 to 8.0.

On the figure below pH profile of free tyrosinase and immobilized onto hybrid matrices are presented (Fig. 3).

The change in optimum pH depends on the charge of the enzyme and/or of the matrix. This change is useful in understanding the structure-function relationship of the enzyme and helps the activity of free and immobilized enzyme as a function of pH. As seen in Fig. 2, the optimum pH for free enzyme was found to be 6.5. In the case of MTES/CAP/H/AA immobilized tyrosinase the optimum pH shifted by 1.0 unit toward the acidic region. The results are the same that reported from *Yahsi and co-authors.* These shifts could be attributed to secondary interaction such as ionic and polar interactions, hydrogen bonding, etc. between the enzyme and the hybrid membrane [30].

On the figure below temperature profile of free tyrosinase and immobilized onto hybrid matrices are presented (Fig. 4).

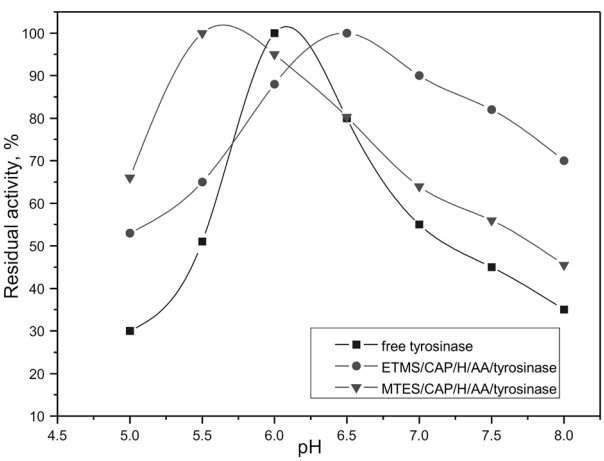

Fig. 3. Residual activity of free and immobilized tyrosinase as a function of pH

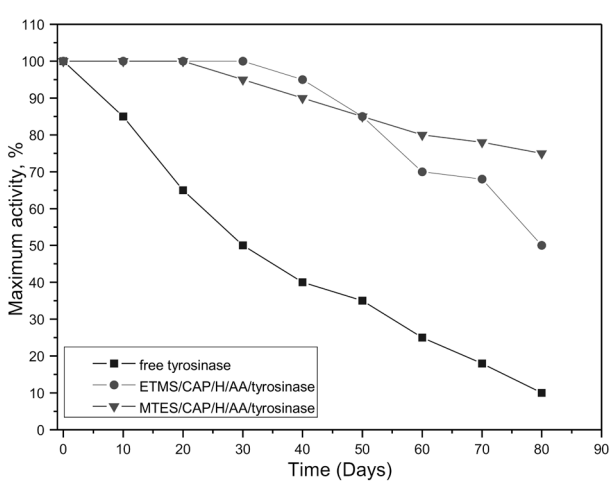

Fig. 2. Stored stability of immobilized tyrosinase activity

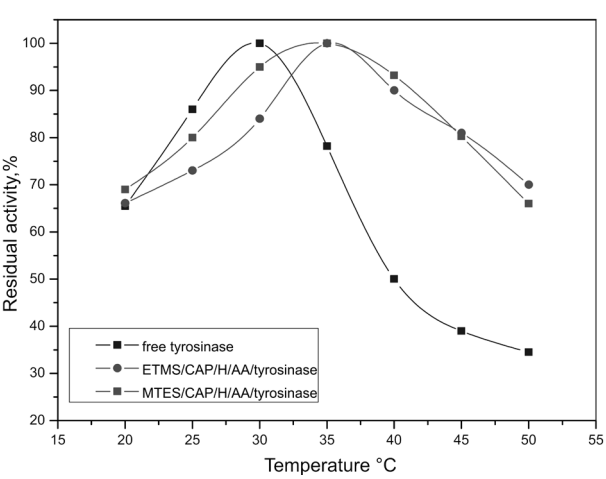

Fig. 4. Residual activity of free and immobilized tyrosinase as a function of temperature

Maximum enzymatic activity was obtained at 35 °C for immobilized enzymes. The optimal reaction temperature was higher than that of the commercial enzymes in its free form or when immobilized on other supports [31, 32], which illustrates a substantial degree of enzyme stabilization [33]. The stability of the obtained preparation demonstrates the advantages of immobilization onto hybrid membranes.

CONCLUSION

In order to construct an optical biosensor, membranes were synthesised with participation of different silica precursors and covalent immobilization was performed. The analysis of the enzymes immobilized on the different membranes showed change in pH optimums for ETMS/CAP/H/AA pH=6.5 and MTES/CAP/H/AA, pH=5.5 and the temperature optimums t = 35 °C for the same membranes compared to the characteristics of the free enzymes. The present research showed that the best membranes with the highest relative activity is (ETMS/CAP/H/AA – 76.48%) for L-DOPA substrate. The efficiency of immobilization depends on the type of the silica precursors and cellulose derivatives, when the other conditions are identical. The constructed optical biosensor based on covalent immobilized enzyme demonstrated excellent operational parameters.This membranes can be potentially applied for biosensors design for analyses in organic solvents, analysis of food and in monitoring of the environment.

Acknowledgments: *This study was supported by "National Found Scientific Research", project DUNK 01/03, 2010.*

REFERENCES

1. S. Padney, S. B. Mishra, *J. Sol-Gel Sci. Technol*., **1**, 59 (2011).
2. Y. Zhang, D. Wu, Y. Sun, S. Peng, *Journal of Sol-Gel Science and Technology*, 33 (2005).
3. V. B. Kandimalla,V. S. Tripathi, H. Ju, *Analalytical Chemistry*, 36 (2006).
4. M. Dragomirescu, T. Vintila, S. Jurcoane, G. Preda, *Romanian Biotechnological Letters*, **15,** 2 (2010).
5. D. J. Monk, D. R. Walt, *Anal. Bioanal. Chem.*, 379 (2004).
6. P. C. A. Jeronimo, A. N. Araujo, M. Conceicao, B. S. M. Montenegro, *Talanta*, 72 (2007).
7. R. Gupta, N. K. Chaudhury, *Biosensors and Bioelectronics*, 22 (2007).
8. J. Michalowicz, W. Duda, *Current Topics in Biophysics*, 30 (2007).
9. K. R. Rogers, *Analytica Chimica Acta*, 568 (2006).
10. D. Fiorentino, A. Gallone, D. Fiocco, G. Palazzo, A. Mallardi, *Biosensors and Bioelectronics*, 25 (2010).
11. A. Lukowiak, W. Strek, *J. Sol-Gel Sci. Technol*., **2**, 50 (2009).
12. S. Tembe, M. Karve, S. Inamda, S. Haram, J. Melo, S. F. D'Souza, *Analytical Biochemistry*, 349 (2006).
13. B. Kuswandi, R. Andres, R. Narayanaswamy, *Analyst*, 126 (2001).
14. S. R. Mozaz, M. J. L. de Alda, M. P. Marco, D. Barcelo, *Talanta*, 65 (2005).
15. J. Zhao, D. Wu, J. Zhi, *Biochemistry*, 75 (2009).
16. Y. Wang, X. Zhang, Y. Chen, H. Hu, Y. Tan, S. Wang, *Am. J. Biomed. Sci.*, **2,** 3 (2010).
17. J. Kochana, *Acta Chim Slov.*, 59 (2012).
18. E. Casero, L. Vazquez, A. M. Parra-Alfambra, E. Lorenzo, *The Analyst*., **8**, 135, (2010).
19. S. A. Ansari, Q. Husain, *J. Am. Ceram. Soc.*, 30 (2012).
20. L. Yotova, T. Ivanov, V. Mironova, V. Chuchuranova, *Bioautomation*, 11 (2008).
21. S. Yaneva, D. Marinkova, L. Yotova, B. Samuneva, *Bioautomation*, 8 (2007).
22. O. Zaborsky, R. Ogletree, *J. Biochem. Biophys Res. Coun.*, 61 (1974).
23. O. H. Lowry, N. J. Rosebrough, A. L. Farr, R. J. Randall, *J. Biol. Chem.*, 193 (1951).
24. Y. Chujo, *Kona*, 25 (2007).
25. L. Yotova, S. Yaneva, D. Marinkova, Serfaty, *Journal of Biotechnology and Bioequipment*, (2013), accepted.
26. H. Zhou, L. Liu, K. Yin, S. Liu, G. Li, *Electrochemistry Communications*, **8**, 7 (2006).
27. M. Y. Arica, G. Bayramoglu, N. Bicak, *Process Biochemistry*, 39 (2004).
28. E. Jahangira, R. Agharafeie, H. J. Kaiser, Y. Tahambasi, R. L. Legge, K. Haghbeen, *Biochemical Engeneering Journal*, 60 (2012).
29. J. Zhao, D. Wu, J. Zhi, *Bioelectrochemistry*, 75 (2009).
30. A. Yahsi F. Sahin, G. Demirel, H. Tumturk, *International Journal of Biological Macromolecules*, 36 (2005).
31. T. Sandu, A. Sarbu, F. Constantin, E. Ocnaru, S. Vulpe, A. Dimitru, H. Iovu, *Rev. Roum. Chim*., **56,** 9 (2011).
32. T. Zhang, B. Tian, J. Kong, P. Yang, A. B. Liu, *Analitica Chimica Acta*, 489 (2003).
33. M. E. M. Zamora, F. R. Melgarejo, F. G. Canovas, A. G. Ruiz, *Journal of Biotechnology*, 126 (2006).

ХИБРИДНИ МАТЕРИАЛИ НА ОСНОВАТА НА СИЛИЦИЕВ ДИОКСИД КАТО БИОСЪВМЕСТИМИ ПОКРИТИЯ ПРИ БИОСЕНЗОРИ ЗА КСЕНОБИОТИЦИ

Л. Йотова*, С. Янева

Катедра Биотехнология, Химикотехнологичен и Металургичен Университет, бул. „Кл. Охридски“ 8, 1756 София, България

Постъпила февруари, 2013 г.; приета май, 2013 г.

(Резюме)

През последните години са разработени много видове биосензори с приложения в медицината, контрол на здравето, при създаването на нови лекарства, за екологичен мониторинг, за регистриране на биологични, химични и токсични агенти и други.

Адаптирането на повърхността на носителя, за да се подобри неговата реакционна способност, биосъвместимост и омокряемост, може да се постигне чрез различни методи за модифициране. Така се създава биофункционална повърхност, което е обект на изследователски интерес. Изборът на носител и метод за имобилизация са от основно значение за постигане на желаната ефективност на сензорната система.

Целта на това изследване е имобилизация на тирозиназа върху хибридни мембрани на основата на етилтриметокси силан (ETMS) и метилтриметокси силан (MTES) и целулозни производни. Тирозиназата бе ковалентно имобилизирана с помощта на съполимер на акриламид/акрилонитрил, включен в хибридния материал. Бяха определени pH и температурният оптимум на свободния и имобилизиран ензим.

Bulgarian Chemical Communications, Volume 45, Number 4 (pp. 522–529) 2013

Crystal structures of Cs^+, Mg^{2+}, Ba^{2+} ion exchanged ETS-4 at RT and 150 K

L. Tsvetanova[1], L. Dimowa[1]*, S. Ferdov[2], R. Nikolova[1]

[1] *Institute of Mineralogy and Crystallography, Bulgarian Academy of Sciences, Sofia, 1113, Bulgaria*
[2] *Department of Physics, University of Minho, 4800-058 Guimarães, Portugal*

Received February, 2013; Revised May, 2013

Ion exchanged ETS-4 samples by Cs^+, Mg^{2+}, and Ba^{2+} cations were analyzed by single crystal X-ray diffraction at 150 K. Structural data obtained from low temperature (LT) experiment are compared with the room temperature (RT) ones obtained from the same samples. The study shows that the low temperature conditions ensure precise determination of atomic positions and minimize the effects of atomic thermal vibration and positional disorder.

Key words: ETS-4, LT experiment, single crystal X-ray diffraction.

INTRODUCTION

ETS-4 (*Engelhard* titanium silicate – 4) is a mixed tetrahedral-octahedral molecular sieve related to the mineral zorite [1–4]. Due to its highly disordered structure various studies aiming at elucidation of ETS-4 framework have been reported [5–7]. The first structural data providing evidence for the framework similarity between Na-ETS-4 and zorite have been published in 1996 [5]. Later reports described ETS-4 as an intergrowth of four hypothetical polymorphs which differ in the arrangement of part of the titano-silicate units [6]. The ETS-4 framework exhibits orthorhombic *Cmmm* symmetry and each of the Ti and Si atoms has two symmetrically independent positions. The Ti1 atom is six coordinated and takes part in –O–Ti–O– chains running parallel to [010]. In the [001] direction the chains are interconnected by Si1 tetrahedra to build layers parallel to (100). The layers are identical for all of the hypothetical polymorphs. The latter differ in the arrangement of the titano-silicate bridging units formed by Ti2 and Si2 polyhedra. The position of the Ti2 atom with respect to the mirror plane perpendicular to *c* axis is supposed to predetermine its coordination environment and has been of significant interest for most of the authors. In earlier structural studies based on powder diffraction data six-coordination environment was suggested for this atom as it was positioned exactly on the mirror plane. The coordination octahedron is built of four oxygen atoms from four $Si2O_4$ tetrahedra and two oxygens (usually marked as O7) symmetrically related to each other with respect to the mirror plane where the Ti2 atom is positioned. [5–6]. Single crystal X-ray diffraction analysis of Na-ETS-4 and Sr-exchanged ETS-4 indicated that the Ti2 atom in the studied samples is situated close to but not on the mirror plane and as a consequence the Ti2 octahedron suffers some distortion expressed in terms of the Ti2–O7 distances (1.70 *vs*. 2.23 Å). The performed refinement of the Ti2 and O7 atoms occupancy gave evidence that Ti2 atom in the studied samples is five-coordinated [7]. However, interpretation of the Ti2 coordination is rather controversial because the low occupancy of the O7 ligand position in it can be due to various reasons e.g. structural defects *etc*. Recently the crystal structures of Cs^+, Mg^{2+}, and Ba^{2+} exchanged forms of as-synthesized Na-K-ETS-4 have been reported [8]. The performed single crystal analyses confirmed that Ti2 in the initial Na-K-ETS-4 is situated outside the mirror plane. It was also found that the incorporation of Cs^+ and Mg^{2+} ions do not provoke significant distortion of the ETS-4 framework, but the Ti2 atom is shifted closer to the mirror plane. In contrast, Ba^{2+} inclusion in the pore system of ETS-4 causes substantial framework contraction, splitting of some of the positions of the framework atoms and shifting of the Ti2 atom to a position lying exactly on the mirror plane perpendicular to the *c* axis. It has been suggested that the coordination of the Ti2 atom remains the same in the Na-K-ETS-4 and its exchanged forms. This puts the question to what extent the position of the Ti2 atom with respect to the mirror plane, defines its coordination.

* To whom all correspondence should be sent:
E-mail: louiza.dimova@gmail.com

The present study aims at structural investigation of the same Cs^+, Mg^{2+}, Ba^{2+} exchanged ETS-4 samples performed at low temperature in order to minimize the effects of atomic thermal vibration and positional disorder. The elastic behavior of the unit cell and the positions of the framework and extra-framework cations from room temperature (RT) and low temperature (LT) experiments are compared. The framework distortion, position and coordination of the Ti2 atom are also discussed.

EXPERIMENTAL

Single-crystal X-ray diffraction data have been collected at low temperature conditions using the same single crystal samples of Cs^+, Mg^{2+} , Ba^{2+} exchanged ETS-4 for which RT experimental data have been published in [8]. LT (150 K) data collection was performed by ω-scan technique, on an Agilent Diffraction SuperNova Dual four-circle diffractometer equipped with Atlas CCD detector using mirror-monochromatized MoKα radiation from micro-focus source (λ = 0.7107 Å). During the low temperature data collection the samples were kept at 150 K with an Oxford Instruments Cobra controller device and a nitrogen atmosphere. The determination of cell parameters, data integration, scaling and absorption corrections were carried out using the CrysAlis Pro program package [9]. The structures were solved by direct methods (SHELXS-97) [10] and refined by full-matrix least-square procedures on F^2 (SHELXL-97) [10]. Further details of the crystal structure investigation may be obtained from Fachinformationszentrum Karlsruhe, 76344 Eggenstein-Leopoldshafen, Germany (fax: (+49)7247 808 666; e-mail: crysdata@fiz-karlsruhe.de, http://www.fizkarlsruhe.de/ request_for_deposited_data.html on quoting the CSD-425730, 425731. The crystal data obtined by the low temperature experiment and the structure refinement indicators for the studied compounds are presented in Table 1.

RESULTS AND DISCUSSION

Chemical composition of the studied Cs- Mg- Ba-ETS-4 samples obtained after the data refinement for RT and LT experiments are presented in Table 2. The discrepancies in the calculated chemi-

Table 1. LT crystal data and structure refinement indicators for Cs- Mg- Ba-ETS-4

Sample	Cs-ETS-4	Mg-ETS-4	Ba-ETS-4
Space group	Cmmm	Cmmm	Cmmm
a (Å)	23.123(2)	23.198(4)	22.939(3)
b (Å)	7.213(4)	7.177(2)	7.169(3)
c (Å)	6.930(3)	6.948(2)	6.721(2)
V (Å^3)	1156.9(2)	1157.0(1)	1105.5(5)
Z	1	1	1
D_x[Mg m^{-3}]	273.5	2.123	2.824
μ [mm$^-$]^1	4.42	1.54	5.16
T_{min}–T_{max}	0.261 – 1	0.916–1	none
measured reflections	2196	2212	2067
independent reflections	723	728	695
parameters	85	75	83
reflections with $I > 2\sigma(I)$	381	479	490
θ_{min}–θ_{max}	2.9°–28.3°	2.9°–28.3°	3.0°–28.2°
F_{000}	648	728	874
T (K)	150(2)	150(2)	150(2)
$R[F^2 > 2\sigma(F^2)]$	0.113	0.077	0.083
wR(F^2)	0.332	0.212	0.222
R_{int}	0.186	0.088	0.086
S	1.105	1.08	1.04

Table 2. Chemical composition of Cs-, Mg-, Ba-ETS-4 calculated after the structure refinement

Compound	RT – structural data	LT – structural data
Cs-ETS-4	$K_{1.18}Na_{1.20}Cs_{4.01}H_{2.61}Si_{12}Ti_5O_{38}(OH) \times 7.12\ H_2O$	$K_{0.86}Na_{1.12}Cs_{3.96}H_{3.06}Si_{12}Ti_5O_{38}(OH) \times 7.36\ H_2O$
Mg-ETS-4	$K_{2.63}Mg_{1.44}H_{3.49}Si_{12}Ti_5O_{38}(OH) \times 7.92\ H_2O$	$K_{2.81}\ Mg_{1.52}\ H_{3.15}Si_{12}Ti_5O_{38}(OH) \times 8.24\ H_2O$
Ba-ETS-4	$Ba_{4.31}H_{0.39}Si_{12}Ti_5O_{38}(OH) \times 4.52\ H_2O$	$Ba_{4.41}H_{0.18}Si_{12}Ti_5O_{38}(OH) \times 4.6\ H_2O$

cal compositions for the RT and LT data are most probably due to statistical reasons of the experimental conditions used. It is also notable that there is no partial dehydration of the samples with N2 gas flow – an effect observed by other authors performed LT experiments of water containing porous materials [11, 12].

A model obtained by superposition of the four hypothetical polymorphs models of the ETS-4 framework (see Introduction) is presented in Figure 1. The complex pore system of the presented framework includes three different kinds of channels. The six-membered-ring channel, where smaller ions as Na^+ and Mg^{2+} reside, is marked with A1. This channel is formed within the titano-silicate layer formed by $Ti1O_6$ and $Si1O_4$ polyhedra. The A2 channel is the one formed between the layer and the titanosilicate bridging units built by $Ti2O_5$ and $Si2O_4$ polyhedra. The channel consists of seven-membered rings and is occupied by bigger cations. In the studied samples K^+, Ba^{2+} or Cs^+ ions are situated there. The eight-membered ring made by four $Si1O_4$ and four $Si2O_4$ tetrahedra is marked as A3. It has been found that water molecules and Cs^+ ions reside in the channels formed by the eight-membered rings and running parallel to [010]. It should be noted that the accessibility of A2 and A3 channels depends on the orientation of the titano-silicate bridging units formed by the $Ti2O_5$ and $Si2O_4$ polyhedra.

Unit cell behavior at LT conditions

The unit cell parameters variation of the studied samples as a function of the cation exchange and low temperature conditions are shown in Figure 2. The elastic behavior of ETS-4 structure is studied by comparing the unit cell parameters in the following order: Na-K-ETS-4 → ETS-4 exchanged samples at RT → ETS-4 exchanged samples at LT. The ion exchange by Cs^+ and Mg^{2+} do not cause significant changes of the ETS-4 unit cell volume. The unit cell parameters of the initial Na-K-ETS-4 and the exchanged samples at RT are almost the same. Interestingly the unit cell volume of ETS-4 decrease by 60 A^3 after the ion exchange of Na-K-ETS-4 by Ba^{2+}. This notable contraction observed at RT measurements is most probably due to the higher ionic potential of barium ion. The low temperature conditions affect differently the structural parameters of the ion exchanged samples. In the Ba-ETS-4 the compression capability of the ETS-4 structure is realized after the ion exchange and no additional contraction is possible with temperature lowering (Fig. 2). However a structural adjustment

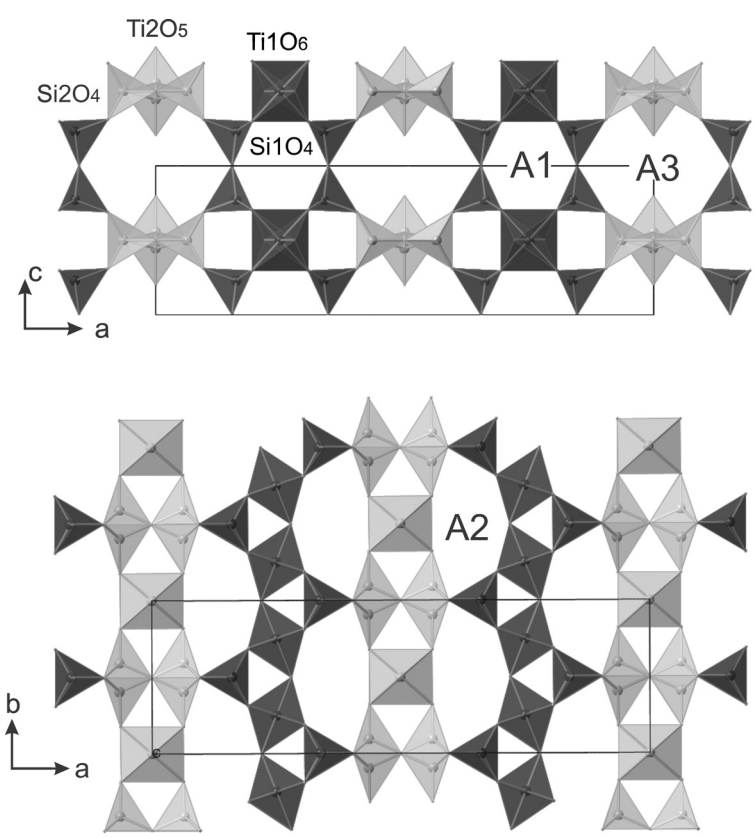

Fig. 1. Superposition model of the ETS-4 framework. The six, seven and eight – membered-ring channels are marked by letters as A1, A2 and A3 respectively. The $Ti1O_6$ and $Si1O_4$ polyhedra, building the layers are dark grey colored. The $Ti2O_5$ and $Si2O_4$ bridging units are marked by light grey color

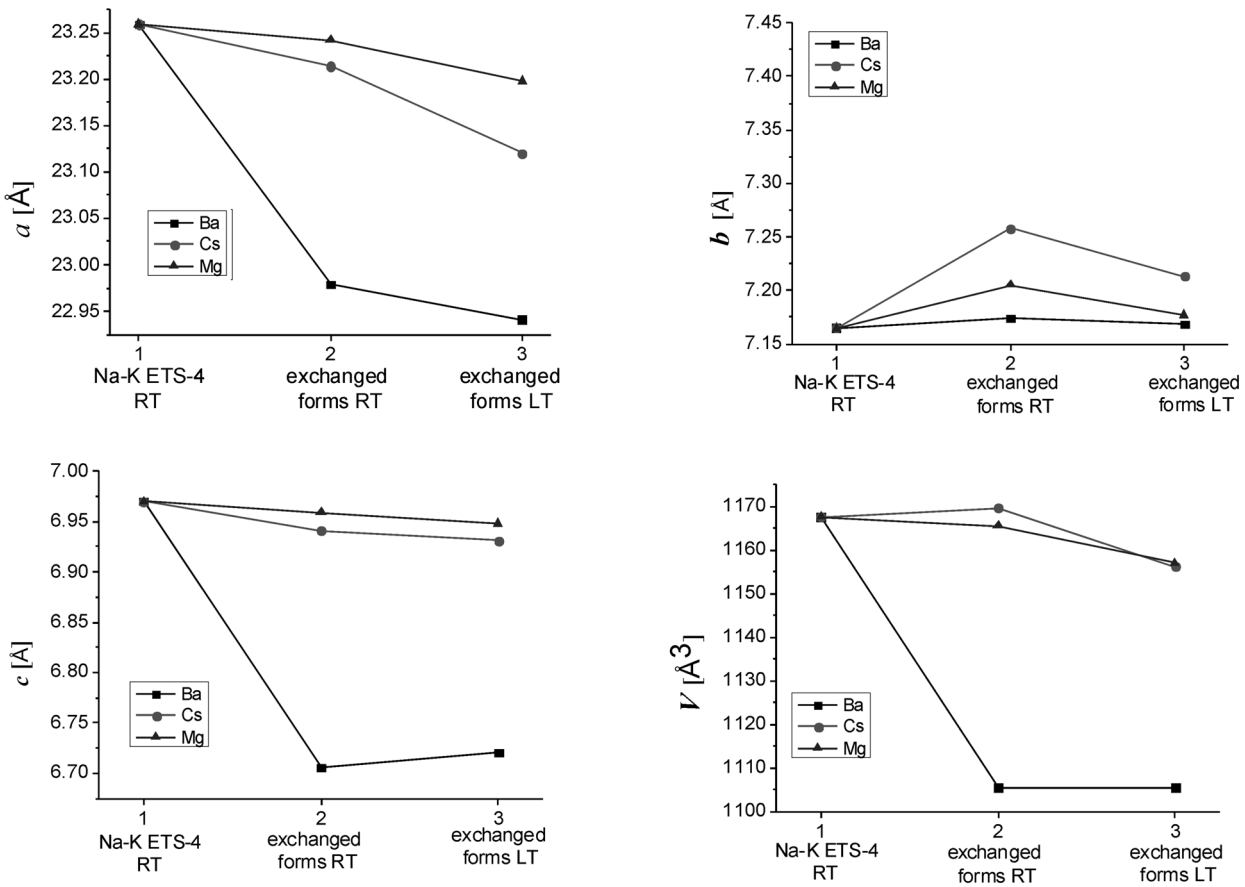

Fig. 2. Unit cell parameters of K-Na-ETS-4 and exchanged forms at RT and LT

to the LT conditions is realized by altering of the deformation directions. This process is expressed by slight increase of the *c* parameter compensated by decreasing of *a* and *b* parameters thus the cell volume remains the same. Although a lowering of the Cs- and Mg-ETS-4 volumes at LT conditions is observed these structures remain less compressed than that one of the Ba- ETS-4 one (Fig. 2).

Framework atoms position at LT conditions

The framework topology of the studied compounds remains stable but some of the fractional coordinates of the framework atoms shift from their positions found for RT experiments in order to adapt the structure to the low temperature conditions (Table 3). Thus the structures contraction accompanied by atom positions shifts influence the bond distances (Table 4) and angles in all the studied compounds.

In the Cs-ETS-4 sample all framework positions remain almost unchanged most probably because all of the channels are occupied by cations (A1 – Na^+, A2 – K^+ and Cs^+ and A3 – Cs^+) and the coordination bonding between the framework oxygens and the extra-framework cations stabilize the structure. The Mg-ETS-4 sample behaves similarly and the framework atoms remain at the same positions except the Ti2 one which shifts along the *c* axis to a position lying exactly on the mirror plane perpendicular to it (Table 3.). Such a shift of the Ti2 atom from general to a special position was reported for Ba-ETS-4 after the ion exchange and a possible change of the Ti2 coordination from five to six was previously suggested [8]. In the case of Mg-ETS-4 the shift of the Ti2 position is most probably due to readjustment of the framework occurring upon the LT conditions of the experiment. In the most distorted Ba-ETS-4 framework the atomic positions of Si1, Ti2 and most of the framework oxygen atoms remain unchanged. In this case the framework responses to the temperature lowering by a cooperative rotation of $Si2O_4$ and $Ti1O_6$ polyhedra. This is expressed by shift of the Si2 and Ti1 atoms from the special positions in [001] direction and split of the O1 and O2 atomic positions. In order to preserve the framework topology and chemical stoichiometry these new positions have been refined as half occupied.

Table 3. Atomic parameters of the studied compounds at RT an LT conditions

ETS sample		*x* (RT)	*x* (LT)	*y* (RT)	*y* (LT)	*z* (RT)	*z* (LT)	Occupancy (RT)	Occupancy (LT)	U_{eq}Å^2 (RT)	U_{eq}Å^2 (LT)
Cs ETS-4	Si1	0.337(2)	0.337(1)	0	0	0.230(2)	0.230(2)	1	1	0.0147(12)	0.0143(16)
Mg ETS-4		0.338(2)	0.338(1)	0	0	0.229(2)	0.230(2)	1	1	0.0144(6)	0.0090(7)
BaETS-4		0.337(2)	0.337(1)	0	0	0.228(2)	0.228(1)	1	1	0.0180(12)	0.0183(12)
Cs ETS-4	Si2	0.063(1)	0.064(1)	0.402(2)	0.406(1)	0.5	0.5	0.5	0.5	0.0139(19)	0.014(3)
Mg ETS-4		0.063(2)	0.063(1)	0.408(1)	0.407(1)	0.5	0.5	0.5	0.5	0.0161(11)	0.0113(11)
BaETS-4		0.064(1)	0.064(1)	0.410(2)	0.410(1)	0.5	0.457(2)	0.5	0.25	0.055(5)	0.018(5)
Cs ETS-4	Ti1	0.25	0.25	0.25	0.25	0.5	0.5	1	1	0.0197(12)	0.0159(16)
Mg ETS-4		0.25	0.25	0.25	0.25	0.5	0.5	1	1	0.0215(7)	0.0157(7)
BaETS-4		0.25	0.25	0.25	0.25	0.5	0.461(2)	1	0.5	0.0421(18)	0.0111(19)
Cs ETS-4	Ti2	0	0	0	0	0.450(3)	0.460(3)	0.25	0.25	0.037(9)	0.06(5)
Mg ETS-4		0	0	0	0	0.468(3)	0.5	0.25	0.5	0.014(4)	0.034(2)
BaETS-4		0	0	0	0	0.5	0.5	0.5	0.5	0.021(3)	0.023(2)
Cs ETS-4	O1	0.155(2)	0.155(2)	0.5	0.5	0	0	1	1	0.023(4)	0.020(5)
Mg ETS-4		0.154(2)	0.154(2)	0.5	0.5	0	0	1	1	0.032(3)	0.024(2)
BaETS-4	O11	0.125(2)	0.127(2)	0	0.5	0	0	0.34(4)	0.48(4)	0.007(8)	0.042(12)
	O12	0.187(1)	0.184(2)	0	0.5	0	0	0.32(4)	0.52(5)	0.007(8)	0.051(13)
	O13	0.343(2)	–	0.074(8)	–	0	–	0.17(2)		0.007(8)	
Cs ETS-4	O2	0.305(1)	0.305(1)	0.184(2)	0.181(2)	0.299(2)	0.299(2)	1	1	0.026(2)	0.025(3)
Mg ETS-4		0.306(2)	0.305(1)	0.186(2)	0.185(3)	0.297(2)	0.298(3)	1	1	0.0250(12)	0.0183(12)
BaETS-4		0.304(2)		0.180(1)		0.291(2)		1		0.11(2)	
	O21		0.310(2)		0.183(2)		0.350(3		0.44		0.013(5)
	O22		0.300(2)		0.177(2)		0.246(3)		0.56		0.022(5)
Cs ETS-4	O3	0.404(2)	0.405(2)	0	0	0.309(1)	0.309(1)	1	1	0.037(3)	0.036(5)
Mg ETS-4		0.404(1)	0.404(2)	0	0	0.313(2)	0.311(1)	1	1	0.0327(19)	0.0240(17)
BaETS-4		0.402(2)	0.403(2)	0	0	0.309(3)	0.313(3)	1	1	0.065(6)	0.064(5)
Cs ETS-4	O4	0	0	0.5	0.5	0.5	0.5	1	1	0.020(5)	0.016(6)
Mg ETS-4		0	0	0.5	0.5	0.5	0.5	1	1	0.018(3)	0.011(3)
BaETS-4		0	0	0.5	0.5	0.559(4)	0.44(1)	0.5	0.5	0.015(8)	0.010(5)
Cs ETS-4	O5	0.058(1)	0.059(2)	0.184(4)	0.192(4)	0.5	0.5	0.5	0.5	0.039(7)	0.036(9)
Mg ETS-4		0.059(2)	0.059(2)	0.184(2)	0.185(2)	0.5	0.5	0.5	0.5	0.054(5)	0.060(7)
BaETS-4		0.060(1)	0.059(1)	0.187(4)	0.186(3)	0.5	0.5	0.5	0.5	0.069(10)	0.064(8)
Cs ETS-4	O6	0.218(2)	0.220(1)	0	0	0.5	0.5	1	1	0.025(4)	0.016(4)
Mg ETS-4		0.220(2)	0.220(1)	0	0	0.5	0.5	1	1	0.0170(19)	0.0093(18)
BaETS-4		0.219(2)	0.219(2)	0	0	0.451(3)	0.452(2)	0.5	0.5	0.009(6)	0.007(4)
Cs ETS-4	O7	0	0	0	0	0.185(3)	0.186(2)	0.25	0.25	0.25(14)	0.04(2)
Mg ETS-4		0	0	0	0	0.218(3)	0.216(2)	0.25	0.25	0.032(10)	0.036(11)
BaETS-4		0	0	0	0	0.215(2)	0.218(3)	0.25	0.25	0.034(17)	0.039(16)

Table 3 (continued)

ETS sample		*x* (RT)	*x* (LT)	*y* (RT)	*y* (LT)	*z* (RT)	*z* (LT)	Occupancy (RT)	Occupancy (LT)	U_{eq}Å^2 (RT)	U_{eq}Å^2 (LT)
Cs ETS-4	Na	0.25	0.25	0.25?	0.25	0	0	0.30(4)	0.28(5)	0.031(5)	0.025(17)
Mg ETS-4	Mg	0.25	0.25	0.25	0.25	0	0	0.36(2)	0.38(2)	0.047(15)	0.033(6)
BaETS-4	–	–		–		–					
Cs ETS-4	K	0.128(1)	0.131(3)	0	0	0.328(6)	0.668(5)	0.14(1)	0.10(2)	0.060(16)	0.004(12)
Mg ETS-4	K	0.134(2)	0.133(6)	0	0	0.260(3)	0.266(3)	0.32(2)	0.35(2)	0.113(8)	0.109(8)
BaETS-4	Ba2	0.139(3)	0.138(1)	0	0	0.236(2)	0.237(1)	0.20(2)	0.21(1)	0.014(3)	0.017(3)
	Ba3	0.116(3)	0.116(1)	0	0	0.333(7)	0.340(5)	0.08(1)	0.07(1)	0.038(10)	0.028(7)
Cs ETS-4	Cs1	0	0	0.387(9)	0.440(4)	0	0	0.89(6)	0.15(9)	0.076(2)	0.05(7)
	Cs3		0		0.361(1)		0		0.22(14)		0.045(8)
Mg ETS-4	O21	0	0.009(4)	0.337(5)	0.338(5)	0	0.170(2)	0.80(7)	0.50(3)	0.173(19)	0.17(2)
BaETS-4	O21(RT)/	0		0.374(8)		0		0.49(2)		0.11(2)	
	O24(LT)		0		0.372(8)		0		0.69(8)		0.013(5)
Cs ETS-4	O22	0.086(5)	0.090(5)	0	0	0	0	0.43(4)	0.21(7)	0.13(6)	0.17(8)
Mg ETS-4		0.078(2)	0.084(2)	0.112(6)	0	0	0	0.23(5)	0.63(9)	0.17(4)	0.17(5)
BaETS-4											
Cs ETS-4	Cs2	0.190(2)	0.189(2)	0	0	0	0	0.51(2)	0.50(2)	0.0442(15)	0.0336(18)
Mg ETS-4	O23	0.206(2)	0.206(2)	0	0	0	0	0.86(6)	0.85(6)	0.127(14)	0.123(15)
BaETS-4	Ba1	0.200(1)	0.200(1)	0	0	0	0	0.50(2)	0.53(2)	0.0114(8)	0.0145(8)
Cs ETS-4	O21	0.094(1)	0.095(2)	0	0	0.466(4)	0.5	0.58(4)	1	0.044(9)	0.053(10)
BaETS-4	O23	0	0	0.173(5)	0.174(5)	0.272(6)	0.276(5)	0.23(4)	0.23(4)	0.008(14)	0.012(14)

Table 4. Framework interatomic distances (Å) for structure refinements at RT and LT

Bond length	Cs ETS-4 RT	Cs ETS-4 LT	Mg ETS-4 RT	Mg ETS-4 LT	Ba ETS – 4 RT	Ba ETS – 4 LT
Si1-O1	1.609(4)	1.605(6)	1.607(3)	1.605(3)	O11 1.761(19) O12 1.632(15) O13 1.63(2)	O11 1.725(16) O12 1.617(12)
Si1-O2 (x2)	1.605(8)	1.588(10)	1.603(5)	1.605(5)	1.555(10)	O21 1.669(15) O22 1.539(13)
Si1-O3	1.644(12)	1.648(16)	1.636(7)	1.626(7)	1.589(15)	1.603(14)
Si2-O3 (x2)	1.673(11)	1.652(15)	1.638(7)	1.648(7)	1.625(19)	1.84(2)
Si2-O4	1.640(9)	1.631(12)	1.620(5)	1.620(5)	1.660(11)	1.728(12)
Si2-O5	1.59(3)	1.54(3)	1.619(16)	1.598(15)	1.60(4)	1.63(3)
mean Si-O	1.63(1)	1.61(1)	1.62(1)	1.617	1.62(4)	1.66(8)
Ti1-O2 (x4)	1.952(8)	1.951(11)	1.961(5)	1.962(4)	1.949(12)	O21 1.651(14)(x2) O22 1.925(15)(x2)
Ti1-O6 (x2)	1.953(6)	1.932(7)	1.925(3)	1.924(3)	1.955(6)	1.930(5)
Ti2-O5 (x4)	1.94(3)	1.97(4)	1.927(15)	1.917(15)	1.93(4)	1.91(3)
Ti2-O7 (x2)	1.87(13)	1.9(2) 2.4(2)	1.74(4)	1.97(4)	O71 1.91(7) O23 1.97(4)	1.89(2)
mean Ti-O	1.93(1)	2.03(1)?	1.88(9)	1.94(3)	1.94(6)	1.86(1)

Extra-framework cations and water molecules positions at LT conditions

The extra-framework atoms positions remain almost unchanged at LT conditions for all of the studied samples. The LT structure refinements confirm a significant reduction of the thermal vibration effects of the extra-framework population, as shown by the magnitude of the thermal displacement ellipsoids at RT (290 K) and LT (150 K) in Table 3. Only in Cs-ETS-4 the Cs1 position splits into two ones – Cs1 and Cs3 thus allowing more isometric displacement ellipsoids to be obtained (Table 3).

CONCLUSIONS

The LT conditions enhance the structure contraction of Mg- and Cs-ETS-4, as the contraction potential of these structures is not fully realized during the ion exchange process. In Ba-ETS-4 the compression ability of the structure is manifested already upon the ion exchange procedure and the structure response to the LT conditions acts mainly through changing of the deformation direction. At 150 K the Cs- and Mg-ETS-4 structures remain less compressed than that one of the Ba-ETS-4.

The LT structure refinements confirm a significant reduction of the thermal vibration effects of the extra-framework population.

The flexibility of the ETS-4 framework is most pronounced for the titano-silicate bridging unit including the $T2O_5$ and $Si2O_4$ polyhedra. Both ion exchange and temperature lowering shift the Ti2 atom to a position closer to or placed on the mirror plane, giving evidence that the position of the Ti2 atom with respect to the mirror plane does not define explicitly its coordination.

REFERENCES

1. S. M. Kuznicki, U.S. *Patent* 4 938 939 (1990).
2. D. M. Chapman, A. L. Roe, *Zeolites*, **10**, 730 (1990).
3. A. Merkov, I. Bussen, E. Goiko, E. Kulchiczka, J. Menshikov, A. Nedorezova, *Zapiski Vses. Mineralog. Obshch*., **54**, 9 (1973).
4. P. A. Sandomirski, N. V. Belov, *Sov. Phys. Crystallogr*., **24**, 686 (1979).
5. G. Cruciani, P. D. Luca, A. Nastro, P. Pattison, *Micropor. Mesopor. Mater*., **21**, 143 (1998).
6. C. Braunbarth, H. W. Hillhouse, S. Nair, M. Tsapatsis, A. Burton, R. F. Lobo, R. M. Jabubinas, S. M. Kuznicki, *Chem. Mater*., **12**, 1857 (2000).
7. S. Nair, H. K. Jeong, A. Chandrasekaran, C. M. Braunbarth, M. Tsapatsis, S. M. Kuznicki, *Chem. Mater.*, **13**, 4247 (2001).
8. R. P. Nikolova, B. L. Shivachev, S. Ferdov, *Micropor. Mesopor. Mater.*, **165**, 121 (2013).
9. Agilent. CrysAlis PRO (version 1.171.35.15). Agilent Technologies Ltd, Yarnton England, 2010.
10. G. M. Sheldrick, *Acta. Cryst.*, A, **64**, 112 (2008).
11. G. D. Gatta, P. Lotti, *Micropor. Mesopor. Mater*., **143**, 467 (2011).
12. G. D. Gatta, P. Cappelletti, N. Rotiroti, C. Slebodnick, R. Rinaldi, *Am. Mineral*., 94, 190 (2009).

КРИСТАЛНИ СТРУКТУРИ НА Cs^+, Mg^{2+}, Ba^{2+} ЙОННО ОБМЕНЕНИ ОБРАЗЦИ НА ETS-4 ПРИ СТАЙНА (290 K) И НИСКА ТЕМПЕРАТУРА (150 K)

Л. Цветанова[1]*, Л. Димова[1], С. Фердов[2], Р. Николова[1]

[1] Институт по минералогия и кристалография, Българска академия на науките, София, 1113, България
[2] Department of Physics, University of Minho, 4800-058 Guimarães, Portugal

Постъпила февруари, 2013 г.; приета май, 2013 г.

(Резюме)

Обменени с Cs^+, Mg^{2+}, and Ba^{2+} катиони образци от титано-силиката ETS-4 са изследвани чрез монокристален рентгеноструктурен анализ при температура от 150 K. Получените структурни данни са сравнени с тези от рентгеноструктурния анализ на същите образци при стайна температура 290 K. Получените резултати потвърждават, че нискотемпературните изследвания позволяват прецизно уточняване на атомните параметри и минимизиране на ефекта на температурните трептения и позиционната неподреденост на атомите.

Bulgarian Chemical Communications, Volume 45, Number 4 (pp. 530–535) 2013

Investigation of newly synthesized biocompatible materials as biofilm carriers

D. Marinkova[1]*, L. Yotova[1], D. Danalev[1], D. Stoykov[1], J.-M. Ringeard[2], M. Michiel[2], S. Serfaty[2], P. Griesmar[2]

[1] *Department of Biotechnology, University of Chemical Technology and Metallurgy, 8 Kl. Ohridski blvd, 1756 Sofia, Bulgaria*
[2] *Université de Cergy-Pontoise, ENS, UMR CNRS 8029, Systèmes et applications des technologies de l'information et de l'énergie (SATIE), F-95000 Cergy-Pontoise, France*

Received February, 2013; Revised May, 2013

The biodegradation of aniline is of a great concern and has attracted many researchers' attention. Because of its toxic and recalcitrant nature as well as the wide application of aniline containing chemicals, aniline is considered to be an increasing threat both to the environment and to human health.

Microbial transformation and degradation are major mechanisms to eliminate aniline from the environment. Most of the microorganisms found in the nature, industrial and clinical environments are attached to a surface.

The aim of this study is to synthesize new hybrid biocompatible materials, to investigate the obtained matrices for their ability to hold biofilm formation.

It was report about comparison of the formation of biofilms from model gram-negative bacteria *Pseudomonas species 1625* onto different, newly synthesized hybrid carriers. Some kinetic investigations on aniline biodegradation applying obtained biofilms are also discussed.

Key words: biodegradation, aniline, biofilms, carrier.

INTRODUCTION

Aniline is a widely distributed environmental pollutant resulting from the manufacture of dye materials [1] and agricultural chemicals such as herbicides [2]. Because of its toxic and recalcitrant nature and the wide application of aniline containing chemicals, aniline is considered to be an increasing threat both to the environment and to human health. Thus, the fate of aniline in the environments is a great concern. Microbial transformation and degradation are major mechanisms to eliminate aniline from the environment.

Most of the microorganisms found in the nature, industrial and clinical environments are attached to a surface. Separated cells attached to the same surface can "communicate", and thus form a complex structure known as biofilm. Biofilms are complex communities of microorganisms attached to any surface or associated with interfaces. They could be successfully used in a process of bioremediation. This is an innovation technology, which controls the pollutants using biological systems for degradation or biotransformation of different toxic compounds. Taking in consideration the efficiency of the bioremediation by means of different microbial strains the aim of this study is to investigate the creation and application of biofilms for wastewater treatment.

The biodegradation of aniline is of a great concern and has been attracted many researchers' attention. Up to date, it is well recognized that aniline can be efficiently removed by aerobic biological treatment [3–5], and many aniline-biodegradation bacteria such as *Pseudomonas sp*. [6]. Microbial transformation and degradation are major mechanisms to eliminate aniline from the environment. Bacterial species of *Pseudomonas* [7–9], *Rhodococcus* [10], *Frateuria* [11], *Moraxella* [12] and *Nocardia* [13] have been shown to be able of aniline and its derivatives degradation.

Some recent investigations show that the isolated strain, PN1001, a member of the *Pseudomonas species* is capable to do degradation of 93% and 89% of pentylamine and aniline, respectively. Additionally, authors revealed that aniline being

* To whom all correspondence should be sent:
E-mail: dmarinkova@yahoo.com

more toxic demonstrates a more complex degradation pathway [14].

The aim of this study is to synthesize new hybrid biocompatible materials, to investigate the obtained matrices for their ability to hold biofilm formation as well as to synthesize and characterize new three-dimensional co-networks based on pure organic N–acryloylglycine. Additionally herein, we report about comparison of the formation of biofilms from model gram-negative bacteria *Pseudomonas species 1625* onto different, newly synthesized hybrid carriers. Some kinetic investigations on aniline biodegradation applying obtained biofilms are also discussed.

EXPERIMENTS AND EQUIPMENT

Reagents

2,2'-azobis(2-methyl proponitrile) (AIBN) and glycine were provided by Acros Organics. Poly (ethylene glycol) dimethacrylate (PEGDM 550, Mw = 550 g/mol) N,N'-methylenebisacrylamide (BIS), N, N-dimethylacetamide (DMAc) and acryloylchloride were purchased by Sigma-Aldrich. All products were used without any further purification. *Pseudomonas species 1625* microbial strain was purchased by the National collection for industrial and cell cultures (NBIMCC) of Bulgaria. Salts for nutrient medium were obtained from Merck (Germany). Glucose and bovine serum albumin were obtained from Fluka (Switzerland). All other chemicals were of reagent grade or better.

Cell culture

Pseudomonas species 1625 were growth on solid agar medium for 24 hours at 28 °C. Further colonies were picked up and suspended in liquid nutrient medium at pH 7.0 (14 g/L yeast extract; 15 g/L potassium aspartate; 8 g/L KNO_3; 0.025 g/L $MnSO_4$; 0.060 g/L $FeCl_3.6H_2O$; 0.025 g/L $(NH_4)_6MoO_{24}.4H_2O$) supplemented with 10% glucose. After incubation for 24 h in bath shaker at 28 °C, pH 7.0, the cells were suspended in the same nutrient medium containing different concentration of aniline under the same conditions.

Carriers for biofilm formation

The following three different polymeric matrices were used for biofilm formation during the experiments:

Ti based matrices were synthesized by incorporation of organic polymer (cellulose acetate butyrate (CAB)) and copolymer of polyacrylonitril and acrylamide (Poly (AN-co-AA)) to inorganic network according to [15]. The other two types of polymer membranes are based on N–acryloylglycine (NAGly) – poly (N-acryloylglycine) (PNAGly).

Preparation of NAGly

NAGly was prepared by adapted method of Bentolila et al. [16]. It was synthesized by a Schotten-Baumann reaction in aqueous phase as following: 4.50 g of glycine (60 mmol) were dissolved in 60 mL of 2M solution of potassium hydroxide. The mixture was cooled at 0ºC with a water ice bath for about 10 minutes. 6 mL of acryloyl chloride (73.6 mmol) were added to the mixture drop wise using a dropping funnel. At the end of the reaction (TLC monitoring) the solution was washed with 2×40 ml of diethyl ether and the separated aqueous phase was acidified to pH = 2. The aim product was extracted with 3×40ml ethyl acetate. After drying the organic phase over $MgSO_4$, the residue was concentrated with a rotary evaporator.

Preparation of membrane based on PNAGly

Two different types of membranes were synthesized according to the methodology described above. The overall composition of the networks was varied from 90 to 10 w% of each compound. All investigated co-networks were reported as PNAGly/PEGDM (x/y) or PNAGly/BIS (x/y). The numbers between brackets (x/y) correspond to the PNAGly and cross linker weight proportions, respectively. For example, a co-network obtained from a mixture of 450 mg of NAGly and 50 mg PEGDM was noted PNAGly/PEGDM (90/10). The mixture was stirred and degassed to remove all traces of oxygen (radical inhibitor). Finally, 25 mg of AIBN were added at the last moment to avoid the rapid decomposition of the initiator. The contents of the flask was taken with a pipette and placed between two glass plates separated by a Teflon film and held together by a clamp system to ensure the sealing of the experimental device. The device was placed in an oven and treated according to the following thermal program: 2.5 h at 60 °C to complete polymerization and then one hour at 120 °C to achieve a post-curing. After polymerization, the crosslinked polymer was detached from the device and vacuum dried at 60 °C.

Formation of biofilm

The obtained matrices were placed in the cell suspension with nutrient medium and the biofilms were formed by cell adhesion. The binding of cells was carried out at pH 7 and temperature 28 °C under continuous stirring in bath shaker (220rpm).

Biofilm formation was studied at 24, 48, 72, 96 and 120 h. Every 24 h the matrixes were washed up by physiological solution and suspended in the fresh nutrient medium.

Methods

Biochemical analyses

The absorbance of the biomass of free cells and this produced by biofilms was measured at 590 nm with a Perkin-Elmer Lambda 2 spectrophotometer (Germany). The renovation of the biofilm was monitored microscopically as well as by means of the turbidity (OD-590) of the effluent. Cell growth of suspended and immobilized cells was also determined as dry cell weight, according to the method described by Mallette [17]. All samples were dried till they reached a constant weight at 105 °C.

The extracellular protein content attach to the matrixes was measured using a modified Lowry method, [18] as described by Raunkjaer et al [19]. The exopolysaccharide content was measured using the anthrone method modified by Raunkjaer et al. [18] to eliminate the effect of a non anthrone-specific color development.

Gas chromatography analysis

In order to detect the biodegradation of aniline by free cells and biofilms from *Pseudomonas species 1625*, samples of 1 ml were taken at a specified hour and were submitted for testing at the Department of Biotechnology, UCTM, Bulgaria using a Shimadzu gas chromatograph GC-2010 with flame ionization detector (FID) and Rtx-5 column. The following temperature gradient was used. Starting with isocratic temperature of 120 °C for 8 min and then increasing to 220 °C with 10/min step. The temperatures of the injector and detector were 305 °C. The carrier gas was helium at 1.7 mL/min.

RESULTS AND DISCUSSION

Initially, we started with investigation of biochemical properties of formed biofilms onto newly synthesized hybrid membranes. The dynamic of proteins and extracellular polysaccharides production by biofilms were studied.

Dynamics of extracellular proteins production from biofilms of Pseudomonas species 1625 formed onto different polymer matrices

After the culture was developed and a biomass was accumulated, polymer carriers were added to the cell suspension for biofilms formation. The kinetic of proteins and polysaccharides produced by biofilms formed on two different types of polymer carriers for 120 hours was tracked and the 24th hour was assumed as initial period for the incubation. The quantity of proteins synthesized from biofilms of *Pseudomonas species 1625* on different types of matrices is shown on Figure 1.

The figure shows that a larger quantity of proteins is produced from biofilms formed on PNAGly/PEGDM matrix. A gradient increase of the quantity of the produced proteins was observed until the 72nd hour of incubation onto two types of biofilms. Further the protein concentration followed by a significant rise to the 96th hour into biofilm formed onto PNAGly/PEGDM matrix. The production again became gradient, reaching 106.87 mg.g^{-1} at the 120th hour.

The concentration of proteins from biofilm formed on a matrix PNAGly/BIS increased proportionally to the incubation time of maturing.

The figure also reveals that considering the produced proteins, the polymer matrix based on PNAGly/PEGDM is a better carrier for biofilm formation.

Dynamics of extracellular polysaccharides production from biofilms of Pseudomonas species 1625 formed onto different polymer matrices

Kinetics of polysaccharide production from the formed biofilms is presented on Figure 2. The figure shows that the quantity of polysaccharides produced from biofilms formed on a matrix of

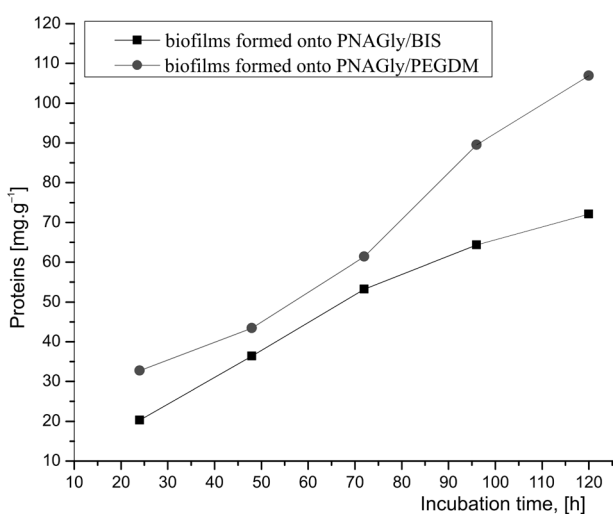

Fig. 1. Kinetic of proteins production from biofilms formed on PNAGly/BIS and PNAGly/PEGDM matrices

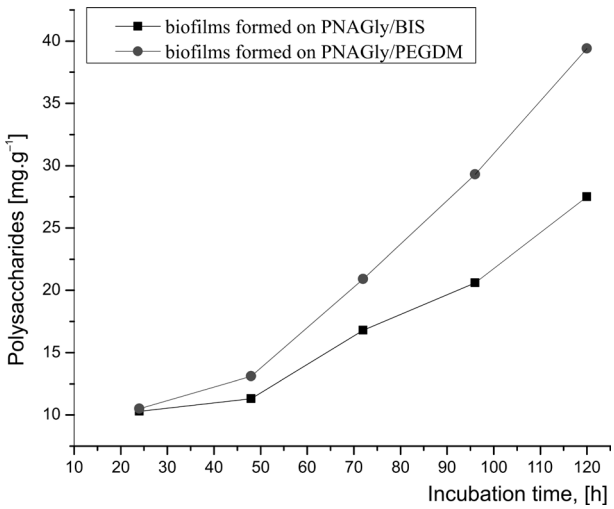

Fig. 2. Kinetics of the polysaccharides production from biofilms formed on PNAGly/BIS matrix and PNAGly/PEGDM matrix

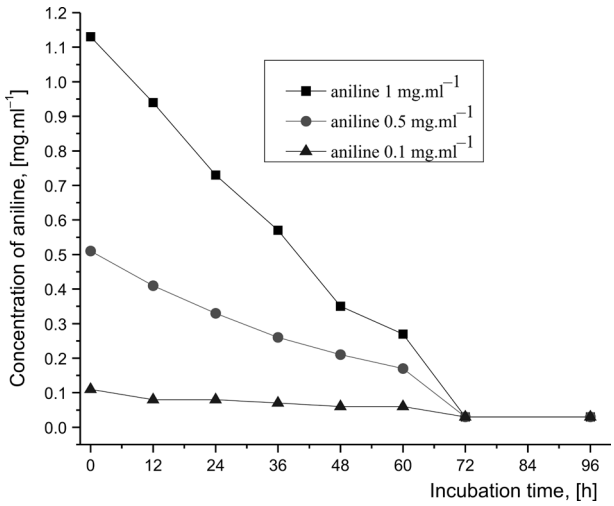

Fig. 3. Dynamics of the aniline degradation by free cells of *Pseudomonas species 1625*

PNAGly/PEGDM is larger. It can be clearly observe that until 48 h of incubation time polysaccharides production of biofilm formed onto PNAGly/BIS membrane is keeping proportional to the incubation time, after that slightly increasing. After 48 h increasing of polysaccharides producing occurring to both biofilms but it is more expressive to biofilm formed onto matrix of PNAGly/PEGDM. The peak about 40 mg.g^{-1} is at 120th hour.

Comparing the proteins and polysaccharides production from biofilms on the two types of carriers we could conclude that the most appropriate matrix for biofilm formation is PNAGly/PEGDM.

Dynamics of the model wastewater purification process of biodegradation of aniline from biofilms formed onto three different types of matrices

In the present study the dynamics of aniline degradation from biofilms formed onto different types of carriers was also investigated. Our study starts with tracking of aniline degradation by free cells of *Pseudomonas species 1625*. Single nutrient source aniline in different concentrations: 0.1 mg.ml^{-1}, 0.5 mg.ml^{-1} and 1 mg.ml^{-1} were used. Samples were taken at every 6 h and they were monitored by gas chromatography.

The results for dynamics of degradation are shown on Figure 3.

Figure 3 shows that decreasing of the concentration of substrate is the best using as an initial concentration 0.5 mg.ml^{-1} and 1 mg.ml^{-1} of aniline. Degradation is proportional to incubation time and after 72 h the aniline is completely biotransformed. Concerning the lowest initial concentration of aniline it is observed a detention and slightly decreasing after 60 h.

On the ground of experimental results mentioned above in this study it was followed biodegradation of aniline by biofilms formed onto three different types of carriers in the initial concentration of 1 mg.ml^{-1}.

On Figure 4 is presented dinamics of aniline degradation by biofilms formed from *Pseudomonas species 1625*.

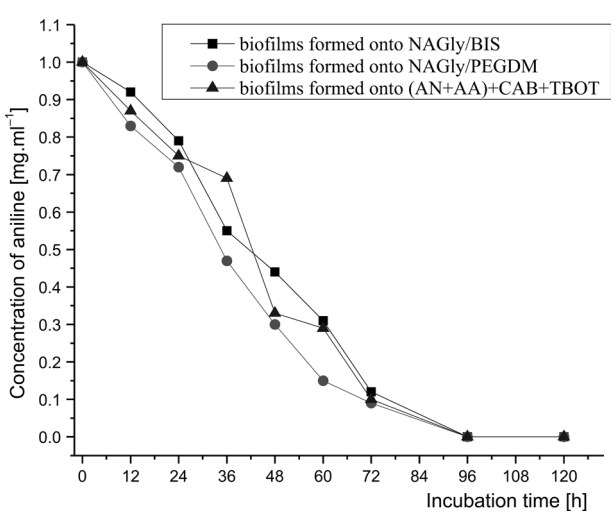

Fig. 4. Dynamics of the aniline degradation in initial concentration of 1 mg.ml^{-1} by biofilms of *Pseudomonas species 1625* formed onto different types of carriers

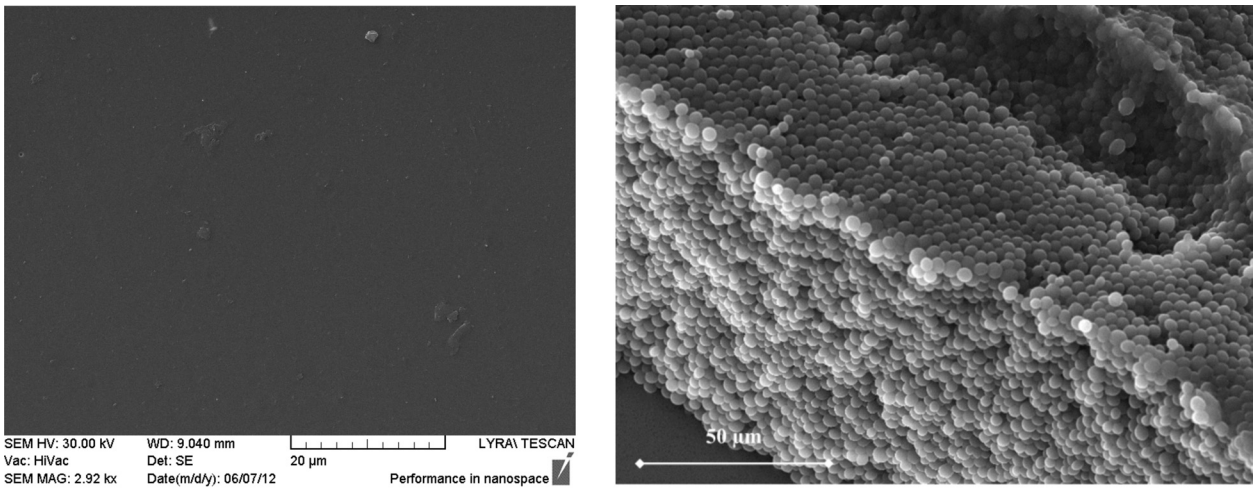

Fig. 5. SEM images of the surfaces of PNAGly/PEGDM sample without (a) and with (b) cells of *Pseudomonas species 1625*

Figure 4 reveals that the application of biofilms is preferable to free cells as it is clearly observed that they are more capable of substrate degradation at initial concentration of 1 mg.ml^{-1}. In addition, it was showed that all three biofilms do completely degradation of aniline after 96 h of incubation time.

In the biofilm formed onto polymer carrier based on (AN+AA)+CAB+TBOT the depletion of aniline is characetrisized with a slightly detention between 24 and 60 h. For biofilms formed onto new hybrid polymer matricies based on PNAGly/BIS and PNAGly/PEGDM is observed that aniline degradation is proportional of the incubation time. From the experimental results is shown that the aniline degradation of biofilm formed onto matrix of PNAGLy/PEGDM is the best expressed.

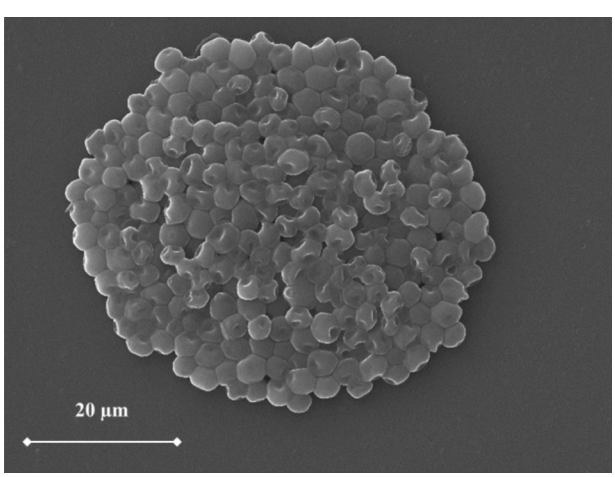

Fig. 6. SEM images of the biofilms formed onto surfaces of PNAGly/BIS

Structure and stability of biofilms

The structure of obtained biofilms was visualized by electronic microscopy. Some of the results are shown in Figure 5 and 6.

SEM images show that *Pseudomonas species 1625* cells are formed a biofilm onto both matrices. But the microscopic analysis clearly presents that the biofilm is thicker onto matrix based on PNAGly/PEGDM.

CONCLUSION

Our study reveals that it is possible to preserve the biological integrity of a living organism (*Pseudomonas species*) in newly obtained matrices. Additionally, the obtained results show that the most appropriate carrier for biofilm formation from the cells of *Pseudomonas species 1625* is the matrix based on NAGly/PEGDM. Finally our results reveal that the matrix obtained by PNAGly/PEGDM is the best according to biofilm formation and aniline biodegradation.

Acknowledgments: *This study was supported by "National Found Scientific Research", project DUNK 01/03, 2010.*

REFERENCES

1. U. Meyer, J (eds), Microbial degradation of xenobiotics and recalcitrant compounds, Academic, London, 1981.
2. P. C. Kearney, D. D Kaufmann, Herbicides: chemistry, degradation and mode of action, 2nd edn, Marcel Dekker, New York SI, 1975.

3. M. Takeo, T. Fujii, K. Y. Takenaka, *Journal of Fermentation and Bioengineering*, **85**(5), (1998).
4. T. Zhang, J. L. Zhang, S. J. Liu, Z. P. Liu, *Journal of Environmental Sciences*, **20** (6), (2008).
5. C. B. Xiao, J. Ning, H. Yan, X. D. Sun, J. Y. Hu, *Chinese Journal of Chemical Engineering*, **17**, (2009).
6. J. G. Anson, G. Mackinnon, *Applied and Environmental Microbiology*, **48**, (1984).
7. C. Hinteregger, M. Loidl, F. Streichsbier, *Microbiology Letters*, **97**, (1992).
8. R. E. Parales, T. A. Ontl, D. T. Gibson, *J. Ind. Microbiol. Biotechnol.*, **19**, (1997).
9. S. I. Kim, S. H. Leem, J. S. Choi, Y. H. Chung, S. Kim, Y. M. Park, Y. N. Lee, K. S. Ha, *J. Bacteriol.*, **179**, (1997).
10. K. Aoki, K. Ohtsuka, R. Shinke, H. Nishira, *Agric. Biol. Chem.*, **47**, (1983).
11. S. Murakumi, A. Takashima, J. Takemoto, S. Takenaka, R. Shinke, K. Aoki, *Gene*, 1999.
12. J. Zeyer, A. Wasserfallen, K. N. Timmis, *Appl. Environ. Microbiol.*, **50**, (1985).
13. R. Bachofer, F. Lingens, W. Schafer, FEBS Lett, **50**, (1975).
14. Li. Wang, S. Barrington, Jin-Woo Kim, *Journal of Environmental Management*, **83**, (2007).
15. L. Yotova, I. Ivanov, *Appl. Biochem. Biotechnol.*, **87**, (2000).
16. A. Bentolila, I. Vlodavsky, C. Haloun, A. Domb, *J. Polym. Adv. Technol.*, **11**, (2000).
17. M. Mallette, T. R. Noris, D. W. Robinsons, *Methods in Microbiology*, vol. 1 ed, Academic Press, London, New York, 1969.
18. O. H. Lowry, N. L. Rosenbrough, A. L Farr, R. J. Randall, *J. Biol. Chem*., **193**, (1951).
19. K. T. Raunkjær, Jacobsen Hvitved, P. H. Nielsen, *Water Res.*, 1994.

ИЗСЛЕДВАНИЯ ВЪРХУ НОВОСИНТЕЗИРАНИ БИОСЪВМЕСТИМИ МАТЕРИАЛИ КАТО НОСИТЕЛИ ЗА БИОФИЛМИ

Д. Маринкова[1]*, Л. Йотова[1], Д. Даналев[1], Д. Стойков[1], Ж. Ринджерард[2], М. Мишел[2], С. Серфати[2], П. Гриесмар[2]

[1] Катедра Биотехнология, Химикотехнологичен и Металургичен Университет, бул. „Кл. Охридски“ 8, 1756 София, България
[2] Университет на Сержи Понтоаз, ENS, UMR CNRS 8029, SATIE, F-95000, Сержи Понтоаз, Париж, Франция

Постъпила февруари, 2013 г.; приета май, 2013 г.

(Резюме)

Биоразграждането на анилина е проблем от голямо значение и привлича вниманието на много изследователи. Съдържанието на анилин в околната среда е заплаха за човешкото здраве, което налага разкриване на нови методи за пречистване. Изследователи докладват за редица случаи на микробна трансформация за разграждане на това токсично съединение. Повечето от микроорганизмите в природата в промишлени и клинични среди са прикрепени към дадена повърхност. Целта на това изследване е да се синтезират нови хибридни биосъвместими материали и да се проучи възможността на получените матрици като носители за формиране на биофилми. В настоящото проучване е разгледано сравнението на биофилми, формирани върху различни матрици от клетки на грам положителните бактерии *Pseudomonas species 1625*, както и възможността на биофилмите да бъдат приложени в процесите на биоразграждане на анилин.

Bulgarian Chemical Communications, Volume 45, Number 4 (pp. 536–542) 2013

Study of zinc borophosphate compositions doped with samarium and manganese

G. I. Patronov*, I. P. Kostova, D. T. Tonchev

Dept. Chem. Technology, Plovdiv University "Paisii Hilendarski", 4000 Plovdiv, Bulgaria

Received February, 2013; Revised May, 2013

Synthesis and characterisation studies of samarium and manganese doped ZnO-rich borophosphate material of composition 0.5M – 71.8ZnO – yP_2O_5 – (27.7 – y)B_2O_3 where: M = Sm_2O_3 or MnO, y = 9.7, 13.85, 18 mol% were presented. The compositions were prepared by a typical high-temperature ceramic syntheses where ZnO, $NH_4H_2PO_4$, H_3BO_3 and Sm_2O_3 (or MnO) of pre-determined ratios were powdered, mixed and placed in alumina crucibles. The synthesis was performed at 950 °C for 3 hours in a muffle furnace. Samples were quenched out of the melt to room temperatures and after that annealed at 250 °C for 2 hours.

Samarium and manganese doped ZnO-rich zinc borophosphate compositions were investigated by powder X-ray diffraction, differential scanning calorimetry, temperature – modulated differential scanning calorimetry, Raman spectra analysis and photoluminescence spectroscopy. The results obtained show that the samples are predominantly amorphous, with the presence of crystalline structure in some of them. The main crystalline phases are zinc borate phosphate $Zn_3(BO_3)(PO_4)$ and zinc borate α-$Zn_5B_4O_{11}$. While samarium doped samples exhibit strong visible (orange to red) immediate photoluminescence (scintillation) signal under UV light, manganese doped samples do not exhibit visible scintillation signal.

Key words: doped zinc borophosphates, samarium, manganese, crystal structure.

INTRODUCTION

Compositions based on ZnO and P_2O_5 are both scientifically and technologically important materials because of their interesting characteristics. Having in view that the addition of rare earth and transition metal ions to such materials usually induces significant changes in their optical, electrical and magnetic behaviour, opening thus opportunities in the finding of new applications, careful structural investigations of compositions containing rare earth and transition metal ions become necessary [1–5].

In this work we present synthesis and characterisation studies of samarium and manganese doped ZnO-rich borophosphate material of composition 0.5M – 71.8ZnO – yP_2O_5 – (27.7 – y)B_2O_3 where: M = Sm_2O_3 or MnO, y = 9.7 mol%, 13.85 mol%, 18 mol%.

Samarium and manganese doped ZnO-rich borophosphate compositions were investigated by powder X-ray diffraction, differential scanning calorimetry (DSC), temperature – modulated DSC (TMDSC), Raman spectra analysis and photoluminescence spectroscopy.

EXPERIMENTAL

Sample preparation

All samples were prepared by high-temperature ceramic methods using ZnO, $NH_4H_2PO_4$, H_3BO_3 and Sm_2O_3 (or MnO) as starting materials. The reagents were thoroughly mixed, placed in alumina crucibles and heated at 950 °C for 3 hours in a muffle furnace. The obtained homogeneous melts were then poured onto a graphite plate and by manual pressing have reached a suitable thickness (1–2 mm). Then the samples were annealed at 250 °C for two hours. Synthesized compositions are homogeneous, not hygroscopic and transparent glass. They are easily reproducible. List of the samples is presented in Table 1.

* To whom all correspondence should be sent:
E-mail: patron@uni-plovdiv.bg

Table 1. List of the non-doped and Sm or Mn doped zinc borophosphate samples

Sample, №	Composition				
	ZnO, mol%	B_2O_3, mol%	P_2O_5, mol%	Sm_2O_3, mol%	MnO, mol%
1	72.31	9.69	18.00	–	–
2	72.31	13.84	13.85	–	–
3	72.31	18.00	9.69	–	–
4	71.81	9.69	18.00	0.50	–
5	71.81	13.84	13.85	0.50	–
6	71.81	18.00	9.69	0.50	–
7	71.81	9.69	18.00	–	0.50
8	71.81	13.84	13.85	–	0.50
9	71.81	18.00	9.69	–	0.50

Density measurements

Density measurements were carried out according to the Archimedes method using deionised water of density 1 gm cm^{-3} as an immersion liquid.

Powder X-ray diffraction analysis

Powder X-ray diffraction data were collected on Bruker diffractometer operating with a Cu –Kα radiation source (λ = 1.5406 nm), in steps of 0.02° over the range of 10–80° 2θ, with a time per step of 2.8 s. The crystalline phases were identified using the powder diffraction files PDF 19-1455 and PDF 86-2017 from database JCPDS – International Centre for Diffraction Data PCPDFWIN v.2.2 (2001) [6–8].

Raman spectroscopy analysis

The Raman studies were conducted using the 1064 nm Nd:YAG laser line at a power of 700 mW and a RAM II spectrometer (Bruker Optics) having a resolution of 2 cm^{-1}.

Differential Scanning Calorimetric and Temperature Modulated DSC analysis

DSC and TMDSC measurements were performed using TA Instruments DSC Q100 and DSC 2910 with attached Fast Air Cooling System (FACS) and Refrigerating Cooling System (RCS). The samples (20–22 mg) were placed in aluminium hermetic pans. A heating rate of 10 K/min was used.

Photoluminescence measurements

The photoluminescence spectra were measured by optical CCD Avantes spectrometer Avaspec 2048, operating at 25 MW in the range 250–1100 nm at room temperature. As a light source was used 450 nm wavelength laser diode.

RESULTS AND DISCUSSION

Density measurements

The data obtained from density measurements of the samples are presented in Table 2. There are some variations in the density as a function of the B_2O_3 content. Addition of B_2O_3 in zinc phosphate glasses causes an increase in oxygen-packing density that may squeeze the structure of the sample. This may be due to the replacement of an equal amount of low bond strength glass former P_2O_5 with B_2O_3, which has high bond strength [9]. Moreover, the doped agents (Sm_2O_3 or MnO) act as a glass modifier, which increases the fraction of non-bridging oxygen atoms and leads to increased porosity and reduced density of the glass.

Table 2. Density of the non-doped and Sm or Mn doped zinc borophosphate samples

Undoped samples			Samples doped with Sm			Samples doped with Mn		
Sample, №	B_2O_3, mol%	Density (ρ), gm cm^{-3}	Sample, №	B_2O_3, mol%	Density (ρ), gm cm^{-3}	Sample, №	B_2O_3, mol%	Density (ρ), gm cm^{-3}
1	9.69	2.035	4	9.69	1.861	7	9.69	1.842
2	13.84	2.157	5	13.84	1.887	8	13.84	1.916
3	18.00	2.023	6	18.00	1.888	9	18.00	1.961

Powder X-ray diffraction data

The results obtained show that the samples are predominantly amorphous, with the presence of crystalline structure in some of them (Fig. 1). The main crystalline phases are zinc borate phosphate $Zn_3(BO_3)(PO_4)$ and zinc borate α-$Zn_5B_4O_{11}$ (Fig. 2). The appearance of borate and phosphate in the crystallization products shows the important role of PO_4 and BO_4 structural units in the structural network of borophosphate glasses. It is possible to suggest based on other authors' studies that these borophosphate glasses contain B–O–P linkages within their structural network [2, 10].

Raman spectroscopy data

Raman spectra of the glass samples are presented in Fig. 3. They contain a vibrational band at 968 cm^{-1} ascribed to the vibrations of isolated PO_4 units in the

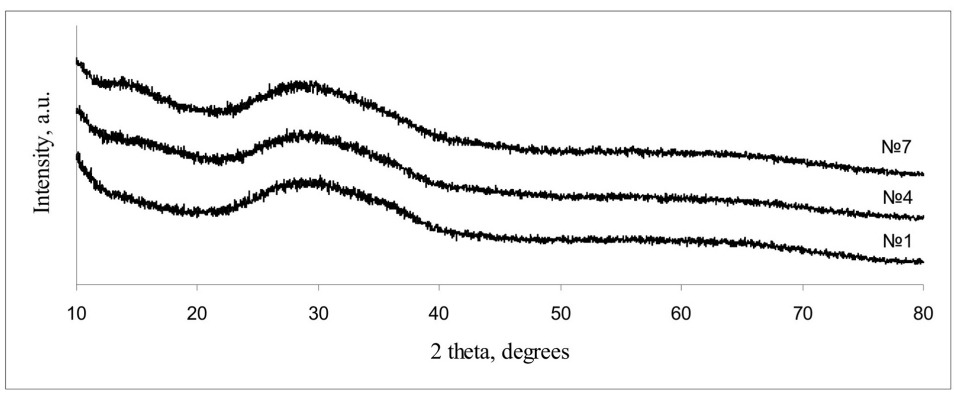

a. Powder X-ray diffraction patterns for samples № 1, 4, 7 (B_2O_3:P_2O_5=1:2)

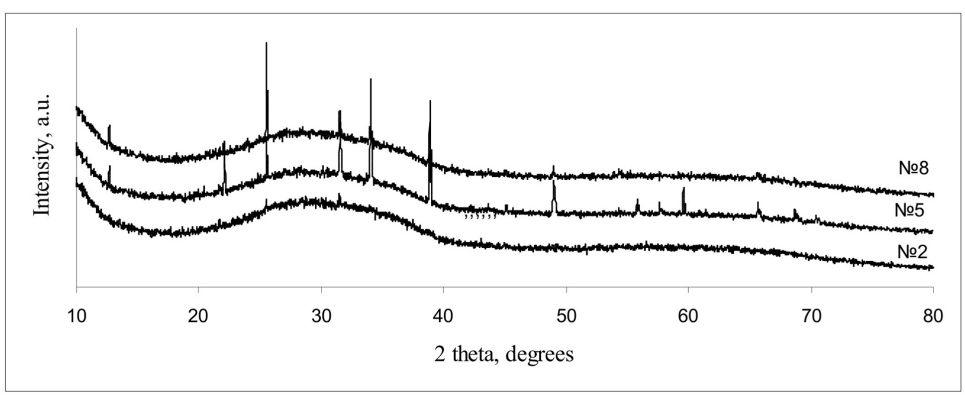

b. Powder X-ray diffraction patterns for samples № 2, 5, 8 (B_2O_3:P_2O_5=1:1)

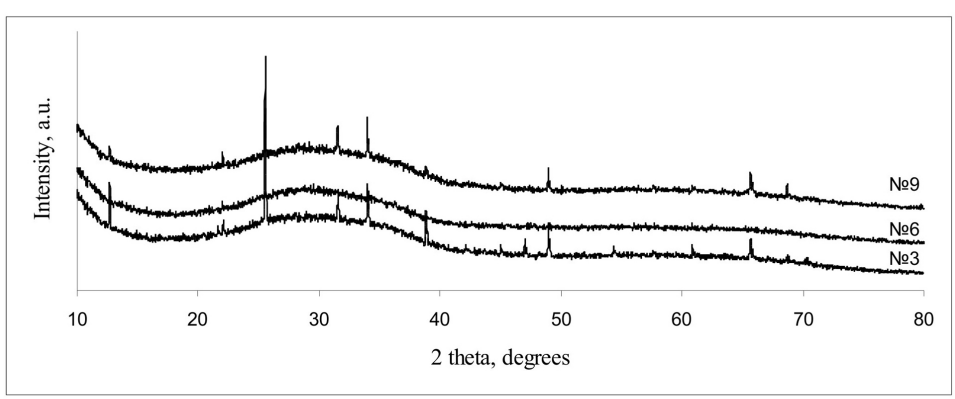

c. Powder X-ray diffraction patterns for samples № 3, 6, 9 (B_2O_3:P_2O_5=2:1)

Fig. 1. Powder X-ray diffraction patterns for synthesized samples

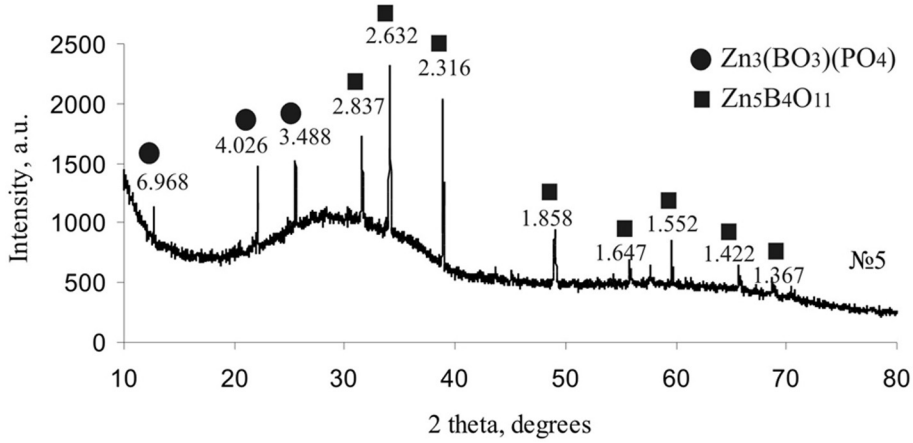

Fig. 2. Powder X-ray diffraction pattern for sample № 5

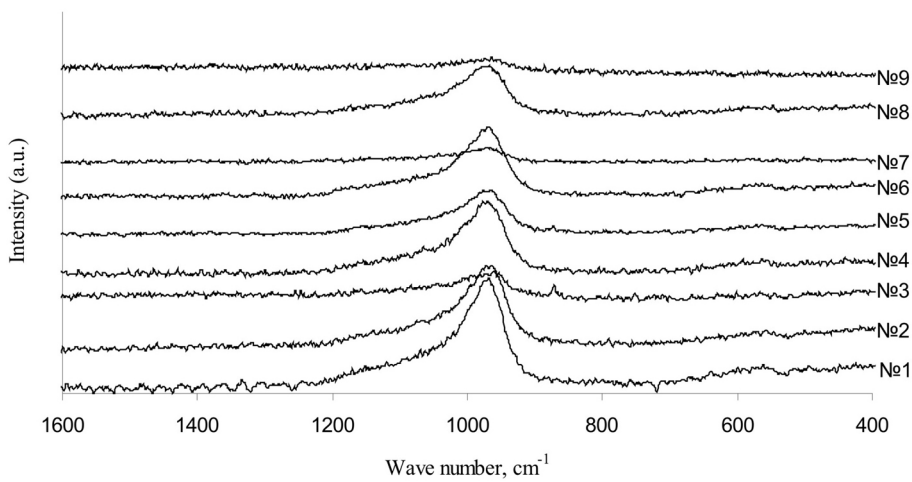

Fig. 3. Raman spectra of the glass samples

structural network of borophosphate glasses at the B_2O_3 – rich side [2].

Differential Scanning Calorimetric and Temperature Modulated DSC data

Figure 4 reveals typical examples of scanning with DSC and TMDSC. Figure 5 presents the dependence of the glass transition temperature obtained by DSC and TMDSC versus the content of B_2O_3. Increasing the content of B_2O_3 is associated with increased glass transition point, indicating a higher stability of the glass.

Values of the glass transition temperature for the same composition as measured by the heat flow (DSC) and the specific heat (TMDSC) differ minimally as shown in Fig. 5. The difference due to the fact that these values characterize the different areas of the same viscosity curve at Tg for the glassy material according to previous studies [11].

Photoluminescence measurements

Representative emission spectra for synthesized samples are illustrated in Figure 6. All of Sm-doped samples display photoluminescence in contrast to undoped samples and those with manganese. Typical photoluminescence of Sm^{3+} ions is observed with three emission bands corresponding to transitions:

564 nm – $^4G_{5/2} \rightarrow {}^6H_{5/2}$
600 nm – $^4G_{5/2} \rightarrow {}^6H_{7/2}$
645 nm – $^4G_{5/2} \rightarrow {}^6H_{9/2}$

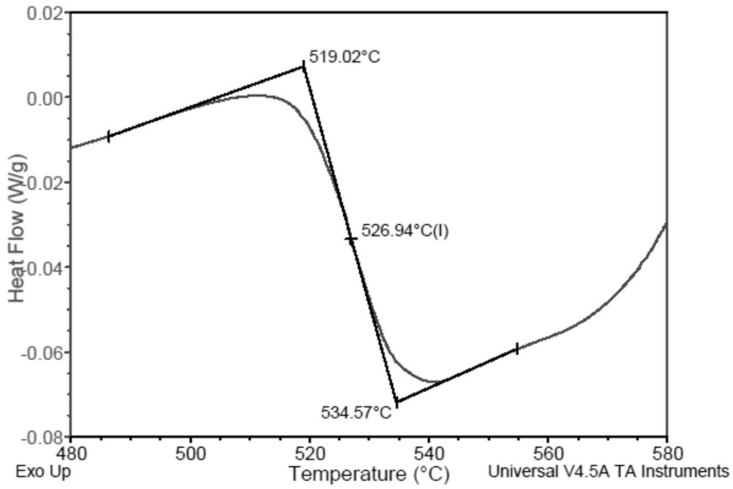

a) DSC data

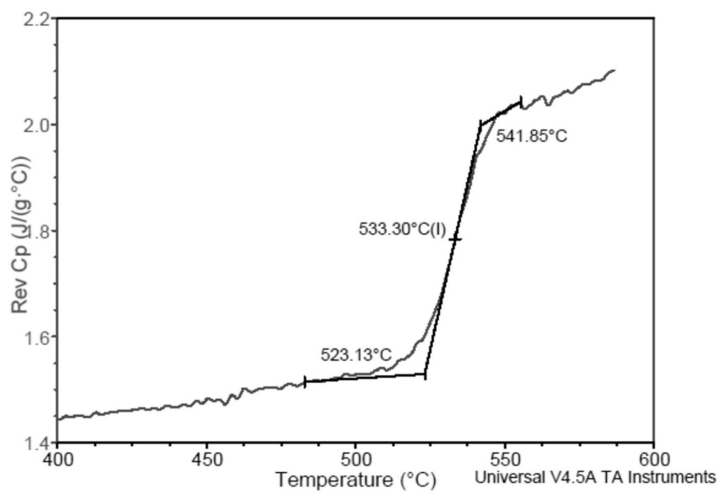

b) TMDSC data

Fig. 4. DSC and TMDSC data of the glass sample № 4

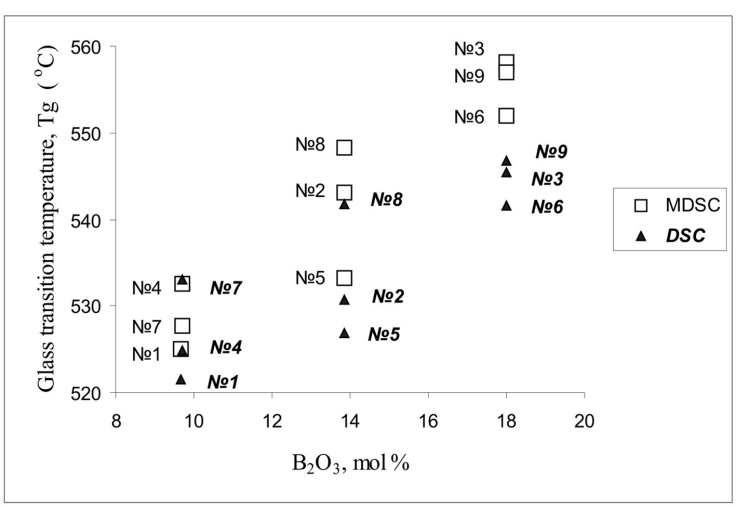

Fig. 5. Dependence of the glass transition temperature obtained by DSC and TMDSC versus the content of B_2O_3

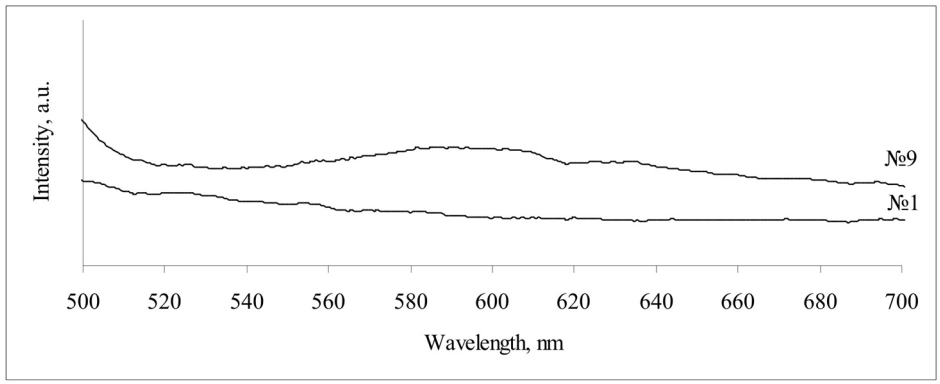

a) Typical photoluminescence spectra of undoped samples (№1) and Mn-doped samples (№9)

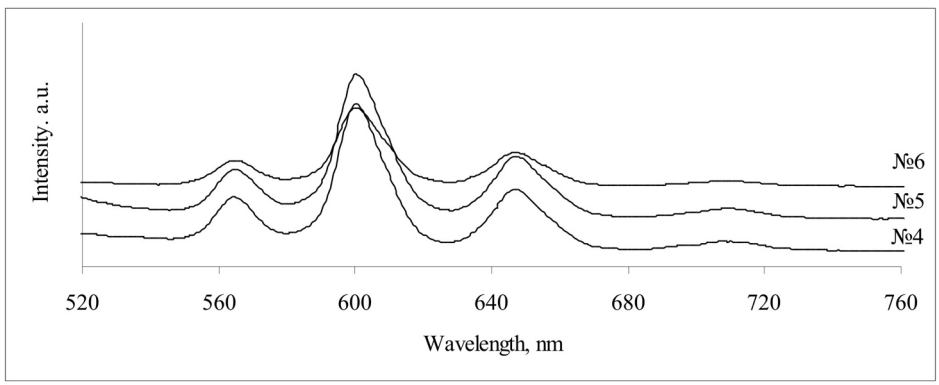

b) Photoluminescence spectra of Sm-doped samples (№4-6)

Fig. 6. Photoluminescence spectra of samples №1, 4–6, 9 at excitation wavelength 450 nm

The band at 600 nm, which corresponds to orange emission, is the most intense [12, 13].

CONCLUSIONS

Samarium and manganese doped ZnO-rich borophosphate compositions were investigated by powder X-ray diffraction, differential scanning calorimetry (DSC), temperature – modulated DSC, Raman spectra analysis and photoluminescence spectroscopy.

The results obtained show that the samples are predominantly amorphous, with the presence of crystalline structure in some of them. The main crystallization phases are zinc borate phosphate $Zn_3(BO_3)(PO_4)$ and zinc borate α-$Zn_5B_4O_{11}$.

When samarium doped samples exhibit strong visible (orange to red) immediate photoluminescence (scintillation) signal under UV light, manganese doped samples do not exhibit visible scintillation signal in glass-ceramics materials we have prepared (Mn doped materials need extra work to reveal their potential).

Synthesized glassy and glass-ceramic materials are all transparent, stable, and strong to mechanical damage. In addition, these materials are not hygroscopic what made them a good candidate for a number of sensing, optical security etc. applications.

Acknowledgments: *We are grateful to Assoc. Prof. Penchev of Plovdiv University and Assist. Prof. Tzvetkov of Institute of General and Inorganic Chemistry (BAS) for their help with the Raman spectra analysis and the powder X-ray diffraction measurements respectively. This research was funded by the "Scientific Research" fund at Plovdiv University, Grant № NI 13 HF 006.*

REFERENCES

1. P. Pascuta, G. Borodi, N. Jumate, I. Vida-Simiti, D. Viorel, E. Culea, *J. Alloys and Compounds*, **504**, 479 (2010).
2. L. Koudelka, P. Mosnerr, *Materials Letters*, **42**, 194 (2000).

3. M. Pal, B. Roy, M. Pal, *Journal of Modern Physics*, **2**, 1062 (2011).
4. S. Khor, Z. Talib, W. Yunus, *Ceramics International*, **38**, 935 (2012).
5. Y. Ravi Babu, P. Naik, K. Kumar, N. Kumar, A. Kumar, *Journal of Quantitative Spectroscopy & Radiative Transfer*, **113**, 1669 (2012).
6. JCPDS – International Centre for Diffraction Data PCPDFWIN v.2.2 (2001).
7. Petzoldt, *Glastech. Ber.*, **39**, 130 (1966).
8. K. Bluhm., C. H. Park, *Z. Naturforsch. B: Chem. Sci.*, **52**, 102 (1997).
9. M. Altaf, M. A. Chaudhry, and T. Bhatti, *Modern Physics Letters B*, **20**(26), 1637 (2006).
10. P. Chen, S. Li, W. Qiao, Y. Li, *Glass Physics and Chemistry*, **37**(1), 29 (2011).
11. S. O. Kasap, D. Tonchev, *J. Mater. Res.*, **16**(8), 2399 (2001).
12. G. Lakshminarayana, H. Yang, Y. Teng, J. Qiu, *J. Luminesc.*, **129**, 59 (2009).
13. G. Patronov, I. Kostova, Z. Stoeva, D. Tonchev, *Bulg. Chem. Comm.*, **44**(3), 307 (2012).

ИЗСЛЕДВАНЕ НА ЦИНК-БОР-ФОСФАТНИ КОМПОЗИЦИИ, ДОТИРАНИ СЪС САМАРИЙ И МАНГАН

Г. И. Патронов, И. П. Костова, Д. Т. Тончев

Катедра Химична технология, Пловдивски Университет „Паисий Хилендарски“, 4000 Пловдив, България

Постъпила февруари, 2013 г.; приета май, 2013 г.

(Резюме)

Настоящото изследване представя синтез и характеристика на богати на ZnO борфасфатни материали, дотирани със Sm и Mn, със състав 0.5M – 71.8ZnO – yP_2O_5 – (27.7-y)B_2O_3, където M = Sm_2O_3 или MnO, y = 9.7, 13.85, 18 mol%. Композициите са получени чрез високотемпературен синтез от ZnO, $NH_4H_2PO_4$, H_3BO_3 и Sm_2O_3 (или MnO) в определено съотношение, които са стрити, смесени и поставени в керамичен тигел. Синтезът е извършен при температура от 950 °C за 3 часа в муфелна пещ. Пробите са охладени до стайна температура и след това темперирани при 250 °C за 2 часа.

Богатите на ZnO борфасфатни композиции, дотирани със Sm и Mn, са изследвани чрез рентгеноструктурен анализ, диференциална сканираща калориметрия, температурно – модулирана диференциална сканираща калориметрия, Раман спектрален анализ и фотолуминесцентна спектроскопия. Получените резултати показват преимуществено аморфния характер на пробите, с наличие на кристална структура в някои от тях. Основните кристални фази са $Zn_3(BO_3)(PO_4)$ и α-$Zn_5B_4O_{11}$. Докато дотираните със Sm проби показват силен видим (оранжев до червен) фотолуминесцентен (сцинтилационен) сигнал под ултравиолетова светлина, дотираните с Mn проби не показват видим сцинтилационен сигнал.

Bulgarian Chemical Communications, Volume 45, Number 4 (pp. 543–548) 2013

Synthesis and crystal structure of magnesium chlorate dihydrate and magnesium chlorate hexahydrate

K. Kossev*, L. Tsvetanova, L. Dimowa, R. Nikolova, B. Shivachev

[1] *Institute of Mineralogy and Crystallography "Acad. Iv. Kostov", Bulgarian Academy of Sciences, Acad. G. Bonchev str., building 107, 1113 Sofia, Bulgaria*

Received February, 2013; Revised May, 2013

Two magnesium chlorate hydrates, $Mg(ClO_3)_2\times6(H_2O)$ (**1**) and $Mg(ClO_3)_2\times2(H_2O)$ (**2**), have been synthesized by slow evaporation from water and ethanol, respectively. The structures were determined by single-crystal X-ray diffraction at 150 K due to the dehydration-rehydration at room temperature leading to multiple phase transitions. Both compounds crystallized in the monoclinic space group $P2_1/c$ (SG 14) with respective unit cell parameters of a = 6.3899(3), b = 6.5139(3), c = 13.8963(6)Å, β = 100.319(5)°, V = 569.05(5) Å^3, Z = 2, R= 0.0210 and a = 6.3707(5), b = 5.4092(3), c = 9.8208(6) Å, β = 97.338(6)°, V = 335.66(4) Å^3, Z = 2, R = 0.0201. The structure solution shows an octahedral coordination of the Mg^{2+} for both compounds **1** and **2**. In the case of $Mg(ClO_3)_2\times6(H_2O)$ the coordination is achieved by the water molecules, while for $Mg(ClO_3)_2\times2(H_2O)$ the coordination involves two water molecules and is complemented by four oxygen atoms from the chlorate moiety.

Key words: magnesium chlorate, hydrates, single crystal.

INTRODUCTION

The coordination chemistry of magnesium is well studied because of its role and participation in a multitude of reactions in the living organisms. Magnesium is an essential component of many enzymes [1]. It binds and thus activates ATP and participates in the process of energy transfer and construction of nucleic acids [2]. The preferred coordination number of magnesium is six [3]. In the majority of known crystal phases involving the participation of magnesium it favors the octahedral coordination.

With the discovery of perchlorates ClO_4^- on Mars by NASA *Phoenix Lander* [4] the interest in studying and modeling the oxidized forms of chlorine increased. Between the chloride (oxidation state –1) and perchlorate (oxidation state +7) there are three other ions – hypochlorite ClO^- (oxidation state +1), chlorite ClO_2^- (oxidation state +3) and chlorate ClO_3^- (oxidation state +5). Chlorates are of peculiar interest due to their stability [5], though, their structural and crystallographic characteristics are similar to those of perchlorates. Alkali or alkaline earth metal chlorates are intensively studied, mostly sodium and magnesium chlorates, which is reasoned by the distribution of those elements in nature and the low eutectic temperatures of the aqueous solutions of $Mg(ClO_3)_2$. Magnesium chlorates have different industrial applications: in paper production; in agro chemistry as herbicide and defoliant; in pyrotechnics; and as antiseptic agent [6].

The first communication about magnesium chlorate hexahydrate was made by Wachter [7], who obtained it in 1841 from the reaction of barium chlorate and magnesium sulfate. Later, Meusser [8] determined the temperature at which $(Mg(ClO_3)_2).6H_2O$ melts in its crystallization water to be 35 °C. In addition to the hexahydrate, magnesium chlorate forms two other crystal hydrates with two (compound **2**) and four water molecules. The phase diagram of the system magnesium chlorate – water was reported by Linke in 1965 [9]. The tetrahydrate form $(Mg(ClO_3)_2).4H_2O$ is stable in the temperature range 35–65 °C, while above that temperature the stable form is $(Mg(ClO_3)_2).2H_2O$.

While the chemical and physicochemical properties of the anhydrous magnesium chlorate, as well as its hydrate forms have been well studied, the crystal structure(s) of none the salts were determined. In this study we report the crystal structures of two of the three magnesium hydrates

* To whom all correspondence should be sent:
E-mail: k_kossev@yahoo.com

namely $Mg(ClO_3)_2 \times 6(H_2O)$, (compound **1**) and $Mg(ClO_3)_2 \times 2(H_2O)$ (compound **2**).

MATERIALS AND METHODS

Synthesis

Magnesium chlorates were obtained via the reaction of barium chlorate monohydrate and magnesium sulfate heptahydrate [7] in equimolar ratio, followed by recrystallization in ethanol solution.

Synthesis of compound 1

Barium chlorate monohydrate (0.322 g, 1.0 mmol) was dissolved in 20 ml distilled water. Magnesium sulfate heptahydrate (0.246 g, 1.0 mmol) was dissolved in 20 ml distilled water. The water solution of magnesium sulfate heptahydrate was slowly added to the barium one under constant stirring. After three hours the mixture is centrifuged for 30 min at 5000 rpm. The barium sulfate pellet was discarded while the supernatant is transferred to a rotary evaporator. The obtained magnesium chlorate was recrystallized in 5 ml ethanol.

Colorless single crystals of magnesium chlorate hexahydrate, $Mg(ClO_3)_2.6H_2O$ (compound **1**), were grown by slow evaporation from an aqueous solution at room temperature.

Synthesis of compound 2

The synthesis of compound **2** followed the same steps as described for compound **1**. Colorless single crystals of magnesium chlorate dehydrate, $Mg(ClO_3)_2.2H_2O$ (compound **2**), were grown by slow evaporation from absolute ethanol at room temperature.

Single crystal X-ray diffraction study

Crystals of compounds **1** and **2** suitable for single crystal XRD analysis were placed on a glass fiber and mounted on an Agilent, SuperNovaDual four-circle diffractometer equipped with Atlas CCD detector and using mirror-monochromatized MoKα (λ = 0.7107 Å) radiation from a micro-focus source. The crystals were flash frozen at 150 K in an N_2 gas stream (Cobra, Oxford cryosystems) and diffraction data were collected at this temperature by ω-scan technique. The determination of cell parameters, data integration, scaling and absorption correction were carried out using the CrysAlisPro program package [10]. The structures were solved by direct methods using ShelxS [11] and refined by full-matrix least-square procedures on F^2 with ShelxL-97 [11]. The hydrogen atoms were located from difference Fourier map and refined as riding on their parent atoms, with $U_{iso}(H) = 1.2U_{eq}(O)$.

RESULTS AND DISCUSSION

The crystal structures of the magnesium chlorate hydrates (di-, tetra- and hexa- hydrates) have not been reported although the synthesis of these three magnesium chlorates has been published [12]. The performed check (ICDD-PDF and ICSD) revealed that similar magnesium chlorates (where the water is replaced by another small highly polar molecule e.g. urea) have been characterized.

The structures of some magnesium oxychlorides have also been reported ($Mg(ClO_4)_2.6H_2O$) [13] and ($Mg(ClO_2)_2.6H_2O$) [14]). The problem with the crystal structure determination of magnesium chlorates is associated with their relative instability at ambient temperature. Actually, the performed room temperature data collection resulted in good diffraction of the crystals for 10–15 minutes after what diffraction disappeared almost instantly. The attempted X-ray powder data collection was also unsuccessful. Thus we performed single crystal data collection by flash freezing the crystals in N_2 at 150 K.

An *ORTEP* view with 50% probability of the molecular structures of compounds **1** and **2** and the atom numbering scheme is shown in Figure 1. The experimental conditions are summarized in Table 1.

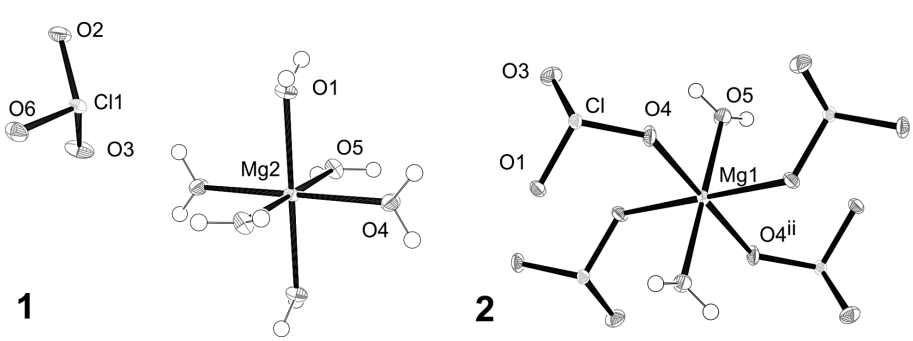

Fig. 1. View of the molecular structures of compounds **1** and **2** with atomic numbering scheme. Displacement ellipsoids for the non-H atoms are drawn at the 50% probability level. The H atoms are presented with spheres with arbitrary radii

Table 1. Crystal data and most important refinement indicators for compounds **1** and **2**

	1	**2**
Empirical formula	$Cl_2H_{12}MgO_{12}$	$Cl_2H_4MgO_8$
Molecular weight	299.31	227.24
Crystal size (mm)	0.32 × 0.30 × 0.28	0.23 × 0.21 × 0.18
Crystal habit, color	prism, colorless	prism, colorless
Crystal system	Monoclinic	Monoclinic
Space group	$P2_1/c$	$P2_1/c$
T(K)	150	150
Radiation wavelength (E)	0.71073 (Mo K*a*)	0.71073 (Mo K*a*)
a (E)	6.3899(3)	6.3707(5)
b (E)	6.5139(3)	5.4092(3)
c (E)	13.8963(6)	9.8208(6)
α (°)	90	90
β (°)	100.319(5)	97.338(6)
γ (°)	90	90
V (E^3)	569.05(5)	335.66(5)
Z	2	2
d (mg. m^{-3})	1.747	2.248
μ (mm^{-1})	0.67	1.06
diffractometer	Agilent SupernovaDual	Agilent SupernovaDual
Detector, resolution mm^{-1}	Atlas CCD, 10.3974 pixels	Atlas CCD, 10.3974 pixels
radiation source, wavelength (Å)	Mova(Mo) X-ray source, λ = 0.7107	Mova(Mo) X-ray source, λ = 0.7107
Absorption correction	multi-scan, CrysAlisPro	multi-scan, CrysAlisPro
Refinement, Least-squares matrix	F^2, Full	F^2, Full
Reflections collected/I>2σ (I)	3955/1288	1388/788
parameters	94	61
R1 ($F^2 > 2\sigma(F^2)$)	0.021	0.02
wR2 (all data)	0.057	0.055
GOF	1.08	0.83
Extinction correction	none	0.049(5)
$\Delta\rho_{max}$/ $\Delta\rho_{min}$ (e $Å^{-3}$)	0.32/–0.45	0.23/–0.33

Table 2. Selected geometrical parameters for compounds **1** and **2** (Å, °)

Bond distance			
compound 1		compound 2	
Cl1 — O2	1.4923(8)	Cl1 — O1	1.5019 (9)
Cl1 — O3	1.4808(9)	Cl1 — O3	1.4793(11)
Cl1 — O6	1.4843(8)	Cl1 — O4	1.4850 (9)
Mg2 — O1	2.0481(8)	Mg1 — O1	2.1039(9)
Mg2 — O4	2.0455(8)	Mg2 — O4	2.0733(10)
Mg2 — O5	2.0703(8)	Mg2 — O5	2.0429(10)
Bond angle			
O1— Mg2 — O5	88.07(3)/91.93(3) [i]	O5— Mg1 — O1	89.48(4)/90.52(4)[ii]
O4— Mg2 — O1	90.62(4)/89.38(4) [i]	O5— Mg1 — O4	88.96(4)/91.04(4)[ii]
O4— Mg2 — O5	90.45(4)/89.55(4) [i]	O4— Mg1 — O1	88.05(4)/91.95(4)[ii]
O3 —Cl1 — O2	107.25(5)	O1— Cl — O3	105.98(6)
O3 —Cl1 — O6	106.62(5)	O1— Cl — O4	106.48(6)
O6 —Cl1 — O2	107.19(5)	O3— Cl — O4	107.41(6)

Symmetry operations: (i) $-x, -y, -z+1$; (ii) $x, y, z-1$.

Selected bond distances and bond angles are listed in Table 2. Hydrogen bonding geometry is presented in Table 3. The data for publication were prepared with WinGX [15], *ORTEP* [16], and Mercury [17] program packages.

As expected, the crystal structure of the hexahydrate consists of discrete $[Mg(H_2O)6]^{2+}$ octahedra and chlorate anions (Fig. 2). The $[Mg(H_2O)6]^{2+}$ octahedra are connected via hydrogen bonds to chlorate anions, where every H atom of the six water

Table 3. Hydrogen bond for compounds **1** and **2** (Å, °)

D—H···A	D—H	d(H···A)	d(D···A)	<(DHA)
Compound **1**				
O1—H1A···O6^{i}	0.801	2.084	2.879(5)	172.0
O1—H1B···O3^{i}	0.804	1.957	2.763(5)	160.7
O4—H4A···O6^{ii}	0.804	1.951	2.739(4)	166.6
O4—H4B ···O2^{iii}	0.809	2.038	2.845(5)	175.3
O5—H5A ···O3^{i}	0.775	2.120	2.886(5)	170.3
O5—H5B···O2^{iv}	0.822	2.087	2.901(5)	177.5
Compound **2**				
O5—H1···O3^{v}	0.751	2.094	2.843(5)	168.8
O5—H2···O3^{vi}	0.745	2.267	2.942(5)	151.2

Symmetry codes : (i) *–x, –1/2+y, 1/2–z*; (ii) *–1+x, 1/2–y, 1/2+z*; (iii) *1–x, -y, 1–z*; (iv) *–1+x, 1/2–y, 1/2+z*; (v) *–1+x, y, z* (vi) *1–x, 1–y, 2–z*.

molecules is in contact with a chlorate anions, with a O…O distances in the range of 1.95–2.15 Å (Table 3), thus arranging 10 chlorate anions around the octahedral unit (Fig. 2). The result is the appearance of a complex three-dimensional hydrogen-bonding network comprising layers of chlorates anions and $[Mg(H_2O)6]^{2+}$ octahedra (Fig. 3).

In compound **2** the Mg coordination is also octahedral. However, in compound **2** a chlorate oxygen participates in the Mg coordination sphere. The magnesium atom (ion) and four chlorate ions lie in one plane, while the water molecules are in axial positions and Mg–O bonds are nearly perpendicular to this plane (89.44(5)°). The chlorate molecule acts as a bridge between two magnesium atoms (Mg–O–ClO–O–Mg) and thus produces layers that are stacked along *a*. The layers are stabilized by internal hydrogen bonds involving water molecules, O5 and chlorate O3. The three-dimensional stabilization of the structure is achieved by a bicyclic hydrogen O5-H…O3 between the adjacent layers (Fig. 4).

CONCLUSIONS

The crystal structures of two elusive magnesium compounds, $Mg(ClO_3)_2\times6(H_2O)$ and $Mg(ClO_3)_2\times2(H_2O)$ were determined. They will help in the understanding of the rapid hydration processes and multiple phase transitions associated with magnesium hydrates and solvates.

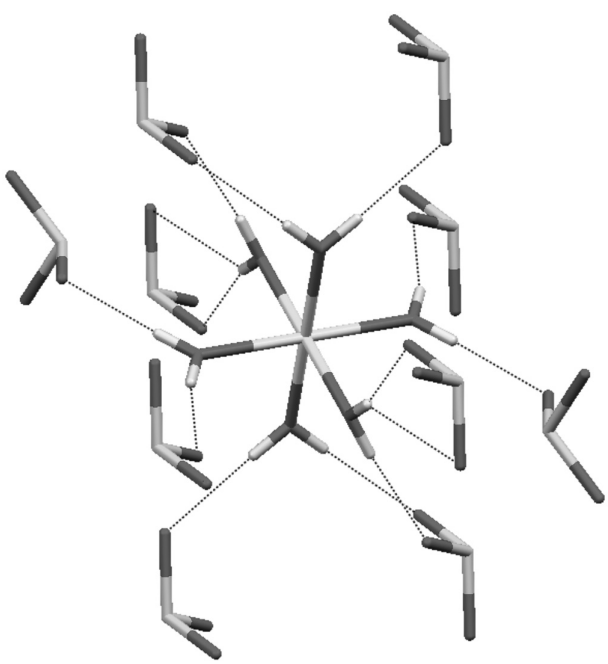

Fig. 2. Hydrogen bonding motif of $Mg(ClO_3)_2\times6(H_2O)$

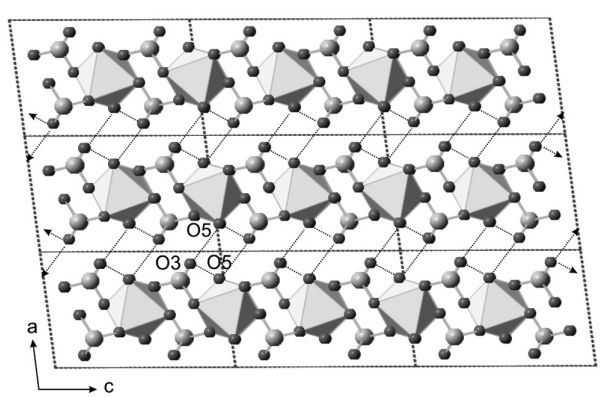

Fig. 3. Three-dimensional hydrogen-bond networks comprising layers of chlorates anions and $[Mg(H_2O)6]^{2+}$ octahedra

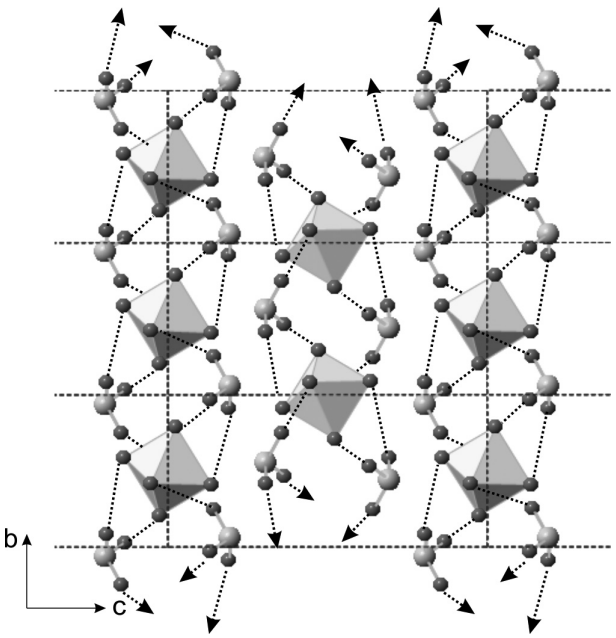

Fig. 4. Three-dimensional stabilization of the structure is achieved by a bicyclic hydrogen O5-H…O3 between the layers

SUPPLEMENTARY MATERIALS

ICSD 425637 and 425637 contain the supplementary crystallographic data for this paper. Further details of the crystal structure investigation(s) may be obtained from Fachinformationszentrum Karlsruhe, 76344 Eggenstein-Leopoldshafen, Germany (fax: (+49)7247-808-666; e-mail: crysdata(at)fiz-karlsruhe.de, http://www.fiz-karlsruhe.de/request_for_deposited_data.html) on quoting the appropriate ICSD number.

Acknowledgment: *This work was supported by the National Science Fund of Bulgaria, contract DRNF 02/1.*

REFERENCES

1. D. Rogolino, M. Carcelli, M. Sechi, N. Neamati, *Coord. Chem. Rev*., **256**, 3063 (2012).
2. J. P. Glusker, A. K. Katz, Ch. W. Bock, *The Rigaku Journal*, **16(2)**, 8 (1999).
3. C. Hsiao, M. Tannenbaum, H. VanDeusen, E. Hershkovitz, G. Perng, A. Tannenbaum, L. D. Williams, Complexes of Nucleic Acids with Group I and II Cations. Nucleic Acid Metal Ion Interactions, N. Hud (ed.), The Royal Society of Chemistry, London, 2008, p. 1–35.
4. M. H. Hecht et al., *Science*, **325**, 64 (2009).
5. J. Hanley et al. *Geophys. Res. Lett*., **39**, L08201, 5 (2012).
6. W. Robbins, A. S. Crafts, R. N. Raynor, Weed Control, Mc Graw-Hill, Inc., New York and London, 1942; *Pulp and Paper Canada*, **97(10)**, 11 (1996).
7. A. Wachter, *J. Prakt. Chem*., (1) 30, 325 (1841).
8. A. Meusser, *Ber.*, **35**, 1415 (1902).
9. W. F. Linke, Solubilities: Inorganic and Metal-Organic Compounds, American Chemical Society, 4th ed., 1965, p. 1914.
10. Agilent. CrysAlisPro (version 1.171.35.15). Agilent Technologies Ltd, Yarnton England, (2010).
11. G. M. Sheldrick, *Acta Cryst. A*, **64**, 112 (2008).
12. T. Todorov, R. Petrova, K. Kossev, J. Macicek, O. Angelova, *Acta Cryst*. C, **54**, 927 (1998).
13. C. D. West, *Zeitschrift fuer Kristallographie, Kristallgeometrie, Kristallphysik, Kristallchemie*, **91**, 480 (1935).
14. Marsh, R.E., *Acta Cryst*., **46**, 1755 (1990).
15. L. J. Farrugia, *J. Appl. Cryst.*, **32**, 837 (1999).
16. L. J. Farrugia, *J. Appl. Cryst.*, **30**, 565 (1997).
17. I. J. Bruno, J. C. Cole, P. R. Edgington, M. Kessler, C. F. Macrae, P. McCabe, J. Pearson, R. Taylor, *Acta Cryst. B*, **58**, 389 (2002).

СИНТЕЗ И КРИСТАЛНА СТРУКТУРА НА МАГНЕЗИЕВ ХЛОРАТ ДИХИДРАТ И МАГНЕЗИЕВ ХЛОРАТ ХЕКСАХИДРАТ

К. Косев, Л. Цветанова, Л. Т. Димова, Р. Николова, Б. Л. Шивачев

Институт по Минералогия и кристалография, БАН, ул. „Акад. Георги Бончев“, бл. 107, София 1113, България

Постъпила февруари, 2013 г.; приета май, 2013 г.

(Резюме)

Получени са монокристални образци на магнезиев хлорат $Mg(ClO_3)_2\times6(H_2O)$ (**1**) и $Mg(ClO_3)_2\times2(H_2O)$ (**2**) при условията на бавно изпарение, съответно от вода (**1**) и етанол (**2**). Поради ниската устойчивост на кристалите на стайна температура монокристалният експеримент е осъществен на 150 K. Рентгеноструктурният анализ разкрива, че двете съединения кристализират в моноклинната $P2_1/c$ пространствена група (No 14) с параметри на елементарната клетка a = 6.3899(3), b = 6.5139(3), c = 13.8963(6) Å, β = 100.319(5)°, V = 569.05(5) Å^3 и a = 6.3707(5), b = 5.4092(3), c = 9.8208(6) Å, β = 97.338(6)°, V = 335.66(4) Å^3. Рафинирането на кристалната структура показа, че Mg^{2+} е октаедрично координиран и при двете съединения. При $Mg(ClO_3)_2\times6H_2O$ координацията е само от водни молекули, докато при $Mg(ClO_3)_2\times2(H_2O)$ координационният октаедър включва две молекули вода, а останалите четири позиции се заемат от кислородни атоми на хлоратни йони.

Bulgarian Chemical Communications, Volume 45, Number 4 (pp. 549–553) 2013

Microstructure and texture analyses on spring steel

L. V. Nikolova*

University of Chemical Technology and Metallurgy – Sofia,
8 St. Kl. Ohridski Blvd. 1756 Sofia, Bulgaria

Received February, 2013; Revised May, 2013

For this study hourglass shaped specimens of spring steel were subjected to rotating-bending fatigue at different stress ranges to fracture. Microstructure observations showed eutectoid (lamellar) structure and characteristics of the lamellar microstructure were described. Deeper observations described the influence of the fatigue process on microstructure and the crystallography – is there a crystallographic influence on the fatigue as it is seen with other materials or not. Electron backscatter diffraction (EBSD) analyses were performed to characterize the crystallography of the specimens at different parts of the fractured surface as well as in direction perpendicular to the fracture surface to investigate crack path.

Key words: spring steel; microstructure, texture, EBSD.

INTRODUCTION

The materials applied for springs are extended to metallic and nonmetallic types, in addition, among the metals there are many types, such as, spring steel, stainless steel, nickel alloy and so on. Their required properties vary accordingly. However, whatever the applications are, it is certain that a high stress during cyclic loading and prolonged reliability should be required. It is generally recognized that the linear fracture mechanics allows to be defined the threshold condition of fatigue crack propagation. In high strength materials such as spring steels very small cracks lead to fatigue fracture. It is well known that the fatigue process can be influenced by many different factors such as temperature, applied stress, environment, microstructure of the material etc. most of the measurements on pearlite structures are pointed to morphology and formation mechanism of pearlite steels and to give more insight into the problem of the nucleation and growth process of pearlite [1, 2, 3, 4, 5, 6]. Not so many researches are pointed to determine the crystallographic orientation in the pearlite colony [7, 8]. The aim of this study was to investigate the influence of the crystallography on specimens tested on specific plastic deformation.

EXPERIMENTAL

Material and specimens: The studied material was steel wire, used for springs, with a diameter φ = 8 mm and tensile strength σ_B = 1522 MPa. The chemical composition of the steel contains 0,819 weight % Carbon i.e. hypereutectoid steel and is presented in Table 1. The specimens were machined from a coiled on reel drawn steel, no additional heat treatment was performed before

Table 1. Chemical composition of the investigated steel (weight %)

C	Mn	P	S	Si	Al	Cr	Ni	Cu	Mo	N_2
0.819	0.760	0.010	0.001	0.257	0.034	0.251	0.016	0.011	0.003	0.005

* To whom all correspondence should be sent:
E-mail: lyubov_nikolova@abv.bg

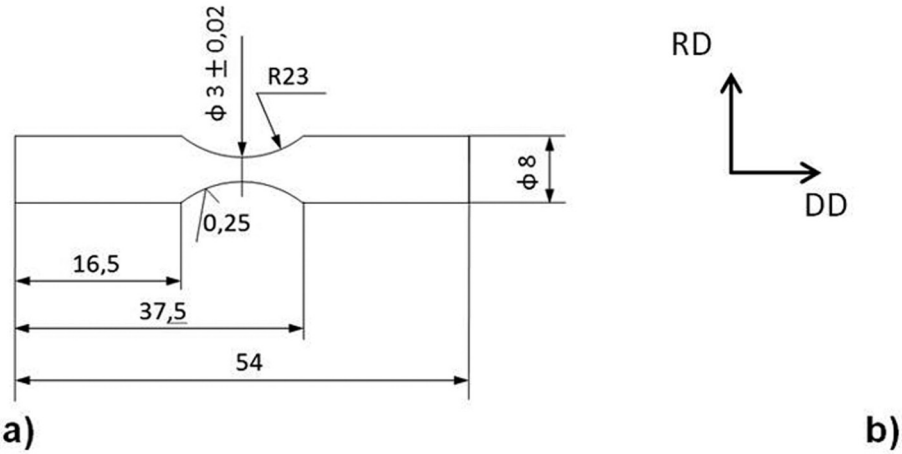

Fig. 1. Geometry of the specimens (a) and the named directions of the axis (b)

testing. The geometry of the specimens is shown on Figure 1(a). Figure 1 (b) represents the directions of the axis of the specimens i.e. DD – drawing direction (longitudinal axis), RD – radial direction (transverse axis). The specimens were polished with silicon carbide papers (starting with 400-grid, after 500-grid, 600-grid, 800-grid, 1000-grid, 2000-grid and 2500-grid) before testing so that all surface defects to be removed.

Testing: Hourglass shaped specimens were subjected to symmetric cyclic rotating-bending fatigue at different stress ranges (R = –1, f = 11 Hz) in air and room temperature to fracture. Tests were performed on a table model Fatigue Rotating Bending Machine, FATROBEM-2004, designed and assembled in "Fracture and Fatigue" Laboratory in UCTM – Sofia [9]. All the tests were done in the range of high cycle fatigue accordingly to the S-N curve of the material.

Equipment for characterization and sample preparation: Scanning electron microscope (SEM) Jeol JSM-6490 was used for microstructure and fatigue fracture surface observations and Jeol JSM-6500F equipped with field emission electron gun (Oxford instruments, HKL technology) for Electron backscattered diffraction (EBSD) analysis. Channel 5 system (HKL Technology) was used for analyzing and presenting the obtained results. A step size of 0,8 μm was used to collect data over the surface of the specimen, accelerating voltage inside of the vacuum camera was 15 kV.

To reveal the microstructure of the samples 4% picric acid solution was used after polishing with a 4000-grid silicon paper. The samples for EBSD analyses were polished with a 4000-grid silicon carbide paper followed by final polishing with colloidal silica solution.

The specimens were characterized in two mutual perpendicular directions (parallel and perpendicular to fracture surface). Successive polishing steps over the fracture surface were performed to identify the microstructure behind the nucleation site using EBSD technology. Because of the fine microstructure of the material and the fact that for the most materials the ferrite could not be read the EBSD analysis for this study were performed with a very small step size i.e. 0,08 μm. The characterization of the material and the EBSD analysis were done in the laboratory LEM3, University of Lorraine – Metz, France.

RESULTS AND DISCUSSION

The steel used in this study contains 0,819 wt.% carbon which accordingly to the Fe-C phase diagram means that it is eutectoid steel with lamellar microstructure (alternate layers of ferrite and cementite). This is confirmed by proceeded microstructure observations (Fig. 2). Typical characteristics of the eutectoid microstructure were noticed such as curvature of cementite lamellae, discontinuous cementite lamellae, bridges connecting two cementite lamellae, branching of the cementite and also primary cementite (Fig. 2 (c)). The presence of primary cementite (Fig. 2 (a)) is explained by the higher percentage of carbon i.e. hypereutectoid steel. Flattening and widening of the lamellae respectively oriented parallel and perpendicular to DD were noticed on specimen's microstructure (//DD) what could be a result of the drawing process. Curvature of the cementite lamellae oriented parallel to DD in the zones close to the fracture surface was also found. The interlamellar spacing λ at different zones (//DD) of the specimens

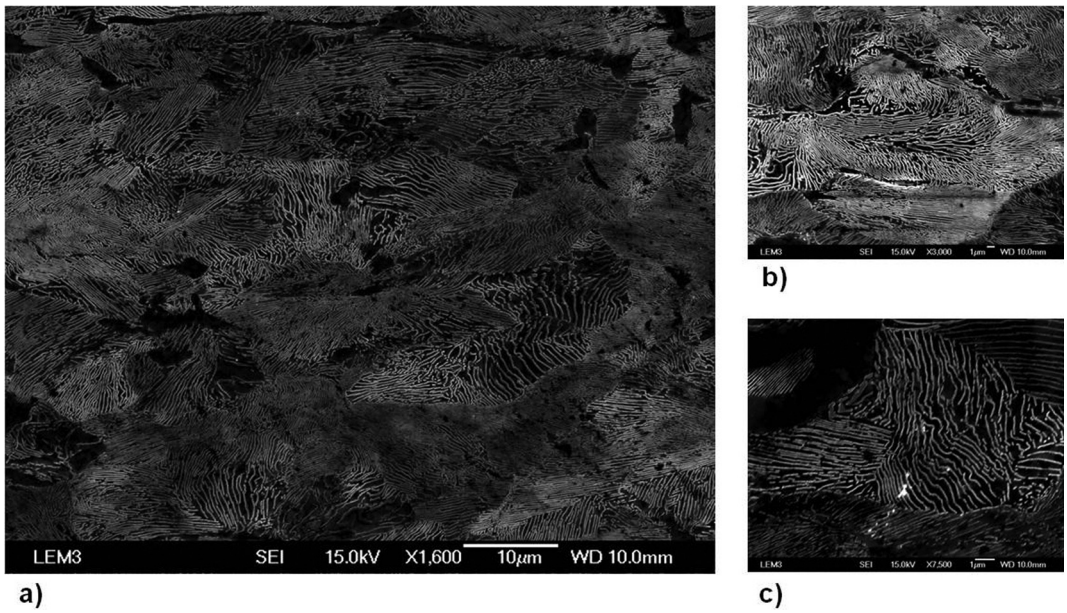

Fig. 2. Lamellar microstructure of the material at different areas and different magnifications: (a) x1600; (b) x3000; (c) x7500;

was measured. Each one of the obtained results for each zone is an average value from 50 to 60 measurements. The values for the different zones are as follows: zones close to the fractured surface (//DD) $\lambda = 0.2808$ μm; zones from the middle part of the specimens (//DD) $\lambda = 0.2847$ μm; zones from the not deformed specimen (//DD) $\lambda = 0.2668$ μm.

EBSD analyses (Fig. 3) were performed to characterize the crystallographic orientation at different parts of the fractured surface as well as in direction perpendicular to the fracture surface to investigate crack path. As could be seen from the performed analysis, the fatigue process in this study was not influenced by the crystallography of the material's microstructure. On Figure 3 are illustrated colored pole figures for both phases obtained by Channel 5 system. The figure is showing the texture analysis of different specimens and different zones of the polished surface. It can be concluded that there is no significant change of the texture, but it can be

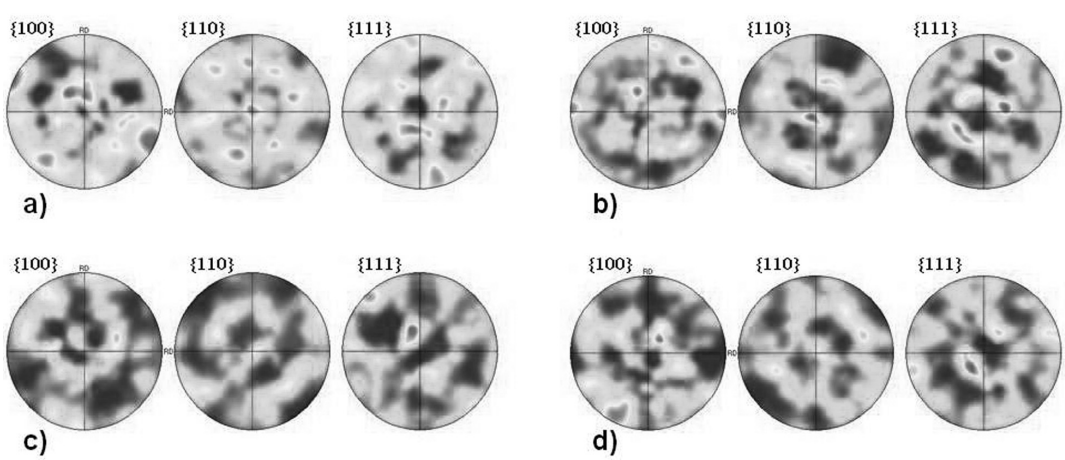

Fig. 3. Pole figures (coloured) illustrating the texture of different specimens and in different directions of geometrical form: (a) zone of the initiation, applied stress $\Delta\sigma = 1500$ MPa; (b),zone of final fracture, applied stress $\Delta\sigma = 1500$ MPa; (c) analysis of surface parallel to RD, applied stress $\Delta\sigma = 1500$ MPa; (d) initial texture of not-deformed material

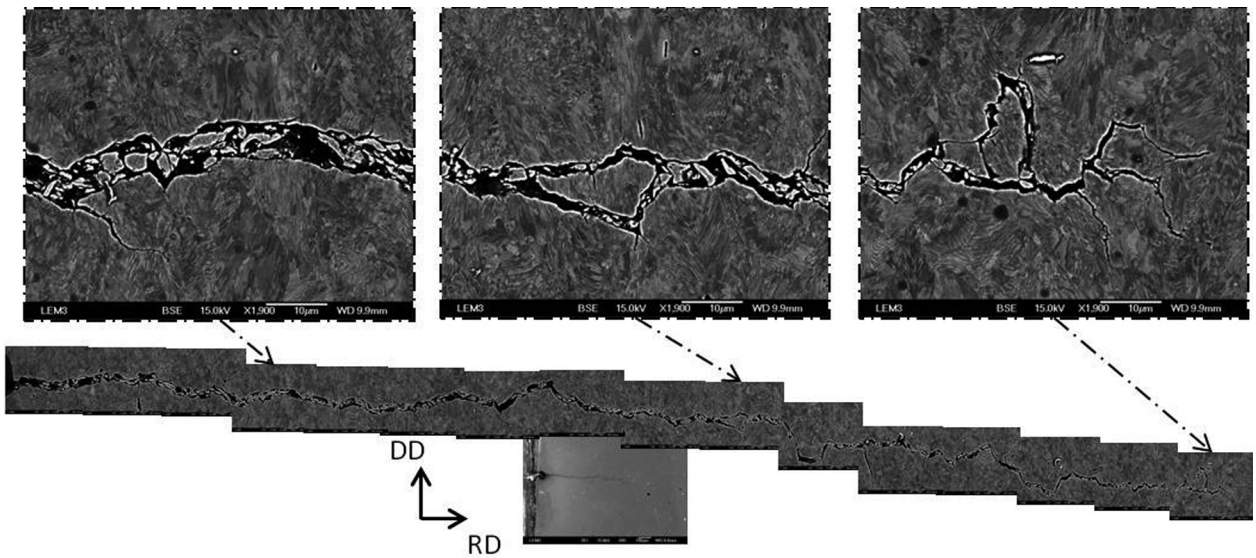

Fig. 4. Crack path on a fractured surface of a specimen subjected to Rotating-Bending Fatigue under $\Delta\sigma = 1200$ MPa

noticed only a small difference in the intensity i.e. zones with a higher rate of deformation (Fig. 3a, b) showed higher rate of texture in comparison to analysis of the surface parallel to RD (Fig. 3c) and of that of not-deformed material (Fig. 3d). As is it seen on Fig. 3a there is expressed a slow rate of fiber texture clearly seen on pole figure {110} showing the texture in planes (101), (110), $(01\bar{1})$.

The initial texture (not-deformed specimens) that had been measured showed slow rate of texture what could be a result of the process of drawing of the material. It is known that by drawing the rate of texture is influenced by the difference in the ratio of initial diameter/final diameter of the drawn material which is confirmed also by other researchers [10, 11].

As it is seen on Figure 4 the fatigue crack propagation also was not influenced by the fatigue process. The crack is not propagating on a specific crystallographic planes or directions. This might be due to very low texture or very high applied stresses when we investigate the mentioned kind of influence. However, more investigations at low stresses are necessary to determine whether the crack propagation in this material could be influenced by the crystallographic orientation.

CONCLUSIONS

In this work the influence of the crystallography on a tested under rotating bending fatigue spring steel has been studied. EBSD analysis were performed and expressed by pole figures obtained for both phases. The results showed higher rate of fiber texture of the more deformed zones of the specimen in comparison to the initial one. But still it cannot be said that the texture was significantly changed by the performed deformation.

From the performed observations it can be concluded that the crack path had not been influenced by the crystallographic orientation. An illustration of that is shown though the crack path of a specimen tested on Rotating-Bending Fatigue at $\Delta\sigma = 1200$ MPa.

Acknowledgements: *I, Lyubov Nikolova would like to express my gratitude to all those who gave me the possibility to complete this report. I am deeply indebted to my supervisor Dr. Nathelie Gey (laboratory LEM3 – Metz, France) whose help, stimulating suggestions, knowledge, experience and encouragement helped me in all the times of study and analysis of the project in the research period. I am also grateful to all other researchers in laboratory LEM3 – Metz who helped to a great extent in the project.*

REFERENCES

1. P. R. Howell, *Materials Characterization*, **40**, 227 (1998).
2. M. X. Zhang, P. M. Kelly, *Materials Characterization*, **60**, 545 (2009).
3. F. G. Caballero, C. Garcia de Andreas, C. Capdevila, *Materials Characterization*, **45**, 111 (2000).

4. A. W. Wilson, G. Spanos, *Materials Characterization*, **46**, 407 (2001).
5. A. Walentek, M. Seefeldt, B. Verlinden, E. Aernoudt, P. Van Houtte, *Materials Science and Engineering A*, **483–484**, 716 (2008).
6. A. Walentek, M. Seefeldt, B. Verlinden, E. Aernoudt, P. Van Houtte, *Journal of Microscopy*, 224, (Pt 3), 256 (2006).
7. N. Guo, Q. Liu,Y. C. Xin, B. F. Luan, Z. Zhou, *Science China – Technological Sciences*, **54** (9), 2368 (2011).
8. N. Nakada, N. Koga, T. Tsuchiyama, S. Takaki, *Scripta Materialia*, **61**, 133 (2009).
9. A. Davidkov, PhD Thesis, UCTM, Sofia, 2006.
10. M. Zidani, S. Messaoudi, T. Baudin, D. Solas, M. H. Mathon, *International Journal of Materials Forming*, **3**, 7 (2010).
11. G. Langford, *Metallurgical Transactionsa*, 8A, 861 (1977).

МИКРОСТРУКТУРНИ И ТЕКСТУРНИ АНАЛИЗИ НА ПРУЖИННА СТОМАНА

Л. В. Николова*

Химикотехнологичен и Металургичен университет – София, бул. „Климент Охридски“ 8, София 1756, България

Постъпила февруари, 2013 г.; приета май, 2013 г.

(Резюме)

За това изследване са използвани образци от пружинна стомана, изработени във форма тип пясъчен часовник и подложени на умора със схема на натоварване „огъване при въртене“ до разрушаване. Микроструктурните наблюдения показаха евтектоидна (ламеларна) структура, като резултатите от тях са описани. По-подробни анализи описват влиянието на уморния процес върху микроструктурата и кристалографията – има ли влияние на кристалографията върху процеса на умора и забелязва ли се и при други материали или не. EBSD анализи бяха проведени за охарактеризиране на кристалографията и изследване на пътя на пукнатината в различни области от образците, както по разрушената повърхност, така и в посока перпендикулярна на нея.

Bulgarian Chemical Communications, Volume 45, Number 4 (pp. 554–559) 2013

Ab initio simulation of crystallization of amorphous Ge–Te–In system

A. Zaidan[1,2]*, Vl. Ivanova[1], P. Petkov[1]

[1] *Department of Physics, Thin Film Technology Lab, University of Chemical Technology and Metallurgy, 8 "Kl. Ohridski" Blvd., 1756 Sofia, Bulgaria*
[2] *Departments of Physics, Faculty of Science and Technology, Airlangga University, Surabaya 60115, Indonesia*

Received February, 2013; Revised May, 2013

Phase change materials are promising candidates for memory materials because their ability to change between amorphous to crystalline state or vice versa with the application of specific profile of heat. Due to fast transition between crystalline and amorphous form, chalcogenide based on Ge-Te has been regarded as potential candidate of phase change materials. Our investigation of amorphous structures of $GeTe_4$ with indium dopant have shown that amorphous Ge–Te–In has a significant number of fourfold rings which are responsible for the rapid crystal growth in crystal-amorphous transition. In the present study, *ab initio* molecular dynamics were used to study crystallization process of $GeTe_4$ with indium dopant (5, 10, 15 and 20 at%). The structural changes in transition process were analyzed by evaluation of ring statistics. Results from *ab initio* simulations show that crystallization of samples with 80–100 atoms occur in hundreds of picoseconds.

Key words: Crystallization, *Ab initio* Molecular Dynamics, Chalcogenide.

INTRODUCTION

Chalcogenide glasses are interesting materials because of their technological applications and commercial importance. Due to their unique properties (low phonon energies, optical transparency in IR region, high index of refraction), chalcogenide glasses have many important applications in optics and optoelectronics. These applications include phase change material [1–4], sensor [5, 6], optical circuits, gratings, waveguides [7–9], and many others.

Phase change materials have been extensively studied by many authors because it is expected to be the future of non-volatile memories [10, 11]. The emerging non-volatile phase change memory holds the potential for the next generation data storage which is faster and more stable than present data storage. Chalcogenide based on Ge–Te has been regarded as a potential candidate of phase change materials due to its fast transition between crystalline and amorphous form. However, very little theoretical guidance is available for chalcogenide materials based on Ge–Te, especially for Ge–Te–In system.

With these motivations, theoretical study of crystallization process in amorphous $GeTe_4$ doped with indium 0, 5, 10, 15, and 20 at% using numerical calculation has been done. Models reported in this work are generated through melt quenching *ab initio* molecular dynamics (AIMD) simulations. This approach, first pioneered by Car and Parrinello, which combines density functional theory (DFT) with molecular dynamics (MD) is a powerful tool for investigating liquid and amorphous structures [12].

CALCULATION DETAILS

Relaxed structure of $(GeTe_4)_{100-x}In_x$ with $x = 0$, 5, 10, 15, 20 were generated by AIMD simulation. The calculations were performed with the SIESTA program [13] using a linear combination of numerical atomic orbitals as the basis set and norm-conserving pseudopotentials. The total energy is approximated in the non-self consistent Harris functional. The SIESTA program was run under periodic boundary conditions and employed one point (k = 0) in the Brillouin zone. Mesh Cutoff 30 Ry was used for calculation and temperature was controlled by a Nosé-Hoover thermostat.

* To whom all correspondence should be sent:
E-mail: zaidan@unair.ac.id

Structures of amorphous $(GeTe_4)_{100-x}In_x$ were investigated using atomic models contain up to 300 atoms. The starting point of these models is model of $GeTe_4$ contains 240 atoms placed randomly inside cubic lattice with periodic boundary condition. The lattice constant of cubic lattice were calculated from mass density of system which is measured from experiment [14]. AIMD was performed to obtain relaxed stucture of $GeTe_4$ system. Indium atoms were then added to relaxed structure of $GeTe_4$ so atomic models of $(GeTe_4)_{100-x}In_x$ with x = 5, 10, 15, 20 contain 300 were obtained. Using relaxed structures, bond angle distributions and ring statistics were calculated and discussed for amorphous state.

Unfortunately up to now there is no standard procedure to model amorphous structure using MD method. Although several amorphous systems were successfully generated from so called "melt quenching" technique, but this technique itself varies in details. Melt quenching can be done using classical MD or AIMD. The "melt and quench" simulation scheme proceeds by carrying out a series of MD simulations. At each step, the structure obtained from the previous MD simulation is used as the starting point for the next one. In this work, process of melt quenching technique contains three AIMD steps, one annealing process and two *NVT* MD processes. First, system is annealed at 1500 K which is higher than melting temperature of system and then system is allowed to reach thermodynamic equilibrium in this temperature using *NVT* MD. The process is then continued with quench of the system to 300 K. Then, the structure is equilibrated at this temperature using *NVT* MD. For each MD step, system is given enough time to reach its thermal equilibrium in order to eliminate its correlation to the previous structure. At each step, system is allowed to run for 10 ps to reach its thermodynamic equilibrium. The time step for the simulations is set to be 2 fs in order to suppress numerical error.

Crystallization process was investigated by carried out AIMD simulations on $(GeTe_4)_{100-x}In_x$ with x = 5, 10, 15, 20 using models contain 80–100 atoms. Each model was first equilibrated at 1500 K followed by a thermal quenching to 900 K slightly above melting points. Then model was quenched with slow cooling rate ($dT/dt = -0.75$ K ps^{-1}) for 400 ps. In this step, structural changes in transition process are analyzed by evaluation of ring statistics.

RESULTS AND DISCUSSION

Bond angle distribution between first neighbor atoms can give information about structural nature of system. As member of group IV chalcogenide we expect that $GeTe_4$ has tetrahedral nature as $GeSe_4$.

The average Ge coordination number in the amorphous models is around 4, but this does not prove that amorphous models only have tetrahedral coordination. Bond angle distributions of Te–Ge–Te for amorphous $(GeTe_4)_{100-x}In_x$ in Figure 1 gives us information that prepared models have maximum angle distribution at around 88–100° and a contribution lower than 180° in amorphous state. The presence of a small peak at around 60° in the angle distribution function is due to a very small fraction of three membered rings. This result indicates that tellurium atoms can lay either in equatorial plane (90°) of a Ge atom or at its vertices (180°). It also shows that amorphous structure doesn't display a full tetrahe-

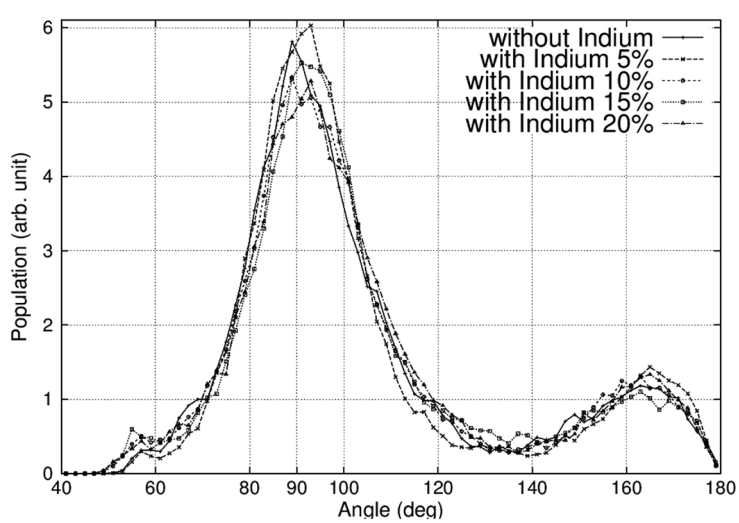

Fig. 1. Bond angle distributions of amorphous state of system $(GeTe_4)_{100-x}In_x$

dral character which should show by max at 109° like in system $GeSe_4$.

With max angle distribution found between 88 and 109° prepared amorphous structures should be made of 4-fold which is partially tetrahedral and defective octahedral-like environment. Structure of $GeTe_4$ show that the distribution peak is around 90° which indicates defective octahedral structure. With indium atom addition, distribution peak shifts to tetrahedral characteristic. It looks like that Ge atom can be bonded as tetrahedral and octahedral structure. Atoms participating in Ge–Te bond favour octahedral coordination and the presence of homopolar Ge–Ge and Ge–In bonds favors the tetrahedral coordination.

Beside bond angle distribution structural information can be gathered from ring statistics. Topology analysis of amorphous, liquid or crystalline systems is often based on part of structural information which can be represented in the graph theory using nodes for the atoms and links for the bonds. A series of nodes and links connected sequentially without overlap is called a path. Following this definition a ring is therefore simply a closed path.

The ring statistics is an important structural parameter to investigate crystal growth in amorphous-crystal transition. Ring calculation in present study uses the definition of ring which was proposed by Guttman [15], who defines a ring as the shortest path which comes back to a given node (or atom) from one of its nearest neighbors.

Bond angle distribution analysis suggests that $(GeTe_4)_{100-x}In_x$ structure should be made from 4-fold rings. 4-fold rings are the basic structural elements of rocksalt crystal. Therefore it is important to investigate their distribution in amorphous state and during crystallization processes.

Result of ring statistics calculation is shown in Figure 2. As expected, ring statistics have good agreement with bond angle distribution analysis. $(GeTe_4)_{100-x}In_x$ structure shows that amorphous $(GeTe_4)_{100-x}In_x$ has a significant number of 4-fold rings with most of them being in the form ABAB (A=Ge, In; B=Te). In 2008, Hegedus and Elliot showed that rapid phase transitions in phase change material GST due to the presence of crystal-nuclei seeds (fragments of octahedral rocksalt structure which is 4-fold rings) in amorphous states [16]. From bond angle distribution and rings statistics result, it looks that Ge-Te-In system has similar characteristics with GST. So it is plausible to assume that 4-fold rings can be responsible to the rapid crystal growth in crystal-amorphous transition in Ge–Te–In system.

Crystallization is very fast in prepared models. Figure 3 shows snapshots of atomic configuration of 80 atoms of $GeTe_4$ in amorphous state and partially crystals form produced by slow cooling of the melt. Crystallization event is starting to occur only after 150 ps. It can be seen that crystals have the rocksalt-like structure characteristic similar with phase change GST materials [16, 17].

The time evolution of 4-fold rings that are crystal-nuclei seeds and the building blocks of the rocksalt structure are presented in Figure 4. Beside Hegedus [16], the significance of four-fold rings to phase transition in phase change materials GST also has been investigated by Kohara [18] using reverse Monte

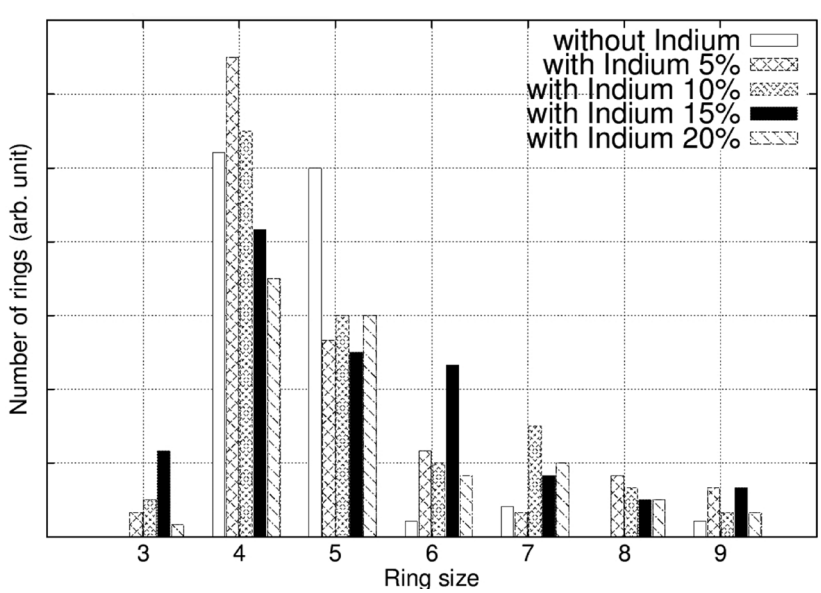

Fig. 2. Ring statistics of amorphous state of system $(GeTe_4)_{100-x}In_x$

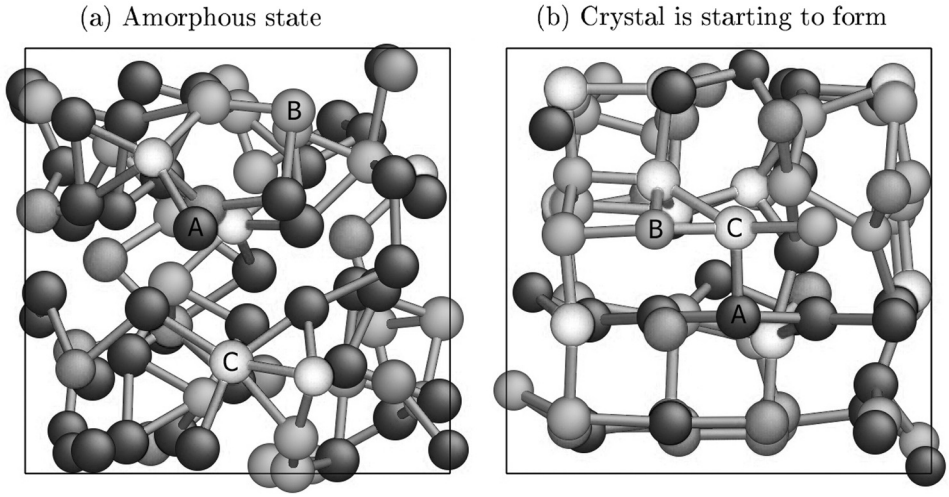

Fig. 3. Snapshots of atomic configuration of (a) amorphous $GeTe_4$ (b) crystallization event that is starting to occur after 150 ps (A: atom with coordination number 3, B: atom with coordination number 4, C: atom with coordination number 5)

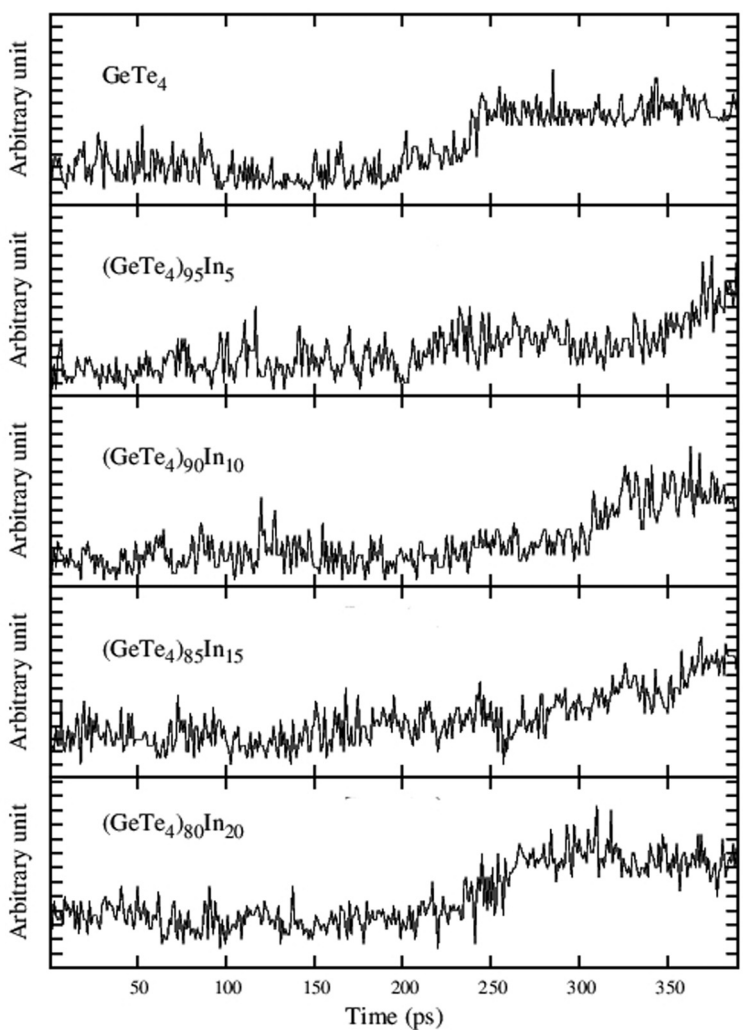

Fig. 4. Number of four-fold rings evolution of system $(GeTe_4)_{100-x}In_x$ with $x = 0, 5, 10, 15, 20$ during 400 ps quench

Carlo simulations and by Akola [20]. Figure 4 shows that crystalline fraction of prepared samples increase after 200 ps. The binary $GeTe_4$ system goes through rapid crystallization between 200–250 ps and for ternary $(GeTe_4)_{100-x}In_x$ rapid crystallization occur after 250 ps. This result is expected because model for binary system has fewer atoms than model for ternary system. For all prepared samples, crystallization occurs in hundreds of picoseconds.

CONCLUSSION

Models of $(GeTe_4)_{100-x}In_x$ with x = 0, 5, 10, 15, 20 have been made using melt quenching AIMD. Calculation results of bond angle distributions suggest that the structure of prepared amorphous system should be made of 4-fold coordinated structure which is partially tetrahedral and defective octahedral-like environment. Ring statistics investigation of amorphous $(GeTe_4)_{100-x}In_x$ suggest that structure of $(GeTe_4)_{100-x}In_x$ with x = 0, 5, 10, 15, 20 have a significant number of 4-fold rings which responsible to the rapid crystal growth in crystal-amorphous transition. Results of time evolution of 4-fold rings investigation show that crystallization of samples with 80–100 atoms occur in hundreds of picoseconds. All these results show promising properties as candidates of phase change material. With further development, Ge-Te-In system has potential to be applied as new phase change materials.

REFERENCES

1. M. Boniardi, D. Ielmini, T. Tortorelli, A. Redaelli, A. Pirovano, M. Allegra, M. Magistretti, C. Bresolin, D. Erbetta, A. Modelli, E. Varesi, F. Pellizzer, A. L. Lacaita, R. Bez, *Solid-State Electronics*, **58**, (2011).
2. V. Sousa, *Microelectronic Engineering*, **88**, 5 (2011).
3. S. A. Kozyukhin, A. I. Popov, E. N. Voronkov, *Thin Solid Films*, **518**, 20 (2010.
4. A. Abrutis, V. Plausinaitiene, M. Skapas, C. Wiemer, O. Salicio, M. Longo, A. Pirovano, J. Siegel, W. Gawelda, S. Rushworth and C. Giesen, *Microelectronic Engineering*, **85**, 12 (2008).
5. K. Kolev, C. Popov, T. Petkova, P. Petkov, I. N. Mihailescu, J. P. Reithmaier, *Sensors and Actuators B: Chemical*, **143**, 1 (2009).
6. V. S Vassilev, S.V Boycheva, *Talanta*, **67**, 1 (2005).
7. A. V. Rode, A. Zakery, M. Samoc, R. B. Charters, E. G. Gamaly, B. Luther-Davies, *Applied Surface Science*, 197 (2002).
8. J. Hu, V. Tarasov, N. Carlie, L. Petit, A. Agarwal, K. Richardson, L. Kimerling, *Optical Materials*, **30**, 10 (2008).
9. C. Florea, J. S. Sanghera, I. D Aggarwal, *Optical Materials*, **30**, 10 (2008).
10. S. Raoux, M. Wuttig (eds), Phase change materials and applications, Springer, 2008.
11. D. Lencer, M. Salinga, B. Grabowski, T. Hickel, J. Neugenauer, M. Wuttig, *Nature Mat*., **7**, 972 (2008).
12. R. Car, M. Parrinello, *Physical Review Letters*, **55**, 22 (1985).
13. E. Artacho, E. Anglada, O. Dieguez, J.D. Gale, A. García, J. Junquera, R.M. Martin, P. Ordejón, J.M. Pruneda, D. Sánchez-Portal, J. M. Soler, *J. Phys.: Condens. Matter*, 20 (2008).
14. V. Ivanova, A. Zaidan, P. Ilchev, Y. Trifonova, P. Petkov, *Advances in Natural Science: Theory & Applications*, **1**, 3 (2012).
15. L. Guttman. *J. Non-Cryst. Solids*., **116**, 145 (1990).
16. J. Hegedus, S. R. Elliot, *Nature Mat*., **7**, 399 (2008).
17. T. Matsunaga, N. Yamada, Y. Kubota, *Acta Crystallogr. B*, **60**, 685 (2004).
18. Kohara, S. et al., *Appl. Phys. Lett*., **89**, 201910 (2006).
19. J. Akola, R. O. Jones, *Phys. Rev. B*, **76**, 235201 (2007).

AB INITIO СИМУЛАЦИЯ НА КРИСТАЛИЗАЦИЯТА НА АМОРФНИ ОБРАЗЦИ ОТ СИСТЕМАТА Ge–Te–In

А. Зайдан[1, 2]*, Вл. Иванова[1], П. Петков[1]

[1] Катедра Физика, Химико-технологичен и металургичен университет, бул. „Кл. Охридски“ № 8, 1756 София, България
[2] Катедра Физика, Факултет по наука и технологии, Университет Аирланга, Сурабая 60115, Индонезия

Постъпила февруари, 2013 г.; приета май, 2013 г.

(Резюме)

Материалите с промяна на фазата са многообещаващи кандидати за изработване на памети, поради способността им да преминават от аморфно в кристално състояние, или обратното, при прилагане на топлина. Поради бързия преход между кристалната и аморфната форма, халкогенидните материали на базата на Ge–Te се разглеждат като потенциален кандидат за материали с промяна на фазата. Изследването на аморфни структури $GeTe_4$, дотирани с индий показва, че аморфната система Ge–Te–In съдържа значителен брой четворни пръстени, които са отговорни за бързия растеж на кристалите при прехода кристал–аморфно състояние. В настоящото проучване е използвана *ab initio* молекулярна динамика за изучаване на процеса на кристализация в $GeTe_4$ при дотиране с индий (5, 10, 15 и 20%). Структурните промени в процеса на прехода са анализирани чрез статистическа оценка на пръстените. Резултатите от *ab initio* симулациите показват, че кристализацията на образци с 80–100 атоми протича за няколко стотин пикосекунди.

Bulgarian Chemical Communications, Volume 45, Number 4 (pp. 560–567) 2013

Polycaprolactam crystal structure. I. Gamma–alpha polymorphic transition

S. Uzova[1], A. Popov[2], V. Velev[3], T. Angelov[4],
S. Mihaleva[2], Ch. Uzov[2]

[1] *PST "Prof. dr. Assen Zlatarov" – Burgas, 8000 Burgas, Bulgaria*
[2] *Assen Zlatarov University, 8010 Burgas, Bulgaria*
[3] *Konstantin Preslavski University, 9712 Shumen, Bulgaria*
[4] *Lukoil Neftochim Burgas JSC, Burgas, Bulgaria*

Received February, 2013; Revised May, 2013

It was examined the polycaprolactam gamma–alpha transition as its major structural transformation. The specific behavior of the polymer in the reversible alpha–gamma transition was established. It was found that the transition progress was accompanied by a critical deformations of the crystal cells. The gamma–alpha transition is presented as the first stage of the polycaprolactam crystalline phase development by forming of a stable configuration in the package of the macromolecular chain segments. The influence of the quantitative accumulation of gamma phase and its development during the transition in the alpha phase has been also investigated. It is proposed a methodology for the realization of the study and criteria for evaluation. A mechanism of the structural transitions has been suggested.

Key words: polycaprolactam, crystal structure, polymorphism.

INTRODUCTION

Crystal structure of poly(ε-caprolactam) (PCL) examination has been intensified since 1942 [1, 2]. It is known for its polymorphic great diversity [1–21]. However, the results are very inconsistent, conflicting and sometimes controversial [1–35]. This applies particularly for thermal initiated polymorphic transitions. They are highly dependent on the conditions of implementation. Most of these conditions are difficult to be controlled precisely. This makes it difficult to predict the structure and performance properties of materials and products.

To establish the relation between structure and properties is necessary to know well the structure. The structural diversity to be well defined. To describe accurately and unambiguously polymorphism of PCL it is necessary to assess the quality of polymorphic forms. Only then its polymorphic transitions can be precisely clarified.

So, first, it is necessary to clarify the terms of the alpha–gamma transition, i.e. to assess the perfection of the crystalline phase of PCL. Only then the perfection of the crystal forms can be evaluated and its structural diversity thoroughly described.

EXPERIMENTAL

Different types of polycaprolactam (PCL) with different molecular weight and molecular mass distribution (characteristic viscosity in 1%-ile sol. N_2SO_4 $\eta_{otn.}$ = 2.11–2.83) were used with a content of low molecular weight compounds in the range 1.0–12.0% fat. and moisture content of 0.1 to 0.01% mass as a prerequisite to obtaining crystal structures of varying sophistication. Thin films were formed in a wide range of molding conditions: $T_{m.}$ = 215–240 °C and $T_{cool.}$ = –196–200 °C.

Using universal powder X-ray diffractometers URD-6 ("Präzisionsmechanik – Freiburg", Germany) and DRON-3 with a high temperature camera ATM-2000 ("Burevestnik – St. Petersburg", Russia) using $Cu_{K\alpha}$-radiation (β-filtered with Ni-Filter, λ = 1,5418 Å), low and high temperature X-ray diffraction at different temperature-time regimes of simultaneous modification was received

Software package "Origin 5.0" was used for decomposition multiply peaks in determining polymorphic forms of PCL.

* To whom all correspondence should be sent:
E-mail: hristo_uzov@abv.bg

RESULTS AND DISCUSSION

The experiment involves heating and cooling under different conditions of thin films of PCL. The main purpose of the experiment is to study the polymorphic forms of PCL and transitions between them, mainly gamma–alpha transition. This is the main polymorphic transition in PCL between the unstable gamma and the stable alpha-crystalline polymorphic modifications. The degree of completeness of the transition forms the structure that determines the operating properties of the polymer. This is the structure on which the possibility for further processing and modification of polymeric material depends in order to optimize its operational properties. The content of the unstable gamma form enhances the compressibility of the structures in terms of thermal, mechanical, heat-mechanical and others complex physical fields. This is extremely important for the tape, foil and fiber-forming materials.

According to recent literature and our data, the heat of a super cooled melt of PCL forms initially its gamma form. The continuation of the process leads to improvement of the crystal structure to the stable alpha form. In this transition, beta form inevitably presents in detectable amounts, regardless of its strong conditional dependence. The impression is of its buffer, intermediate, facilitating role in the gamma–alpha transition. On the other hand, its satellite presence in the advanced stable structure is observed after the apparent depletion of the gamma form. It is not certain that there no traces of the beta-form remain even after prolonged annealing, because it is structurally very similar to the alpha form[8, 24].

For the first time the beta-form is mentioned by Holmes and coworkers'1955 together with the alpha-form definition [8]. In this sense, the beta-form can be called alpha-imperfect form. Because of its presence and influence on the determination of the partial coordinates of the basic alpha-form by Holmes it is necessary their later correction by Simon [24].

It is not accidental that some authors have assumed its presence in the form of a mixture from alpha and gamma forms. Thus, the transition delta–gamma–beta–alpha can be represented as a continuous process of improvement of the PCL crystalline phase. The whole structural reorganization occurs without cardinal displacement and geometrical modifications, while the delta–gamma and beta–alpha stages are realized permanently and almost unnoticed. Therefore, in first approximation, we can say that the compaction of the PCL structure through repacking of chain segments in the crystalline phase is realized by gamma–alpha transition. This transition is realized through the redistribution of hydrogen bonds (H-bonds) from the nearest neighboring segments in different crystallographic directions, especially in the plains of molecular folding.

The carried out experiments showed the presence of extremely rich possibilities of structural conversions. Depending on the type of polymer, the geometry of the samples, their starting structures, schemes and the conditions of temperature modification and simultaneous X-ray scanning and so on, get the impression of infinite structural diversity and ambiguous reorganization behavior.

This sets the need for criteria and systems of quantitative evaluation of the crystalline phase perfection. The need for such qualifying of the crystalline phase quality at each stage and every moment of the structural adjustment comes from the need to assess the degree of completion of polymorphic transitions. Moreover, the characterization of the crystalline phase is necessary for elucidation of simultaneous presence of the possible PCL crystal forms with different amounts and perfection. This fact determines the possibility and necessity of the simultaneous running of the possible polymorphic transitions. Under different conditions, however, it can change the direction of the various processes and increase the ambiguity of the results and their interpretation.

Some of the results from the study on the gamma–alpha transition of PCL are shown in Fig. 1 and in Table 1. When heating the δ-form (super cooled melt) from 20–30 °C to 70–80 °C with heating rate of 50 °C/min no significant changes in its dust diffraction occur. It is observed the appearance of γ-form in the range from 80–90 °C to 100–110 °C. Its improvement continued up to 160 °C. The diffraction reflection (100γ) is migrating into the diffraction of about 21.1 to about 22.6–22.7 θ. The gamma–alpha transition is realized within the interval 160–190 °C.

The intensity of overlaid reflections $(200)_{\beta,\alpha}$ and $(002)_{\beta,\alpha}/(202)_{\beta,\alpha}$ grows and their positions divide noticeably at a temperature about 180 °C. The angular positions at the time of occurrence are about 20, 60 °2θ and 22.85 °2θ, respectively. At the same time, the position of the reflection (100γ) started reverse migration to the value of 21.15 °θ. The probable cause of the observed effects is the started redistribution of the hydrogen bonds from all closest neighboring segments in different crystallographic directions only in the plains of folding of the macromolecular chains.

The position 21.15 °2θ, of $(100)_{\gamma}$ corresponds to the largest (about 4.2 Å) achievable for gamma-form distance between the segments axes in the crystalline phase. It is probably possible because of the optimal heating speed of 5 °C/min up to that temperature, the tempering during the X-ray scanning and the appropriate objects geometry. This dis-

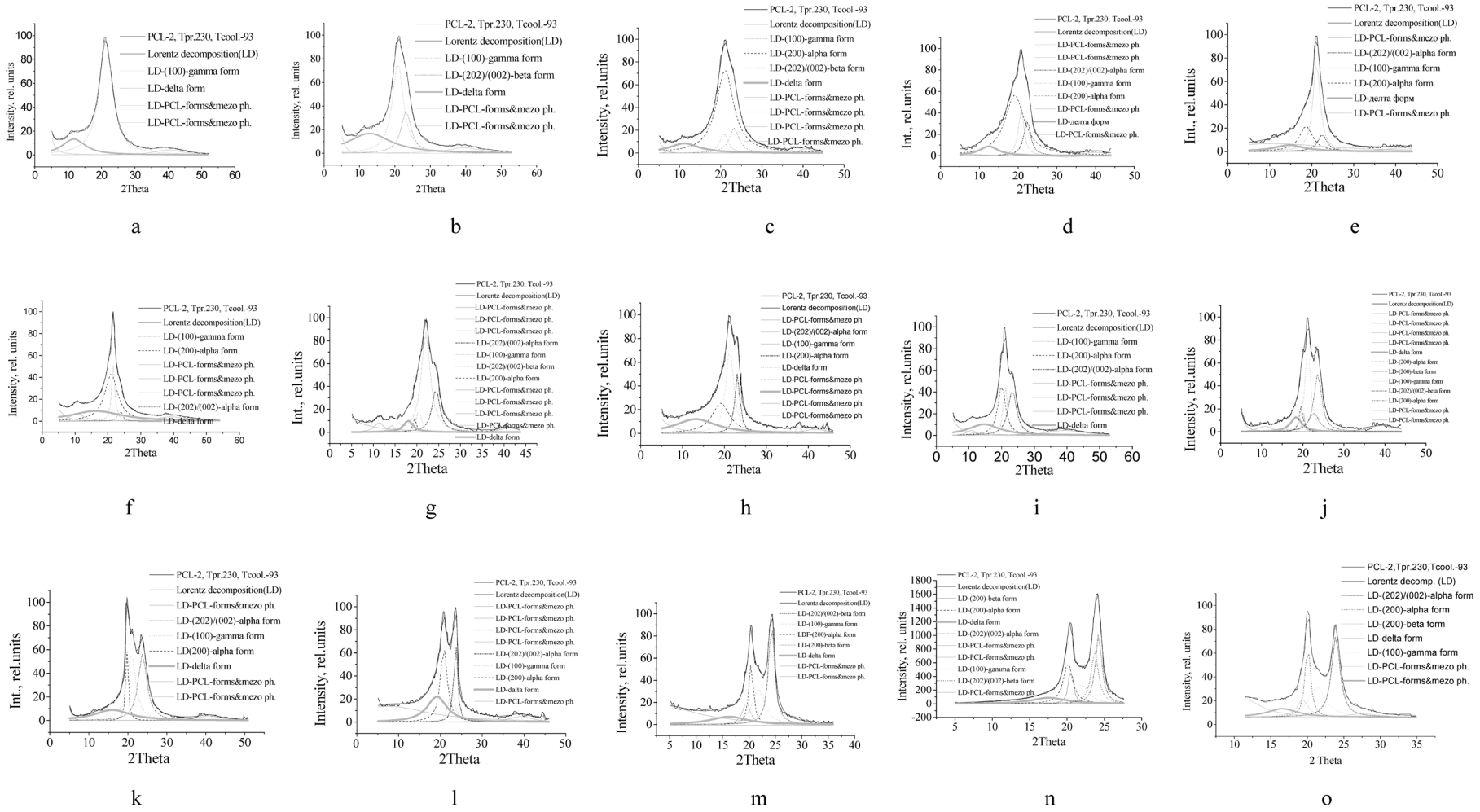
a
PCL-2, Tpr.230, Tcool.-93
Lorentz decomposition(LD)
LD-(100)-gamma form
LD-delta form
LD-PCL-forms&mezo ph.
LD-PCL-forms&mezo ph.
Intensity, rel. units
2Theta
b
PCL-2, Tpr.230, Tcool.-93
Lorentz decomposition(LD)
LD-(100)-gamma form
LD-(202)/(002)-beta form
LD-delta form
LD-PCL-forms&mezo ph.
LD-PCL-forms&mezo ph.
Intensity, rel. units
2Theta
c
PCL-2, Tpr.230, Tcool.-93
Lorentz decomposition(LD)
LD-(100)-gamma form
LD-(200)-alpha form
LD-(202)/(002)-beta form
LD-delta form
LD-PCL-forms&mezo ph.
LD-PCL-forms&mezo ph.
LD-PCL-forms&mezo ph.
LD-PCL-forms&mezo ph.
Intensity, rel.units
2Theta
d
PCL-2, Tpr.230, Tcool.-93
Lorentz decomposition(LD)
LD-PCL-forms&mezo ph.
LD-PCL-forms&mezo ph.
LD-(202)/(002)-alpha form
LD-(100)-gamma form
LD-(200)-alpha form
LD-PCL-forms&mezo ph.
LD-делта форм
LD-PCL-forms&mezo ph.
Int., rel.units
2Theta
e
PCL-2, Tpr.230, Tcool.-93
Lorentz decomposition(LD)
LD-PCL-forms&mezo ph.
LD-(202)/(002)-alpha form
LD-(100)-gamma form
LD-(200)-alpha form
LD-делта форм
LD-PCL-forms&mezo ph.
Int., rel.units
2Theta
f
PCL-2, Tpr.230, Tcool.-93
Lorentz decomposition(LD)
LD-(100)-gamma form
LD-(200)-alpha form
LD-PCL-forms&mezo ph.
LD-PCL-forms&mezo ph.
LD-PCL-forms&mezo ph.
LD-(202)/(002)-alpha form
LD-delta form
Intensity, rel. units
2Theta
g
PCL-2, Tpr.230, Tcool.-93
Lorentz decomposition(LD)
LD-PCL-forms&mezo ph.
LD-PCL-forms&mezo ph.
LD-PCL-forms&mezo ph.
LD-(202)/(002)-alpha form
LD-(100)-gamma form
LD-(202)/(002)-beta form
LD-(200)-alpha form
LD-PCL-forms&mezo ph.
LD-PCL-forms&mezo ph.
LD-PCL-forms&mezo ph.
LD-PCL-forms&mezo ph.
LD-delta form
Int., rel.units
2Theta
h
PCL-2, Tpr.230, Tcool.-93
Lorentz decomposition(LD)
LD-PCL-forms&mezo ph.
LD-(202)/(002)-alpha form
LD-(100)-gamma form
LD-(200)-alpha form
LD-delta form
LD-PCL-forms&mezo ph.
LD-PCL-forms&mezo ph.
LD-PCL-forms&mezo ph.
Intensity, rel.units
2Theta
i
PCL-2, Tpr.230, Tcool.-93
Lorentz decomposition(LD)
LD-(100)-gamma form
LD-(200)-alpha form
LD-(202)/(002)-alpha form
LD-PCL-forms&mezo ph.
LD-PCL-forms&mezo ph.
LD-PCL-forms&mezo ph.
LD-delta form
Intensity, rel.units
2Theta
j
PCL-2, Tpr.230, Tcool.-93
Lorentz decomposition(LD)
LD-PCL-forms&mezo ph.
LD-PCL-forms&mezo ph.
LD-PCL-forms&mezo ph.
LD-PCL-forms&mezo ph.
LD-delta form
LD-(200)-alpha form
LD-(200)-beta form
LD-(100)-gamma form
LD-(202)/(002)-beta form
LD-(200)-alpha form
LD-PCL-forms&mezo ph.
LD-PCL-forms&mezo ph.
Intensity, rel.units
2Theta
k
PCL-2, Tpr.230, Tcool.-93
Lorentz decomposition(LD)
LD-PCL-forms&mezo ph.
LD-(202)/(002)-alpha form
LD-(100)-gamma form
LD(200)-alpha form
LD-delta form
LD-PCL-forms&mezo ph.
LD-PCL-forms&mezo ph.
Int., rel.units
2Theta
l
PCL-2, Tpr.230, Tcool.-93
Lorentz decomposition(LD)
LD-PCL-forms&mezo ph.
LD-PCL-forms&mezo ph.
LD-PCL-forms&mezo ph.
LD-PCL-forms&mezo ph.
LD-(202)/(002)-alpha form
LD-(100)-gamma form
LD-(200)-alpha form
LD-dalta form
LD-PCL-forms&mezo ph.
Intensity, rel.units
2Theta
m
PCL-2, Tpr.230, Tcool.-93
Lorentz decomposition(LD)
LD-(202)/(002)-beta form
LD-(100)-gamma form
LDF-(200)-alpha form
LD-(200)-beta form
LD-delta form
LD-PCL-forms&mezo ph.
LD-PCL-forms&mezo ph.
Intensity, rel.units
2Theta
n
PCL-2, Tpr.230, Tcool.-93
Lorentz decomposition(LD)
LD-(200)-beta form
LD-(200)-alpha form
LD-delta form
LD-(202)/(002)-alpha form
LD-PCL-forms&mezo ph.
LD-PCL-forms&mezo ph.
LD-(100)-gamma form
LD-(202)/(002)-beta form
LD-PCL-forms&mezo ph.
Intensity, rel. units
2Theta
o
PCL-2,Tpr.230,Tcool.-93
Lorentz decomp. (LD)
LD-(202)/(002)-alpha form
LD-(200)-alpha form
LD-(200)-beta form
LD-delta form
LD-(100)-gamma form
LD-PCL-forms&mezo ph.
LD-PCL-forms&mezo ph.
Intensity, rel. units
2 Theta

←

Fig. 1. Some of the high-temperature powder X-ray diffraction, showing gamma–alpha transition in PCL: a) Lorentz decomposition of part of the powder diffraction curve from thin isotropic PCL film, molded by pressing at 235 °C and tempered at –93°C, scanned at 20 °C. The main single peak of the decomposed doublet, almost coinciding with the diffraction curve at the distribution about 21 °2θ can be accepted as an equivalent to a 100_{γ} on the diffuse halo of the super cooled melt (δ-phase); b) Lorentz decomposition of part of the powder diffraction curve from thin isotropic PCL film, molded by pressing at 235 °C and tempered at –93 °C, scanned at 120 °C, after heating from 20 °C with a speed of 5°/min and tempering for 3 min. Minor change of the profile of the multiple experimental peak after decomposition shows the appearance of additional peak (right to larger diffraction angles), corresponding to possible $202/002_{\beta,\alpha}$; c) Lorentz decomposition of part of the powder diffraction curve from thin isotropic PCL film, molded by pressing at 235 °C and tempered at –93 °C and scanned at 140 °C (after 120 °C). Again, minor modification of the profile of the multiple peak does not hide, however, the possibility for significant structural changes through repackaging of chain segments and possible decomposition of $200_{\alpha,\beta}$, 100_{γ}, $202/002_{\alpha,\beta}$, respectively; d) Lorentz decomposition of part of the powder diffraction curve from thin isotropic PCL film, molded by pressing at 235 °C and tempered at –93 °C and scanned at 160 °C (after 140 °C) shows a strong change in the proportion of co-existing with different perfection phases; e) Lorentz decomposition of part of the powder diffraction curve from thin isotropic PCL film, molded by pressing at 235 °C and tempered at –93 °C and scanned at 180 °C (after 160 °C) already shows a strong increase with the temperature increasing of the amount of γ-crystalline form; f) Lorentz decomposition of part of the powder diffraction curve from thin isotropic PCL film, molded by pressing at 235 °C and tempered at –93 °C and scanned at 190 °C (after 180 °C). It is observed a picture of approximation and intensity decrease of reflections of different phases at the expense of maintaining priority wheelbase of around 4.22 Å (priority baseline condition for obtaining α-perfect shape after polymorphic transition γ-β-α at sufficient cooling); g) Lorentz decomposition of part of the powder diffraction curve from thin isotropic PCL film, molded by pressing at 235 °C and tempered at –93 °C, scanned at 180 °C (after cooling from 220, 200 and 190 °C with a speed of 5°/min and tempering for 3 min). Shows improvement (away of the decomposed peaks corresponding to the reflections about 20 and 24 °2θ) and quantitative growth of α-and β-forms; h) Lorentz decomposition of part of the powder diffraction curve from thin isotropic PCL film, molded by pressing at 235 °C and tempered at –93 °C, scanned at 160 °C (after cooling from 220, 200, 190, 180 and 170 °C with a speed of 5°/min and tempering for 3 min). Shows improvement (away of the decomposed peaks corresponding to the reflections about 20 and 24 °2θ) and quantitative growth of α-and β-forms; i) Lorentz decomposition of part of the powder diffraction curve from thin isotropic PCL film, molded by pressing at 235 °C and tempered at –93 °C, scanned at 150 °C (after cooling from 220 200, 190, 180, 170 and 160 °C with a speed of 5°/min and tempering for 3 min). Shows improvement (away of the decomposed peaks corresponding to the reflections about 20 and 24 °2θ) and quantitative growth of α-and β-forms; j) Lorentz decomposition of part of the powder diffraction curve from thin isotropic PCL film, molded by pressing at 235 °C and tempered at –93 °C, scanned at 140 °C (after cooling from 220, 200, 190, 180, 170, 160 and 150 °C with a speed of 5°/min and tempering for 3 min). Shows improvement (away of the decomposed peaks corresponding to the reflections about 20 and 24 °2θ) and quantitative growth of α-and β-forms; k) Lorentz decomposition of part of the powder diffraction curve from thin isotropic PCL film, molded by pressing at 235 °C and tempered at –93 °C, scanned at 130 °C (after cooling from 220, 200, 190, 180, 170, 160, 150 and 140 °C with a speed of 5°/min and tempering for 3 min). Shows improvement (away of the decomposed peaks corresponding to the reflections about 20 and 24 °2θ) and quantitative growth of α-and β-forms; l) Lorentz decomposition of part of the powder diffraction curve from thin isotropic PCL film, molded by pressing at 235 °C and tempered at –93 °C, scanned at 120 °C (after cooling from 220, 200, 190, 180, 170, 160, 150, 140 and 130 °C with a speed of 5°/min and tempering for 3 min). Shows improvement (away of the decomposed peaks corresponding to the reflections about 20 and 24 °2θ) and quantitative growth of α-and β-forms; m) Lorentz decomposition of part of the powder diffraction curve from thin isotropic PCL film, molded by pressing at 235 °C and tempered at –93 °C, scanned at 110 °C (after cooling from 220, 200, 190, 180, 170, 160, 150, 140, 130 and 120 °C with a speed of 5°/min and tempering for 3 min). Shows improvement (away of the decomposed peaks corresponding to the reflections about 20 and 24 °2θ) and quantitative growth of α-and β-forms; n) Lorentz decomposition of part of the powder diffraction curve from thin isotropic PCL film, molded by pressing at 235 °C and tempered at –93 °C, scanned at 100 °C (after cooling from 220, 200, 190, 180, 170, 160, 150, 140, 130, 120 and 110 °C with a speed of 5°/min and tempering for 3 min). Shows improvement (away of the decomposed peaks corresponding to the reflections about 20 and 24 °2θ) and quantitative growth of α-and β-forms; o) Lorentz decomposition of part of the powder diffraction curve from thin isotropic PCL film, molded by pressing at 235 °C and tempered at –93 °C, scanned at 20 °C (after cooling from 220, 200, 190, 180, 170, 160, 150, 140, 130, 120, 110 and 100 °C with a speed of 5°/min and tempering for 3 min). Multiply peaks observed in the geometry of the intensity distribution in the diffraction experiments are decomposed by Gaussian and Lorentzian distributions corresponding to the main polymorphic forms of PCL.; This allows control of the polymorphic composition of PCL during thermal modification.

Table 1. Illustratively represent a double cycle of heating and cooling of 50 μm PCL-2 foil, pressed at 498 K and cooled to 293 K in air

No	$T_{ск.}$, °C	Angle deviation on thermal modification of the diffraction reflections of the PCL																					
		Alpha-form								Beta-form*								Gamma-form					
		V = 5 °C/min				V = 10 °C/min				V = 5 °C/min				V = 10 °C/min				V = 5 °C/min		V = 10 °C/min	
		heating		cooling		heating		cooling		heating		cooling		heating		cooling		heating	cooling	heating	cooling
		(200)	(002)/(202)	(200)	(002)/(202)	(200)	(002)/(202)	(200)	(002)/(202)	(200)	(002)/(202)	(200)	(002)/(202)	(200)	(002)/(202)	(200)	(002)/(202)	(100)	(100)	(100)	(100)
		2θ	2θ	2θ	2θ	2θ	2θ	2θ	2θ	2θ	2θ	2θ	2θ	2θ	2θ	2θ	2θ	2θ	2θ	2θ	2θ
1	20	20.10	23.90	20.36	23.50	20.10	23.90	20.36	23.49	20.00	24.11	20.08	24.11	20.00	24.10	20.09	24.09	22.30	22.28	22.30	22.31
2	30	20.10	23.90	20.37	23.49	20.10	23.90	20.37	23.48	20.00	24.10	20.08	24.10	20.00	24.10	20.09	24.09	22.30	22.28	22.30	22.31
3	40	20.10	23.90	20.37	23.49	20.10	23.90	20.37	23.48	20.00	24.10	20.09	24.10	20.00	24.10	20.09	24.09	22.40	22.28	22.33	22.31
4	50	20.11	23.90	20.37	23.48	20.10	23.90	20.37	23.48	20.01	24.09	20.09	24.09	20.01	24.09	20.10	24.08	22.40	22.28	22.38	22.31
5	60	20.11	23.89	20.38	23.48	20.11	23.89	20.38	23.47	20.01	24.09	20.09	24.09	20.01	24.09	20.10	24.08	22.50	22.28	22.45	22.31
6	70	20.11	23.89	20.38	23.47	20.11	23.89	20.38	23.47	20.01	24.09	20.10	24.09	20.01	24.09	20.11	24.07	22.50	22.29	22.46	22.31
7	80	20.12	23.88	20.38	23.47	20.11	23.89	20.38	23.47	20.01	24.08	20.10	24.08	20.01	24.08	20.11	24.07	22.50	22.29	22.47	22.31
8	90	20.12	23.87	20.39	23.46	20.11	23.88	20.39	23.46	20.02	24.07	20.10	24.08	20.02	24.07	20.12	24.06	22.60	22.29	22.51	22.31
9	100	20.13	23.87	20.39	23.45	20.12	23.87	20.39	23.45	20.03	24.07	20.10	24.08	20.02	24.07	20.13	24.05	22.70	22.29	22.55	22.31
10	110	20.14	23.86	20.39	23.44	20.12	23.86	20.39	23.44	20.04	24.06	20.11	24.07	20.02	24.06	20.14	24.05	22.80	22.29	22.66	22.32
11	120	20.15	23.85	20.40	23.42	20.12	23.85	20.40	23.43	20.06	24.05	20.13	24.07	20.03	24.05	20.16	24.05	22.81	22.29	22.72	22.32
12	130	20.20	23.80	20.40	23.41	20.14	23.80	20.40	23.42	20.08	24.00	20.15	24.07	20.04	24.00	20.17	24.04	22.83	22.29	22.74	22.33
13	140	20.25	23.70	20.40	23.40	20.23	23.70	20.40	23.40	20.09	24.00	20.17	24.07	20.05	24.00	20.18	24.03	22.85	22.29	22.76	22.33
14	150	20.30	23.60	20.41	23.35	20.27	23.60	20.41	23.35	20.10	24.00	20.19	24.06	20.06	24.00	20.19	24.02	22.87	22.30	22.78	22.36
15	160	20.35	23.50	20.41	23.35	20.31	23.50	20.41	23.35	20.11	24.00	20.21	24.05	20.07	24.00	20.20	24.01	22.90	22.30	22.82	22.34
16	165	20.40	23.40	20.41	23.35	20.35	23.40	20.49	23.35	20.12	24.00	20.22	24.00	20.08	24.00	20.22	23.95	22.92	22.30	22.88	22.34
17	170	20.45	23.30	20.44	23.35	20.41	23.30	20.52	23.34	20.16	23.90	20.25	23.90	20.09	23.90	20.25	23.82	22.95	22.30	22.90	22.35
18	175	20.50	23.20	20.48	23.30	20.45	23.20	20.58	23.34	20.22	23.80	20.29	23.80	20.11	23.80	20.30	23.75	22.98	22.31	22.95	22.35
19	180	20.55	23.10	20.51	23.20	20.49	23.10	20.65	23.24	20.28	23.70	20.32	23.70	20.16	23.70	20.32	23.61	23.01	22.31	23.00	22.36
20	185	20.60	23.00	20.58	23.00	20.65	23.00	20.69	23.05	20.33	23.60	20.39	23.60	20.25	23.60	20.35	23.50	23.03	22.31	23.03	22.36
21	190	20.65	22.90	20.62	22.90	20.69	22.90	20.70	22.95	20.39	23.50	20.44	23.50	20.36	23.50	20.46	23.39	23.05	22.33	23.05	22.35
22	195	20.70	22.80	20.68	22.80	20.74	22.80	20.79	22.82	20.44	23.40	20.51	23.40	20.43	23.40	20.55	23.27	23.07	22.35	23.07	22.36
23	200	20.75	22.70	20.71	22.70	20.80	22.70	20.85	22.77	20.49	23.30	20.61	23.30	20.48	23.30	20.63	23.15	23.09	22.50	23.09	22.51
24	205	20.80	22.60	20.74	22.60	20.85	22.60	20.87	22.66	20.55	23.20	20.69	23.20	20.52	23.20	20.78	23.09	23.11	22.71	23.11	22.73
25	210	20.85	22.50	20.85	22.50	20.87	22.50	20.88	22.54	20.60	23.10	20.72	23.10	20.69	23.10	20.73	23.03	23.14	22.85	23.14	22.86
26	215	20.90	22.40	20.84	22.40	20.88	22.40	20.88	22.42	20.66	23.00	20.77	23.00	20.65	23.00	20.74	22.97	23.17	23.02	23.17	23.02
27	220	20.95	22.35	20.94	22.35	20.89	22.35	20.89	22.35	20.72	22.95	20.79	22.95	20.71	22.95	20.76	22.93	23.22	23.21	23.22	23.21
28	225	21.00	22.30	21.00	22.30	20.90	22.30	20.90	22.30	20.79	22.90	20.79	22.90	20.77	22.90	20.77	22.90	23.31	23.31	23.31	23.31

* Note: Often the angular deviations of the beta-form are within the boundaries of the method uncertainty and methodology of recording of the peak positions as compared with the same peaks of the alpha-form. But the gravity center of the integrated intensity of the delta-form coincides with the position of the gamma form peak. Furthermore, gamma and alpha forms fully characterized the PCL structure. Therefore, beta and delta forms can not be illustrated.

tance is close to the thermodynamic advantageous fold width during the PCL chains folding. Thus it makes possible to create H-bonds between the opposite targeted segments in the folding planes that forms its alpha form.

After this point, the amount of the gamma form reduces and it loses its perfection. The smaller the peak of the diffraction reflection (100)γ is, so much the visual reporting position is inaccurate.

In the geometry of the intensity distribution of the high-temperature powder diffraction, it is highly overlapping with $(200)_{\beta,\alpha}$. If the heating rate is higher, the gamma–alpha transition is realized later and on smaller average statistically distances between the segments in the polymer volume. Then it gets mainly the beta form that improved in alpha.

This is indicated by the increased intensity of the $(002)_{\beta,\alpha}/(202)_{\beta,\alpha}$ [8]. Then, the near located peak $(100)_{\gamma}$ overlaps and geometric "draws" from the higher intensity. Decomposition, however, shows the true positions of the diffraction reflections in the Table. They allow the definition of some, albeit rel-

Table 2. An illustrative example of the formation of same structures (Fig. 1, h) by different ways

Object formation and measurement	Thermal modification				
	$V_{modification}$, °C/min	$\tau_{tempering}$, min	n, number of ful cycles	↑↓, heating cooling processes	~α:β:γ:δ, %
$T_{mold.}$=235 $T_{crystall.}$=–93 $PCL-1^{T_{modif.}=120-220}_{T_{scann.}=165}$	5	3	3	3	9:37:45:9
$T_{mold.}$=235 $T_{crystall.}$=20 $PCL-1^{T_{modif.}=120-220}_{T_{scann.}=170}$	4	4	2	2	9:37:45:9
$T_{mold.}$=235 $T_{crystall.}$=200 $PCL-1^{T_{modif.}=120-220}_{T_{scann.}=175}$	3	5	1	1	9:37:45:9
$T_{mold.}$=235 $T_{crystall.}$=–93 $PCL-2^{T_{modif.}=120-220}_{T_{scann.}=180}$	5	3	3	3	9:37:45:9
$T_{mold.}$=235 $T_{crystall.}$=20 $PCL-2^{T_{modif.}=120-220}_{T_{scann.}=185}$	4	4	2	2	9:37:45:9
$T_{mold.}$=235 $T_{crystall.}$=200 $PCL-2^{T_{modif.}=120-220}_{T_{scann.}=185}$	3	5	1	1	9:37:45:9

Table 3. An illustrative example of the formation of different structures by the same ways

Object formation and measurment	Thermal modification				
	$V_{modif.}$, °C/min	$\tau_{tempering}$, min	n, number of ful cycles	↑↓, heating cooling processes	~α:β:γ:δ, %
$T_{mold.}$=235 $T_{crystall.}$=–93 $PCL-1^{T_{modif.}=120-220}_{T_{scann.}=165}$	10	1	5	2	34:34:24:8
$T_{mold.}$=235 $T_{crystall.}$=20 $PCL-1^{T_{modif.}=120-220}_{T_{scann.}=170}$	10	1	5	2	36:33:23:8
$T_{mold.}$=235 $T_{crystall.}$=200 $PCL-1^{T_{modif.}=120-220}_{T_{scann.}=175}$	10	1	5	2	38:36:19:7
$T_{mold.}$=235 $T_{crystall.}$=–93 $PCL-2^{T_{modif.}=120-220}_{T_{scann.}=180}$	10	1	5	2	37:33:22:8
$T_{mold.}$=235 $T_{crystall.}$=20 $PCL-2^{T_{modif.}=120-220}_{T_{scann.}=185}$	10	1	5	2	38:34:21:7
$T_{mold.}$=235 $T_{crystall.}$=200 $PCL-2^{T_{modif.}=120-220}_{T_{scann.}=185}$	10	1	5	2	39:35:19:7

ative temperature-time intervals of the transitions. We can come in many other ways to similar reflections positions, for example, via other schemes, speeds of heating and X-ray scan, other times and exposures of tempering, using other PCL, source structures and geometry of its objects, other combinations etc.

The best justifications for that are the different results by different authors [1–35]. It is therefore necessary to create a unified system for study of the structural reorganization of PCL, with the ability to quantitative assessment of the crystalline phase quality. This would allow an unambiguous and accurate assessment of the implementation of the polymorphic transition.

CONCLUSION

1. It was found that the structural diversity in PCL temperature modification in a wide range of conditions is difficult to be realized by X-ray diffraction interpretation and evaluation. It is proposed simultaneous control with a high temperature powder diffraction and interpretation of information obtained from the structural studies of thin films of PCL with different initial structure after the necessary corrections and decomposition of multiple intensity distribution.

2. Detailed information about the temperature dependence of the possible angular deviations, intensity proportions and profile changes of the polymorphic diffraction reflections in the observed experimental peaks has been obtained. An attempt to analyze the polymorphic reorganizations and especially the main alpha-gamma transition in PCL has been made. Difficulties in the interpretation of the observed effects related to their qualitative and quantitative ambiguities have been shown.

3. The impossibility for precise and positive interpretation of the diffraction (powder diffraction) results from the structural changes in PCL without satisfactory quantitative evaluation of the quality and quantity of polymorphic forms has been assumed. It is very difficult without a quantitative assessment of their perfection as a measure of the completeness of the polymorphic transitions.

4. A conclusion has been drawn about the need to establish the basis of criteria and methodology for practical assessment of the crystalline phase perfection of the main polymorphic forms.

Acknowledgements: *The authors are grateful to the Fund "Scientific investigations" of the Projects NIH-244 from University "Prof. Dr. Assen Zlatarov", Burgas and № 8268 from the University of Shumen, for the support.*

REFERENCES

1. R. Bril, *Zeitschrift fur physikalische Chemie (DDR)*, B, **53**, 61 (1942).
2. R. Brill, *J. Prakt. Chem.*, **161**, 49 (1942).
3. I. Sandeman, A. Keller, *J. Polym. Sci.*, **19**, 401 (1956).
4. H.-J. Radusch, M. Stolp, R. Androsch, *Polymer*, **35**, 3568 (1994).
5. C. W. Bunn, E. V. Garner, *Proc. Roy. Sot.*, A189, 39 (1947).
6. R. Brill, *Makromol. Chem.*, 18/19, 294 (1956).
7. L. G. Wallner, *Makromol. Chem*., **79**, 279 (1948).
8. D. R. Holmes, C. W. Bunn, D. J. Smith, *Journal of Polymer Sci.*, **XVII**, 159 (1955).
9. W. P. Slichter, *Journal of Polymer Sci*., **XXXVI**, 259 (1959).
10. I. Kinoschita, *Makromol. Chem*., **33**, 1 (1959).
11. Ch. Ruscher, V. Gröbe, H. Versaumer, *Faserforsch. und Textiltechn*., **12**, 214 (1961).
12. D. C. Vogelsong, *Journal of Polymer Sci., A*, **1**, 1055 (1963).
13. H. Arimoto, M. Ishibashi, M. Hirai, *J. Polym. Sci*., *A*, **3**, 317 (1965).
14. P. F. Dismore, W. O. Statton, *J. of Polym. Sci. Part C*., **13**, 133 (1966).
15. J. Tomka, J. Šebenda, O. Wichterle, *J. Polym. Sci. Part C: Polym. Symp.*, **16**, 53 (1967).
16. J. Baldrian, *Faserforschung und Textiltechnik*, **18** (4), 174 (1967).
17. A. Sh. Goikhman, G. A. Osokin, A. A. Konkin, *Polymer Science U.S.S.R.*, **10** (7), 1903 (1968).
18. Sh. Goyihman, T. P. Tantstyura, in: Visokomol. Soed., **A**, т. **10**, 1968, p. 724; (*Polym. Sci. U.S.S.R.*, **10**, 4, p. 839).
19. F. Danausso, in: Uspehi Himii, т. **39**, 1970, p. 304.
20. K.-H. Illers, H. Haberkorn, *Die Macromolare Chemie*, **142**, Nr. 3463, 31 (1971).
21. J. Baldrian, Z. Pelzbauer, *J. of Polym. Sci. Part C*., **38**, 289 (1972).
22. V. A. Marikhin, L. P. Myasnikova, *Journal of Polymer. Sci., Polym. Symp.*, **58**, 97 (1977).
23. J. P. Parker, *J. Appl. Polym. Sci*., **21**, 821 (1977).
24. P. Simon, G. Avgay, *J. Polym. Sci., Polym. Phys. Ed.,* **16** (5), 935 (1978).
25. K.-H Illers, *Makromol. Chem*., **179**, 497 (1978).
26. H. M. Heuvel, R. Huisman, *J. Polym. Sci., Polym. Phys. Ed.,* **19** (1), 121 (1981).
27. H. H. Chush, R. S. Porter, *Polymer*, **27**, 241 (1986).
28. N. S. Murthy, H. Minor, R. A. Latif, *Journal of Macromolecular Sci.*, B **26** (4), 427 (1987).
29. O. V. Startsev, A. L. Yordanskiy, G. E. Zaykov, *Visokomol. Soed. A*, **XXX**, 1539 (1988).
30. J. Koszkul, *Archiwum Nauki o Materialach*, **9** (2), 115 (1988).
31. T. Karstens, V. Rossbach, *Macromol. Chem.,* **190**, 3033 (1989).
32. N. Avramova, S. Fakirov, *Polymer*, **31** (6), 1025 (1990).
33. H. J. Biangardi, *J. Macromol. Sci., Phys.* B, **29**, 139 (1990).
34. C. Ramesh, *Macromolecules*, **32**, 3721 (1999).
35. Y. Liu, L. Gui, F. Guan, Y. Gao, N. Hedin, L. Zhu, H. Fong, *Macromolecules*, **40** (17), 6283 (2007).

КРИСТАЛНА СТРУКТУРА НА ПОЛИКАПРОЛАКТАМА. I. ГАМА–АЛФА ПОЛИМОРФЕН ПРЕХОД

С. Узова[1], А. Попов[2], В. Велев[3], Т. Ангелов[4], С. Михалева[2], Х. Узов[2]

[1] ПГТ „Проф. д-р Ас. Златаров", 8000 Бургас, България
[2] Университет „Проф. д-р Ас. Златаров" – Бургас, 8010 Бургас, България
[3] Университет „Еп. Константин Преславски", 9712 Шумен, България
[4] Лукойл Нефтохим Бургас АД, Бургас, България

Постъпила февруари, 2013 г.; приета май, 2013 г.

(Резюме)

На база предположението за перманентна реорганизация на опаковката на макромолекулните верижни сегменти на поликапролактама, вследствие динамично изменящите се равновесни мрежи от водородни връзки при температурна или термомеханична модификация, е изучаван богатия му полиморфизъм в интервала 20–240 °C.

Изследван е основният гама–алфа полиморфен преход на поликапролактама. Установено е специфично поведение на полимера при обратимия алфа–гама преход. Установено е, че прехода се съпровожда с достигане на критични деформации на елементарните кристални клетки. Гама–алфа преходът е представен като първи етап от развитието на кристалната фаза на поликапролактама при формирането на стабилна конфигурация в опаковката на макромолекулните верижни сегменти. Изследвано е влиянието на количественото натрупване и усъвършенстване на гама формата върху прехода и в алфа форма. Предложена е методика за провеждане и критерии за оценка на изследванията. Предположен е механизъм за реализиране на структурните преходи.

Установено е едновременното съвместно съществуване в различно количествено съотношение и с различно съвършенство на алфа, бета, гама и делта формите му в комплексни структури в зависимост от вида на полимера, предисторията на обектите, начина и условията на водене на кристализационния или рекристализационния процес. В зависимост от начина и пътя на температурна модификация е разгледана възможността за получаване на подобни комплексни структури при различни условия или различни комплексни структури при еднакви условия на формирането им. Това затруднява силно изучаване на полиморфизма и полиморфните му преходи.

Bulgarian Chemical Communications, Volume 45, Number 4 (pp. 568–574) 2013

Structure of hybrid materials containing natural and synthetic organic compounds

G. E. Chernev[1]*, E. V. Todorova[1], S. P. Djambazov[1], I. M. Miranda Salvado[2]

[1] *Department of Silicate Technology, University of Chemical Technology and Metallurgy, 8 Kl. Ohrydski blvd. 1756 Sofia, Bulgaria*
[2] *Department of Materials and Ceramics Engineering, CICECO, University of Aveiro, Aveiro, Portugal*

Received February, 2013; Revised May, 2013

Hybrid materials are innovative and extensively studied, because of the incorporation organic compounds in inorganic network, combining their properties. The properties of the hybrid material can be controlled by variation of the nature and amounts of the components. Recently, the sol-gel synthesis of hybrid materials has been extensively studied due to the possibility of controlling the chemical conditions, as well as it allows the introduction of organic and bioorganic molecules within the inorganic network.

In the present work, results on sol-gel synthesis and structure of hybrid materials containing silica and natural (chitosan) and synthetic (methyl methacrylate) organic compounds are described and discussed. Two and three component hybrid materials were prepared by mixing inorganic precursor – tetraethylortosilicate with the organic components. The structure of the obtained hybrid materials was studied by XRD, FT-IR, SEM and AFM. With the help of SEM the presence of spheres in the synthesized material was observed. The presence of a heterogeneous structure with well-defined nano units was suggested by AFM studies.

Key words: hybrids, sol-gel, silica, chitosan, methyl methacrylate.

INTRODUCTION

Hybrid materials are extensively studied, because of the incorporation organic compounds in inorganic network, combining their properties. Sol-gel method allows to synthesized materials with high homogeneity and purity at a molecule level [1]. Sol-gel process involves hydrolysis of silica precursor and condensation of Si–OH groups into SiO_4 tetrahedra. These building units are bridges by oxygen and lead to formation of Si–O–Si network. Silica materials obtained via sol-gel route exhibit good thermal and mechanical properties and long-term stability at different pH [2, 3]. Thermodynamic stability of Si–O bond enables interactions with many biomolecules and allows them to function normally in the presence of silicates [4]. Many researcher groups work on synthesis of biomaterials (biosensors and biocatalysts) and their interaction effect with different biomolecules–enzymes, proteins, living cells and others [5–7]. Most of them combine inorganic matrix on the base of silica precursors with organic polymers, with potential application in different fields: biotechnology, medicine, optics, pharmacy and etc.

The addition of organic constituent improves the plasticity of the silicate matrix. Furthermore, using sol-gel synthesis we can easily insert functional groups from polymer into the silicate matrix and that will afford entrapment of biomolecules [8].

In the last few years intensive investigations of silicate materials with participation of acrylates [9–11], alginates [12] and polysaccharides have been carried out. Chitosan (CS) is the second most abundant natural polysaccharide, composed of glucosamine and *N*-acetyl-glucosamine units [13, 14]. It has three reactive groups – primary amino or amide group and secondary hydroxyl groups [15]. Chitosan is insoluble in water and organic solvents, but soluble in acid water solution (pH <6.5) [16]. In low pH conditions amino groups are protonated and become positively charged, which makes CS a cationic polyelectrolyte [17]. Most of the bacteria's and enzymes are negative charged and can easy form bounds with amino groups of CS [18].

* To whom all correspondence should be sent:
E-mail: georgi_chernev@yahoo.com

Many investigations for the structure and properties of silica/chitosan hybrid materials are available [19–23]. Si/CS hybrid materials can be used as biomaterials in medicine, pharmacy, as materials for enzyme immobilization, for adsorption of toxic metals and dyes in waste water [24–28] etc.

Materials based on silica and different acrylates lead to formation of hybrids with good protective properties [29]. Adsorption of different biomolecules is limited by the length of the synthetic organic chain. With increasing chain length of acrylates, adsorption of biomolecules decreases.

For improving characteristics of silica/organic hybrids, they can be modified, by using combinations of polymers. Modified by grafting method polysaccharide (chitosan) with synthetic organic compound improves adsorption and mechanical properties of materials [30, 31].

The main objectives of the present study were the synthesis and structural characterization of hybrid materials on the base of silicate matrix, cross linked with chitosan and methyl methacrylate by the sol-gel method.

EXPERIMENTAL

Hybrid materials in the systems silica/chitosan (SiCS), silica/methyl methacrylate (SiM) and silica/chitosan/methyl methacrylate (SiCSM) were prepared using sol-gel method.

Tetraethyl orthosilicate (TEOS) was used as silica precursor, chitosan and methyl methacrylate (MMA) were used as organic constituents. Silica precursor was hydrolyzed in the presence of distilled water (dH_2O) and 1 N HCl for 1 hour under vigorous stirring. Ratio of TEOS/dH_2O/HCl is kept constant for all mixtures (sol). Chitosan was dissolved in 1% acetic acid and stirred until fully dissolved. Then silica sol was mixed with chitosan solution and MMA, respectively. The ratios between silica/CS and silica/MMA were varied from 1 to 4 wt.%.

Obtained hybrid sols (SiCS, SiM, SiCSM) were dried at room temperature until formation of solid gels.

The structure of synthesized hybrid materials was investigated using follow methods:

X-Ray diffraction (XRD) measurements were performed by a brucker D8 Advance. The diffracted intensity of CuKα radiation was measured with scan rate of $0.02°.min^{-1}$ in 2θ range between 10 and 80°. Infrared Spectra (FT-IR) were obtained using a MATSON 7000 Forier Transforming Infra Red spectrometer. Pellets of 2 mg of hybrid samples were mixed with 200 mg of spectroscopic grade KBr. Information about surface characteristics of synthesized hybrids was obtained using EDS (Rentec EDS system), SEM (Philips 515) and AFM (Nano Scope Tapping Mode TM).

RESULTS AND DISCUSSION

All synthesized samples were investigated with powder XRD and obtained results are presented on Figure 1. In the three investigated systems a halo is observed at ~ 23° 2θ. This halo shows the amorphous character of the obtained hybrid materials. In the systems with chitosan peak at ~23° 2θ is overlap with anhydrous crystalline form of chitosan.

FT-IR spectra of SiM, SiCS, and SiCSM hybrids are shown on Fig. 2–4. In FT-IR spectra of obtained hybrids characteristic absorption bands of silica network and organic components, as well as new absorption peaks, proved chemical interac-

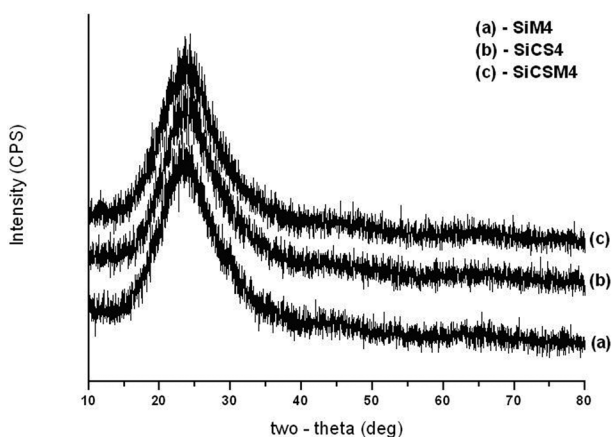

Fig. 1. XRD patterns of SiCS, SiM and SiCSM hybrids

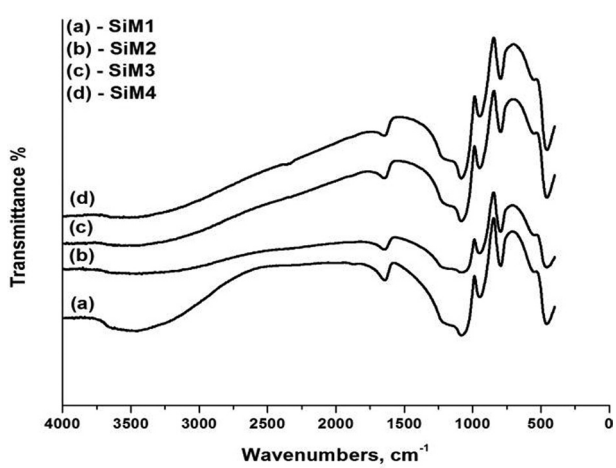

Fig. 2. FT-IR spectra of SiM hybrids

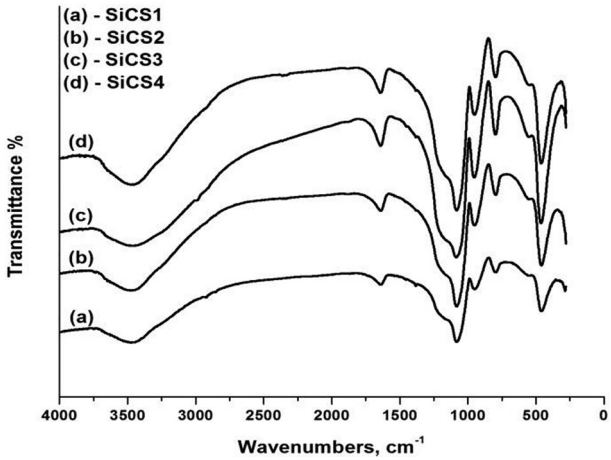

Fig. 3. FT-IR spectra of SiCS hybrids

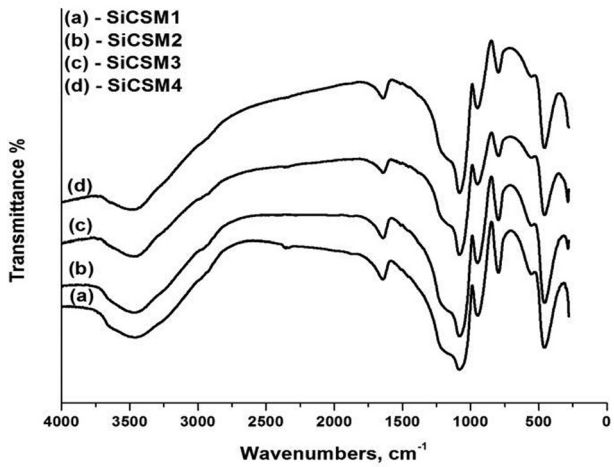

Fig. 4. FT-IR spectra of SiCSM hybrids

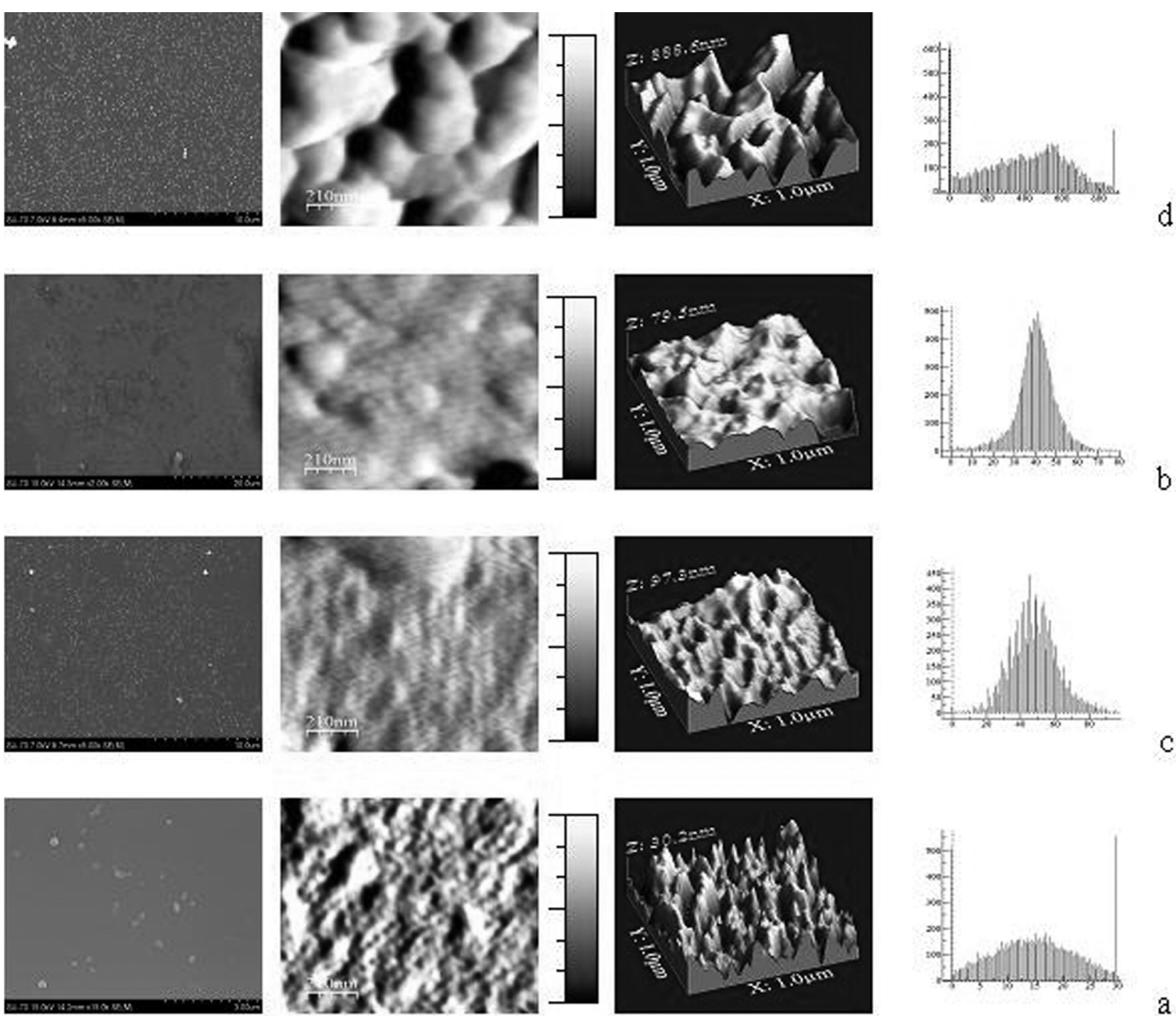

Fig. 5. SEM and AFM images on the surface of hybrids in the system SiCS

tion between them is detected. As a result of hydrolysis and condensation of TEOS, characteristic peaks at 795, 550 and 458 cm^{-1} corresponding for Si–O–Si symmetric stretching vibration. Intensive peak 1081 cm^{-1} show Si–O–Si asymmetric stretching mode [32]. On the other hand these peaks corresponding to Si–O–C band, which can be prove for new band between silica and organic sources. The presence of free Si–OH mode is associated with peak at 950 cm^{-1}. Wide band of absorption in the field of 3400 cm^{-1} related to symmetrical valent vibration of free NH_2 and OH groups and H-bonding interactions. Absorption peaks of chitosan at 2980–2850 cm^{-1} (–OH и –CH stretching band) are detected [26]. The decrease in peak intensity around 1250 cm^{-1} is due to co-condensation of –OH groups of chitosan with silicate matrix [26]. A new absorption peak in spectra of SiCS hybrid at 1643 cm^{-1} can be attributed to the asymmetric N–H deformation vibration and confirm the $–NH_3^+$ ion formation [33].

In the FT-IR spectra of hybrid containing MMA the peak of C=C bond at 1642 cm^{-1} validates the incorporation of MMA in silica network, because no such C = C is present in TEOS.

In the system SiCSM typical characteristic bands of Si–O–Si network are detected, which are widely described above. The peak at 1643 cm^{-1} can be attributed to formation of –NHCO linkage between chitosan and MMA [34]. These results proved cross linking of chitosan in Si-O-Si network and incorporation of two organic components by the grafting method.

The surface of obtained hybrids was investigated by SEM and AFM analysis (Fig. 5–7). All samples had smooth surface with distributed spherical par-

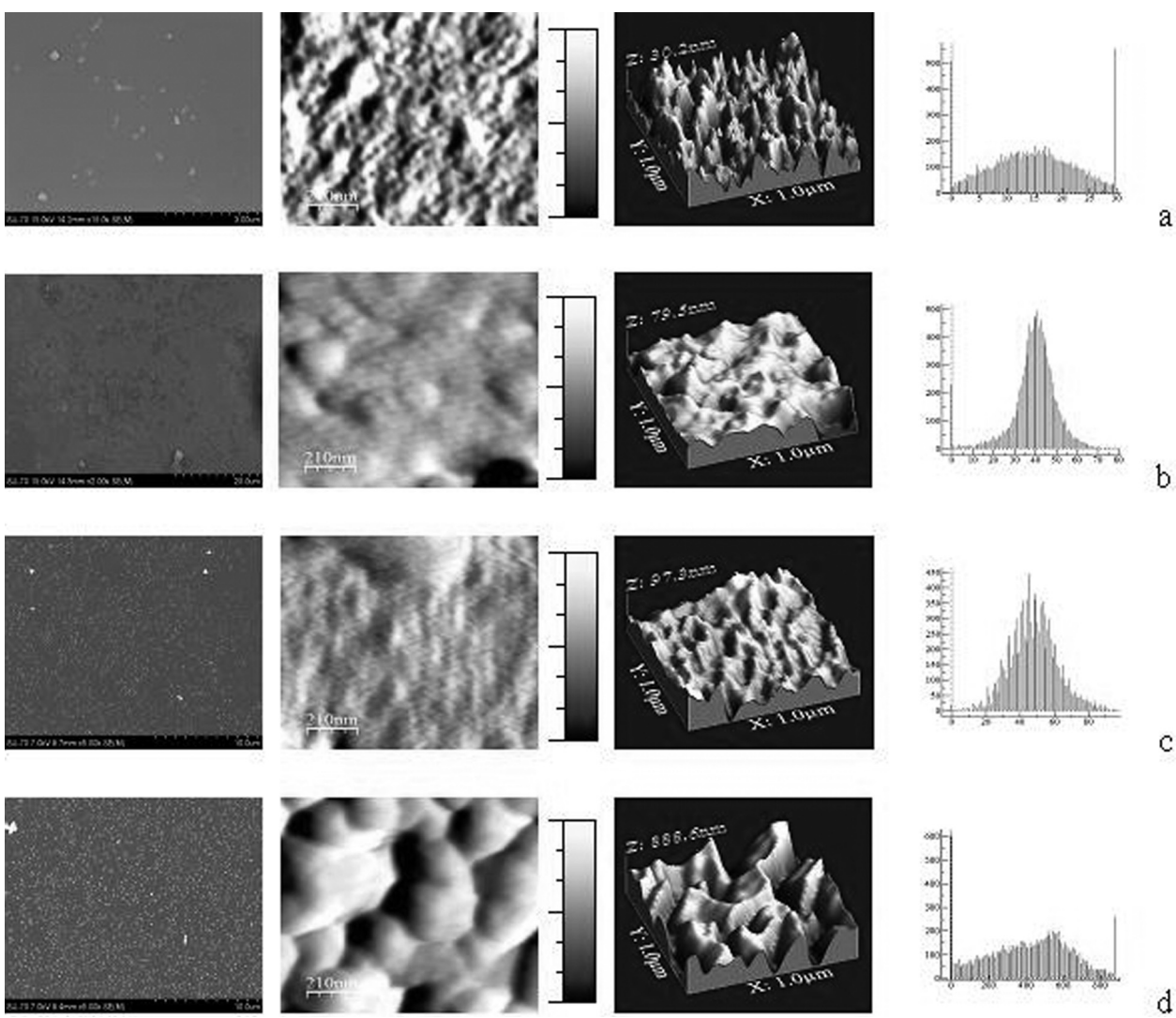

Fig. 6. SEM and AFM images on the surface of hybrids in the system SiM

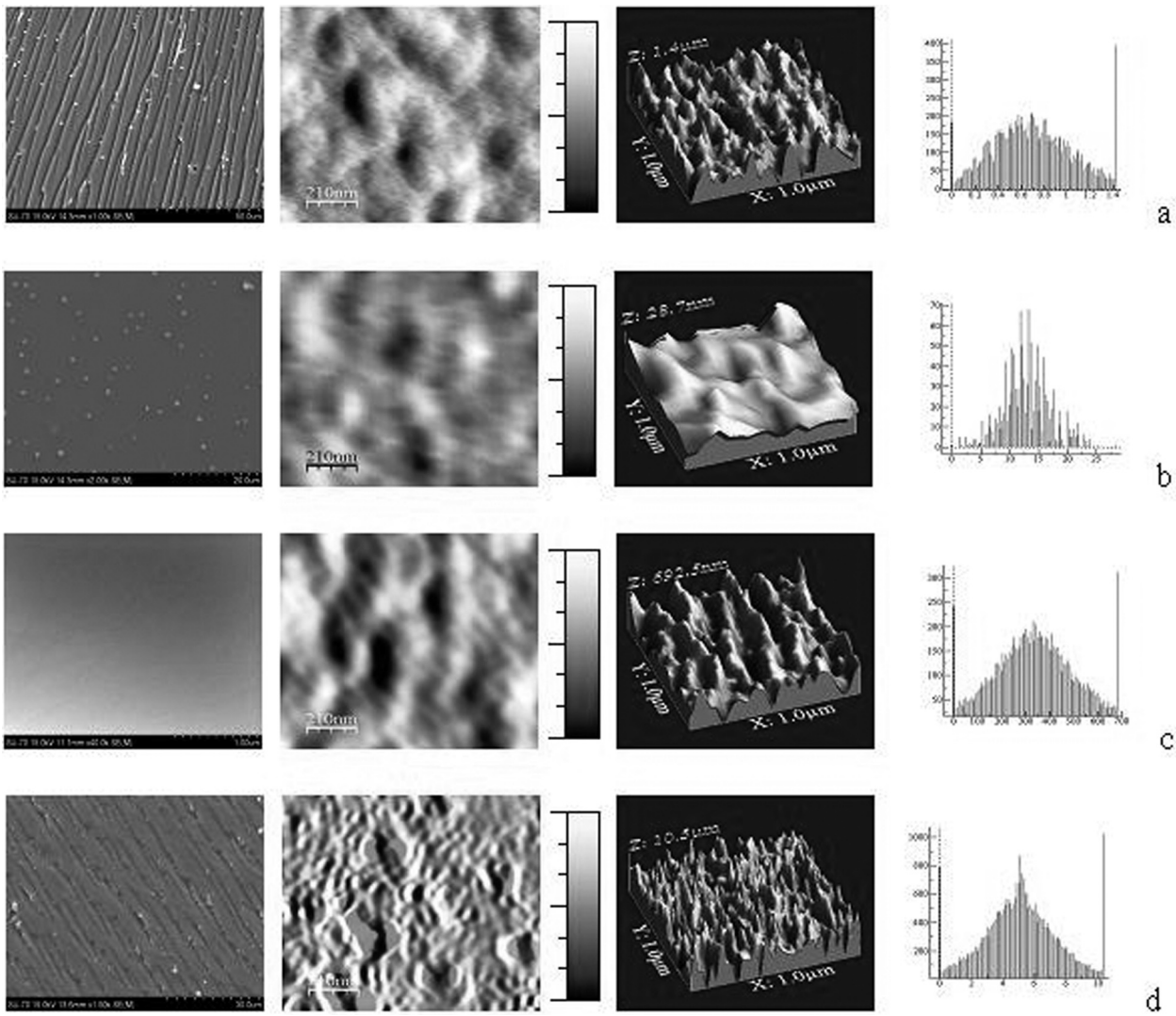

Fig. 7. SEM and AFM images on the surface of hybrids in the system SiCSM

ticles. Formed units proved the incorporation and cross linkage of chitosan in silica network.

SEM micrographs of SiCS system (Fig. 5) showed decreasing trend of particle size with increasing amount of chitosan solution.

Influence of partial substitution of chitosan with MMA on the structure is shown on Fig.7. Adding MMA to Si/CS mixture, rough surface is observed. The change of morphology is due to grafting process between chitosan and MMA. Distribution and spherical size followed the same tendency. Particles with diameter 61 nm at equal amount of inorganic and organic components are formed.

AFM investigations of obtained samples in 2d, 3d topography and roughness analysis are presented on Figures 5, 6 and 7. Samples, containing TEOS and chitosan formed smooth structure, where z-direction increase from 30, 2 nm (SiCS1) to 888, 6 nm (SiCS4).Variations of unit size on their surface are confirmed with roughness analysis (Fig. 5).

AFM topographies of SiCSM hybrid materials presented transformation from smooth (Fig. 7b) to rough surfaces (Fig. 7d) with increasing organic amount. When organic and inorganic components are in equal amount, rough surface with maximum z-direction (10, 4 μm) is observed. From AFM surface analysis can be concluded for random distribution of hybrid units.

CONCLUSIONS

Hybrid materials, containing silica, chitosan and methyl methacrylate were successfully synthesized

using sol-gel method. Obtained results of XRD proved the amorphous structure of hybrids. FT-IR spectra showed result of hydrolysis and condensation of silica source, formed reactive amino and hydroxyl groups and interaction between methyl methacrylate and chitosan in SiCSM hybrids. SEM images showed random distribution of chitosan in silica network. With increasing amount of organic component formed spherical particles become smaller. Partial replacement of chitosan with methyl methacrylate, formed spherical particles is better distributed in the structure. The existing reactive groups in obtained materials ensured different application of obtained hybrids in the field of biotechnology.

Acknowledgements: *The authors are grateful to the CICECO of the Project Pest-C/CTM/LA001/2011 from the University of Aveiro, Portugal for the support.*

REFERENCES

1. G. S. Silva, P. C. Oliveira, D. S. G., H. F. de Castro, *J. Braz. Chem. Soc.*, **22**, 8, 1407 (2011).
2. T. Godjevargova, R. Nenkova, V. Konsulov, *J. Mol. Cat. B: Enzymatic*, **38**, 59 (2006).
3. D. H. Lee, Ch. H. Park, J. Mo Yeo, S. W. Kim, *J. Ind. Eng. Chem.,* **12**, 5, 777 (2006).
4. K. Sakai-Kato, *Anal. Sc.*, **25**, 969 (2009).
5. I. Gill, *Chem. Mater.*, **13**, 3404 (2001).
6. W. Jin, J. D. Brennan, *Analytica Chim. Acta*, **461**, 1 (2002).
7. R. Nenkova, D. Ivanova, J. Vladimirova, T. Godjevargova, *Sensors and Actuators*, **B 148**, 59 (2010).
8. K. Kawakami, S. Yoshida, *J. of Fermentation and Bioengineering*, **82**, 239 (1996).
9. R. T. Sakai, F.M. Di L. da Cruz, H.G. de Melo, A. V. Benedettib, C. V. Santilli, P. H. Suegama, *Progress in Org. Coat.*, **74**, 288 (2012).
10. E. Rubio, J. Almaral, R. Ramírez-Bon, V. Castaño, V. Rodríguez, *Opt. Mat.*, **27**, 1266 (2005).
11. W. M. Chiu, C. F. Yang, Y. S. Zhang, Polymer-*Plastics Techn. and Eng.*, **46:8**, 767 (2007)
12. T. Coradin, J. Livage, J. of Sol-Gel *Sci. and Techn.,* **26**, 1165 (2003).
13. C. K. S. Pillai, W. Paul, Ch. P. Sharma, *Progress. in Pol. Sci.*, **34**, 641 (2009).
14. M. Dasha, F. Chiellini , R. M. Ottenbrite, E. Chiellini, *Progress in Pol. Sci.*, **36**, 981 (2011).
15. D. Enescu, V. Hamciuc, L. Pricop, T. Hamaide, V. Harabagiu, B. C. Simionescu, *J. Polym. Res.*, **16**, 73 (2009).
16. M. Kamburov, L. Lalov, *Biotech. and Biotech. Eq*., **26**, 156 (2012).
17. V. R. Sinha, A. K. Singla, S. Wadhawan, R. Kaushik, R. Kumria, K. Bansal, S. Dhawan*, Int. J. of Pharm.*, **274**, 1 (2004).
18. M. R. Avadi, A. M. M. Sadeghi, A. Tahzibi, Kh. Bayati, M. Pouladzadeh, M. J. Zohuriaan-Mehr, M. Rafiee-Tehrani, *Eur. Pol. J.*, **40**, 1355 (2004).
19. Y. M. Yang, J. W. Wang, R. X. Tan, *Enz. and Micr. Techn.*, **34**, 126 (2004).
20. V. K. Konaganti, R. Kotaa, S. Patil, G. Madras, *Chem. Eng. J.*, **158**, 393 (2010).
21. S. Jenjob, P. Sunintaboon, Pr. Inprakhon, N. Anantachoke, V. Reutrakul, *Carb. Pol.*, **89**, 842 (2012).
22. M. Chellapandian, M. R. V. Krishnan, *Pr. Bioch*., **33**, 595 (1998).
23. Z. Lei , Sh. Bi, *Enz. and Micr. Techn.*, **40**, 1442 (2007).
24. G. J. Copello, A. M. Meberta, M. Raineria, M. P. Pesentia, L. E. Diaz, *J. of Hazard. Mat.*, **186**, 932 (2011).
25. Y. L. Liu, Y. H. Su, K. R. Lee, J. Y. Lai, *J. of Membr. Sci.*, **251**, 233 (2005).
26. S. Dhanasingh, Mallesha, J. J. Hiriyannaiah, *Biointerface Research in Applied Chemistry*, **1**, 48 (2011).
27. M. N. V. Ravi Kumar, *React. Funct. Pol*., **46**, 1 (2000).
28. S. Spirk, G. Findenig, A. Doliska, *Carbohydrate Polymers*, in press.
29. A. Khan, T. Huq, R. A. Khan, D. Dussault, St. Salmieri, M. Lacroix, *Rad. Phys. and Chem.*, **81**, 941 (2012).
30. T. Sun, P. Xu, Q. Liu, J. Xue, W. Xie, *Eur. Pol. J.*, **39**, 189 (2003).
31. V. Singh, A.K. Sharma, D.N. Tripathi, R. Sanghi, *J.of Hazard. Mat*., **161**, 955 (2009).
32. S. H. Jun, E. J. Lee, S. W. Yook, H. E. Kim, H. W. Kim, Y. H. Koh, *Acta Biom*., **6**, 302 (2010).
33. J. Ostrowska-Czubenko, M. Gierszewska-Druzynska, *Carbohydrate Pol*., **77**, 590 (2009).
34. R. Jayakumar, R. L. Reis, J. F. Mano, *Drug Delivery*, **14,** 9 (2007).

СТРУКТУРА НА ХИБРИДНИ МАТЕРИАЛИ, СЪДЪРЖАЩИ ЕСТЕСТВЕНИ И СИНТЕТИЧНИ ОРГАНИЧНИ СЪЕДИНЕНИЯ

Г. Е. Чернев[1]*, Е. В. Тодорова[1], С. П. Джамбазов[1],
И. М. Миранда Салвадо[2]

[1] Катедра „Технология на силикатите“, Химикотехнологичен и Металургичен Университет, бул. „Климент Охридски“ 8, 1756 София, България
[2] Департамент по инженерна керамика, СИСЕКО, Университет на Авейро, Авейро, Португалия

Постъпила февруари, 2013 г.; приета май, 2013 г.

(Резюме)

Хибридните материали са иновативни и широко изучавани материали, поради възможността за съчетаване на неорганична матрица и органични компоненти, което позволява промяна на свойствата на поплучените материали. Свойствата на хибридните материали зависят от природата и количествата на изходните компоненти. През последните години интересът към синтезиране по зол-гел на хидридни материали е голям, заради възможността условията на синтез да бъдат контролирани, както и внасянето на органични и биоорганични молекули в неорганичната матрица.

В настоящата работа са представени и дискутирани резултатите върху структурните изследвания на хибридни материали синтезирани по зол-гелен метод, съдържащи естествени (хитозан) и синтетичин (метил метакрилат) органични компоненти. Синтезирани са дву- и трикомпонентни системи използвайки неорганичен прекурсор-тетраметилортосиликат и горепосочените органични компоненти. Структурата на получените хибриди е охарактеризирана с помощта на РФА, ИЧ, СЕМ и АСМ анализи.

Bulgarian Chemical Communications, Volume 45, Number 4 (pp. 575–583) 2013

Polycaprolactam crystal structure. II. Crystal phase perfection

S. Uzova[1], A. Popov[2], V. Velev[3], T. Angelov[4],
S. Mihaleva[2], Ch. Uzov[2]

[1] *PST "Prof. dr. Assen Zlatarov" – Burgas, 8000 Burgas, Bulgaria*
[2] *Assen Zlatarov University, 8010 Burgas, Bulgaria*
[3] *Konstantin Preslavski University, 9712 Shumen, Bulgaria*
[4] *Lukoil Neftochim Burgas JSC, Burgas, Bulgaria*

Received February, 2013; Revised May, 2013

An attempt was made to optimize the valuation methods of the polycaprolactam crystalline phase perfection. Criteria for the evaluation of the perfection of the alpha form are established.

It is proposed a methodology for the practical determination of the alpha-form perfection. Formulas are derived for its quantification.

Approaches have been proposed for the evaluation of other polymorphic forms of the polycaprolactam. The intensity ratio of the main diffraction reflections is used to determine the quantitative assessment of the presence and perfection of the beta form. Changes in angular displacement of the main diffraction reflection of the gamma-form in the powder diffractograms were analyzed to determine the perfection of gamma crystalline form.

Key words: polycaprolactam, crystal phase, perfection.

INTRODUCTION

The perfection of the crystalline phase in the polymer has different dimensions than that of low molecular weight substances. Partly this is due to skeletal chemical bonds in long-chain polymer molecules. Restricting the freedom of the nearest neighbors in the base of elementary crystal cells, they significantly affect the far order in the grid. They are the basis and for the specific type of defects in the polymers, too. This necessitated the creation of the theory of polymer pseudocrystal. All factors affecting the quality of the crystalline phase otherwise impact in varying degrees to perfection pseudocristal polymer lattice. And they are very complex and their simultaneous impact is ambiguous. An additional complicating factor in polycaprolactam (PCL) are dynamically changing balances arising from shatter and recombine hydrogen bonds (H-bonds). These may be other chemical, physical or purely complex networks or just any steric factor and geometric specificity. Especially in the process of crystallization, recrystallization, and any type of structural reorganization of the atomic-molecular level in terms of thermal, thermo-mechanical or other type of complex physical fields. And these are all real thermal fluctuation processes of structural adjustment and fine-crystal crystallographic and morphological level.

Fortunately, most accurate and complete uniformity in the definition of similar processes and structures is rarely attainable and seldom necessary. For example, in the study of polymorphic transitions PCL, knowledge and ability to control the perfection of the crystalline phase is required. Because the wide variety of polymorphic transitions is not nothing but a permanent process of improvement of the crystal structure of the PCL. And just tracking the change of the lattice perfection we can study the polymorphism of PCL. To do so, however, is not complete determinism of the studied physical reality. We need to know only what quality (crystalline perfection – CP) structure, respectively, way and packing density (chain packing density – CPD) of macro-molecular chain segments arises a crystalline phase, under what conditions and how does it change. When and how to improve and to what extent violates the order to destroy the crystal structure of phase or move to another crystallographic modification.

* To whom all correspondence should be sent:
E-mail: hristo_uzov@abv.bg

EXPERIMENTAL

High-temperature powder X-ray diffractometers are best suited for the study of temperature-initiated restructuring of the crystalline phase of PCL. Structural changes are controlled by changes in the geometry of the intensity distribution of X-ray radiation. Angular positional deviations, intensity variations and profile changes of the diffraction reflections have been observed and compared. They specify the dimensions and distances between structural elements, the quantity and type of packaging in the different structures of the polymer. Key structural elements are chain segments in the elementary crystal cell. Usually they are the symmetrical version or parts from it in the basis of the cell.

The behavior of α-, β-, γ- and δ-PCL forms were studied in a wide temperature range (20–240 °C) and in more detail in the range 160–190 °C. The temperature dependences of the angular deviations of all major diffraction reflections of polymorphic forms and above all $(200)_\alpha$, $(100)_\gamma$ and $(002)_\alpha/(202)_\alpha$ are controlled. By using suitable software such as "ORIGIN" decomposition of multiply peaks was performed to establish the statistical characteristics of the actual characteristics of the diffraction reflections. Experienced subjects were scanned at speeds 1, 2 and 3° 2θ/min, if necessary, in the interval 20–24 °2θ, 15–30 °2θ 2–60 °2θ and a URD-6 (Freiburg "Precizionsmechanik", Germany), and DRON-3 ("Burevestnik", St. Petersburg, Russia) equipped with a high-temperature chamber ATM-2000. Used $Cu_{K\alpha av.}$ = 1.5418 Å radiation filtered β-nickel filter.

Different types of polycaprolactam (PCL-1 with $\eta_{rel.1\%\ sol.\ H2SO4}$ = 2.64; $W_{mass.\%}$ = 1.0 and PCL-2 with $\eta_{rel.1\%sol.\ H_2SO_4}$ = 2.32; $W_{mass.\%}$ = 0.01) with different molecular masses and molecular-mass distribution (characteristic viscosity in 1% solution of H_2SO_4 η_{rel} = 2.11–2.83) were used with contents of low-molecular tie in the interval 1.0–12.0% mass, moisture content W from 0.1 to 0.01 mass%, as a necessary condition about the obtaining of crystal structures with different perfection. Thin folios were formed in a large diapason of forming conditions: T_m = 210–240 and T_c = –196–200 °C.

The high temperature X-ray investigations were carried out by repeated cyclical heating and cooling in the temperature interval from 293 K to 513 K with heating rate of 5 K/min and 5 min tempering for every scanned temperature at interval of 5 K. A software package "Origin 5.0" was used for decomposition of multiple peaks in determining polymorphic forms of PCL.

The initial isotropic structure of the pressed folios was characterized by light-microscopy, electron-microscopy and with powder X-ray diffraction methods using a polarization light-microscopy Amplival Pol, Karl Zeiss, Jena, Germany, SEM BS – 340, Tesla, Brno, Cheh Republic, TEM Opton 10B, Feintechnik, Oberkochen, Germany.

The crystal phase perfection was defined by the packing compactness of the macromolecular chain segments in the crystal phase of the α-crystal modification [1, 2].

RESULTS AND DISCUSSION

It is impossible to talk about precise and unambiguous quantitative and even qualitative structural study of the polymers, if there is not an opportunity to identify and assess the quality of their crystalline phase. For chain-flexible polymers and PCL not much information on similar research is available [1–8]. The main quantitative criterion in the X-ray structural studies is the integral diffraction intensity of the X-ray radiation in a given crystallographic direction. On the other hand, the integral intensity is strongly connected with the quality of the studied structure at the atomic-molecular level. This kind of "dualism" can lead to ambiguous experimental solutions. In the more perfect low molecular crystal lattices the polymorphic resolution is better. In some cases, depending on the conditions and objectives of the study, the profile of diffraction effects can successfully arbitrate and decide such dualism.

Mathematical and statistical characteristics of the profile distributions as a design may be sufficient for this. Moreover, if they are representatives of various relevant statistics such as Gauss, Lorentz, Lorentz quadratic, Void, Pseudo-Void, Pearson VII, etc., for polymers, in particular PCL, such a decision is unthinkable. All major diffraction reflections of his polymorphic diversity are nesting in the range of 1–2 Bragg degrees. This strongly hampers the qualitative and quantitative analysis of the diffraction pattern. But the study of polymorphic transitions requires precise control of the qualitative and quantitative simultaneous polymorphic composition. This requires the creation of a criteria basis for recognition, separation, correction, evaluation and comparison of the diffraction reflections of co-existing in different proportions polymorphic modifications of PCL. At first glance, the undeniable correlation between the quality and quantity of each polymer crystallographic modifications looks facilitating the identification of real forms in the crystalline phase of PCL. It seems that the existing relations lower degrees of freedom and the apparent ambiguity in permanently changing structures studied. In practice, however, this is not so. The limited selection of practical approaches and techniques for detection of the crystalline forms in PCL would not allow its use even in synchronous excellent knowledge.

It appears unlikely the exact establishment of the moment of polymorphic transition relation by the quantity–quality of the polymorphic crystal forms. The definition of the polymer polymorphic transitions as a continuous process of change in the packaging of the macromolecular chain segments, and the technical difficulties in the experimental implementation of the evaluations guarantee this. What is the system of approaches and techniques for implementation of the planned experiment? The main objective is the study of polymorphic transformations of PCL in a wide range of conditions. This can be investigated with high-temperature X-ray powder diffraction under different conditions of thin films of PCL with different starting structure. The need to be thin foils is determined by the low coefficient of thermal conductivity of the polymer that must be heated and cooled quickly and homogeneously. A detailed interpretation of the geometry of the intensity distribution of high-temperature powder diffraction, especially in the angle range from 20 to 24 °2θ of diffraction scan. The basic diffraction reflections of the known polymorphic crystal forms of the polymer are in this interval. To them the proportion between the crystal forms in simultaneous coexistence may be established. By varying temperatures in different modifications can be studied the geometry, mechanism and kinetics of the polymorphic transitions. For this purpose is needed data for the angular deviation, intensity and profile modification of the diffraction reflections. It can be obtained after splitting of the overlap in complex multiple peak of diffraction reflections of individual alpha- beta-and gamma-crystalline forms of PCL. The processing of the multiple peaks can be done with a computer program Origin. As supporting information can be used theoretical diffraction curves of known crystal forms of PCL and simulation of particle diffraction images with their software as, for example, Crystallographica, Material Studio, etc.

The alpha form perfection can be defined as a CPP (crystalline phase perfection) = $83(d_{(200)}/d_{(002),(202)})$, [%], and the density of the chains packing as a CPD (chains packing density) = $137(d_{(200)} - d_{(002),(202)})$, [%]. Thus, through the angular deviation of the main diffraction reflections can be controlled quantitatively, evaluated and compared the changes in the crystalline phase quality and the distance between the chains.

The normalizing coefficients estimated, namely "83" (in front of the ratio of the distances between the planar) and "137" (in front of the their difference) determine the maximum value (100%), respectively of perfection and density. Of course, the values of the normalizing coefficients have been estimated at the maximum possible experimentally reachable values of the used ratio and difference of the distance between the planar, at the angular positions values of the diffraction reflection $(200)_\alpha$ – 20.00 °2θ and of $(002)_\alpha$,$(202)_\alpha$ – 24.00 °2θ.

It is established that within the boundaries of possible deviation of reflections CPP is between 91–100%, a CPD varies in the range of 54–100%. The perfection climate out these borders means critical deformation of the unit cell, polymorphic transition and the crystalline phase destruction, depending on conditions.

The change of the density of packing of the chains has no direct sense of a change in the distance between them, and the percentage of the maximum difference between the planar distances of family's crystallographic planes that lie in the chains.

This indicator shows rather tendencies to increase or decrease of distances in trigonometric relationships. It can be seen that the perfection decrease of the alpha form leads to a percentage lower of the chains packing density in times fast for the defined range.

Intensity ratio (the linear intensities) of (200) to (002)/(202) in the alpha form is about 3/2 = 1.5. In beta form, it is back to 2/3 ~ 0.667. So the most easily recognized and percentage calculation can be done using intensity ratio $CPP^\beta = 150(I_{(200)\alpha\beta}/I_{(002)\alpha\beta/(202)\alpha,\beta})$, [%]. The detailed justification and output of the analytical dependence is as follows.

The simulation of the theoretical powder diffraction of the known PCL polymorphic forms shows the declared above dependencies of the intensity ratios.

After simulation and experimental confirmation was considered as the maximum of the beta form on scanned objects is $I_{(200)\alpha\beta}/I_{(002)\alpha\beta/(202)\alpha\beta}$ = 0,667. After the standardization it to 100% as $(I_{(200)\alpha\beta}/I_{(002)\alpha\beta/(202)\alpha\beta})$/ 0,667).100, [%], the expression was a little simplistic to $150(I_{(200)\alpha\beta}/I_{(002)\alpha\beta/(202)\alpha\beta})$, by introducing a correction coefficient 150 ~ 0.00667. Coefficient 150 is connected with the idea of 150% intensity of the second line to the first PCL peak in the powder diffraction of the monoclinic crystallographic alpha and beta modifications.

It is easy to reduce in percentage the beta-crystalline phase. Higher accuracy is possible, but in most cases it is not necessary. In the remaining cases are used the algorithms for the alpha form. It should be noted that alpha and beta forms always coexist in different proportions and perfection. When we talk about 100 percentage of beta-form, that means their 100% possible participation in such polymorphic mixture.

Determination of the gamma-form perfection is reasonable in the light of the clarification of the so-called Brill transition (gamma–alpha, or gamma–beta–alpha transition). From maximum amorphized (deep hardened) condition close to ideal

Table 1. Dependence of d-spacing of PCL-2 thin foil in cyclic thermal modification and simultaneous X-ray scan

T_{sk}, °C	Alpha crystal form of PCL								Beta crystal form of PCL								Gamma crystal form of PCL			
	$T°_{\uparrow}$	$T°_{\downarrow}$	$T_{\uparrow}$	$T_{\downarrow}$	$T_{\uparrow}$	$T_{\downarrow}$	$T_{\uparrow}$	$T_{\downarrow}$	$T_{\uparrow}$	$T_{\downarrow}$	$T_{\uparrow}$	$T_{\downarrow}$	$T_{\uparrow}$	$T_{\downarrow}$	$T_{\uparrow}$	$T_{\downarrow}$	$T_{\uparrow}$	$T_{\downarrow}$	$T_{\uparrow}$	$T_{\downarrow}$
	(200)	(002)	(200)	(002)	(200)	(002)	(200)	(002)	(200)	(002)	(200)	(002)	(200)	(002)	(200)	(002)	(100)	(100)	(100)	(100)
	4.42	3.72	4.36	3.79	4.42	3.72	4.36	3.79	4.44	3.69	4.42	3.69	4.44	3.69	4.42	3.69	3.99	3.99	3.99	3.99
	4.42	3.72	4.36	3.79	4.42	3.72	4.36	3.79	4.44	3.69	4.42	3.69	4.44	3.69	4.42	3.69	3.99	3.99	3.99	3.99
	4.42	3.72	4.36	3.79	4.42	3.72	4.36	3.79	4.44	3.69	4.42	3.69	4.44	3.69	4.42	3.69	3.97	3.99	3.98	3.99
	4.42	3.72	4.36	3.79	4.42	3.72	4.36	3.79	4.44	3.69	4.42	3.69	4.44	3.69	4.42	3.70	3.97	3.99	3.97	3.99
	4.42	3.73	4.36	3.79	4.42	3.73	4.36	3.79	4.44	3.69	4.42	3.69	4.44	3.69	4.42	3.70	3.95	3.99	3.96	3.99
	4.42	3.73	4.36	3.79	4.42	3.73	4.36	3.79	4.44	3.69	4.42	3.69	4.44	3.69	4.42	3.70	3.95	3.99	3.96	3.99
	4.41	3.73	4.36	3.79	4.42	3.73	4.36	3.79	4.44	3.70	4.42	3.70	4.44	3.70	4.42	3.70	3.95	3.99	3.96	3.99
	4.41	3.73	4.36	3.79	4.42	3.73	4.36	3.79	4.44	3.70	4.42	3.70	4.44	3.70	4.41	3.70	3.93	3.99	3.95	3.99
	4.41	3.73	4.36	3.79	4.41	3.73	4.36	3.79	4.43	3.70	4.42	3.70	4.44	3.70	4.41	3.70	3.92	3.99	3.94	3.99
	4.41	3.73	4.36	3.80	4.41	3.73	4.36	3.80	4.43	3.70	4.42	3.70	4.44	3.70	4.41	3.70	3.90	3.99	3.92	3.98
	4.41	3.73	4.35	3.80	4.41	3.73	4.35	3.80	4.43	3.70	4.41	3.70	4.43	3.70	4.41	3.70	3.90	3.99	3.91	3.98
	4.40	3.74	4.35	3.80	4.41	3.74	4.35	3.80	4.42	3.71	4.41	3.70	4.43	3.71	4.40	3.70	3.90	3.99	3.91	3.98
	4.39	3.75	4.35	3.80	4.39	3.75	4.35	3.80	4.42	3.71	4.40	3.70	4.43	3.71	4.40	3.70	3.89	3.99	3.91	3.98
	4.38	3.77	4.35	3.81	4.38	3.77	4.35	3.81	4.42	3.71	4.40	3.70	4.43	3.71	4.40	3.71	3.89	3.99	3.90	3.98
	4.36	3.79	4.35	3.81	4.37	3.79	4.35	3.81	4.42	3.71	4.39	3.70	4.42	3.71	4.40	3.71	3.88	3.99	3.90	3.98
	4.35	3.80	4.35	3.81	4.36	3.80	4.33	3.81	4.41	3.71	4.39	3.71	4.42	3.71	4.39	3.72	3.88	3.99	3.89	3.98
	4.34	3.82	4.35	3.81	4.35	3.82	4.33	3.81	4.41	3.72	4.39	3.72	4.42	3.72	4.39	3.74	3.88	3.99	3.88	3.98
	4.33	3.83	4.34	3.82	4.34	3.83	4.32	3.81	4.39	3.74	4.38	3.74	4.42	3.74	4.38	3.75	3.87	3.99	3.88	3.98
	4.32	3.85	4.33	3.83	4.33	3.85	4.30	3.83	4.38	3.75	4.37	3.75	4.41	3.75	4.37	3.77	3.87	3.99	3.87	3.98
	4.31	3.87	4.32	3.87	4.30	3.87	4.29	3.86	4.37	3.77	4.36	3.77	4.39	3.77	4.36	3.79	3.86	3.99	3.86	3.98
	4.30	3.88	4.31	3.88	4.29	3.88	4.29	3.88	4.36	3.79	4.35	3.79	4.36	3.79	4.34	3.80	3.86	3.98	3.86	3.98
	4.29	3.90	4.30	3.90	4.28	3.90	4.27	3.90	4.35	3.80	4.33	3.80	4.35	3.80	4.32	3.82	3.86	3.98	3.86	3.98
	4.28	3.92	4.29	3.92	4.27	3.92	4.26	3.91	4.33	3.82	4.31	3.82	4.34	3.82	4.31	3.84	3.85	3.95	3.85	3.95
	4.27	3.93	4.28	3.93	4.26	3.93	4.26	3.92	4.32	3.83	4.29	3.83	4.33	3.83	4.28	3.85	3.85	3.92	3.85	3.91
	4.26	3.95	4.26	3.95	4.26	3.95	4.25	3.95	4.31	3.85	4.29	3.85	4.29	3.85	4.29	3.86	3.84	3.89	3.84	3.89
	4.25	3.97	4.26	3.97	4.25	3.97	4.25	3.97	4.30	3.87	4.28	3.87	4.30	3.87	4.28	3.87	3.84	3.86	3.84	3.86
	4.24	3.98	4.24	3.98	4.25	3.98	4.25	3.98	4.29	3.88	4.27	3.88	4.29	3.88	4.28	3.88	3.83	3.83	3.83	3.83
	4.23	3.99	4.23	3.99	4.25	3.99	4.25	3.99	4.27	3.88	4.27	3.88	4.28	3.88	4.28	3.88	3.82	3.82	3.82	3.82
	4.42	3.72	4.36	3.79	4.42	3.72	4.36	3.79	4.44	3.69	4.42	3.69	4.44	3.69	4.42	3.69	3.99	3.99	3.99	3.99

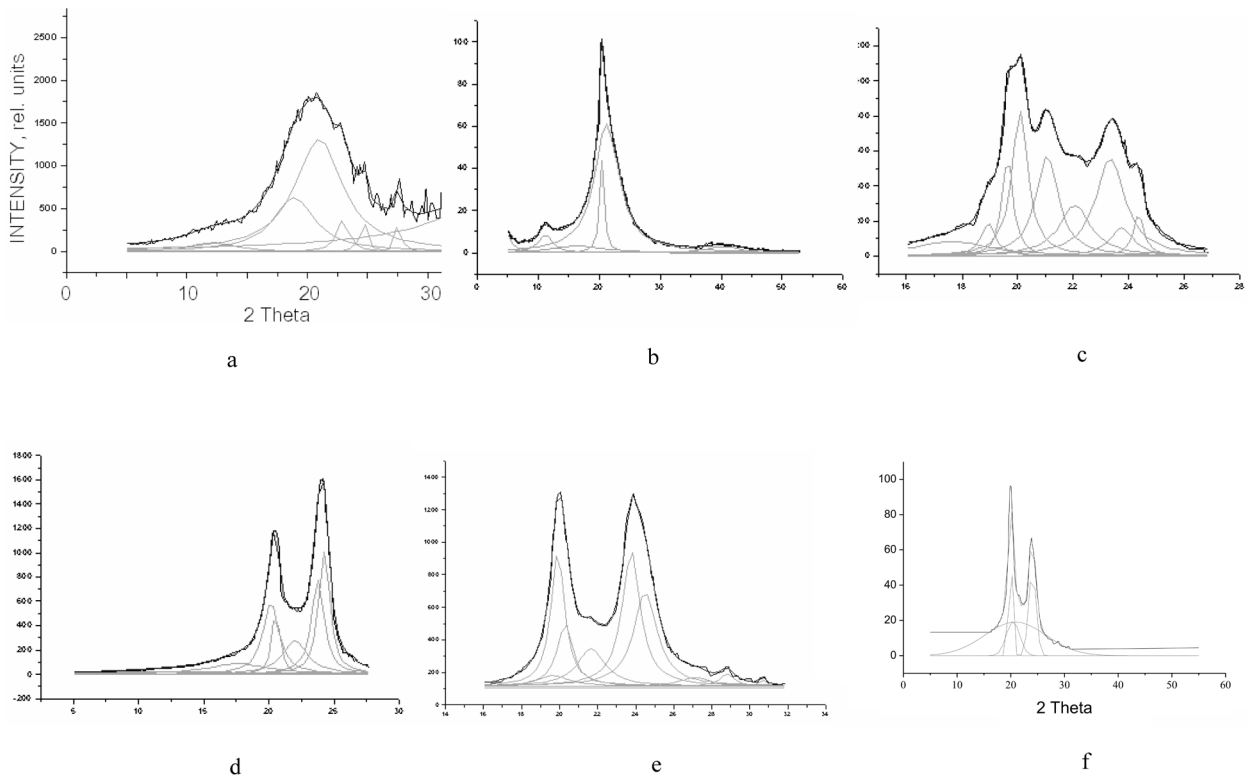

Fig. 1. High temperature X-ray powder diffraction of thin films of PCL-2, pressed at 225 °C (T_m = 225 °C), crystallized at 0 °C (T_c = 0 °C). X-ray scans temperatures: a – 20 °C; b – 170 °C; c – 165 °C after heating (V_{heat} = 5°/min) to 225, then cooling (V_{cool} = 5°/min); d – 145 after heated (V_{heat} = 5°/min) to 225, then cooling (V_{cool}=5 °/min); e – 120 °C after heating (V_{heat} = 5°/min) to 225, then cooling (V_{cool} = 5°/min); f – 20 °C after heating (V_{heat} = 5°/min) at 165 °C for 5 min, and 225 °C for 5 min, then cooling to 165 °C for 5 min and cooling (V_{cool} = 1°/min) to 20 °C.

super cooled melt of PCL called delta-form up to gamma-transition has no structural secrets. This transition occurs secret, as well as the beta-alpha transition with improvement of the more stable and perfect form.

In contrast to the gamma-alpha transition consisting of a significant structural adjustment and cardinal modification of the hydrogen bonds between the segments. In the delta-form the segments packaging showed an average statistical distance between the chains around 4.20–4.22 Å. The appearance of the minimum sufficient for structural formation segmental mobility at the expense of recombination of the hydrogen bonds compacts container to 4.17–4.18 Å. The trend is stable, albeit within the margin of uncertainty. Perfecting, the gamma form compacts the segment package by mutual hydrogen bonding of all neighbors to 3.90 Å (22.770 °θ).

The newly established system of hydrogen bonds is dynamically changing and the distances fluctuate greatly. With temperature modification under certain conditions, in the range 160–1900 S stable alpha form starts forming. It forms two spacing of chain segments and, more specifically, between the crystallographic planes in which they lie. 4.44 Å – the distance between the targeted alternative circuits in the plains of folding. It is fixed to free from tension, conveniently located hydrogen bonds [Holms] and least varying in temperature modification. 3.71 Å – distance crystallographic axis "c" between stitched by hydrogen bonds sheets (planes of segments folding).

Sewing together by hydrogen bonds between alternative targeted segments (folds) in the same chain is folded and sewn together between neighboring segments, defining the width of the folds. Because on a number of thermodynamic and geometric reasons, they are extremely stable and large enough, 4.44 Å, can slipping through each other (in the direction perpendicular to the "b" molecular axes – i.e. a crystallographic axis "a") to wedge each other their Van-der-Waals interactions. This further helps compaction of stitched leaves and small lattice periodicity in the direction of "c".

It is clear that in this situation, a more imperfect and unstable, but more homogeneous and isotropic

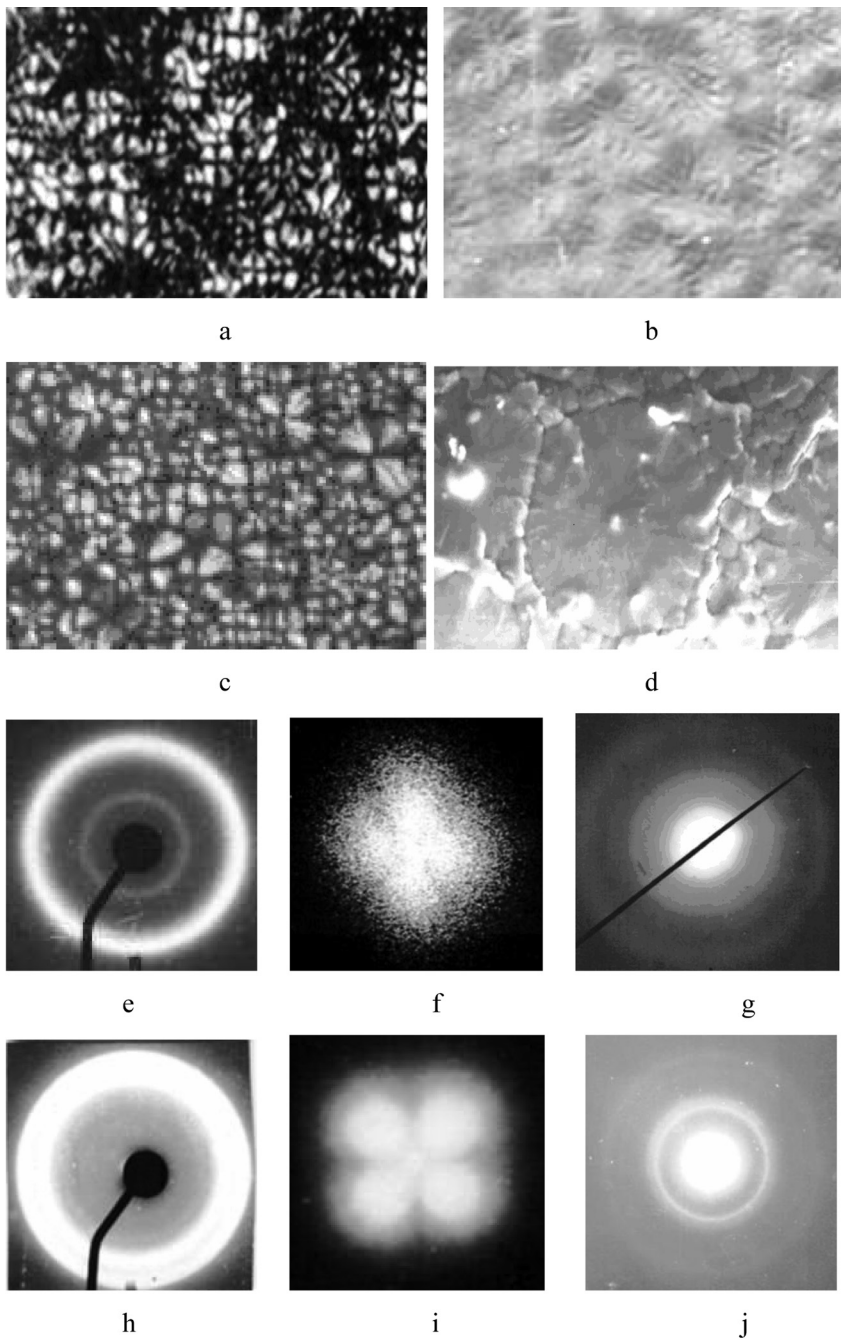

Fig. 2. Polarization (a, c) and scanning (b, d) photomicrography, X-ray (e, h), light (f, i - Small Angle Light Scattering, SALS) and electron (g, j) photo diffraction of thin films of PCL-2 (T_m = 225 °C; T_c = 20 °C): crystallization temperature 20 °C after free cooling (a, b, e, f, g); crystallization temperature 200 °C (c, d, h, I, j).

perpendicular to the macromolecular axes structure with average distances between the chains around 3.90 Å should be transformed into more non isometric the plain "ac" with periods in the crystallographic directions [200] and [002] 4.44 Å and 3.71 Å, respectively. This can occur spontaneously in increased segmental mobility due to thermal modification by pulling in an appropriate direction of dynamic equilibrium in the processes of fragmentation and recombination of hydrogen bonds between the amide groups of adjacent segments.

The appropriate direction in this case is between the different directions oriented segments of the same chain in the plains of folding them. That is, the realization of hydrogen bonds (H-bonds) between the amide groups of the two neighboring alterna-

Table 2. Perfection in % for thermal modification of the crystalline phase of the films of 50 microns PCL-2, 225 °C when pressed and crystallized at 200 °C

№	$T_{modif.}$, °C	Perfection of alpha form of PCL				Perfection of gamma form of PCL			
		V = 5 °C/min		V = 10 °C/min		V = 5 °C/min		V = 10 °C/min	
		heating	cooling	heating	cooling	heating	cooling	heating	cooling
1	20	98.48	95.63	98.48	95.59	99.66	99.75	99.66	99.62
2	30	98.48	95.55	98.48	95.51	99.66	99.75	99.66	99.62
3	40	98.48	95.55	98.48	95.51	99.22	99.75	99.53	99.62
4	50	98.43	95.51	98.48	95.51	99.22	99.75	99.31	99.62
5	60	98.39	95.46	98.39	95.42	98.79	99.75	99.00	99.62
6	70	98.39	95.42	98.39	95.42	98.79	99.71	98.96	99.62
7	80	98.30	95.42	98.39	95.42	98.79	99.71	98.92	99.62
8	90	98.26	95.33	98.35	95.33	98.36	99.71	98.74	99.62
9	100	98.21	95.29	98.26	95.29	97.93	99.71	98.57	99.62
10	110	98.13	95.25	98.22	95.25	97.50	99.71	98.10	99.57
11	120	98.04	95.13	98.18	95.17	97.46	99.71	97.84	99.57
12	130	97.60	95.09	97.88	95.13	97.38	99.71	97.76	99.53
13	140	96.95	95.05	97.05	95.05	97.29	99.71	97.67	99.53
14	150	96.31	94.80	96.46	94.80	97.21	99.66	97.59	99.40
15	160	95.68	94.80	95.87	94.80	97.08	99.66	97.42	99.49
16	165	95.05	94.80	95.28	94.43	97.00	99.66	97.17	99.49
17	170	94.42	94.66	94.60	94.26	96.88	99.66	97.08	99.44
18	175	93.79	94.28	94.02	93.99	96.75	99.62	96.88	99.44
19	180	93.17	93.75	93.44	93.28	96.63	99.62	96.67	99.40
20	185	92.55	92.64	92.32	92.35	96.54	99.62	96.54	99.40
21	190	91.93	92.06	91.75	91.91	96.46	99.53	96.46	99.44
22	195	91.31	91.40	91.14	91.00	96.38	99.44	96.38	99.40
23	200	90.70	90.88	90.49	90.55	96.30	98.79	96.30	98.74
24	205	90.09	90.35	89.88	90.03	96.21	97.89	96.21	97.80
25	210	89.49	89.49	89.40	89.52	96.09	97.29	96.09	97.25
26	215	88.88	89.14	88.97	89.05	95.97	96.59	95.97	96.59
27	220	88.48	88.52	88.73	88.73	95.76	95.81	95.76	95.81
28	225	88.07	88.07	88.49	88.49	95.40	95.40	95.40	95.40

tively targeted segments (branches) of a fold. Such connections are steric favorable to the molecular geometry and form thermodynamically favorable structures. The slightly folded sheets stitched also fit comfortably on matrix van-der-Waals curves planar contours using small fluctuation cooperative untangling. The latter, according to the common or micro local conditions may be replaced by other mechanisms.

For example, first may be adjusted the relief, and then to be fixed the network by suitable H-bonding, etc. in the space and time as one not a quick process, but thermodynamically favorable and therefore stable trend. The relatively isotropic gamma structure should be slightly deformed, forming H-bonds in stitched sheets and, more importantly, congesting these lists – improve packaging segments approximating crystallographic planes which lie in stable (200) of monoclinic alpha form 3.71 Å distance.

In practice, the distance increases with 0.54 Å from 3.90 up to 4.44 Å and the reduction with 0.19 Å from 3.90 to 3.71 Å within specified crystallographic directions are realized at the expense of minor reorganizations in basis of the unit cell. Like less permanent change in the partial coordinates of the basis change the structural amplitude so that the $(100)_\gamma$ migrates slightly from item 21.3 °θ (4.17 Å) up to 21.1 °2θ, in reaching the distance between the chaotically adjacent chains around 4.21 Å, then gradually migrate to 22,85 °2θ (3.89 Å). Then: BRILL (gamma–alpha) $(\gamma\leftrightarrow\alpha) = (d_{(100)\gamma}/3.88).100$, [%], – $0.258d_{(100)\gamma}$, %, $25d_{(100)\gamma}$, [%].

The delta form, present always and everywhere as a transitional phase between amorphous others may present average statistical distances between segments axes about 4.0 and 4.5 Å, an average of 4.22 Å. Rarely implemented in practice so deep hardening to form in the pure state.

Sometimes, the apparent displacement of the center of gravity of the amorphous halo of the most frequently observed angular position 21.05 °2θ, corresponding to the distance of 4.22 Å, probably due to the different quantitative relationship between the other polymer forms. Because the delta-form in the transition zones around the crystalline of different polymorphic forms with different perfection has a different density and different geometric statistical properties. It is difficult to find adequate criteria, however, for such assessments. Such precision is not necessary.

CONCLUSION

1. It was found that the control on the perfection change of the crystalline phase as the density of chain segments packing is adequate and convenient method about study of the PCL polymorphic transitions and their mechanism.

2. Algorithm and methodology for convenient practical control of the PCL crystalline phase perfection have been created. Analytical dependences of quantitative evaluation of the packing density and the perfection of its main polymorphic forms have been proposed.

3. The obtained results allow the assumption that the rich polymorphism and the transitions between the polymorphic phases are the most natural and thermodynamically entropy most comfortable steps in improving of the PCL crystal structure.

4. The assumptions and conclusions give reason to plan a detailed study of the specifics of segment packaging of all meso phases and phases of PCL from the structure of super cooled melt up to the perfect state of the stable crystalline α-form in practical the widest possible range of conditions. The need for such a study is determined by the requirement for the formation of an appropriate structure for obtaining the desired performance properties. Refinement and extension of the results of these studies show that this possibility is feasible.

Acknowledgements: *The authors are grateful to the Fund "Scientific investigations" of the Project NIH-244 from University "Prof. Dr. Assen Zlatarov", Burgas, and № 8268 from the University of Shumen, for the support.*

REFERENCES

1. N. S. Murthy, H. Minor, R. A. Latif, J. Macromol. *Sci. Phys. B*, **26**б(4), 427 (1987).
2. N. S. Murthy , S. A. Curran , S. M. Aharoni, H. Minor, Macromolecules, **24**(11), 3215 (1991).
3. Ch. Ruscher, I. Schroder, U. Fasrforsch, *Textiltechn*., **11**(4), 165 (1960).
4. A. Reicle, A. Prietzschk, *Angew. Chem*., **74**, 562 (1964).
5. J. B. Park, K. L. Devries, W. O. Statton, *J. Macromol. Sci. – Phys*., **B15**, 229 (1978).
6. P. F. Dismore, W. O. Statton, *J Polym. Sci. C*, **13**, 133 (1966).
7. A. Guinier, X-Ray Diffraction in Crystals, Imperfect Crystals and Amorphous Bodies, Freeman, San Francisco, 1963.
8. A. Ziabicki, *Kolloid-Zeitschrift*, **167**(2), 132 (1959).

КРИСТАЛНА СТРУКТУРА НА ПОЛИКАПРОЛАКТАМА. II. СЪВЪРШЕНСТВО НА КРИСТАЛНАТА ФАЗА

С. Узова[1], А. Попов[2], В. Велев[3], Т. Ангелов[4], С. Михалева[2], Х. Узов[2]

[1] ПГТ „Проф. д-р Ас. Златаров“, 8000 Бургас, България
[2] Университет „Проф. д-р Ас. Златаров“ – Бургас, 8010 Бургас, България
[3] Университет „Еп. Константин Преславски“, 9712 Шумен, България
[3] Лукойл Нефтохим Бургас АД, Бургас, България

Постъпила февруари, 2013 г.; приета май, 2013 г.

(Резюме)

Посредством комплексен анализ на интензитетни, профилни и позиционни характеристики на пиковете на дифракционните отражения от праховите рентгенови дифрактограми на поликапролактама се търсят подходи за определяне количественото съдържание и качествено състояние на кристалографските модификации в кристалната му фаза, като способ за оценка степента на завършеност на полиморфните му преходи при кристализация и рекристализация.

Установено е, че за обективност, адекватност и сравнимост на резултатите при определяне механизма и кинетиката на структурна реорганизация е необходима гарантирана условна еднозначност при събиране геометрично-чувствителната дифракционна експериментална информация посредством високо-температурната прахова рентгенова дифрактометрия. Необходима е адекватна еднозначна декомпозиция на интегрално-интензитетната дифрактометрична крива. Еднозначно разделяне и разпознаване на фазите, индексация на дифракционните отражения. Подобен подход би гарантирал точното определяне на количественото и качествено съотношение на полиморфните форми, определящо степента на реализиране на полиморфните преходи с близката предистория и перспектива. Точността на прогнозата зависи от това.

Направен е опит да се оптимизират методите за оценка съвършенството на кристалната фаза при поликапролактама. Установени са критерии за оценка на съвършенството на алфа формата му. Предложена е методика за практическото му определяне. Изведени са формули за неговата количествена оценка. Предложени са подходи за оценяване и на други полиморфни форми на поликапролактама. Интензитетното съотношение на основните дифракционни отражения се използва за количествена оценка и усъвършенстването на бета формата. Измененията в ъгловите девиации на основното дифракционно отражение на гама формата се анализират за определяне съвършенството ѝ.

Bulgarian Chemical Communications, Volume 45, Number 4 (pp. 584–591) 2013

Experimental study of the surface chemical composition of sea salt crystallized during evaporation of seawater under natural conditions

H. Kolev[1]*, G. Tyuliev[1], C. Christov[2], K. L. Kostov[2]

[1] *Institute of Catalysis, Bulgarian Academy of Sciences*
[2] *Institute of General and Inorganic Chemistry, Bulgarian Academy of Sciences*

Received February, 2013; Revised May, 2013

Under natural atmospheric conditions (at 45–55% RH and 25–30 °C) three sea-salt samples have been obtained by evaporation of sea waters from the Black Sea, Mediterranean Sea and Dead Sea, respectively, and then studied by XPS. The results show that the salt surfaces are enriched in Mg^{2+} ions as the Na^{+} ion amount is ~6 and ~20 times **lower** than that of the Mg^{2+} ions in the Black sea and Mediterranean Sea samples, respectively. Also enriched content of Br^{-} ions in all crystallized sea salts with respect to the chlorine concentration on the surface has been measured. Bromine ions are supposed to be localized in the top surface layer. Probably the first step of the crystallization sequence includes the formation of NaCl crystallites, followed by creation of a layer containing mainly $MgCl_2$ and $MgSO_4$ compounds. Additionally, this layer contains K^{+} ions, $(HCO_3)^{1-}$ and $(CO_3)^{2-}$ groups and also Ca^{2+} ions in the case of Dead Sea salt. Relatively high surface concentrations of the $(HCO_3)^{1-}$ and $(CO_3)^{2-}$ anions have been detected. Therefore, these ions together with the surface localized Br^{-} anions could play a significant role in the interaction dynamics on the surface of crystalized sea salts.

Key words: Sea salt, Ion concentration, Salt crystallization, XPS.

INTRODUCTION

The extents to which atmospheric particles affect the radiative balance of atmosphere depend on their chemical composition, physical state, and on their size as these properties depend on the relative humidity (RH). Sea salts aerosols are the largest species being highly hygroscopic and they initiate changes taking up water vapor from the atmosphere and forming aqueous droplets. Enhanced halide concentrations have been suggested at their liquid/vapor interface, which is important for the understanding of the atmospheric reactions [1]. Because the interactions occur on the surfaces of particles their surface chemical compositions have to be studied. This is the main motivation for the present study to investigate the chemical state and concentration of ions on the surface during the formation of sea-salt particles by evaporation of seawater.

The sequence of precipitation of the various ions, present in seawater during its evaporation, is crucial for the understanding the properties and reactivity of the formed sea salt particles. In that case the use of X-ray Photoelectron Spectroscopy (XPS) is particularly appropriate because it provides information about the chemical composition of the solid surfaces. There are a few studies on model laboratory samples using XPS, which contribute to the understanding of the surface segregation of different seawater ions. Zangmeister et al. [2] have studied the segregation of NaBr during the precipitation of mixed NaBr/NaCl crystals from aqueous solutions containing Br:Cl concentration ratio similar to that observed in seawater. The surface NaBr concentration has been found to be appr. 35 times higher than that in the crystal bulk but regardless of this NaBr segregation, most of the surface (~95%) remains occupied by NaCl [2]. The authors assume that a similar surface segregation of NaBr should be expected also in the case of the sea salt crystallization. However, based on the high Cl concentration found in seawater they have considered that also the sea-salt surface should be enriched mainly in NaCl.

Oppositely, Ghosal et al. [3] have used a significantly higher Br:Cl ratio, compared to that in sea-

* To whom all correspondence should be sent:
E-mail: hgkolev@ic.bas.bg

water, to a grown mixed NaBr/NaCl crystal. Their XPS measurements have shown higher Br:Cl ratio in the bulk of the crystals than the one measured by Zangmeister et al. [2]. An important result is that after water adsorption this ratio increases drastically leading to the conclusion that on the sea-salt surface the NaBr segregation should also be enhanced. Also segregation of Br^- ions has been observed on the surface of bromide-doped NaCl crystal at relative humidity above 40% due to water adsorption [4]. The Br-enrichment of the salt surfaces can play an important role in some global atmosphere processes like depletion of atmospheric ozone layer [3]. This makes the quantitative and qualitative researches on marine salt, from which salt aerosols are formed particularly important.

Harviee and Weare [5] have developed Na–K–Mg–Ca–Cl–SO_4–H_2O model in order to predict the mineral solubility and to understand the sequence of the mineral depositions at equilibrium evaporation of brine chemically similar to seawater. As an extension to the model Eugster et al. [6] have calculated phase relations within the same system Na–K–Mg–Ca–Cl–SO_4–H_2O at 25 °C and 1 atm pressure. The authors have noted that it is possible to estimate quantitatively the process of mineral precipitation for the natural carbonate-free waters based on the obtained results. Also, for this system a model called Spencer-Møller-Weare model has been parameterized not only at 25 °C but also at the subzero temperatures [7, 8].

The previous theoretical calculations of Christov [9, 10] and recent chemical kinetics experimental studies [11] show that assuming the sea salt as a simple halite (NaCl(cr)) salt, which is the main sea salt component, is a wrong approximation in the construction of a model for sea salt wetting behavior. It has been shown that the formation of surface solutions in equilibrium with magnesium chloride solids (bishofite ($MgCl_2.6H_2O$(s); DRH ≈ 34%), and carnallite ($KCl.MgCl_2.6H_2O$(s); MDRH = 34–52%) determined to a great extent the deliquescence behavior of sea salt under natural wet atmospheric conditions [9–11].

Now, using XPS we study experimentally the surface chemical composition of the sea-salt surface in order to shed more light and aid understanding of the bulk-surface disproportion of ions. XPS is a surface sensitive method, monitoring the chemical states of the elements and their concentrations within surface layers up to 2–3 nm depth [12]. Therefore, we expect to obtain results about the ion concentrations on the surface of crystalized sea salt leading to the understanding of the sequence of precipitation of various salts under natural evaporation conditions of sea water (45–55% RH and temperature of 25–30 °C).

EXPERIMENTAL

X-ray photoelectron measurements have been carried out on the ESCALAB MkII (VG Scientific) electron spectrometer at a base pressure in the analysis chamber of 5×10^{-10} mbar using twin anode MgKα/AlKα X-ray source with excitation energies of 1253.6 and 1486.6 eV, respectively. The spectra are recorded at the total instrumental resolution (as it was measured with the FWHM of $Ag3d_{5/2}$ photoelectron line) of 1.06 and 1.18 eV for MgKα and AlKα excitation sources, respectively. The energy scale has been calibrated by normalizing the C1s line of adsorbed adventitious hydrocarbons to 285.0 eV. The processing of the measured spectra includes a subtraction of X-ray satellites and Shirley-type background. The peak positions and areas are evaluated by a symmetrical Gaussian-Lorentzian curve fitting. The relative concentrations of the different chemical species are determined based on normalization of the peak areas to their photoionization cross-sections, calculated by Scofield [13].

The sea salt samples have been obtained by evaporation (at the natural conditions) of sea waters from Black Sea (BS), Mediterranean Sea (MS) and Dead Sea (DS). The ion concentrations on the salt surfaces measured by XPS are compared with the bulk data determined by the EUROTEST – CONTROL EAD Company (Sofia, Bulgaria). The temperature is maintained at about 25–30 °C, whereas the relative humidity is controlled within 45–55% RH. The temperature is measured by a *Pt100* thermometer. The relative humidity is being monitored by *808H5V6* Humidity transmitter during the whole evaporation period.

RESULTS AND DISCUSSION

Surface chemical composition of sea salts

As it was mentioned above, the three sea-salt samples obtained by evaporation of sea water from the Black Sea (BS), Mediterranean Sea (MS) and Dead Sea (DS), respectively, have been studied by XPS. One of the most intensive photoelectron peaks is located at about 200 eV and it originates from Cl2p core-level, characteristic of Cl^- ions giving respectively the largest concentration of these ions compared to all the other surface salt particles.

The presentation of our results begins with the C1s core-level region because the energy of the most intensive peak here is used for energy-scale calibration (Fig. 1). This peak at binding energy of 285.0 eV is characteristic of the C-H and/or C-C functional groups [14] most probably due to adsorbed hydrocarbons from residual gases in the vacuum chamber. Fig. 1 shows the different peak contributions, derived from

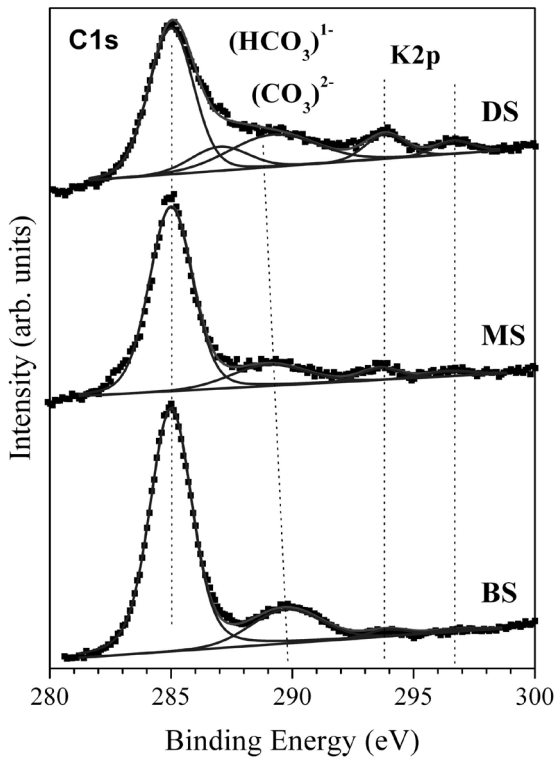

Fig. 1. C1s- and K2p-spectral regions of sea salts crystallized from different seawaters

the fitting procedure described in Sect. Experimental. The next two low-intensity broad peaks centered in a region of 287–290 eV can be attributed to negatively charged $(HCO_3)^-$ and $(CO_3)^{2-}$ functional groups as the higher negative charge of $(CO_3)^{2-}$ group determines its higher C1s binding energy [12]. The peak contribution of the $(HCO_3)^-$ group is more distinctly seen for the DS salt although the two functional groups are present in all the studied seawaters. Their bulk concentrations in seawaters are very small, between 70–300 times lower than the bulk-seawater concentration of Cl^- ions (Table 1) but in the surface layers of crystallized sea salts the corresponding ratio is significantly higher: the concentrations of $(HCO_3)^-$ and $(CO_3)^{2-}$ groups are only 6–8 times lower than that of chloride.

In the spectral region, shown in Fig. 1, the $K2p_{3/2}$ and $K2p_{1/2}$ peaks are measured at binding energies of 293.6 and 296.2 eV, characteristic of K^+ ions. No significant differences are detected for the K^+ ion concentrations with respect to those of the surface Cl^- species. The K^+:Cl^- concentration ratio varies between ~70 for BS salt and ~43 for both MS and DS salts (Table 1). It should be noted that the concentration ratio of the same order is measured in the bulk seawaters. There is significant deviation only for DS seawater, which will be discussed at the end of this section. These K^+:Cl^- ratio similarities between bulk and surface of liquid and crystallized phases, respectively, can be explained assuming that K^+ ions originate from the KCl compound. Surprisingly, the most intensive feature in XPS spectra cannot be connected with Na but rather with the presence of large amount of Mg on the surface. This is clearly shown in Fig. 2. The binding energies of the indicated peaks are characteristic of Mg^{2+}, Na^+, Br^- and Ca^{2+}-ions [15]. The Na2s peak intensity is almost invisible, while the Mg2s peak dominates the whole spectral region, although their photoionization cross-sections are comparable, 0.422 and 0.575, respectively [13]. The ion concentrations in the surface layers of the crystalline salts are shown in Table 1. While in the bulk sea water from BS and MS the Na^+ ion concentration is 10 times *higher* than the Mg^{2+} concentration, on the surface of crystallized salt phase the Na^+ ion amount is ~6 and ~20 times *lower* compared to the Mg^{2+} amount, respectively. Again a deviation is observable in the Dead Sea sample results. In the bulk seawater the amounts of Mg^{2+} and Na^+ ions are almost equal, which can

Table 1. Surface ion concentrations (at. %) of salts evaporated from Black Sea (BS), Mediterranean Sea (MS) and Dead Sea (DS) water sample solution compared to the ion concentrations (at. %) in sea water from corresponding seas

Ions	BS water (at. %)	BS salt (at. %)	MS water (at. %)	MS salt (at. %)	DS water (at. %)	DS salt (at. %)
Na^+	43.82	6.6	42.12	1.8	17.85	0.8
Mg^{2+}	4.29	37.6	4.60	37.6	18.71	29.6
K^+	0.73	0.6	0.83	1.1	2.33	1.3
Ca^{2+}	0.90	-	0.99	-	3.10	3.7
Cl^-	47.40	41.2	48.93	46.2	57.12	56.7
$(SO_4)^{2-}$	2.09	5.8	2.29	6.8	0.04	0
$(HCO_3)^-$	0.40	7.2	0.08	6.0	0.28	6.9
$(CO_3)^{2-}$	0.26		0.08		0.06	
Br^-	0.06	1.1	0.08	0.5	0.50	1.0

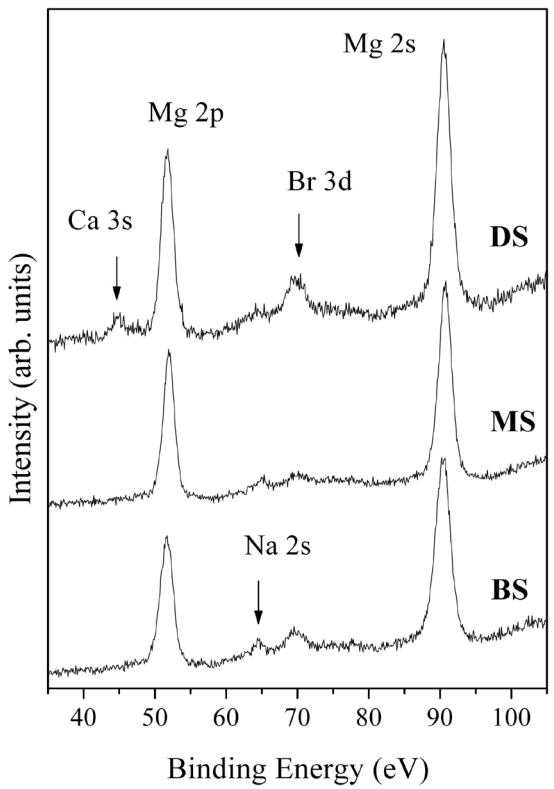

Fig. 2. Low binding-energy regions of crystallized sea salts from different seawater samples

be explained by the already started crystallization leading to the formation of small NaCl crystallites on the walls of the container with DS water. With respect to BS and MS waters the smaller amount of Na^+ ions in DS water leads to their smaller quantity in the surface layers of crystallized phase: 37 times lower than Mg^{2+} ion concentration (Table. 1). However, for all three crystallized samples one can conclude that the surfaces of sea salts are enriched in Mg^{2+} ions.

Another remarkable feature, which follows from our measurements, is the enriched content of Br^- ions with respect to the chlorine concentration on the surface of all crystallized samples. In the bulk of seawaters the Br^-:Cl^- concentrations ratio is 0.001 for BS and MS, respectively, and 0.009 for the DS sample while on the sea-salt surfaces this ratio is measured to be 27, 10 and 2 times higher in the salts evaporated from BS, MS and DS, respectively (Table 1). Despite the very small bromide amounts they can be reliably measured by XPS due to the relatively high photoionization cross-sections of Br3d (5/2+3/2) electrons, calculated to be 1.68+1.16=2.84, respectively [13]. For comparison this value is about 5–7 times higher than the cross-sections of Mg2s and Na2s electrons, respectively, as it was mentioned above. In addition to the analysis of the results represented in Fig. 2 we should note here that only for the salt crystallized from DS water a small amount of Ca^{2+} ions is detected with corresponding weak peak of Ca3s electron core-level at 44.8 eV.

To complete the discussion of the surface chemical composition of sea salts the next intensive photoelectron lines of S2p, Cl2p and O1s should also be considered (Fig. 3). The sulfur amount is detected

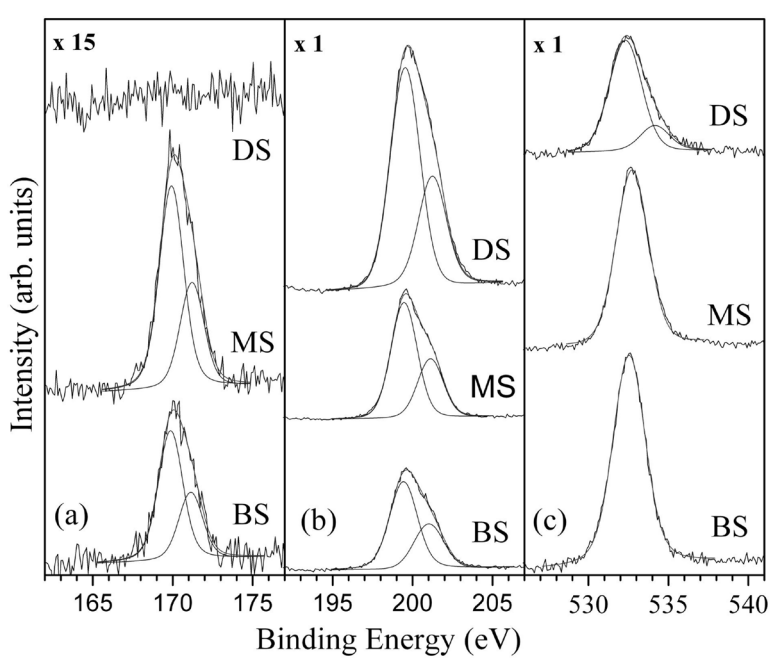

Fig. 3. Different spectral regions of crystallized sea salts: (a) S2p; (b) Cl2p; (c) O1s

only in the salts, crystallized from BS and MS waters. From the fitted S2p spectra a $S2p_{3/2}$ binding energy of 169.9 eV has been derived as well as 2p (3/2–1/2) spin-orbital splitting of 1.2 eV (Fig. 3a). This energy shows that the sulphur is in $(SO_4)^{2-}$ chemical state (Fig. 3a) [15]. The $(SO_4)^{2-}$:Cl^- ions concentration ratio is almost equal (0.14) on the surfaces of both BS and MS crystallized salts, whereas in the bulk of seawaters this ratio is about 3 times lower (Table 1).

The spectral Cl2p region is characterized by one asymmetrical peak containing $2p_{3/2}$ and $2p_{1/2}$ components with separation energy difference of 0.7 eV (Fig. 3b). Although, the peak intensities for different crystallized salts increase in the order BS<MS<DS, the chloride concentration remains almost the same for BS and MS salts and it is higher by approximately 20% for the DS salt (Table 1). These results can be convincingly explained making a balance between the two possible $MgCl_2$ and $MgSO_4$ compounds, which may exist on the sea-salt surfaces using the concentrations of Mg^{2+}, Cl^- and $(SO_4)^{2-}$ ions from Table 1. On the DS salt surface no sulfur is detected and therefore almost all the Mg^{2+} and Cl^- ions are probably included in the $MgCl_2$ whereas on the BS and MS salt surfaces there are ~5–7% $(SO_4)^{2-}$ ions and therefore part of the Mg-ions is involved in the form of $MgSO_4$ compound. For this reason the amount of $MgCl_2$ compound and respectively Cl^- ions should be lower than those in DS salt. This concentration balance leads to the conclusion that $MgCl_2$ and $MgSO_4$ compounds may exist on the surfaces of BS and MS salts in $MgCl_2$:$MgSO_4$ amount ratio of ~3.

For the salts crystallized from BS and MS no differences are to be seen in their O1s peaks as evidenced by the spectra shown in Fig. 3c. Both O1s peaks are located at 532.5 eV which binding energy is characteristic of oxygen in organic molecules and/or $(HCO_3)^-$ groups [16], $(CO_3)^{2-}$ groups [17] as well as of $(SO_4)^{2-}$ groups [18]. Therefore the oxygen ions in chemically different environments in these three groups cannot be resolved based on their binding energies. For the sea salt evaporated from the DS water we detect an additional O1s peak at 534.1 eV, which can be attributed to OH^- groups [19]. As this peak does not exist in the BS and MS salt spectra and also having in mind that the only significant difference between the three sea-salt samples is the presence of Ca^{2+} ions in DS salt surface, one can suppose that the OH^- groups are connected with some compound also containing Ca^{2+}.

Sequence of mineral precipitation

As it was demonstrated in the previous sections, the chemical compositions of the surfaces of crystallized sea salts at 45–55% RH and 25–30 °C showed a high concentration of Mg^{2+} ions, whereas the Na^+ ion amount was ~6 and ~20 times **lower** than the Mg^{2+} amount in the BS and MS salts, respectively. In addition, the Br^-:Cl^- and $(SO_4)^{2-}$:Cl^- ion concentrations ratios are established to be significantly higher than that in the bulk of seawaters. These surprising results can be explained by precisely determined sequence of deposition of the various minerals, contained in sea waters. Therefore, to examine this sequence it is necessary to analyze the amounts of different ions in the depth of the samples. For this purpose the sample surface has been "washed" with deionized water for a short time interval and the chemical composition of the treated newly formed surface has also been studied by XPS. Here, we present the results for the MS salt crystallized under natural conditions like the samples discussed in Sect. 3.2. The only difference is that the MS salt has been left for a few months under the conditions of its formation (at 45–55% RH and 25–30 °C), and as a result, the salt has been humidified. It should be noted that the original (before washing) and treated surfaces have been dried in vacuum before the analysis.

The most informative XPS spectra of the original and treated surfaces are shown in Fig. 4. Obviously,

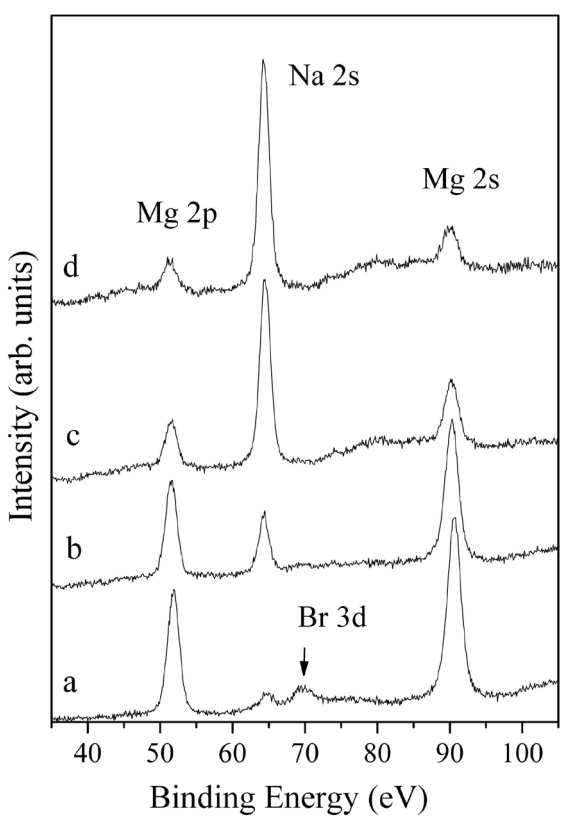

Fig. 4. Comparison of low binding-energy regions of treated sea salts: (a) before "washing" procedure and after (b) first, (c) second and (d) third lavement, respectively

Table 2. Surface ion concentrations (at. %) of wetted salt ontained by evaporation of Mediterranean Sea (MS) water and after three lavements of the salt surface with deionized water

Ions	Wetted MS salt (at.%)	1st lavement (at.%)	2nd lavement (at.%)	3rd lavement (at.%)
Na^+	3.4	12.7	37.8	47.4
Mg^{2+}	36.2	31.5	11.4	7.1
K^+	0.9	2.6	1.4	0.8
Ca^{2+}	–	–	~0	~0
Cl^-	47.4	35.9	41.7	45.7
$(SO_4)^{2-}$	5.6	12.9	4.7	3.3
$(HCO_3)^-$ $(CO_3)^{2-}$	5.7	4.0	3.0	2.6
Br^-	0.8	0.2	0	0

the concentration of Mg-ions is significantly reduced after "the washing" treatment, while gradually the Na2s peak begins to dominate. The 3d peak of the bromide almost disappears after the first lavement of the salt surface. The concentrations of all ions are shown in Table 2. The results for the original salt surface are in good agreement with those for MS salt concentration, presented in Table 1, which shows the good reproducibility of our measurements. Several conclusions can be drawn on the basis of the results listed in Table 2.

After the first lavement the Mg^{2+} ions concentration is slightly reduced while that of $(SO_4)^{2-}$ is increased 2 times. Also 25% reduction of Cl^- ions concentration is observed. The explanation can be found assuming the presence of a significant amount of $MgSO_4$ immediately below the top surface layers of the salt crystal. After the next steps of washing Mg^{2+} and $(SO_4)^{2-}$ ion concentrations are decreased simultaneously but the Na^+ and Cl^- amounts increase to a level characteristic of NaCl stoichiometry. Therefore, we believe that after the washing treatment of the salt surface relatively clean NaCl crystallites should appear indicating that their formation should be the first step in the crystallization sequence of the sea salt under natural conditions of seawater evaporation. Indeed, Table 2 shows that the concentrations of all ions are decreased except for those of Cl^- and Na^+. Note, that in these considerations, the differences in the initial dissolution rates of the various salt components have been ignored.

Observed differences in DS salt features

Similar study to that, explained in previous section, has been performed with the salt evaporated from Dead Sea water. This salt has been stationed for five months under laboratory conditions. Because of the humidity in the room the salt becomes moisturized and has been separated in two volume layers. The bottom layer in the container consists of wet precipitated crystallites, whereas above this layer an aqueous salt solution is observed. The top liquid layer has been dried first and then studied by XPS. Its corresponding XP spectrum is shown in Fig. 5 and it is compared with the spectrum of the original DS salt. The measured concentrations of the Na^+, Mg^+, K^+, Ca^{2+}, Cl^-, and Br^- ions on the surface of the salt, obtained from the top aqueous layer, are 3.0%, 13.5%, 0.9%, 16.3%, 57.6% and 2.5%, respectively. In comparison to the original DS salt (see Table 1) the amounts of Ca^{2+} and Br^- ions are increased strongly

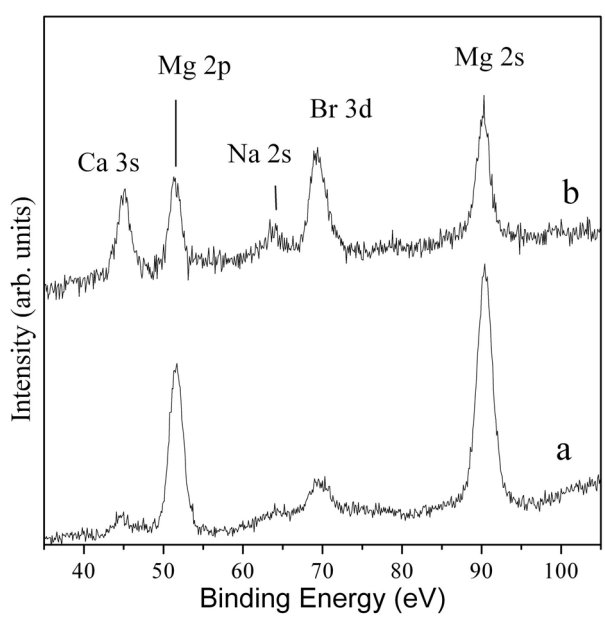

Fig. 5. Comparison of XP spectra of (a) original DS sea salt and (b) salt received from the top liquid layer as it is described in the text

more than 4 and 2.5 times, respectively. Therefore, we can suggest that these are the ions, dissolved in the formed liquid top layer, which were originally located on the salt crystal surface.

CONCLUSIONS

Three sea-salt samples obtained by evaporation of sea water from the Black Sea, Mediterranean Sea and Dead Sea, have been studied by XPS. The highest ion concentrations of about 41–46% are measured for the Cl^- ions in the BS and MS salts, and ~57% in the DS salt. In all the samples, the salt crystal surfaces are enriched in Mg^{2+} ions, while the bulk is dominated by the presence of Na^+ ions. While the Na^+ ion concentration in the bulk sea water from BS and MS is 10 times *higher* than the Mg^{2+} concentration, on the surface of crystallized salt phase the Na^+ ion amount is ~6 and ~20 times *lower* with respect to the Mg^{2+} amount, respectively. Another remarkable feature is the enriched content of Br^- ions with respect to the chloride ions concentration on the salt surface, which suggests that the bromide ions are supposed to be localized mainly in the top surface layer.

In an attempt to examine the sequence of salt crystallization we reached the conclusion that the first step should include the formation of NaCl crystallites followed by creation of a layer containing mainly $MgCl_2$ and $MgSO_4$ compounds. This second layer contains also small amounts of K^+, $(HCO_3)^-$ and $(CO_3)^{2-}$ groups and also Ca^{2+} in the case of DS salt. The $(HCO_3)^-$ and $(CO_3)^{2-}$ concentrations in the bulk of seawaters are very low: 70–300 times lower than the bulk concentration of Cl^- ions. It is worth noting that in the surface layers the $(HCO_3)^-$ and $(CO_3)^{2-}$ ion concentrations are only 6–8 times lower than that of the chloride. These relative high surface concentrations of the $(HCO_3)^{1-}$ and $(CO_3)^{2-}$ groups, together with the surface localized Br^- ions, might play a significant role in the interaction dynamics on the surface of crystallized sea salts.

Acknowledgements: *The authors gratefully acknowledge the financial support by the National Science Fund of Bulgaria (Grant No DO-02-243). The EUROTEST – CONTROL EAD (http://www.eurotest-control.bg) Company assistance is acknowledged for the determination of the bulk concentrations of ions presented in sea water. Dr. Alexander Eliyas is acknowledged for critical reading of this paper.*

REFERENCES

1. S. Ghosal, J. C. Hemminger, H. Bluhm, B. S. Mun, E. L. D. Hebenstreit, G. Ketteler, D. F. Ogletree, F. G. Requejo, M. Salmeron, *Science*, **305**, 563 (2005).
2. C. D. Zangmeister, J. A. Turner, J. E . Pemberton, *Geophys. Res. Lett*., **28**, 995 (2001).
3. S. Ghosal, A. Shbeeb, J. C. Hemminger, *Geophys. Res. Lett*., **27**, 1879 (2000).
4. S. Ghosal, A. Verdaguer, J. C. Hemminger, M. Salmeron, *J. Phys. Chem. A*, **109**, 4744 (2005).
5. C. E. Harvie, J. H. Weare, *Geochim. Cosmochim. Acta*, **444**, 981 (1980).
6. H. P. Eugster, C. E. Harvie, J. H. Weare, *Geochim. Cosmochim. Acta*, **44**, 1335 (1980).
7. R. J. Spencer, N. Møller, J. H.Weare, *Geochim. Gosmochim. Acta*, **54**, 575 (1990).
8. G. M. Marion, R. E. Farren, *Geochim. Gosmochim. Acta,* **63**, 1305 (1999).
9. C. Christov, *J. Chem. Eng. Data,* **54**, 627 (2009).
10. C. Christov, *J. Chem. Eng. Data,* **54**, 2599 (2009).
11. J.-H. Park, C. Christov, A. Ivanov, M. Molina, *Geophys. Res. Lett*., **36**, LO2802 (2009).
12. D. Briggs, in: Surface Analysis by Auger and X-Ray Photoelectron Spectroscopy, J. G. D. Briggs (ed), IM Publications and Surface Spectra Ltd, 2003, p. 31.
13. J. H. Scofield, *J. Electron Spectrosc. Relat. Phenom*., **8**, 129 (1976).
14. D. Karpuzov, K. L. Kostov, E. Venkova, P. Kirova, I. Katardjiev, G. Carter, *Nuc. Instr. Meth. Phys. Res*., **B 39**, 787 (1989).
15. C. D. Wagner, W. M. Riggs, L. E. Davis, J. F. Moulder, G. E. Mullenberg, Handbook of X-ray Photoelectron spectroscopy, G. Mullenberg (ed), Perkin-Elmer Corporation, 1979.
16. B. J. Tyler, B. D. Ratner, D. G. Castner and D. Briggs, *J. Biomed. Mater. Res*., **26**, 273 (1992).
17. F. Voigts, F. Bebensee, S. Dahle, K. Volgmann, W. Maus-Friedrichs, *Surf. Sci.*, **603**, 40 (2009).
18. S. Sugiyama, T. Miyamoto, H. Hayashi, J.B. Moffat, *Bull. Chem. Soc. Jpn*., **69**, 235 (1996).
19. N. Martensson, P. A. Malmquist, S. Svensson, E. Basilier, J. J. Pireaux, U. Gelius, K. Siegbahn, *J. Chim*., **1**, 191 (1977).

ЕКСПЕРИМЕНТАЛНО ИЗСЛЕДВАНЕ НА ХИМИЧЕСКИЯ СЪСТАВ НА ПОВЪРХНОСТТА НА МОРСКА СОЛ, ПОЛУЧЕНА ПРИ ИЗПАРЕНИЕ НА МОРСКА ВОДА В ЕСТЕСТВЕНИ УСЛОВИЯ

Х. Колев[1], Г. Тюлиев[1], Х. Христов[2], К. Костов[2]

[1] *Институт по катализ, Българска академия на науките*
[2] *Институт по обща и неорганична химия, Българска академия на науките*

Постъпила февруари, 2013 г.; приета май, 2013 г.

(Резюме)

При естествени атмосферни условия (45–55% RH и 25–30 °C) три проби от морска сол са получени чрез изпарение на морска вода от Черно море, Средиземно море и Мъртво море, съответно, след което са изследвани с РФС. Резултатите показват, че повърхността на солта е обогатена с Mg^{2+} йони, като концентрацията на Na^{+} йоните е ~6 пъти по-ниска от тази на Mg^{2+} йоните в Черно море и съответно ~20 пъти по-ниска от тази на Mg^{2+} йоните в Средиземно море. Регистрирано е повишено съдържание на Br-йони на повърхностите на всички кристализирали морски соли спрямо концентрацията на хлор. Бромните йони най-вероятно са локализирани в най-горния повърхностен слой. Вероятно първата стъпка на кристализационния процес включва образуването на кристали от NaCl, последвано от създаването на слой, съдържащ предимно $MgCl_2$ и $MgSO_4$ съединения. Освен това, този слой съдържа K^{+} йони, $(HCO_3)^{1-}$ и $(CO_3)^{2-}$ групи, а също и Ca^{2+} йони в случая на сол от Мъртво море. На повърхността на образците концентрациите на $(HCO_3)^{1-}$ и $(CO_3)^{2-}$ йони са относително високи. Следователно, тези йони заедно с локализираните на повърхността Br^{-} аниони могат да играят важна роля в динамиката на взаимодействията върху повърхностите на кристализиралите морски соли.

Bulgarian Chemical Communications, Volume 45, Number 4 (pp. 592–600) 2013

Physical bases of thermal stability of proteins: A comparative study on homologous pairs from mesophilic and thermophilic organisms

E. K. Salamanova*, D. T. Tsoneva, A. D. Karshikoff

Institute of Molecular Biology "Akad. Rumen Tsanev", Bulgarian Academy of Sciences, Acad. G. Bonchev st., bl. 21, 1113 Sofia, Bulgaria

Received February, 2013; Revised May, 2013

We used classical molecular dynamics simulation method to investigate physical factors responsible for the increased thermal stability of proteins from thermophilic and hyperthermophilic organisms. Subject of investigation were two pairs of homologous proteins from the functional classes of: 1) cold shock proteins from *Escherichia coli* (mesophilic) and *Bacillus caldolyticus* (thermophilic) and 2) acylphosphatases from *Bos taurus* (mesophilic) and *Pyrococcus horicoshii* (hyperthermophilic). The simulations were performed for three different temperatures: 298 K, 373 K and 500 K. The results confirmed the common opinion that salt bridges and internal hydrogen bond networks stabilize thermostable proteins at high temperature. In addition, we found that at high temperatures the packing defects, in terms of cavity formation, increase with a preference to the mesophilic protein. Since cavities are a destabilizing factor, we conclude that due to specific packing organisation of proteins of extremophilic organisms, these proteins are more resistant to temperature induced cavity formation, which contributes to their enhanced tolerance towards increase in temperature.

Key words: Thermostability, extremophiles, molecular dynamics, packing defects.

INTRODUCTION

Proteins from thermostable organisms are characterized by higher thermal stability in comparison with their mesophilic counterparts. The most discussed factors contributing to thermal stability of proteins are the optimization of electrostatic interactions [1], the optimization of protein-solvent interactions [2], salt bridges and hydrogen bond networks [3, 4]. Molecular packing and reduction of packing defects (cavity formation) can also be considered as a factor involved in the mechanism of thermal stabilization of proteins [5].

There are a few overall structural characteristics that discriminate proteins from mesophilic and (hyper)thermophilic organisms such as amino acid content, secondary and quaternary structure. These differences preferably occur at the protein-solvent interface rather than in the protein interior. Polar non-charged residues in thermophilic proteins have been found to change into glutamate and lysine and non-polar amino acids to substitute isoleucine [6]. In hyperthermophiles, isoleucine and to a lesser extent valine residues have been proved to form most of the hydrophobic contacts of the structurally conserved regions [7]. The secondary structure accounts for a larger fraction of residues with α-helices and β-strands conformations in the thermophilic proteins. Consequently, it has been discovered that the content of lower structured irregular regions is smaller in thermophiles [8]. The comparison between Fe-Superoxide dismutases (Fe-SOD's) has revealed that the thermophilic counterparts have fewer and longer loops, more α-helices and turns, and decreased length of β-strands [9]. α-Helices have showed to be involved in the greater apolar contact area in the hyperthermophilic proteins. Despite all the differences in amino acid contents and secondary structures, there are practically no or very small differences in the three-dimensional organization of the homologous mesophilic/thermostable proteins.

The above observations, however, do not reveal in detail the driving forces responsible for the shift of the melting point to higher temperature of proteins from (hyper)thermophilic species. Since the chemical content of these classes of proteins is practically the same, the answer to the question of thermal stability should be sought in the delicate balance of

* To whom all correspondence should be sent:
E-mail: esalamanova@bio21.bas.bg

non-covalent interactions. Vogt et al. [10] have investigated 16 families of proteins in which 80% have manifested correlation between the thermal stability and the increase in the number of internal hydrogen bonds, salt bridges and existence of polar surface. These authors have found that proteins connect to 22 extra solvent molecules per 10 °C rise in melting temperature by increasing their polar surface area. It has also been found that the increase in the internal hydrogen bonding in thermophilic proteins is mainly due to links between buried donor/acceptor pairs belonging to the main chains. The abundance of stable intermolecular and intramolecular hydrogen bonds has been found to attribute to the mechanical rigidity of the proteins, a factor enhancing their thermal stability [11]. In thermostable proteins a large number of side chain alternative H-bonds are formed with rise in temperature[12].

The electrostatic interactions have been found to have an important role for the thermal stability of proteins, especially in increasing the number of the salt bridges [13]. Danciulescu et al. [14] have investigated the electrostatic interactions calculating the free energy contributions for the nucleotide-binding domain of homologous mesophilic and hyperthermophilic Glutamate dehydrogenises from *E. Coli* and *T. maritima*. The mobility and the dynamics of the salt bridges proved to be crucial. According to their calculations the specific heat capacity of the hyperthermophilic protein is higher than the heat capacity of the mesophilic one.

In our earlier investigations we have noticed that protein from (hyper)thermophilic organisms are characterized by somewhat lower packing density [5]. We have also confirmed that the packing defects in term of cavity formation are reduced in (hyper)thermophilic proteins. Hence, the destabilizing effect of the cavities is diminished in these proteins. These results, as well as the vast majority of the conclusions discussed above, are based on three-dimensional X-ray protein structures. It is well documented that proteins in solution are dynamic and occupy more than a single conformation. It is interesting to see to what extent the above observations can be confirmed when dynamic properties of proteins are taken into account. For this purpose we employed MD simulation for two pairs of homologous proteins from mesophilic and (hyper) thermophilic organisms. The first homologous pair consists of the cold shock proteins from *Escherichia coli* (mesophilic, in the following abbreviated as M-csp) and *Bacillus caldolyticus* (thermophilic, T-csp) and 2) acylphosphatases from *Bos taurus* (mesophilic, M-acp) and *Pyrococcus horicoshii* (hyperthermophilic, H-acp). The structures of the two pairs are illustrated in Figure 1. As seen, the

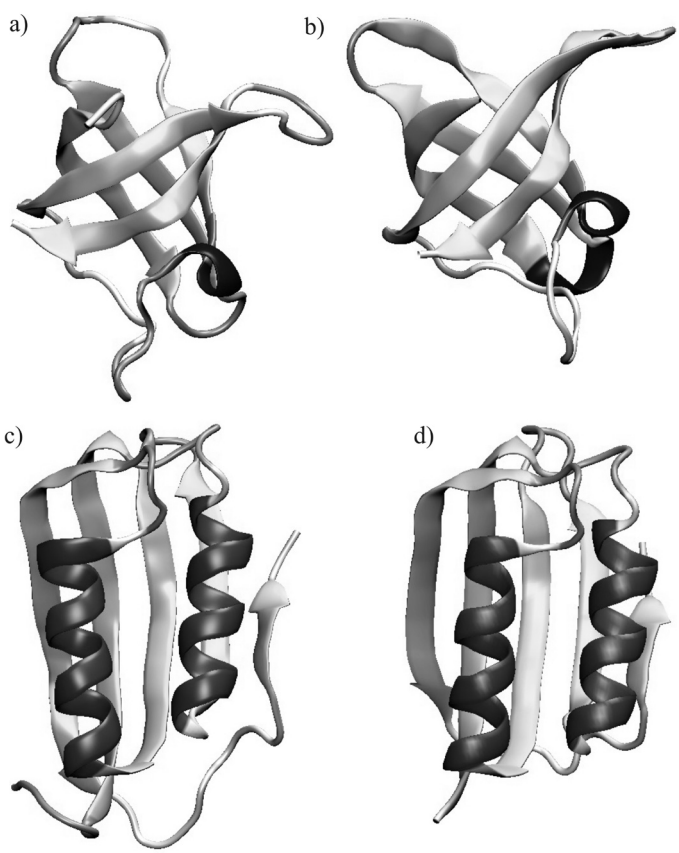

Fig. 1. X-ray crystal structures of the investigated proteins: a) M-csp; b) T-csp; c) M-acp and d) H-acp

three dimensional similarity within the pairs is remarkable, nevertheless the unfolding temperatures differ dramatically (see also Table 1).

Their X-ray structures were downloaded from Protein Data Bank (PDB) [15]. Our results are in accord with the common opinion that electrostatic interactions and hydrogen bonding are important factor for the thermal stability of proteins from extremophiles. The average percentage of occupancy per amino acid pair, participating in a salt bridge and per hydrogen bond in hyperthrmophilic proteins has showed distinct separation compared to the mesophilic and thermophilic proteins. The hyperthermophiles formed longer-lasting, stable hydrogen bonds. In addition, we have shown that thermophilic and especially hyperthermophilic proteins from the investigated pairs are more resistant towards temperature induced cavity formation. Since cavities are destabilizing component of protein structure, we conclude that proteins from thermophiles gain stability via diminishing temperature induced cavity formation.

COMPUTATIONAL METHODS

Classical Molecular Dynamics (MD) simulations were carried out for two pairs of homologous proteins. The biological units of the mesophilic proteins are monomers, whereas those of the thermophilic and hyperthermophilic proteins are dimers. For the consistency of our calculations only the monomers were used.

The possible contribution of intermolecular interactions within the tertiary structures to thermal stability is out of the scope of this study.

Based on the sequence analysis performed using BLASTP algorithm [16], we found that the thermostable cold shock protein and the acylphosphatase have a structural identity with their mesophilic counterparts of 92% and 84%, respectively.

All the MD simulations were performed, using GROMACS v.4.5.3 [17, 18] with CHARMM27 force field [19] and TIP3P explicit water model [20]. The systems were set up in dodecahedron boxes with 1nm distance between the sides of the box and the protein surfaces. Water molecules were added, along with sodium (Na^+) and chloride (Cl^-) counter ions in order to achieve ionic strength of 0.1 M. The systems were minimized using Steepest Descent method. The restraints of the atoms were released at three stages: 1) the minimizations were performed with all non-hydrogen atoms, restrained with 500 kJ/mol/nm^2; 2) only non-hydrogen atoms of the main chain restrained with 200 kJ/mol/nm^2 and 3) the minimizations were performed without position restraints. Next, MD simulations were conducted in periodic boundary conditions, in NVT ensemble. The systems were heated by 10 K every 2 ps to the desired temperatures: 298, 373 and 500 K. For the purpose of keeping the temperature constant, Berendsen thermostat was used. The constant temperature MD simulations were performed using leap-frog integrator with 2 fs time step. The hydrogen atoms were constrained with LINKS algorithm, implemented in GROMACS. The length of simulations was 6 ns at 298 K and 10 ns at 373 K and 500 K.

The analysis of the trajectories with rmsd, the salt bridges and hydrogen bonding evaluation was processed with VMD [21]. The secondary X-ray structure of all the molecules was investigated with STRIDE [22].

For the purposes of this study we define a void as room within the protein moiety which is inaccessible to the solvent and small enough so that no solvent molecules can be situated there. Cavity is an internal space in the protein where at least one solvent molecule can be introduced. The identification of voids and cavities as well as their volumes were calculated using the method and the parameters described earlier [5].

Salt bridge/hydrogen bond and void/cavity formation were calculated taking 50 snapshots over the last 2 ns of the MD simulations at all temperatures. The length of simulation at 298 K was 6 ns, during which time the protein structures reached equilibrium. The high temperature simulations were stopped

Table 1. Mesophilic/thermophilic and mesophilic/hyperthermophilic pairs

Organism	Functional class	PDB entry	Name	Number of residues	Biological unit	Melting temperature, T_m [°C]
Escherichia coli	Cold shock protein	1MJC	M-csp	69	Monomer	57.60 [31]
Bacillus caldolyticus	Cold shock protein	1C9O	T-csp	66	Dimer	76.90 [32]
Bos taurus	Acyl-phosphatase	2ACY	M-acp	98	Monomer	53.80 [33]
Pyrococcus horicoshii	Acyl-phosphatase	1W2I	H-acp	91	Dimer	111.50 [25]

at 10 ns when they began to show increased deviations from the X-ray structure in the last 2 ns. For the analysis of the results, we took the averages of the rmsd values when the temperature perturbation starts to affect the protein structure. Then the first step of denaturation occurs and the structures leave their equilibrium conformation(s).

The assessment of salt bridge and hydrogen bonds formation was made of the basis of a cut-off distance of 3.6 Å and 3.2 Å respectively, whilst the cut-offs of 40° and 20° of the acceptor-donor-hydrogen angle (according VMD nomenclature) were used. Data were collected over the last 2 ns of the simulation.

RESULTS AND DISCUSSION

Rmsd and rmsf (root mean square deviation and fluctuation) analysis. The average rmsd values for the non-hydrogen atoms of the proteins simulated at different temperatures are summarized in Table 2. At almost all simulated temperatures the T-csp and H-acp proteins were characterized by smaller changes in the average rmsd values than their mesophilic counterparts, which relates to their greater structural stability. The fluctuations of residues in the structures were investigated by calculating the rmsf for the non-hydrogen atoms from an average structure for the last 2 ns at all temperatures. Structural elements fluctuating more than the threshold of 0.15 nm are presented in Table 3. During the last 2 ns of the simulations all the proteins fluctuated at distance-separated unique residues with preferably highly mobile, solvent-exposed secondary structures such as turns and coils. Fluctuations in α-helices and β-strands were either in their beginnings or ends where they are followed or preceded by the mobile residues.

At 373 K the difference in rmsd values of the cold shock proteins was minimal (M-csp-2.105 Å and T-csp-2.002 Å). The rmsf per residue involved fluctuation in coordinates of coils, turns and a β-strand (Glu56) in M-csp and well-structured elements as parts of β-strands (Lys5, Gly23-Ser24; Gln53- Gly54 and Lys65) in T-csp. The rmsf difference between the M-acp and H-acp acylphosphatases at 373 K became 0.244 Å. The alternations in M-acp consist of fluctuations in turns, α-helices (Lys31; His60; Lys68) and β-strand (Arg77). In H-acp the fluctuating regions were mostly parts of β-strands and α-helices (Arg13, Arg28, Leu53, Arg70, Arg77).

At 500 K M-csp experienced greater structural fluctuations in larger number of residues than its thermophilic homolog. The change in coordinates preferably included big blocks of β-strands and a visual loss of its 3–10 helix structure (Phe34-Ala36), which was transformed into a turn and

Table 1. Average rmsd and standard deviation (sd) values of the non-hydrogen atoms from the X-ray structure of the M-csp/T-csp and M-acp/H-acp homologous pairs at 298 K, 373 K and 500 K

Protein	Average rmsd [Å] at 298 K	Average rmsd [Å] at 373 K	Average rmsd [Å] at 500 K	Average Δrmsd [Å] (298K-373K)	Average Δrmsd [Å] (298K-500K)
M-csp	1.915 ± 0.260	2.105 ± 0.219	2.635 ± 0.468	0.190	0.720
T-csp	1.515 ± 0.206	2.002 ± 0.272	2.418 ± 0.287	0.487	0.903
M-acp	1.231 ± 0.089	1.684 ± 0.197	2.815 ± 0.675	0.453	1.584
H-acp	1.356 ± 0.199	1.440 ± 0.133	1.849 ± 0.308	0.084	0.493

Table 3. Total number of amino acid pairs, participating in the formation of salt bridges and their population over 50 frames of the last 2 ns of the simulations

	Total number of amino acid pairs participating in salt bridges			Average occupancy of salt bridges per amino acid pair [%]		
Protein Id	298 K	373 K	500 K	298 K	373 K	500 K
M-csp	1	3	5	40.38	35.9	18.46
T-csp	6	6	11	42.66	49.36	27.97
M-acp	6	9	17	52.20	38.46	25.11
H-acp	17	16	20	54.44	59.62	39.13

coil. The flexibility of a turn (Asn39- Tyr42) and a bend (Ser57- Pro62) caused larger deviation from the X-ray structure and distortion of the structure. During the simulations similar changes were observed for T-csp, which also fully lost one of its 3-10 helix (Asn11- Lys13) and partially another 3-10 helix (Phe30- Ala32) structures to irregular regions (turn and coil).

The second pair of proteins, which has difference in the melting temperatures bigger than the first homologous pair, showed significant separation in the rmsd values (~ 1 Å). The mesophilic protein reached higher rmsd values especially in the last 2 ns of the simulation- consistent with changes in the secondary structure and initial stage of denaturation. The main change in the secondary structure in M-acp was in one β-strand (Ile75- Val85). In some of the snapshots the β-strand was disrupted in residues His81, Asn82 and Glu83. Residues from another β-strand and residues close to the N- and C- termini (Asn41, Tyr11, Val85) manifested high fluctuations. These structural deviations are displayed as major peaks in Figure 2c. The major difference between the X-ray of H-acp and the simulated structure at 500 K was in β-strand and α-helix (Tyr11- Arg13; Trp21; Arg25; Arg28; Gln64, Arg70- Arg73).

The Δrmsd values in Table 2 were calculated as difference between rms deviations of the simulated structures at 373 K and 500 K and the average rms deviations of the equilibrated molecule at 298 K. The average Δrmsd of H-acp does not show large deviation in coordinates from the equilibrated structure at 298 K unlike the other simulated proteins.

In the acylphospatase pair the fluctuations around the average structure over the trajectory of the hyperthermophilic protein, were smaller in average than its mesophilic counterpart.

The 1MJC/1C9O pair are proteins with small molecular weight per chain (7280 Da and 7547 Da) [23, 24], without or with small hydrophobic cores, which would lead to high, close rates of fluctuations for both structures. Fluctuation difference should be sought in the M-acp/H-acp pair (weights of 11.326 kDa and 10.369 kDa per chain) [25, 26]. The mesophilic proteins are less fluctuating at 373 K with change in position mainly in irregular regions compared to their thermostable counterparts, where the fluctuations occur mostly in α-helices and β-strands. Therefore, the thermostable proteins are more mobile at moderately high temperatures (373 K) without experiencing overall significant distortion in structure at 500 K.

Salt bridges and internal hydrogen bonds. The number of salt bridges for the homologous pairs of proteins was calculated over the last 2 ns of the MD trajectories for 298 K, 373 K and 500 K (Table 3).

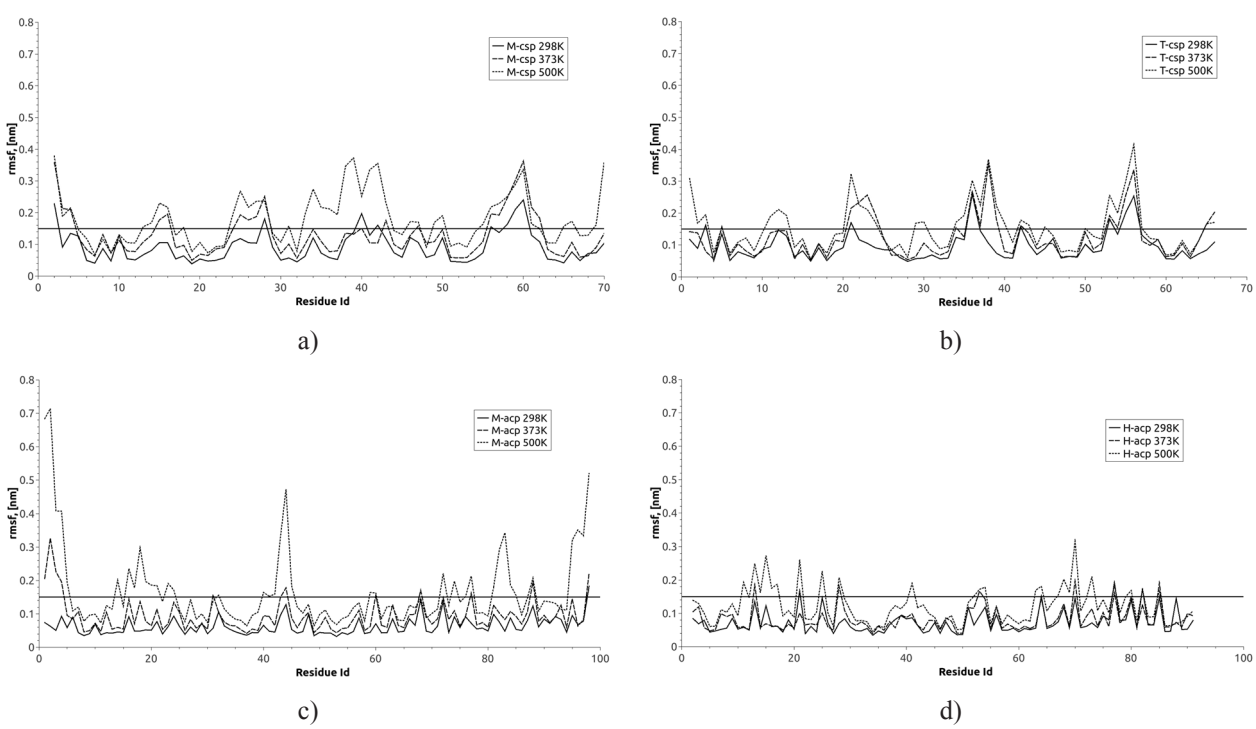

Fig. 2. Average rmsf plots per residue for the last 2 ns of the MD simulation at 298 K, 373 K and 500 K: a) M-csp; b) T-csp; c) M-acp and d) H-acp

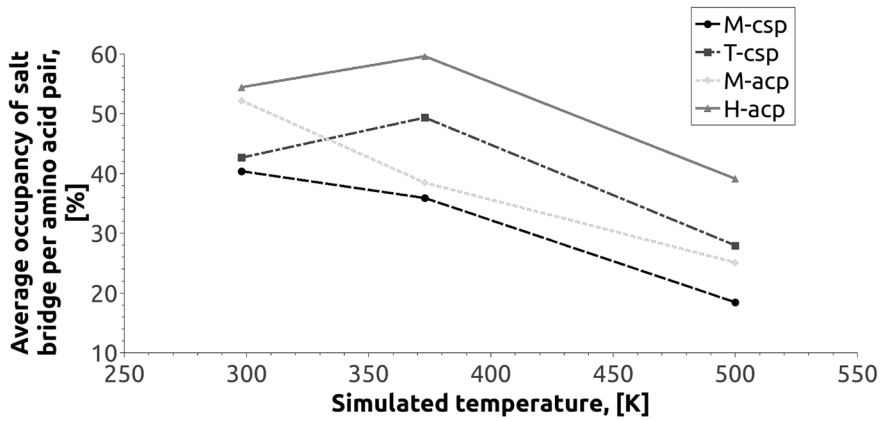

Fig. 3. Average population of salt bridges per amino acid pair at 298 K, 373 K and 500 K in mesophilic M-csp (dashed line) and thermophilic T-csp (dash-dotted line) cold shock proteins and mesophilic M-acp (dotted line) and hyperthermophilic H-acp (solid line) acylphospatases

As expected [2] the proteins from thermostable organisms are characterized by a larger number of salt bridges than their mesophilic counterparts (Table 3). Since salt bridges are dynamic formation, i.e. they may break and form during simulations [27, 28], the quantity relevant for the structural stability of proteins is their lifetime. As seen in Figure 3 and Table 3 there is a weak tendency the proteins from the extremophilic organisms to have a longer lifetime at room temperature. Due to increasing of the kinetic energy when temperature increases the overall salt bridge lifetime (occupancy) reduces. However, this reduction is lower for the thermostable and especially for the hyperthermostable protein. Hence, the role of salt bridges as stabilizing factor is less reduced in proteins from (hyper)thermophilic organisms. The physical foundation of this effect has been discussed [29]. Based on X-ray structure and continuum dielectric model it has been shown that due to reduction of permittivity of solvent water, the charge-charge interaction energy increases, whereas the desolvation penalty reduces. These two factors increase the stabilization effect of electrostatic interactions. In this work we illustrate the same effect using more detailed representation of the protein/solvent system, including structural flexibility of the protein molecule.

In contrast to salt bridges, the number of intramolecular hydrogen bonds at room temperature practically does not differ within the counterparts of the two types of investigated proteins (Table 4). This reflects the similarity of the three-dimensional structures of the counterparts. As mentioned above, the measure of the contribution of hydrogen bonds to structural stability is their lifetime (the occupancy) rather than their number. Similarly to salt bridge occupancy, that of intramolecular hydrogen bonds reduces with temperature. However, in this case the reduction is practically the same for all four proteins under consideration (see also Figure 4). The thermostable protein shows a bit longer average lifetime at 500 K MD simulation run, however the difference between the counterparts is too small to make general conclusion. In the case of Acp pair, the average hydrogen bond lifetime for the hyperthermophilic protein at 500 K simulation is about

Table 4. Values of the hydrogen bonds for the proteins at all the simulated temperatures for 50 frames of the last 2 ns of each of the simulations

	Total number of hydrogen bonds			Average occupancy per hydrogen bond [%]		
Protein Id	298 K	373 K	500 K	298 K	373 K	500 K
M-csp	62	66	103	30.02	24.07	12.19
T-csp	60	83	97	30.71	22.10	14.71
M-acp	102	130	167	32.13	22.71	14.19
H-acp	100	107	127	33.73	28.59	18.88

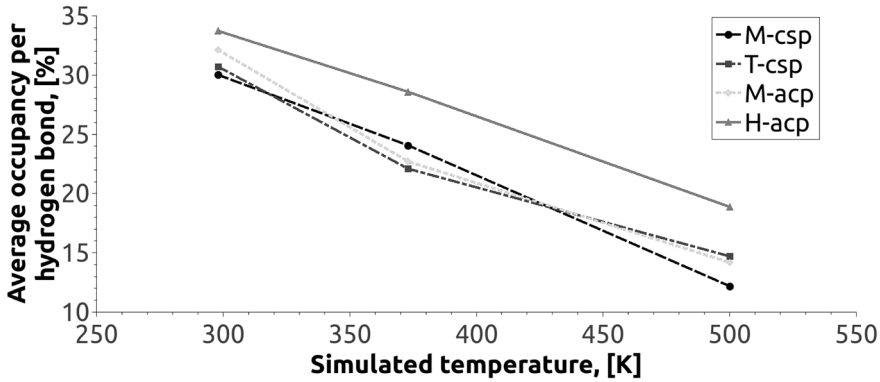

Fig. 4. Average population per hydrogen bond at 298 K, 373 K and 500 K in mesophilic M-csp (dashed line) and thermophilic T-csp (dash-dotted line) cold shock proteins and mesophilic M-acp (dotted line) and hyperthermophilic H-acp (solid line) acylphospatases

25% longer than that for the mesophilic counterpart. Thus, on the basis of the two pairs of proteins we conclude that in the case of meso/thermophilic pair the contribution of intramolecular hydrogen bonds to protein thermal stability is not so pronounced as that of salt bridges. We hypothesise that the hydrogen bonding is "used" as stabilising instrument for hyperthermophilic proteins.

Void volumes and cavities. Voids and cavities are integral characteristics, which result from all non-covalent interactions, as well as from the amino acid content of the protein molecules. It is well documented that amino acid substitution leads to cavity formation, which reduces the stability of the protein molecule [30]. In general, cavities are considered as packing defects destabilizing the native structure. Voids also may lead to decreasing of the thermal stability, due to reduction of Van der Waals interactions. On the other hand, voids make folded protein structure to tolerate the increase of vibrational entropy with elevation of temperature. It is a general question to investigate to what extent thermo- and hyperthermophilic proteins can be discriminated from their mesophilic counterparts in terms of voids and cavities.

The calculated void and cavities volumes are presented in Table 5. The void volumes remain almost unchanged in the simulation at 298 K and 373 K. In

Table 5. Average number of cavities and void volumes per atom over 50 frames of the last 2 ns of the MD simulations at 298 K, 373 K and 500 K. In brackets are given the calculated void volumes per atom/average number of cavities/cavity volumes over the last 2 ns of additional 5 ns simulations for H-acp

	M-csp mesophile			T-csp thermophile		
Temperature [K]	Average number of cavities	Average cavity volume [Å^3]	V_{void}/atom [Å^3]	Average number of cavities	Average cavity volume [Å^3]	V_{void}/atom [Å^3]
298	0.57	14.35	3.76	0.96	14.14	3.92
373	1.80	21.23	3.90	0.73	15.19	3.86
500	1.92	18.13	3.77	1.75	17.11	3.91
	M-acp mesophile			H-acp hyperthermophile		
Temperature [K]	Average number of cavities	Average cavity volume [Å^3]	V_{void}/atom [Å^3]	Average number of cavities	Average cavity volume [Å^3]	V_{void}/atom [Å^3]
298	1.78	12.92	4.19	1.35	14.24	4.15
373	2.39	17.41	4.18	1.96 (1.66)	14.78 (17.45)	4.17 (4.15)
500	4.10	13.90	3.06	2.29	21.47	4.00

the case of the 500 K MD simulations, the mesophilic M-acp showed dramatic reduction of the void volume. The same tendency but with smaller magnitude is observed for the mesophilic M-csp. It can be attributed to initiation of unfolding at which the protein interior becomes accessible to the solvent. The overall similarity of void volumes within the two pairs suggests that this parameter does not reveal difference between mesophilic and (hyper) thermophilic proteins.

The number of cavities gradually increases with temperature in all investigated proteins. This dependency on temperature is clearly pronounced for the mesophilic proteins. Another interesting feature uncovered by the computations is that, for these proteins the increase in the cavities' number and volume is observed already at 373 K, compared to the thermostable proteins, where this change occurs at 500 K. The larger structure of H-acp needed to be simulated longer for this phenomenon to be observed. Therefore, we performed MD simulations with H-acp at 373 K for 5 more nanoseconds, and collected statistics over the last 2 ns. The void volumes and average number of cavities changed their values from 4.17 $Å^3$ and 1.96 to 4.15 $Å^3$ and 1.66, respectively. These results suggest that thermophilic and hyperthermophilic proteins are characterized by structural organization resistant to temperature induced packing defects. This resistance correlates with the melting temperatures of the investigated proteins.

CONCLUSIONS

Our comparative computational study on two homologous pairs of mesophilic- thermophilic/ hyperthermophilic proteins showed that the molecules from the extremophilic species have a larger flexibility than that of the mesophilic counterparts. It has been observed that the number of charged groups participating in salt bridges increases, as obeying the correlation mesophilic<thermophili c<hyperthermophilic proteins. In parallel the reduction of salt bridge lifetimes at high temperature is less for the proteins from extremophiles, hence salt bridges as stabilising factor are more resistant towards increasing of temperature. It was hypothesized that the hydrogen bond network becomes relevant stabilizing factor in hyperthermophilic proteins, whereas for the thermophilic species its stabilizing role is not pronounced. Finally, the results have showed that thermophilic and hyperthermophilic proteins are characterized by structural organization resistant to temperature induced packing defects.

Acknowledgements: *This work was financially supported by the Bulgarian National Research Fund (grant DRG-02/05).*

REFERENCES

1. V. Z. Spassov, A. D. Karshikoff, R. Ladenstein, *Protein Sci.*, **3**(9), 1556 (1994).
2. V. Z. Spassov, A. D. Karshikoff, R. Ladenstein, *Protein Sci.*, **4**(8), 1516 (1995).
3. V. Z. Spassov, R. Ladenstein, A. D. Karshikoff, *Protein Sci.*, **6**(6), 1190 (1997).
4. S. Kumar, C. J. Tsai, B. Ma, R. Nussinov, *J. Biomol. Struct. Dyn*., 17 Suppl 1, 79 (2000).
5. A. Karshikoff, R. Ladenstein, *Protein Eng*., **11**(10), 867 (1998).
6. K. Mizuguchi, M. Sele, M. V. Cubellis, *BMC Bioinformatics*, 8 Suppl 1, S15 (2007).
7. A. Paiardini, R. Sali, F. Bossa, S. Pascarella, *BMC Struct. Biol*., **8**, 14 (2008).
8. A. Szilagyi, P. Zavodszky, *Structure*, **8**(5), 493 (2000).
9. Y. Ding, Y. Cai, Y. Han, B. Zhao, L. Zhu, *Biopolymers*, **97**(11), 864 (2012).
10. G. Vogt, S. Woell, P. Argos, *J. Mol. Biol.*, **269**(4), 631 (1997).
11. D. S. Vieira, L. Degreve, R. J. Ward, *Biochim. Biophys. Acta*, **1790**(10), 1301 (2009).
12. N. N. Khechinashvili, M. V. Fedorov, A. V. Kabanov, S. Monti, C. Ghio, K. Soda, *J. Biomol. Struct. Dyn.*, **24**(3), 255 (2006).
13. M. Robinson-Rechavi, A. Alibes, A. Godzik, *J. Mol. Biol.*, **356**(2), 547 (2006).
14. C. Danciulescu, R. Ladenstein, L. Nilsson, *Biochemistry*, **46**(29), 8537 (2007).
15. F. C. Bernstein, T. F. Koetzle, G. J. Williams, E. F. Meyer Jr., M. D. Brice, J. R. Rodgers, O. Kennard, T. Shimanouchi, M. Tasumi, *Eur. J. Biochem*., **80**(2), 319 (1977).
16. S. F. Altschul, T. L. Madden, A. A. Schaffer, J. Zhang, Z. Zhang, W. Miller, D. J. Lipman, *Nucleic Acids Res.*, **25**(17), 3389 (1997).
17. H. J. C. Berendsen, D. Vanderspoel, R. Vandrunen, *Comput. Phys. Commun*., **91**(1–3), 43 (1995).
18. S. Pronk, S. Pall, R. Schulz, P. Larsson, P. Bjelkmar, R. Apostolov, M. R. Shirts, J. C. Smith, P. M. Kasson, D. van der Spoel, B. Hess, E. Lindahl, *Bioinformatics*, **29**(7), 845 (2013).
19. A. D. MacKerell Jr., N. Banavali, N. Foloppe, *Biopolymers*, **56**(4), 257 (2000).
20. W. L. Jorgensen, J. Chandrasekhar, J. D. Madura, R. W. Impey, M. L. Klein, *J. Chem. Phys*., **79**(2), 926 (1983).
21. W. Humphrey, A. Dalke, K. Schulten, *J. Mol. Graph*., **14**(1), 27 (1996).
22. D. Frishman, P. Argos, *Proteins*, **23**(4), 566 (1995).
23. H. Schindelin, W. Jiang, M. Inouye, U. Heinemann, *Proc. Natl. Acad. Sci. U. S. A*., **91**(11), 5119 (1994).
24. U. Mueller, D. Perl, F. X. Schmid, U. Heinemann, *J. Mol. Biol*., **297**(4), 975 (2000).

25. Y. Y. Cheung, S. Y. Lam, W. K. Chu, M. D. Allen, M. Bycroft, K. B. Wong, *Biochemistry*, **44**(12), 4601 (2005).
26. M. M. Thunnissen, N. Taddei, G. Liguri, G. Ramponi, P. Nordlund, *Structure*, **5**(1), 69 (1997).
27. A. Koumanov, A. Karshikoff, E. P. Friis, T. V. Borchert, *J. Phys. Chem. B*, **105**, 9339 (2001).
28. S. Bjelic, S. Wieninger, I. Jelesarov, A. Karshikoff, *Proteins*, **70**(3), 810 (2008).
29. A. Karshikoff, R. Ladenstein, *Trends Biochem. Sci*., **26**(9), 550 (2001).
30. E. Durr, I. Jelesarov, *Biochemistry*, **39**(15), 4472 (2000).
31. S. A. Petrosian, G. I. Makhatadze, *Protein Sci.*, **9**(2), 387 (2000).
32. B. N. Dominy, D. Perl, F. X. Schmid, C. L. Brooks III, *J. Mol. Biol*., **319**(2), 541 (2002).
33. K. Ghosh, K. Dill, *Biophys. J.*, **99**(12), 3996 (2010).

ФИЗИЧНИ ОСНОВИ НА ТЕРМИЧНАТА УСТОЙЧИВОСТ НА ПРОТЕИНИ: СРАВНИТЕЛНО ИЗСЛЕДВАНЕ НА ХОМОЛОЖНИ ДВОЙКИ ОТ МЕЗОФИЛНИ И ТЕРМОФИЛНИ ОРГАНИЗМИ

Е. К. Саламанова*, Д. Т. Цонева, А. Д. Кършиков

Институт по молекулярна биология „Акад. Румен Цанев“, БАН, ул. „Акад. Георги Бончев“, бл. 21, 1113 София

Постъпила февруари, 2013 г.; приета май, 2013 г.

(Резюме)

За изследване на физичните фактори, отговорни за повишена термична стабилност на белтъци от термофилни и хипертермофилни организми, използвахме симулационен метод, базиран на класическата молекулна динамика. Предмет на изследването са две двойки хомоложни белтъци от функционалните класове на: 1) „студ–стрес“ (cold shock) белтъци от *Escherichia coli* (мезофилен) и *Bacillus caldolyticus* (термофилен) и 2) ацил фосфатази от *Bos Taurus* (мезофилен) и *Pyrococcus horicoshii* (хипертермофилен). Проведени бяха симулации на белтъците при три различни температури: 298, 373 и 500 K. Резултатите потвърдиха общото мнение, че солеви мостове и мрежи от вътрешномолекулни водородни връзки стабилизират термостабилните белтъци при висока температура. В допълнение ние установихме, че при „високи“ температури дефектите на пакетиране се увеличават (чрез формиране на кухини), най-осезаемо при мезофилните белтъци. Тъй като кухините са дестабилизиращ фактор, ние стигнахме до заключението, че особеното опаковане на белтъци от екстремофилни организми, по-устойчиви към температурно-индуцираното формиране на кухини, допринася за подобряване на тяхната толерантност към висока температурата.

Bulgarian Chemical Communications, Volume 45, Number 4 (pp. 601–606) 2013

The high energy milling effect on positional redistribution of CO_3-ions in the structure of sedimentary apatite

B. V. Kostova[1], N. L. Petrova[2], V. Petkova[2]*

[1] *New Bulgarian University, Department of Natural Sciences, 1618 Sofia, 21 Montevideo str., Bulgaria*
[2] *Institute of Mineralogy and Crystallography, Bulgarian Academy of Sciences, Acad. G. Bonchev Str. Bid. 107, 1113 Sofia, Bulgaria*

Received February, 2013; Revised May, 2013

Different types of isomorphic substitutions in the apatite structure are well known, as the substitution of PO_4 by CO_3-ion is the most common. This specifies the existence of various members of the apatite isomorphic series.

Carbonate-hydroxyl-flour apatite sample (B-type with Ca/P ratio >1.67) from Tunisia sedimentary phosphorite ore deposit are investigated.

The high energy milling is an environmentally friendly technological alternative for ore processing, to the conventional acid leaching methods. The high energy milling creates defects in the apatite structure with simultaneous accumulation of mechanic energy. The impact of the mechanical forces over the solids is mostly revealed through the changes of the quantities being related to the energetic stability and reactivity of the solid phase. Under high energy milling process the isomorphic substitution increases mainly ~~of~~ on the account of CO_2 and partly of water vapor.

Thermal with gas-mass analysis in the temperature interval 600–900 °C in air medium has been used to evaluate the achieved effect of the high energy milling on the positional redistribution of CO_3-ions and the structural phase-transformations occurring in the investigated sample. The experimental analysis shows liberation of CO_3-ions in three temperature stages with varying mass losses. Peaks intensities are determined from the high energy milling effect, the high temperature heating and the gas medium during the measurements.

Key words: high energy milling, apatite, structure.

INTRODUCTION

Different types of isomorphic substitutions in the apatite structure are well known. The end members of the apatite (Ap) isomorphic series are hydroxyl-apatite (HAp), flour-apatite (FAp) and chlorine-apatite (ClAp) [1–3]. Two types of substitutions are the most common: (i) PO_4 by CO_3-ions in tetrahedral position (B-type position of CO_3) and (ii) F^- by OH^- (Cl^-) and and vice versa in the channels located nearby the hexagonal crystallographic axes [2]. This specifies the existence of various members of apatite isomorphic series: carbonate-flour apatite (CFAp), carbonate-chlorine apatite (CClAp), carbonate-hydroxyl-flour apatite (CHFAp), etc. Under high energy milling process the isomorphic substitution increases mainly through incorporation of CO_2 and partly of water vapor [2, 4, 5].

Previously we investigated the phase transitions of sedimentary apatite ores from Tunisia and Syria, using Infra-Red spectroscopy (IR) and powder X-Ray Diffraction (XRD), and the results show the isomorphic transitions from B- to A-type apatite through positional migration of CO_3^{2-}-ions (from tetrahedral B-type to channel A-type position of CO_3, where CO_3 occupy the OH^-/F^- position in channels located nearby the hexagonal crystallographic axes [2]) and F^- additional incorporation of CO_2 from the air during the high energy milling [2, 4–6]. The incorporated CO_2 occupy the A-type position of CO_3. The high energy milling activation also leads to decreasing of samples particle size and formation of highly defective nano-particles with high degree of reactivity. The obtained nano-samples are undersized (amorphous) for investigation with powder XRD, so the identification of the phase composition is not possible by this method.

The aim of the study is to evaluate the achieved effect of the high energy milling on the possitional migration of CO_3-ions and the structural phase-transformations occurring in the investigated sam-

* To whom all correspondence should be sent:
E-mail: vilmapetkova@gmail.com

ple – natural fluorine-apatite (FAp) from Tunisia using thermogravimetric and differential thermal analyses with attendant mass-spectrometer analysis of the gas phases.

MATERIALS AND METHODS

We investigated FAp (with Ca/P ratio >1.67) from Tunisia sedimentary phosphorite ore deposit [8, 9]. The chemical composition of the material includes (main components): 29.6% $P_2O_5^{total}$; from which assimilated (ass.) is 6.9% $P_2O_5^{ass}$ (by 2% citric acid); 3.5% F; 46.5% CaO; 0.55% R_2O_3 (R = Al, Fe); 1.1% SO_3; 1.9% SiO_2; 0.35% MgO; 0.05% Cl; 6.6% CO_2; moisture content 3.14% and a granulometric size of the particles of 0.8 mm. There are different forms of P_2O_5 – water-soluble, assimilable, and insoluble in water. They are reflected in the application of P_2O_5 as a phosphate fertilizers. The assimilable forms of $P_2O_5^{ass.}$ are insoluble in water but are soluble in soil solutions. Evaluation of the forms of P_2O_5 is performed on the basis of their solubility in the so-called conditional solvents – solution of ammonium citrate or 2% solution of citric acid. The choice of the reagent is based on its similarity with the soil solutions. In the resent years greater advantage is given to the assimilable fertilizers because their solubility is slower than that of the water-soluble ones and thus they feed the plants for a longer time. The method used for high energy milling is intended to enhance the transformation of the insoluble forms of P_2O_5 in $P_2O_5^{ass.}$.

The high energy milling activation was carried out in a planetary mill Pulverisette-5, Fritsch Co (Germany), for activation times 120 and 150 min, milling bodies of unalloyed steel, diameter of the milling bodies of 20 mm, and a sample weight 0.020 kg.

Thermogravimetric and differential thermal analyses (TG-DTG-DTA) were performed on a SETSYS2400 thermal analyzer (SETARAM, France) in the temperature range 20–950 °C in air medium, with a heating rate of 10 °C.min^{-1} combined with an OmniStar mass-spectrometer.

RESULTS

Our previous powder XRD studies on untreated phosphorite ores from Tunisia have given evidence that the sample contains the following mineral phases: FAp, calcite and traces of quartz [10]. Our earlier IR measurements have confirmed that the investigated FAp actually is CHFAp B-type, where two types of isomorphic substitution take place: PO_4^{3-}-group by CO_3^{2-}-ions and F^- by OH^--ions [5, 11, 12, 13]. The thermal decomposition mechanism of untreated sample is described in details elsewhere [9, 11–13]. In this work we are focused on the thermal reactions in the temperature interval 600–900 °C only, where decarbonization of CO_3-ions from the CHFAp-structure and impurity carbonate-containing phases occurs.

The obtained results of the present thermal investigations are shown on Figs 1–3 and in Table 1.

Table 1 shows the results from the thermal experiments (temperature data for the inflex points) together with calculated mass losses for the three samples: untreated (TF0), high-energy milled for 120 min (TF120) and for 150 min (TF150), respec-

Table 1. Multi-peak fitting of dTG-curves for untreated and high energy milled samples within the temperature interval 600–850 °C

Thermal decomposition of mineral phases	Activation time (min)								
	Untreated apatite (TF0)			120 (TF120)			150 (TF150)		
	Peak position, T °C	Peak area	ML*, %	Peak position, T °C	Peak area	ML, %	Peak position, T °C	Peak area	ML, %
A-type CHFAp		–	–	613.73	–3.73	0.49	630.32	–3.82	0.52
B-type CHFAp	701.2	–18.54	1.70	673.28	–16.22	1.65	692.16	–14.45	0.84
							720.16	–1.10	0.50
$CaMgCO_3$ (dolomite)	724.0	–1.68	0.80	741.32	–10.19	0.87	741.97	–4.70	0.70
$CaCO_3$ (calcite)	773.7	–8.47	1.66				770.67	–5.81	0.91
A-B type CHFAp	–	–	–	798.85	–7.14	0.55	810.1	–3.8	0.46
				816.40	–3.50	0.81	828.5	–5.2	0.86
		Sum	4.23		Sum	4.37		Sum	4.06

* Mass losses

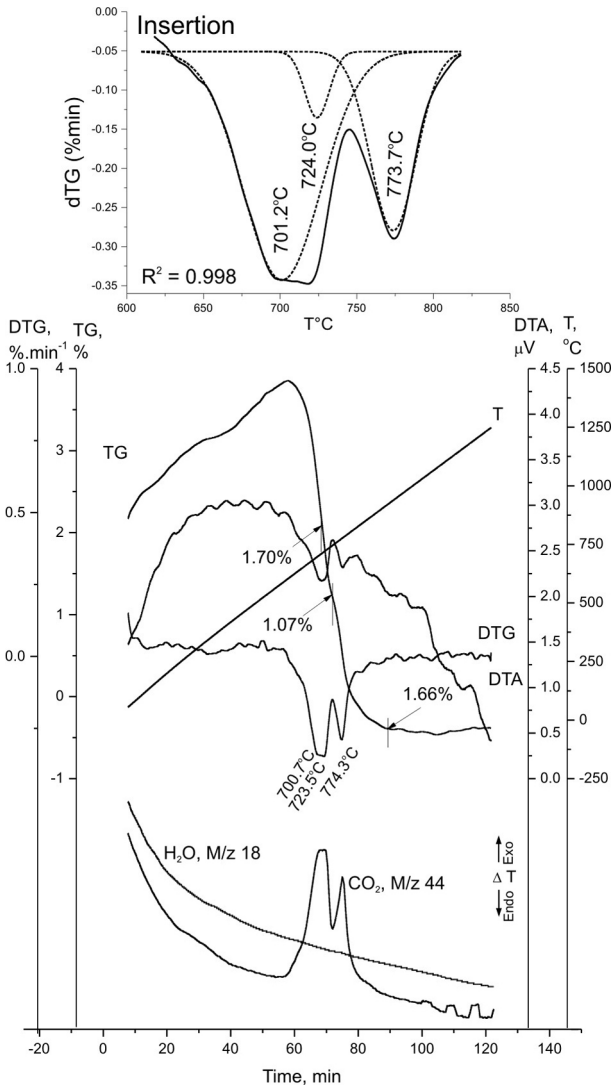

Fig. 1. Thermal with gas-mass analysis of TF0. *Insertion*: Multi-peak fitting (dashed line) of dTG in temperature interval 600–850 °C.

tively. There exist three main temperature intervals for TF0, where thermal reactions are accompanied by mass losses as following: 1.70% between 650–720 °C, 1.07% between 720–770 °C and 1.66% between 770–850 °C. At high energy milled samples appear two new temperature ranges 620–650 °C and 770–850 °C. The range 770–850 °C coincides with the third range for the TF0 (770–850 °C) but differs in new thermal reactions proven in a thermal dependencies (TG, dTG, dTA) and mass losses. The analysis of thermal dependencies for TF120 and TF150 shows overlapping of the thermal reactions. The gas-mass analysis shows existence of CO_2 in all samples (Figs 1–3) and H_2O – only for the TF120 (Fig. 3). For more detailed visualization of these processes, the Gauss decomposition of the dTG-curves is made and the results are presented as insertions in the figures.

DISCUSSIONS

Within the investigated temperature range (600–850 °C) the decarbonization from CHFAp – B-type, calcite and dolomite occurs [2, 7, 9, 11–13]. For sample TF0 (Fig. 1), peak situated at 701 °C corresponds to decarbonization of CHFAp – B-type positions, the peak at 724 °C – to CO_3 –ions from dolomite and the peak at 773 °C – to CO_3–ions from

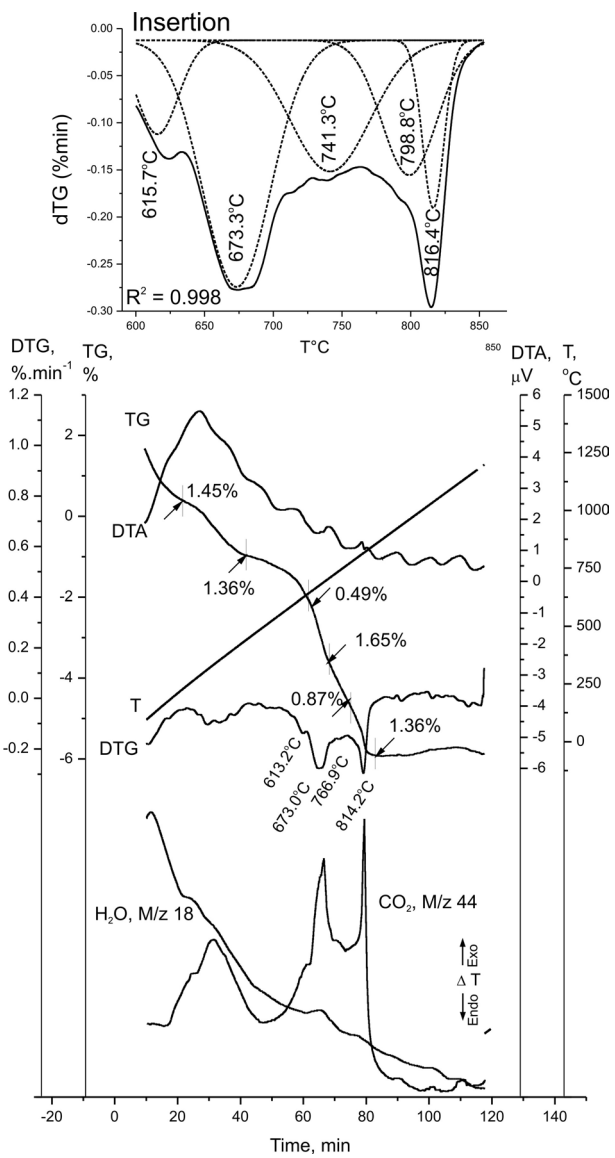

Fig. 2. Thermal with gas-mass analysis of TF120. *Insertion*: Multi-peak fitting of dTG in temperature interval 600–850 °C.

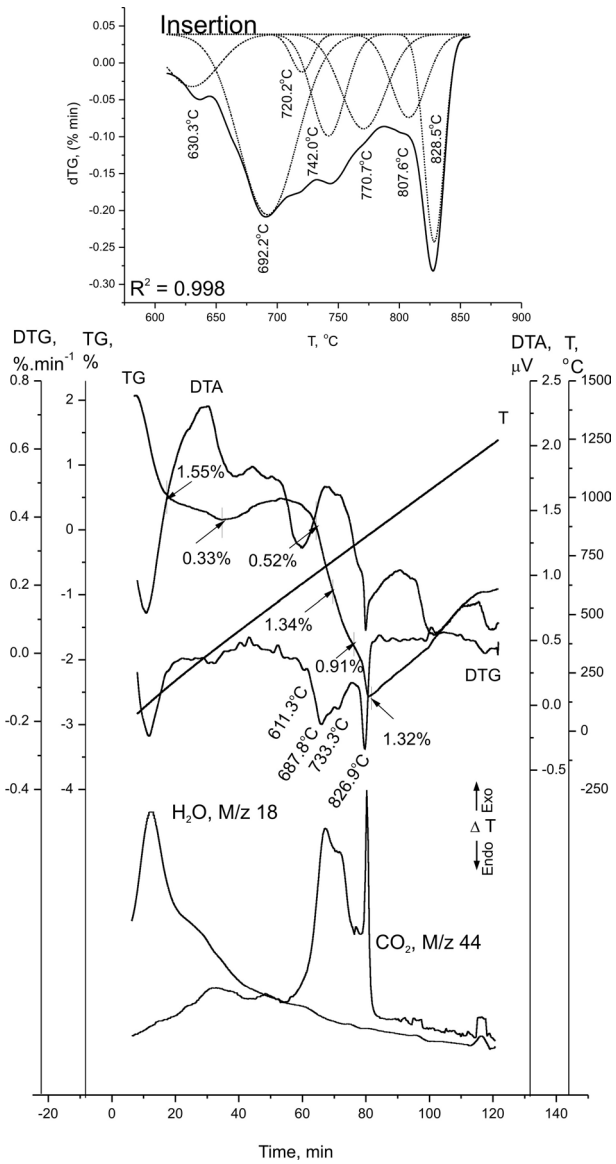

Fig. 3. Thermal with gas-mass analysis of TF150. *Insertion*: Multi-peak fitting of dTG in temperature interval 600–850 °C.

calcite (Table 1). The decarbonization of B-type position proceeds at lower temperatures because of the weak chemical bonds in CHFAp, predetermined by isomorphism of PO_4 by CO_3, as the ionic radii of PO_4-group is bigger than that of CO_3-ion [2].

The high-energy milled samples changed the temperature of decarbonization in comparison to TF0:

– for the ions of B-type position: in TF120 temperature decreases, whereas in TF150 the temperature increases and splitting of dTG-peaks is observed (Table 1, Figs 2–3);

– for calcite and dolomite: in TF120 the temperature decreases, and falls down in the area where overlay of the process is observed; in TF150 the temperature increases and splitting of the dTG-peaks is observed (Table 1, Figs 2–3).

The sum of the peaks areas and mass losses are nearly constant which is determined from the permanent quantities of the mineral phases in the experiment. The temperature changes during the decarbonization process can be explained with the alterations of the particle sizes of the samples after the high energy milling activation. At the beginning of the milling stage, the particles reach nanosize [4, 6, 10], the next stages of milling are followed by particle agglomeration. The increasing level of agglomeration depends contrariwise on the specific surface area and determines: (i) diffusion difficulties in the thermal decomposition and (ii) splitting of the dTG-peaks and increasing of decarbonization temperatures.

During the thermal experiments of high energy milled samples new peaks situated in the two temperature intervals appear: 590–630 °C and 770–850 °C.

The peaks in the interval 590–630°C are assigned to be due to decarbonization of weakly bonded ions in the apatite structure. According to literature [2, 3, 14–16] and our previously published data [5, 6, 10] it is known that in this temperature interval the decarbonization of CO_3-ions from the A-type apatite occurs, where these ions substitute OH^--groups in the channels with weak bonds. It is important to note that mass losses are nearly 0.50% and are constant and independent from the activation time of the samples. It could be explained with the incorporation of CO_2 from the air, but in limited quantities, uncontrolled by the activation time.

The peaks situated in the 770–850 °C temperature range are a result from the emission of CO_3-ions, as evidenced by the gas-mass analysis. Until now, it was thought that at these temperatures OH^--groups replacing F^--ions in the apatite structure are released. As it has already been reported [3, 5, 17] these peaks originate from the decarbonization of mixed A-B-type apatite [3, 15]. In mixed A-B-type apatite substitution of PO_4 and Ca-vacancy by CO_3-ions occur. That type isomorphism influences the length of the Ca-O-bonds, and the degree of substitution depends on the activation time (i. e. size of the particles) and water presence [2]. That is why, the mass loses of TF120 are bigger than those ones of TF150. The splitting of the dTG-peak of TF150 could be explained with liberation of CO_3-ions from different crystallographic positions. The diffusion difficulties of TF150 are caused by particle agglomerationas manifested by the increased temperature of decarbonization and the decreased mass loses.

The TG-dTA-dTG analysis of untreated and activated samples (Figs. 1–3) reveals that the decomposition runs after the following main reaction:

- 590–630 °C – decarbonization of CO_3^{2-} from A type positions of CHFAp
- 660–710 °C – decarbonization of CO_3^{2-} from B type positions of CHFAp
- 730–770 °C – $CaCO_3 = CaO + CO_2$
- 770–30 °C – decarbonization of CO_3^{2-} from A-B type positions of CHFAp
- >850 °C – $Ca_{10}FOH(PO_4)_6 = 2Ca_3(PO_4)_2 + Ca_4P_2O_9 + HF$
  $Ca_3(PO_4)_2 + 2CaO + SiO_2 = Ca_3(PO_4)_2.Ca_2SiO_4$

CONCLUSIONS

High energy milling activation causes structural and phase changes in the studied samples.

(i) The gas-phase analysis, clarified the mechanism of chemical reactions and isomorphic substitutions as a result of the high energy milling: all samples absorbed CO_2 from the air, as the TF120 exhibits the highest level of absorption, which is controlled from the specific surface area of the powdered samples and does not depend on the structural type.

(ii) The formation of two new apatite phases – CHFAp-A and A-B-types via isomorphic substitution of CO_2–ionsis detected. Their existence is evidenced by gas-mass analysis.

(iii) The temperature ranges and mass-losses for each particular isomorphously substituted apatite phase are determined and this new information supplements the existing up to now data.

(iv) The isomorphic substitution is a result from the obtained defects and energy-metastable structure condition achieved via high-energy milling.

(v) The activation effect in different samples has no functional dependence with the high energy milling activation time, because of agglomeration processes.

Acknowledgments: *The study is a part of cooperation work between University of Chemical Technology and Metallurgy, Sofia, Institute of Mineralogy and Crystallography of Bulg. Acad. Sci. and Tallinn University of Technology. Authors gratefully acknowledge the financial support of this work by the Bulgarian National Scientific Research Fund by contracts DRNF02/10, DNTS/Slovakia/01/3, DNTS/Makedonia/01/3, ДО1-1122 the "European Territorial Cooperation" Operational Programme Greece–Bulgaria 2007-2013 by contract B1.11.02/ 14.03.2011 and New Bulgarian University, Natural Sciences Department.*

REFERENCES

1. J. Elliott, Structure and chemistry of the apatites and other calcium orthophosphates, Amsterdam, Elsevier, 1994.
2. M. V. Chaikina, Mechanochemistry of natural and synthetic apatites. (Ed. by prof. E.G. Avvakumov) Novosibirsk, Publishing house of SB RAS, Branch "GEO", 2002.
3. T. Kaia, K. A. Gross, L. Pluduma, M. Veiderma, *J. Therm. Anal. Calorim.*, **110**, 2 (2012).
4. V. Yaneva, O. Petrov, V. Petkova, *Mat. Res. Bull.*, **44** (2009).
5. V. Koleva, V. Petkova, *Vibr. Spectr.*, **58** (2012).
6. V. Petkova, V. Yaneva, *JEPE*, **13**, 2A (2012).
7. V. Petkova, V. Yaneva, I. Dombalov, Y. Pelovski, *JEPE*, ISSN 1311-5065, **13,** 2A (2012).
8. V. Petkova, Y. Pelovski, I. Dombalov, K. Tonsuaadu, *J. Therm. An. Cal.*, **80** (2005).
9. V. Petkova, E. Serafimova, N. Petrova, Y. Pelovski, *J. Therm. An. Cal.*, **105**, 2 (2011).
10. K. Tõnsuaadu, T. Kaljuvee, V. Petkova, R. Traksmaa, V. Bender, K. Kirsimäe, *Int. J. Min. Pro.*, **100** (2011).
11. V. Petkova, V. Yaneva, Y. Pelovski, *JBTA*, **15**, 4 (2009).
12. V. Petkova, V. Yaneva, *JBTA*, **16**, 1 (2010).
13. V. Petkova, V. Yaneva, *JBTA*, **16**, 3 (2010).
14. T. I. Ivanova, O. V. Frank-Kamenetskaya, A. B. Kol'tsov, V. L. Ugolkov, *J. Sol. St. Chem.*, **160** (2001).
15. J. P. Lafon, E. Championa, D. Bernache-Assollant, *J. Eur. Cer. Soc.*, **28** (2008).
16. J. P. Lafon, E. Champion, D. Bernache-Assollant, R. Gibert, A. M. Danna, *J. Ther. Anal. Cal.*, **73** (2003).
17. F. C. Driessens, R. M. Verbeeck, Lc. P. Kiekens, *Zeitschrift für anorganische und allgemeine Chemie*, **504**, 9 (1983).

ЕФЕКТ ОТ ИНТЕНЗИВНО ЕНЕРГИЙНО СМИЛАНЕ ВЪРХУ ПРЕРАЗПРЕДЕЛЕНИЕ НА КАРБОНАТНИТЕ ЙОНИ В СТРУКТУРАТА НА СЕДИМЕНТЕН АПАТИТ

Б. В. Костова[1], Н. Л. Петрова[2], В. Петкова[2]*

[1] Нов български университет, Департамент Природни науки, 1618 София, ул. „Монтевидео“ № 21, България
[2] Институт по минералогия и кристалография, Българска академия на науките, ул. „Акад. Г. Бончев“, бл. 107, 1113 София, България

Постъпила февруари, 2013 г.; приета май, 2013 г.

(Резюме)

Изследван е седиментационен карбонат-хидроксил-флуор апатит (B-type) от Тунис. За повишаване на химичната реакционна способност на апатита е използван сух метод за високоенергетична активация в планетарна мелница.

Този метод се прилага като алтернатива на киселинните методи за преработване на фосфатни суровини за получаване на фосфорни торове и неорганични киселини. Под влияние на сухата активация се извършва внедряване на на CO_2 и водни пари от въздуха в в различни кристалографски позиции в подрешетката на апатита – във ваканциите на Ca^{2+} или заместайки частично F. Изоморфните заместявания са анализирани чрез термичен метод с анализ на изходящите гозаве с масспектрометър. Доказва се изоморфно заместване на карбонатни йони с образуване на A-type и A-B type и са определени температурните интервали и масови загуби на отделните типове изоморфно заместени фази на апатита.

Bulgarian Chemical Communications, Volume 45, Number 4 (pp. 607–610) 2013

The structural distortion and Zeeman splitting of the complexes $CrCl_2(H_2O)_4^{2+}$ and $Cr(H_2O)_6^{2+}$

P. Petkova*, V. Nedkov, J. Tacheva,
P. Vasilev, I. Dimitrov

Shumen University "Konstantin Preslavsky", 115 Universitetska street, 9712 Shumen, Bulgaria

Received February, 2013; Revised May, 2013

In this work, we discuss the physicochemical properties of the complex $CrCl_2(H_2O)_4^{2+}$ in 1% solution of C_2H_5OH and the complex $Cr(H_2O)_6^{2+}$ in 1% aqueous solution of $CrCl_2.6H_2O$. The spin magnetic moment and the magnetic susceptibility are calculated after Zeeman splitting in the complexes.

Key words: structural distortion, Zeeman splitting, $CrCl_2(H_2O)_4^{2+}$, $Cr(H_2O)_6^{2+}$.

INTRODUCTION

The alcoholic solutions of 3d ions salts manifest optical activity and interesting properties in magnetic field. This fact helped us when we decided to investigate these ionic liquids. In this work, the most important accent is on the existence and influence of $CrCl_2(H_2O)_4^{2+}$ complex. Our analyses give answer of questions which are connected with the peculiarities of electron transitions in the complex and with the stability in this complex. Many authors have studied the absorption of the compound $CrCl_2.6H_2O$, but they not give information about the exact number of d electron transitions and about Zeeman splitting there. This is the main aim in our work.

EXPERIMENTAL

The experimental set up for the measurement of the absorption coefficient in the visible region consisted of the following: a halogen lamp with a stabilized 3H-7 rectifier, a SPM-2 monochromator, a system of quartz lenses, a polarizer, a crystal sample holder, and a Hamamatsu S2281-01 detector. The thickness of the used cuvette is d = 0.995 cm.

* To whom all correspondence should be sent:
E-mail: Petya232@abv.bg

RESULTS AND DISCUSSION

The familiar colors of the transition metal ions in solutions are due to absorption bands which have their origins in electronic transitions within the 3d shell. The electric field of the nearest neighbour anions splits the energy levels of the unpaired d-electrons and electronic transitions between these split energy levels give rise to the observed "crystal field" spectra [1]. The measurement of absorption spectrum of 3d metal ions solutions helps us to understand how many unpaired d electrons are in the different complex structures. The absorption coefficient of $CrCl_2(H_2O)_4^{2+}$ and $Cr(H_2O)_6^{2+}$ complexes has been measured to be between 450 and 850 nm (Figs.1a and 2a). The calculated first derivative of the absorption coefficient at photon energy $[d\alpha/d(h\nu)]$ determines only the number of electron transitions in a Cr^{2+} ions and it does not give an exact information about the energy position of these transitions (Figs.1b and 2b). This is the reason for the calculation of the second derivative of the absorption coefficient $[d^2\alpha/d(h\nu)^2]$ (Figs.1c and 2c). The absorption coefficient is calculated using the formula: (1) $\alpha = (1/d)\ln(I_0/I)$, where I_0 is the intensity of the incident light, I is the intensity of the passing light and d is the sample thickness. The interesting peculiarity in the absorption spectrum of $CrCl_2(H_2O)_4^{2+}$ is the presence of the "double exciton" at 450 nm (Fig. 1a). This exciton corresponds to the double excitation of two neighboring Cr^{2+} ions and the transition $^5T_2 \rightarrow {}^5E$ realizes at this wavelength [2]. The three

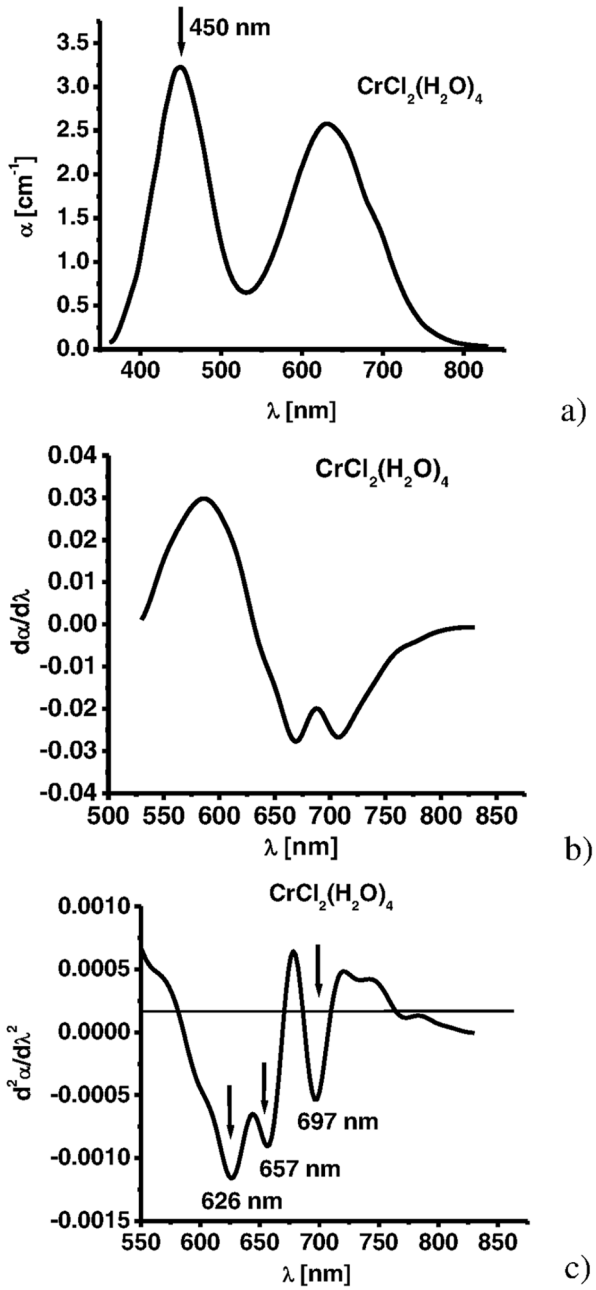

Fig. 1. a) The absorption coefficient α(E), b) first derivative dα/dE and c) second derivative $d^2\alpha/dE^2$ of the complex $CrCl_2(H_2O)_4^{2+}$

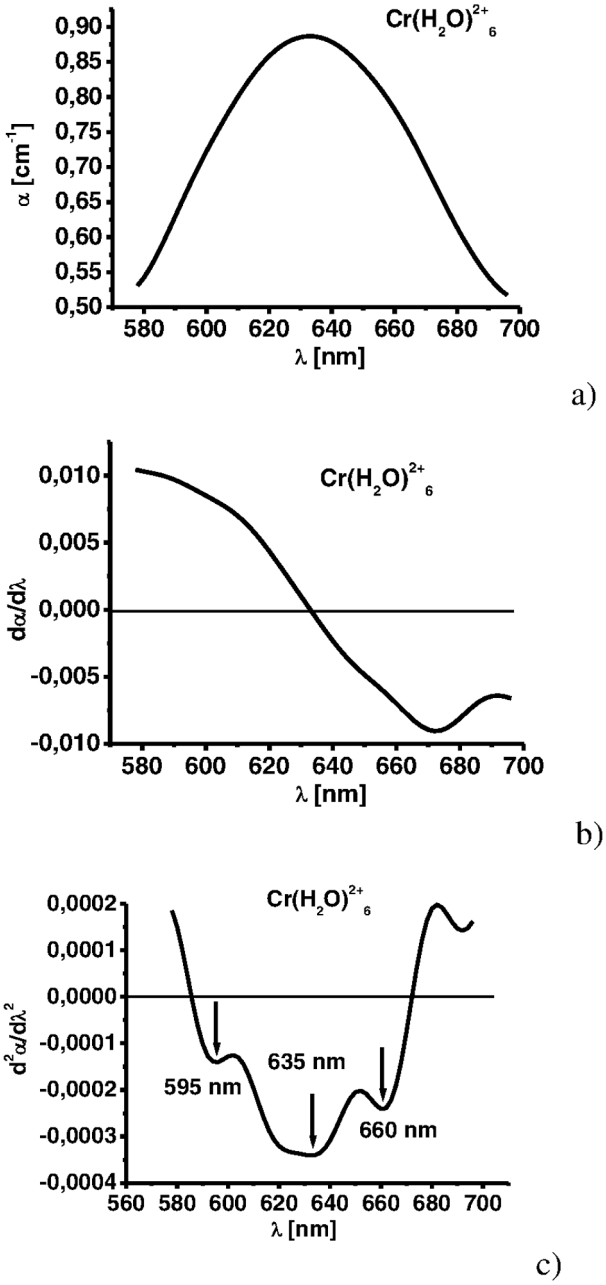

Fig. 2. a) The absorption coefficient α(E), b) first derivative dα/dE and c) second derivative $d^2\alpha/dE^2$ of the complex $Cr(H_2O)_6^{2+}$

electron transitions in the chromium ion realize from the level $^5E(^5D)$ to the level $^3T_1(^3H)$ (Fig. 3). The Cr^{2+} ions are paramagnetic. If the metal complexes $CrCl_2(H_2O)_4^{2+}$ and $Cr(H_2O)_6^{2+}$ interact with the external magnetic field then the spin magnetic moment is expressed as

$$\mu_{eff} = \sqrt{N(N+2)}\,,$$

where N is the number of the unpaired electrons. In our case N = 3 and μ_{eff} = 3.87 (S = 3/2). On the other hand

$$\mu_{eff} = g_e\sqrt{S(S+1)}$$

and g_e = 2. The magnetic susceptibility can be calculated by the formula

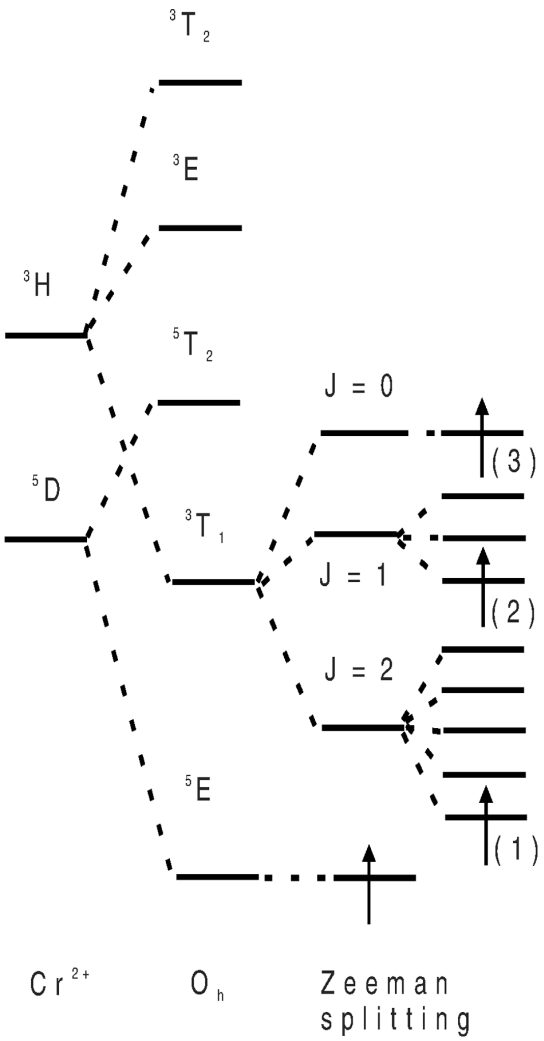

Fig. 3. The energetic diagram of Cr^{2+} ion in the octahedral symmetry

$$\chi = \frac{N}{kT}\sum_n (E_n^{(1)})^2 \ ,$$

where $N = 3$, k is Boltzmann constant, $T = 300$ K and $E_n^{(1)}$ are the values of the energy on Fig. 1c and 2c. The values of χ for the complexes $CrCl_2(H_2O)_4^{2+}$ and $Cr(H_2O)_6^{2+}$ are respectively: $\chi_1 = 728$ and $\chi_2 = 800$.

CONCLUSIONS

The interesting peculiarity in the absorption spectrum of $CrCl_2(H_2O)_4^{2+}$ is the presence of the "double exciton" at 450 nm.

Zeeman splitting appears at the level $^3T_1(^3H)$ in the chromium structure.

The magnetic susceptibility of the complex $Cr(H_2O)_6^{2+}$ has bigger value than this of the complex $CrCl_2(H_2O)_4^{2+}$.

Acknowledgments: *Partial financial support by project of Shumen University (2012) is gratefully acknowledged.*

REFERENCES

1. D. M. Gruen, R. L. McBeth, The coordination chemistry of 3d transition metal ions in fused salt solutions, Argonne; Illinois, USA: Argonne National Laboratory.
2. A. B. P. Lever, Inorganic Electronic Spectroscopy, Toronto, 1984.
3. R. S. Drago, Physical Methods in Chemistry, W. B. Saunders Company, London, 1981.

СТРУКТУРНА ДЕФОРМАЦИЯ И ЗЕЕМАНОВО РАЗЦЕПВАНЕ НА КОМПЛЕКСИТЕ $CrCl_2(H_2O)_4^{2+}$ И $Cr(H_2O)_6^{2+}$

П. Петкова*, В. Недков, Й. Тачева,
П. Василев, И. Димитров

*Шуменски университет „Епископ Константин Преславски“,
ул. „Университетска“ №115, 9712 Шумен, България*

Постъпила февруари, 2013 г.; приета май, 2013 г.

(Резюме)

В тази работа ние разглеждаме физикохимичните свойства на комплекса $CrCl_2(H_2O)_4^{2+}$ в 1% разтвор на C_2H_5OH и на комплекса $Cr(H_2O)_6^{2+}$ в 1% воден разтвор на $CrCl_2.6H_2O$. Изчислени са магнитният спинов момент и магнитната възприемчивост след Зееманово разцепване в комплексите. Интересна особеност в спектъра на поглъщане на $CrCl_2(H_2O)_4^{2+}$ е наличието на „двоен екситон“ при 450 nm. Зеемановото разцепване се проявява при нивото $^3T_1(^3H)$ в структурата на хрома. Магнитната възприемчивост на комплекса $Cr(H_2O)_6^{2+}$ има по-голяма стойност отколкото стойността ѝ за комплекса $CrCl_2(H_2O)_4^{2+}$.

Bulgarian Chemical Communications, Volume 45, Number 4 (pp. 611–616) 2013

Nanosized composite thin films of SiO_2-ZnO for photocatalytic decomposition of organic dyes – structure and characterization

N. V. Kaneva[1], S. A. Siuleiman[1], A. S. Bojinova[1]*, K. I. Papazova[1], D. T. Dimitrov[1], I. Gracheva[2], S. Karpova[2], V. A. Moshnikov[2]

[1] *Laboratory of Nanoparticle Science and Technology, Department of General and Inorganic Chemistry, Faculty of Chemistry and Pharmacy, University of Sofia, Sofia 1164, Bulgaria*
[2] *Micro- and Nanoelectronics Department, Saint-Petersburg State Electrotechnical University, Saint-Petersburg 197376, Russia*

Received February, 2013; Revised May, 2013

In this study we present pure ZnO and $20SiO_2$–80ZnO (mol %) nanocomposite photocatalysts, prepared on glass substrates via spin coating technique and sol-gel method from starting solutions of zinc nitrate and tetraethoxysilane. The as-prepared films are annealed in air at 500 °C for 1 h. The films are characterized by XRD and SEM analysis. The photocatalytic action of the films is checked and compared in photodegradation of two organic dyes Malachite Green and Methylene Blue under UV and visible light illumination. The change in dye concentration with time of irradiation is monitored by UV-visible spectroscopy.

Key words: SiO_2–ZnO films, photocatalytic degradation, sol–gel, spin coating, Malachite Green, Methylene Blue.

INTRODUCTION

The organic dyes belong to one of the most common and large group of pollutants in wastewaters from textile industries, dye manufacturing, and various other industrial processes such as food and paper production, pharmaceuticals, cosmetics and etc. The worldwide dye production is more than 7.10^5 tones per year. The losses in wastewaters at different stages of manufacturing and during application are about 10–15% of the total produced amount [1]. Organic dyes can undergo transformation in aquatic media and can form harmful carcinogenic and mutagenic intermediates, this way causing a serious risk for survival of microorganisms, aquatic life and environmental media – water and soil [2, 3]. The effect of such contamination on human health may be unpredictable hazardous inflicting different diseases like immune-suppression, respiratory, central nervous, neurobehavioural disorders presage as allergy, tissue necrosis, skin or eye infections and irritation and even lung edema [4, 5].

Different biological, physical and chemical methods have been successfully applied to solve the problems in purification of dye contaminated wastewaters. All these conventional methods have also some disadvantages: large amounts of biological sludge and the problem of their disposal; transfer of the toxic compounds just from one phase to another instead of their decomposition; need of regular regeneration of the adsorbents. Recently the advanced oxidation processes based on generation of highly reactive species (hydroxyl radicals, superoxide anion radicals or hydrogen peroxide as initiators of oxidative degradation), are an attractive alternative to traditional methods for wastewaters purification. Among these processes, heterogeneous photocatalysis seems to be promising advanced method and has been successfully applied in photodecomposition of large number organic pollutants including dyes [6, 7]. In general the photocatalytic process is governed by combined interaction between semiconductor catalyst and light irradiation, which leads to formation of free radicals from the photogenerated on the catalysts surface charge carriers and further degradation of the organics. One of the most popular semiconductor catalysts is ZnO. Zinc oxide is a natural compound with band gap energy of 3.2 eV, which makes it an alternative potential catalyst due to its high quantum efficiency. For that

* To whom all correspondence should be sent:
E-mail: nhasb@wmail.chem.uni-sofia.bg

reasons ZnO has been applied and studied in various organic pollutants photodegradation [2, 8]. The surface modification [9–11], semiconductor coupling [12–14], metal [15–17] and non-metal [18–20] doping of ZnO also have been investigated in terms of their influence on the catalyst effectiveness.

In this work we present a study on photocatalysis with films, prepared of ZnO and ZnO–SiO_2 heterostructures, aimed to enhance the degradation efficiency and activity in visible region as well as solar irradiation in future applications. The organic dyes malachite green (MG) and methylene blue (MB) are chosen as modal pollutants for dye contaminated wastewaters.

EXPERIMENTAL

The reagents and materials, used in the experiments, were as follows: zinc nitrate ($Zn(NO_3)_2.6H_2O$, Fluka); tetraethyl orthosilicate (TEOS, $Si(OC_2H_5)_4$, Sigma-Aldrich); microscopic glass slides (25×75 ×1.2 mm, ISOLAB Germany). Prior films deposition the glass substrates were thoroughly cleaned by ultrasound with acetone, ethanol and deionized water. As model pollutant were chosen the commercial dyes malachite green oxalate ($C_{48}H_{50}N_4O_4.2C_2H_2O_4$, dye content >90%, λ_{max} = 618 nm) and methylene blue ($C_{16}H_{18}ClN_3S.\times H_2O$, dye content >95%, λ_{max} = 665 nm) supplied from Sigma-Aldrich. All dye solutions, used in the photocatalytic tests, were prepared with distilled water.

The ZnO and 20SiO_2–80ZnO nanocomposite films were deposited by sol gel method [21, 22] from sol solutions, based on binary heterochain inorganic polymers. The 20:80 (SiO_2 to ZnO) ratio of the composite is selected based on our previous morphological study on porous silicon with embedded metal oxide nanocomposites [22]. In this case more uniform coatings with better adhesion to substrate were achieved. The films were finally annealed at 520 °C 1.5 h in air for complete organics decomposition. The initial precursors contain easily hydrolyzed components, such as TEOS, which interact with water with formation of polymolecules. For the preparation of the two-component oxide coatings, based on silica and zinc oxide, the hydrolysis and polycondensation of TEOS was carried out in the presence of the zinc inorganic salt $Zn(NO_3)_2$. The precursor sols were deposited onto glass substrates via spin coating technique at rotation speed of 3000 rpm.min^{-1}. The as-obtained gel films were finally annealed at 500 °C for 1.5 h in air for completing the organics decomposition.

The as-obtained ZnO and ZnO–SiO_2 films were checked for photocatalysis by standard testing procedure in photodegradation of 5 ppm MG or MB in water solutions under UV or visible-light illumination. The volume of treated dye solution was 150 ml. The sources of radiation were as follows: (i) for the UV light – Sylvania 18W BLB T8, emitting mainly in the range 315–400 nm UVA lamp fixed 10 cm above the pollutants solution; (ii) for the visible light – linear Tungsram lamp 500 W K1R7s 9700 Lm, maximal emission at 700 nm placed at 25 cm above the treated solution. The photocatalytic tests were carried out in four series. Photocatalysis with composite ZnO–SiO_2 thin and thick films under UV and visible light irradiation was compared to photocatalytic experiments with ZnO thin and thick films and under both types of illumination. Regularly taken aliquot samples from the pollutants aqueous solution at determined time intervals were analyzed by spectrophotometer (Jenway 6400) at the maximal absorption of the dye. After the measurements the aliquots were returned back to the purified solution. The solution was constantly stirred by electromagnetic stirrer at constant rotation speed of 400 rpm. The experiments were conducted at constant temperature of 23±2 °C.

The samples surface morphology was observed by scanning electron microscopy (SEM) (JSM-5510 JEOL). The phase composition and crystallinity of ZnO and ZnO-SiO_2 films was characterized by X-ray diffraction (Siemens D 500 diffractometer, CuKα source of radiation at a step of 0.05 deg for 2Θ and counting time 2s/step).

RESULTS AND DISCUSSION

The comparison of surface morphology observation by SEM shows that the ZnO and ZnO–SiO_2 film samples are textured, the effect is more pronounced in the case of composite film (Figs. 1 and 2). The porous structure of the nanocomposite is formed as a result from spinoidal decomposition of the sol, with a simultaneous release of the solvent by evaporation from the formed gel net. The latter leads to formation of macropores with overall size of 0.2–0.5 μm (Fig. 2a). The conductive branches of the macropores are from unhomogeneous mesoporous material, build by conducting ZnO spherical structures and insolating SiO_2 grains. The film thickness of the composite coatings is found to be 200 nm (Fig. 2b).

The nanostructured films are analyzed by X-ray diffraction in order to determine the phase composition of the samples (Fig. 3). The ZnO in the films is identified as wurtzite, with main characteristic peaks at 32.1, 34.8 and 36.5 2θ degrees. The SiO_2 in the composite structures is amorphous and therefore is not represented in the XRD spectrum.

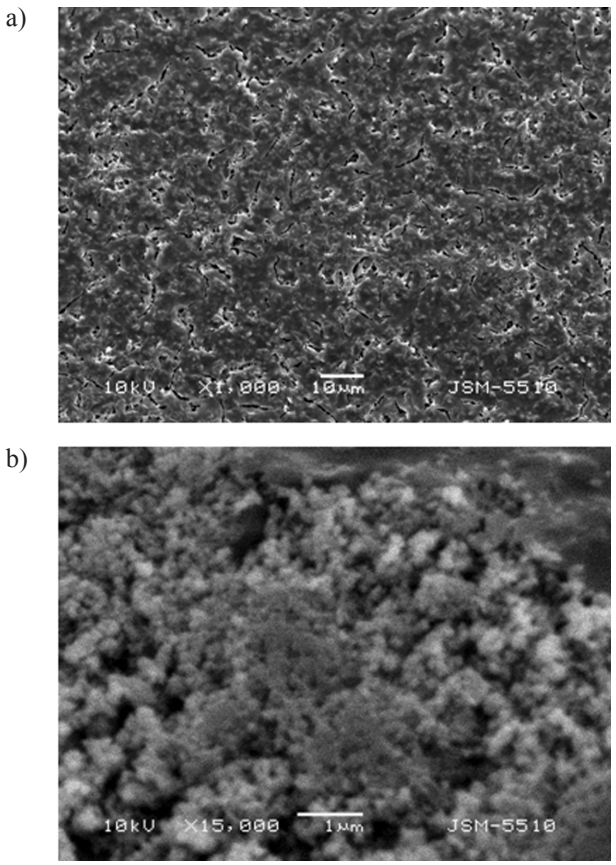

Fig. 1. SEM micrographs of zinc oxide films: (a) typical top view of the films surface at lower magnification; (b) a structure of spherical particles inside the pores at higher magnification

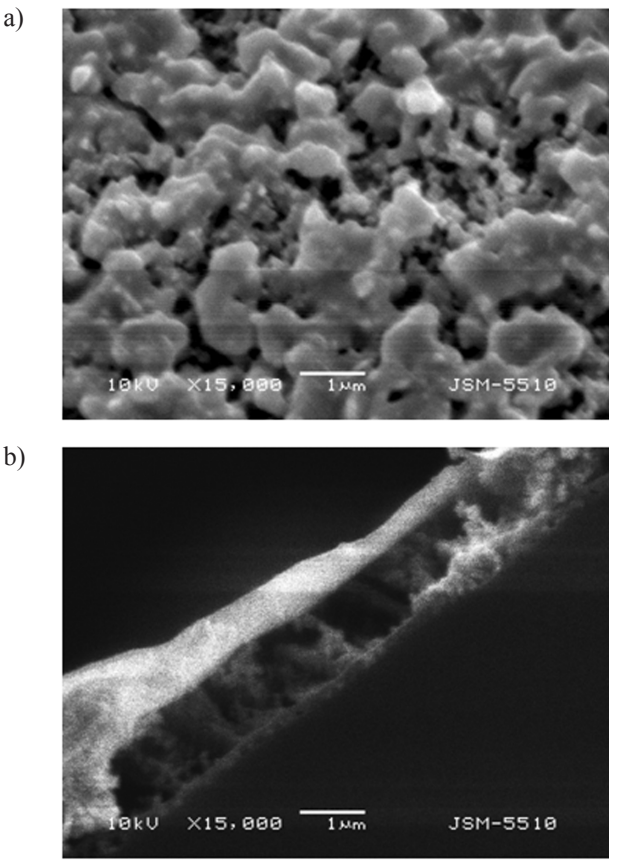

Fig. 2. SEM images of $20SiO_2$–$80ZnO$ films: (a) top view of the coatings surface morphology; (b) cross section of the nanocomposite film

Two series of photocatalytic experiments are performed upon UV and visible light irradiation – with methylene blue and with malachite green aqueous solutions. The results from the photocatalytic tests for MB degradation with the ZnO and composite films are presented in Figure 4. As seen from the experimental data, the photocatalytic efficiency of all the films (ZnO and ZnO–SiO_2) is low. In case of visible light illumination the ZnO thin film is more effective than the composite one. Similar trend is observed from the tests under UV illumination – all the thin film samples manifest higher rates of MB photodegradation in comparison to the thicker ones irrespective of type of light irradiation. From the comparison of visible light induced photocatalysis by samples with thicker layers is seen that the ZnO-SiO_2 composite sample shows higher degree of pollutants degradation than the ZnO film. The rate constants values of photocatalysis, calculated following the equation $\ln (C/C_0) = -kt$ are given in Table 1.

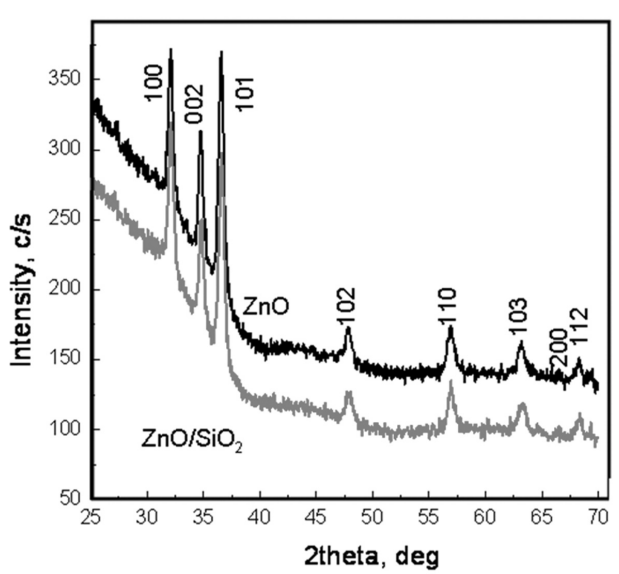

Fig. 3. Comparative XRD of ZnO and ZnO–SiO_2 composite films

Figure 5 represents kinetics of photocatalysis of MG with the ZnO and ZnO–SiO_2 film samples under UV and visible light illumination. In general an increased photocatalytic efficiency of all samples is observed in this case. From the presented data one can see clear tendency for regular rise in the samples photocatalytic efficiency with the film thickness irrespective of the type of light irradiation. Double layered films reach 43.45% of dye degradation under UV and 55.70% under visible light irradiation. This effect can be seen also from the rate constants of photocatalysis, presented in Table 1. The differ-

Table 1. Rate constants of photodegradation, calculated from the tests, conducted with different film samples

Samples	Rate constants, min^{-1}			
	Methylene Blue		Malachite Green	
	UV	Visible	UV	Visible
ZnO, thin	0.0009	0.0014	0.001	0.0014
ZnO, thick	0.0003	0.0005	0.0021	0.0031
SiO_2-ZnO, thin	0.0003	0.001	0.0007	0.0013
SiO_2-ZnO, thick	0.0002	0.0006	0.0024	0.0033

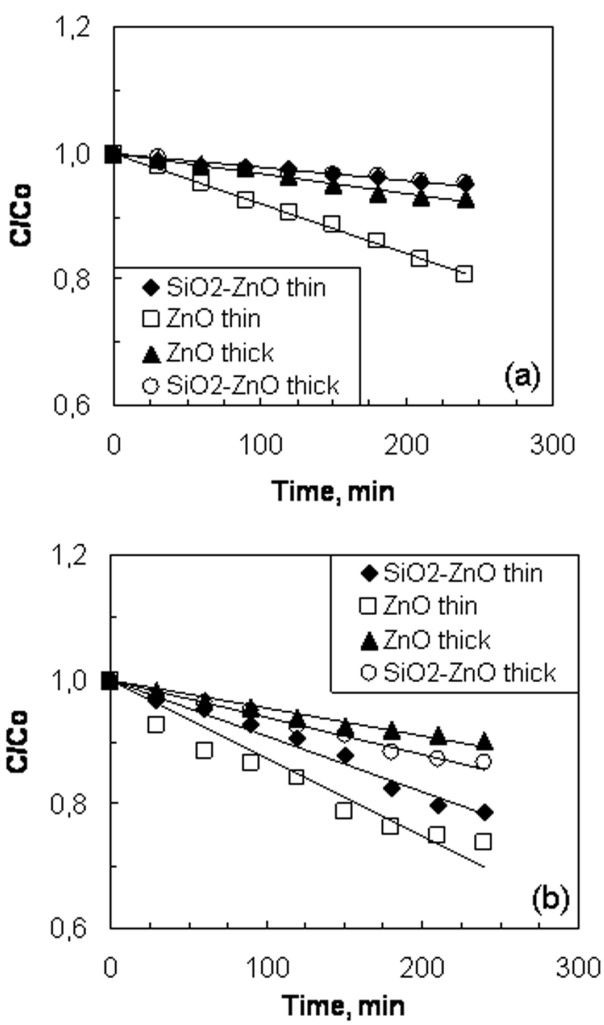

Fig. 4. Change in methylene blue concentration versus time of photocatalysis with the different film samples under: (a) UV illumination and (b) visible light. The initial MB concentration is 5 ppm

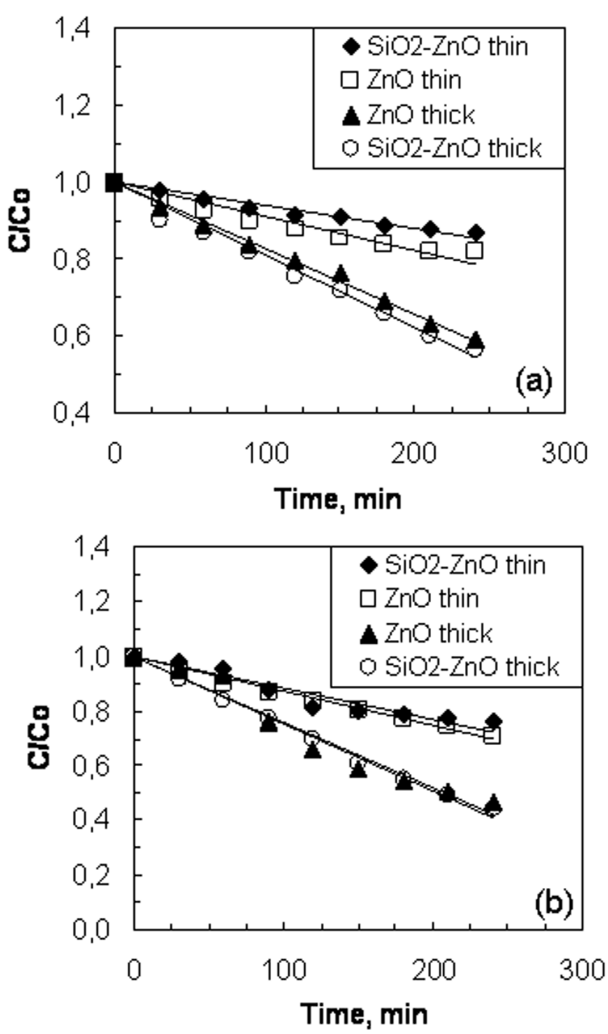

Fig. 5. Comparison of the photodegradation kinetics of malachite green with the photocatalytic films under catalytic action under: (a) UV irradiation and (b) visible light. The initial MG concentration is 5 ppm

ences, observed in photocatalytic decomposition of both pollutants can be attributed to geometrical factor, which is different for the different dye molecules. The structural formulas of Methylene blue and Malachite green oxalate are shown in Fig. 6.

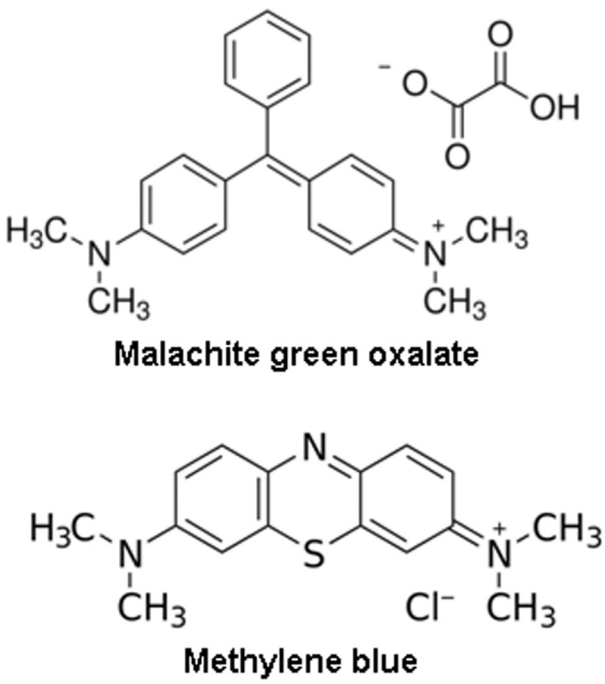

Fig. 6. Structural formulas of Methylene blue and Malachite green oxalate

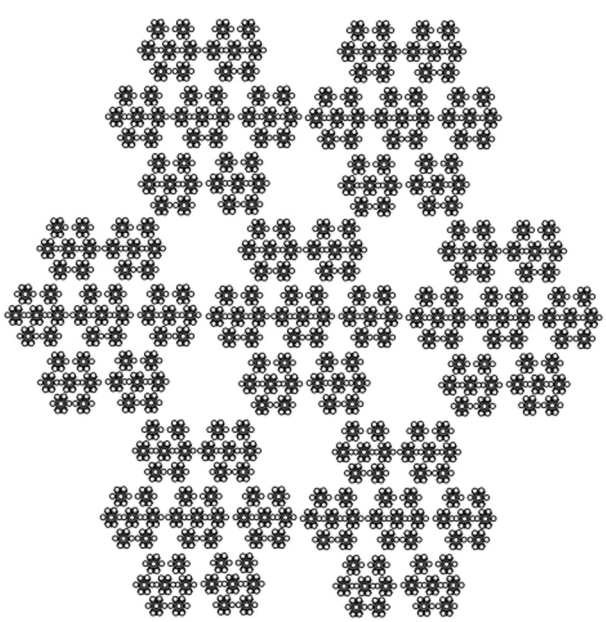

Fig. 7. Scheme of 3-D Julien fractal

The main advantages of using hierarchical assembled SiO_2/ZnO nanocomposite photocatalyst, consisting micro- and nanocrystals, are connected with the possible control over size and morphology towards desirable chemical properties of the obtained materials. The hierarchical self-assembly materials consist of constructive "blocks" with different sizes and shapes (and size-dependent properties) and have hierarchical porous structure. Hierarchical self-assembly can be a multilevel one, when the integrated blocks are basic elements for larger consolidations (with lager interaction radius). Figure 7 represents Julien fractal, which is one of the simplest idealized examples of self-assembly [22]. It is an appropriate example for understanding of the principal possibility to obtain materials with calibrated pores size. That is very important for development of new-generation devices, because the pores with different sizes have different functions (adsorption centers, canals for import and export of reaction products, nanoreactors with different capillary phenomena etc.).

CONCLUSIONS

Thin solid films of ZnO–SiO_2 are prepared via sol-gel process and spin coating technique. The films consist of micro- and nanostructures as shown by SEM and XRD investigations. The photocatalytic tests with respect to destruction of MG prove that of best performance is always the composite ZnO–SiO_2 thick film sample. This result is confirmed with both UV and visible light illumination using lamps of different power. The double layered films manifest much higher photocatalytic efficiency, compared with the rest film samples under UV and visible light irradiation. All films have higher photocatalytic efficiency in malachite green degradation in comparison to methylene blue.

Acknowledgements: *This research is financially supported by FP7 project Beyond Everest and the Federal target program "Scientific and Pedagogical Personnel of Innovative Russia" (state contract № 14.B37.21.1089).*

REFERENCES

1. C. A. Martinez-Huitle and E. Brillas, *Appl. Catal. B:*, **87**, 105 (2009).
2. S. M. Lam, J. C. Sin, A. Z. Abdullah and A. R. Mohamed, *Desalin. Water Treat.*, **41** (1–3), 131, (2012).
3. R. M. Christie, Environmental Aspects of Textile Dyeing, CRC Press, Cambridge, 2007.

4. K. Y. Foo and B. H. Hameed, *Adv. Colloid. Interface Sci.*, **159**, 130 (2010).
5. S. Srivastava, R. Sinha and D. Roy, *Aquatic Toxicology*, **66**, 319 (2004).
6. M. N. Chong, B. Jin, C. W. K. Chow and C. Saint, *Water Res.*, **44**, 2997 (2010).
7. D. Chatterjee and S. Dasgupta, *J. Photochem. Photobiol. C:*, **6**, 186 (2005).
8. M. D. Hernandez-Alonso, F. Fresno, S. Suarez and J. M. Coronado, *Energy Environ. Sci.*, **2**, 1231 (2009).
9. R. Comparelli, E. Fanizza, M.L. Curri, P.D. Cozzoli, G. Mascolo and A. Agostiano, *Appl. Catal. B:*, **60**, 1 (2005).
10. J. Xie, Y. T. Li, W. Zhao, L. Bian and Y. Wei, *Powder Technol.*, **207**, 140 (2011).
11. M. S. Mohajerani, A. Lak and A. Simchi, *J. Alloys Compounds*, **485,** 616 (2009).
12. R. Iordanova, A. Bachvarova-Nedelcheva, Y. Dimitriev and Tz. Iliev, *Bulg. Chem. Commun.*, **43** (3), 378 (2011).
13. A. Shalaby, Y. Dimitriev, R. Iordanova, A. Bachvarova-Nedelcheva and Tz. Iliev, *J. Univ. Chem. Technol. Metallurgy*, **46** (2), 137 (2011).
14. A. Stoyanova, Y. Dimitriev, A. Shalaby, A. Bachvarova-Nedelcheva, R. Iordanova and M. Sredkova, *J. Optoelectronic and Biomedical Materials*, **3**, (1), 24 (2011).
15. J. Li, H. Q. Fan, X. P. Chen and Z. Y. Cao*, Colloids Surf. A:*, **349**, 202 (2009).
16. S. Fernandez, O. D. Abril, F. B. Naranjo and J. J. Gandıa, *Solar Energy Mater. Solar Cells*, **95**, 2281 (2011).
17. S. K. L. Devi, K. S. Kumar and A. Balakrishnan, *Mater. Lett.*, **65**, 35 (2011).
18. D. Li and H. Haneda, *J. Photochem. Photobiol. A:*, **155**, 171 (2003).
19. S. H. Cho, J. W. Jang, J. S. Lee and K. H. Lee, *Cryst. Eng. Comm.*, **12**, 3929 (2010).
20. S. Ahmad, M. Kharkwal, Govind and R. Nagarajan, *J. Phys. Chem. C*, **115**, 10131 (2011).
21. V. A. Moshnikov, I. E. Gracheva, V. V. Kuznezov, A. I. Maximov, S. S. Karpova and A. A. Ponomareva, *J. Non-Cryst. Solids*, **356** (37), 2020 (2010).
22. I. E. Gracheva, V. A. Moshnikov, E. V. Maraeva, S. S. Karpova, O. A. Alexsandrova, N. I. Alekseyev, V. V. Kuznetsov, G. Olchowik, K. N. Semenov, A. V. Startseva, A. V. Sitnikov and J. M. Olchowik, *J. Non-Cryst. Solids*, **358**, 433 (2012).

НАНОРАЗМЕРНИ КОМПОЗИТНИ ТЪНКИ ФИЛМИ ОТ SiO_2–ZnO ЗА ФОТОКАТАЛИТИЧНО РАЗЛАГАНЕ НА ОРГАНИЧНИ БАГРИЛА – СТРУКТУРА И ХАРАКТЕРИЗИРАНЕ

Н. В. Кънева[1], С. А. Сюлейман[1], А. С. Божинова[1*], К. И. Папазова[1], Д. Т. Димитров[1], И. Грачева[2], С. Карпова[2], В. А. Мошников[2]

[1] Лаборатория по наука и технология на наночастици, катедра Обща и неорганична химия, Факултет по Химия и Фармация, Софийски университет, София 1164, България
[2] Катедра „Микро-Наноелектроника“, Държавен Университет по Електротехника, Санкт Петербург , 197376, Русия

Постъпила февруари, 2013 г.; приета май, 2013 г.

(Резюме)

В това изследване ние представяме чист ZnO и нанокомпозитни фотокатализатори $20SiO_2$–80ZnO (мол. %), получени върху стъклени подложки чрез техника на цетробежно отлагане (spin coating) и золгелен метод от изходни разтвори на цинков нитрат и тетраетоксисилан. Така получените филми са накалени при 500 °C за 1 час. Филмите са характеризирани чрез рентгенова дифракция и СЕМ анализи. Фотокаталитичното действие на филмите е изпитано и сравнено при фоторазграждането на две органични багрила Малахитово Зелено и Метиленово Синьо под облъчване с УВ и видима светлина. Промяната в концентрацията на багрилото с времето на облъчване е проследена с УВ-видима спектроскопия.

Bulgarian Chemical Communications, Volume 45, Number 4 (pp. 617–624) 2013

Structure and reducibility of the mixed metal oxides obtained from Ni-Al layered double hydroxides. Catalytic activity in CO_2 methanation reaction

M. V. Gabrovska[1]*, R. M. Edreva-Kardjieva[1], D. D. Crişan[2], K. K. Tenchev[1], D. A. Nikolova[1], M. Crişan[2]

[1] *Institute of Catalysis, Bulgarian Academy of Sciences, Acad. G. Bonchev Str. Bl. 11, 1113 Sofia, Bulgaria*
[2] *"Ilie Murgulescu" Institute of Physical Chemistry, Romanian Academy, 202 Splaiul Independentei Str., 060021 Bucharest-12, Romania*

Received February, 2013; Revised May, 2013

The effect of nickel amount on the structure, reducibility and activity of the mixed metal oxides generated by controlled thermal treatment of co-precipitated Ni-Al layered double hydroxides as catalyst precursors for CO_2 removal by methanation reaction, was examined by variation of the Ni^{2+}/Al^{3+} molar ratio (Ni^{2+}/Al^{3+} = 0.5, 1.5, and 3.0), the reduction and reaction temperatures. The powder X-ray diffraction of the thermally treated samples (200−1000 °C) established the formation of nano-sized NiO- and spinel $NiAl_2O_4$-like phases in different proportion and degree of crystallinity. The calcination temperature of 500 °C was selected as most convenient one because of the high dispersion of the mixed oxide phases predetermining the high dispersion of the metallic nickel.

It was revealed that after preliminary '*in situ*' reduction at 400, 450, 530 and 600 °C, all studied catalysts hydrogenated CO_2 effectively at reaction temperatures from 400 to 280 °C and space velocities between 3000 and 22000 h^{-1}. All three catalysts demonstrated similar activity at lower reduction and reaction temperatures due to the formation of readily reducible Ni^{2+}–O species which generated sufficient number of accessible Ni^0 surface active sites. Partial regeneration of the original layered structure was registered in the higher nickel containing solids after finishing of the catalytic test.

The advantage of the catalyst with the lowest nickel amount is disclosed at low reaction and reduction temperatures. Its performance dominates after reduction at higher temperatures because of the role of $NiAl_2O_4$ spinel-like phase to act as a "reservoir" generating fresh Ni^0. The decrease of activity in the rest of the catalysts is attributed mainly to the Ni^0 sintering.

Key words: Ni-Al layered double hydroxides, Ni-Al mixed oxides, structure, reducibility, CO_2 removal by methanation.

INTRODUCTION

The Ni-Al layered double hydroxides (LDHs), which are also known as takovite-like (TKl) compounds, belong to a great group of natural or synthetic inorganic lamellar compounds with chemical composition expressed by the general formula $[Ni^{2+}_{1-x}Al^{3+}_x(OH)_2]^{x+}[A^{n-}_{x/n}]\cdot mH_2O$, where Ni^{2+} and Al^{3+} ions are located in the brucite-like hydroxide layers, while the charge compensating exchangeable anions A^{n-} such as CO_3^{2-}, NO_3^-, SO_4^{2-}, Cl^-, etc., as well as water molecules, are situated in the interlayer space of the layered structure. Herewith, x represents the fraction of the Al^{3+} cation, and m is the number of the water molecules [1].

The research efforts have been focused on the assessment of the potential use of these layered systems as catalysts, either as-synthesized or mainly after thermal treatment. Typically, the thermal decomposition of the materials, includes dehydration, dehydroxylation and loss of the charge compensating anions, results in formation of finely dispersed Ni-Al mixed oxides of $Ni^{2+}(Al^{3+})O$ type. The latter represent promising catalysts due to their high specific surface area, high distribution of both Ni^{2+} and Al^{3+} ions after calcination despite of the high content of Ni^{2+} ions, high metal (inter)dispersion after

* To whom all correspondence should be sent:
E-mail: margo@ic.bas.bg

reduction, small crystal size, and stability against sintering [1−4].

The effective utilization of CO_2 originating from the production processes and flue gases of CO_2-intensive sectors is an important area of research because CO_2 is a major greenhouse gas and makes a significant contribution to global warming and climate change. Among the catalytic reactions, the catalytic hydrogenation of CO_2 over supported nickel metal catalysts to form methane, simply called methanation, is a particularly promising technique for CO_2 removal [5, 6]. The methanation reaction is commonly applied in ammonia plants at the final stage of purification of the synthesis gas in which low concentrations of CO and CO_2 (0.1−0.5%) are catalytically removed by a reaction with hydrogen. The reaction is of crucial importance due to the poisonous effect of carbon oxides on the ammonia synthesis. At present, the methanation became also attractive for reducing the residual carbon oxides in hydrogen-rich reforming gases, and to satisfy the requirements of polymer electrolyte fuel cell anodes [7, 8]. Although many different catalytic systems based on supported group VIII metals (e. g. Ru, Rh) on various oxide carriers (TiO_2, SiO_2, Al_2O_3, CeO_2, ZrO_2) have been applied to catalyze the reaction, the industrial methanation catalyst is essentially nickel metal at a large scale of concentrations (25−77 wt.%) due to its high activity, selectivity toward methane formation in preference to other hydrocarbons, high thermal stability, and relatively low cost [5, 9].

In a series of articles [10−13] Kruissink et al. have claimed that a thermal treatment of co-precipitated Ni-Al precursors of Ni^{2+}/Al^{3+} = 2.0−3.0 molar ratio in the interval of 450−900 °C and a following high-temperature reduction at 500−600 °C lead to the formation of very active catalysts for CO methanation at ≈300 °C. However, the authors have reported neither variations of the reduction and reaction temperatures, nor variations of the flow rates of the gaseous reaction mixture to obtain a detailed picture of catalyst performance.

In our recent paper [14] it was established that the Ni-Al LDHs with TKl structure are potential catalyst precursors for the fine CO_2 removal from hydrogen-rich gas streams through the methanation reaction, depending on the Ni^{2+}/Al^{3+} molar ratio and temperature of treatment in hydrogen ambience of the as-synthesized precipitates without preliminary calcination to the related oxides. It was found that after reduction at 400 and 450 °C the catalyst of the highest nickel amount has demonstrated the highest conversion degree at all reaction temperatures and space velocities, while the catalyst of the lowest nickel prevailed in the methanation activity after reduction within 530–600 °C.

The objective of this study is to examine the phase composition of the mixed oxides obtained by a controlled thermal treatment of the Ni-Al TKl systems aiming to select the catalyst with the most beneficial characteristics for the methanation reaction ($CO_2 + 4H_2 = CH_4 + 2H_2O$) by variation of the Ni^{2+}/Al^{3+} molar ratio, the reduction and reaction temperatures.

EXPERIMENTAL

Sample preparation

Carbonate forms of TKl precursors with Ni^{2+}/Al^{3+} molar ratios of 0.5, 1.5 and 3.0 were obtained by co-precipitation of the mixed Ni-Al nitrate solution with Na_2CO_3 at constant temperature of 80 °C and pH = 8 under vigorous stirring. More detailed description of the preparation procedure was presented in Ref. 14. The obtained precipitate was further dried at 80 °C for 20 h and named takovite-like precursor, designated as *x*NiAl, where *x* represents the Ni^{2+}/Al^{3+} molar ratio, for example 3.0NiAl (Table 1). The precursors were calcined in air at 500 °C for 2 h before the catalytic activity test. The catalysts after the reaction run (the tested catalysts) were labeled as *x*NiAl-t.

The unsupported NiO was prepared as a reference sample by the same preparation procedure. The sample was calcined in air at 500 °C for 2 h and denoted as reference NiO.

Table 1. Chemical composition of the as-synthesized TKl samples

Sample	Chemical composition (wt. %)				Ni^{2+}/Al^{3+} molar ratio
	Ni	Al	NiO	Al_2O_3	
0.5NiAl	21.3	19.6	42.3	57.7	0.49
1.5NiAl	32.9	10.1	68.7	31.3	1.48
3.0NiAl	42.6	6.5	81.5	18.5	2.98

Sample characterization

Powder X-ray diffraction data was collected on a Bruker D8 Advance diffractometer employing CuK_α radiation (λ = 0.15418 nm), operated at U = 40 kV and I = 40 mA. The mean crystallite sizes (*L*) were determined using computer program X'Pert HighScore (PW3209) Version 1.0f (2004). The crystalline phases were identified using Joint Committee on Powder Diffraction Standards (JCPDS) files.

Specific surface area was measured employing the single point BET method using a FlowSorb II 2300 Micromeritics apparatus with a N_2–He mixture (15% N_2) at the boiling temperature of liquid nitrogen.

Temperature-programmed reduction was evaluated in the measurement cell of a SETARAM differential scanning calorimeter (DSC-111) directly connected to a gas chromatograph. The temperature was linearly raised from 25 to 700 °C at a heating rate of 10°C/min. The experiments (~0.025 g sample) were accomplished by a gaseous mixture of 10% H_2 in Ar at a flow rate of 25 cm^3/min.

Gas-phase hydrogenation of CO_2 to CH_4 was carried out in a fixed-bed flow reactor set-up under ambient pressure. The activation of the catalysts was performed by preliminary '*in situ*' reduction in the equipment at 400, 450, 530, and 600 °C for 3 h with pure hydrogen at a gas hourly space velocity (GHSV) of 2000 h^{-1} and a heating rate of 1.7°/min. The catalytic activity measurements were accomplished by means of gaseous mixture of $CO_2/H_2/Ar$=0.65/34.35/65 vol.% in the temperature interval 220−400 °C and GHSV from 3000 to 22000 h^{-1} after each reduction procedure. A liquate N_2 trap after reactor eliminated water as a reaction product. The amount of residual CO_2 was determined using online-connected Uras 3G gas analyzer (Hartmann-Braun AG) in the range 0−0.0050 vol.% CO_2 (0−50 ppm).

RESULTS AND DISCUSSION

The chemical composition of the TKl samples, measured by ICP analysis, is listed in Table 1.

Powder X-ray diffraction (PXRD)

In our recent paper [14] it was documented that a well-crystallized TKl structure containing carbonate anions in the interlayer space is formed only in 3.0NiAl precipitate (Fig. 1a): sharp and symmetrical reflections for (003), (006), (110) and (113) planes and broad and asymmetric for (012), (015), and (018), respectively. It was established that a decrease in nickel loading of 1.5NiAl sample causes lowering of the peak intensities and broadening of the TKl reflections (Fig. 1b), as well as the coexistence of two phases in 0.5NiAl solid (Fig. 1c): a poorly crystallized TKl phase accompanied by a gibbsite one. It was found that the increase in Ni amount of the samples leads to (i) increase of the lattice param-

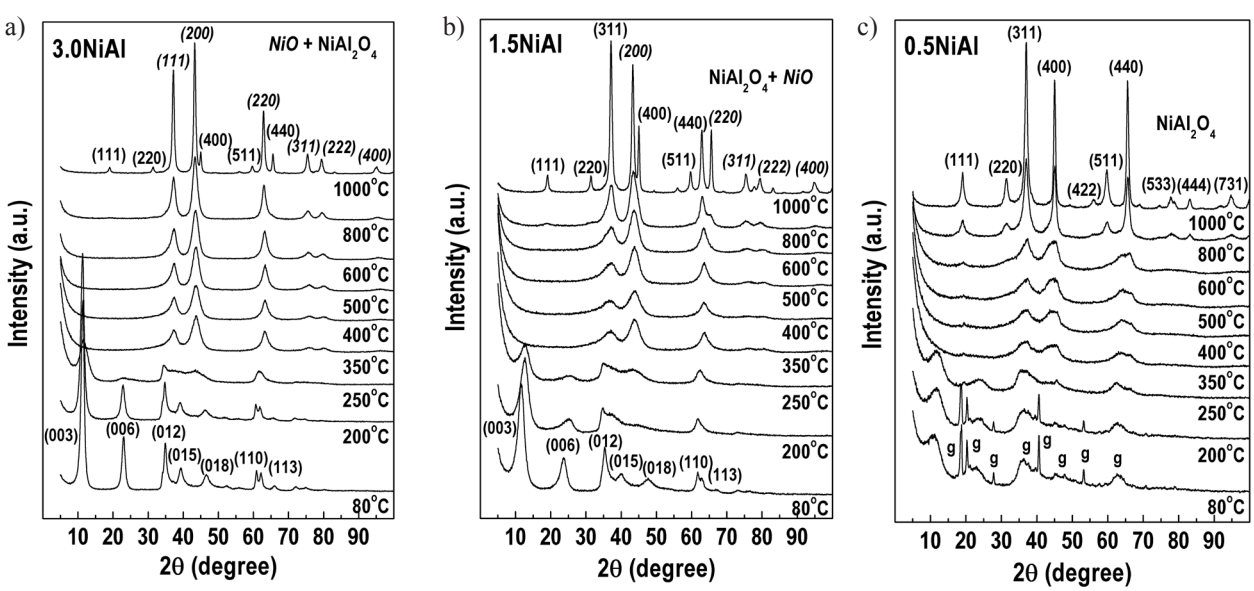

Fig. 1. PXRD patterns of the samples thermally treated at various temperatures: (a) 3.0NiAl, (b) 1.5NiAl and (c) 0.5NiAl, where **g** is gibbsite

eters, (ii) crystallite growth and (iii) decrease of the specific surface area (SSA).

The investigated Ni-Al layered systems were thermally treated in the temperature range 200−1000 °C for 120 min in an air atmosphere. The corresponding PXRD patterns were used for elucidation of the structure evolution with the temperature increase, i.e. appearance, formation and transformation of the resultant phases.

PXRD patterns of the calcined at 200 °C solids (Figs. 1−3) displayed reflections similar to the as-synthesized ones, however slightly shifted to higher angles. This finding is ascribed to the beginning of the interlayer water molecules losing. The diffraction lines of the thermally treated at 250 °C samples indicate partial decomposition of the TKl structure in all samples. It is observed an appearance of badly organized reflections (200) of NiO phase (JCPDS file 00-047-1049) in 1.5NiAl and 3.0NiAl samples, being better organized in the later. An additional broad reflections (111), (311) and (440) of a non-stoichiometric spinel-type $NiAl_2O_4$ phase (JCPDS file 00-010-0339) are detected in 0.5NiAl. The characteristic diffraction lines of TKl structure disappear completely at 350 °C and rather amorphous calcination products are formed in all samples. This observation is attributed to both dehydroxylation of the brucite-type layers and decarbonation of the interlayer space as result of the destruction of the layered structure [15−17]. With further increase in the temperature to 500 and 600 °C, the diffraction peaks of NiO and $NiAl_2O_4$ phases become narrower and more intense, due to the growth of crystallites and improvement of crystallization. PXRD patterns of the calcined at 800 °C solids detect reflections of: (i) a well formed single $NiAl_2O_4$ phase in 0.5NiAl; (ii) an appearance of badly organized $NiAl_2O_4$ phase in 1.5NiAl sample together with a better crystallized NiO phase, and (iii) a well formed single NiO phase in 3.0NiAl solid. The diffraction lines of the calcined at 1000 °C materials show existence of two phases in 1.5NiAl and 3.0NiAl samples: NiO and $NiAl_2O_4$, however, differing in proportion. NiO is a predominant phase in 3.0NiAl solid and conversely, spinel $NiAl_2O_4$ phase is the dominant phase in 1.5NiAl and 0.5NiAl materials. No separate Al-containing phase was observed may be because of segregation of Al^{3+} cations to an amorphous components.

The calculated crystallographic parameters of NiO phase (a_{NiO}) in calcined 1.5NiAl and 3.0NiAl solids up to 1000 °C (Fig. 2a) demonstrate values which are lower than of both reference NiO (a_{NiO} = 0.4176 nm) and standard NiO (a_{NiO} = 0.4177 nm) according to JCPDS file 00-047-1049. As it was reported [18], this finding is a consequence of the partial incorporation of Al^{3+} ions into the cubic framework of the NiO, reducing its cell dimensions (a_{NiO}) of the pure NiO because of the smaller radius of Al^{3+} ions (0.053 nm) as compared to Ni^{2+} ones (0.069 nm) [19]. The increase of Al^{3+} cations' incorporation into NiO lattice on decreasing Ni^{2+}/Al^{3+} molar ratio is in line with decreasing the NiO lattice parameter in the samples.

The mean crystallite sizes of NiO (L_{NiO}) and $NiAl_2O_4$ ($L_{NiAl_2O_4}$) phases in 1.5NiAl and 3.0NiAl samples were determined from the full-width at half-maximum values of (200) diffraction line for NiO phase and (311) line for $NiAl_2O_4$, respectively. It is observed that the increase of the calcination temperature up to 500 °C and the nickel content lead to the slightly enlargement of NiO crystallite sizes (Fig. 2b). The treatment of both samples at 800 and

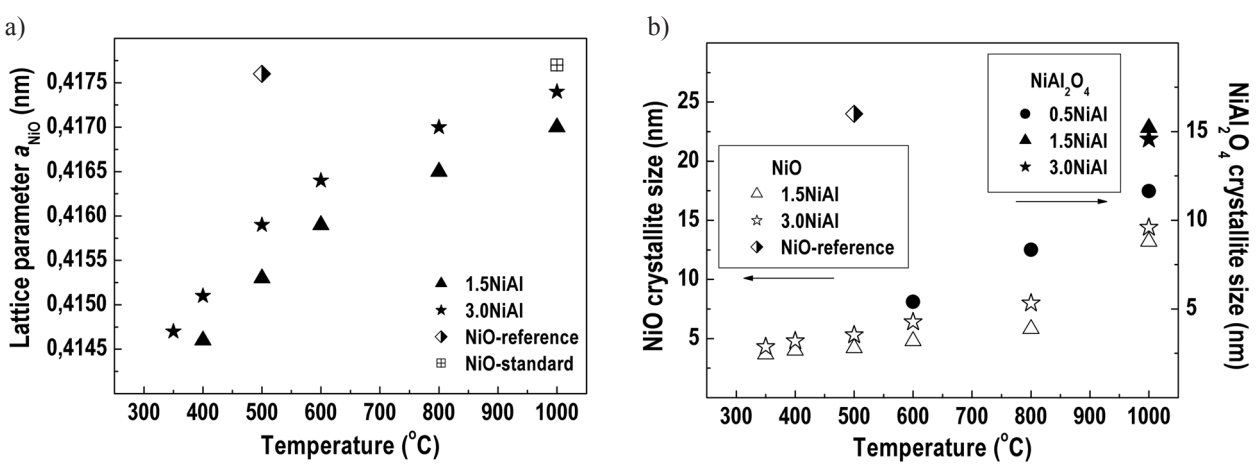

Fig. 2. Crystallographic characteristics of the samples thermally treated at various temperatures: (a) lattice parameter of NiO (a_{NiO}) and (b) crystallite size (L) of NiO and $NiAl_2O_4$ phases

1000 °C causes sharply increase and alignment of the NiO crystallite sizes, suggesting complete separation of NiO and $NiAl_2O_4$ phases. The values of L_{NiO} and $L_{NiAl_2O_4}$ comply with the degree of crystallization of both phases in the studied solids remaining in the nano-scaled region.

The PXRD analyses documented that the decomposition of the TKl structure at 500 °C attracts special attention. The resulting structurally disordered oxide mixture crystallizes to form NiO-like phase in 3.0NiAl and 1.5NiAl samples with L_{NiO} of 5.3 and 4.2 nm, respectively, and poorly organized $NiAl_2O_4$-like phase in 0.5NiAl. In addition the SSA (m^2/g) values of the calcined Ni-Al samples at 500 °C demonstrate well developed surface: 141 (0.5NiAl) > 128 (1.5NiAl) > 112 (3.0NiAl) in comparison with 15 m^2/g of the reference NiO sample.

Obviously, the NiO-like phase obtained by calcination of the Ni-Al TKl compounds exhibits a high thermal stability in comparison with the reference NiO. The Al^{3+} ions are concentrated onto and in the NiO surface, forming other phases such as alumina or spinel-type phases, so that the NiO surface is wholly modified [20]. The spinel-type phase plays a major role in the thermal properties of the mixed oxides, because there is no possibility of direct physical contact between two adjacent nickel crystallites. In such a way the growth and sintering of the NiO is hindering, thus increasing the SSA [21].

The high dispersion of NiO-like phase is presumed to generate also highly dispersed metallic nickel particles after the activation of the precursors by reduction with hydrogen. All these arguments lead to the conclusion that the thermal treatment of Ni-Al TKl systems as precursors of catalysts for CO_2 removal by methanation should be carried out at a temperature of 500 °C.

Temperature programmed reduction (TPR) study

The reducibility of the calcined at 500 °C precursors was investigated by means of TPR technique. TPR experiments were applied to elucidate the nature of reducible Ni^{2+}–O species present in the samples and to reveal the temperature at which reduction to metallic Ni^0 occurs depending on the nickel loading in the solids.

The TPR profile of the reference sample NiO, displays a large temperature peak in the range 280−550 °C with T_{max} at 393 °C and a shoulder at ≈450 °C. It may be assumed that full reduction of bulk Ni^{2+} ions to Ni^0 has occurred (Fig. 3). The appearance of broad asymmetric TPR profiles spreading throughout a wide temperature range from 290 to 700 °C in all solids documented the presence of Al^{3+} ions. A shift of LT shoulders as well as T_{max} towards higher temperatures upon decreasing of Ni content (increase of Al), are clearly observed with the samples under study.

The TPR profile of the highest nickel containing sample 3.0NiAl demonstrates low-temperature (LT) shoulders at ≈310 °C and ≈390 °C, temperature maxima (T_{max}) ≈550 °C and high-temperature (HT) shoulder at ≈645 °C. The profile of 1.5NiAl indicates a presence of LT shoulders at ≈312 °C and ≈405 °C, shoulder at ≈545 °C, T_{max} at ≈615 °C and HT shoulder at ≈670 °C. LT shoulders at ≈335 °C and ≈440 °C, T_{max} at ≈615 °C and HT shoulder at ≈670 °C are registered in 0.5NiAl sample.

The impeded reducibility as compared to the reference NiO pointed undoubtedly to the presence of $A1^{3+}$ ions in the NiO lattice. According to the models, proposed for decomposition and reduction of the LDH compounds [20−22], the LT shoulders from TPR profiles of all solids are ascribed to reduction of NiO intimately mixed with a small quantity of Al^{3+} ions (Phase I). The T_{max} of 3.0NiAl sample is attributed to reduction of the quasi-amorphous Ni-Al spinel-like phase (Phase II) which decorates the surface of the NiO particles and/or acts as their support. The T_{max} of 1.5NiAl and 0.5NiAl solids, as well as the HT shoulders of all samples are assigned to the reduction of the alumina-type phase doped with some amount of Ni^{2+} ions (Phase III), probably 'grafted' on the spinel-like phase. All TPR profiles identify incomplete reduction of Phase III because the profiles do not recover the baseline. It is associated with the appearance of hardly reducible spinel-like $NiAl_2O_4$ phases.

It may be generalized that the reduction of the Ni^{2+} ions in the mixed Ni-Al oxides, is realized at different temperatures due to different amounts,

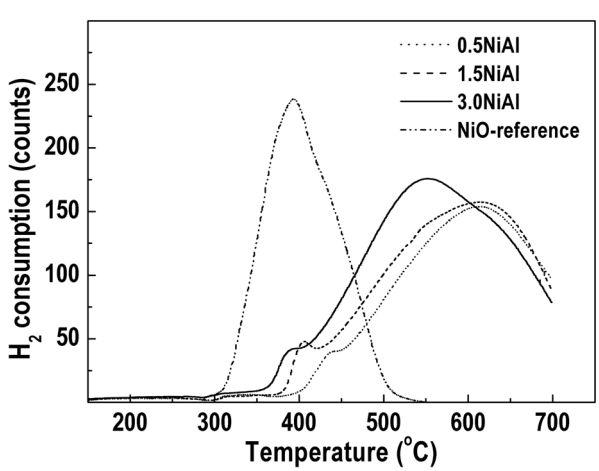

Fig. 3. TPR profiles of the samples calcined at 500 °C

location and strength of interaction of Ni^{2+}–O and Al^{3+} moieties.

CO_2 removal by methanation reaction

The catalytic activity of the calcined at 500 °C catalysts is evaluated by the highest GHSV at which the residual concentration of CO_2 at the reactor outlet is 0.0010 vol.% (10 ppm). This level is an admissible limit in modern industrial ammonia production. The catalytic runs show that after preliminary reduction at 400, 450, 530 and 600 °C all three catalysts hydrogenate CO_2 successfully to residual content of CO_2 levels of 0−10 ppm at reaction temperatures between 400 and 280 °C and GHSV within 3000–22000 h^{-1}. The differences in activity become evidently at lower reaction temperatures, namely at 260, 240 and 220 °C (Fig. 4).

As it can be seen, the 0.5NiAl catalyst demonstrates higher methanation activity at a reaction temperature of 260 °C after reduction at 400 °C. The catalyst purifies the reaction mixture from CO_2 to residual content of 10 ppm at GHSV = 12000 h^{-1}. Further increase of the reduction temperature brings about effective purging of the reaction mixture at GHSV = 22000 h^{-1} to residual content of 5.7 ppm CO_2 after reduction at 450 °C and 0 ppm CO_2 after reduction at 530 and 600 °C. The rest of catalysts comply with the following order of activities: 1.5NiAl>3.0NiAl after reduction at all examined temperatures.

Lowering of the reaction temperature to 240 °C leads to similar activity of all catalysts after reduction at 400 °C and to indistinguishable one, after reduction at 450 °C. In contrast, an enhancement in activity is registered after reduction at 530 °C, being more pronounced in the 0.5NiAl catalyst. Further increase of the reduction treatment to 600 °C reveals the priority of the 0.5NiAl catalyst which removes CO_2 to 10 ppm level at GHSV = 15000 h^{-1}. The activity of the rest of catalysts decrease in the order: 1.5NiAl>3.0NiAl.

The CO_2 removal at reaction temperature of 220 °C shows lower values almost independent of the reduction temperature. The purification seems effective only at low space velocities (4−5 h^{-1}).

The interpretation of the demonstrated activity may be partially found in the TPR experiments (Fig. 3). TPR profiles suggest the existence of two types of Ni^{2+}-O species on the surface of the all mixed oxides under study: readily and hardly reducible. The methanation activity of the catalysts after reduction at 400 and 450 °C may be easily ascribed to the presence of readily reducible Ni^{2+}-O species. The close activity indicates that the amount of active Ni^0 species is enough even in the 0.5NiAl in spite of the different nickel loading.

The higher activity of 0.5NiAl catalyst after reduction above 500 °C may be attributed to the retarding effect of Al^{3+} ions on the Ni^0 sintering due to the presence of spinel-type $NiAl_2O_4$ phase at higher temperatures. The sintering of the reduced metal lead to decrease of the activity, more pronounced in the catalyst with the highest nickel content 3.0NiAl. Moreover, it is suggested by McArthur [23] that nickel aluminates or some similar compounds act

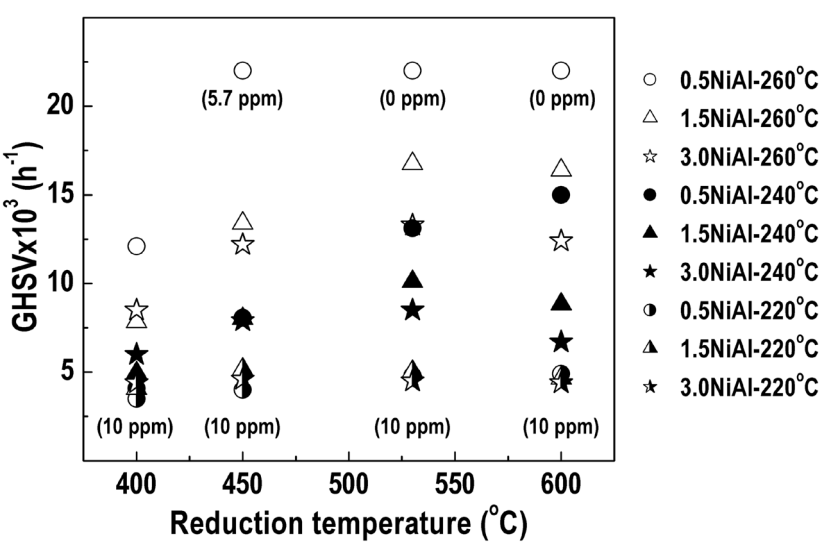

Fig. 4. Comparison of the methanation activity (0–10 ppm) of the calcined catalysts at reaction temperatures of 260, 240 and 220 °C *vs* reduction temperatures

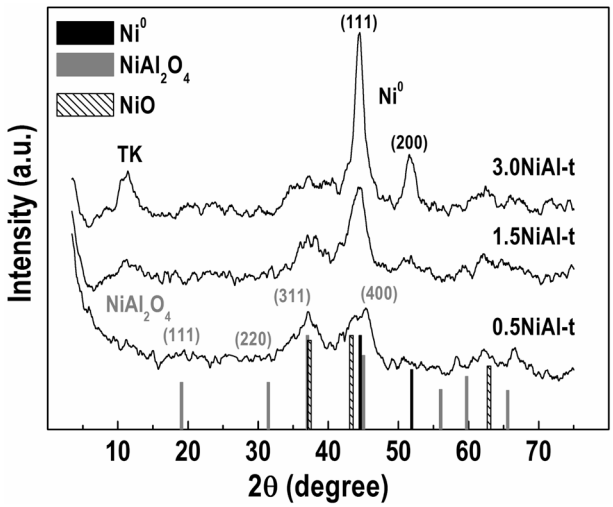

Fig. 5. PXRD patterns of the catalysts after the reaction run (tested samples)

somewhat as a "reservoir" which, upon gradual reduction in the presence of hydrogen-containing gases, continually generates fresh metallic nickel, thus accounting for the remarkable activity maintenance of the catalyst.

All these considerations are related to the incorporation of Al^{3+} cations into NiO lattice.

Additional explanation of the methanation activity is suggested by the diffractograms of the catalysts after the reaction run (Fig. 5), namely reduction at 600 °C, testing in the range 400–220 °C and passivation after cooling down to room temperature by a gas mixture of O_2/N_2. Some findings must be pointed: (i) Formation of Ni^0 phase (JCPDS file 00-004-850), in all the tested catalysts, being better organized in 3.0NiAl-t; (ii) Presence of NiO-like phase in 1.5NiAl-t and 0.5NiAl-t catalysts; (iii) Prevalent $NiAl_2O_4$ phase in 0.5NiAl-t; (iv) Registration of the reflections characteristics of TKl structure in 1.5NiAl-t and 3.0NiAl-t catalysts, more expressive in 3.0NiAl-t.

The appearance of diffraction lines typical of TKl compounds may be attributed to the property of the mixed oxides generated from LDHs to regenerate the initial layered structure in the presence of water with natural content of dissolved CO_2 [24, 25]. Evidently, a hydrolysis of the unreduced surface Ni^{2+} ions is realized upon the methanation reaction medium. The hydrolyzed Ni^{2+} species together with some Al^{3+} ions partially re-crystallized in original TKl structure. The partial formation of TKl phase may be implied as an additional reason for the lowest activity of 3.0NiAl and 1.5NiAl catalysts, namely, the amount of Ni^0 on the catalyst surface should be diminished thus provoking decrease in activity.

The low degree of crystallization of the tested catalysts hinders the determination of the Ni^0 size. The SSA (m^2/g) measurements suggest greater dispersion of the phases in 0.5NiAl-t catalyst: 122 (0.5NiAl-t) > 114 (1.5NiAl-t) > 79 (3.0NiAl-t). Moreover, the SSA of 3.0NiAl-t catalyst (79 m^2/g) shows value very close to the SSA of takovite-like 3.0NiAl solid (71 m^2/g) [14] thus evidencing the partial formation of TKl structure.

CONCLUSIONS

The structure, reducibility and CO_2 methanation activity of the Ni-Al mixed oxides generated by controlled thermal treatment of Ni-Al takovite-like LDHs depend on the amount, location and strength of interaction of Ni^{2+}–O and Al^{3+} species and temperature. NiO- and spinel $NiAl_2O_4$-like phases are formed in the nano-sized region in different proportion and degree of crystallinity as a function of the nickel content.

The calcination temperature of 500 °C is selected as most convenient one because of the high dispersion of the mixed oxide phases predetermining the high dispersion of the metallic nickel. All preliminary reduction temperatures of the three catalysts provoke effectively CO_2 hydrogenation down to 280 °C and high space velocities. Partial regeneration of the original layered structure was registered in the higher nickel containing solids after finishing of the catalytic test.

The advantage of the catalyst with the lowest nickel amount is revealed at low temperature of reaction (260 °C) and reduction (400 °C). Its performance dominates at higher reduction temperatures due to the role of spinel $NiAl_2O_4$-like phase to act as a "reservoir" generating fresh metallic nickel. The decrease of activity in the rest of the catalysts is mainly attributed to sintering of the reduced metal nickel.

Note: This article has been realized in the frame of inter-academic collaboration between Institute of Catalysis, Bulgarian Academy of Sciences, and "Ilie Murgulescu" Institute of Physical Chemistry, Romanian Academy.

REFERENCES

1. F. Cavani, F. Trifirò, A. Vaccari, *Catal. Today*, **11**, 173 (1991).
2. A. Vaccari, *Catal. Today*, **41**, 53 (1998).
3. A. Vaccari, *Appl. Clay Sci*., **14**, 161 (1999).
4. B. Zümreoglu-Karan, A. Ay, *Chemical Papers* **66**, 1 (2012).

5. W. Wang, J. Gong, *Front. Chem. Sci. Eng*., **5**, 2 (2011).
6. W. Wang, Sh. Wang, X. Ma, J. Gong, *Chem. Soc. Rev*., **40**, 3703 (2011).
7. K. Xavier, R. Sreekala, K. Rashid, K. Yusuff, B. Sen, *Catal. Today*, **49**, 17 (1999).
8. G. Xu, X. Chen, Z.-G. Zhang, *Chem. Eng. J*., **121**, 97 (2006).
9. A. Mills, F. Steffgen, *Catal. Rev. –Sci. Eng*., **8**, 159 (1974).
10. G. van Veen, E. C. Kruissink, E. B. Doesburg, J. R. Ross, L. L. van Reijen, *React. Kinet. Catal. Lett*., **9**, 143 (1978).
11. E. Kruissink, L. van Reijen, J. Ross, *J. Chem. Soc. Trans*. I, **77**, 649 (1981).
12. L. Alzamora, J. Ross, E. Kruissink, L. van Reijen, *J. Chem. Soc. Faraday Trans.* I, **77**, 665 (1981).
13. E. Kruissink, H. Pelt, J. Ross, L. van Reijen, Appl. *Catal*., **1**, 23 (1981).
14. M. Gabrovska, R. Edreva-Kardjieva, D. Crişan, P. Tzvetkov, M. Shopska, I. Shtereva, *React. Kinet. Mech. Cat.*, **105**, 79 (2012).
15. D. Bish, G. Brindley, *Am. Mineral*., **62**, 458 (1977).
16. S. Palmer, R. Frost, T. Nguyen, *Coord. Chem. Rev*., **253**, 250 (2009).
17. T. Sato, H. Fujita, T. Endo, M. Shimada,A. Tsunashima, *React. Solids*, **5**, 219 (1988).
18. D. Puxley, I. Kitchener, C. Komodromos, et al., *Stud. Surf. Sci. Catal*., **16**, 237 (1983).
19. R. Shannon, *Acta Crystallogr. A*, **32**, 751 (1976).
20. O. Clause, B. Rebours, E. Merlen, F. Trifirò, A. Vaccari, *J. Catal*., **133**, 231 (1992).
21. O. Clause, M. Goncalves Coelho, M. Gazzano, D. Matteuzzi, F. Trifirò, A. Vaccari, *Appl. Clay Sci*. **8**, 169 (1993).
22. F. Trifirò, A. Vaccari, O. Clause, *Catal. Today*, **21**, 185 (1994).
23. D. McArthur, US Patent 4,191,664, Mart 1980.
24. Ts. Stanimirova, G. Kirov, E. Dinolova, *J. Mater. Sci. Lett*., **20**, 453 (2001).
25. Ts. Stanimirova, V. Balek, *J. Therm. Anal. Calorim*., **94**, 477 (2008).

СТРУКТУРА И РЕДУЦИРУЕМОСТ НА СМЕСЕНИ МЕТАЛНИ ОКСИДИ, ПОЛУЧЕНИ ОТ Ni-Al СЛОИСТИ ДВОЙНИ ХИДРОКСИДИ. КАТАЛИТИЧНА АКТИВНОСТ В РЕАКЦИЯТА НА МЕТАНИРАНЕ НА CO_2

М. В. Габровска[1]*, Р. М. Едрева-Кърджиева[1], Д. Д. Кришан[2], К. К. Тенчев[1], Д. А. Николова[1], М. Кришан[2]

[1] Институт по катализ, Българска академия на науките, ул. Акад. Г. Бончев, бл. 11, 1113 София, България
[2] „Илие Мъргулеску“ Институт по физикохимия, Румънска академия, 202 бул. Индепенденцей, 060021 Букурещ-12, Румъния

Постъпила февруари, 2013 г.; приета май, 2013 г.

(Резюме)

Изследван е ефектът от количеството на никела върху структурата, редуцируемостта и активността на сместените метални оксиди, получени чрез контролирана термична обработка на съутаени Ni-Al слоисти двойни хидроксиди, като прекурсори на катализатори за очистване от CO_2 чрез реакцията на метаниране, променяйки молното съотношение Ni^{2+}/Al^{3+} (Ni^{2+}/Al^{3+} = 0.5, 1.5 и 3.0) и температурите на редукция и реакция. Чрез прахова дифракция на рентгенови лъчи на термично обработваните образци (200−1000 °C) е установено образуването на нано-размерни NiO- и шпинело $NiAl_2O_4$-подобни фази в различно съотношение и степен на кристалност. Като най-подходяща за накаляване на образците е избрана температурата от 500 °C поради високата дисперсност на смесените оксидни фази, което предопределя висока дисперсност и на металния никел след редукция.

Разкрито е, че след предварителна редукция *in situ* при 400, 450, 530 и 600 °C, всички изследвани катализатори ефективно хидрогенират CO_2 при реакционни температури от 400 до 280 °C и обемни скорости между 3000 и 22000 $ч^{-1}$. И трите катализатора показват сравнима активност при по-ниски редукционни и реакционни температури поради образуването на лесно редуцируеми Ni^{2+}-O видове, които пораждат достатъчен брой от достъпни Ni^0 активни места на повърхността. Регистрирано е частично възстановяване на първоначалната слоиста структура в образците с по-високо съдържание на никел след приключване на каталитичният тест.

Предимството на катализатора с най-ниско съдържание на никел проличава при ниски редукционни и реакционни температури. Неговата производителност доминира след редукция при по-високи температури поради ролята на $NiAl_2O_4$ шпинело-подобна фаза да действа като „резервоар“, пораждащ нови количества метален никел. Понижаването на активността на останалите катализатори се приписва главно на синтерованието на металният никел.

Bulgarian Chemical Communications, Volume 45, Number 4 (pp. 625–630) 2013

Synthesis and characterization of ZnO and TiO_2 powders, nanowire ZnO and TiO_2/ZnO thin films for photocatalyc applications

L. K. Krasteva[1], K. I. Papazova[1], A. S. Bojinova[1]*,
N. V. Kaneva[1], A. A. Apostolov[2]

[1] *Laboratory of Nanoparticle Science and Technology, Department of General and Inorganic Chemistry, Faculty of Chemistry and Pharmacy, University of Sofia, 1 James Bourchier Blvd.,1164 Sofia, Bulgaria*
[2] *Laboratory on Structure and Properties of Polymers, Department on Applied Organic Chemistry, Faculty of Chemistry and Pharmacy, University of Sofia, 1 James Bourchier Blvd.,1164 Sofia, Bulgaria*

Received February, 2013; Revised May, 2013

The study concerns vertically well-aligned ZnO nanowires and TiO_2–ZnO films on Si substrates. They were prepared by a two-step chemical bath deposition (CBD) method, witch includes seed deposition and growth of ZnO nanowires. SEM and X-ray diffraction are used for the ZnO and TiO_2/ZnO thin films characterization. The film thickness is of 3–3.5 μm and the average diameter of ZnO nanowires is 100-150 nm, as determinated by SEM. Thus prepared films (pure ZnO nanowires and mixed with TiO_2 nanoparticles) are tested in comparison to TiO_2 and ZnO powder catalysts. TiO_2 doped ZnO nanowire films show a significant rise in the photocatalytic efficiency. The photocatalytic tests are performed in cylindrical glass reactors under UV and visible light irradiation. The effect is due to the successful separation of photogenerated charge carriers in the prepared TiO_2/ZnO photocatalytic film. The pollutants concentrations are 20 ppm Orange II for slurry and 10 ppm for film photocatalysis. The photodegradation of organic dye Orange II is observed spectrophotometrically.

Key words: ZnO nanowires, TiO_2, composite films, Orange II, photocatalysis.

INTRODUCTION

Nanomaterials are of tremendous interest due to their noticeable application in electronics, optics, and photonics. Nanomaterials are generaly classified into three groups: 0-dimensional, 1-dimensional, and 2-dimensional. Zero-dimensional nanostructures, referred to as quantum dots or nanoparticles with an aspect ratio near unity, have been extensively used in biological applications [1]. Two-dimensional nanomaterials, such as thin films, have also been widely used as optical coatings, corrosion protection, and semiconductor thin film devices. One-dimensional (1D) semiconductor nanostructures such as nanowires, nanorods (short nanowires), nanofibres, nanobelts, and nanotubes have been of intense interest in both academic research and industrial applications. This is due to their potential as building blocks for other structures [1]. 1D nanostructures are useful materials for investigating the dependence of electrical and thermal transport or mechanical properties on dimensionality and size reduction (or quantum confinement) [2]. They are also important because of their interconnections and functional units in the fabrication of electronic, optoelectronic, electrochemical, and electromechanical nanodevices [3]. In todays research zinc oxide (ZnO) nanowire is one of the most important among the one-dimensional (1D) nanostructures [4].

The band gap energy plays a significant role in the photocatalytic process. Figure 1 shows the band gap energies and the band edge positions of a common semiconductor photocatalysts [5–7]. It is important to have in mind that, the band gap values of ZnO, reported in the literature, are not all equivalent due to the different levels of the O vacancyes in ZnO [8]. ZnO has also been considered as a suitable alternative of TiO_2 because of its comparability with TiO_2 band gap energy and its relatively lower cost of production [9, 10].

ZnO is a semiconductor with a direct wide band gap energy (3.37 eV) and has a large exciton binding energy (60 meV) at room temperature [11]. TiO_2 has similar large band gap – 3.2 eV for anatase modification. It is most widely used photocatalyst since it is chemically stable, nontoxic and natural

* To whom all correspondence should be sent:
E-mail: nhasb@wmail.chem.uni-sofia.bg

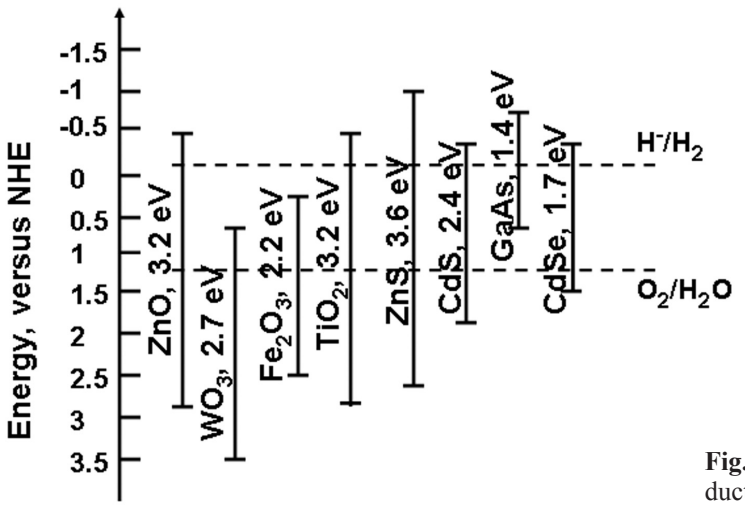

Fig. 1. Band edge positions of common semiconductor photocatalysts (data from [5–7])

material [12].The band gaps values of TiO_2 and ZnO show that near UV irradiation is needed for photo activation of both oxides.

Different authors apply various methods of modification like ball-milling [13], doping and co-doping [14, 15] to obtain efficient photocatalysis under visible light with ZnO and TiO_2. Composite materials are another approach to achieve this goal. There is a number of investigations reporting such effect, achieved by addition of variety of oxides such as SnO_2 [16, 17], SiO_2 [18], CeO_2 [19], ZnO [20–23], WO_3 [24] and ZrO_2 [25]. Application of supported bycomponent catalysts from two semiconductor oxides also alters the electronic properties, as compared to the initial material, in turn affecting charge photogeneration, charge separation and transfer, as found for ZnO overlayers on TiO_2 [26]. Other study reports about significant inhibition of the particle-to-particle electron transfer established for thin ZnO shell on a TiO_2 core [27].

To clarify this effect, ZnO films with TiO_2 overlayer have been studied. The new element here is investigation of the photocatalytic effect due to the combination of the two semiconductors, presented in different forms as nanowires and nanoparticles. This effect is checked in degradation of the commonly used organic dye Orange II in aqueous solution and compared using TiO_2 and ZnO nanowire film. The aim is to prepare and characterize ZnO nanowire film and TiO_2/ZnO photocatalyc film, suitable for application under illumination with UV and visible light irradiation.

EXPERIMENTAL

The reagents and materials used in the experiments were: Zn $(CH_3COO)_2.2H_2O$ and 2 methoxyethanol from Fluka, methenamine from Reidel de Haen, TiO_2 anatase and Orange II (λmax = 484 nm) from Sigma Aldrich. Si substrates (50×50×2 mm) from ISO-LAB (Germany) were used as supports for the films. The ZnO nanorods used in this investigation were grown on Si substrates by chemical bath deposition (CBD). It is a two step process, on a substrate treatment prior to the CBD growth. The first stage was ZnO seed deposition for next growth of nanowires. The pretreatment of the substrates is conducted by spin-coating (spin coater KW-4A, Chemat Technology Inc, 2200 rpm). A substrate with a solution of zinc acetate dihydrate ($Zn(C_2H_3O_2)_2 2H_2O$), dissolved in pure ethanol with a concentration of 5 mM, was used to control the diameter of ZnO nanorods. Then the seeded substrate was rinsed with distilled water, dried and annealed at 320 °C for 20 min. The next step was growth of ZnO nanowires on the as-prepared seeds. For this purpose the seeded substrates were kept for 3h placed in aqueous solutions of zinc nitrate hexahydrate [$Zn(NO_3)_2 6H_2O$, 99.9% purity grade] and methenamine ($C_6H_{12}N_4$, 99.9% purity grade) containing also methenamine (25 mM). After that the substrates were rinsed with distilled water and placed again in new precursor solution. In the CBD growth, the concentrations of both reagents were fixed at 0.1M. The pretreated Si substrates were immersed into the aqueous solution, and ZnO was grown at an constant temperature of 93 °C. This step was repeated 8 times and the final films were dried in air [28]. The mixed films were prepared by impregnation of the ZnO coating with TiO_2 suspension in ethanol in selected ZnO:TiO_2 ratio 3:1 (weight) [27].

The prepared ZnO and mixed films were characterized by X-ray analysis (diffractometer Siemens D 500, CuKα source radiation at a step of 0.05Θ for 2h and counting time 2 s/step) and scanning electron microscopy (SEM, JEOL JSM-5510).

The photocatalytic action of the films was examined in photoinitiated degradation of the organic dye Orange II in water solution (10 ppm, 150 ml) under UV (Sylvania 18 W BLB T8 lamp, emitting mainly in the range 315–400 nm) and visible (linear TUNGSRAM lamp 500 W K1R7 s, 9700 Lm) light irradiation. Three series of experiments were performed with the powder and with the film samples: under UV and visible light irradiation. Photocatalytic experiments with commercial and prepared by us powder samples were conducted prior testing of the films. The detailed procedure of photocatalytic experiments is described elsewhere [29, 30]. Spectrophotometer (Jenway 6400) determined the change in the dye concentration within the time of photocatalysis.

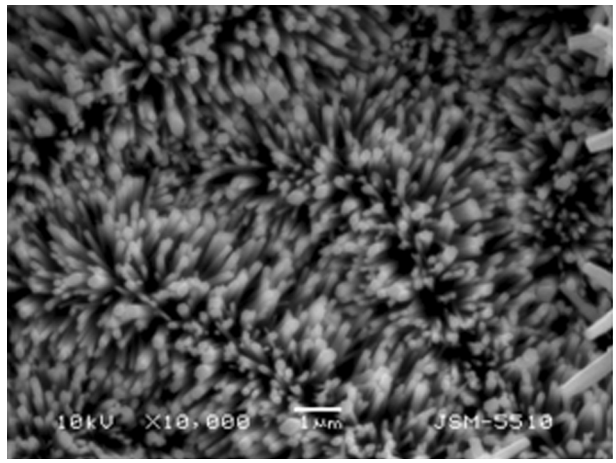

Fig. 2. SEM images of top view of the ZnO nanowires

RESULTS AND DISCUSSION

SEM analysis is used to study the morphology of as-prepared films. Figure 2 shows a schematic view of ZnO nanowires film produced by chemical bath deposition (CBD). The ZnO nanowires obtained are of hexagonal crystal structure. The SEM micrographs show uniform films of high density (3.1×10^9 numbers of nanowires per cm^{-2}). The ZnO nanowires grown on Si substrate are of approximately 3–3.5 μm length and 100-150 nm in diameter.

The microscopic observations of the ZnO nanowires and TiO_2 nanoparticles in the TiO_2/ZnO film on Si substrate are shown in Fig. 3.

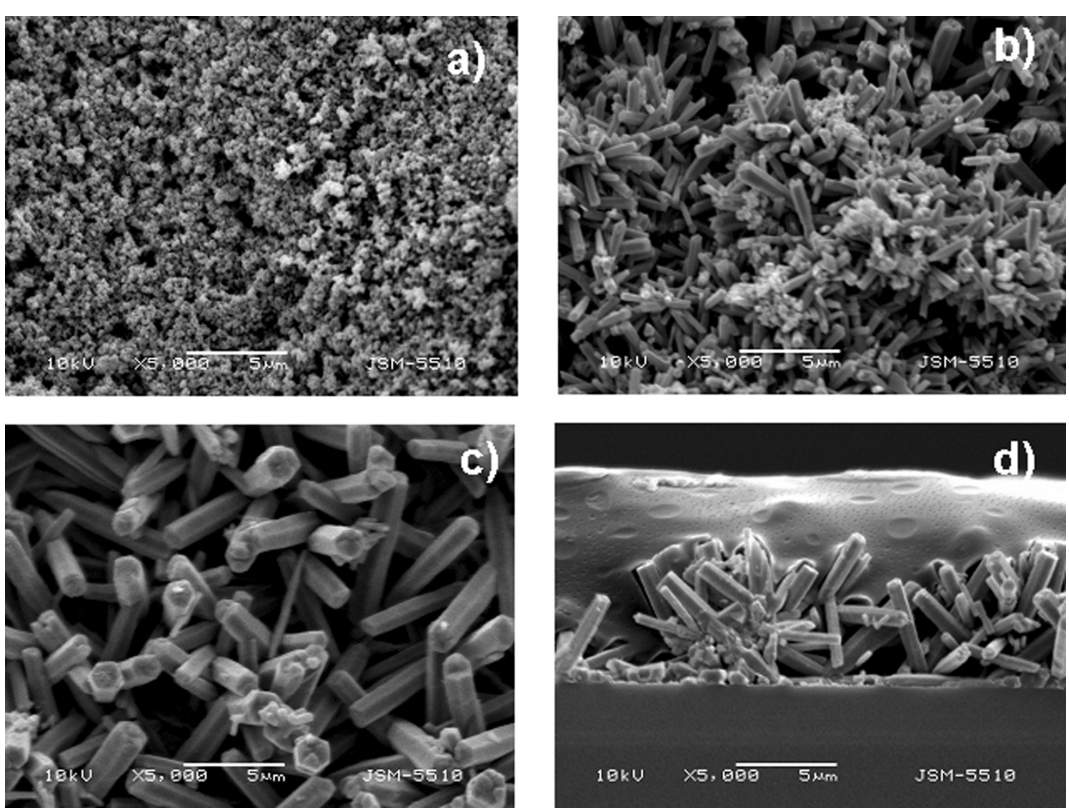

Fig. 3. SEM images of TiO_2/ZnO nanowire arrays: (a), (b), (c) TiO_2/ZnO arrays (top view) at different magnifications; (d) shows films cross section – TiO_2/ZnO nanowire array with TiO_2 nanoparticles film on the top

Figure 3 shows impregnated ZnO:TiO_2 of weight ratio 3:1. Samples are 100% crystalline. TiO_2 nanoparticles of about 0.05 μm average diameter can be clearly seen unevenly distributed between the ZnO nanowires along the entire films surface (Fig. 3a). The bottom layer of ZnO nanowires and upper layer of TiO_2/ZnO nanoparticles can be clearly seen in Fig. 3b and 3c. Figure 3d shows the composite films cross section.

Figure 4 represents XRD patterns of commercial TiO_2 anatase, ZnO powder from Aldrich and ZnO nanowire films.

It is clear from Fig. 4a that the nanowires can be classified as hexagonal wurtzite ZnO, and the dominating (002) peak at 34.4° indicates that the nanowire is well crystallized and grows in preferred orientation perpendicular to the substrate, which is in perfect agreement with the data from SEM observations. The XRD of mixed TiO_2/ZnO powder and nanosized film with pointed characteristic peaks of anatase and zinc oxide is presented in Fig. 4b. The intensities of the main peaks of ZnO differ from those of a mechanical mixture. After addition of TiO_2, the two ZnO peaks (100) and (002) are the strongest, indicating a slight change of the preferred orientation. The size of crystallites is calculated following Sherrers equation for ZnO from the (100) peak and for TiO_2 from the (101) peak (Fig. 4b) as they are relatively strong and single for the respective metal oxide. The crystallite size in direction perpendicular to the (101) plane remains the same (33.9 nm) as in the nanowire ZnO film, whereas the crystallite size in direction (100) changes from 33.0 before the preparation procedure to 35.9 nm after it.

The results from the photocatalytic experiments with commercial powders of TiO_2 and ZnO samples are shown in Table 1. The adsorption degree of Orange II onto different catalysts surface at 30th minute of contact without any illumination are also presented. Blank experiments with pure dye solutions, irradiated with the respective lamps (UV or visible), are performed prior the photocatalytic tests. No significant photobleaching of the pollutants solution is observed upon UV or visible light illumination, meaning that the direct dye photoly-

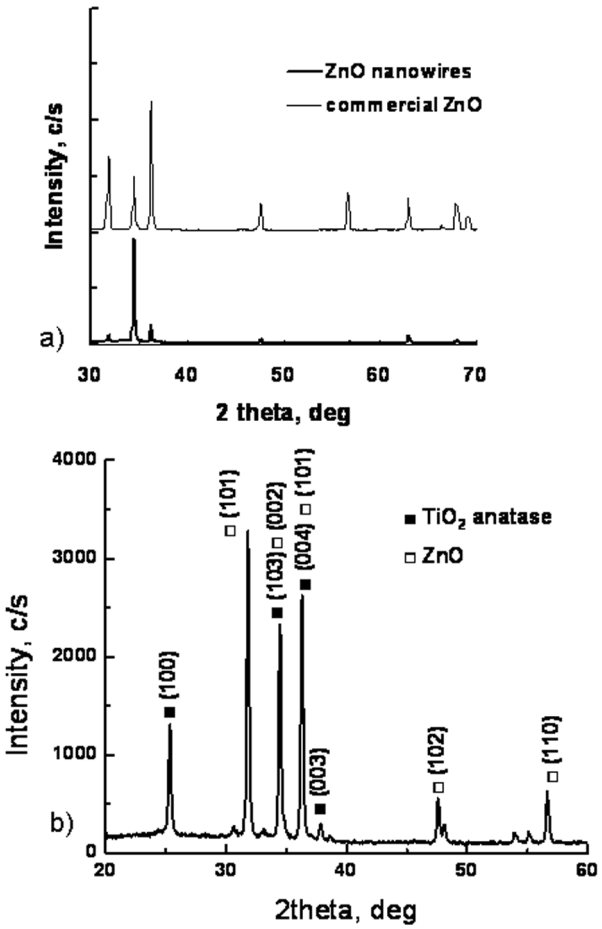

Fig. 4. Comparative XRD patterns of (a) commercial ZnO powder to nanowire ZnO film and (b) XRD pattern of mixed TiO_2/ZnO film of weight ratio 3:1

Table 1. Rate constants, adsorption and photodegradation degrees reached in the experiments with different photocatalytic samples. The duration of photocatalytic tests is 1 h for all powders (denoted as *) and 2.5 h for film samples (denoted as **)

Type of Illumination	Darkness (0.5 h)	UV		VIS	
Sample \ Quantity	Absorption, %	Degradation, %	Rate constant, min^{-1}	Degradation, %	Rate constant, min^{-1}
Orange II	0	0	–	0	–
ZnO powder*	5	98	0.157	21	0.028
TiO_2 powder*	2	100	0.162	2	–
ZnO nanowire film**	15	29	0.0015	35	0.0019
TiO_2/ZnO nanowire film**	20	53	0.0038	73	0.0058

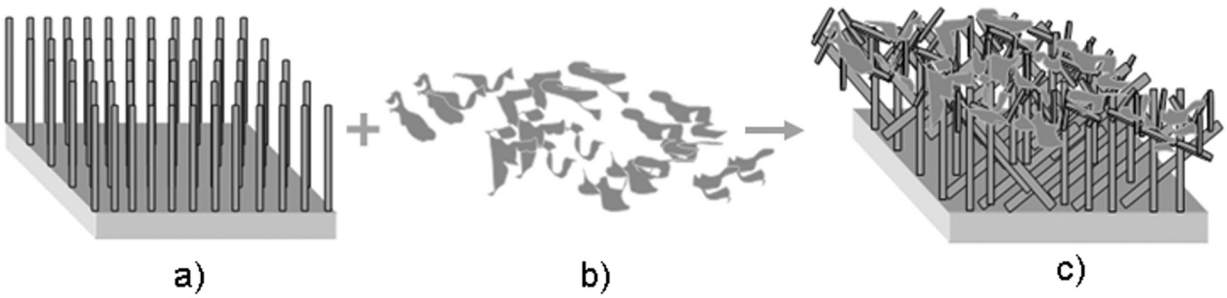

Fig. 5. Schematic illustration of (a) ZnO nanowires; (b) TiO_2 suspension in ethanol; (c) ZnO nanowires with TiO_2 nanoparticles

sis of is negligible at the particular experimental conditions.

As seen from the experimental data, both TiO_2 and ZnO successfully degrade Orange II under UV illumination approximately – the achieved after 1 h of photocatalysis dye degradation is 100% and 98% respectively. Zinc oxide has also photocatalytic activity under visible light irradiation (19% dye degradation at 1st h of illumination).

A comparison of the photocatalytic tests, conducted with prepared by us ZnO nanowire and mixed TiO_2/ZnO films is presented in Table 1. As seen from the Table, the ZnO films have not very high efficiency: 28% of Orange II degradation is reached for the UV and 35% for the visible light photocatalysis at 2.5 h of irradiation. The composite TiO_2/ZnO films express more efficient degradation of Orange II in aqueous solutions in both cases of UV or visible illumination. Highest degree of dye degradation for UV (53%) and for visible light (72%) irradiation, are achieved with the mixed TiO_2/ZnO photocatalytic films.

The observed higher rate of degradation with mixed TiO_2/ZnO than that with ZnO films is a complex result of at least two effects and can be explained by the change in the surface morphology as represented in the scheme of the mixed photocatalyst below (Fig. 5). As seen from the scheme, the addition of titania nanoparticles to the dense nanowire structure drastically increases the amount of illuminated catalysts surface and allows more efficient utilization of ZnO nanowires in the photocatalytic reaction. On another hand, the combination of two nanosized semiconductors with close band gaps (Fig. 1) in form of wires and particles increases the contact between TiO_2 and ZnO and favors effective charge separation of the photogenerated charge carriers under light excitation and therefore reduces the losses of recombination.

CONCLUSIONS

Nanowire TiO_2/ZnO films of 3–3.5 μm thickness are prepared on Si substrate. The zinc and titania oxides are present in the composite film as wurtzite and anatase respectively. The films exhibit a good homogeneity and nanocrystallinity as shown by SEM and XRD analysis. The average diameter of ZnO nanowires is 100–150 nm, as determined by SEM. The as-prepared films (pure and mixed with TiO_2) are tested in light induced degradation of the organic dye Orange II from water solutions. Significant rise in the photocatalytic efficiency is established with the composite TiO_2/ZnO nanowire film. The trend is confirmed under both sources of illumination – UV and visible light and is due to composites morphology and successful charge separation.

Acknowledgements: *This research is financially supported by FP7 project Beyond Everest.*

REFERENCES

1. B. Weintraub, Z. Zhou, Y. Li, Y. Deng, *Nanoscale*, **2** (9), 1573 (2010).
2. Y. Xia, P. Yang, Y. Sun, Y. Wu, B. Mayers, B. Gates, Y. Yin, F. Kim, H. Yan, *Advanced Materials*, **15** (5), 353 (2003).
3. G. C. Yi, C.Wang, W. I. Park, *Semiconductor Science and Technology*, **20**, S22 (2005).
4. Z. L. Wang, *Chinese Science Bulletin*, **54** (22), 4021 (2009).
5. S. Linic, P. Christopher, D. Ingram, *Nature Materials*, **10**, 911 (2011).
6. S. S. Srinivasan, J. Wade, E.K. Stefanakos, *Journal of Nanomaterials*, **2006**, Article ID 45712, (4 pages) (2006).
7. D. S. Bhatkhande, V. G. Pangarkar, A. C. M. Beenackers, *Journal of Chemical Technology and Biotechnology*, **77** (1), 102 (2002).

8. A. Alkauskas, A. Pasquarello, *Physical Review B*, **84**, Article ID 125206, (11 pages) (2011).
9. M. Ladanov, M. K. Ram, G. Matthews, A. Kumar, *Langmuir*, **27** (14), 9012 (2011).
10. D. M. Fouad, M. B. Mohamed, *Journal of Nanomaterials*, **2012**, Article ID 524123, (8 pages) (2012).
11. F. Lu, W. Cai, Y. Zhang, *Advanced Functional Materials*, **18** (7), 1047 (2008).
12. A. Fujishima, T. N. Rao, D. A. Tryk, *J. Photochem. Photobiol. C*, **1**, 1 (2000).
13. M. Uzunova-Buinova, D. Dimitrov, D. Radev, A. Bojinova, D. Todorovsky, *Mater. Chem. Phys*., **110** (2–3), 291 (2008).
14. O. Lorret, D. Francova, G. Waldner, N. Stelzer, *Appl. Cat. B*, **91**, 39 (2009).
15. B. Donkova, D. Dimitrov, M. Kostadinov, E. Mitkova, D. Mehandjiev, *Mater. Chem. Phys.*, **123**, 563 (2010).
16. Z. J. Li, B. Hou, Y. Xu, D. Wu, Y. H. Sun, *Journal of Colloid and Interface Science*, **288**, 149 (2005).
17. I. N. Martyanov, K. J. Klabunde, *Journal of Catalysis*, **225**, 408 (2004).
18. M. S. P. Francisco, V. R. Mastelaro, *Chemistry of Materials*, **14**, 2514 (2002).
19. J. J. Zou, B. Zhu, L. Wang, X. Zhang, Z. Mi, *Journal of Molecular Catalysis A* **286**, 63 (2008).
20. H. Y. Song, H. F. Jiang, X. Q. Liu, G.Y. Meng, *J. Photochem. Photobiol. A*, **181**, 421 (2006).
21. A. Shalaby, Y. Dimitriev, R. Iordanova, A. Bachvarova-Nedelcheva, Tz. Iliev, *Journal of the University of Chemical Technology and Metallurgy*, **46** (2), 137 (2011).
22. R. Iordanova, A. Bachvarova-Nedelcheva, Y. Dimitriev, Tz. Iliev, *Bulgarian Chemical Communications*, **43** (3), 378 (2011).
23. A. Stoyanova, Y. Dimitriev, A. Shalaby, A. Bachvarova-Nedelcheva, R. Iordanova, M. Sredkova, *Journal of Optoelectronic and Biomedical Materials*, **3**, (1), 24 (2011).
24. H. Y. Song, H. F. Jiang, X. Q. Liu, G. Y. Meng, *J. Photochem. Photobiol. A*, **181**, 421 (2006).
25. M. Hirano, C. Nakahara, K. Ota, O. Tanaike, M. Inagaki, *Journal of Solid State Chemistry*, **170**, 39 (2003).
26. D. Chen, H. Zhang, S. Hu, J. Li, *Journal of Physical Chemistry C*, **112**, 117 (2008).
27. T. V. Peshkova, K. I. Papazova, A. S. Bojinova, N. V. Kaneva, A. A. Apostolov, *Journal of Nanoscience and Nanotechnology* (2013) in press.
28. Q. X. Zhao, L. L. Yang, M. Willander, B. E. Sernelius, P. O. Holtz, *Journal of Applied Physics*, **104**, 073526 (2008).
29. A. Bojinova, R. Kralchevska, I. Poulios, C. Dushkin, *Mater. Chem. Phys*., **106**, 187 (2007).
30. A. Bojinova, C. Dushkin, *Reac. Kinet. Mech. Cat*., **103**, 239 (2011).

СИНТЕЗ И ХАРАКТЕРИЗИРАНЕ НА ПРАХОВЕ ОТ ZnO И TiO_2, ТЪНКИ ФИЛМИ ОТ ZnO НАНОЖИЧКИ И TiO_2/ZnO ЗА ФОТОКАТАЛИТИЧНИ ПРИЛОЖЕНИЯ

Л. К. Кръстева[1], К. И. Папазова[1], А. С. Божинова[1]*,
Н. В. Кънева[1], А. А. Апостолов[2]

[1] Лаборатория по наука и технология на наночастици, катедра Обща и неорганична химия, Факултет по Химия и Фармация, Софийски университет, София 1164, България
[2] Лаборатория по структура и свойства на полимери, катедра Приложна органична химия, Факултет по Химия и Фармация, Софийски университет, София 1164, България

Постъпила февруари, 2013 г.; приета май, 2013 г.

(Резюме)

Обект на настоящата работа са филми от вертикално подредени ZnO наножички върху Si подложка, както и такива дотирани с TiO_2. Изследваните образци са получени по метода на химично отлагане чрез двуетапна процедура, включваща зародишообразуване и последващ кристален растеж на наножичките от ZnO. Тънките филми от ZnO и TiO_2/ZnO са характеризирани със сканираща електронна микроскопия (СЕМ) и рентгенова дифракция. Определената със СЕМ дебелина на филма е 3–3.5 μm, а средният диаметър на наножичките от ZnO е 100–150 nm. Получените от нас филми (от чисти ZnO наножички и дотирани с наночастици TiO_2) са изпитани за фотокатализа и действието им е сравнено с това на каталитични прахове от TiO_2 и ZnO. Фотокаталитичните експерименти са проведени в цилиндричен стъклен реактор при облъчване с УВ или видима светлина. Изходната концентрация на замърсителя Оранжево II е 20 ppm за суспензия и 10 ppm за фотокатализа с филми. Фоторазграждането на багрилото е проследено спектрофотометрично. Дотираните с TiO_2 филми от ZnO наножички показват значително повишена фотокаталитична ефективност. Наблюдаваният ефект се дължи на успешно реализирано разделение на фотогенерираните заряди в синтезираните TiO_2/ZnO филми.

Bulgarian Chemical Communications, Volume 45, Number 4 (pp. 631–634) 2013

The behaviour of osmium ions in the tetrahedral oxygen coordination

P. Petkova*, P. Vasilev, I. Dimitrov

Shumen University "Konstantin Preslavsky", 115 Universitetska street, 9712 Shumen, Bulgaria

Received February, 2013; Revised May, 2013

In this work, the absorption spectrum of $Bi_{12}SiO_{20}$:Os is investigated. The crystal changes its state from the untreated to the illuminated. The experiment is conducted at the room temperature in the spectral region 1.6–2.2 eV. The energetic diagram of the electron transitions in Os^{5+} is presented. The Schrödinger equation is solved for the Os^{5+} ions which are chemically bonded with the oxygen ions.

Key words: Schrödinger equation, doped sillenites, transition metal ions.

INTRODUCTION

The sillenite-type $Bi_{12}SiO_{20}$ (BSO) crystals display optical activity and a strong photochromic effect. They are applied in dynamic holography, optical information processing, optical phase conjugation and real-time interferometry [1, 2]. This is the reason for the investigation of their optical properties. The determination of the valence and the local symmetry of the involved dopants in the crystal structure is very important for the optimization of the synthesis conditions of these materials. That is why the aim of the present work is to present the energy level diagram of Os^{5+} in BSO:Os.

EXPERIMENTAL

The crystals were prepared from a stoichiometric solution using the Czochralski method. The purity of the starting oxides used was 99.9999% for Bi_2O_3 and SiO_2. The structure of the sillenite is the final result from Si^{4+} tetrahedrons and Bi^{3+} octahedrons. The dopant was placed in the melt solution in the form of the oxide OsO_4.The concentration of the ruthenium ions in the crystal lattice was Os – 6.33×10^{20} cm^{-3}. The maximum ruthenium concentration in the melt was established by several experiments which determined the optically homogeneous doped crystals without other phase inclusions. The diameter of the synthesized crystals was 30–45 mm and their lenght was 70–100 mm. The experimental set up for the measurement of the absorption coefficient in the visible region consisted of the following: a halogen lamp with a stabilized 3H-7 rectifier, a SPM-2 monochromator, a system of quartz lenses, a polarizer, a crystal sample holder, and a Hamamatsu S2281-01 detector. The investigation was carried out with an untreated sample that has been illuminated with UV light for 30 min.

RESULTS AND DISCUSSION

The absorption coefficient of the investigated samples has been measured to be between 564 and 775 nm (Figs.1a and 2a). The first derivative of the absorption coefficient at photon energy is calculated to be in the 564–775 nm spectral region. The $[d\alpha/d(h\nu)]$ determines only the number of electron transitions in a Os^{5+} ions and it does not give an exact information about the energy position of these transitions (Figs.1b and 2b). This is the reason for the calculation of the second derivative of the absorption coefficient $[d^2\alpha/d(h\nu)^2]$ (Figs.1c and 2c). The absorption coefficient is calculated using the formula: (1) $\alpha = (1/d)\ln(I_0/I)$,where I_0 is the intensity of the incident light, I is the intensity of the passing light and d is the sample thickness. The components of the Os^{5+} structure that are connected with the electron transitions are $^4T_{1g}(^4F) \rightarrow {}^4T_{2g}(^4F)$ (Fig. 3). Our assumption is that Os^{5+} replaces Si^{4+} in the silicon tetrahedrons. The ionic radius of Os^{5+} ion is 0.575 Å and the ionic radius of Si^{4+} ion is 0.40 Å. Thus the oxygen tetrahedrons are shortened along z axis and Jahn-Teller effect is bigger than the

* To whom all correspondence should be sent:
E-mail: Petya232@abv.bg

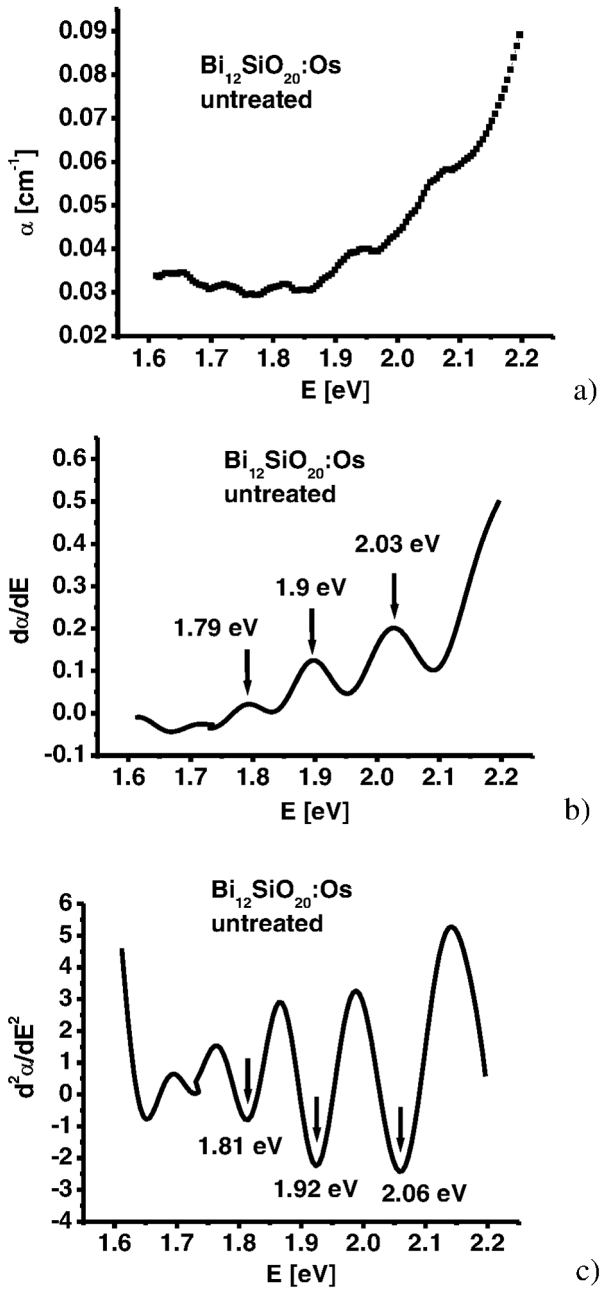

Fig. 1. a) The absorption coefficient α(E), b) first derivative dα/dE and c) second derivative $d^2\alpha/dE^2$ for the untreated $Bi_{12}SiO_{20}$:Os

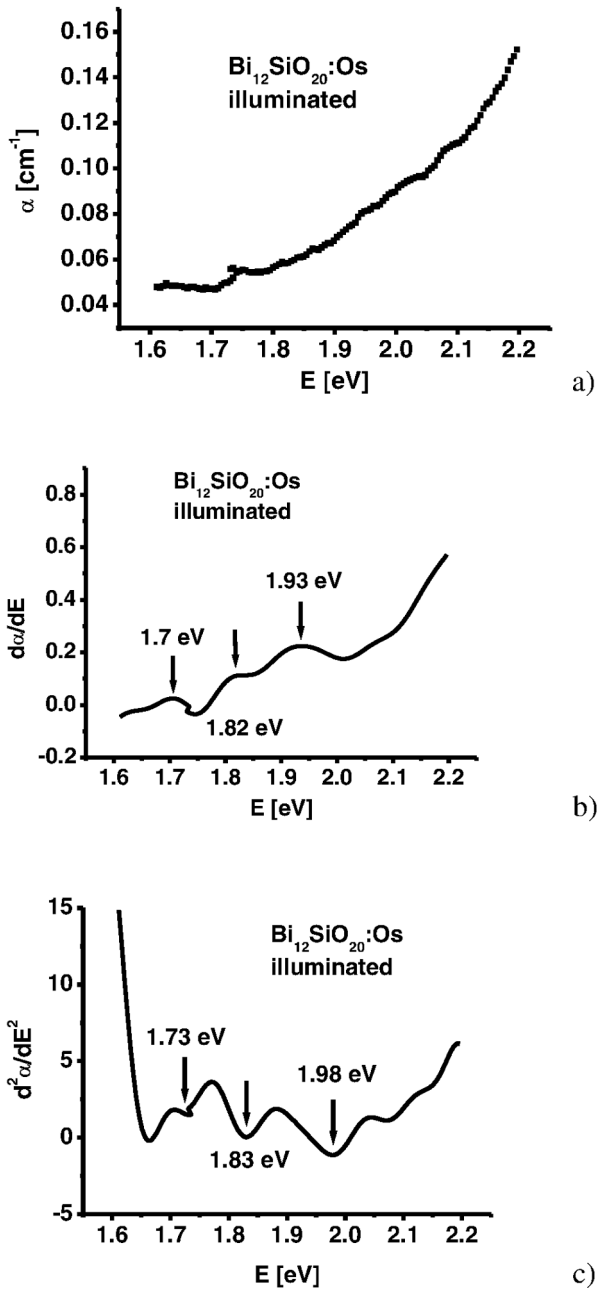

Fig. 2. a) The absorption coefficient α(E), b) first derivative dα/dE and c) second derivative $d^2\alpha/dE^2$ for the illuminated $Bi_{12}SiO_{20}$:Os

spin-orbit interaction there. If the Os^{5+} ion is caught by a one-dimensional hole than its potential can be described as: 1) V = 0, a≤x≤b (a, b are the borders of the hole) and 2) V = ∞ in the other cases. In the first case the Schrödinger equation has the following form: (2) $E\psi(x) = -(\hbar^2/2m)*(d^2\psi/dx^2)$ [3]. If $k = (2mE)/\hbar^2$ after some transformations we will find that (3) $(d^2\psi/dx^2) + k^2\psi = 0$. The solution of the last equation is (4) ψ(x) = Asin(kx) + Bcos(kx). The constants A and B are determined by normalizing the wavefunction i.e.

$$\int_{-\infty}^{+\infty} |\psi(x)|^2 dx = 1.$$

In our situation $A = \sqrt{(2/a)}$ and $B = \sqrt{(2/b)}$. When ψ(a) = 0 than ka = nπ and kb = (2n+1)π. Thus k = [(n+1)π]/(b–a), n = 1, 2, … Therefore the final

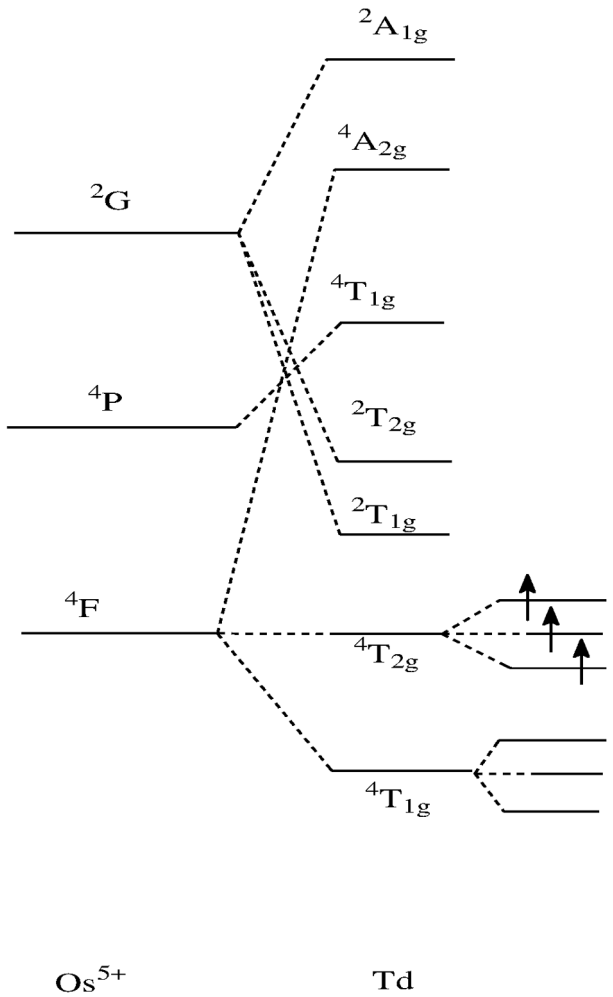

Fig. 3. The energetic diagram of Os^{5+} ion in the tetrahedral symmetry

form of the solution (4) is $\psi(x) = A\sin\{[(n+1)\pi]/(b-a)\} + B\cos\{[(n+1)\pi]/(b-a)\}$. When the Os^{5+} ion is caught by a one-dimensional hole than its wavefunction is $\psi(x) = 0.0592*\sin\{[(2+1)\pi]/(775-564)\} + 0.51*\cos\{[(n+1)\pi]/(b-a)\}$ or in the end $\psi(x) = 0.0592*\sin(0.0446x) + 0.51*\cos(0.0446x)$. This is the way to calculate $\psi(x)$ at each minimum on the Figs. 1c and 2c. The values of the wavefunction are respectively $\psi_3(2.06) = 0.4817$; $\psi_2(1.92) = 0.4754$; $\psi_1(1.81) = 0.4693$ for the untreated BSO:Os and $\psi_3(1.98) = 0.4783$; $\psi_2(1.83) = 0.4704$; $\psi_1(1.73) = 0.464$ for the illuminated doped sample. The energy of the basic state of Os^{5+} ion is $E_1 = (\pi^2*\hbar^2)/[2m(b-a)^2]$ and the energy of the first excited state is $E_2 = [2^2*(\pi^2*\hbar^2)]/[2m(b-a)^2]$. The difference between these two energies is $\Delta E = 8.7$ cm^{-1}. The distance between the energy levels $^4T_{1g}(^4F)$ and $^4T_{2g}(^4F)$ is the same (Fig. 3).

CONCLUSIONS

The illumination with UV light leads to the shifting of the energy position of the electron transitions to the bigger wavelengths.

Jahn-Teller effect is bigger than the spin-orbit interaction in the oxygen tetrahedrons.

The Schrödinger equation is solved in the spectral region of the osmium absorption structure.

The values of $\psi(x)$ decrease with the increasing of the wavelength in the spectral region of the Os^{5+} structure.

Acknowledgments: *Partial financial support by project of Shumen University (2012) is gratefully acknowledged.*

REFERENCES

1. G. Raciukaitis, V. Gavryushin, V. Kubertavicius, G. Puzonas, *Jpn. J. Appl. Phys.*, **32**, 645 (1993).
2. V. Marinova, M. Veleva, D. Petrova, I. M. Kourmoulis, D. G. Papazoglou, A. G. Apostolidis, E. D. Vanidhis, N. C. Deliolanis, *Journal of Applied Physics*, **89**, 2686 (2001).
3. D. McMahon, Quantum Mechanics, "McGraw-Hill", New York, 2005.

ПОВЕДЕНИЕ НА ОСМИЕВИ ЙОНИ В ТЕТРАЕДРИЧНО КИСЛОРОДНО ОБКРЪЖЕНИЕ

П. Петкова*, П. Василев, И. Димитров

Шуменски университет „Епископ Константин Преславски“,
ул. „Университетска“ №115, 9712 Шумен, България

Постъпила февруари, 2013 г.; приета май, 2013 г.

(Резюме)

В тази работа е изследван спектъра на поглъщане на $Bi_{12}SiO_{20}$:Os. Състоянието на кристала се променя от нетретирано в осветено. Експериментът е проведен при стайна температура в спектралната област 1.6–2.2 eV. Представена е енергетичната диаграма на електронните преходи в Os^{5+}. Решено е уравнението на Шрьодингер за йоните Os^{5+}, които са химически свързани с обкръжаващите ги кислородни йони. Облъчването с ултравиолетова светлина води до отместване на енергетичното положение на преходите на електроните към по-големите дължини на вълната. Ефектът на Ян-Телер е по-голям в сравнение със спин-орбиталното взаимодействие в кислородните тетраедри. Стойностите на $\psi(x)$ намаляват с нарастване на дължината на вълната в спектралната област на абсорбционната структура на Os^{5+}.

Bulgarian Chemical Communications, Volume 45, Number 4 (pp. 635–643) 2013

Surface and photocatalytic properties of nanostructured ZnO thin films doped with iron

N. Kaneva[1], A. Ponomareva[2], L. Krasteva[1], D. Dimitrov[1], A. Bojinova[1]*, K. Papazova[1], G. Suchaneck[2], V. Moshnikov[3, 4]

[1] *Laboratory of Nanoparticle Science and Technology, Department of General and Inorganic Chemistry, Faculty of Chemistry and Pharmacy, University of Sofia, Sofia 1164, Bulgaria*
[2] *Solid State Electronics Laboratory, TU Dresden, Dresden 01062, Germany*
[3] *Micro- and Nanoelectronics Department, Saint-Petersburg State Electrotechnical University (LETI), Saint-Petersburg 197376, Russia*
[4] *Department of Integrated Electronics, Saint-Petersburg State Polytechnical University, Saint-Petersburg 195251, Russia*

Received February, 2013; Revised May, 2013

In this work, we investigate nanosized Fe-ZnO thin films, deposited on glass substrates by sol-gel method and dip-coating technique. The precursor sol is prepared by dissolving of $Zn(CH_3COO)_2.2H_2O$ and $Fe(NO_3)_3.9H_2O$ in 2-methoxyethanol with addition of monoethanolamine as surfactant. The Fe content in the ZnO thin films is selected to be 0.25, 0.5 and 1 wt.%. Thin nanostructured films with two different coatings structures are prepared for the photocatalytic tests. The first one is formed by deposition of Fe-doped layer by 5 dip-coating cycles on standard microscopic glass slides. The second type of hierarchically structured films is deposited onto glass substrates by two – step procedure. The photocatalytic efficiency of the prepared films is tested using a textile dye, Reactive Black 5 (RB5) in aqueous solutions at different initial dye concentration, under UV or visible light irradiation. The dependence of photocatalytic activity on the (i) Fe content, (ii) presence or absence of ZnO sublayer under Fe doped layer, (iii) frequency of irradiation and (iv) initial concentration of dye are investigated. For explanation of the observed results a comprehensive AFM investigation including fractal analysis of surface topography is performed. The relationship between the observed photocatalytic behavior of the film samples and the obtained by AFM surface features is discussed.

Key words: ZnO:Fe thin films, sol gel, photocatalysis, Reactive Black 5, UV and visible light.

INTRODUCTION

In the last decades, a large number of research groups worldwide focused their attention on investigations on the use of sunlight, (5–7% UV, 46% visible and 47% infrared radiation) as a beneficial natural energy source for photocatalytic applications [1, 2]. Nowadays, there is a large problem in water purification from harmful pollutants (such as dyes, drugs, hormones, heavy metals traces) in low concentrations. The most widely used photocatalyst TiO_2, has a relatively large band gap (for anatase modification E_g=3.2 eV) and is low a cost, natural, chemically stable and nontoxic material [3]. Zinc oxide has similar band gap (E_g=3.2 eV) and is favored is favored in comparison to TiO_2, in some applications due to its higher quantum efficiency [4–6]. However, the band gap of the above mentioned semiconductors require near UV irradiation for their photoactivation. Therefore, different methods have been used to achieve an efficient visible light photocatalysis by these oxides, such as doping and co-doping with nonmetals [7–9] and transition metals [10, 11], surface modification [12, 13] and composite materials [14–16]. However, no matter of its unique optical [17–20], magnetic [21, 22], electrical [23] and gas-sensing properties [24–27], only few investigations have reported on the photocatalytic photodegradation of organic contaminants with Fe-doped ZnO [28, 29].

There are a large number of commonly used dyes available at the market. Between them, the most used are reactive azo dyes. Additionally, these dyes are the most problematic pollutants in textile waste-

* To whom all correspondence should be sent:
E-mail: nhasb@wmail.chem.uni-sofia.bg

waters. The reason is that after the reactive dyeing process is finished, more than 15% of the textile dyes is lost in wastewaters during dyeing operation [30]. So, in this work, we have selected Reactive Black 5 dye (RB5), one of the most used reactive dyes for textile finishing, as representative azo dye pollutant for contaminated wastewaters from textile manufacturing.

Textile wastewaters are large problem for conventional treatment plants in the entire world. The release of these wastewaters into enviroment is harmful to aquatic life and mutagenic to human beings. The removal of organic pollutants from wastewater by heterogeneous photocatalysis is an important method in environmental protection. As a well-known photocatalyst, much attention has been paid to ability of ZnO in degradation and complete mineralization of dyes and other environmental pollutants.

In this study we present for the first time nanosized hierarchical Fe-ZnO (Fe-content 0.25, 0.5 and 1 wt.%) thin photocatalytic films, deposited on glass substrates via sol-gel method and dip-coating technique. The aim of this research is to investigate and establish the dependence of photocatalytic activity on the: (i) Fe content; (ii) existence or absence of ZnO sublayer under Fe doped layer; (iii) frequency of irradiation and (iv) initial concentration of dye.

EXPERIMENTAL

Materials and reagents

The following materials were used to manufacture ZnO thin films: zinc acetate dehydrate, $Zn(CH_3COO)_2.H_2O$, (≥99.5%), 2-methoxyethanol (≥99.5%), monoethanolamine (≥99.0%) and iron nitrate hydrate, $Fe(NO_3)_3.9H_2O$, (≥99.0%) from Fluka. The glass slides (ca. 76×26 mm) for substrates of ZnO films were from ISO-LAB (Germany). Reactive Black 5 ($C_{26}H_{21}N_5Na_4O_{19}S_6$, λ_{max}=595 nm, dye content ca. 55%) was from Sigma-Aldrich. Distilled water was used in the preparation of dye solutions.

ZnO and ZnO:Fe synthesis

Zinc oxide thin films with different concentrations of Fe^{3+} doping (0.25, 0.5 and 1 wt.%) were deposited on glass substrate by sol–gel method. The precursor sol is obtained using zinc acetate dihydrate, 2-methoxyethanol and monoethanolamine. As starting materials, zinc acetate dihydrate [$Zn(CH_3COO)_2.2H_2O$] and iron nitrate hydrate [$Fe(NO_3)_3.9H_2O$] were dissolved in 2-methoxyethanol. Then, sol stabilizer, monoethanolamine (MEA) equimolar to the [Zn^{2+} + Fe^{3+}], was added to the above solution. The substances were mixed together in a round-bottom flask and stirred at room temperature for 15 min. The obtained clear solution was heated up at 60 °C upon magnetic stirring for 60 min and let to age overnight. The resultant solution was clear and homogenous to serve as the coating substance for films. No visible changes were observed in the sol upon standing of the precursor at room temperature for at least 2 months.

Preparation of the coating solution

The dip coating is a simple and cheap technique for deposition of thin oxide films. The deposition of a layer of oxide material can be optimized by controlling precisely the immersion and withdrawal speed, number of dipping cycles and solution viscosity for the purpose of deposition of a layer of oxide material.

The ZnO films were prepared by dip coating, drying and sintering of the material. Glass surfaces (5×5 cm) were coated with the coating solution by means of dip coating apparatus and withdrawing it at rates of 0.9 cm/min at room temperature deposited the gel films. It was found that higher withdrawal rates result in films of lower quality. The films were dried for 15 min at 80 °C in air after each successive coating. The as-prepared gel films were annealed at 500 °C for 60 min in order to obtain the final ZnO films.

Thin nanostructured films with two different coatings configurations were prepared for the photocatalytic tests. The first one was formed by deposition of the Fe doped layer by 5 dip-coating cycles onto standard microscopic glass slides. For producing of the second configuration, the glass slides are covered firstly with a pure ZnO layer formed by 2 dip-coatings, prior the deposition of doped with Fe ZnO layer produced by 3 dip-coating cycles. The final iron doped films had slight orange-brownish coloration, typical for the formation of Fe_2O_3, as expected at the particular experimental conditions, applied for films preparation.

Characterization of the films

The as-obtained at different annealing temperatures ZnO thin films were analyzed by scanning electron microscope (SEM) JSM-5510 (JEOL), operated at 10 kV of acceleration voltage. Before imaging, the investigated samples were coated with gold by JFC-1200 fine coater (JEOL). The surface morphology of ZnO films (pure and doped with iron) was additionally examined by atomic force microscopy (AFM) using an INTEGRA Therma scanning probe microscope (NT-MDT, Zelenograd,

Russia). Tapping mode imaging was performed in air using silicon cantilevers (Type NSG01, NDT-MDT, Zelenograd, Russia). In this work, fractal dimension analysis was performed by means of the Open Source Software Gwyddion 2.21 [31] using two different approaches: the cube counting method and the triangulation method [32]. The crystalline phase identification and unit cell parameters evaluation was performed by X-Ray diffraction analysis using Siemens D 500 diffractometer (CuKα source of radiation at a step of 0.05 deg for 2Θ and counting time 2s/step).

Photocatalytic degradation tests

The photocatalytic performance of the films was examined using the degradation of Reactive Black 5 dye in aqueous solution. Nanostructured films with two different configurations of the coating structures were studied and compared for decolorization of textile dye (initial concentration was 3, 5 or 10 ppm).

The measurement was conducted in cylindrical glass vessel of 150 ml volume, equipped with a magnetic stirrer and UV-lamp above (maximum emission at 370 nm). The light power density at the sample position was 0.66 mW/cm^2. The light irradiation was measured with research radiometer of Ealing Electro-optics, Inc. The lamp was fixed at ~15cm above the treated solution. The decolorization process of RB5 was monitored by UV-Vis absorbance spectroscopy after aliquot sampling at regular time intervals. Each aliquot sample was returned back to the reaction vessel immediately after the spectrophotometrical measurement. All photocatalytic tests were performed at a constant stirring rate (500 rpm) and room temperature (23±2 °C). The effect of initial concentration of RB5 (3, 5 and 10 ppm) on the photocatalytic performance of the films was also investigated. In all experiments the optical absorbance spectra were measured by spectrophotometer Jenway 6400 in the wavelength range from 400 to 800 nm. Control experiments without any illumination (the reaction system was kept in darkness) were also performed. The decolorization rate of RB5 is followed with time spectrophotometrically at a wavelength of 595 nm (the wavelength of maximum absorbance).

The degradation degree of Reactive Black 5 (%) was calculated as:

$$D\% = \frac{C_0 - Ci}{C_0} x100 \qquad (1)$$

Here C_0 is the initial concentration of dye and C_i is the concentration of the dye after irradiation at selected time interval t_i.

To investigate the photoinstability of pure and doped ZnO films, produced in the current work, some of the photocatalytic experiments were repeated three times, using a new dye solution with the same initial concentration in each measurement. All the results were reproducible. The absence of photocorrosion was also checked by Scanning Electron Microscopy after finishing of all the three photocatalytic experiments of the samples. No changes of the ganglia-like hills and wrinkled morphology of the films was observed, which make us to conclude that this kind of structure may increase somehow photostability of the films and this is the subject of our future investigations.

RESULTS AND DISCUSSION

Structure characterization

Recent review [33] summarizes the main chemical routes used in the sol–gel synthesis of ZnO thin coatings and highlights the chemical and physical parameters (precursors nature and concentration, type of additive, coatings method, pre- and post-heat treatment) influencing films structural properties. SEM images of the films, prepared by first method were investigated in order to show how their surface morphology influences the photocatalytic properties (Fig. 1). The morphology is homogenous with the ganglia-like hills of a width 0.5–1 μm, length ~5 μm and height about 1μm (Fig. 1a). The Fe-doped ZnO films express similar morphology, as seen from the surface micrographs of samples with 0.25–1 wt.% Fe^{3+} (Fig. 1b and 1c). In the case of Fe-containing films, the ganglia are of a typical width 0.1–0.5 μm, length from 1 μm to 5 μm and height of about 2.5–3 μm. The increase of Fe^{3+} content leads to decrease of the volume and size of ganglia-like hills, which look more distorted and branched at their ends. The ganglia-like hills are smaller and the morphology is not homogenous.

Fig. 2 shows the AFM-images of the samples recorded in tapping mode. It is well known that AFM provides already a digitized image suitable for numerical evaluation. Surface texture is characterized by the height of its peaks, the depths of its valleys and the distances that separate them. Surface topography is usually described in terms of surface roughness. Sometimes the root mean square roughness (RMS) is associated to grain size of film. However, surface roughness is solely a function of height, that is, information about lateral topography is lost. The calculation of the fractal dimension gives a more general description than the RMS surface roughness alone.

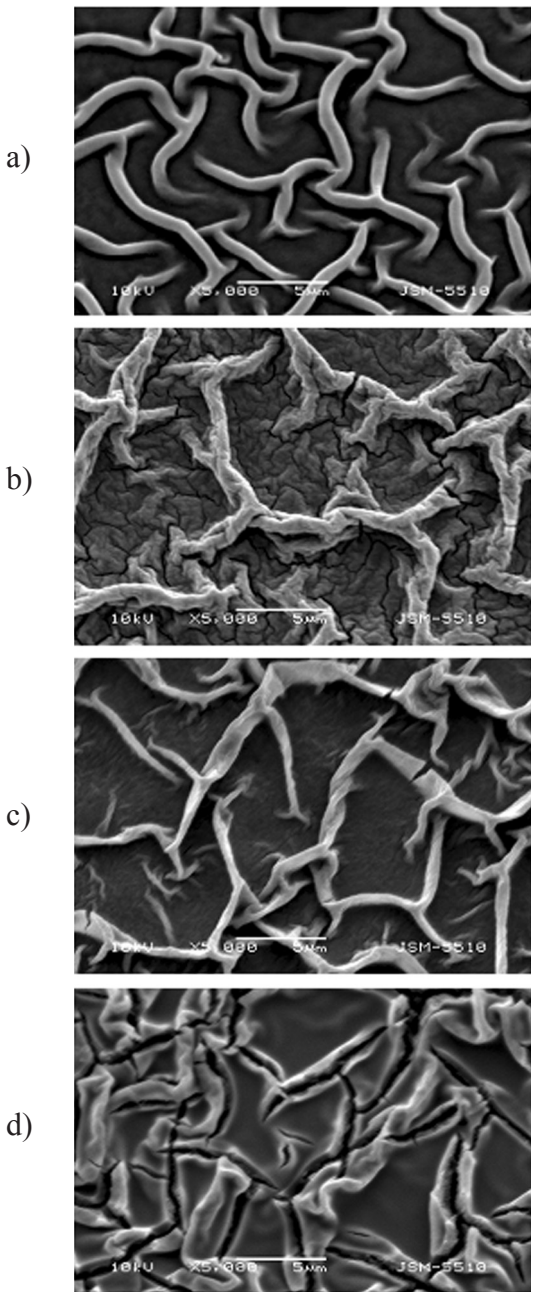

Fig. 1. SEM images of ZnO films prepared by first method at different concentrations of Fe^{3+} doping: (a) 0%; (b) 0.25%; (c) 0.5% and (d) 1%

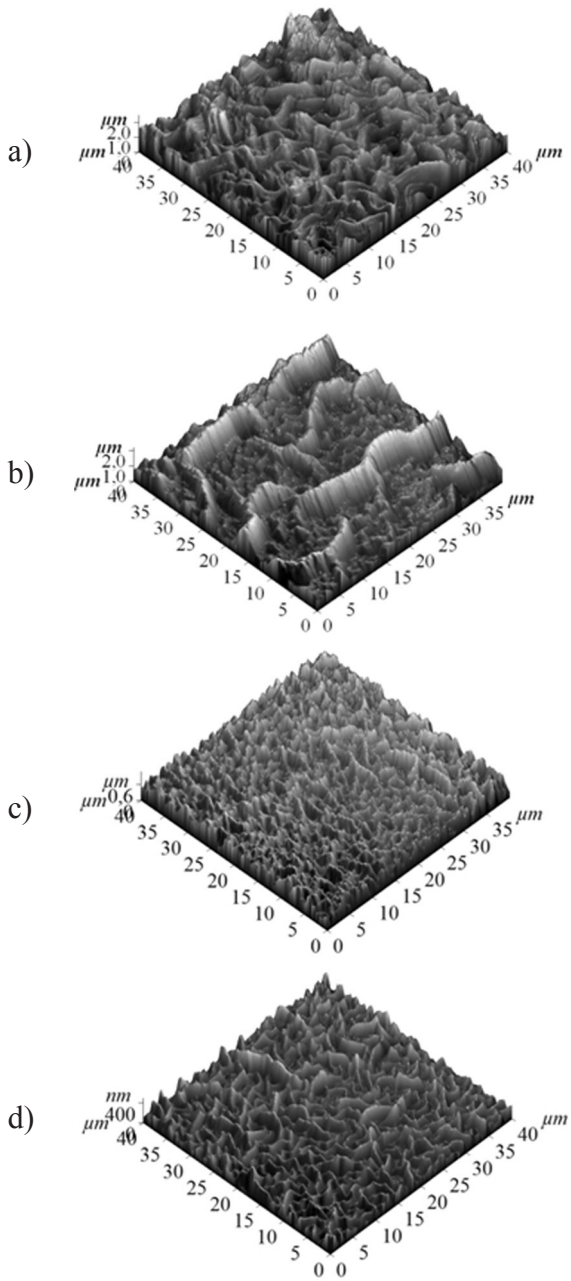

Fig. 2. AFM images of ZnO doped with Fe^{3+}: (a) 0%, (b) 0.25 wt%, (c) 0.5 wt% and (d) 1 wt%

A fractal is a set for which the so called fractal dimension D_f always exceeds the topological dimension, but it is smaller than Euclidian dimension of the space where the fractal is embedded. Fractal dimension of a line in two-dimensional space characterizes the ratio of the change in detail to the change in scale of a fractal pattern [32].

$$D_f = \lim_{\varepsilon \to 0} \frac{\lg N}{\lg(1/\varepsilon)} \tag{2}$$

where N is the number of sticks measured using the scaling factor ε. Surfaces in three-dimensional spaces are approximated using scaled cubes or tri-

Table 1. Fractal dimensions and the roughness characteristics of ZnO nanocomposites in dependence on iron doping concentration

Composition	*Ra*, μm	*RMS*, μm	D_f
Pure ZnO	0.412	0.513	2.47
ZnO+0.25 wt% Fe	0.293	0.373	2.43
ZnO+0.5 wt% Fe	0.250	0.306	2.41
ZnO+1 wt% Fe	0.159	0.190	2.37

angles. In case of film growth on a two-dimensional substrate, the fractal dimension lies within the range $2 \leq D_f \leq 3$, where a flat surface has a value $D_f = 2$ and an increasing value of D_f represents an increasing surface roughness [32]. An advantage of AFM images is that they are already digitized as required for numerical evaluation of fractal dimension. Here, the scaling factors range from pixel size to half of the scan length of the image.

Fractal analysis of AFM-images allows detecting surfaces local fractal dimensions. Due to a self-affine surface (self-affinity refers to a fractal whose units are scaled by different amounts in the x- and y-directions), a local fractal dimension appears which characterizes the increase in surface size compared to a smooth surface.

The surface topography plays a crucial role in predicting catalytic properties [32]. Obviously, the larger surface area and roughness provide greater number of activation centers which can fit on it. Therefore the higher value of fractal dimension can indicate higher catalytic activity. Both the cube counting and triangulation methods of fractal analysis [31, 32] gave similar values. All roughness characteristics the arithmetic average roughness (*Ra*), the root mean square roughness (RMS) and the fractal dimension (D_f) are significantly affected by Fe^{3+} fraction. These parameters decrease with the increasing of iron content (Table 1). The decrease of fractal dimension with increasing of Fe^{3+} content is correlated with results of photocatalytic activity investigation, as described below.

The XRD spectrum (Fig. 3) of the clear ZnO thin film consists of well-defined diffraction peaks showing good crystallinity. The (100), (002), (101) diffraction peaks of the sol-gel films appear clearly at the annealing temperature, which can be attributed to the hexagonal wurtzite structure of ZnO. The thin films consist in this case of polycrystalline grains with no preferential growth observed. The calculated by Scherer crystallite size is 30 nm. Nanostructure doped films contains a small amount of iron (0.25, 0.5 and 1 wt.%), which is not captured by the X-ray diffraction.

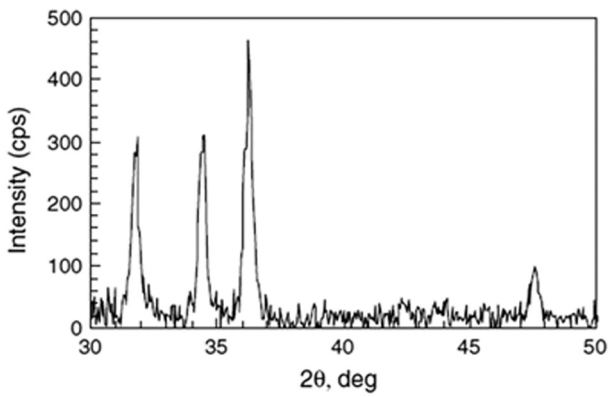

Fig. 3. XRD spectra of clear ZnO films annealed for 1 h at 500 °C.

Photocatalytic activity

In this work we photodegrade the dye Reactive Black 5 (RB5), one of the most used reactive dyes for textile finishing, as a representative dye pollutant for industrial wastewaters. The bleaching rate of RB5 is followed with time spectrophotometrically at a wavelength of 595 nm (the wavelength of maximum absorbance).

The photodegradability of the dye is investigated by exposing the dye solution under UV light in the presence of undoped and doped ZnO photocatalyst, prepared by the two different methods. The dependence of the degradation rate on time under UV-light is illustrated in Fig. 4. The figure compares the kinetic curves of RB5 decolorization of undoped and doped ZnO photocatalyst with the irradiation time. The pure ZnO films have the highest decolorization percentage under UV-light illumination (more than 90% in 180 min of irradiation). The ZnO doped with Fe^{3+} samples (0.25 wt%, obtained by the first method) have higher photocatalytic efficiency and faster mineralization RB5 (D = 68.75%) than those, prepared by the second method (D = 52.25%, Fig. 4). Therefore, we investigated more completely

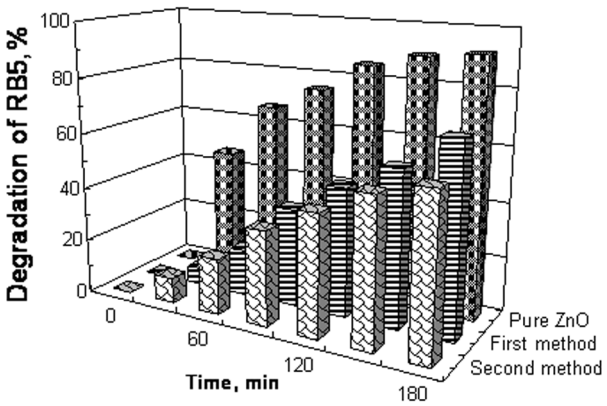

Fig. 4. Photocatalytic degradation of the Reactive Black 5 concentration (3 ppm) in aqueous solutions under UV-light illumination of ZnO and ZnO-Fe (0.25 wt%) films, deposited by two methods

the photocatalytic properties of the films, obtained by the first method.

Fig. 5 shows bleaching kinetics of RB5 in aqueous solutions by ZnO and ZnO:Fe films under UV and visible light illumination. The reaction kinetics is revealed by plotting the natural logarithm of concentration ratio, $\ln(C/C_0)$, versus the irradiation time, t. The solid lines indicate that the reaction is of first order kinetics. They are plotted following the equation below:

$$\ln(C/C_0) = -kt \tag{3}$$

where, C_o is the initial absorbance of dye solution, C is the absorbance at time t, and k is the reaction rate constant. The value k is evaluated from the respective logarithmic plots of the experimental data.

As seen from Fig. 5, the pure ZnO film has the highest photocatalytic activity, which corresponds to a highest k value (under UV and visible, $k_1 = 0.0153$ min^{-1} and $k_2 = 0.0095$ min^{-1}). The photocatalytic activity of the doped ZnO is rather low. It is interesting to note that the k values of composite film with ZnO:Fe (under UV and visible, $k_1 = 0.0013$ min^{-1} and $k_2 = 0.0008$ min^{-1}) is considerably lower than that of pure ZnO. These experimental results are obtained for two independent series of experiments – under UV or visible light illumination.

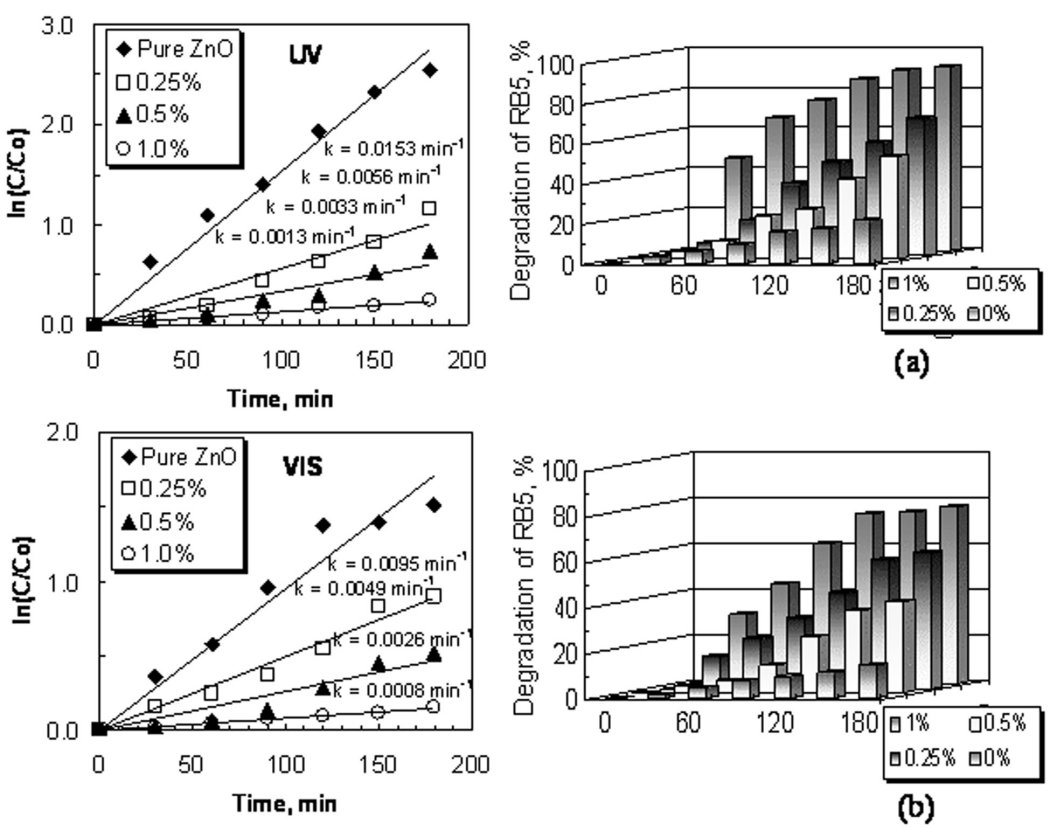

Fig. 5. Bleaching kinetics of RB5 in aqueous solutions by ZnO and ZnO-Fe films under (a) UV and (b) visible light illumination. The initial concentration of dye was 3 ppm

Nanostructured ZnO films degrade faster the dye (under UV and visible, D_1 = 97.76% and D_2 = 78.45%) and have the better photocatalytic properties compared to ZnO films doped with 1 wt.% iron. They degrade 21.88% of RB5 under UV-light illumination at the end of the process (180 min). The experimentally established results that the pure films are better catalysts compared to ZnO:Fe are in good agreement with the observed difference in the surface morphology for these samples (SEM images in Fig. 1).

The results confirm that the prepared films with significantly developed surface are better photocatalysts, as the higher surface area favors the rates of the heterogeneous photocatalytic reaction.

Decolorization of RB5 by ZnO films in darkness

The results from experiments without any illumination (Fig. 6) are compared with respect to the apparent rate constant *k*. The concentration of RB5 decreases also without illumination, but much slower in comparison with the respective photocatalytic counter parts. As seen from the data in Fig. 6, the rates of dye decolorization are very low for all the investigated samples. Among them highest degree of RB5 bleaching is achieved with the ZnO film – a trend, similar to the observed from photocatalytic experiments. This fact leads to the conclusion that the absorption stage plays significant role in photocatalytic reactions on ZnO surface. In case of experiments without illumination there is no crucial dependence of the rate constant *k* on the percent of the dopant, as well as on the initial dye concentration (C_0). As seen, linear fits for first-order kinetics are not much appropriate in this case. The decrease of RB5 concentration in these cases can be considered as the interplay of at least two processes: (i) adsorption of RB5 on the ZnO films surface and (ii) some kind of dye destruction process, taking part on the ZnO films even without illumination. This assumption needs further proofs and will be a subject of future studies. Despite these complications, we assume the simplification to fit the experimental data (from the experiments in darkness) as a single reaction process with rate constant *k* in order to compare this result to the results from the photocatalytic experiments.

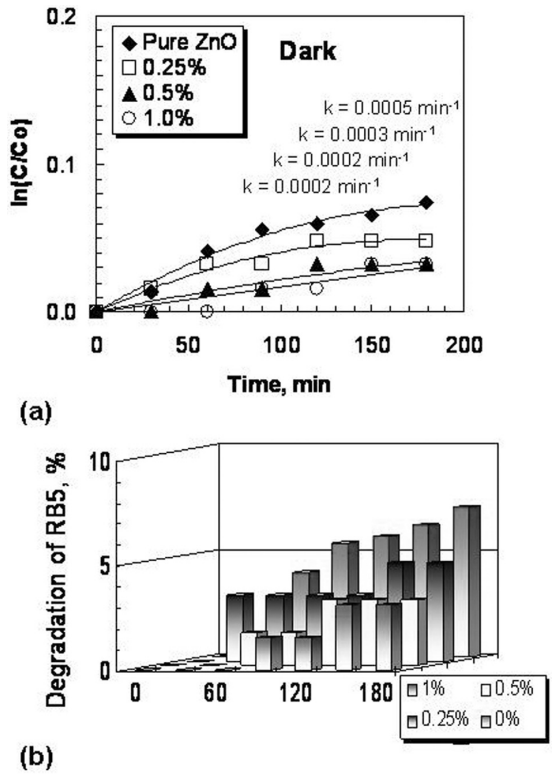

Fig. 6. Decrease of Reactive Black 5 by ZnO and ZnO-Fe films in darkness. The initial concentration was 3 ppm

CONCLUSIONS

Pure and iron doped ZnO films with two different coating configurations structure are deposited by sol–gel via dip coating technique. The films were characterized by SEM, AFM and UV-Vis spectroscopy. Nanostructured films manufactured by the first method demonstrate higher photocatalytic efficiency and faster mineralization of RB5 in comparison with these, prepared with the one of the second procedure. The addition of 0.25–1 wt.% of Fe^{3+} ions to the precursor modifies the film morphology (decreases the ganglia-like hills) and reduces the photocatalytic activity of ZnO. The kinetics of photocatalytic reaction is systematically studied under UV or visible light illumination and in darkness at different system parameters – amount of iron doping and the initial concentration of Reactive Black 5 in aqueous solution. The photocatalytic efficiency of pure ZnO films is higher than the activity, achieved by iron doped film under UV-light illumination, with a rate constant of 0.0153 min^{-1} (ZnO) much greater than that of 0.0013 min^{-1} (ZnO:Fe(1%)). The undoped films have the highest photocatalytic activity in comparison with the doped ones under visible light illumination. Our results are promising for the development of doped ZnO photocatalysts and their future application under visible light.

Acknowledgements: *This research is financially supported by FP7 project Beyond Everest and by the Erasmus Mundus External Co-operation Window Programme of the European Union (A.P.).*

REFERENCES

1. A. Fujishima, X. Zhang, D. Tryk, *Surface Science Reports*, **63**, 515 (2008).
2. A. Fujishima, X. Zhang, C. R. *Chimie*, **9**, 21 (2006).
3. A. Fujishima, X. Zhang, D. A. Tryk, *Internat. J. Hydrogen Energy*, **32**, 2664 (2007).
4. A. Ennaoui, M. Weber, R. Scheer, H. Lewerenz, *Sol. Energy Mater. Sol. Cells*, **54**, 277 (1998).
5. M. Vafaee, M. Ghamsari, *Mater. Lett*., **61**, 3265 (2007).
6. Y. Kim, W. Tai, S. Shu, *Thin Solid Films*, **491**, 153 (2005).
7. Y. Wang, J. Li, P. Peng, T. Lu, L. Wang, *Appl. Surf. Sci*., **254**, 5276 (2008).
8. T. Ohno, M. Akiyoshi, T.Umebayashi, K. Asai, T. Mitsui, M. Matsumura, *Appl. Catal. A*, **265**, 115 (2004).
9. R. Asahi, T. Morikawa, T. Ohwaki, K. Aoki, Y. Taga, *Science*, **293**, 269 (2001).
10. A. Eliyas, L. Dimitrov, V. Iliev, E. Stoyanova, S. Rakovsky, *Nanoscience and Nanotechnology*, Eds. E. Balabanova, I. Dragieva, BPS Publ. Co., **11**, 146 (2011).
11. A. Bojinova, C. Dushkin, *Reaction Kinetics, Mechanisms and Catalysis*, **103** (1), 239 (2011).
12. M. Uzunova-Buinova, D. Dimitrov, D. Radev, A. Bojinova, D. Todorovsky, *Mater. Chem. Phys.*, **110** (2–3), 291 (2008).
13. A. Eliyas, V. Iliev, I. Mitov, S. Rakovsky, *Nanoscience and Nanotechnology*, Eds. E. Balabanova, I. Dragieva, BPS Publ. Co., **10**, 38, (2010).
14. A. Shalaby, Y. Dimitriev, R. Iordanova, A. Bachvarova-Nedelcheva, Tz. Iliev, *J. Univ. Chem. Technology and Metallurgy*, **46** (2), 137 (2011).
15. R. Iordanova, A. Bachvarova-Nedelcheva, Y. Dimitriev, Tz. Iliev, *Bulg. Chem. Commun.*, **43** (3), 378 (2011).
16. A. Stoyanova, Y. Dimitriev, A. Shalaby, A. Bachvarova-Nedelcheva, R. Iordanova, M. Sredkova, *Journal of Optoelectronic and Biomedical Materials*, **3** (1), 24 (2011).
17. W. Zhang, Z. Liu, Z. Liu, J. Zhao, *Appl. Surf. Sci.*, **258**, 6103 (2012).
18. L. Xu, X. Li, *J. Cryst. Growth,* **312**, 851 (2010).
19. C. Wang, Z. Chen, Y. He, L. Li, D. Zhang, *Appl. Surf. Sci.*, **255**, 6881 (2009).
20. C. Ton-That, M. Foley, L. L. C. Lem, G. McCredie, M. R. Phillips, B. C .C. Cowie, *Mater. Lett.*, **64**, 386 (2010).
21. R. Saleh, S.P. Prakoso, A. Fishli, *J. Magnetism Magnetic Mater.*, **324**, 665 (2012).
22. A. K. Mishra, D. Das, *Mater. Sci. Eng. B*, **171**, 5 (2010).
23. M. L. Dinesha, H. S. Jayanna, S. Ashoka, G. T. Chandrappa, *J. Alloys Compd.*, **485**, 538 (2009).
24. F. Paraguay, D. M. Miki-Yoshida, J. Morales, J. Solis, W. L. Estrada, *Thin Solid Films*, **373**, 137 (2000).
25. G.-H. Kuo, H. Paul Wang, H. H. Hsu, J. Wang, Y. M. Chiu, C.-J. G. Jou, T. F. Hsu, F.-L. Chen, *J. Nanomat.*, **2009**, Article ID 316035 (3 pages) (2009) doi:10.1155/2009/316035.
26. A. Yu, J. Qian, H. Pan, Y. Cui, M. Xu, L. Tu, Q. Chai, X. Zhou, *Sens. Actuators B*, **158**, 9 (2011).
27. N. Han, L. Chai, Q. Wang, Y. Tian, P. Deng, Y. Chen, *Sens. Actuators B*, **147**, 525 (2010).
28. Q. Xiao, C. Yao, *Mater. Chem. Phys.*, **130**, 5 (2011).
29. S. Dong , K. Xu, J. Liu, H. Cui, *Physica B*, **406**, 3609 (2011).
30. H. Park, W. Choi, *Journal of Photochemistry and Photobiology A: Chemistry*, **159**, 241 (2003).
31. Gwyddion - data analysis software:///gwyddion.net.
32. T. Vicsek, Fractal Growth Phenomena, *World Scientific*, Singapore, 1992.
33. L. Znaidi, *Materials Science and Engineering B*, **174**, 18 (2010).
34. J. H. Sinfelt, *Surface Science*, **500**, 923 (2002).

ПОВЪРХНОСТНИ И ФОТОКАТАЛИТИЧНИ СВОЙСТВА НА ДОТИРАНИ С ЖЕЛЯЗО НАНОСТРУКТУРИРАНИ ТЪНКИ ФИЛМИ ОТ ZnO

Н. Кънева[1], А. Пономарева[2], Л. Кръстева[1], Д. Димитров[1], А. Божинова[1]*, К. Папазова[1], Г. Сучанек[2], В. Мошников[3,4]

[1] Лаборатория по наука и технология на наночастици, катедра Обща и неорганична химия, Факултет по химия и фармация, Софийски университет, София 1164, България
[2] Лаборатория по електроника на твърдото състояние, ТУ Дрезден, Дрезден 01062, Германия
[3] Катедра „Микро-наноелектроника“, Държавен университет по електротехника, Санкт Петербург , 197376, Русия
[4] Катедра „Интегрирана електроника“, Санкт Петербург, Държавен политехнически университет, Санкт Петербург, 195251, Русия

Постъпила февруари, 2013 г.; приета май, 2013 г.

(Резюме)

В настоящата работа изследваме наноразмерни Fe-ZnO тънки филми, отложени върху стъклени подложки чрез зол-гел метод и техника на потапяне на подложката (dip-coating). Прекурсорният зол е получен чрез разтваряне на $Zn(CH_3COO)_2.2H_2O$ и $Fe(NO_3)_3.9H_2O$ в 2-метоксиетанол, с добавка от моноетаноламин като повърностно активен агент. Съдържанието на желязо в ZnO тънки филми е 0.25, 0.5 или 1 мас.%. Тънките наноструктурирани филми са с две различни покрития за фотокаталитичните тестове. Първите са получени чрез отлагане на 5 слоя от дотиран с желязо зол върху стандартни микроскопски стъкла. Вторият тип йерархично структурирани филми се отлагат върху стъклени подложки чрез двуетапна процедура. Фотокаталитичната ефективност на получените филми е тествана върху текстилно багрило, Реактично Черно 5 (RB5) във воден разтвор при различни начални концентрации на багрилото, при облъчване с УВ или видима светлина. Изследвана е зависимостта на фотокаталитичната активност спрямо (i) съдържанието на желязо, (ii) наличието или отсъствието на ZnO подслой под Fe дотирания слой, (iii) честотата на облъчване и (iv) началната концентрация на багрилото. За обяснение на наблюдаваните резултати са извършени цялостни АФМ изследвания включително и фрактален анализ на повърхността (топография). Обсъдена е връзката между наблюдаваното фотокаталитично поведение на филмите и получените АФМ повърхностни характеристики.

Bulgarian Chemical Communications, Volume 45, Number 4 (pp. 644–648) 2013

Researches on the structure and properties of heat treated, nickel alloyed, molybdenum modified aluminum bronze

R. Vl. Gavrilova, R. I. Petkov*

University of Chemical Technology and Metallurgy – Sofia; Faculty of Metallurgy and Material Science, 1756 Sofia, blvd. Kl. Ochridski 8

Received February, 2013; Revised May, 2013

The changes, after heat treatment, in the microstructure and hardness of copper-aluminum alloys, additionally alloyed with Ni and modified with Mo are investigated and described in the present study. The changes in the microstructure largely are determined by the presence of Ni in the composition of the alloy. The investigations were made for a case when the content of additional alloying element is fixed on 3%. Modification was made by addition of 0.1% Mo.

Key words: copper-aluminum alloys, modifiers, heat treatment, structure.

INTRODUCTION

The increase of aluminum content, in two-phase (duplex) Cu-Al alloys, from 8% up to10% leads to a progressive strengthening, due to the appearance of harder, body centered cubic beta-phase, which additionally makes the bronzes more suitable for hot working and casting. Ni alloyed, heat treated aluminum bronzes are ones with the highest strength among the nickel-bearing aluminum bronzes. They exhibit excellent yield and compressive strength, high hardness and adequate elongation. They are a good load-bearing material, suitable for heavy-duty machine details and such exposed of high impact. The additional increase of the strength is achieved through a heat treatment. The material exhibits excellent corrosion and heat resistance, good machinability and weldability. It is used for bushings and bearings of heavy duty, gears, and wear parts. It find application in the marine as pump parts, machine tool parts, aircraft parts, as well for military applications. The most often is used in the aircraft landing gear as bearing components [1, 2, 6, 8].

The primary fine-grain structure in aluminum bronzes are achieved by adding different refractory elements during the casting process. The changes in the microstructure (the magnitude and shape of the metal grains) of the alloys are provoked by modifying effect of these elements, and to large extent from the presence of Fe in the alloys. The optimum concentration of modifiers, according to the data cited in popular scientific literature, is between 0.05 to 0.5%.

EXPERIMENTAL EQUIPMENT, METHODS AND MATERIALS

Melting of the charge materials (electrolytic copper, aluminum, nickel and molybdenum) was carried out in a laboratory induction furnace MRA8-25 with graphite crucible. The casting temperature was 1130–1140 °C. The produced samples are cylindrical, with diameter 25 mm.

The effect of nickel alloying and molybdenum modifying was evaluated on the obtained alloys of a type CuAl9. Data for changes in the structure and hardness of the specimens as well for the effect of different heat treatments (Fig. 2–5) have been obtained, as these characteristics change in the cases of alloying (Fig. 1b–5b) and modifying with molybdenum (Fig. 1c–5c). The samples are prepared for examination by a standard technique [4] and micro-photographs of the alloys were made at a magnification 63x.

HEAT TREATMENT

The heat treatment of samples was conducted in a laboratory electric resistance furnace in several

* To whom all correspondence should be sent:
E-mail: r.gavrilova@abv.bg

Table 1. Regimes of heat treatment on the investigated alloys

Regimes	Heat treatment	Temperature	Time	Cooling
1	Quenching	875 °C	60 min	In water
2	Ageing	300 °C	120 min	In furnace
3	Ageing	400 °C	120 min	In furnace
4	Ageing	500 °C	120 min	In furnace

stages. Initially, they were subjected to quenching, then to artificial aging regimes [7–9] (annealing temperatures) shown in Table 1:

INVESTIGATION OF THE STRUCTURE

Nickel-aluminum bronzes, generally, are two-phase duplex alloys containing aluminum and additionally nickel for increase of the strength. The different aluminum content of the cast alloys (Fig. 1a–1c) and alloying with 3% Ni (Fig. 1b–5b) and on the other hand alloying with 3% Ni and modifying by molybdenum (Fig. 1c–5c) resulted in markedly different microstructures. Hence, seemingly small variations in composition can lead to changes of the phases, developing in the stucture.

ESTIMATION OF THE HARDNESS

The hardness was determined to Brinell method (BS 1SO 6506). Measurement was made by a sphere with a diameter 2.5 mm, 187.5 kgf (1840N). Graphically, on Fig. 6 are presented measurements of the hardness for different regimes of heat treatment of investigated cuprum-aluminum alloys. The analysis of the results shows that the hardness tends to increasing with the increase of ageing temperature for specimens in cast, well as in quenched condition. This most likely is due to the partial dissolution of the phase, obtained in a time of the primary crystallization of the (α+γ) eutectoid, whose hardness and brittleness are higher.

RESULTS AND DISCUSSION

The subject of this paper was the evaluation of the effect of a small change in composition of aluminum bronzes on the microstructure, as well the evaluation the effect of alloying with Ni, modifying by Molybdenum and heat treatment on the hardness . Based on only three compositions and four regimes of heat treatment we make the next primary conclusions: Nickel alter and improve uniformity of the cast structure, raises hardness, and act as microstructure stabilizer. Nickel-aluminum bronzes are complex alloys in which small variations in composition can result in the development of markedly different microstructures, which can, in turn to result in wide variations in properties. Specifically:

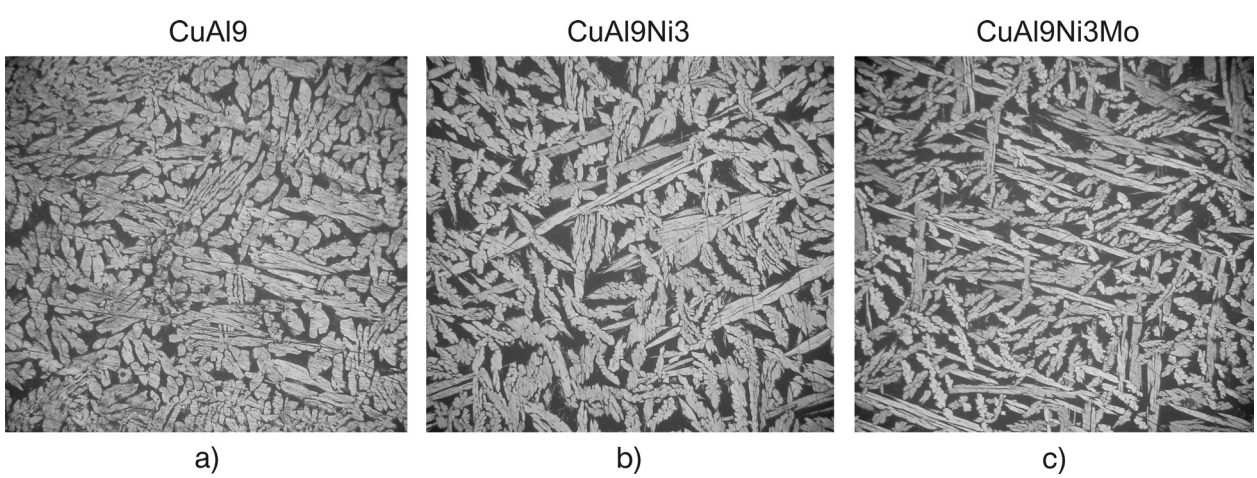

Fig. 1. Microstructures of investigated alloys in cast condition

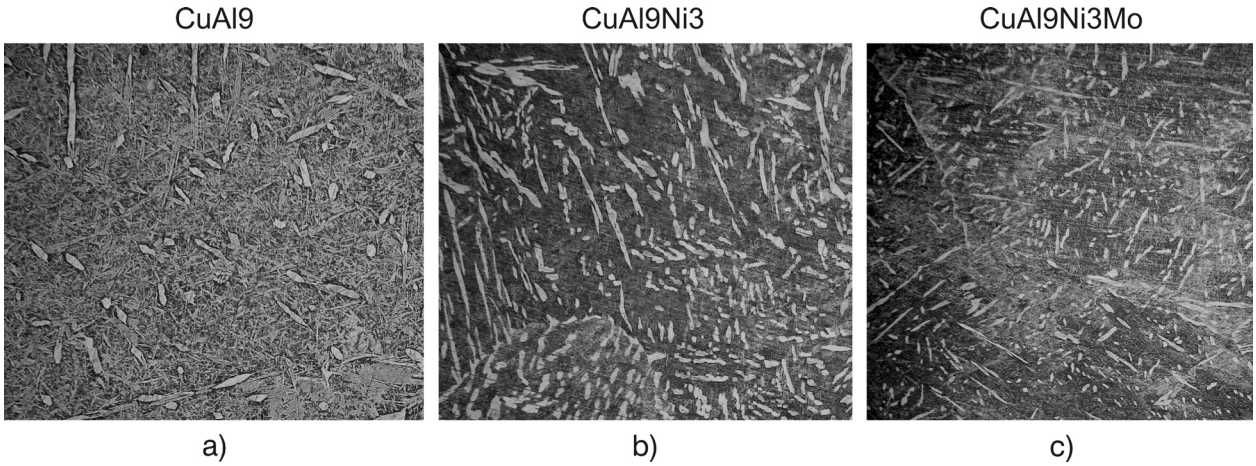

Fig. 2. Microstructures of investigated alloys in quenched condition

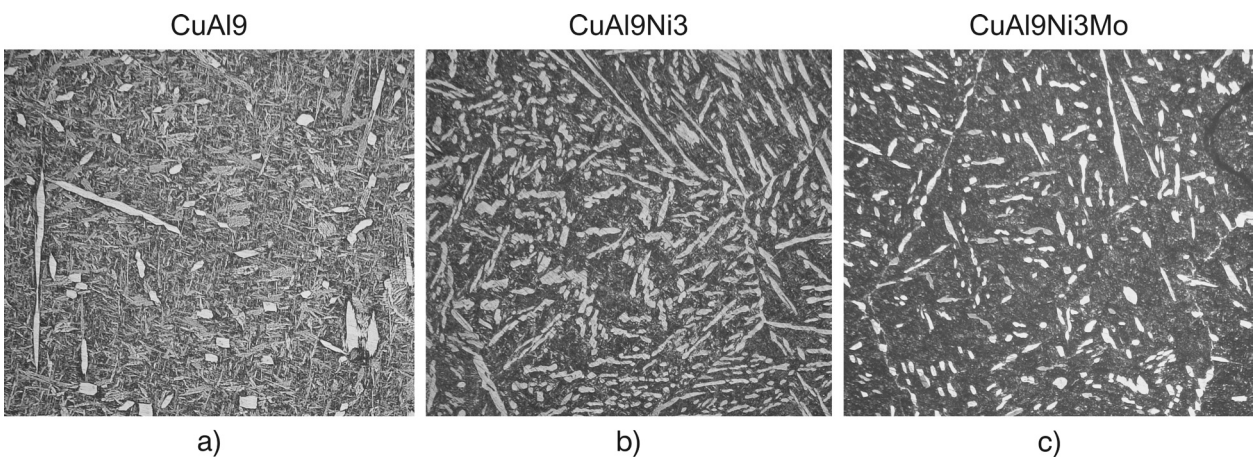

Fig. 3. Microstructures of investigated alloys after ageing at 300 °C for 2 hours

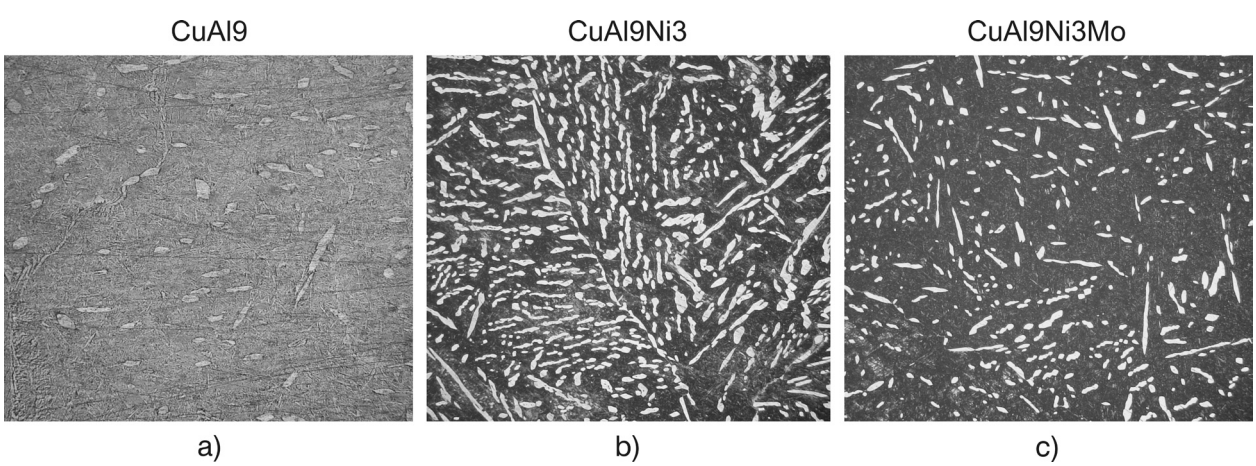

Fig. 4. Microstructures of investigated alloys after ageing at 400 °C for 2 hours

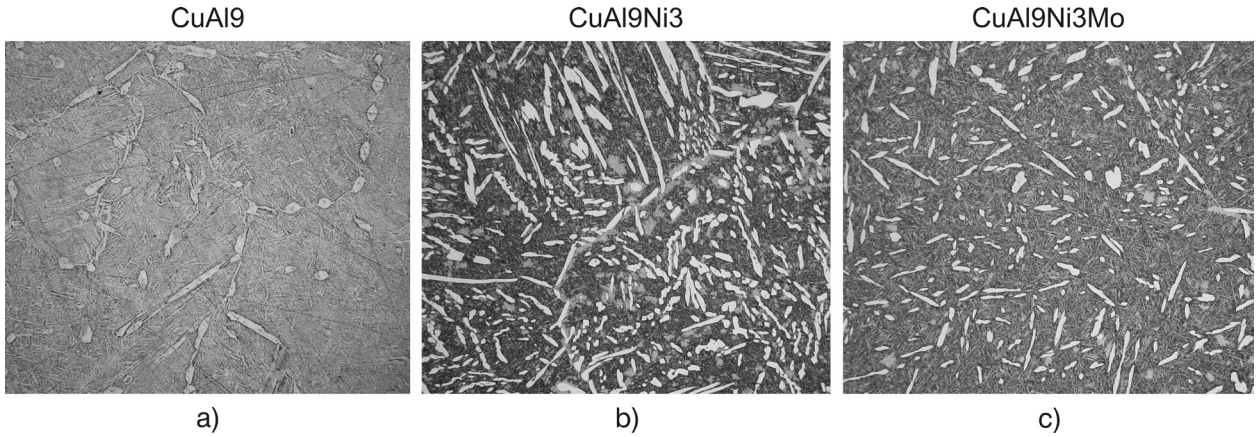

Fig. 5. Microstructures of investigated alloys after ageing at 500 °C for 2 hours

• The analysis of the structures shows, that for the basic CuAl9 alloy (Fig. 1a–5a) after the different heat treatments the structure becomes finer and with a relative decrease in the amount of the eutectoid component.

• Adding of nickel in aluminum bronze (Fig. 1b–5b) leads to a change in the form of eutectoid crystals - they elongate and acquire form similar to Widmanstatten structure plus intercepts of martensite or bainite between releases of the second phase (Fig. 2b–5b). This can be confirmed with certainty at higher microscopic magnification and by measuring the micro-hardness of the different structural elements. (These studies will be the subject of our next work).

• The modification of a nickel-aluminum bronze with molybdenum leads to keeping the acicular nature of the structure and visible refinement of the eutectoid component (Fig. 1c–5c).

• In regard to the hardness, adding of nickel in the aluminum bronze leads to an overall increase of the hardness (Fig. 6) compared with the base alloy. The explanation is that nickel hampers the eutectoid decomposition. The β-phase is kept, and the struc-

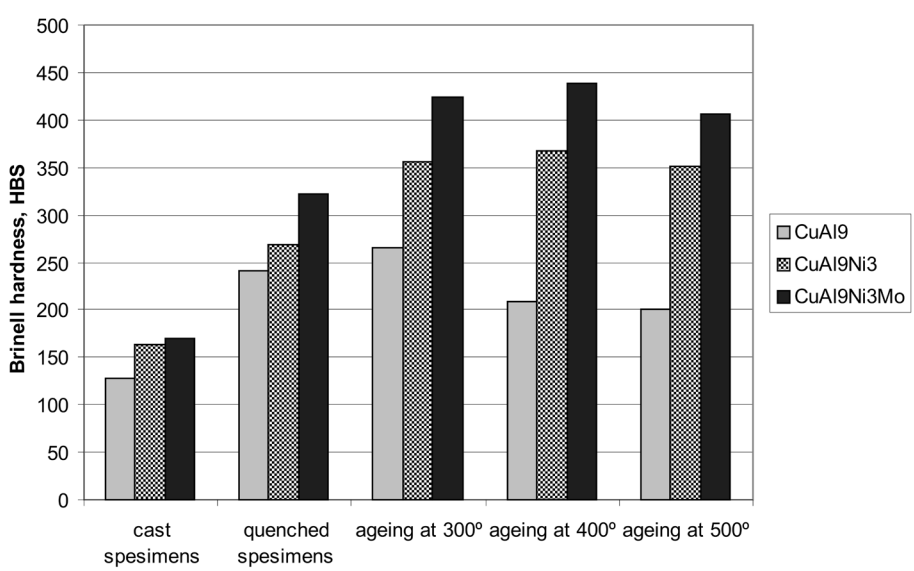

Fig. 6. Influence of the alloying with Ni and modifying with Mo on the hardness of copper-aluminum alloy

ture became fine-grained. Modification of the alloy with molybdenum causes refinement of the structure, a base for further increase of the hardness. The tendency of hardness increasing with the increasing of ageing temperature to 400 °C is kept.

• At high temperature aging – 500 °C, and holding time 2 hours, the measured hardness values marked fall. This fact shows that the optimal mode of heat treatment after quenching of alloys of this type should not exceed 400 °C.

REFERENCES

1. R. E. Smallman, R. J. Bishop, Modern Physical Metallurgy and Materials Engineering, Science, process, applications, Sixth Edition, Butterworth-Heinemann, Linacre House, Jordan Hill, Oxford OX2 8DP, 225 Wildwood Avenue, Woburn, MA 01801-2041, 1999.
2. U. K. Korzunin, V. P. Razshtupkin, B. I. Matjuhin, Study of the microstructure of non ferrous alloys, Materialovedenie, Omsk, 2008, 20.
3. Kay Geels, Metallographic and Materialographic Specimen Preparation, Light Microscopy, Image Analysis and Hardness Testing, Printed in U.S.A., ASTM, No. MNL46, 2007.
4. H. Schumann, Metallography, VEB DVG, Leipzig, 1997.
5. M. Jablonska, A. Jasik, A. Hanc, *Archives of Materials Science and Engeneering*, **29**(1), 16 (2008).
6. P. R. Subramanlan, D. E. Laughlin, *Bulletin of Alloy Phase Diagrams*, **11**(2), (1990).
7. P. Brezina, Heat treatment of complex aluminum bronzes, *International Metals Reviews*, **27**, 77 (1982).
8. Source: Thermal Properties provided by SAE, www.morganbronze.com.
9. H. J Meigh, Cast and wrought aluminum bronzes – properties, processes and structure, Institute of Materials, London, 2000.

ИЗСЛЕДВАНЕ НА СТРУКТУРАТА И СВОЙСТВАТА СЛЕД ТЕРМИЧНО ОБРАБОТВАНЕ НА МЕДНО-АЛУМИНИЕВИ СПЛАВИ, ДОПЪЛНИТЕЛНО ЛЕГИРАНИ С Ni И МОДИФИЦИРАНИ С Mo

Р. Гаврилова, Р. Петков

Химико-технологичен и Металургичен университет – София,
1756 София, бул. „Кл. Охридски“ № 8

Постъпила февруари, 2013 г.; приета май, 2013 г.

(Резюме)

Настоящото проучване установява промените в микроструктурата и твърдостта, настъпили в резултат на термично обработване на медно-алуминиеви сплави, допълнително легирани с 3% Ni и модифицирани с 0.1% Mo. Закаляването на легираните с никел алуминиеви бронзи води до общо повишаване на твърдостта в сравнение с базовата сплав, а допълнителното модифициране с молибден предизвиква издребняване на структурата и също води до повишаване на стойностите ѝ. В резултат на приложените различни режими на отвръщане, в изследваните структури са констатирани промени по отношение на едрината и разпределението на отделената втора фаза, а стойностите на твърдостта значително се повишават.

Bulgarian Chemical Communications, Volume 45, Number 4 (pp. 649–654) 2013

Nanosized composite ZnO/TiO_2 thin films for photocatalytic applications

S. A. Siuleiman, D. V. Raichev, A. S. Bojinova*,
D. T. Dimitrov, K. I. Papazova

Laboratory of Nanoparticle Science and Technology, Department of General and Inorganic Chemistry, Faculty of Chemistry and Pharmacy, University of Sofia, 1 James Bourchier Blvd., Sofia 1164, Bulgaria

Received February, 2013; Revised May, 2013

This study is focused on preparation, characterization and photocatalysis with ZnO, TiO_2 and nanocomposite thin films of ZnO/TiO_2, prepared by spin coating method from suspensions of the commercial metal oxide powders in ethanol, with addition of PEG as stabilizer. The content of ZnO in the composite samples is selected to be 90%. The phase composition and morphology of the ZnO, TiO_2 and mixed composite thin films of ZnO/TiO_2 is characterized by X-Ray Diffraction and SEM analysis. The photocatalytic efficiency of the prepared films is tested in photooxidation of organic azo dye Orange II from aqueous solutions under irradiation with UV and visible light. The influence of the number of coated layers on the efficiency of dye photodegradation is also investigated. Comparative photocatalytic experiments with ZnO and TiO_2 films are performed. It is found out that the nanocomposite film of 90% ZnO content with 3 coated layers manifests the highest photocatalytic efficiency under UV irradiation.

Key words: ZnO/TiO_2 composite film, spin coating, photocatalysis, Orange II, UV, visible light.

INTRODUCTION

Heterogeneous photocatalysis is an attractive advanced technology for removal of organic pollutants from water and air under light illumination. Titania and zinc oxide are the most popular semiconductor oxides used as photocatalysts due to their unique blend of properties [1]. The coupling of two semiconductors, possessing different energy levels for their corresponding conduction and valence bands, provides an approach to achieve a more efficient charge separation, an increased lifetime of the charge carriers and an enhanced interfacial charge transfer to the adsorbed species favoring their photooxidation and further mineralization [2]. There is significant interest in the scientific research on nanostructured ZnO/TiO_2 composites with different configurations and morphologies in order to obtain more efficient photocatalytic degradation [3–5]. In addition to classical mechanochemical processing used to manufacture nanoparticulate $(TiO_2)_x(ZnO)_{1-x}$ photocatalytic powders [6], the photocatalityc performance is investigated for coated with titania shell ZnO nanorods [7], junction type p-ZnO/n-TiO_2 powder photocatalyst [8], powdered ZnO–TiO_2 nanocomposites prepared by wet chemical methods [9–11], nanosized ZnO/TiO_2 [12] and Zn-TiO_2-ZnO [13] nanocomposite films. To the best of our knowledge, we have not found in the available literature, investigation on ZnO/TiO_2 films, prepared via spin coating method from suspensions.

In this study we present a procedure for obtaining thin solid films of TiO_2/ZnO from slurry by spin coating and their characterization as a first step to enhance the photocatalitic efficiency of the composite film under UV-light. For this reason, our goal is to find the conditions for preparation of good and reproducible coatings by studying the influence of different factors on the photocatalytic properties of the composite films.

EXPERIMENTAL

The reagents and materials used in the experiments were as follows: TiO_2 anatase from KRONOS-Germany, ZnO and Orange II (O II) ($C_{16}H_{11}N_2NaO_4S$, dye content ~85%, absorption

* To whom all correspondence should be sent:
E-mail: nhasb@wmail.chem.uni-sofia.bg

maximum at λ_{max} = 484 nm) from Sigma Aldrich. Absolute ethanol and PEG (2000) were purchased from the Institute of Pure Substances, University of Sofia. Standard microscopic glass slides of dimensions 75×26×1 mm (Isolab, Germany) were used as substrates of the coatings. The glass slides were preliminary cleaned thoroughly with detergent and then consecutively rinsed with isopropanol, acetone and ethanol in order to eliminate organic residues and assure better adhesion of the coatings [14].

The coating suspension, containing commercial TiO_2 or ZnO powders, was obtained by addition of the corresponding metal oxides (7% weight ratio) to ethanol. The ZnO content in the composite TiO_2/ZnO film samples was selected to be 90% with respect to titanium oxide, based on our previous investigation [15]. To assure better films adhesion and porosity, 7% (weight) polyethylene glycol 2000 was also added to the slurry [16]. Then the coating suspension was homogenized by ultrasonic bath (IKEDARIKA BU95001) for 20 minutes and was let to age overnight. The substrates were coated using spin-coater (KW-4A, Chemat Technology Inc) at two speeds of rotation: first – 1000 rpm (3 sec) and second – 2000 rpm (30 sec). Three series of film samples of each composition were prepared – with one, two and three coated layers. The films were allowed to dry at 100 °C for 10 min between the successive coating cycles. The as-coated substrates were finally annealed in a high temperature oven (Barnstead Thermolyne, Furnace 1400) for 1.5 h at 500 °C in air atmosphere to obtain complete organics decomposition and crystalline films.

The phase composition and crystallinity of as-prepared thin films was established by Siemens D 500 diffractometer (CuKα source of radiation at a step of 0.05 deg for 2Θ and counting time 2s/step). The surface morphology of the samples was observed via scanning electron microscope (SEM) (JSM-5510 JEOL). The film thickness was determined by weight method for series of films from ZnO, TiO_2 and TiO_2/ZnO, prepared with 1, 2 and 3 spin coated layers.

The as-prepared ZnO, TiO_2 and TiO_2/ZnO films were tested in photodegradation of Orange II from water solution by a standard testing procedure [14]. The volume of dye solution was 100 ml. The initial O II concentration was 8 ppm. The sources of irradiation were as follows: UVA lamp (Sylvania 18W BLB T8, emitting mainly in the range 315–400 nm) placed 10 cm above and a linear Tungsram lamp (500 W K1R7s 9700 Lm, maximal emission at 700 nm) for the visible irradiation fixed at 25 cm above the investigated solution. Aliquot samples were regularly taken from the dye solution at fixed time intervals and analyzed for absorption at the maximal absorption of O II by UV-VIS spectrophotometer (Thermo scientific, Type Evolution 300 BB). After absorption measurement, the aliquots were immediately returned back to the treated solution. The solution was constantly stirred by electromagnetic stirrer at constant rotation speed of 400 rpm. All photocatalytic experiments were conducted at constant temperature of 23±2 °C.

RESULTS AND DISCUSSION

The crystalline phase of the prepared ZnO, TiO_2 and TiO_2/ZnO films, identified by X-ray diffraction analysis is represented in Fig. 1. It is clear from the XRD pattern that zinc oxide is well crystallized and can be classified as hexagonal wurtzite modification, with dominating (101) peak. The titanium dioxide, in the thin films, is of anatase form (with main peak at (101)). The diffractogram of mixed TiO_2/ZnO composite film with pointed characteristic peaks of anatase and zinc oxide is presented also in Fig. 1. The intensities of the main peaks of ZnO and TiO_2 in case of composite do not differ from those in case of pure ZnO or TiO_2 film – both oxides are present in the composite as separate phases, there is no indication for formation of mixed compound. The size of crystallites is calculated following Sherrers equation (k = 1.5406 Å) for ZnO from the (101) peak and for TiO_2 from the (101) peak (Fig. 1) as they are relatively strong and single for the respective metal oxide. The sizes of crystallites are found to be 40.7 nm for TiO_2 and 24 nm for ZnO.

The surface morphology of TiO_2 and TiO_2/ZnO composite film is represented in Fig. 2. From the SEM images in Fig. 2 is seen that the films are uni-

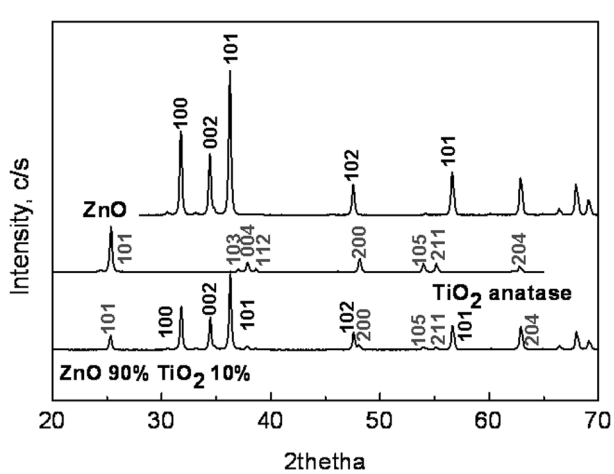

Fig. 1. Comparative XRD pattern of TiO_2, ZnO and composite TiO_2/ZnO thin films

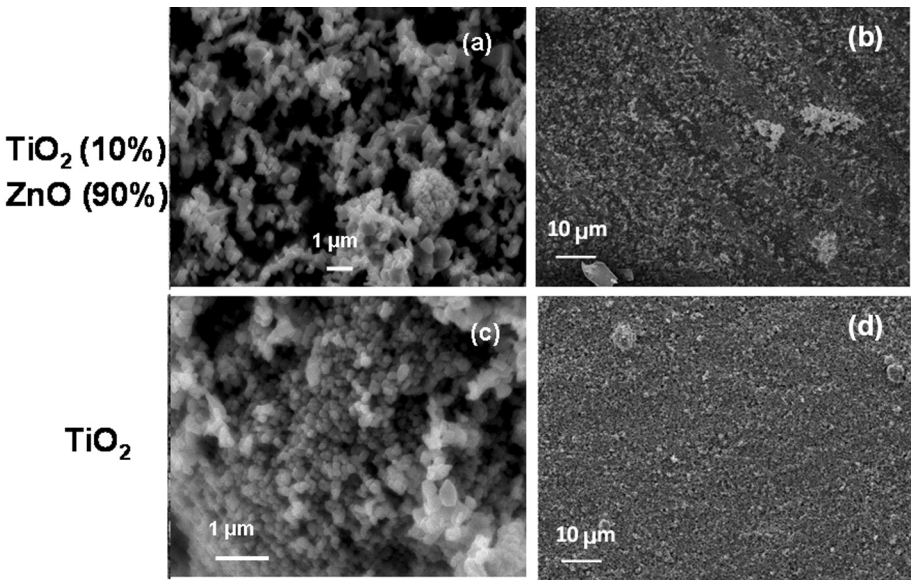

Fig. 2. SEM images of the prepared catalysts in form of thin films at different magnifications

form and homogeneous. The size of the particles in the films is calculated following the equation:

$$D_{av} = \sum_{N}^{i=1} \left(D_{i\max} + D_{i\min}\right)/2N \qquad (1)$$

Where N is the number of observed particles, and D_{av}, D_{max} and D_{min} are the average, maximum and minimum diameter of the particle, respectively. In our case N=300–500. The average particle size is found to be 0.2 µm for TiO_2 and 0.45 µm for ZnO in all the prepared films. The observed film thickness by SEM is 2.5 µm.

Series of experiments are made in order to obtain the optimal number of coated layers of the prepared films. The dependence of the film weight on the number of spin coating cycles is presented in Fig. 3. As seen from Fig. 3a, in case of ZnO and TiO_2 films, the weight of the first layer is greater, compared to that of the next ones. The second and third coatings, for each of the pure oxide films, have approximately equal weigh. In general – the ZnO films have greater weight (0.49 µg.cm^{-2} per 3 coatinds), than these of TiO_2 (0.43 µg.cm^{-2}) due to the different density of the respective oxides (ρ_{ZnO} = 5.6 g.cm^{-3}, ρ_{TiO2} = 3.9 g.cm^{-3}). The average film weight in case of 3 coated film of TiO_2/ZnO composite (Fig. 3b) is found to be 0.43 µg.cm^{-2}.

The photocatalytic action of the titania, zinc oxide and titania/zinc oxide nanocomposite films is investigated, as mentioned above, in the photo initi-

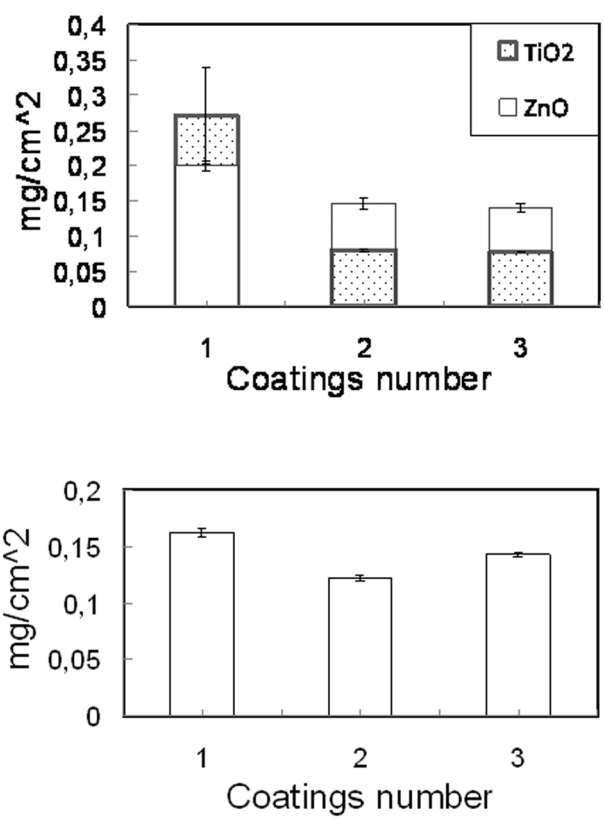

Fig. 3. Weight of the successive coatings for the films of: (a) TiO_2 and ZnO; (b) thin composite films of 90% ZnO content. The experimental data points represent the average from three independent measurements; the error bars show the respective deviations

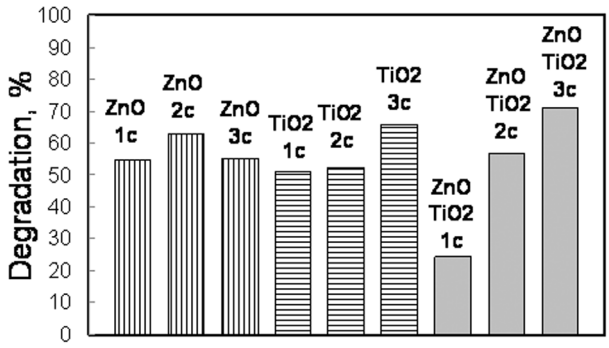

Fig. 4. Comparison of the achieved degree of photocatalytic decomposition of O II in 8 ppm water solution with all film samples at 3th h of UV light irradiation

ated decomposition of Orange II from 8 ppm water solutions. The photocatalytic experiments are carried out with films coated by 1, 2 and 3 spin coated layers. The results of the photocatalytic experiments after 180 min of UV illumination are shown in Fig. 4. The experimental data in case of TiO_2 and TiO_2/ZnO composite films show clear tendency for higher photocatalytic efficiency with the number of film coatings. The effect is most expressive for the TiO_2/ZnO composite films. The photocatalytic activity of ZnO films undergoes maximum (62% dye degradation) for the film prepared with 2 spin coatings and then slightly decreases. Higher degree of pollutants photodegradation (65%) is observed with TiO_2 films, prepared with 3 layers. The titania/zinc oxide films, prepared with 3 coatings, manifest the best photocatalytic efficiency (72% O II degradation) under UV irradiation due to successful charge separation in the prepared composite and therefore avoiding losses from recombination of the photogenerated charge carriers.

The experimental results from the photocatalytic tests at the 180th minute of visible light illumination are presented in Fig. 5. Generally the photocatalytic activity of all film samples under visible light is lower, compared to the results obtained upon UV irradiation. In this case a trend, reverse to the case of photocatalysis under UV light, is observed for the TiO_2 and TiO_2/ZnO film samples – the photocatalytic activity decreases with the number of coated layers. Here the TiO_2 and TiO_2/ZnO films have lower efficiency in comparison with the ZnO films. In case of films of zinc oxide, the photodegradation efficiency regularly increases with the number of the film coatings. The ZnO films prepared with 3 coated layers have the highest efficiency – 14% Orange II photodegradation.

The apparent rate constants of photocatalytic process are determined following the equation:

$$C = C_{in}.e^{-kt} \quad (2)$$

where C is the concentration of the dye solution at the moment t, C_{in} – the initial dye concentration and t is the illumination time in minutes.

The rate constants values (K), calculated by Eq. (2) with the data, obtained from the photocatalytic experiments under both types of illumination, are plotted in Fig. 6. From the figure one can see, that highest rate constants values are observed in case of photocatalysis under UV light with TiO_2/ZnO nanocomposite films, where the process of photocatalysis is the most effective.

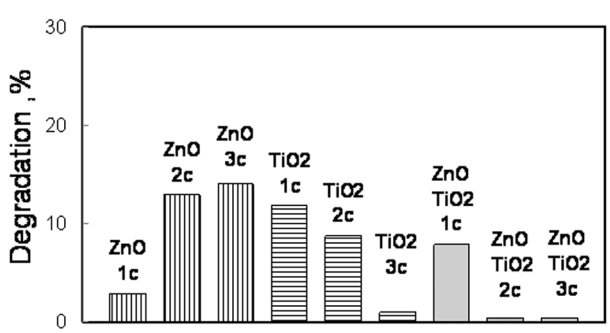

Fig. 5. Degradation degree (%) of Orange II after 3 h photocatalysis with the different film samples under visible light illumination. The initial dye concentration is 8 ppm

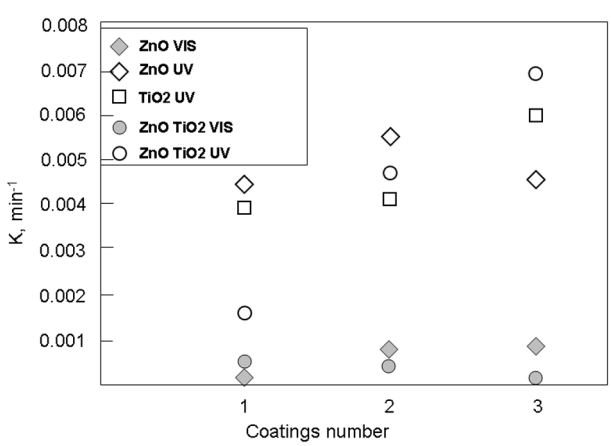

Fig. 6. Rate constants of photocatalysis versus number of the films coatings

CONCLUSIONS

Nanocomposite films of TiO_2/ZnO are prepared using for the first time dip coating method from ethanol suspensions. The films exhibit a good homogeneity and nanocrystallinity as shown by XRD and SEM analysis. The titania and zinc oxides in the composite film exist as separate phases in form of anatase and wurtzite modification, respectively. The determined by weight method composite film weight is found to be 0.43 $\mu g.cm^{-2}$. The photocatalytic action of the TiO_2/ZnO films is tested and compared with that of ZnO and TiO_2 films in UV and visible light induced purification of aqueous solutions from the organic dye Orange II. Most efficient dye photodegradation is achieved with the composite films of TiO_2/ZnO under UV irradiation. The investigation will be developed further upon visible light illumination, where a better photocatalytic performance of the composite TiO_2/ZnO films might be expected.

Acknowledgements: *This research is financially supported by FP7 project Beyond Everest.*

REFERENCES

1. S. Rehman, R. Ullah, A. M. Butt, N. D. Gohar, *J. Hazard. Mater.*, **170** (2–3), 560 (2009).
2. O. Carp, C. L. Huisman, A. Reller, *Progress in Solid State Chemistry*, **32**, 33 (2004).
3. A. Shalaby, Y. Dimitriev, R. Iordanova, A. Bachvarova-Nedelcheva, Tz. Iliev, *Journal of the University of Chemical Technology and Metallurgy,* **46** (2), 137 (2011).
4. R. Iordanova, A. Bachvarova-Nedelcheva, Y. Dimitriev, Tz. Iliev, *Bulgarian Chemical Communications*, **43** (3), 378 (2011).
5. A. Stoyanova, Y. Dimitriev, A. Shalaby, A. Bachvarova-Nedelcheva, R. Iordanova, M. Sredkova, *Journal of Optoelectronic and Biomedical Materials*, **3** (1), 24 (2011).
6. A. Dodd, A. McKinley, T. Tsuzuki, M. Saunders, *Journal of Alloys and Compounds*, **489**, L17 (2010).
7. M. Y. Guo, M. K. Fung, F. Fang, X. Y. Chen, A. M. C. Ng, A. B. Djurisic, W. K. Chan, *Journal of Alloys and Compounds*, **509**, 1328 (2011).
8. C. Shifu, Z. Wei, L. Wei, Z. Sujuan, *Applied Surface Science*, **255**, 2478 (2008).
9. Y. Jiang, Y. Sun, H. Liu, F. Zhu, H. Yin, *Dyes and Pigments*, **78**, 77 (2008).
10. C. Karunakaran, G. Abiramasundari, P. Gomathisankar, G. Manikandan, V. Anandi, *Materials Research Bulletin*, **46**, 1586 (2011).
11. J. Wang, Z. Jiang, L. Zhang, P. Kang, Y. Xie, Y. Lv, R. Xu, X. Zhang, *Ultrasonics Sonochemistry*, **16**, 225 (2009).
12. Z. Zhang, Y. Yuan, Y. Fang, L. Liang, H. Ding, L. Jin, *Talanta*, **73**, 523 (2007).
13. A. Abdel Aal, M. A. Barakat , R. M. Mohamed, *Applied Surface Science*, **254**, 4577 (2008).
14. A. Bojinova, C. Dushkin, *Reaction Kinetics, Mechanisms and Catalysis*, **103** (1), 239 (2011).
15. Deyan Daychev, M. Thesis, Faculty of Chemistry, Sofia University, 2012.
16. C. Dushkin, S. Stoianov, A. Bojinova, S. Russev, *Annuire L'Universite Sofia, Faculte Chimie*, **98–99**, 73 (2006).

НАНОРАЗМЕРНИ КОМПОЗИТНИ ТЪНКИ ФИЛМИ ОТ ZnO/TiO_2 ЗА ФОТОКАТАЛИТИЧНИ ПРИЛОЖЕНИЯ

Ш. А. Сюлейман, Д. В. Райчев А. С. Божинова*,
Д. Ц. Димитров, К. И. Папазова

Лаборатория по наука и технология на наночастици, катедра Обща и неорганична химия, Факултет по химия и фармация, Софийски университет, София 1164, България

Постъпила февруари, 2013 г.; приета май, 2013 г.

(Резюме)

Представеното изследване е насочено към синтез, характеризиране и фотокаталитична активност на ZnO, TiO_2 и нанокомпозитни тънки филми от ZnO/TiO_2, отложени по метода на центробежно въртене (spin coating) от етанолни суспензии на търговските прахове метални оксиди, съдържащи стабилизираща добавка от полиетиленгликол. Избраното съдържание на ZnO в композитните проби е 90%. Фазовият състав и морфологията на ZnO, TiO_2 и смесените композитни тънки филми от ZnO/TiO_2 са характеризирани с рентгенова дифракция и сканираща електронна микроскопия. Фотокаталитичното поведение на получените филми е изпитано при фотоокислението на органичното азо багрило Оранжево II във воден разтвор при облъчване с ултравиолетова и видима светлина. Изследвано е и влиянието на броя на покритията върху ефективността на фоторазграждане на багрилото. Проведени са сравнителни фотокаталитични тестове с филми от чистите ZnO и TiO_2. Установено е, че филмите със съдържание на 90% ZnO и 3 покрития показват най-висока фотокаталитична ефективност под действието на ултравиолетова светлина.

AUTHOR INDEX

Abedini I., See Tabatabaee et al. 90
Adonyi R., Kirilova E.G., Vaklieva-Bancheva N.Gr., Systematic approach for designing and activities' scheduling of supply chain network.....288
Aidan A., See Dobrudzhaliev et al. 214
Alias Z., See Sidek et al. 93
Allen S.J., See Yaneva et al. 161
Al Nashef I.M, See Hayyan et al. 394
Andreeva L.A., See Petrov et al. ….....455
Angelov T., See Uzova et al. 560,575
Apostolov A.A., See Krasteva et al. 625
Ashrafi A. R., See Ghorbani et al. 5
Atanasova G., See Grigorova et al. 280
Atanassova-Vladimirova S., See Piroeva et al. ..494,510
Avramov I., See Avramova N., Avramov I 43
Avramova N., Avramov I.,Properties of nickel (II) doped silica xerogels. ….....43

Bachvarova-Nedelcheva A.D., See Iordanova et al. .485
Bachvarova-Nedelcheva A.D., See Stoyanova et al. 497
Bangov I.P., See Moskovkina et al. 9
Bojinova A.S., See Kaneva et al. 611,635
Bojinova A.S., See Krasteva et al. … 625
Bojinova A.S., See Siuleiman et al. … 649

Cheng F., See Mei et al. ….....385
Cherkezova R.Ts., See Mitova et al.....114
Chernev G. E., Todorova E. V., Djambazov S. P., Miranda Salvado I.M., Structure of hybrid materials containing natural and synthetic organic compounds 238
Chesnaud A., See Mladenova et al. 366
Chethan J., See Shubakar et al. 274
Christov C., See Kolev et al. 584
Crişan D.D., See Gabrovska et al. …….....617
Crişan M, See Gabrovska et al.....617

Davaajav Y., See Purevsuren et al. 157
Danalev D., See Marinkova et al. 530
Daskalova N., See Velitchkova et al.....229
Díaz-Cedillo F., See Figueroa-Valverde et al. 71,332
Dimitriev Y.B., See Iordanova et al.....485
Dimitrov D.T., See Kaneva et al.....611,635
Dimitrov D.T., See Siuleiman et al.....649
Dimitrov I., See Petkova et al 607,631
Dimowa L.T., Petrov S.L., Shivachev B.L., Natural and Zn exchanged clinoptilolite: *in situ* high temperature XRD study of structural behavior and cation positions, ...466
Dimowa L., Kossev K., Sbirkova H.I., Nikolova R.P., Shivachev B.L., Synthesis and crystal structure of oxonium 2,4,8,10-tetra-hydroxy-1,3,5,7,9,11-hexaoxa-2,4,6,8,10-penta-boraspiro [5.5]undecan-6-uide hydrate.....505
Dimowa L., Shivachev B., Petrov S., Design and application of a cost effective high temperature holder for *in-situ* powder X-ray diffraction experiments 479
Dimowa L., See Piroeva et al. 491,510
Dimowa L., See Tsvetanova et al.....522
Dimowa L., See Kossev et al. 543
Djambazov S. P., See Chernev et al. 568
Dobrovolska Ts., See Stefanova et al.....144,151
Dobrudzhaliev D., Nikolova D., Ivanov B., Aidan A., Optimal energy saving and management in antibiotics production 214
Dochev S., Penkova A., Retailleau P., Manolov I.,Synthesis and crystal structure of an ammonium salt of 4-hydroxy-3-[(2-oxo-2H-chromen-3-yl)-(3,4,5-trimethoxyphenyl)-methyl]chromen-2-one 301
Dochev St., Ströbele M., Meyer H.-J., Manolov I., Synthesis, crystal structure and theoretical study of two isomeric poly-substituted derivatives of 1,4-dihydropyridine 100

Edreva-Kardjieva R. M., See Gabrovska et al.....617
Exner G.K., See Krastev 411

Fathi A., See Refat et al.....250
Ferdov S., See Tsvetanova et al. 522
Figueroa-Valverde L., Díaz-Cedillo F., García-Cervera E., Pool Gómez., E., Rosas-Nexticapa M., López-Ramos M., Design and synthesis of two sulfathiazole derivatives using a three-component system. 332
Figueroa-Valverde L., Díaz-Cedillo F., García-Cervera E.., Pool-Gómez E., López-Ramos M., Design and Synthesis of *N*-[2- (2,3-dimethoxy-strychnidin-10-ylidenamino)-ethyl]-succinamic acid 4-allyl-2-methoxy-phenyl ester. 71

Gabrovska M.V., Edreva-Kardjieva R.M., Crişan D.D., Tenchev K.K., Nikolova D.A., Crişan M., Structure and reducibility of the mixed metal oxides obtained from Ni-Al layered double hydroxides. Catalytic activity in CO_2 methanation reaction. 617
García-Cervera E. See Figueroa-Valverde et al. ..71,332
Gavrilova R.Vl., Petkov R.I., Researches on the structure and properties of heat treated, nickel alloyed, molybdenum modified aluminum bronze.....644
Gegova R.D., See Iordanova et al. 485
Genadiev V.R., See Purevsuren et al.....157
Gentscheva G., See Nikolova et al. 244
Georgiev M., See Stefanova et al. 144,151
Gharib A., Khorasani B.R.H., Jahangir M., Roshani M., An efficient catalytic synthesis of 1,2-dihydro-1-aryl-3H-naphth[1,2-e][1,3]oxazin-3-one derivatives using silica supported Preyssler heteropolyacid, H14[NaP5W30O110]/SiO2 (50%) as a heterogeneous catalyst 59
Gharib A., Khorasani B.R.H., Jahangir M., Scheeren J.W., A convenient catalytic synthesis of 2*H*-indazolo[2,1-*b*]phthalazine-triones on reusable silica supported Preyssler heteropolyacid 64
Gharib A., Pesyan N.N., Jahangir M., Roshani M., Scheeren J.W., A catalytic crossed-aldol condensation of ketones with aromatic and non-aromatic aldehydes

by silica supported Preyssler heteropolyacids catalyst 314
Gharib A., Pesyan N. N., Khorasani B. R. H., Roshani M., Scheeren J. W., Silica-bonded *N*-propyl sulfamic acid: A recyclable catalyst for microwave-assisted synthesis of spirooxindoles via three-component reaction .. 371
Ghassemzadeh M., See Tabatabaee et al 90
Ghorbani M., Ashrafi A. R., Hemmasi M, Eccentric Connectivity Polynomial of C18*n*+10 Fullerenes 5
Glavchev I.K., See Purevsuren et al. 157
Gracheva I., See Kaneva et al. 611
Griesmar P., See Marinkova et al. 530
Grigorova E., Khristov M., Peshev P., Nihtianova D., Velichkova N., Atanasova G., Hydrogen sorption properties of a MgH_2 - V_2O_5 composite prepared by ball milling 280

Hadavi Moghadam B., Hasanzadeh M., Haghi A. K., On the contact angle of electrospun polyacrylonitrile nanofiber mat 169
Hadavi Moghadam B., See Hasanzadeh el al. 178
Haghi A. K., See Hadavi Moghadam et al. 169
Haghi A. K., See Hasanzadeh et al. 178
Haghi A. K., See Mohammadian 336
Hamta A., See Mobinikhaledi et al. 353
Harizanova R., Gugov Iv., Rüssel C., Novel catalyst of mixed SiO_2-TiO_2 supported tungsten for metathesis of ethene and 2-butene 84
Hasanzadeh M., Hadavi Moghadam B., Moghadam Abatari M. H., Haghi A. K, On the production optimization of polyacrylonitrile electrospun nanofiber 178
Hasanzadeh M., See Hadavi Moghadam el al. 169
Hashim M.A., See Hayyan et al. 394
Hayyan A., Mjalli F.S., Hashim M.A., Hayyan M., Al Nashef I.M, Conversion of free fatty acids in low grade crude palm oil to methyl esters for biodiesel production using chromosulfuric acid 394
Hemmasi M, See Ghorbani et al. 5
Hitkova H.Y., See Stoyanova et al. 497
Hourani M. K., Wehbeh A.I., Electrochemical characterization of Jordanian coins 347
Hristov P. I., See Sbirkova et al. 440
Hristov P.,.See Piroeva et al. 510
Hristova I.L., See Kralchevska et al. 131
Hosseinzadeh R., See Hosemi et al. 379
Huang G., See Mei et al. 385
Hubenova Y.V., Mitov M.Y., Electricity generation during sauerkraut fermentation process. 197

Ignatova K., Electrodeposition of Ag and Ag-Ni powders in potentiostatic and pulse potential modes 357
Iordanova R.S., Bachvarova-Nedelcheva A.D., Gegova R.D., Dimitriev Y.B., Synthesis and characterization of TeO_2/TiO_2 powders obtained through Te (Vi) acid 485
Iordanova R.S., See Stoyanova et al. 497
Ivanov B., See Dobrudzhaliev et al. 214
Ivanova E. See Nikolova et al. 244
Ivanova N.K., Se Stoyanova et al. 497
Ivanova Vl., See Zaidan et al. 554

Jahangir M., See Gharib et al. 59,64
Jain P.K., See Meena et al. 388
Kaneva N.V., Siuleiman S.A., Bojinova A.S., Papazova K.I., Dimitrov D.T., Gracheva I., Karpova S., Moshnikov V.A., Nanosized composite thin films of SiO_2-ZnO for photocatalytic decomposition of organic dyes – structure and characterization 611
Kaneva N.V., See Krasteva et al. 625
Kaneva N., Ponomareva A., Krasteva L., Dimitrov D., Bojinova A., Papazova K., Suchaneck G., Moshnikov V., Surface and photocatalytic properties of nanostructured ZnO thin films doped with iron.... 635
Karimipour G., Mousavinejad T., Biomimetic oxidative dehydrogenation of 1,4-dihydro-pyridines with m-chloroperoxybenzoic acid (m-CPBA) in the presence of tetraphenyl-porphyrinatoiron(III) chloride [Fe(TPP)Cl] 55
Karpova S., See Kaneva et al. 611
Karshikoff A. D., See Salamanova et al. 592
Khorasani B.R.H., See Gharib et al. 59,64,314,371
Khristov M.,, See Grigorova et al. 280
Kirilova E.G., See Adonyi et al. 288
Kirilova E.G., See Vaklieva-Bancheva. 47
Kokate S. J., Kuchekar S.R., Reverse phase extraction chromatography of rhodium(III) with N-n-octylaniline 37
Kolev H., Tyuliev G., Christov C., Kostov K.L., Experimental study of the surface chemical composition of sea salt crystallized during evaporation of seawater under natural conditions 584
Koleva K.V., Velinov N.I., Tsoncheva T.S., Mitov I.G., Kunev B.N., Preparation, structure and catalytic properties of $ZnFe_2O_4$ 434
Kossev K., Sbirkova H., Petrova N., Shivachev B., Nikolova R., Crystal structure and properties of urea and thiourea adducts of tetraalkyl ammonium hydrogen sulphate 446
Kossev K., Tsvetanova L., Dimowa L., Nikolova R., Shivachev B., Synthesis and crystal structure of magnesium chlorate dihydrate and magnesium chlorate hexahydrate 543
Kossev K., See Dimowa et al. 505
Kostov K. L., see Kolev et al. 584
Kostov-Kytin V., See Nikolova 418
Kostova B.V., Petrova N.L., Petkova V., The high energy milling effect on positional redistribution of CO_3-ions in the structure of sedimentary apatite 601
Kostova I.P., See Patronov et al. 536
Kotzev Il.V., See Purevsuren et al. 157
Koumanova B.K., See Yaneva et al. 161
Kovacheva D., See Markova-Velichkova et al. 427
Kozhukharov S., Machkova M., Kozhukharov V., Simeonov S.P., Evaluation of the potential application of $La_{2-x}Sr_xCuO_{4-\delta}$ and $Nd_{2-x}Sr_xNiO_{4-\delta}$ as alternative cathode materials for solid oxide fuel cells 207
Kozhukharov V., See Kozhukharov et al. 207
Kralchevska R.P., Milanova M.M., Hristova I.L., Todorovsky D.S., Some endocrine disrupting

compounds in the environment and possibilities for their removal and degradation 131
Krapchanska M., See Mladenova et al. 366
Krastev V., Exner G. K., 100 years of X-ray diffraction: from Röntgen's discovery to top-of-the-art synchrotron source applications 411
Krasteva L., See Kaneva et al. 635
Krasteva L.K., Papazova K.I., Bojinova A.S., Kaneva N.V., Apostolov A.A., Synthesis and characterization of ZnO and TiO_2 powders, nanowire ZnO and TiO_2/ZnO thin films for photocatalyc applications 625
Krushna Tripathy J., See Panda 77
Kuchekar S.R., See Kokate 37
Kumar N., See Meena et al 388
Kunev B.N., See Koleva et al. 434
Kuneva M., Surface phase detection of proton-exchanged layers in $LiNbO_3$and $LiTaO_3$ by IR reflection spectroscopy 474

Lasemi Z., Hosseinzadeh R., Tajbakhsh M., Mohadjerani M., Ethylene bis (N-methyl imidazolium) ditribromide: An efficient and reusable reagent for oxidation of thiols and sulfides 379
Lazarova Tz.I., See Petrov et al. 455
López-Ramos M. See Figueroa-Valverde et al. 71
López-Ramos M. See Figueroa-Valverde et al. 332

Machkova M., See Kozhukharov et al. 207
Maichle-Moessmer C.,See Manolov et al. 109,224
Manolov I., Maichle-Moessmer C., Synthesis and crystal structure of 4-hydroxy-3-[(3E)-3-(hydroxyimino)-1-(4-nitrophenyl)butyl]-2H-chromen-2-one 109
Manolov I., Maichle-Mössmer C., Crystal structures of two polysubstituted derivatives of cyclohexanone 224
Manolov I., See Dochev et al. 100,301
Marinkova D., Yotova L., Danalev D., Stoykov D., Ringeard J.-M., Michiel M., Serfaty S., Griesmar P., Investigation of newly synthesized biocompatible materials as biofilm carriers 530
Markov P., See Velitchkova et al. 229
Markova-Velichkova M., Veleva S., Tumbalev V., Stoyanov L., Nihtianova D., Mladenov M., Raicheff R., Kovacheva D., XRD and TEM characterization of the morphology of ZnO powders prepared by different methods 427
Meena A.S., See Meena et al. 388
Meena K.S., See Meena et al. 388
Meena P.L., Kumar N., Meena A.S., Meena K.S., Jain P.K., Calculation of atomic spectroscopic terms for f^2 and f^{12} orbital configuration, assigning the term symbols and comparative study 388
Mei X., Shu Sh., Cheng F., Huang G., Synthesis of di-N-acetyl-β-chitobiosyl N-glycothiazoline 385
Meyer H.-J. See Dochev et al. 100
Michiel M., See Marinkova et al. 530
Mihaleva S., See Uzova et al. 560,575
Mikli V., See Petrov et al. 455
Milanova M.M., See Kralchevska et al. 131
Milanova M.M., See Zaharieva et al. 32
Miletiev R., See Stefanova et al. 144,151
Miranda Salvado I.M., See Chernev et al. 568
Mitić, J.Lj., See Mitić et al. 26
Mitić S.S., Stojanović B.T., Stojković M.B., Mitić, J.Lj., Pavlović M.N., Total phenolics, flavonoids and antioxidant activity of different apple cultivars ...326
Mitov I.G., See Koleva et al. 434
Mitov M.Y., See Houbenova 197
Mitova V.A., Cherkezova R.Ts., Troev K.D., Chemical transformations of β-hydroxyethyl esters of n-2-hydroxyalkyl carbamic acids 114
Mjalli F.S., See Hayyan et al. 394
Mladenov M., See Markova-Velichkova et al. 427
Mladenova E., Vladikova D., Stoynov Z., Chesnaud A., Thorel A., Krapchanska M., Gases permeability study in dual membrane fuel cell 366
Mobinikhaledi A., Sasani F., Hamta A., Shariatzadeh S.M., Molecular iodine catalyzed synthesis of some biologically active dihydroperimidines 353
Moghadam Abatari M.H., See Hasanzadeh et al. 178
Mohadjerani M., See Lasemi et al. 379
Mohamed G.G., See Refat et al. 250
Mohammadian M., Haghi A. K., Some aspects of multilayer chitosan electrospun nanofibers web .. 336
Moshnikov V.A., See Kaneva et al. 611,635
Moskovkina M.N., Bangov I.P., Patleeva A.Zh., Retention modeling in gas chromatography by QSSR approach 9
Mousavinejad T., See Karimipour 55
Mozafari A.A., See Tabatabaee et al. 90

Nagaraj S., See Venkatram et al. 269
Nedkov V., See Petkova et al. 607
Netiworaruksa B., Phatanasri S., Praserthdam P., Phongsawat W., Suriye K., Propene yield enhancement from metathesis of ethene and 2-butene on mixed HBeta-alumina supported molybdenum-based catalysts using aluminum nitrate as alumina precursor 191
Nihtianova D., See Grigorova et al. 280
Nihtianova D., See Markova-Velichkova et al. 427
Nikolova D.A., See Gabrovska et al. 617
Nikolova D., See Dobrudzhaliev et al. 214
Nikolova R., See Tsvetanova et al. 522
Nikolova K., Gentscheva G., Ivanova E., Survey of the mineral content and some physico-chemical parameters of Bulgarian bee honeys 244
Nikolova L.V., Microstructure and texture analyses on spring steel. 549
Nikolova R., Kostov-Kytin V., Crystal chemistry of "glaserite" type compounds 418
Nikolova R., See Kossev et al. 446,543
Nikolova R.P., See Dimowa et al. 505

Pai V.K., See Venkatram et al. 269
Panda S., Krushna Tripathy J., A comparative study of inclusion complexes of substituted indole derivatives with β-cyclodextrin 77
Papazova K.I., See Kaneva et al. 611
Papazova K.I., See Krasteva et al. 625
Papazova K.I, See Siuleiman et al. 649

Patleeva A.Zh., See Moskovkina et al. 9
Patronov G.I., Kostova I.P., Tonchev D.T, Study of zinc borophosphate compositions doped with samarium and manganese. 536
Pavlović M.N., See Mitić S.S. 326
Penkova A., See Dochev et al. 301
Peshev P., See Grogorova et al. 280
Pesyan N.N., See Gharib et al. 314,371
Petkov P., See Zaidan et al. 554
Petkov R.I., See Gavrilova.....644
Petkova P., Nedkov V., Tacheva J., Vasilev P., Dimitrov I., The structural distortion and Zeeman splitting of the complexes $CrCl_2(H_2O)_4^{2+}$ and $Cr(H_2O)_6^{2+}$..... .607
Petkova P., Vasilev P., Dimitrov I., The behaviour of osmium ions in the tetrahedral oxygen coordination 631
Petkova V., See Kostova et al. 601
Petrov S.L., See Dimowa et al. 466,479
Petrov V.G., Terzieva S.D., Lazarova Tz.I., Mikli V., Andreeva L.A., Stoyanova-Ivanova A.K., Corrosive changes and chemical composition of the orthodontic archwires' surface during treatment. 455
Petrova N., See Piroeva et al.....491
Petrova N., See Kossev et al. 446
Petrova N.L., See Kostova et al. 601
Phatanasri S., See Netiworaruksa et al. 191
Phongsawat W., See Netiworaruksa et al. 191
Piroeva I., Atanassova-Vladimirova S., Dimowa L., Sbirkova H., Radoslavov G., Hristov P., Shivachev, B.L, A simple and rapid scanning electron microscope preparative technique for observation of biological samples: application on bacteria and DNA samples510
Piroeva I., Dimowa L., Atanasova-Vladimirova S., Petrova N., Shivachev B. L., Synthesis, structural and optical characterization of TeO_2–GeO_2–Nd_2O_3 glasses 491
Ponomareva A., See Kaneva et al. 635
Pool Gómez E. See Figueroa-Valverde et al..... 71,332
Popov A., See Uzova et al. 560,575
Pourvaghar M. J., Assessing the nano scale variation of the ferritin and iron level following two months of progressively increasing interval physical activity 296
Praserthdam P., See Netiworaruksa et al. 191
Purevsuren B., Davaajav Y., Genadiev V.R., Kotzev Il.V., Glavchev I.K., Investigation of the liquid tar product from the pyrolysis of yak-milk casein and its application in curing of epoxy resin 157

Radoslavov G., See Piroeva et al. 510
Radoslavov G. A., See Sbirkova et al. 440
Raicheff R., See Markova-Velichkova et al. 427
Raichev D.V., See Siuleiman et al. 649
Refat M.S., Mohamed G.G., Fathi A., Spectrophotometric determination of sildenafil citrate drug in tablets. Spectroscopic characterization of the solid charge transfer complexes 250
Retailleau P., See Dochev et al. 301
Reza Bozorgmehr M., See Reza Housaindokht M. et al. 201
Reza Housaindokht M., Sargolzaei M., Reza Bozorgmehr M., *Ab initio* study of ion replacement in Spinach plastocyanin protein 201
Reza Nateghi M., See Tabatabaee et al. 90
Ringeard J.-M., See Marinkova et al. 530
Rosas-Nexticapa M., See Figueroa-Valverde et al.... 332
Roshani M., See Gharib et al. 59,314,371

Salamanova E. K., Tsoneva D. T., Karshikoff A.D., Physical bases of thermal stability of proteins: A comparative study on homologous pairs from mesophilic and thermophilic organisms 592
Sargolzaei M., See Reza Housaindokht et al. 201
Sasani F., See Mobinikhaledi et al. .....
Sbirkova H.I., Radoslavov G.A., Hristov P.I., Shivachev B.L., Crystallographic conditions of the heterologically expressed recombinant metal-binding protein Ts-PCHTP. 440
Sbirkova H.I., See Dimowa et al. 505
Sbirkova H.I., See Kossev et al. 446
Sbirkova H., See Piroeva et al. 510
Scheeren J.W. See Gharib et al. 64,314,371
Serfaty S., See Marinkova et al. 530
Shariatzadeh S.M., See Mobinikhaledi et al. 353
Shivachev B.L., See Sbirkova et al. 440
Shivachev B., DHA, a program for calculating hydrogen atom coordinates of solvent atom involved in hydrogen bonding interactions 461
Shivachev B.L., See Dimowa et al. 466,479,505
Shivachev B.L., See Kossev et al. 446
Shivachev, B.L. See Piroeva et al. 491,510
Shivachev B., See Kossev et al. 543
Shu Sh., See Mei et al. 385
Shubakar K., Umesha K.B., Srikantamurthy N., Chethan J., Synthesis and antimicrobial evaluation of novel derivatives of 1,3,4-thiadiazine incorporated with pyrazole-4-carboxylic acid moiety. 274
Sidek N.A .A., Alias Z., Tayyab S., Gel chromatographic analysis of ficin under native and under denaturing conditions 93
Simeonov I., See Stefanova et al. 144,151
Simeonov S.P.,, See Kozhukharov et al. 207
Siuleiman S.A.**,** Raichev D.V., Bojinova A.S., Dimitrov D.T., Papazova K.I, Nanosized composite ZnO/TiO_2 thin films for photocatalytic applications. 649
Siuleiman S.A., See Kaneva et al. 611
Sredkova M.P, See Stoyanova et al. 497
Srikantamurthy N., See Shubakar et al.....274
Stefanova V., Dobrovolska Ts., Miletiev R., Georgiev M., Simeonov I., Investigation of electrode reactions in hydrogen peroxide alkaline medium onto Pt and Au electrodes by cyclic voltammetry - Part I 144
Stefanova V., Dobrovolska Ts., Miletiev R.,. Georgiev M., Simeonov I., Investigation of electrode reactions in hydrogen peroxide alkaline medium onto Co, In and Ni by cyclic voltammetry – Part II 151
Stojanović B.T., See Mitić et al.....326
Stojković M.B., See Mitić et al. 326
Stoyanov L., See Markova-Velichkova M. et al. 427

Stoyanova A.M., Hitkova H.Y., Ivanova N.K., Bachvarova-Nedelcheva A.D., Iordanova R.S., Sredkova M.P, Photocatalytic and antibacterial activity of Fe-doped TiO_2 nanoparticles prepared by non-hydrolytic sol-gel method 497
Stoyanova-Ivanova A.K., See Petrov et al. 455
Stoykov D., See Marinkova et al. 530
Stoynov Z., See Mladenova et al. 366
Ströbele M., See Dochev et al. 100,274
Suchaneck G., See Kaneva et al. 635
Suriye K., See Netiworaruksa et al. 191

Tabatabaee M., Mozafari A.A., Ghassemzadeh M., Reza Nateghi M., Abedini I., A simple method for synthesis of cadmium oxide nanoparticles using polyethylene glycol 90
Tacheva J., See Petkova et al. 607
Tajbakhsh M., See Lasemi et al. 379
Tayyab S., See Sidek et al. 93
Tenchev K.K., See Gabrovska et al. 617
Terzieva S.D., See Petrov et al. 455
Thorel A., See Mladonova et al. 366
Todorova E.V., See Chernev et al. 568
Todorovsky D.S., See Kralchevska et al. 131
Todorovsky D.S., See Zaharieva et al. 32
Tonchev D.T, See Patronov et al. 536
Troev K.D., See Mitova et al. 114
Tsoncheva T.S., See Koleva et al. 434
Tsoneva D.T., See Salamanova et al. 592
Tsvetanova L., See Kossev et al. 543
Tsvetanova L., Dimowa L., Ferdov S., Nikolova R., Crystal structures of Cs_+, Mg_{2+}, Ba_{2+} ion exchanged ETS-4 at RT and 150 K 522
Tumbalev V., See Markova-Velichkova M., et al. ... 427
Tyuliev G., See Kolev et al. 584

Umesha K.B., See Shubakar et al. 274
Uzov Ch., See Uzova et al. 560,575
Uzova S., Popov A., Velev V., Angelov T., Mihaleva S., Uzov Ch., Polycaprolactam crystal structure. I.Gamma–alpha polymorphic transition. 560
Uzova S., Popov A., Velev V., Angelov T., Mihaleva S., Uzov Ch., Polycaprolactam crystal structure. II. Crystal phase perfection 575
Vaklieva-Bancheva N.Gr., See Adonyi et al. 288
Vaklieva-Bancheva N.Gr., Kirilova E.G., Reduction of the impact of peak emissions of pollutants from multipurpose batch chemical and biochemical plants 47
Vasilev P., See Petkova et al. 607,631
Velev V., See Uzova et al. 560,575
Veleva S., See Markova-Velichkova et al. 427
Veleva O., See Velitchkova et al. 229
Velichkov S., See Velitchkova et al. 229
Velichkova N., See Grigorova et al. 280
Velinov N.I., See Koleva et al. 434
Velitchkova N., Veleva O., Velichkov S., Markov P., Daskalova N., Determination of As, Zn, Pt, B, Hg, Cd, Tl and U in environmental materials by high resolution radial viewing 40.68 MHz inductively coupled plasma optical emission spectrometry (ICP-OES) 29
Venkatram R., Pai V.K., Nagaraj S., Novel enantioselective synthesis and dissolution studies on enteric coated pellets of (*S*)-duloxetine hydrochloride 269
Vladikova D., See Mladenova et al. 366

Wehbeh A.I., See Hourani. 347

Yancheva D.Y., Characterization of the structure, electronic conjugation and vibrational spectra of the radical anions of p- and m-dinitrobenzene: a quantum chemical study 24
Yaneva S., See Yotova 516
Yaneva Z.L., Koumanova B.K., Allen S.J., Applicability comparison of different kinetic/diffusion models for 4-nitrophenol sorption on Rhizopus oryzae dead biomass 161
Yavari M., Permutation symmetry of fullerene isomers of C82 310
Yotova L., See Marinkova et al. 530
Yotova L., Yaneva S., Silica-based hybrid materials as biocompatible coatings for xenobiotics sensors 516

Zaharieva J.Ts., Milanova M.M., Todorovsky D. S., Some limitations using optical sensors for determination of dissolved oxygen in wine 32
Zaidan A., Ivanova Vl., Petkov P., Ab initio simulation of crystallization of amorphous Ge–Te–In system ... 554

АВТОРСКИ УКАЗАТЕЛ

Абедини И., Виж Табатабае и др. 92
Аврамов И., Виж Аврамова 46
Аврамова Н., И. Аврамов, Свойства на никел (II) дотирани ксерогели 46
Адоньи Р., Е.Г. Кирилова, Н.Гр. Ваклиева-Банчева, Редуциране на пиковите въздействия от замърсители върху околната среда за многоцелеви периодични и биохимични производства 295
Айдан А., Виж Добруджалиев и др. 223
Алиас З., Виж Сидек и др. 213
АлНашеф И.М., Виж Хайян и др. 399
Алън С.Д., Виж Янева и др. 168
Амролахи М.А., Виж Мобинихаледи и др. 356
Ангелов Т., Виж Узова и др. 567,583
Андреева Л.А., Виж Петкова и др. 460
Апостолов А.А., Виж Кръстева и др. 630
Атанасова Г., Виж Григорова и др. 287
Атанасова-Владимирова С., Виж Пироева и др. ... 496,515
Ашрафи А.Р., Виж Гхорбани и др. 5

Бангов И.П., Виж Московкина и др. 23
Бодаги Фард М.А., Виж Мобинихаледи и др. 356
Божинова А.С., Виж Кънева и др. 616,643
Божинова А.С., Виж Кръстева и др. 630
Божинова А.С., Виж Сюлейман и др. ..... .634
Бъчварова-Неделчева А.Д.,Виж Йорданова и др. 490
Бъчварова-Неделчева А.Д.,Виж Стоянова и др. .. 509

Ваклиева-Банчева Н.Гр., Е.Г. Кирилова, Редуциране на пиковите въздействия от замърсители върху околната среда за многоцелеви периодични химични и биохимични производства 54
Ваклиева-Банчева Н.Гр., Виж Адоньи и др. 295
Василев П., Виж Петкова и др. ..... .610,634
Велев В., Виж Узова и др. 567,583
Велева О., Виж Величкова и др. 243
Велева С., Виж Маркова-Величкова и др. 433
Велинов Н.И., Виж Колева и др. 439
Величков С., Виж Величкова и др. 243
Величкова Н., Виж Григорова и др. 287
Величкова Н., О. Велева, С. Величков, П. Марков, Н. Даскалова, Определяне на As, Zn, Pt, B, Hg, Cd, Tl и U в проби от околната среда чрез оптична емисионна спектрометрия с индуктивни свързана плазма с радиално наблюдение и високо разделяне 243
Венкатрам Р., В.К. Паи, С. Нагарадж, Нова енантиоселективна синтеза и разтваряне на филмови таблетки от (S)-дулоксетин хидрохлорид с ентеро-приложение 273
Владикова Д., Виж Младенова и др. 370

Гаврилова Р., Р. Петков, Изследване на структурата и свойствата след термично обработване на медно-алуминиеви сплави, допълнително легирани с Ni и модифицирани с Mo..... 648
Габровска М. В., Р. М. Едрева-Кърджиева, Д. Д. Кришан, К. К. Тенчев, Д. А. Николова, М. Кришан, структура и редуцируемост на смесени метални оксиди, получени от Ni-Al слоисти двойни хидроксиди. каталитична активност в реакцията на метаниране на CO_2 624
Гариб А., Б.Р.Х .Кхорасани, М. Джахангир, М. Рошани, Ефективен каталитичен синтез на 1,2-дихидро-1-арил-3H-нафт[1,2-E][1,3] оксазин-3-он производни при използване на хетерополи-киселина върху носител силициев диоксид $H_{14}[NAP_5W_{30}O_{110}]/SiO_2$ (50%) като Preissler-ов хетерогенен катализатор..... 63
Гариб А., Б.Р.Х. Кхорасани, М. Джахангир, Й.В. Схеерен, Удобен каталитичен синтез на 2 n-индазоло[2,1-B]фталазин-три-они върху възобно-вяема Preyssler-ова хетерополи-киселина върху силициев диоксид..... 70
Гариб А., Н.Н. Песян М. Джахангир, М. Рошани, Й. В. Схеерен,. Кръстосана алдолна кондензация на кетони с ароматни и не-ароматни алдехиди с Preyssler‘ов хетерокиселинен катализатор върху силициев диоксид като носител..... 325
Гариб А., Н.Н. Песян, Б.Р.Х. Кхорасани, М. Рошани, Й.В. Схеерен, N-пропил-сулфаминова киселина, свързана със силициев диоксид: рециклируем катализатор за синтеза на спиро-оксиндоли чрез три-компонентна реакция, стимулирана от микровълни 378
Гарсия-Сервера, Е. Виж Фигероа-Валверде и др. 76,335
Гасемзаде М., Виж Табатабае и др. 92
Гегова Р.Д.,Виж Йорданова и др. 490
Генадиев В.Р., Виж Пуревсурен и др. 160
Генчева Г., Виж Николова и др. 249
Георгиев М., Виж Стефанова и др. 150,156
Главчев И.К., Виж Пуревсурен и др. 160
Грачева И., Виж Кънева и др. 616
Гриесмар П., Виж Маринкова и др. 535
Григорова Е., М. Христов, П. Пешев, Д. Нихтянова, Н. Величкова, Г. Атанасова, Сорбционни свойства по отношение на водород на композит MgH_2 - V_2O_5 получен чрез механоактивиране 287
Гугов И., Виж Харизанова и др. 89
Гхорбани М., А.Р. Ашрафи, М. Хемаси, Полином на ексцентрична свързаност на фулерени 5

Даваажав И., Виж Пуревсурен и др. 160
Даналев Д., Виж Маринкова и др. 535
Димитриев Я.Б., Виж Йорданова и др. 490
Димитров Д.Т., Виж Кънева и др. 616,643
Димитров Д.Ц., Виж Сюлейман и др. 634
Димитров И., Виж Петкова 610,634
Даскалова Н., Виж Величкова и др. 243
Джайн П.К., Виж Меена и др. 393
Джамбазов С.П., ВижЧернев и др. 574
Джахангир М., Виж Гариб и др. 63,70,325
Диас-Седийо Ф., Виж Фигероа-Валверде и др.... 76,335
Димова Л.Т., С.Л. Петров, Б.Л. Шивачев, Природен и Zn обменен клиноптилолит: in situ високотемпературно прахово рентгено-структурно изследване на поведението на структурата и катионните позиции. 473
Димова Л. Т., С.Л. Петров, Б.Л. Шивачев, Дизайн и приложение на лесна за направа високо-температурна приставка подходяща за *in-situ* прахови рентгенодифракциони изследвания ... 484
Димова Л., К. Косев, Х.И. Сбиркова, Р.П. Николова, Б.Л. Шивачев, синтез и кристална структура на оксониев 2,4,8,10-тетрахидрокси-1,3,5,7,9,11-хексаокса-2,4,6,8,10-пента-биспиро[5.5]ундекан-6-оид хидрат 509
Димова Л.Т., Виж Косев и др. 548
Димова Л., Виж Пироева и др. 496,515
Димова Л., Виж Цветанова и др. 529
Доброволска Ц., Виж Стефанова и др. 150,156
Добруджалиев Др., Д. Николова, Б. Иванов, А. Айдан, Оптимално управление потреблението на енергията при производството на антибиотици 223
Дочев С.М., М. Щрьобеле, Х.Ю. Майер, И. Манолов, Синтеза, структура и теоретично изследване на две изомерни поли-заместени производни на 1,4-дихидропиридин 108

Дочев С., А. Петкова, П. Ретайльо, И. Манолов, Синтез и кристална структура на амониева сол на 4-хидрокси-3-[(2-оксо-2H-хромен-3-ил)-(3,4,5-триметоксифенил)метил] хромен-2-он 309

Едрева-Кърджиева Р.М., Виж Габровска и др. 614
Екснер Г., Виж Кръстев 417

Зайдан А., Вл. Иванова, П. Петков, *Ab initio* симулация на кристализацията на аморфни образци от системата Ge–Te–In 559
Захариева Й. Цв., М. М. Миланова, Д. Ст. Тодоровски, Някои ограничения при използване на оптични сензори за определяне на разтворен във вино кислород.....

Иванов Б., Виж Добруджалиев и др. 223
Иванова Вл., Виж Зайдан и др. 559
Иванова Е., Виж Николова и др. 249
Иванова Н.К., Виж Стоянова и др.....509
Игнатова К., Електроотлагане на Ag и на Ag-Ni прахове в стационарен и в импулсен режим ... 365

Йорданова Р.С., Виж Стоянова и др. 509
Йорданова Р.С., А.Д. Бъчварова-Неделчева, Р.Д. Гегова, Я.Б. Димитриев, Синтез и характеризиране на TeO_2/TiO_2 прахове получени от Te(VI) киселина 490
Йотова Л., С. Янева, Хибридни материали на основата на силициев диоксид като биосъвместими покрития при биосензори за ксенобиотици..... 521
Йотова Л., Виж Маринкова и др 535

Каримипур Г., Т. Мусавинеджад, Сравнително изследване комплекси на включване на заместените индол деривати с β- циклодекстрин .. 58
Карпова С., Виж Кънева и др 616
Кирилова Е.Г, Виж Ваклиева-Банчева..... 54
Кирилова Е.Г., Виж Адоньи и др. 295
Ковачева Д., Виж Маркова-Величкова и др. 433
Кожухаров В., Виж Кожухаров и др. 213
Кожухаров С., М. Мачкова, В. Кожухаров, С. П. Симеонов, Изследване и оценка на потенциалното приложение като алтернативни катодни материали за твърдоокисни горивни клетки на $La_{2-x}Sr_xCuO_{4-\delta}$ и $Nd_{2-x}Sr_xNiO4-\delta$ 213
Кокате С.Дж., С.Р. Кучекар, Обратнофазова екстракционна хроматография на родий(III) с N-n-октиланилин 42
Колев Х., Г. Тюлиев, Х. Христов, К. Костов, експериментално изследване на химическия състав на повърхността на морска сол, получена при изпарение на морска вода в естествени условия. 591
Колева К.В., Н.И. Велинов, Т.С. Цончева, И Г. Митов, Б.Н. Кунев, Синтез, структура и каталитични свойства на $ZnFe_2O_4$..... 439
Косев К., Х. Сбиркова, Н. Петрова, Б. Шивачев, Р. Николова, Кристална структура и свойства на уреа и тиоуреа адукти на тетраетил амониев хидроген-сулфат 454
Косев К., Виж Димова и др. 509
Косев К., Л. Цветанова, Л.Т. Димова, Р. Николова, Б.Л. Шивачев, Синтез и кристална структура на магнезиев хлорат дихидрат и магнезиев хлорат хексахидрат 548
Костов К., Виж Колев и др. 591
Костов-Китин В., Виж Николова.....426
Костова Б.В., Н.Л. Петрова, В. Петкова, Ефект от интензивно енергийно смилане върху преразпределение на карбонатните йони в структурата на седиментен апатит.....606
Костова И.П., Виж Патронов и др. 542
Коцев Ил.В., Виж Пуревсурен и др. 160
Кралчевска Р.П., М.М. Миланова, Ил.Л. Христова, Д.Ст. Тодоровски, Някои съединения с ендокринно въздействие в околната среда и възможностите за тяхното отстраняване/разграждане 143
Кришан М., Виж Габровска и др. 624
Кришан Д. Д., Виж Габровска и др. 624
Крушна Трипати Дж., Виж Панда 83
Кръпчанска М., Виж Младенова и др. 370
Кръстев В., Г. Екснер, 100 години рентгенова дифракция: от откритието на Рьонтген до модерните приложения на синхротронните източници. 41
Кръстева Л.К., К.И. Папазова, А.С. Божинова, Н.В. Кънева, А.А. Апостолов, Синтез и характеризиране на прахове от ZnO и TiO_2, тънки филми от ZnO наножички и TiO_2/ZnO за фотокаталитични приложения.....630
Кръстева Л., Виж Кънева и др. 643
Куманова Б.К., Виж Чнева и др. 168
Кумар Н., Виж Меена и др. 393
Кунев Б.Н., Виж Колева и др. 439
Кучекар С.Р., Виж Кокате 42
Кхорасани Б.Р.Х., Виж Гариб и др. 63,76,378
Кънева М., Определяне на повърхнинната фаза на протонно-обменени слоеве в $LiNbO_3$ и $LiTaO_3$ чрез отражателна ИЧ-спектроскопия.....478
Кънева Н.В.,Виж Кръстева и др. 630
Кънева Н.В., С.А. Сюлейман, А.С. Божинова, К.И. Папазова, Д.Т. Димитров, И. Грачева, С. Карпова, В.А. Мошников, наноразмерни композитни тънки филми от SiO2–ZnO за фотокаталитично разлагане на органични багрила–структура и характеризиране.....616
Кънева Н., А. Пономарева, Л. Кръстева, Д. Димитров, А. Божинова, К. Папазова, Г. Сучанек, В. Мошников, повърхностни и фотокаталитични свойства на дотирани с желязо наноструктурирани тънки филми от ZnO.....643
Кършиков А.Д., Виж Саламанова и др. 600

Лазарова Ц.И., Виж Петкова и др. 460
Ласеми З., Р. Хосеинзаде, М. Таджбакш, М. Мохаджерани, Етилен бис-(N-метил имидазол) ди-

трибромид: ефективен и многократно използван реагент за окислението на тиоли и сулфиди... 384
Лопес-Рамос М., Виж Фигероа-Валверде и др. 76,335

Майер Х.Ю., Виж Дочев и др. 108
Майхле-Мьосмер Ц., Виж Манолов..... 113,228
Манолов И., Виж Дочев и др. 108 Манолов И., Виж Дочев и др. 309
Манолов И., Ц. Майхле-Мьосмер, Синтеза и кристална структура на 4-хидрокси-3-[(3E)-3-(хидроксиимино)-1-(4-нитрофенил)бутил]-2H-хромен-2-он. 113
Манолов Ил., Ц. Майхле-Мьосмер, Кристални структури на две полисубституирани производни на циклохексанона 228
Маркова-Величкова М., С. Велева, В. Тумбалев, Л. Стоянов, Д. Нихтянова, М. Младенов, Р. Райчев, Д. Ковачева, Рентгенографско и TEM характеризиране на морфологията на прахообразен ZnO, получен по различни методи 433
Маринкова Д., Л. Йотова, Д. Даналев, Д. Стойков, Ж. Ринджерард, М. Мишел, С. Серфати, П. Гриесмар, Изследвания върху новосинтезирани биосъвместими материали като носители за биофилми 535
Марков П., Виж Величкова и др. 243
Мачкова М., Виж Кожухаров и др. 213
Мджали Ф.С., Виж Хайян и др. 399
Меена А.С., Виж Меена и др. 393
Меена, К.С. Виж Меена и др. 393
Меена П.Л., Н. Кумар, А.С. Меена, К.С. Меена, П.К. Джайн, Изчисляване на атомни спектроскопски термове за f2 и f12орбитални конфигурации чрез сравнително изследване и символи на термовете 393
Мей Кс., Ш. Шу, Ф. Ченг, Г. Хуанг, Синтеза на ди- N-ацетил-β-хитобиозил N-гликотиазолин 387
Микли В.,Виж Петкова и др. 460
Миланова М.М., Виж Захариева и др. 36
Миланова М. М., Виж Кралчевска и др. 143
Милетиев Р., Виж Стефанова и др. 150,156
Миранда Салвадо И.М., Вуж Чернев и др……...574
Митич М.Н., Виж Митич и др. 331
Митич С.С., Б.Т. Стоянович, М.Н. Стойкович, М.Н. Митич, Й.Л. Павлович, Общи феноли, флавоноиди и антиоксидантна активност на различни ябълкови сортове 331
Митов И. Г., Виж Колева и др. 439
Митов М.Й., Виж Хубенова..... 200
Митова В.А., Р.Ц. Черкезова, К.Д. Троев, Химични трансформации на β-хидроксиетилови естери на n-2-хидроксиалкил карбаминови киселини 120
Михалева С., Виж Узова и др. 567,583
Мишел М., Виж Маринкова и др. 535
Младенов М., Виж Маркова-Величкова и др. 433
Младенова Е., Д. Владикова, З. Стойнов, А. Чесно, А. Торел, М. Кръпчанска, Изследване на газовата пропускливост в двойно мембранна горивна клетка. 370
Мобинихаледи А., М.А. Бодаги Фард, Ф. Сасани, М.А. Амролахи, Синтеза на някои биологично-активни дихидропиримидини, катализирани от молекулен йод 356
Могадам Абатари М.Х., Виж Хасанзаде и др. 190
Мохаджерани М., Виж Ласеми и др. 384
Мозафари А.А., Виж Табатабае и др. 92
Московкина М.Н., И.П. Бангов, А.Ж. Патлеева, Моделиране на газхроматографско задържане с помощта на хемометричен подход..... 23
Мохамадиан М., А. К. Хаги, Някои аспекти на мрежа от многослойни хитозанови нановлакна, получени при електропредене 346
Мохамед Г.Г., Виж Рефат и др. 258
Мошников В.А., Виж Кънева и др. 616,643
Мусавинеджад Т., Виж Каримипур 58

Нагарадж С., Виж Венкатрам и др..... 273
Недков В., Виж Петкова и др…. 610
Нетиворарукса Б., С. Фатанасри, П. Прасертдам, В. Фонгсават, К. Сурийе, Ускоряване на превръщането на пропен чрез прегрупиране на етилен и 2-бутен върху смесен катализатор на основата на молибден, нанесен върху Hß-алуминиев триоксид, получен от алуминиев нитрат 196
Николова Д., Виж Добруджалиев и др. 223
Николова Д.А., Виж Габровска и др..... 624
Николова Л.В., Микроструктурни и текстурни анализи на пружинна стомана 553
Николова К., Г. Генчева, Е. Иванова, Преглед на минералното съдържание и физико-химичните параметри на български пчелен мед 249
Николова Р., В. Костов-Китин,Кристалохимия на съединения с “glaserite”тип структура..... 426
Николова Р.П., Виж Димова и др. 509
Николова Р., Виж Косев и др. 454,548
Николова Р., Виж Цветанова и др. 529
Нихтянова Д., Виж Григорова и др. 287
Нихтянова Д., Виж Маркова-Величкова и др. 433

Павлович Й.Л., Виж Митич и др. 331
Паи В.К., Виж Венкатрам и др..... 273
Панда С., Дж. Крушна Трипати, Сравнително изследване комплекси на включване на замес-тените индол деривати с β-циклодекстрин 83
Папазова К.И., Виж Кръстева и др. 630
Папазова К.И., Виж Кънева и др. 616,643
Папазова К.И., Виж Сюлейман и др. 634
Патлеева А.Ж., Виж Московкина и др. 23
Патронов Г.И., И.П. Костова, Д.Т. Тончев, изследване на цинк-бор-фосфатни композиции, дотирани със самарий и манган 542
Песян Н.Н., Виж Гариб и др. 325,378
Петков П., Виж Зайдан и др. 559
Петков Р., Виж Гаврилова 648
Петкова А., Виж Дочев и др. 309
Петкова В., Виж Костова и др. 606
Петкова П., В. Недков, Й. Тачева, П. Василев, И. Димитров, Структурна деформация и зееманово

разцепване на комплексите $CrCl_2(H_2O)_4^{2+}$и $Cr(H_2O)_6^{2+}$ 610
Петкова П., П. Василев, И. Димитров, Поведение на осмиеви йони в тетраедрично кислородно обкръжение 634
Петров В.Г., С.Д. Терзиева, Ц.И. Лазарова, В. Микли, Л.А. Андреева, А.К. Стоянова-Иванова, Корозионни промени в химичния състав на повърхността на ортодонтски дъги при използването им за лечение 460
Петров С.Л., Виж Димова и др. 473,486
Петрова Н., Виж Косев и др. 454
Петрова Н., Виж Пироева и др. 496
Петрова Н.Л., Виж Костова и др. 606
Пешев П., Виж Григорова и др. 287
Пироева И., Л. Димова, С.Атанасова-Владимирова, Н.Петрова, Б.Шивачев, Синтез, структурна и оптична характеристика на TeO_2-GeO_2-Nd_2O_3 стъкла 496
Пироева И., С.Атанасова-Владимирова, Л.Т. Димова, Х.И. Сбиркова, Г. Радославов, П. Христов, Б.Л. Шивачев, Бърза и опростена препаративна процедура на биологични проби, позволяваща последваща визуализация чрез сканираща електронна микроскопия 515
Поол Гомес Е., Виж Фигероа-Валверде и др. . 76,335
Попов А., Виж Узова и др. 567,583
Пономарева А.. Виж Кънева и др. 643
Прасертдам, П. Виж Нетиворарукса и др. 196
Пуревсурен Б., И. Даваажав, В. Р. Генадиев, Ил.В. Коцев, И. К. Главчев, Изследване на течният катранен продукт от пиролиз на казеин от мляко на як и неговото приложение при втвърдяване на епоксидна смола 160
Пурвагар М. Дж., Определяне на нивата на феритин и на желязо в наномащаби след двумесечно прогресивно физическо натоварване..... 300

Радославов Г., Виж Сбиркова и др. 445
Радославов Г., Виж Пироева и др. 515
Райчев, Д.В., Виж Сюлейман и др. 634
Райчев Р., Виж Маркова-Величкова и др. 433
Реза Бозоргмер М., Виж Реза Хусаиндокт и др. .. 206
Реза Натеги М., Виж Табатабае и др. 92
Реза Хусаиндокт М., М. Сарголзаеи, М. Реза Бозоргмер, *Ab initio*-изследване на заместването на йони в протеина пластоцианин в спанака 206
Ретайльо П., Виж Дочев и др. 309
Рефат М.С., Г.Г. Мохамед, А. Фатхи, Спектрофотометрично определяне на силденафил цитрат в таблетки. Спектрофотометрично определяне на твърди комплекси с пренос на заряда 258
Ринджерард Ж., Виж Маринкова и др 535
Росас-Нехтикапа М., Виж Фигероа-Валверде и др. 335
Рошани М., Виж Гариб и др. 63,325,378
Рюсел К., Виж харизанова и др. 89

Саламанова Е.К., Д.Т. Цонева, А.Д. Кършиков, Физични основи на термичната устойчивост на протеини: сравнително изследване на хомоложни двойки от мезофилни и термофилни организми 600
Сарголзаеи М., Виж Реза Хусаиндокт и др. 206
Сасани Ф., Виж Мобинихаледи и др. 356
Сбиркова Х.И., Виж Димова и др. 509
Сбиркова Х.И., Виж Косев и др. 454
Сбиркова Х.И., Виж Пироева и др. 515
Сбиркова Х.И., Г.А. Радославов, П.И. Христов, Б.Л. Шивачев, Кристализационни условия на хетероложно експресиран рекомбинантен металосвързващ белтък Ts-PCHTP 445
Серфати С., Виж Маринкова и др. 535
Сидек Н. А. А., З. Алиас, С. Таййаб, Гел - хроматографски анализ на фицин при естествени условия и при денатуриране 99
Симеонов И., Виж Стефанова и др. 150,156
Симеонов С.П., Виж Кожухаров и др. 213
Срикантамурти Н., Виж Шубакар и др. 279
Стефанова В., Ц. Доброволска, Р. Милетиев, М. Георгиев, И. Симеонов, Изследване на електродни реакции на водороден пероксид в алкална среда върху Pt и Au електроди чрез циклична волтамперометрия – част I 150
Стефанова В., Ц. Доброволска, Р. Милетиев, М. Георгиев, И. Симеонов, Изследване на електродни реакции върху Co, In и Ni алкален разтвор на водороден пероксид чрез циклична волтамперометрия – част II 156
Стойков Д., Виж Маринкова и др. 535
Стойкович М.Н., Виж Митич и др 331
Стойнов З., Виж Младенова и ср 370
Стоянов Л., Виж Маркова-Величкова и др 433
Стоянова А.М., Х.Й. Хиткова, Н.К. Иванова, А.Д. Бъчварова-Неделчева, Р.С. Йорданова, М.П. Средкова, фотокаталитична и антибактериална активност на дотирани с желязо TiO_2 наночастици, получени по нехидролитичен зол-гел метод 504
Стоянова-Иванова А.К., Виж Петкова и др 460
Стоянович Б.Т., Виж Митич и др 331
Средкова М.П., Виж Стоянова и др. 509
Сурийе К., Виж Нетиворарукса и др. 196
Сучанек Г., Виж Кънева и др. 643
Схеерен Й.В., Виж Гариб и др. 70,325,378
Сюлейман С.А., Виж Кънева и др. 616
Сюлейман Ш.А., Д.В. Райчев, А.С. Божинова, Д.Ц. Димитров, К.И. Папазова, Наноразмерни композитни тънки филми от ZnO/TiO_2 за фотокаталитични приложения 654

Табатабае М., А.А. Мозафари, М. Гасемзаде, М. Реза Натеги, И. Абедини, Прост метод за синтеза за синтеза на наночастици от кадмиев оксид при използването на полиетиленгликол 92
Таджбакш М., Виж Ласеми и др. 384
Таййаб С., Виж Сидек и др. 213
Тачева Й., Виж Петкова и др. 610
Тенчев К. К., Виж Габровска и др. 624
Терзиева С.Д.,Виж Петров и др. 460
Тодорова Е.В., Виж Чернев и др. 574
Тодоровски Д.Ст., Виж Захариева и др. 36

Тодоровски Д.Ст., Виж Кралчевска и др. 143
Торел А., Виж Младенова и др. 370
Троев К.Д., Виж Митова и др. 120
Тумбалев В., Виж Маркова-Величкова и др. 433
Тюлиев Г., Виж Колев и др. 591

Уехбе А.И., Виж Хурани.....352
Узов Х., Виж Узова и др. 567,583
Узова С., А. Попов, В. Велев, Т. Ангелов, С. Михалева, Х. Узов, кристална структура на поликапролактама. I. Гама–алфа полиморфен преход.....567
Узова С., А. Попов, В. Велев, Т. Ангелов, С. Михалева, Х. Узов, кристална структура на поликапролактама. II. Съвършенство на кристалната фаза 583
Умеша К.Б., Виж Шубакар и др. 279

Фатанасри С., Виж Нетиворарукса и др. 196
Фатхи А.,Виж Рефат и др. 258
Фердов С., Виж Цветанова и др. 529
Фигероа-Валверде М.Л., Ф. Диас-Седийо, Е. Гарсия-Сервера, Е. Поол Гомес, М. Лопес-Рамос, Дизайн и синтез на 4-алил-2-метокси-фенил естер на N-[2-(2,3-диметокси-стрихнин-10-илиден амино)етил] аминоянтарна киселина 76
Фигероа-Валверде М.Л., Ф. Диас-Седийо, Е. Гарсия-Сервера, Е. Поол Гомес, М. Росас-Нехтикапа, М. Лопес-Рамос, Конструиране и синтеза на две производни на сулфотиазола в три-компонентна система.....335
Фонгсават В., Виж Нетиворарукса и др. 196

Хаги А.К., Виж Хадави Могадам и др. 177
Хаги А.К., Виж Хасанзаде и др. 190
Хаги А.К., Виж Мохамадиан 346
Хадави Могадам Б., М. Хасанзаде, А.К. Хаги, Относно контактия ъгъл с подложката на електропредени влакна от поли-акрилонитрил 177
Хадави Могадам Б., Виж Хасанзаде и др 190
Хайян А., Ф.С. Мджали, М.А. Хашим, М. Хайян, И.М. АлНашеф, Използването на хлор-сулфонова киселина за превръщане на свободните мастни киселини от ниско-качествено палмово масло в метилови естери при производството на биодизел 399
Хайян М., Виж Хайян и др. 399
Харизанова Р., И. Гугов, К. Рюсел, Кристализация и магнитни свойства на стъкла от натриев силикат, съдържащи железни и манганови окиси 89
Хасанзаде М., Виж Хадави-Могадам и др. 177
Хасанзаде М., Б. Хадави Могадам, М.Х. Могадам Абатари, А.К. Хаги, Относно оптимизацията на производството на електропредени нановлакна от полиакриламид 190
Хашим М.А., Виж Хайян и др.. 399
Хемаси М., Виж Гхорбани и др. 5
Хиткова Х.Й., Виж Стоянова и др. .....
Хосеинзаде Р., Виж Ласеми и др. 384
Христов М., Виж Григорова и др. 287
Христов П., Виж Сбиркова и др. 445
Христов П., Виж Пироева и др. 515
Христов Х., Виж Колев и др. 591
Христова Ил.Л., Виж Кралчевска и др. 143
Хуанг Г., Виж Мей и др. 387
Хубенова Й.В., М.Й. Митов, Генериране на електричество по време на ферментация на зеле 200
Хурани М. К., А. И. Уехбе, Електрохимично охарактеризиране на йордански монети 352

Цветанова Л., Виж Косев и др. 548
Цветанова Л., Л. Димова, С. Фердов, Р. Николова, Кристални структури на Cs^{+}, Mg^{2+}, Ba^{2+} йонно обменени образци на ETS-4 при стайна (290 K) и ниска температура (150 K).....529
Цонева Д.Т., Виж Саламанова и др. 600
Цончева Т.С., Виж Колева и др. 439

Ченг Ф., Виж Мей и др. 387
Четхан Дж., Виж Шубакар и др. 279
Черкезова Р.Ц., Виж Митова и др. 120
Чернев Г.Е., Е.В. Тодорова, С.П. Джамбазов, И.М. Миранда Салвадо, структура на хибридни материали, съдържащи естествени и синтетични органични съединения 574
Чесно А., Виж Младенова и др. 370
Шивачев Б., DHA-програма за изчисляване на координатите на водороден атом към атом разтворител, участващ във водородна връзка..465
Шивачев Б.Л., Виж Димова и др.....73,486,509
Шивачев Б.Л., Виж Косев и др.....454,548
Шивачев Б.Л., Виж Пироева и др. 496,515
Шивачев Б.Л., Виж Сбиркова и др. 445
Шу Ш., Виж Мей и др…. 387
Шубакар К., К.Б. Умеша, Н. Срикантамурти, Дж. Четхан, Синтеза и антимикробни свойства на нови производни на 1,3,4-тиадиазин включени в среда от пиразол-4-карбонова киселина 279

Щрьобеле, М., Виж Дочев и др. 108

Явари М., Пермутационна симетрия на изомери на фулерен с 82 въглеродни атома. 313
Янева З.Л., Б.К. Куманова, С.Д. Алън, Сравняване на приложимостта на различни кинетични/дифузионни модели за сорбция на 4-нитрофенол върху мъртва биомаса Rhizopus oryzae. 168
Янева С., Виж Йотова 521
Янчева Д.Я., Охарактеризиране на структурата, електронното спрежение и вибрационните спектри на радикал-анионите на p- и m-динитробензен: теоретично изследване 31

SUBJECT INDEX

1,4-Dihydropyridines; Synthesis; DFT, HF, AM1 and PM3 Study 100
2,4-Diacetyl-5-hydroxy-5-methyl-3-(4-nitrophenyl)-cyclohexanone, 2,4-Diacetyl-3-(4-fluorophenyl)-5-hydroxy-5-methylcyclohexanone, 1,3-dicarbonyl compounds, crystal structure, aldol condensation reaction 224
2-Amino-1,3,4-thiadiazine, pyrazole-4-carboxylic acid, antimicrobial activity 274
4-Hydroxy-3-[(2-oxo-2H-chromen-3-yl)-(3,4,5-trimethoxyphenyl)-methyl] chromen-2-one 109
4-Hydroxy-3-[(3E)-3-(hydroxyimino)-1-(4-nitrophenyl) butyl]-2H-chromen-2-one, crystal structure, coumarin derivatives 109

Alloyed metal powders, pulse potential mode, morphology, phase structure 357
Aluminum nitrate; molybdenum-based catalyst; metathesis; propene 191
Apatite, structure, high energy milling, ... 601

Biodegradation, aniline, biofilms, carrier 530
Biodiesel, esterification, free fatty acids, chromosulfuric acid .....
Boroxine, single crystal, ^{11}B NMR..……..……505
Brucine, ethylenediamine, succinic acid, carbodiimide 71

Chitosan, nanofibers web, filtration, lamination 336
Clinoptilolite, ion exchange, thermal stability 463
Copper-aluminum alloys, modifiers, heat treatment, structure 644
Crystallization, *ab initio* molecular dynamics, chalcogenide 554
Cyclic voltammetry
Electrochemical characterization of coins 347
Hydrogen peroxide, calcium peroxide, Co, In, Ni, electrode 151
Platinum, gold, electrode, hydrogen peroxide, calcium peroxide 144

Dairy industry, environmental impact peaks reduction, shifting of production starting times, batch plants 47
Decarboxylation; m-Chloroperoxybenzoic Acid (m-CPBA); 1,4-Dihydropyridine (1,4-DHP); Tetraphenylporphyrinatoiron(III) chloride [Fe(TPP)Cl] 55
Di-N-acetyl-β-chitobiosyl N-glycothiazoline, synthesis, glycosylation, analogue 385
Doped sillenites, Schrödinger equation, transition metal ions 631
Doped zinc borophosphates, samarium, manganese, crystal structure 536
Dual membrane fuel cell, gases permeability, porous mixed conducting ceramics, electrochemical impedance spectroscopy 366

Electrospinning
Average fiber diameter, contact angle, response surface methodology 178
Contact angle, response surface methodology, artificial neural network 169
Ethylene bis (N-methyl imidazolium) ditribromide, thiols, sulfides, oxidation, sulfoxide 379
Eudragit L30 D 55, duloxetine hydrochloride, enantioselective synthesis, enteric coated pellets, powder layering 269
Extraction chromatography, rhodium(III), separation, alloys 37
Extremophiles, thermostability, molecular dynamics, packing defects 592

Fe-doped titanium dioxide, sol-gel, photocatalytic, antibacterial activity 497
Ferritin, iron, increasing intensity interval exercise... 296
Ficin, gel chromatography, guanidine hydrochloride, Stokes radius, urea 93
Fullerene
C82, symmetry, isomers 310
Eccentric Connectivity Index, Eccentric Connectivity Polynomial, Diameter of graph 5

Gas chromatography, QSRR, substituted phenols, molecular indices, Kovats retention index, phase polarity, McReynolds constants 9
Glaserite, "glaserite" type topology, "glaserite" type compounds 418

Heat integration, batch reactors, Heat storages, Antibiotics ..... .214
Honey, mineral content, sugar content, thermophysical and optical parameters 244
Hybrid membranes, enzymes, optical biosensors 516
Hybrids, sol-gel, silica, chitosan, methyl methacrylate. 568
Hydrogen atom coordinates 461
Hydrogen storage materials; composite materials; electron microscopy; photoelectron spectroscopy 280

ICP-OES, environmental materials, spectral interferences, line selection, detection limits 229
Iodine, catalyst, perimidine, antibacterial 353
Iron oxide and manganese oxide, crystallization kinetics, nano-scale materials, magnetic properties ..... .84

$LiNbO_3$, $LiTaO_3$, optical waveguides, proton exchange, phase composition 474
Liquid tar product, pyrolysis, casein, epoxy resin, hardener 157

Magnesium chlorate, hydrates, single crystal 543
Microbial fuel cell, sauerkraut fermentation..... 197

Nanoparticles; Cadmium oxide, Polyethylene glycol. 90
Ni-Al layered double hydroxides, Ni-Al mixed oxides, structure, reducibility, CO_2 removal by methanation 617
Nickel doping, silica xerogels, thermal analysis, activation energy ..... .43
Nitrobenzenes; Radical anions; Electronic structure; IR spectra; DFT..... 24

Optical oxygen sensors, wine, Ru(II) complexes, immobilization matrices, Stern-Volmer constant, fluorescence microscopy..... 32
Orthodontic wires, XRD, SEM, EDX, surface chemical composition..... 455

Phenolics; flavonoids; antioxidant capacity; apple.... 326
Photocatalysis,environmental pollution, estrogens, photolysis, TiO2 131
Polycaprolactam
Crystal phase, perfection..... 575
Crystal structure, polymorphism..... 560
Preyssler heteropolyacid
Catalyst, naphtho-oxazine; aromatic aldehyde 59
Indazolo[2,1-*b*]phthalazine-trione, phthalhydrazide, dimedone, heteropolyacid 64
Protein active site, electronic structure, *ab initio*; DFT; AIM; NBO 201

Recombinant protein; his tag affinity chromatography; metal binding protein; dynamic light scattering; protein crystallization..... 440
Rhizopus oryzae dead fungi, adsorption, 4-nitrophenol, kinetics 161
Russell-Saunders coupling, term symbol, microstate, singlet, triplet 388

Scanning electron microscopy, *Esherichia coli*, *Thermobispora bispora*..... 510
Sea salt, Ion concentration, Salt crystallization, XPS 584
Sildenafil citrate, DDQ, p-CLA, spectrophotometry, charge transfer complexes..... 250
Silica-bonded N-propyl sulfamic acid (SBNPSA); spirooxindoles; isatin; three-component; irradiation microwave..... 371
SiO2–ZnO films, photocatalytic degradation, sol–gel, spin coating, malachite green, methylene blue 611
SOFC,cathodes, La2–xSrxCuO4–δ, Nd2–xSrxNiO4–δ, perovskites 207
Spring steel; microstructure, texture, EBSD..... 549
structure, coumarin derivatives, Knoevenagel reaction, Hantzsch reaction and Pechmann condensation... 301
Substituted indole, β-cyclodextrin, inclusion complex, antimicrobial activity 77
Supply chain, design, activities scheduling, S -graph, mathematical programming 288
Sulfathiazole derivatives, synthesis 332

Telluric (VI) acid, TeO_2, $TiTe_3O_8$ 485
Tellurite glasses, multiband filter, XRD, FTIR 491

Urea, thiourea; inclusion complex; hydrogen bonding; thermal decomposition..... 446
UV-Vis and IR spectra 100

X-Ray diffraction
Analysis 100
ETS-4, LT experiment, single crystal 522
High-temperature XRD holder, *in situ* heating..... 479
History, Bulgarian X-rays science history 411
in situ HT X-ray diffraction 463

Zeeman splitting, structural distortion, $CrCl2(H2O)_4^{2+}$, $Cr(H2O)_6^{2+}$. 607
Zinc ferrite, Mössbauer spectroscopy, methanol decomposition..... 434
ZnO nanowires, TiO_2, composite films, Orange II, photocatalysis..... .625
ZnO, synthesis, morphology, zinc electrodes 427
ZnO/TiO2 composite film, spin coating, photocatalysis, Orange II, UV, visible light 649
ZnO:Fe thin films, sol gel, photocatalysis, Reactive Black 5, UV and visible light..... 635

α,β-unsaturated aldol, catalysts, aldehyde, ketone, condensation 314
β-Hydroxyethyl esters of N-2-hydroxyalkyl derivatives of carbamic acid, chemical transformations..... 114

ПРЕДМЕТЕН УКАЗАТЕЛ

1,4-дихидроксипиридини; синтеза; DFT, HF, AM1 и PM3-изследванев..... 108
2,4-диацетил-5-хидрокси-5-метил-3-(4-нитрофенил)-циклохексанон, 2,4-дисцетил-3-(4-флуорофенил)-5-хидрокси-5-метилциклоохексанон, 1,3-дикарбомилови съединения, кристална структура, алдолна кондензация 228
2-амино-1,3,4-тиадиазин, пиразол-4-карбонова киселина, антимикробно действие 279
4-хидрокси-3-[(2-оксо-2H-хромен-3-ил)-(3,4,5-триметоксифенил)-метил]хромен-2-он, кристална структура..... 113
4-хидрокси-3-[(3E)-3-(хидроксиимино)-1-(4-нитрофенил)бутил]-2H-хромен-2-он, кристална структура, кумаринови приизводни 113
N-пропил-сулфаминова киселина, носител силициев диоксид (SBNPSA), спиоксиндоли, изатин, трикомпонентна система, микровълново лъчение 378

Адсорбция, мъртви гъбички *Rhizopus oryzae* 4-нитрофенол, кинетика. 168
Алуминиев нитрат; катализатор на молибденова основа; метатеза; пропен..... 196

Атомно-абсорбционна спектрофотометрия, ICP - OES, спектрални взаимодействия, подбор на линии, граници на откриваемост 243

Биодеградация, анилин, биофилм, носители..... 535
Биодизел, естерификация, свободни мастни киселини, хромо-сярна киселина..... 399
Бороксин, монокристали, ^{11}B ЯМР 509
Бруцин, етилендиамин, янтарна киселина, карбодиимид..... 76

Вериги снабдителни, проектиране, разписания на дейсноти, S-граф, математично прграмиране.. 295
Водород, материали за складиране, композитни материали, електронна микроскопия, фотоелектронна микроскопия..... 287

Газопроницаемост, горивна клетка с дуални мембрани, порьозна смесена проводима керамика, електро-импедансна спектроскопия 370
Газ-хроматография, QSRR, заместени феноли, молекулни индекси, индекс на задържане на Kovats, полярност на фазите, кнстанти на McReynolds 23
Глазерит, глазеритова топология, съединения тип „глазерит“. 426

Декарбоксилиране; m-хлороперoксибензоена киселина (m-CPBA); 1,4-дихидропиридин (1,4-DHP); тетрафенилпорфиринат-желязо(III) хлорид [Fe(TPP)Cl]..... 58
Ди--N-ацетил-β-хитобиозилN-гликотиазолин, синтеза, гликозилиране, аналог 387

Екстракционна хроматография, родий(III), разделяне, сплави ..... .42
Екстремофили, термична стабилност, молекулна динамика, дефекти на опаковката. 600
Електропредене, среден диаметър на влакната, контактен ъгъл..... 190
Електропредене, среден диаметър на влакната, контактен ъгъл, невронни мрежи 177
Етилен бис(N-метил имидазол) дитрибромид, тиоли, сулфиди, окисление,сулфоксид 384
Еудрагит L30 D 55, енантиоселективна синтеза, дулоксетин хидрохлорид, филм-таблетки за чревни болести 273

Желязо-дотиран титанов диоксид, зол-гел, фотокатализ, антибактериално действие.....504
Железен оксид и манганов оксид, кунетик на кристализация, нано-материали, магнитни свойства..... 89

Зееманово разцепване, $CrCl_2(H_2O)_4^2$, $Cr(H_2O)_6^{2+}$ ... 610

Индол, субституиран, β-циклодекстрин, комплекс на включване, антимикробно действие..... 83

Йод, катализатор, перимидин, антибактериано действие 356

Карбамид, тиокарбамид; комплекси на включване, водородни връзки, термично разлагане. 454
Катоди за горивни клетки SOFC, La2–xSrxCuO4–δ, Nd2–xSrxNiO4–δ, перовскити..... 213
Катран течен, пиролиза, казеин, епоксидна смола, втвърдители. 160
Координати на водородния атом..... 465
Кристализация, *ab initio* молекулна динамика, халкогениди..... 559
Клиноптилолит, йонообмен, термична стабилност, *in situ* HT рентгенова дифракция 473
Кумарин, производни, структура, реакции на Knoevenagel и Hantzsch, кондензация на Pechmann..... 309
Куплиране на Russell-Saunders, термове, микросъстояния, синглет, триплет 393

Магнезиев хлорат, хидрати, монокристали..... 548
Мед, минерален състав, съдържание на захар, термофизични и оптични параметри..... 249
Микробни горивни клетки, ферментация на зеле, генериране на електричество. 200
Млечна промишленост, намаляване на шоковете върху околната среда, промяна на пусковите времена, периодични процеси 54

Наночастици, кадмиев оксид, полиетилен гликол . 92
Никелово-алуминиеви оксиди с покрития от никел-алуминий, структири, редукционна способност, отстраняване на CO_2 при получаването на метан 624
Никел-дотиране, ксерогелове от силициев диоксид46
Нитробензени, анион-радикали; електронна структура, ИЧ-спектри, DFT..... 31

Оптични вълноводи, $LiNbO_3$, $LiTaO_3$, обмен на протонни, фазов състав. 478
Оптични кислородни сензори, вино, Ru(II)-комплекси, имобилизация, константа на Stern-Volmer constant, флуорсцентна микроскопия.... 36
Ортодонтски дъги, XRD, SEM, EDX, химически състав на повърхността 460

Поликапролактам
Кристална фаза, завършеност..... 583
Кристална структура, полиморфизъм..... 567
Протеини, активен център, електронна структура, *ab initio*, DFT; AIM; NBO 206
Протеини рекомбинантни, His Tag афинитетна хроматография, метал-свързващи протеини, динамично разсейване на светлината кристализация на протеини..... 445

Рентгено-структурен анализ
Рентгенов дифракционен анализ, УВ и ИЧ-спектри. 108

История, рентгеноструктурен анализ в България 417
ETS-4, LT експеримент, монокристал..... 529
Високотемпературен XRD-носител, *in situ*, нагряване..... 484

Силенити дотирани, уравнение на Schrödinger, йони на преходни метали..... 634
Силделафилов цитрат, DDQ, p-CLA, спектрофотометрия, комплекси на пренос на заряда..... 258
Синтеза на две сулфотиазолови производни 335
Сканираща електронна микроскопия (SEM), *Esherichia coli*, *Thermobispora bispora*..... 515
Смилане, висока енергия, апатит. 606
Сол морска, концентрация на йони, кристализация XPS 591
Сплави, медно-алуминиеви, модификатори, термично третиране, структура 648
Сплавени метални прахове, импулсен потенциал, морфология, фазова структура..... 365
Стомана за пружини, микроструктура, текстура, EBSD 553

Телурит (стъкла), многолентов филтър, XRD, FTIR. 496
Телурова (VI) киселина, TeO_2, $TiTe_3O_8$.-485-490
Топлинна интеграция, съхранения на топлина, антибиотици, периодични реактори..... 23

Феритин, желязо, нарастващ интензитет..... 300
Феноли, флавоноиди, антиоксиданен капацитет, ябълкови сортове..... 331
Филми от SiO_2–ZnO, фотокаталитично разграждане, зол-гел, малахитовозелено, метиленово синьо. 616
Фицин, гел-хроматография, гванидин хидрохлорид, Стоксов радиус, карбамид..... 99
Фотокатализ
Замърсяване на околната среда, естрогени, фотолиза, TiO_2 143
Цинков оксид, нано-проводници, TiO_2, композитни филми,оранж II..... 630
Филми композитни, ZnO/TiO_2, оранж II, UV, видима светлина. 654
ZnO:Fe тънки филми, зол-гел, реактивно черно 5, UV и видима светлина..... 643
Фулерени
Индекс на ексцентрична проводимост, полином на ексцентрична проводимост, диаметър на графа 8
C82, симетрия, изомери 313

Хетерополикиселини на Preyssler
Катализатор, нафто-оксазини, ароматни алдехиди 59
Индазоло [2,1-*b*] фталазин-трион, фталхидразид, димедон..... 64
Хибридни мембрани, ензими, оптични биосензори 521
Хибриди, зол-гел, силициев диоксид, хитозан, метил-метакрилат 574
Хитозан, прежда от нанвлакна, филтруване, ламиниране 346

Циклична волтамперометрия
Електрохимично охарактеризиране на монети 347
водороден пероксид, калциев пероксид, Co, In, Ni, електрод 151
платина, злато, електрод водороден пероксид, калциев пероксид. 144
Цинкови борофосфати, дотирани, самарий, манган, кристална структура 542
Цинков оксид, синтеза, морфология, цинкови електроди..... 433
Цинков ферит, спектроскопия на Mössbauer, разлагане на метанол. 439

α,β-ненаситени алдоли, катализатори, алдехиди, кетони, кондензация 325
β–хидрокдиетилови естери на N-2-хидроксиалкилови производни на карбаминовата киселина, химични превръщания..... 120

BULGARIAN CHEMICAL COMMUNICATIONS

Instructions about Preparation of Manuscripts

General remarks: Manuscripts are submitted in English by e-mail or by mail (in duplicate). The text must be typed double-spaced, on A4 format paper using Times New Roman font size 12, normal character spacing. The manuscript should not exceed 15 pages (about 3500 words), including photographs, tables, drawings, formulae, etc. Authors are requested to use margins of 3 cm on all sides. For mail submission hard copies, made by a clearly legible duplication process, are requested. Manuscripts should be subdivided into labelled sections, e.g. **Introduction, Experimental, Results and Discussion**, *etc*.

The title page comprises headline, author's names and affiliations, abstract and key words.

Attention is drawn to the following:

a) **The title** of the manuscript should reflect concisely the purpose and findings of the work. Abbreviations, symbols, chemical formulas, references and footnotes should be avoided. If indispensable, abbreviations and formulas should be given in parentheses immediately after the respective full form.

b) **The author**'s first and middle name initials, and family name in full should be given, followed by the address (or addresses) of the contributing laboratory (laboratories). **The affiliation** of the author(s) should be listed in detail (no abbreviations!). The author to whom correspondence and/or inquiries should be sent should be indicated by asterisk (*).

The abstract should be self-explanatory and intelligible without any references to the text and containing not more than 250 words. It should be followed by key words (not more than six).

References should be numbered sequentially in the order, in which they are cited in the text. The numbers in the text should be enclosed in brackets [2], [5, 6], [9–12], etc., set on the text line. References, typed with double spacing, are to be listed in numerical order on a separate sheet. All references are to be given in Latin letters. The names of the authors are given without inversion. Titles of journals must be abbreviated according to Chemical Abstracts and given in italics, the volume is typed in bold, the initial page is given and the year in parentheses. Attention is drawn to the following conventions:

a) The names of all authors of a certain publications should be given. The use of "*et al*." in the list of references is not acceptable.

b) Only the initials of the first and middle names should be given.

In the manuscripts, the reference to author(s) of cited works should be made without giving initials, e.g. "Bush and Smith [7] pioneered...". If the reference carries the names of three or more authors it should be quoted as "Bush *et al*. [7]", if Bush is the first author, or as "Bush and co-workers [7]", if Bush is the senior author.

Footnotes should be reduced to a minimum. Each footnote should be typed double-spaced at the bottom of the page, on which its subject is first mentioned.

Tables are numbered with Arabic numerals on the left-hand top. Each table should be referred to in the text. Column headings should be as short as possible but they must define units unambiguously. The units are to be separated from the preceding symbols by a comma or brackets.

Note: The following format should be used when figures, equations, *etc*. are referred to the text (followed by the respective numbers): Fig., Eqns., Table, Scheme.

Schemes and figures. Each manuscript (hard copy) should contain or be accompanied by the respective illustrative material as well as by the respective figure captions in a separate file (sheet). As far as presentation of units is concerned, SI units are to be used. However, some non-SI units are also acceptable, such as °C, ml, l, etc.

The author(s) name(s), the title of the manuscript, the number of drawings, photographs, diagrams, etc., should be written in black pencil on the back of the illustrative material (hard copies) in accordance with the list enclosed. Avoid using more than 6 (12 for reviews, respectively) figures in the manuscript. Since most of the illustrative materials are to be presented as 8-cm wide pictures, attention should be paid that all axis titles, numerals, legend(s) and texts are legible.

The authors are asked to submit **the final text** (after the manuscript has been accepted for publication) in electronic form either by e-mail or mail on a 3.5'' diskette (CD) using a PC Word-processor. The main text, list of references, tables and figure captions should be saved in separate files (as *.rtf or *.doc) with clearly identifiable file names. It is essential that the name and version of

the word-processing program and the format of the text files is clearly indicated. It is recommended that the pictures are presented in *.tif, *.jpg, *.cdr or *.bmp format, the equations are written using "Equation Editor" and chemical reaction schemes are written using ISIS Draw or ChemDraw programme.

The authors are required to submit the final text with a list of three individuals and their e-mail addresses that can be considered by the Editors as potential reviewers. Please, note that the reviewers should be outside the authors' own institution or organization. The Editorial Board of the journal is not obliged to accept these proposals.

EXAMPLES FOR PRESENTATION OF REFERENCES

REFERENCES

1. D. S. Newsome, *Catal. Rev.–Sci. Eng*., **21**, 275 (1980).
2. C.-H. Lin, C.-Y. Hsu, *J. Chem. Soc. Chem. Commun*., 1479 (1992).
3. R. G. Parr, W. Yang, Density Functional Theory of Atoms and Molecules, Oxford Univ. Press, New York, 1989.
4. V. Ponec, G. C. Bond, Catalysis by Metals and Alloys (Stud. Surf. Sci. Catal., vol. 95), Elsevier, Amsterdam, 1995.
5. G. Kadinov, S. Todorova, A. Palazov, in: New Frontiers in Catalysis (Proc. 10th Int. Congr. Catal., Budapest, 1992), L. Guczi, F. Solymosi, P. Tetenyi (eds.), Akademiai Kiado, Budapest, 1993, Part C, p. 2817.
6. G. L. C. Maire, F. Garin, in: Catalysis. Science and Technology, J. R. Anderson, M. Boudart (eds), vol. 6, Springer-Verlag, Berlin, 1984, p. 161.
7. D. Pocknell, *GB Patent* 2 207 355 (1949).
8. G. Angelov, PhD Thesis, UCTM, Sofia, 2001.
9. JCPDS International Center for Diffraction Data, Power Diffraction File, Swarthmore, PA, 1991.
10. CA **127**, 184 762q (1998).
11. P. Hou, H. Wise, *J. Catal.*, in press.
12. M. Sinev, private communication.
13. http://www.chemweb.com/alchem/articles/1051611477211.html.

CONTENTS

PREFACE 409
V. Krastev, G. K. Exner, 100 years of X-ray diffraction: from Röntgen's discovery to top-of-the-art synchrotron source applications..... 411
R. Nikolova, V. Kostov-Kytin, Crystal chemistry of "glaserite" type compounds 418
M. Markova-Velichkova, S. Veleva, V. Tumbalev, L. Stoyanov, D. Nihtianova, M. Mladenov, R. Raicheff, D. Kovacheva, XRD and TEM characterization of the morphology of ZnO powders prepared by different methods..... 427
K. V. Koleva, N. I. Velinov, T. S. Tsoncheva, I. G. Mitov, B. N. Kunev, Preparation, structure and catalytic properties of $ZnFe_2O_4$..... 434
H. I. Sbirkova, G. A. Radoslavov, P. I. Hristov, B. L. Shivachev, Crystallographic conditions of the heterologically expressed recombinant metal-binding protein Ts-PCHTP 440
K. Kossev, H. Sbirkova, N. Petrova, B. Shivachev, R. Nikolova, Crystal structure and properties of urea and thiourea adducts of tetraalkyl ammonium hydrogen sulphate..... 446
V. G. Petrov, S. D. Terzieva, Tz. I. Lazarova, V. Mikli, L. A. Andreeva, A. K. Stoyanova-Ivanova, Corrosive changes and chemical composition of the orthodontic archwires' surface during treatment..... 455
B. Shivachev, DHA, a program for calculating hydrogen atom coordinates of solvent atom involved in hydrogen bonding interactions 461
L. T. Dimowa, S. L. Petrov, B. L. Shivachev, Natural and Zn exchanged clinoptilolite: *in situ* high temperature XRD study of structural behavior and cation positions 466
M. Kuneva, Surface phase detection of proton-exchanged layers in $LiNbO_3$ and $LiTaO_3$ by IR reflection spectroscopy 474
L. Dimowa, B. Shivachev, S. Petrov, Design and application of a cost effective high temperature holder for in-situ powder X-ray diffraction experiments 479
R. S. Iordanova, A. D. Bachvarova-Nedelcheva, R. D. Gegova, Y. B. Dimitriev, Synthesis and characterization of TeO_2/TiO_2 powders obtained through Te (Vi) acid 485
I. Piroeva, L. Dimowa, S. Atanasova-Vladimirova, N. Petrova, B. L. Shivachev, Synthesis, structural and optical characterization of TeO_2–GeO_2–Nd_2O_3 glasses 491
A. M. Stoyanova, H. Y. Hitkova, N. K. Ivanova, A. D. Bachvarova-Nedelcheva, R. S. Iordanova, M. P. Sredkova, Photocatalytic and antibacterial activity of Fe-doped TiO2 nanoparticles prepared by nonhydrolytic sol-gel method..... 497
L. Dimowa, K. Kossev, H. I. Sbirkova, R. P. Nikolova, B. L. Shivachev, Synthesis and crystal structure of oxonium 2,4,8,10-tetra-hydroxy-1,3,5,7,9,11-hexaoxa-2,4,6,8,10-penta-boraspiro[5.5]undecan-6-uide hydrate 505
I. Piroeva, S. Atanassova-Vladimirova, L. Dimowa, H. Sbirkova, G. Radoslavov, P. Hristov, B. L. Shivachev, A simple and rapid scanning electron microscope preparative technique for observation of biological samples: application on bacteria and DNA samples..... 510
L. Yotova, S. Yaneva, Silica-based hybrid materials as biocompatible coatings for xenobiotics sensors..... 516
L. Tsvetanova, L. Dimowa, S. Ferdov, R. Nikolova, Crystal structures of Cs^+, $Mg^{2+,}$ Ba^{2+} ion exchanged ETS-4 at RT and 150 K..... 522
D. Marinkova, L. Yotova, D. Danalev, D. Stoykov, J.-M. Ringeard, M. Michiel, S. Serfaty, P. Griesmar, Investigation of newly synthesized biocompatible materials as biofilm carriers. 530
G. I. Patronov, I. P. Kostova, D. T. Tonchev, Study of zinc borophosphate compositions doped with samarium and manganese..... 536
K. Kossev, L. Tsvetanova, L. Dimowa, R. Nikolova, B. Shivachev, Synthesis and crystal structure of magnesium chlorate dihydrate and magnesium chlorate hexahydrate 543
L. V. Nikolova, Microstructure and texture analyses on spring steel..... 549
A. Zaidan, Vl. Ivanova, P. Petkov, Ab initio simulation of crystallization of amorphous Ge–Te–In system..... 554
S. Uzova, A. Popov, V. Velev, T. Angelov, S. Mihaleva, Ch. Uzov, Polycaprolactam crystal structure. I. Gamma–alpha polymorphic transition..... 560

G. E. Chernev, E. V. Todorova, S. P. Djambazov, I. M. Miranda Salvado, Structure of hybrid materials containing natural and synthetic organic compounds..... 568
S. Uzova, A. Popov, V. Velev, T. Angelov, S. Mihaleva, Ch. Uzov, Polycaprolactam crystal structure. II. Crystal phase perfection..... 575
H. Kolev, G. Tyuliev, C. Christov, K. L. Kostov, Experimental study of the surface chemical composition of sea salt crystallized during evaporation of seawater under natural conditions..... 584
E. K. Salamanova, D. T. Tsoneva, A. D. Karshikoff, Physical bases of thermal stability of proteins: A comparative study on homologous pairs from mesophilic and thermophilic organisms..... 592
B. V. Kostova, N. L. Petrova, V. Petkova, The high energy milling effect on positional redistribution of CO_3-ions in the structure of sedimentary apatite..... 601
P. Petkova, V. Nedkov, J. Tacheva, P. Vasilev, I. Dimitrov, The structural distortion and Zeeman splitting of the complexes $CrCl_2(H_2O)_{42+}$ and $Cr(H_2O)_{62+}$..... 607
N. V. Kaneva, S. A. Siuleiman, A. S. Bojinova, K. I. Papazova, D. T. Dimitrov, I. Gracheva, S. Karpova, V. A. Moshnikov, Nanosized composite thin films of SiO_2-ZnO for photocatalytic decomposition of organic dyes – structure and characterization..... 611
M. V. Gabrovska, R. M. Edreva-Kardjieva, D. D. Crişan, K. K. Tenchev, D. A. Nikolova, M. Crişan, Structure and reducibility of the mixed metal oxides obtained from Ni-Al layered double hydroxides. Catalytic activity in CO_2 methanation reaction..... 617
L. K. Krasteva, K. I. Papazova, A. S. Bojinova, N. V. Kaneva, A. A. Apostolov, Synthesis and characterization of ZnO and TiO_2 powders, nanowire ZnO and TiO_2/ZnO thin films for photocatalyc applications..... 625
P. Petkova, P. Vasilev, I. Dimitrov, The behaviour of osmium ions in the tetrahedral oxygen coordination..... 631
N. Kaneva, A. Ponomareva, L. Krasteva, D. Dimitrov, A. Bojinova, K. Papazova, G. Suchaneck, V. Moshnikov, Surface and photocatalytic properties of nanostructured ZnO thin films doped with iron..... 635
R. Vl. Gavrilova, R. I. Petkov, Researches on the structure and properties of heat treated, nickel alloyed, molybdenum modified aluminum bronze..... 644
S. A. Siuleiman, D. V. Raichev, A. S. Bojinova, D. T. Dimitrov, K. I. Papazova, Nanosized composite ZnO/TiO_2 thin films for photocatalytic applications..... 649
AUTHOR INDEX..... 655
AUTHORS INDEX (IN BULGARIAN)..... 659
SUBJECT INDEX..... 665
SUBJECT INDEX (IN BULGARIAN)..... 666
INSTRUCTIONS TO THE AUTHORS..... 669

СЪДЪРЖАНИЕ

ПРЕДГОВОР 409

В. Кръстев, Г. Екснер, 100 години рентгенова дифракция: от откритието на Рьонтген до модерните приложения на синхротронните източници..... 417

Р. Николова, В. Костов-Китин, Кристалохимия на съединения с "glaserite" тип структура..... 426

М. Маркова-Величкова, С. Велева, В. Тумбалев, Л. Стоянов, Д. Нихтянова, М. Младенов, Р. Райчев, Д. Ковачева, Рентгенографско и ТЕМ характеризиране на морфологията на прахообразен ZnO, получен по различни методи..... 433

К. В. Колева, Н. И. Велинов, Т. С. Цончева, И. Г. Митов, Б. Н. Кунев, Синтез, структура и каталитични свойства на $ZnFe_2O_4$.....л..... 439

Х. И. Сбиркова, Г. А. Радославов, П. И. Христов, Б. Л. Шивачев, Кристализационни условия на хетероложно експресиран рекомбинантен металосвързващ белтък Ts-РСНТР 445

К. Косев, Х. Сбиркова, Н. Петрова, Б. Шивачев, Р. Николова, Кристална структура и свойства на уреа и тиоуреа адукти на тетраетил амониев хидроген-сулфат 454

В. Г. Петров, С. Д. Терзиева, Ц. И. Лазарова, В. Микли, Л. А. Андреева, А. К. Стоянова-Иванова, Корозионни промени в химичния състав на повърхността на ортодонтски дъги при използването им за лечение 460

Б. Шивачев, DHA, програма за изчисляване на координатите на водороден атом към атом разтворител, участващ в водородна връзка 465

Л. Т. Димова, С. Л. Петров, Б. Л. Шивачев, Природен и Zn обменен клиноптилолит: in situ високотемпературно прахово рентгеноструктурно изследване на поведението на структурата и катионните позиции 473

М. Кънева, Определяне на повърхнинната фаза на протонно-обменени слоеве в $LiNbO_3$ и $LiTaO_3$ чрез отражателна ИЧ спектроскопия 478

Л. Т. Димова, С. Л. Петров, Б. Л. Шивачев, Дизайн и приложение на лесна за направа високотемпературна приставка подходяща за *in-situ* прахови рентгенодифракциони изследвания 484

Р. С. Йорданова, А. Д. Бъчварова-Неделчева, Р. Д. Гегова, Я. Б. Димитриев, Синтез и характеризиране на TeO_2/TiO_2 прахове получени от Te (VI) киселина 490

И. Пироева, Л. Димова, С. Атанасова-Владимирова, Н. Петрова, Б. Шивачев, Синтез, структурна и оптична характеристика на TeO_2-GeO_2-Nd_2O_3 стъкла 496

А. М. Стоянова, Х. Й. Хиткова, Н. К. Иванова, А. Д. Бъчварова-Неделчева, Р. С. Йорданова, М. П. Средкова, Фотокаталитична и антибактериална активност на дотирани с желязо TiO2 наночастици, получени по нехидролитичен зол-гел метод... 504

Л. Димова, К. Косев, Х. И. Сбиркова, Р. П. Николова, Б. Л. Шивачев, Синтез и кристална структура на оксониев 2,4,8,10-тетрахидрокси-1,3,5,7,9,11-хексаокса-2,4,6,8,10-пента-биспиро[5.5]ундекан-6-оид хидрат..... 509

И. Пироева, С. Атанасова-Владимирова, Л. Т. Димова, Х. И. Сбиркова, Г. Радославов, П. Христов, Б. Л. Шивачев, Бърза и опростена препаративна процедура на биологични проби, позволяваща последваща визуализация чрез сканираща електронна микроскопия..... 515

Л. Йотова, С. Янева, Хибридни материали на основата на силициев диоксид като биосъвместими покрития при биосензори за ксенобиотици..... 521

Л. Цветанова, Л. Димова, С. Фердов, Р. Николова, Кристални структури на Cs^+, Mg^{2+}, Ba^{2+} йонно обменени образци на ETS-4 при стайна (290 K) и ниска температура (150 K)..... 529

Д. Маринкова, Л. Йотова, Д. Даналев, Д. Стойков, Ж. Ринджерард, М. Мишел, С. Серфати, П. Гриесмар, Изследвания върху новосинтезирани биосъвместими материали като носители за биофилми..... 535

Г. И. Патронов, И. П. Костова, Д. Т. Тончев, Изследване на цинк-бор-фосфатни композиции, дотирани със самарий и манган..... 542

К. Косев, Л. Цветанова, Л. Т. Димова, Р. Николова, Б. Л. Шивачев, Синтез и

кристална структура на магнезиев хлорат дихидрат и магнезиев хлорат хексахидрат……. 548
Л. В. Николова, Микроструктурни и текстурни анализи на пружинна стомана…….. 553
А. Зайдан, Вл. Иванова, П. Петков, Ab initio симулация на кристализацията на аморфни образци от системата Ge–Te–In…… 559
С. Узова, А. Попов, В. Велев, Т. Ангелов, С. Михалева, Х. Узов, Кристална структура на поликапролактама. I. Гама–алфа полиморфен преход……... 567
Г. Е. Чернев, Е. В. Тодорова, С. П. Джамбазов, И. М. Миранда Салвадо, Структура на хибридни материали, съдържащи естествени и синтетични органични съединения. 574
С. Узова, А. Попов, В. Велев, Т. Ангелов, С. Михалева, Х. Узов, Кристална структура на поликапролактама. II. Съвършенство на кристалната фаза..... 583
Х. Колев, Г. Тюлиев, Х. Христов, К. Костов, Експериментално изследване на химическия състав на повърхността на морска сол, получена при изпарение на морска вода в естествени условия..... 591
Е. К. Саламанова, Д. Т. Цонева, А. Д. Кършиков, Физични основи на термичната устойчивост на протеини: сравнително изследване на хомоложни двойки от мезофилни и термофилни организми..... 600
Б. В. Костова, Н. Л. Петрова, В. Петкова, Ефект от интензивно енергийно смилане върху преразпределение на карбонатните йони в структурата на седиментен апатит..... 606
П. Петкова, В. Недков, Й. Тачева, П. Василев, И. Димитров, Структурна деформация и Зееманово разцепване на комплексите $CrCl_2(H_2O)_{42+}$ и $Cr(H_2O)_{62+}$…… 610
Н. В. Кънева, С. А. Сюлейман, А. С. Божинова, К. И. Папазова, Д. Т. Димитров, И. Грачева, С. Карпова, В. А. Мошников, Наноразмерни композитни тънки филми от SiO_2–ZnO за фотокаталитично разлагане на органични багрила – структура и характеризиране..... 616
М. В. Габровска, Р. М. Едрева-Кърджиева, Д. Д. Кришан, К. К. Тенчев, Д. А. Николова, М. Кришан, Структура и редуцируемост на смесени метални оксиди, получени от Ni-Al слоисти двойни хидроксиди. Каталитична активност в реакцията на метаниране на CO_2..... 624
Л. К. Кръстева, К. И. Папазова, А. С. Божинова, Н. В. Кънева, А. А. Апостолов, Синтез и характеризиране на прахове от ZnO и TiO_2, тънки филми от ZnO наножички и TiO_2/ZnO за фотокаталитични приложения..... 630
П. Петкова, П. Василев, И. Димитров, Поведение на осмиеви йони в тетраедрично кислородно обкръжение..... 634
Н. Кънева, А. Пономарева, Л. Кръстева, Д. Димитров, А. Божинова, К. Папазова, Г. Сучанек, В. Мошников, Повърхностни и фотокаталитични свойства на дотирани с желязо наноструктурирани тънки филми от ZnO..... 643
Р. Гаврилова, Р. Петков, Изследване на структурата и свойствата след термично обработване на медно-алуминиеви сплави, допълнително легирани с Ni и модифицирани с Mo..... 648
Ш. А. Сюлейман, Д. В. Райчев А. С. Божинова, Д. Ц. Димитров, К. И. Папазова, Наноразмерни композитни тънки филми от ZnO/TiO_2 за фотокаталитични приложения *654*
Авторски указател на английски..... 655
Авторски указател на български..... 659
Предметен указател на английски……..……..…….. 665
Предметен указател на български…….....……..…… 666
Инструкция за авторите..... 669